

**HIGH SPEED TRAIN GEOTECHNICS: NUMERICAL AND EXPERIMENTAL
SIMULATION OF SOME EMBANKMENT PROBLEMS**

A Dissertation

by

SOMAYEH REZAEI TAFTI

Submitted to the Office of Graduate and Professional Studies of
Texas A&M University
in partial fulfillment of the requirements for the degree of

DOCTOR OF PHILOSOPHY

Chair of Committee,	Jean-Louis Briaud
Committee Members,	Charles Aubeny
	Mark Everett
	Gary Fry
Head of Department,	Robin Autenrieth

May 2018

Major Subject: Civil Engineering

Copyright 2018 Somayeh Rezaei Tafti

ABSTRACT

This dissertation explores some of the geotechnical challenges associated with implementing high-speed railway (HSR) systems. These challenges are mostly related to HSR embankments. Three special geotechnical issues addressed in this project are long-term softening of compacted unsaturated embankments due to water absorption, potential derailment when trains break through the Rayleigh wave barrier, and the tolerable bump (or any other type of irregularity) in the track.

Soil softening due to water level rise in compacted embankments is investigated through an extensive experimental study that provides a better understanding of unsaturated soil and its impact on soil modulus degradation, which has a great impact on the other two issues. In fact, too much water content in the natural soil under the embankment can cause serious problems, such as unexpected large, uneven deflections. Through these experiments, it was confirmed that the soil modulus can considerably change as the water content in the soil varies.

To evaluate both the track responses to breaking the Rayleigh wave barrier and bump along HSR lines, a series of four-dimensional (4-D) finite element models (FEMs) using LS-DYNA have been developed. These 4-D FEMs include all track substructural and superstructural components.

Breaking the Rayleigh wave barrier, especially when traveling on soft soils, results in large deflection in the track structures and substructure components due to the combination of static and dynamic loads. Using the developed 4-D FEMs, the effect of train speed on the large track deflection is investigated. Through this study, it was

confirmed that at a particular speed called the critical speed, the maximum track deflection occurs. This train speed should be avoided because the resultant maximum track deflection leads to either high maintenance cost or, in the worst-case scenario, train derailment. These extensive numerical simulation results are compiled into proposed guideline charts to enable the design of safe embankment for HSR lines while keeping the train speed below 70% of the critical speed, which is considered as the safe train speed zone.

The problems of stiffness transition and irregularity along HSR are investigated using a 4-D FEM of both faulted and non-faulted track, considering passenger safety and comfort criteria. Although the main source of bump development is found to be the track modulus differential alone, track modulus variation alone has only minor impact on the train/track responses. It should be noted that track modulus differential instigates the formation of different types of irregularities along HSR, which significantly increases the wheel/rail interaction force and train body acceleration. The parametric study conducted to look at the effect of different parameters such as train speed, subsoil modulus, and irregularity type and size on the train/track responses results in proposed guideline charts defining tolerable irregularity size for HSR lines such that the vertical train body acceleration and wheel/rail interaction force are kept below the permissible values.

DEDICATION

*My beloved parents, Mohammadali Rezaei Tafti and Shayesteh Sadeghi Tafti for
their endless support and kindness*

*My amazing husband, Mehdi Mohammadrajabi for his continuous love, faith,
encouragement, care, and patience*

My beloved kids, Mana and ...

and

Whoever teaches me even only one word.

ACKNOWLEDGEMENTS

My first sincere appreciation and thanks definitely belong to my committee chair, Professor Jean-Louis Briaud for his continuous support, direction, patience, encouragement, and enthusiasm throughout the course of this research study and also my graduate study. Without his valuable and essential advice, this work would not have been completed. I would like to thank him for providing me with this great opportunity to enhance my knowledge in the geotechnical engineering field. Not only has he been a great advisor and mentor, but also he has set an example of excellence as a role model in my whole life.

I would like to thank Professor Charles Aubeny, one of my committee members who took the time to help me when I had any problem with numerical modeling. His great ideas and feedback have been absolutely invaluable.

I would like to express my gratitude to my other committee members: Professor Gary Fry and Professor Mark Everett, for their guidance and support.

Reyhaneh Navabzadeh, Adel Khodakarami, Alireza Mirdamadi, Amir Nekooienejad, Mohammadreza Keshavarz, Mojdeh Asadolahi Pajooh and my other friends and colleagues in the geotechnical engineering faculty also deserve thanks for making my time at Texas A&M University a great experience.

Appreciation and thanks are also reserved for Professor Jose Roeset for providing me with great ideas while I was working on geodynamic problems associated with the project. Also, my sincere thanks go to Dr. Akram Abu-Odeh, who used his valuable time to help me whenever I was faced with any problem related to finite element modeling in

LS-DYNA. I also would like to express my appreciation to Jennifer Elizabeth Nicks, who helped me with numerical modeling.

Funding for this project was provided by the University Transportation Center for Railway Safety (UTCRS) at the Texas A&M Transportation Institute and Texas Transportation Institute (TTI). Also, an extensive numerical study would not have been completed without computer resources provided by the Texas A&M Super Computer (SC) facilities.

Finally, I reserve my special thanks and appreciation for my husband who took the time to help me while I was conducting the laboratory tests. We were working together even after midnight to complete the experiments and obtain the results. His bright ideas also were a great help for me when I suffered difficulty with some numerical simulations. Thanks go to him not only because he is my husband but also because he is always indeed my friend, classmate, and colleague.

CONTRIBUTORS AND FUNDING SOURCES

This work was supported by a dissertation committee consisting of my committee chair, Professor Jean-Louis Briaud, and Professors Charles Aubeny and Gary Fry of the Department of Civil Engineering and Professor Mark Everett of the Department of Geology and Geophysics.

This study was supported by the University Transportation Center for Railway Safety (UTCRS) at the Texas A&M Transportation Institute and Texas Transportation Institute (TTI).

TABLE OF CONTENTS

	Page
ABSTRACT	ii
DEDICATION	iv
ACKNOWLEDGEMENTS	v
CONTRIBUTORS AND FUNDING SOURCES	vii
TABLE OF CONTENTS	viii
LIST OF FIGURES	xi
LIST OF TABLES	xxv
1 INTRODUCTION.....	1
1.1 Overview	1
1.2 Problem Statement and Research Questions	4
1.3 Research Objectives	6
1.4 Research Outline	8
1.5 Research Significance	11
2 BACKGROUND.....	13
2.1 Overview of High-Speed Railways Worldwide.....	13
2.2 Geotechnical Challenges of High-Speed Railways.....	16
2.3 Track Mechanics	19
2.3.1 Track/Embankment Components	19
2.3.2 Track Stiffness.....	34
2.3.3 Track/Embankment Settlement	50
2.4 Loading on Tracks.....	52
3 LONG-TERM MOISTURE SOFTENING OF COMPACTED EMBANKMENTS	61
3.1 Introduction	61
3.2 Review of Previous Studies.....	62
3.2.1 Subgrade Problems.....	63
3.2.2 Effects of Water Content Factor on Fine-Grained Soil Stiffness	66

3.2.3	Literature Review of the Effect of Water Content Variation on Soil Softening	77
3.2.4	Soil Softening Consequences in Railroad Industry	81
3.3	Laboratory Tests.....	87
3.3.1	Unconsolidated Undrained Triaxial Test	87
3.3.2	Test Procedures	93
3.3.3	Data Processing.....	97
3.4	Test Results and Discussion.....	106
3.4.1	Unconsolidated Undrained Triaxial Test Results.....	107
3.4.2	Chilled-Mirror Psychrometers Test Results	108
3.4.3	Salt Solution Equilibrium Test Results	112
3.5	Design Solutions	116
3.5.1	Sources of Moisture in Tracks.....	117
3.5.2	Track Drainage	118
3.6	Conclusions and Recommendations.....	128
4	BREAKING THE RAYLEIGH WAVE BARRIER.....	131
4.1	Introduction	131
4.2	Background	132
4.2.1	Source of Vibration in High-Speed Railways	132
4.2.2	Wave Propagation in Soil Skeleton.....	133
4.2.3	Critical Speed and Ground Mach 1.0	136
4.3	Review of Previous Studies.....	138
4.3.1	Experimental Evidence.....	140
4.3.2	Numerical Simulations	148
4.3.3	Purpose of this Study.....	152
4.4	Computer Model: LS-DYNA.....	153
4.5	Development of Four-Dimensional Finite Element Model: Numerical Simulation	155
4.5.1	Track/Embankment/Soil Model Description.....	155
4.5.2	Train Model Configuration	158
4.5.3	Material Properties	161
4.5.4	Boundary Conditions.....	167
4.5.5	Model Verification	169
4.6	Ground Mach 1.0 Problem	184
4.7	Parametric Studies.....	186
4.7.1	Effect of Train Speed on Track Dynamic Responses.....	188
4.7.2	Effect of Embankment Thickness on Critical Speed.....	197
4.7.3	Embankment Modulus Effect.....	218
4.7.4	Subgrade Modulus Effect.....	235
4.8	Proposed Guideline Charts.....	247
4.8.1	Parametric Study Results.....	248
4.8.2	The Threshold Value	268
4.9	Proposed Design Procedure	277

4.10	Design Solutions	281
4.10.1	Strengthening of the Ground Techniques.....	282
4.10.2	Stiffening of the Embankment Techniques.....	285
4.11	Conclusions and Recommendations.....	289
5	BUMPS IN HIGH-SPEED RAILS	292
5.1	Introduction	292
5.2	Causes Involved in Development of the Irregularities.....	294
5.2.1	Differential Modulus	295
5.2.2	Quality of Approach Fill or Subgrade.....	297
5.2.3	Wheel/Rail Interaction Force	298
5.3	Different Types of Irregularities	298
5.4	Track Response Criteria.....	305
5.4.1	Wheel/Rail Forces	306
5.4.2	Train Body Acceleration	307
5.5	Review of Previous Studies.....	308
5.6	Development of Four-Dimensional Finite Element Model: Numerical Simulation	318
5.6.1	Track Model Configurations	319
5.6.2	Irregularity Model	322
5.6.3	Train Model Configuration	324
5.6.4	Train/Track Contact	329
5.6.5	Boundary Condition	331
5.6.6	Model Verification	332
5.7	Parametric Studies.....	340
5.7.1	Non-Faulted Transition	341
5.7.2	Faulted Transition.....	353
5.8	Proposed Guideline Charts.....	385
5.9	Design Solutions	409
5.9.1	Stiffer Approach Structures.....	410
5.9.2	Reduce Stiffness on Bridges.....	412
5.10	Conclusions and Recommendations.....	413
6	CONCLUSIONS AND RECOMMENDATIONS.....	415
6.1	Conclusions	415
6.1.1	Long-Term Moisture Softening of Compacted Embankments	416
6.1.2	Breaking the Rayleigh Wave Barrier	420
6.1.3	Bumps in High-Speed Rails	427
6.2	Future Related Research.....	432
6.2.1	Long-Term Moisture Softening of Compacted Embankments	432
6.2.2	Breaking the Rayleigh Wave Barrier	433
6.2.3	Bumps in High-Speed Rails	434
	REFERENCES	436

LIST OF FIGURES

	Page
Figure 1.1. Schematic view of different irregularity types: (a) a drop, (b) a rise, (c) a dip, and (d) a bump (Nicks 2009).....	3
Figure 2.1. The historical development of HSR over time (UIC 2017).....	15
Figure 2.2. Map of the plan for the US HSR system to be completed by 2030 (USHSR 2017).....	16
Figure 2.3. Ballasted track structure components (a) side view (b) cross-section (Selig and Waters 1994)	21
Figure 2.4. Components of some discrete rail support systems using sleepers or blocks encased in concrete.....	24
Figure 2.5. Components of several different discrete rail support systems in the subcategory sleepers on top of an asphalt-concrete layer.....	25
Figure 2.6. Components of several discrete rail support systems in the subcategory prefabricated concrete slabs	27
Figure 2.7. Components of several monolithic design, discrete rail support slab track systems.....	29
Figure 2.8. Components of 2 Continuous rail support systems, subcategory embedded rail structures	32
Figure 2.9. Components of 2 continuous rail support systems in the subcategory clamped rail structures	33
Figure 2.10. Track deflection under a single point load (wheel load) (Adapted Kerr 2000).....	37
Figure 2.11. General caption that explains how the two images are connected.....	40
Figure 2.12. Impact hammer technique (Wang et al. 2016).....	41
Figure 2.13. FWD technique (Reddy et al. 2004)	42
Figure 2.14. Components of the track load vehicle technique	43
Figure 2.15. Schematic view of the rolling measurement method for track modulus developed by CARS (Wangqing et al. 1997).....	45

Figure 2.16. KTH rolling measurement method for track modulus (Wang et al. 2016)	46
Figure 2.17. Principal of rolling measurement system developed by UNL (Norman et al. 2004).....	48
Figure 2.18. The effects of track components on track modulus (Selig and Waters 1994)	49
Figure 2.19. Dynamic wheel loads on BR as a function of train speed, static axle load, and unsprung masses (Railway Gazette 1970)	58
Figure 2.20. The comparison of DAF formulas (Adapted Doyle 1980)	60
Figure 3.1. Soil state above ground water level (Briaud 2013).....	68
Figure 3.2. Examples of water normal stress (u_w) profile (a) below and (b) above ground water level (Briaud 2013).....	69
Figure 3.3. Water tension at the contact between two particles (Briaud.....	70
Figure 3.4. (a) osmotic suction experiment (Briaud 2013) (b) semi-permeable membrane	71
Figure 3.5. Error band for suction and water content (Briaud 2013)	75
Figure 3.6. An example of a soil water retention curve (SWRC) (Briaud 2013).....	76
Figure 3.7. Soil water retention curves (SWRC) of different soil types (Briaud 2013)	77
Figure 3.8. Modulus –suction relationship.....	79
Figure 3.9. Schematics of (a) cross-sectional view of the full-scale model (b) top view of water control pipes (Chen et al. 2014; Jiang et al. 2015, Bian et al. 2016)	83
Figure 3.10. Accumulative settlement as a function of the number of train axle load passage (Bian et al. 2016)	84
Figure 3.11. Measured time history of vibration velocity at track slab and roadbed at train speed of 216 km/h (before and after water level rising) (Bian et al. 2016)	85
Figure 3.12. Maximum measured vibration velocity as a function of train speed at track slab and roadbed (before and after water level rising) (Bian et al. 2016)	86

Figure 3.13. Unconsolidated undrained (UU) triaxial test set-up (Briaud 2013).....	88
Figure 3.14. The process of creating the samples for the unconsolidated undrained (UU) triaxial tests	91
Figure 3.15. Membrane fitting	93
Figure 3.16. Six samples on top of the sieves to air dry uniformly	94
Figure 3.17. Two different series of time intervals leading to have soil specimens with different water content ranges	95
Figure 3.18. A photo summary of the UU triaxial test procedure and failure plane.....	96
Figure 3.19. UU triaxial test data processing	98
Figure 3.20. (a) a WP4 device; (b) a schematic representative of the inside of a WP4 device (Leong et al. 2003)	101
Figure 3.21. Schematic cross-sectional view of the salt solution equilibrium (SSE) container (Briaud 2013)	104
Figure 3.22. Preparing samples and the salt solution to run the SSE tests.....	106
Figure 3.23. The relationship between water content and Young’s soil modulus	108
Figure 3.24. Soil water retention curves obtained from WP4 tests.....	110
Figure 3.25. Young’s soil modulus vs. suction.....	111
Figure 3.26. Raw data obtained from the salt solution equilibrium (SSE) tests	114
Figure 3.27. Calculation of the asymptotic value of Y	115
Figure 3.28. Comparison of Soil Water Retention Curve calculated using different methods	116
Figure 3.29. Sources of moisture in train tracks (Li et al. 2016)	118
Figure 3.30. A schematic view of surface and subsurface flow (CE 2303 Railway Engineering)	119
Figure 3.31. Grain size distribution plots of typical aggregate drain material and common sandy subgrade (Li et al. 2016).....	121
Figure 3.32. Geomembrane used to raise drainage surface within substructure (Li et al. 2016)	121

Figure 3.33. Using hot mixed asphalt (HMA) to raise drainage surface within track substructure (Li et al. 2016).....	122
Figure 3.34. Example of surface drainage system design (a) plan (b) cross-sectional view (Li et al. 2016)	124
Figure 3.35. An external drainage system using sand piles	125
Figure 3.36. Cross-sectional view of an ideal track for good subsurface drainage (Li et al. 2016)	126
Figure 3.37. Ground water removal and capillary protection of railways ballast.....	126
Figure 3.38. An inverted filter.....	127
Figure 4.1. Different waves propagating in soil skeleton (Braiud 2013).....	135
Figure 4.2. Passing (a) the sound barrier ($M > 1.0$) and (b) the Rayleigh wave barrier ($GM > 1.0$)	137
Figure 4.3. Calculation of (a) the Mach number and Mach angle; (b) the Ground Mach Cone number and Mach Cone Angle (Adapted Woodward 2013)	138
Figure 4.4. (a) Cross sectional view of the real in-situ test in Japan; (b) Vertical displacement of roadbed vs. train speed (Sunaga et al. 1990).....	142
Figure 4.5. Peak-to-peak displacement of ballast as a function of train speed (Woldright and New 1999).....	143
Figure 4.6. Normalized peak-to-peak vertical track displacement as a function of normalized train speed (Madshus et al. 2004).....	145
Figure 4.7. Model verification of (a) dynamic vertical stress-time in roadbed at train speed equal to 330 km/h and (b) vibration velocity vs. train speed (Bian et al. 2014)	147
Figure 4.8. GRAFT facilities (Kennedy 2011)	148
Figure 4.9. (a) Train configuration and its axle loads in measured and simulated vertical track displacement at (b) cut-off train speed and (c) speed close to critical speed (Madshus and Kaynia 2000).....	150
Figure 4.10. Measured and simulated peak vertical track displacement amplitude vs. train speed (Madshus and Kaynia 2001)	151
Figure 4.11. S-wave speed vs. depth at Ledsgard site (Sweden) (Madshus and Kaynia 2000)	153

Figure 4.12. (a) Cross section and (b) side view of the finite element model.....	157
Figure 4.13. Train run time calculation.....	157
Figure 4.14. X2000 specification (load and dimension) (a) Adapted Kaynia et al. (2000) and Madshus and Kaynia (2000) and (b) as used in the current numerical simulation	159
Figure 4.15. CRH2 specification (load and dimension) (a) Adapted Chen et al. (2014) and (b) as used in the current numerical simulation	160
Figure 4.16. Wheel/rail contact surface (Adapted Nicks 2009).....	161
Figure 4.17. The effect of nonlinearity on the critical speed (Abu Saeed et al. 2016)	163
Figure 4.18. Ballast vertical displacement under train load (a) at train speed of 50 m/s and linear ballast, (b) at train speed of 50 m/s and nonlinear ballast, (c) at train speed of 70 m/s and linear ballast, and (d) at train speed of 70 m/s and nonlinear ballast	164
Figure 4.19. Equivalent linear approach: (a) Hysteretic, nonlinear response of soil; (b) modulus degradation and damping curves of organic clay from the Ledsgard site (Sweden) (Madshus and Kaynia 2000)	166
Figure 4.20. Boundary conditions: (a) cross section (b) side view	168
Figure 4.21. (a) A cross section of the embankment at the Ledsgard, Sweden, site (Madshus and Kaynia 2001) (b) The embankment cross section for the numerical simulation	171
Figure 4.22. (a) to (d) Dynamic soil properties of the embankment/soil vs. depth for Ledsgard site (Sweden) (Madshus and Kaynia 2000), and (e) material properties adopted for FEM.....	173
Figure 4.23. Time history of the vertical track displacement at train speeds of (a) 70 km/h and (b) 185 km/h	176
Figure 4.24. (a) Peak track displacement amplitudes as a function of train speeds and (b) Normalized track displacement vs. normalized train speed: measured and simulated.....	177
Figure 4.25. Side views of (a) the full-scale experimental study of slab track in China (Bian et al. 2014) and (b) the finite element model in LS-DYNA, and cross section views of (c) the full-scale experimental study of slab track in China (Bian et al. 2014) and (d) the finite element model in LS-DYNA.....	179

Figure 4.26. (a) The sequential loading system components and (b) the loading program (Bian et al. 2014).....	180
Figure 4.27. The plate load test results for the deformation modulus: (a) subgrade, (b) roadbed (Bian et al. 2014)	181
Figure 4.28. Dynamic soil stress distribution along the depth from roadbed surface at different train speeds of (a) 108 km/h; (b) 216 km/h; (c) 360 km/h.....	183
Figure 4.29. Ground deformation (Top View) (a) at subsonic train speed and (b) at supersonic train speed.....	185
Figure 4.30. Effect of train speed on the development of the GM cone	186
Figure 4.31. Cross sectional view of the finite element model used in the parametric study.....	188
Figure 4.32. FEM dimension used for simulation: (a) cross-section view, (b) side view.....	189
Figure 4.33. Predicted vertical track displacement at different train speeds.....	192
Figure 4.34. Cross-section view of track displacement contour at different train speeds: (a) VT=108 km/h (GM=0.43), (b) VT=180 km/h (GM=0.71), (c) VT=252 km/h (GM=1.0), and (d) VT=324 km/h (GM=1.29)	193
Figure 4.35. Plan view of track displacement contour at different train speeds: (a) VT=108 km/h (GM=0.43), (b) VT=180 km/h (GM=0.71), (c) VT=252 km/h (GM=1.0), and (d) VT=324 km/h (GM=1.29)	194
Figure 4.36. Predicted peak vertical track displacement vs. train speed.....	195
Figure 4.37. Simulated normalized track displacement vs. normalized train speed or Ground Mach number (GM)	197
Figure 4.38. The geometry of the FEM used in section 4.7.2.....	199
Figure 4.39. Predicted vertical track displacement time history at VT=108 km/h with (a) He=0 (GM=0.75), (b) He=2 m (GM=0.43), (c) He=4 m (GM=0.27), (d) He=6 m (GM=0.25), (e) He=8 m (GM=0.20)	200
Figure 4.40. Predicted vertical track displacement time history at VT=216 km/h with (a) He=0 (GM=0.75), (b) He=2 m (GM=0.43), (c) He=4 m (GM=0.27), (d) He=6 m (GM=0.25), (e) He=8 m (GM=0.20)	201

Figure 4.41. Predicted vertical track displacement time history at VT=324 km/h with (a) He=0 (GM=0.75), (b) He=2 m (GM=0.43), (c) He=4 m (GM=0.27), (d) He=6 m (GM=0.25), (e) He=8 m (GM=0.20)	202
Figure 4.42. Cross-section view of track displacement contour at train speed of 108 km/h with (a) He=0 (GM=0.75), (b) He=2 m (GM=0.43), (c) He=4 m (GM=0.27), (d) He=6 m (GM=0.25), (e) He=8 m (GM=0.20)	204
Figure 4.43. Cross-section view of track displacement contour at train speed of 216 km/h with (a) He=0 (GM=0.75), (b) He=2 m (GM=0.43), (c) He=4 m (GM=0.27), (d) He=6 m (GM=0.25), (e) He=8 m (GM=0.20)	205
Figure 4.44. Cross-section view of track displacement contour at train speed of 324 km/h with (a) He=0 (GM=0.75), (b) He=2 m (GM=0.43), (c) He=4 m (GM=0.27), (d) He=6 m (GM=0.25), (e) He=8 m (GM=0.20)	206
Figure 4.45. Plan view of track displacement contour at train speed of 108 km/h with (a) He=0 (GM=0.75), (b) He=2 m (GM=0.43), (c) He=4 m (GM=0.27), (d) He=6 m (GM=0.25), (e) He=8 m (GM=0.20)	207
Figure 4.46. Plan view of track displacement contour at train speed of 216 km/h with (a) He=0 (GM=0.75), (b) He=2 m (GM=0.43), (c) He=4 m (GM=0.27), (d) He=6 m (GM=0.25), (e) He=8 m (GM=0.20)	208
Figure 4.47. Plan view of track displacement contour at train speed of 324 km/h with (a) He=0 (GM=0.75), (b) He=2 m (GM=0.43), (c) He=4 m (GM=0.27), (d) He=6 m (GM=0.25), (e) He=8 m (GM=0.20)	209
Figure 4.48. Maximum track vertical displacement vs embankment thickness (He) at train speed of (a) 108 km/h (b) 216 km/h, and (c) 324 km/h	210
Figure 4.49. Predicted peak vertical track displacement vs. train speed for different case studies: (a) No embankment, (b) He=2 m, (c) He=4 m, (d) He=6 m, and (e) He=8 m	211
Figure 4.50. Summary of the predicted peak vertical track displacement vs. train speed for different case studies (He=0 to 8 m)	214
Figure 4.51. Effect of embankment thickness on simulated normalized track displacement: (a) normalized track displacement vs. normalized train speed or ground Mach number (GM), (b) normalized track displacement vs. embankment thickness	216
Figure 4.52. Effect of embankment thicknesses on critical speed	217
Figure 4.53. Effect of Ee on simulated vertical track displacement amplitude at VT=108 km/h.....	220

Figure 4.54. Effect of Ee on simulated vertical track displacement amplitude at VT=252 km/h.....	221
Figure 4.55. Effect of Ee on simulated vertical track displacement amplitude at VT=396 km/h.....	222
Figure 4.56. Cross-section view of track displacement contour at train speed of 108 km/h under different embankment conditions (different embankment modulus).....	223
Figure 4.57. Figure 4.57. Cross-section view of track displacement contour at train speed of 252 km/h under different embankment conditions (different embankment modulus)	224
Figure 4.58. Cross-section view of track displacement contour at train speed of 396 km/h under different embankment conditions (different embankment modulus).....	224
Figure 4.59. Plan view of track displacement contour at train speed of 108 km/h under different embankment conditions (different embankment modulus)	225
Figure 4.60. Plan view of track displacement contour at train speed of 252 km/h under different embankment conditions (different embankment modulus)	225
Figure 4.61. Plan view of track displacement contour at train speed of 396 km/h under different embankment conditions (different embankment modulus)	226
Figure 4.62. Maximum vertical track displacement vs. train speeds (a) Ee=100 MPa, (b) Ee=150 MPa, (c) Ee=200 MPa, (d) Ee=250 MPa, (e) Ee=300 MPa, (f) summary of all cases	227
Figure 4.63. Effect of embankment moduli on critical speed	230
Figure 4.64. Maximum vertical track displacement vs. train speeds (a) Ee=100 MPa, (b) Ee=150 MPa, (c) Ee=200 MPa, (d) Ee=250 MPa, (e) Ee=300 MPa, (f) summary of all cases	231
Figure 4.65. Effect of embankment moduli on critical speed (He=2.0 and 4.0 m).....	233
Figure 4.66. Maximum vertical track displacement vs. train speed.....	235
Figure 4.67. Finite element model dimension used for parametric study (assessing the effect of subgrade modulus on the critical speed) (a) cross-section view (b) side view	236

Figure 4.68. Effect of E_s on simulated vertical track displacement amplitude at VT=108 km/h.....	238
Figure 4.69. Effect of E_s on simulated vertical track displacement amplitude at VT=216 km/h.....	239
Figure 4.70. Effect of E_s on simulated vertical track displacement amplitude at VT=324 km/h.....	240
Figure 4.71. Cross-section view of track displacement contour at 108 km/h under different embankment conditions (different subgrade modulus).....	241
Figure 4.72. Cross-section view of track displacement contour at 216 km/h under different embankment conditions (different subgrade modulus).....	241
Figure 4.73. Cross-section view of track displacement contour at 324 km/h under different embankment conditions (different subgrade modulus).....	242
Figure 4.74. Plan view of track displacement contour at 108 km/h under different embankment conditions (different subgrade modulus)	242
Figure 4.75. Plan view of track displacement contour at 216 km/h under different embankment conditions (different subgrade modulus)	243
Figure 4.76. Plan view of track displacement contour at 324 km/h under different embankment conditions (different subgrade modulus)	243
Figure 4.77. Maximum vertical track displacement vs. train speeds (a) $E_s=6.51$ MPa, (b) $E_s=14.65$ MPa, (c) $E_s=26.1$ MPa, (d) $E_e=41$ MPa, (e) summary of all cases.....	244
Figure 4.78. Effect of subgrade moduli on critical speed ($H_e=0$).....	247
Figure 4.79. Maximum vertical track displacement vs. train speeds with embankment modulus $E_e=100$ MPa, different embankment heights (0 $\leq H_e \leq 8.0$ m) at (a) $E_s=6.51$ MPa, (b) $E_s=14.65$ MPa, and (c) $E_s=26.1$ MPa.....	252
Figure 4.80. Maximum vertical track displacement vs. train speeds with embankment modulus $E_e=150$ MPa, different embankment heights (0 $\leq H_e \leq 8.0$ m) at (a) $E_s=6.51$ MPa, (b) $E_s=14.65$ MPa, (c) $E_s=26.1$ MPa, (d) $E_s=41$ MPa.....	254
Figure 4.81. Maximum vertical track displacement vs. train speeds with embankment modulus $E_e=200$ MPa, different embankment heights (0 $\leq H_e \leq 8.0$ m) at (a) $E_s=6.51$ MPa, (b) $E_s=14.65$ MPa, (c) $E_s=26.1$ MPa, (d) $E_s=41$ MPa.....	256

Figure 4.82. Maximum vertical track displacement vs. train speeds with embankment modulus $E_e=250$ MPa, different embankment heights ($0 \leq H_e \leq 8.0$ m) at (a) $E_s=6.51$ MPa, (b) $E_s=14.65$ MPa, (c) $E_s=26.1$ MPa, (d) $E_s=41$ MPa.....	258
Figure 4.83. Maximum vertical track displacement vs. train speeds with embankment modulus $E_e=300$ MPa, different embankment heights ($0 \leq H_e \leq 8.0$ m) at (a) $E_s=6.51$ MPa, (b) $E_s=14.65$ MPa, (c) $E_s=26.1$ MPa, (d) $E_s=41$ MPa.....	260
Figure 4.84. Maximum vertical track displacement vs. train speeds with embankment modulus $E_e=2e4$ MPa (Concrete slab), different embankment heights ($0 \leq H_e \leq 1.0$ m) at (a) $E_s=6.51$ MPa, (b) $E_s=14.65$ MPa, (c) $E_s=26.1$ MPa, (d) $E_s=41$ MPa.....	262
Figure 4.85. Effect of embankment thicknesses (H_e), embankment moduli (E_e) and subgrade moduli (E_s) on the critical speeds (VC) (a) $E_e=100$ MPa (b) $E_e=150$ MPa, (c) $E_e=200$ MPa, (d) $E_e=250$ MPa, (e) $E_e=300$ MPa, and (f) $E_e=2e4$ MPa (Concrete slab)	265
Figure 4.86. Definitions of different speed zones	270
Figure 4.87. Effect of embankment heights (H_e), embankment modulus (E_e) and subgrade modulus (E_s) on the Ground Mach (GM) (a) $E_e=100$ MPa (b) $E_e=150$ MPa, (c) $E_e=200$ MPa, (d) $E_e=250$ MPa, (e) $E_e=300$ MPa, and (f) $E_e=2e4$ MPa (Concrete slab)	272
Figure 4.88. Proposed design procedure of HSR track based on the 3-D FEM (Banimahd 2008)	279
Figure 4.89. Flowcharts of design procedure	281
Figure 4.90. (a) lime-cement column method for soil stabilization, (b) measured track displacement before and after soil improvement at train speed between 190 and 200 km/h (Madshus et al. 2004), (c) peak-to-peak track displacement before (May) and after (December).....	284
Figure 4.91. Cost distribution of countermeasure (Holm et al. 2002)	285
Figure 4.92. Simulated effect of countermeasures (Kaynia et al. 2001).....	287
Figure 4.93. (a) Application of the polymer XiTRACK to the ballast surface, (b) schematic cross-sectional view of the XiTRACK polyurethane reinforcement used at Manningtree North Junction UK (Woodward et al. 2012)	288

Figure 5.1. Different aspects contributing to irregularity formation along highway or railway lines (Briaud et al. 1997)	294
Figure 5.2. Dynamic amplification factor of wheel/rail interaction force at different train speeds (VT=108, 180, 252 km/h) for different subgrade conditions (Es= 25 to 100 MPa) (Banimahd 2008).....	296
Figure 5.3. Track displacement with non-faulted transition at a train speed of 252 km/h for (a) Es=40 MPa (b) Es=100 MPa (Banimahd 2008).....	297
Figure 5.4. Schematic view of different types of irregularities: (a) a bump, (b) a dip at the transition zone near bridges (Nicks 2009)	299
Figure 5.5. Static beam deflection as loads move along the track with variable track modulus (Hunt 1997).....	300
Figure 5.6. Differential settlement along the track at the transition zone for different numbers of load cycles (Hunt 1997).....	301
Figure 5.7. Differential rail deflection at the transition zone under moving load (Banimahd and Woodward 2007).....	303
Figure 5.8. Bump model in transition zone used by Banimahd (2008)	303
Figure 5.9. Bump profile at transition zone (Lei and Mao 2004)	304
Figure 5.10. Dip profile (Adapted Banimahd and Woodward 2007).....	304
Figure 5.11. Maximum vertical wheel/rail interaction forces as a function of bump angles at different train speeds (Lei and Mao 2004)	313
Figure 5.12. Effect of bump variables (L and h) on the DAF at train speed (a) 108 km/h, (b) 180 km/h, and (c) 252 km/h (Banimahd 2008).....	315
Figure 5.13. Effect of dip height (h) and train speeds on the DAF (Woodward and Banimahd 2007).....	316
Figure 5.14. Tolerable bump/dip size vs. train speed based on permissible DAF of 2.0 (Nicks 2009)	318
Figure 5.15. (a) Cross section and (b) side view of the finite element model.....	321
Figure 5.16. Schematic view of the bogie with its suspension system	325
Figure 5.17. (a) Equivalent damper coefficient, (b) spring constant, and (c) side view of the finite element model of the train suspension system	326

Figure 5.18. Train dimensions (Nicks, 2009).....	328
Figure 5.19. Continuous single-point contact (Banimahd 2008)	330
Figure 5.20. Contact between the wheel and the rail (Adapted Nicks 2009).....	330
Figure 5.21. Free body diagram of forces acting on the bogie model (Nicks 2009).....	331
Figure 5.22. Boundary conditions: (a) cross-section and (b) side view	332
Figure 5.23. Train body and bogie components (Popp et al. 1999)	335
Figure 5.24. (a) Rise profile (b) the finite element model of rise along track.....	336
Figure 5.25. Model verification result: Dynamic Amplification Factor (DAF) vs. Irregularity Size	337
Figure 5.26. Rise profile.....	339
Figure 5.27. Model verification result: Dynamic Amplification Factor (DAF) vs. Irregularity Size	340
Figure 5.28. Track displacement under the moving load on embankment and bridge sides of the transition at (a)VT=144 km/h, (b)VT=288 km/h, (c)VT=432 km/h	343
Figure 5.29. Effect of train speed (VT) on wheel/rail interaction force.....	344
Figure 5.30. Effect of train speed (VT) on train body vertical acceleration	345
Figure 5.31. Effect of train speed (VT) on track vertical displacement.....	345
Figure 5.32. Dynamic amplification factor (DAF) vs. train speed (VT).....	346
Figure 5.33. Maximum dynamic vertical train body acceleration(amax) vs. train speed (VT)	346
Figure 5.34. Track displacement under the moving load on embankment and bridge sides of the transition at VT=360 km/h, (a) Es=10 MPa, (b) Es=20 MPa, (c) Es=80 MPa, (d) Es=100 MPa.....	348
Figure 5.35. Effect of subgrade modulus (Es) on track vertical displacement in the vicinity of a non-faulted transition zone	350
Figure 5.36. Effect of subgrade modulus (Es) on wheel/rail interaction force	350
Figure 5.37. Effect of subgrade modulus (Es) on train body vertical acceleration.....	351

Figure 5.38. Effect of subgrade (E_s) and train speed (V_T) on dynamic amplification factor (DAF)	352
Figure 5.39. Effect of subgrade (E_s) and train speed (V_T) on maximum train body acceleration (a_{max}).....	352
Figure 5.40. Track displacement along track as a function of train speed, (b) zoom on track displacement along irregularity (rise)	355
Figure 5.41. Effect of train speed on train body acceleration at (a) $V_T=72$ km/h, (b) $V_T=144$ km/h, (c) $V_T=288$ km/h, (d) $V_T=432$ km/h	356
Figure 5.42. Effect of train speed on wheel/rail interaction force at (a) $V_T=72$ km/h, (b) $V_T=144$ km/h, (c) $V_T=288$ km/h, (d) $V_T=432$ km/h.....	357
Figure 5.43. Maximum train body acceleration vs. train speed	359
Figure 5.44. Dynamic amplification factor (DAF) vs. train speed.....	360
Figure 5.45. Track displacement comparison for different irregularity (rise) sizes of equal length ($L=12$ m) (a) along the track profile, (b) zoom on displacement along irregularity length	362
Figure 5.46. Train body acceleration comparison for different irregularity (rise) sizes of equal length ($L=12$ m)	363
Figure 5.47. Wheel/rail interaction force comparison for different irregularity (rise) sizes of equal length ($L=12$ m).....	363
Figure 5.48. Maximum train body acceleration vs. train speed comparison for various rise sizes of equal rise length ($L=12$ m).....	364
Figure 5.49. Dynamic amplification factor (DAF) vs. train speed comparison for various rise sizes of equal rise length ($L=12$ m).....	364
Figure 5.50. Cross-section view of the FEM used to assess the effect of irregularity length (L)	365
Figure 5.51. Maximum train body acceleration vs. train speed comparison for various rise sizes (effect of bump length (L) and bump height (h))	366
Figure 5.52. Dynamic amplification factor (DAF) vs. train speed comparison for various rise sizes (effect of bump length (L) and bump height (h))	366
Figure 5.53. Cross-section view of the FEMs used to assess the effect of irregularity Types (a) Drop, (b) Rise, (c) Bump, (d) Dip	367

Figure 5.54. Track displacement comparison for different irregularity types of equal irregularity size ($s=400$) at train speed of 360 km/h (a) Drop, (b) Rise, (c) Bump, (d) Dip	368
Figure 5.55. Vertical train body acceleration comparison for different irregularity types of equal irregularity size ($s=400$) at train speed of 360 km/h (a) Drop, (b) Rise, (c) Bump, (d) Dip	370
Figure 5.56. Wheel/rail interaction force comparison for different irregularity types of equal irregularity size ($s=400$) at train speed of 360 km/h (a) Drop, (b) Rise, (c) Bump, (d) Dip	372
Figure 5.57. Maximum train body acceleration vs. train speed comparison for various irregularity types	374
Figure 5.58. Dynamic amplification factor (DAF) vs. train speed comparison for various irregularity types	374
Figure 5.59. Maximum train body acceleration vs. train speed comparison for various irregularity types and irregularity sizes (a) Drop, (b) Rise, (c) Bump, (d) Dip	375
Figure 5.60. Dynamic amplification factor (DAF) vs. train speed comparison for various irregularity types and irregularity sizes (a) Drop, (b) Rise, (c) Bump, (d) Dip	377
Figure 5.61. Maximum train body acceleration vs. train speed comparison for subgrade modulus changes and various irregularity sizes (a) $s=100$, (b) $s=200$, (c) $s=400$, (d) $s=800$, (e) $s=1600$	380
Figure 5.62. Dynamic amplification factor vs. train speed comparison for subgrade modulus changes and various irregularity sizes (a) $s=100$, (b) $s=200$, (c) $s=400$, (d) $s=800$, (e) $s=1600$	382
Figure 5.63. Flowchart of proposed design procedure.....	386
Figure 5.64. Schematic plan and cross-section view of the proposed solution by Nicks (2009)	412

LIST OF TABLES

	Page
Table 2.1. Different Slab (Ballast-less) Track Systems (Esveld 1997, Bastin 2005, Lichtberger 2005, Michas 2012).....	22
Table 2.2. Components of Ballasted and Slab Tracks (Michas 2012; Nigel and Franz 2001).....	34
Table 2.3. Summary of Models Used to Estimate the Dynamic Amplification Factor (DAF) (Adapted Doyle 1980)	55
Table 2.4. Parameters Used in the Various DAF Formulas (Adapted Doyle 1980).....	56
Table 2.5. Values of t and ϕ for Eisenmann’s DAF Model (Adapted Esveld 2001).....	56
Table 3.1. Subgrade Problems, Their Causes, and Their Features (Adapted Li & Selig 1995).....	65
Table 3.2. Range of Water Tension and Water Compression for Different Conditions (Briaud 2013)	68
Table 3.3. Osmotic Suction with Various Salt Solutions at 25oC (Briaud 2013).....	72
Table 3.4. Sample Information.....	99
Table 3.5. Water Content Calculation.....	100
Table 3.6. WP4 Results for Suction	102
Table 3.7. Water Content Calculation.....	103
Table 3.8. Salt Solution Equilibrium Test Parameters	105
Table 3.9. Different Techniques for Measuring Suction or Water Tension (Briaud 2013).....	111
Table 3.10. Results of the Salt Solution Equilibrium Tests	115
Table 4.1. Different Sources of Track/Ground Vibration Induced by HST (Hall 2000).....	133
Table 4.2. Elastic Material Properties of Rail, Ties and Train Wheels.....	162

Table 4.3 . Embankment/Soil Parameters for Train Speeds of 200 and 70 km/h (Adapted Kaynia et al. 2000).....	174
Table 4.4. Physical Pproperties of Subgrade and Subsoil (Bian et al. 2014).....	181
Table 4.5. Materials Results of the Plate Load Tests for The Deformation.....	182
Table 4.6. Material Properties of The Different Sections Used in FEM.....	182
Table 4.7. Material Properties of Track/Embankment/Ground System.....	189
Table 4.8. Effect of Embankment Thickness (He) on the Critical Speed or the Equivalent Rayleigh Wave Speed (VReq) of Track/Embankment/Ground System	213
Table 4.9. Material Properties of Embankment	218
Table 4.10. Embankment Modulus (Ee) Effect on the Equivalent Rayleigh Wave Speed (VReq) of Track/Embankment/Ground Systems (Embankment Thickness (He)=2.0 m)	229
Table 4.11. Embankment Modulus (Ee) Effect on the Equivalent Rayleigh Wave Speed (VReq) of track/embankment/Ground Systems (Embankment Thickness (He)=4.0m)	233
Table 4.12. Subgrade Material Properties.....	236
Table 4.13. Matrix Cases Selected for Proposed Guideline Charts	249
Table 4.14. Summary of the Parametric Studies’ Results.....	275
Table 4.15. Comparison of Different Codes and Design Procedures (Banimahd 2008).....	278
Table 4.16. Predicted Critical Speed of Embankment/Subsoil System (Woldringh and New 1999).....	289
Table 5.1. Different Types of Irregularities along Railway Lines (Steffens 2005).....	305
Table 5.2. Dynamic Amplification Factor Threshold Limit Values	307
Table 5.3. Threshold Limit Values for Vertical Train Body Acceleration	308
Table 5.4. Track/Soil Properties.....	321
Table 5.5. Irregularity Profile.....	323

Table 5.6. Irregularity Size.....	324
Table 5.7. HST Specifications (Train Model: X2000).....	326
Table 5.8. Material Properties of Different Parts of the Bogie	328
Table 5.9. Train Specifications	334
Table 5.10. Train Specifications	338
Table 5.11. Parametric Study Summary.....	387
Table 5.12. Evaluation of Tolerable Limits for Different Cases.....	398

1 INTRODUCTION

1.1 Overview

Over the last few decades, development of high-speed railways (HSR) has accelerated rapidly throughout Europe, Asia, and Australia; and in recent years, North America has also become interested. High-speed lines have been constructed to provide a safe, fast, comfortable, affordable, and environmentally friendly ride. Based on the survey published in Railway Gazette International (Takagi 2005), average high-speed train (HST) speed (VT) exceeded 300 km/h (83 m/s). For example, in Germany, the fastest speed on conventional railways was 330 km/h (92 m/s) in 2005. High-speed trains (HST) exceed the maximum speed of 350 km/h (97.2 m/s) in France and China (Railway Gazette International 2015). The experimental France's Train à Grande Vitesse (TGV) HST has reached the speed of 575 km/h (160 m/s). The United States (US) HSR network has been planned to create trains that reach a speed of around 360 km/h (100 m/s) by 2050 (USHSR 2017). However, this evolution has brought a number of new geodynamic challenges to railway engineering that are different from those of conventional freight and passenger trains.

The high speeds have brought many new issues to the old railways in use which were not designed for these high speeds (Banimahd 2008). The high cost of maintenance and less comfortable ride are a result of running HST on the non-HSR.

In addition to high costs and comfort issues, in some countries such as Sweden and Japan, running HST on old tracks has caused safety issues. Major deflections in non-HSR

tracks bearing HST led to a need to decrease train speeds in Sweden to increase safety (Adolfsson et al. 1999). Running HST on the conventional tracks can also result in high levels of vibrations in soft soils under the embankment (Sunaga et al 1990, Woldright and New 1999, Kaynia et al., 2000, Madshus and Kaynia 2000, Madshus et al., 2004, Banimahd 2008, Chen et al. 2014, Bian et al., 2014, Jiang et al. 2015). In worst-case scenarios, the dynamic effects of these high speeds can result in ground failure and train derailment. In Japan, because many railroads were constructed on soft alluvium soils, the dynamic performance of the embankment is a serious concern due to the dynamic nature of HST loads (Sunaga et al 1990).

In recent years, these issues resulted in research studies to investigate a number of such challenges associated with using old traditional railways for HST. Banimahd (2008) conducted an extensive study on some common geotechnical problems regarding HSRs. In the near future, HSTs are expected to pass an average speed of 400 km/h (110 m/s); thus, the range of train speeds (V_T) ($V_T \leq 252$ km/h (70 m/s)) that he considered was not high enough.

Another issue of key concern is the problem of irregularity in general or bumps and dips along HSRs. Different types of irregularities are shown in Figure 1.1. These different types of irregularities are generated due to the frequent passage of HSTs. Indeed, frequent passage of HST leads to permanent track settlement. After each HST load cycle, a very small permanent settlement of track and soil under the track at transition zone remains that accumulates over thousands of load cycles, eventually generating an unbearable irregularity along HSR causing comfort and safety issues (Banimahd 2008, Nicks 2009).

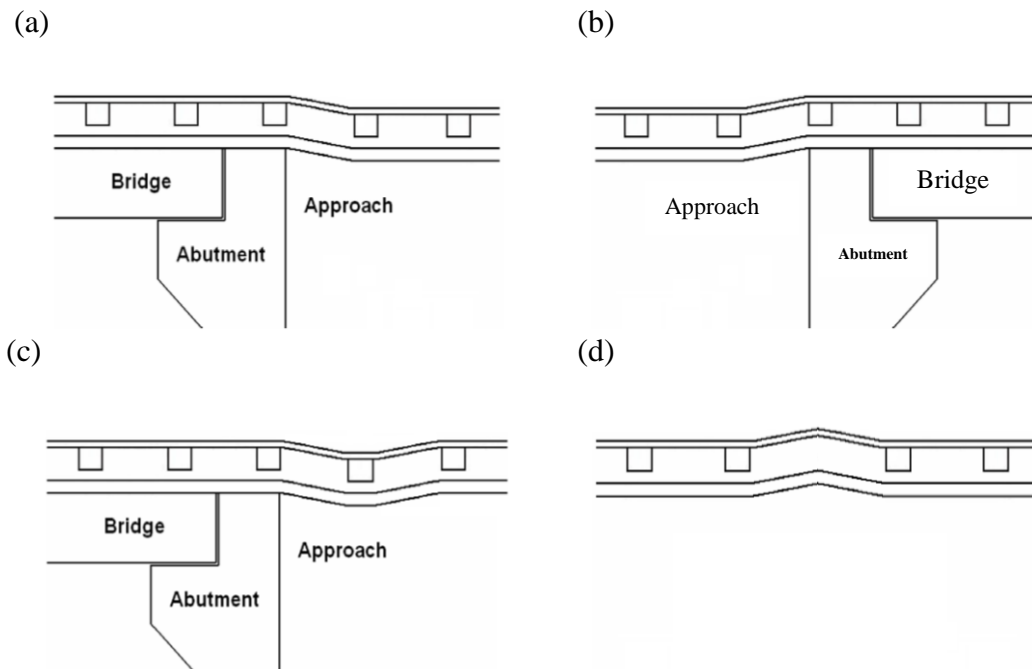


Figure 1.1. Schematic view of different irregularity types: (a) a drop, (b) a rise, (c) a dip, and (d) a bump (Nicks 2009)

The effect of water level changes in compacted embankments is another critical issue related to the both conventional and high-speed railway lines because it results in soil softening. During their service life, railway embankments are exposed to changing water content due to weather events such as heavy rainfall, floods, drought, groundwater level variation, and weak drainage. Such elemental factors impact the mechanical behavior of the subgrade soil resulting in large track deformation (Li and Selig 1995, Berggren 2009, Chen et al. 2014, Sanchez et al. 2014, Cui 2014 Jiang et al. 2015, Bian et al. 2016).

1.2 Problem Statement and Research Questions

The current study will address three main geotechnical issues (GI) associated with embankments for HST with the goal of answering specific research questions (RQ) in each area.

GI1. When trains pass the Rayleigh wave barrier while traveling on soft soils, it results in larger vertical deflections in the subsoil due to the combination of the static and dynamic loads (Kaynia et al., 2000, Madshus and Kaynia 2000, Madshus et al., 2004, Banimahd 2008). In order to better understand what is happening so that better HSR can be created, the answers to the following questions are of key importance.

- RQ1: Why does the large track deflection occurs when an HST passes certain speed called critical speed (V_C)?

- RQ2: Is there a relationship between the critical speed, the speed at which the largest track deflection occurs, and the track/embankment system properties?

- RQ3. How effective is constructing higher and stiffer embankments on soft subsoil in reducing the dynamic effect of running a HST on soft subsoil?

GI2. In embankments and soil under HSTs where the groundwater level is rising, track stiffness is likely to be degraded over time. In fact, too much water content in the subsoil or subgrade can cause a series of problems such as large, unexpected, uneven deflections. The presence of water in the subsoil and compacted embankment can reduce the strength and stiffness of soils dramatically and lead to large deflection (Chen et al. 2014; Bian et al. 2016). Therefore, the answers to the following questions are important.

▪RQ4: How does the soil modulus change as the water level in soil changes?

GI3. The roughness of the ride due to the surface on which the tracks rest is also a source of concern at high speeds. One of the concerns is comfort, but roughness can also result in high maintenance costs. Technically, this issue is referred to as the roughness at the transition zone between the bridge and the embankment.

One source of such roughness is presence of any types of irregularities near bridges. It should be mentioned that there are different types of irregularity considered in this study (Figure 1.1); however, for brevity, the phrase "bump" will be used to refer to either types of irregularities throughout this dissertation. Due to presence of a steep bump in HSRs, high levels of acceleration are generated in car body which leads to an uncomfortable ride. In addition, this track roughness near the bridges causes a large reaction force between rails and wheels, which leads to rail and wheel and rail defects over time. As a result, the maintenance cost increase.

Although much research (Davis et al. 2003, Li et al. 2003, Li and Davis 2005, Plotkin et al. 2006, Davis and Li 2006, Banimahd 2008, Nicks 2009) has been done on conventional and high-speed railway lines and they have been successfully implemented around the globe for several decades already, to date, research has not addressed the effect of the current range of train speeds, ($V_T > 252$ km/h (70 m/s)). The studies in this project will rectify that, filling gaps in the current knowledge as well as in today's technology. It should be noted that tolerable bump size with respect to current train speed ranges is of critical. The following question will be answered throughout the current study.

- RQ5: does the differential modulus alone (non-faulted tracks) in the vicinity of the transition zone play an influential role in train/track responses including wheel/rail interaction force and train body acceleration?

- RQ6: How effective is the train speed in defining tolerable bump size considering safety and comfort criteria?

- RQ7: what are the tolerable bump size with respect to the specific irregularity shape, subsoil modulus at a given train speed when the wheel/rail interaction force as a safety criteria and train body acceleration as a comfort criterion is kept below the threshold values?

1.3 Research Objectives

As mentioned earlier in this chapter, among all geotechnical challenges regarding HSR, our main overall goals for this work is addressing three main issues including long-term soil softening due to water level changes in compacted embankment, breaking the Rayleigh wave barrier and its consequent resonance effect, and the problem of bump along HSR lines.

Design and maintenance of the HSRs have usually been based on empirical relationships and simple models which cannot represent the complex mechanics of track/embankment under the high-speed regimes. Therefore, developing a 4-D finite element model (FEM) representing multi-layered subsoils and embankments, train-track

interactions, and track irregularities that more accurately represents reality is essential part of this work. Thus, one main goal of this study is to develop an effective numerical model to evaluate the coupled train/track/embankment dynamic responses under different geotechnical and operational conditions. The numerical model is a 4-D FEM of trains, tracks, and embankments using LS-DYNA (Livermore Software Technology Corporation (LSTC), 2006). This 4-D finite element model has two objectives: (1) simulating an HST passing the Rayleigh wave barrier and (2) modeling the bumps along HSRs in general. Using this well-developed 4-D FEM, all research questions except for RQ4 will be answered.

This study also includes a series of laboratory tests which allow the effects of rising groundwater levels on HST tracks to be analyzed. This is important because rising water level in compacted embankment and subsoil underneath results in change of water content of the soil material. The compacted embankment and subsoil are considered as unsaturated soil whose mechanical and hydraulic properties are extremely sensitive to the change of water content. Change of water content in this type of material results in modulus variation causing accelerating soil degradation and forming large track deflection. Therefore, this issue need to be analyzed more in detail through an experimental study. Also, it should be noted that change in mechanical properties of the soil due to water level change are connected to the other two issues, i.e. breaking Rayleigh wave barrier and bump problem along HSR lines. The effect of change of water content on the subsoil modulus will be addressed experimentally and then the influence of modulus variation on the track responses will be simulated using FEM through the current work. Together, the research on these three issues lead to proposing the guideline charts providing data necessary for

the design of safe embankment for HST. In addition, using the guidelines can help to minimize/eliminate an uncomfortable ride. Even though Banimahd (2008) and Nicks (2009) addressed some of these issues through their valuable work, the effect of current train speed has not been fully. Our main focus on this research is to fill this gap because the main objective of HST is providing fast, safe and comfortable ride for passengers.

1.4 Research Outline

In this dissertation, three different geotechnical issues for HSRs are addressed, and each is presented in a separate section (sections 3–5). Therefore, the literature review is not presented all together. Instead, the general background is presented in section 2 while rest of reviewing important past works is given in its corresponding sections (sections 3-5).

Embankment and supporting soil stiffnesses are the basis parameters of track design that influences the bearing capacity, the dynamic behavior of passing Rayleigh wave speed by trains, and the formation of irregularities. Water level changes due to either rising ground water levels or events like heavy rainfall can cause soil softening. HSR compacted embankments can be exposed to high water levels which results in a decrease in its performance and jeopardizes the safety of the HST and its passengers. An extensive laboratory study was conducted to evaluate the effects of soil water changes on soil stiffness (section 3). The study included three different tests: unconsolidated undrained

triaxial test (UUT), chilled-mirror psychrometers (WP4¹), and salt solution equilibrium test (SSE). The unconsolidated undrained triaxial test was chosen to assess the soil modulus at different water contents. WP4 and SSE were selected to find the soil water retention curve; in fact, these two test results were used to find the relationship between soil water content and suction. The reasons of choosing these tests to analyze the hydro-mechanical behavior of the soil will be explained more in detail in section 3.

One primary concern of railway engineers is avoiding the train speed called critical speed (Kaynia et al., 2000, Madshus and Kaynia 2000, Madshus et al., 2004, Banimahd 2008). Critical speed (V_C) is defined as the train speed at which the maximum track/embankment/supporting soil dynamic movement occurs. Section 4 addresses the problem of critical speed (V_C) associated with HSR embankments on soft soils and excessive dynamic track movement as trains approach the critical speed (V_C). Different numerical and experimental studies have been confirmed that this critical speed is very close to the Rayleigh wave speed of the track/soil system (Sunaga et al. 1990, Woldright and New 1999, Kaynia et al. 2000, Madshus and Kaynia 2000, Madshus et al. 2004, Banimahd 2008, Chen et al. 2013, Bian et al. 2014, Jiang et al. 2015). Through an extensive numerical simulation, the dynamic nature of the track/embankment/underlying soil response is investigated with a 4-D FEM using LS-DYNA. This model, the 4-D FEM, was developed to simulate the effect of train speed on HSR track response. Tracks were located on multi-layered ground. Two measurements were used to verify the numerical simulations, and the verified model was then used to perform a parametric study to find a

¹ WP4 is the name of the device used in this test.

method suited to overcome the critical speed problem. In this parametric study, the effects of different ground stiffnesses, embankment stiffnesses, and embankment depths on critical speed were investigated.

Formation of any type of irregularity (Figure 1.1) along HSRs is inevitable due to the presence of many site-dependent factors involved in the formation of said irregularities. An important goal of this part of the work was to find a way to minimize them to a tolerable level. A tolerable slope has yet to be precisely specified for different types of irregularities along HSRs at different train speeds. A second series of 4-D dynamic FEMs of train/track/embankment were developed using LS-DYNA with the goal of determining the tolerable irregularity size at a given speed for various irregularities (section 5). This model was used to conduct parametric studies to assess acceptable slopes for different types of irregularities considering comfort and safety criteria. Using this model, 4-D FEM, different types of irregularities including bumps, dips, rises, and drops of different sizes were imposed onto track structures. In addition to testing the effect of irregularity type, the effect of train speed on defining the tolerable value for irregularity size was investigated. The last parameter considered in section 5 was the embankment modulus and its effect on identifying the acceptable value for irregularity size. To define the allowable size for different types of irregularities, two track response criteria were considered: wheel/rail interaction force and train body acceleration. The allowable values for these two criteria are also defined in this section.

1.5 Research Significance

Valuable research regarding geotechnical issues for HSR has been conducted; however, in these works, the overall goal was to define a reasonable range of HST speeds which has an influential effect on the three geotechnical issues defined above. It has long been a main issue for high-speed railroads to provide safe and fast ride for their passengers. It is a competitive issue among different countries that own their high-speed lines to increase the possible train speed in their line considering passengers comfort and safety. A reasonable train speed range of current and future HSTs has rarely been included in numerical models to date. For example, Banimahd's work (2008) is a remarkable numerical simulation studying different geo-challenges with HSR, but the maximum train speed that his study tested was 252 km/h (70 m/s). This range of train speed is not high enough to be useful for current HSTs, which operate at speeds starting at 350 km/h (97.2 m/s) minimum speed today. In the current study, the maximum train speed is 720 km/h (200 m/s).

This research was conducted to investigate three main geotechnical issues: Rayleigh wave propagation effects, the influence of rising ground water levels on track stiffness, and the interaction problems of train/track interaction in transition zones, i.e. the bump problem. The current experimental studies provide a better understanding of unsaturated soil and its impact on soil modulus degradation. Guidelines with charts providing data necessary for designing safe embankments for HST are proposed based on the extensive numerical analyses resulting from the FEM models and experiments. In addition, to minimize, or even eliminate, an uncomfortable ride, tolerable comfort

irregularity sizes for HSR lines for different subsoil conditions and at varied train speeds has been defined.

The proposed guidelines include

- Charts for the design of safe embankments for HSR while keeping the train speed below 70% of the critical speed. This train speed zone is considered as the safe zone at which the dynamic effect of running HST is not significant.
- Charts defining the size of tolerable irregularities for HSR lines for keeping the vertical acceleration of the train cars below the chosen threshold value.
- Charts predicting the wheel/rail interaction force and keep it below the chosen threshold value in order to define tolerable irregularity size.

2 BACKGROUND

A comprehensive literature review was conducted to provide a general overview of HSR lines, which play an important role in transferring passengers safely and quickly. This section addresses several geotechnical issues of major concern to high-speed railroads engineers, some important aspects of HSR track mechanics, and finally load on track. As previously mentioned, a more specific literature review is present in each section (sections 3-5).

2.1 Overview of High-Speed Railways Worldwide

Defining HSRs and understanding which elements make this type of railway different from conventional lines and unique are of key importance. However, industry does not have a single standard definition of HSR. The International Union of Railways (UIC) and the European Union Directive define HSR similarly as a rail system which regularly operates at or above 250 km/h (155 mph) on new tracks or 200 km/h (124 mph) on existing tracks. The European Union Directive defines HSR as railroad lines with a minimum operational speed of 250 km/h (155 mph) on lines built especially for high speeds and of about 200 km/h (124 mph) on existing lines which have been upgraded specifically for this purpose. In contrast, the United States Department of Transportation considers rail service with top speeds of 180 km/h (110 mph) to 240 km/h (150 mph) or

higher as HSR lines. This definition is based on the criteria of operational train speed on HSR lines. In the current study, the effect of speed is the primary concern; therefore, HSR is defined according to this criterion. In this study. It is tried to select a reasonable range of train speed covering all these definitions.

According to Feigenbaum (2013), four types of HSR systems exist (Feigenbaum 2013):

- **Dedicated:** New lines designed exclusively to serve high-speed trains. One example of dedicated service is Japan's Shinkansen, which was built because the existing lines were heavily overburdened with conventional passenger and freight trains.
- **Mixed high-speed:** This category includes railway lines using both dedicated and upgraded existing lines serving HST, for instance, France's Train à Grande Vitesse (TGV).
- **Mixed conventional:** This model has dedicated standard-gauge tracks that serve both HSTs and conventional trains equipped with a gauge-changing system, and conventional, nonstandard gauge tracks serving only conventional trains. It is exemplified by Spain's Alta Velocidad Española (AVE) system.
- **Fully mixed:** In this model, all HSTs, conventional passenger trains, and freight trains in the system use compatible tracks. Germany's InterCity Express (ICE) trains are a good example of this.

The speed of passenger trains has been a crucial aspect of the railway industry around the world since its inception in the early 1800s. During the Industrial Revolution,

operational train speeds constituted evidence of development in advanced countries. Figure 2.1 shows how train speed on rails has changed since 1830. The real birthdate of high-speed rails was 1 October 1964 when Japanese national railways started the operation of a train with an average speed of 210 km/h.

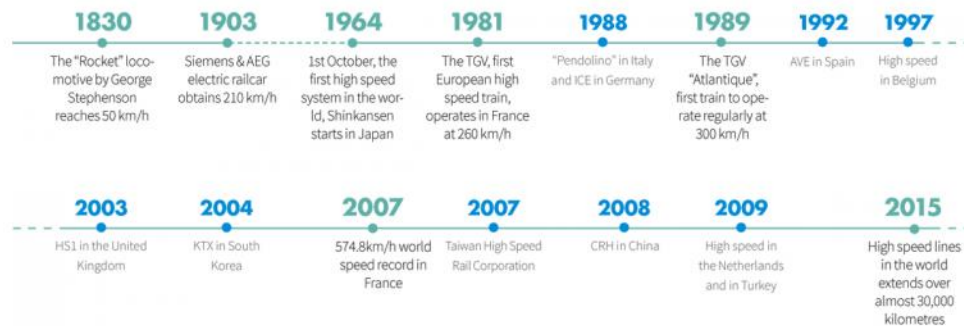


Figure 2.1. The historical development of HSR over time (UIC 2017)

After Japan, HSR was born in various European countries such as France, Germany, Italy, and the United Kingdom (UK). In 1981, the French national railway company (Société nationale des chemins de fer français, SNCF) started the operation of the first European high-speed line with a maximum speed of 260 km/h. In 30 years, TGVs carried more than 2 billion passengers at average speeds of over 350 km/h without any fatal accidents. HSR is currently in operation in more than 20 countries, including the Belgium, China, France, Germany, Italy, Japan, Korea, Spain, Taiwan, Turkey, and UK.

Since 2009, the United States has been planning an HSR system of 17,000 miles to be built in 4 phases and intended for completion by 2030 (Figure 2.2). This plan calls

for a national system of HSR express lines connecting major cities at speeds of 350 km/h (220 mph) and smaller cities and other towns at speed of 177 km/h (110 mph). For example, California is planning to link Los Angeles, San Francisco, and Sacramento with the new system. The California project is estimated at 68.4 billion USD for 1300 km of rail, about 53M USD/km.

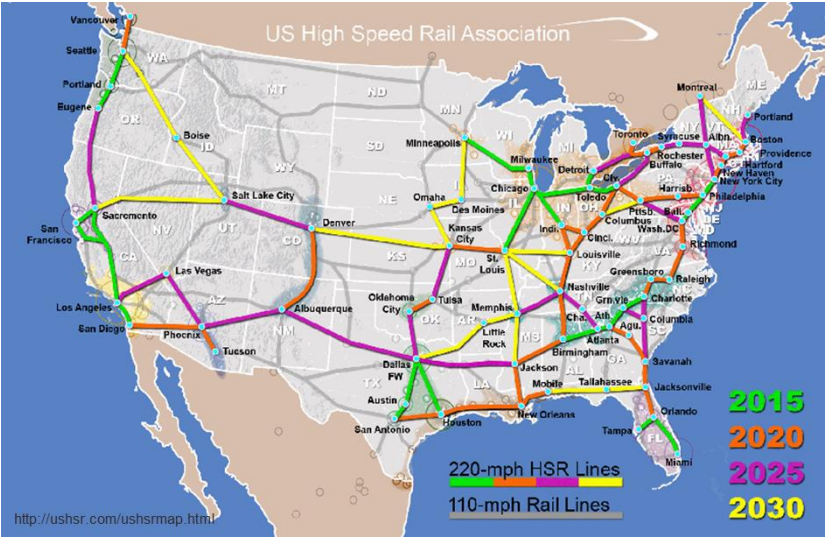


Figure 2.2. Map of the plan for the US HSR system to be completed by 2030 (USHSR 2017)

2.2 Geotechnical Challenges of High-Speed Railways

Numerous challenges regarding both new standard design and conventional railway tracks particularly geotechnical track problems. Several traditional railways’ tracks, embankment, and supporting soil currently in use have not been designed

specifically for HST axial loads and train speed ($V_T \geq 130$ km/h) (Sunaga2001, Banimahd 2008). Because of the high level of vibrations induced by running HSTs, these conventional tracks consequently require a high level of maintenance to provide a safe, fast, and comfortable ride for passengers when used for HST (Banimahd 2008). This results in high maintenance costs. Most of the HSR geotechnical challenges (geochallenges) are due to the presence of soft ground under the HST embankments. Many railroads, for example in Sweden and Japan, have been constructed by laying tracks and making embankments overlaying very soft soils and thus requiring much attention. Due to the dynamic nature of HST loads, high levels of vibrations threaten the performance of HSR embankments; in fact, the dynamic performance of all HSR embankments need to be observed (Sunaga 2001). The problems associated with vibrations induced by HST operation do not decrease with time. Existing lines need upgrades to remain safe for more frequent, faster, and heavier trains, and future lines should be designed for these new conditions.

Some of the main issues related to HSR are as follow (Madshus et al. 2004, Banimahd 2008):

- *Critical speed (V_C) and its resonance effect on HSR tracks/embankment/supporting soils.* Breaking the Rayleigh wave barrier or critical speed (V_C) issue is the most important geotechnical issue of all those facing HSR. Excessive dynamic track response is a result of train speeds approaching the natural Rayleigh wave speed of track structure and supporting soil under the track. To ensure safety and reduce maintenance costs, train speeds should be kept below the speed zone that results in

dynamic responses of the track/soil system. In cases in which soft soil layers with low Rayleigh wave speeds are present under the HST embankment, this problem escalates.

- *Accelerating the degradation of track structures.* The higher the train speed is, the higher the dynamic load generated in the track structure is. Therefore, the embankment and ground under the track must be designed to sustain this high dynamic load. If the embankment/supporting soil is subjected to a high level of vibration or dynamic load, the result will be accelerated degradation of the track/ground systems or excessive settlement.
- *Inconveniencing people and disturbing sensitive equipment near the HSR tracks due to high levels of vibrations induced by operating HSTs in track-side.* HST can create high levels of vibrations that propagate through the ground, potentially affecting buildings and sensitive equipment near the railway lines. The waves induced by HST, called Rayleigh waves, are surface waves that propagate near the surface and can inconvenience people who live near HSR lines and disturb any sensitive equipment nearby. These negative effects should be minimized.
- *Accelerating bump generation due to the frequent passage of trains.* Thousands of loading/unloading cycles due to the frequent passage of trains subject the track and supporting ground to a faster rate of permanent settlements. This settlement, called an irregularity or bump, along the HSR

track increases the dynamic wheel/rail interaction force and, consequently, causes severe, accelerated track deterioration.

This research focuses on the problems of critical speed and bumps in HSR.

2.3 Track Mechanics

In this section, the areas of track mechanics of key relevance to this research are described and defined. First, the components of tracks and embankments are detailed. Then, track and embankment stiffness are reviewed. Finally, track and embankment settlement are discussed.

2.3.1 Track/Embankment Components

Currently, two types of tracks are used: traditional ballasted tracks and non-ballasted, also termed ballast-less or slab, tracks (Indraratna et al. 2006). In this section, track components for both types are addressed.

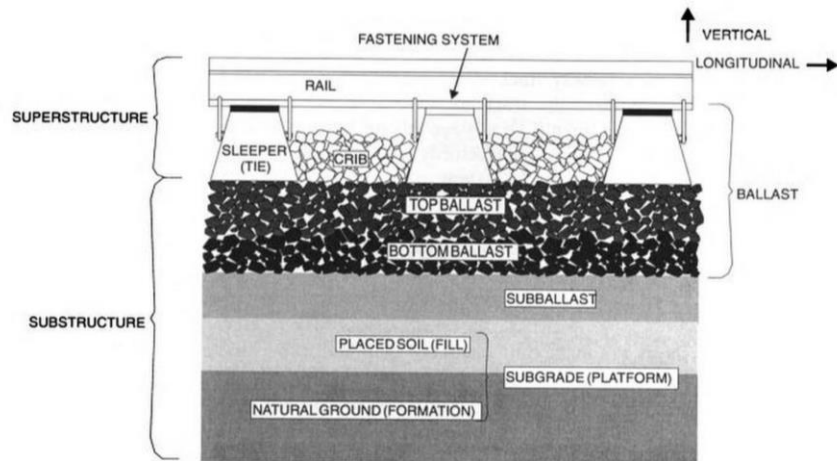
2.3.1.1 Ballasted Tracks

Ballasted tracks have been widely used all over the world. The tracks include a superstructure and a substructure component (Figure 2.3). The rails, ties or sleepers, and fastening system comprise the superstructure while the substructure consists of the ballast, subballast, and subgrade. The superstructure can be separated from the substructure by the element called the tie-ballast interface, which plays an important role in governing load distribution to the deeper track sections.

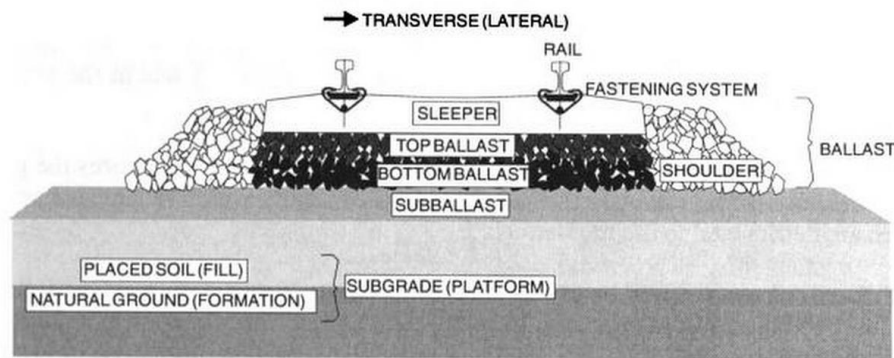
The substructure elements are not thoroughly known because they are made of natural material whose behavior is full of uncertainties. The ballast is made of a granular material and is typically 250–300 mm thick (Indraratna et al. 2006). It serves as a shock absorber for the load, acting on track superstructures to prevent the sleepers and rails from movement by resisting vertical, transverse, and longitudinal forces transmitted by the sleepers. In addition, this layer provides immediate drainage and attenuates the vibrations HSTs create (Selig and Waters 1994).

The subballast is a layer of finer aggregates located between the ballast and subgrade. Its function is to prevent both the penetration of coarse ballast grain into the subgrade and the migration of fine grain subgrade particles into the ballast. Indeed, the subballast separates the other 2 layers and simultaneously transmits and distributes the stress from the ballast into the lower layers.

The subgrade could be either naturally deposited soil or artificially placed fill material. The subgrade is the ultimate foundation for the track structure (Indraratna et al. 2006).



(a) Side view



(b) Cross-section

Figure 2.3. Ballasted track structure components (a) side view (b) cross-section (Selig and Waters 1994)

2.3.1.2 Slab Tracks

Recent studies have indicated that slab tracks are more cost effective than ballasted tracks (Esveld 2001, Indraratna et al. 2006, Lechner 2011, Michas 2012). In different countries such as China, Japan, and Germany slab tracks were used to construct new HSR.

For new HSR lines, slab (ballast-less) tracks are being increasingly used due to several advantages they have over ballasted tracks. Compared to ballasted tracks, slab tracks are more stable both longitudinally and laterally, and they are less sensitive to differential settlement (Steenbergen et al. 2007). From an operational point of view, slab tracks are a more suitable choice for high-traffic high-speed lines because they are almost maintenance free with a long service life (Esveld 2001, Indraratna et al. 2006). Different slab track systems are used with HSRs (Michas 2012). They can be classified into 2 main types: discrete rail support systems and continuous rail systems (Table 2.1). In discrete rail support systems, the rail is fastened to sleepers and continuously, elastically supported by a concrete bearing layer either embedded in or clamped to. Table 2.1 presents different subcategories of each slab track types. Different components of several slab track systems are illustrated in Figures. 2.4 to 2.9. The main components of track systems (ballasted and ballast-less) are summarized in Table 2.2 (Michas 2012).

Table 2.1. Different Slab (Ballast-less) Track Systems (Esveld 1997, Bastin 2005, Lichtberger 2005, Michas 2012)

Subcategory	Discrete Rail Support
<i>With sleepers or blocks encased in concrete</i>	Rheda Rheda-Berlin BTD ¹ ZÜBLIN Stedef SONNEVILLE-LVT ² Heitkamp SBV ³ WALO
<i>Sleepers on top of an asphalt-concrete layer</i>	ATD ⁴ BTD SATO ⁵ FFYS

Table 2.1. Continued

Subcategory	Discrete Rail Support
<i>Sleepers on top of an asphalt-concrete layer</i>	Getrac Walter
<i>Prefabricated concrete slabs</i>	Shinkansen Bögl ÖBB-Porr IPA
<i>Monolithic designs</i>	Rasengleis (Lawn track) FFC ⁶ Hochtief BES ⁷ BTE-BWG/HILTI PACT ⁸
	Continuous Rail Support
<i>Embedded rail structure</i>	Deck-Track INFUNDO -Edilon BBERS ⁹
<i>Clamped and continuously supported rail</i>	Cocon Track ERL Vanguard and KES SFF ¹⁰ SAARGUMMI

¹BTD: BetonTragschicht mit Direktauf Lagerung - Concrete supportive layer with direct support

²LVT: Low Vibration Track

³SBV: Schwellen mit BitumenVerguss (German) - Sleepers with bituminous poured mass

⁴ATD: AsphaltTragschicht mit Direktauf Lagerung - Asphalt rail span with direct Support

⁵SATO: Studiengesellschaft Asphalt Oberbau - study group for asphalt superstructure

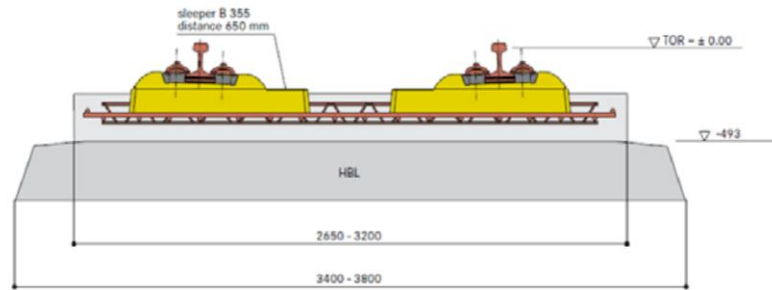
⁶FFC: Feste Fahrbahn Crailsheim - Slab track Crailsheim

⁷BES Betontragschicht mit Einzelstützpunkten - Concrete bearing layer with individual support points

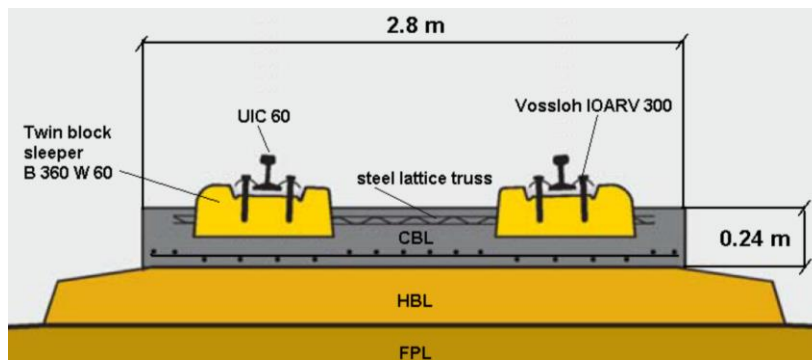
⁸PACT: Paved Concrete Track

⁹BBERS: Balfour Beatty Embedded Rail System

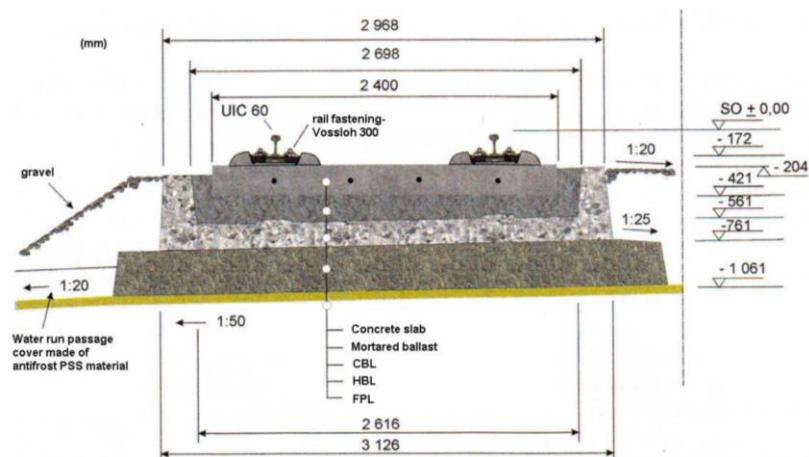
¹⁰SSF: Schwingungsgedämpfte Feste Fahrbahn - Vibration damped slab track



(a) Rheda system (Michas 2012)

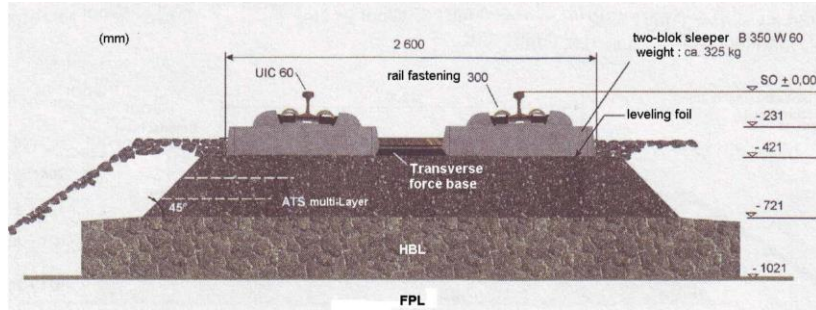


(b) ZÜBLIN system (Michas 2012)

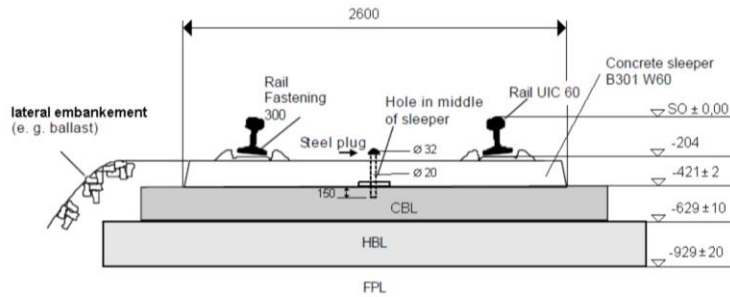


(c) Heitkamp slab track system (Darr and Fiebig 2006)

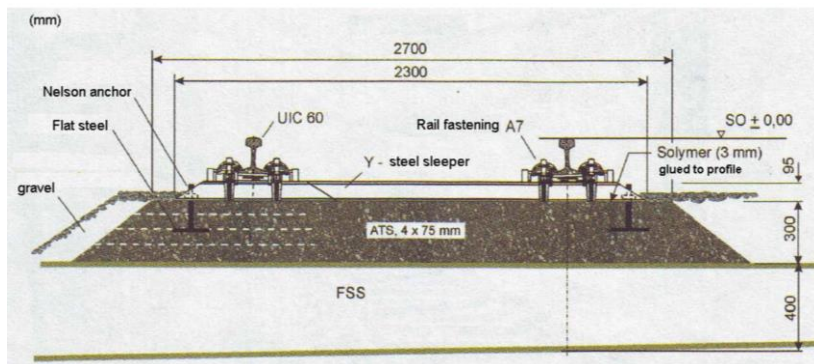
Figure 2.4. Components of some discrete rail support systems using sleepers or blocks encased in concrete



(a) ATD (Darr and Fiebig 2006)

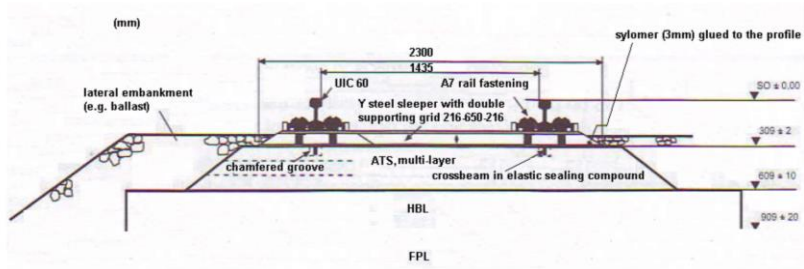


(b) BTD (Darr and Fiebig 2006; Franz 2001)

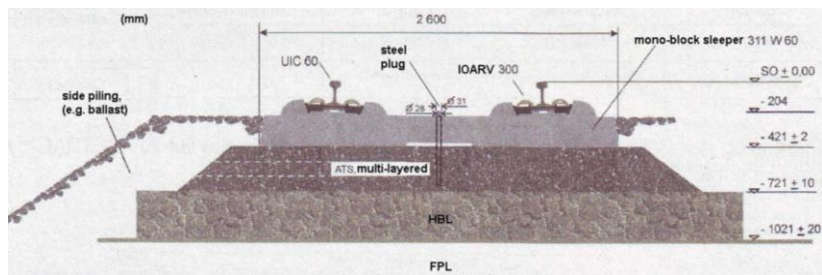


(c) Sato (Darr and Fiebig 2006)

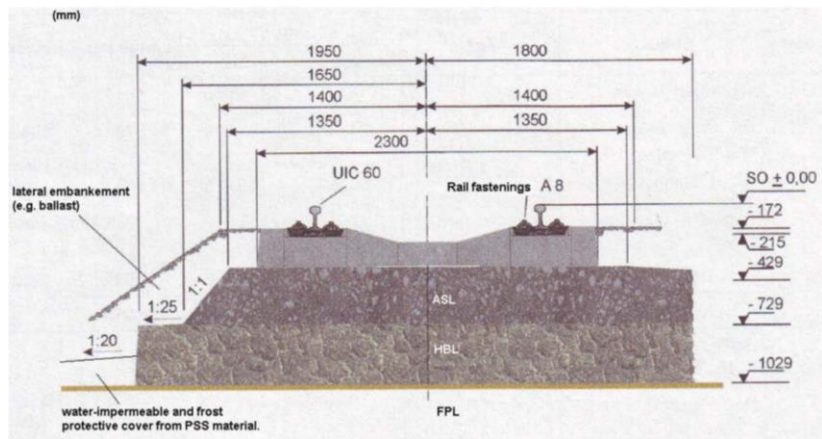
Figure 2.5. Components of several different discrete rail support systems in the subcategory sleepers on top of an asphalt-concrete layer



(d) FFYS system (Darr and Fiebig 2006)

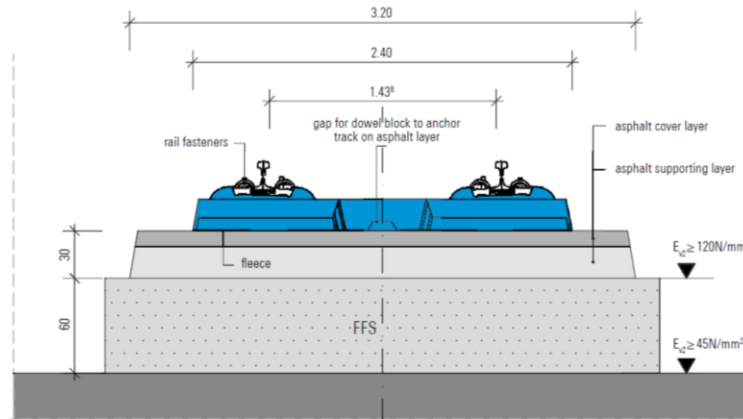


(e) Walter (Darr and Fiebig 2006)



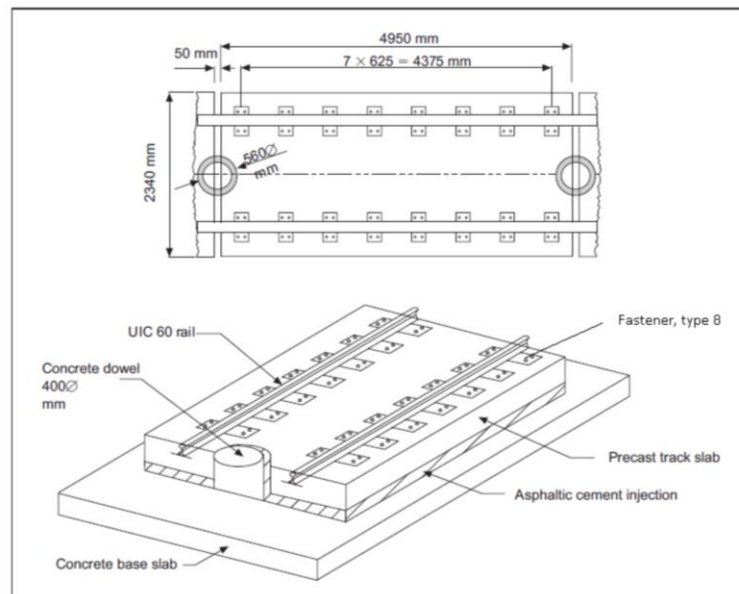
(f) FFBS-ATS-SATO (Darr and Fiebig 2006)

Figure 2.5. Continued



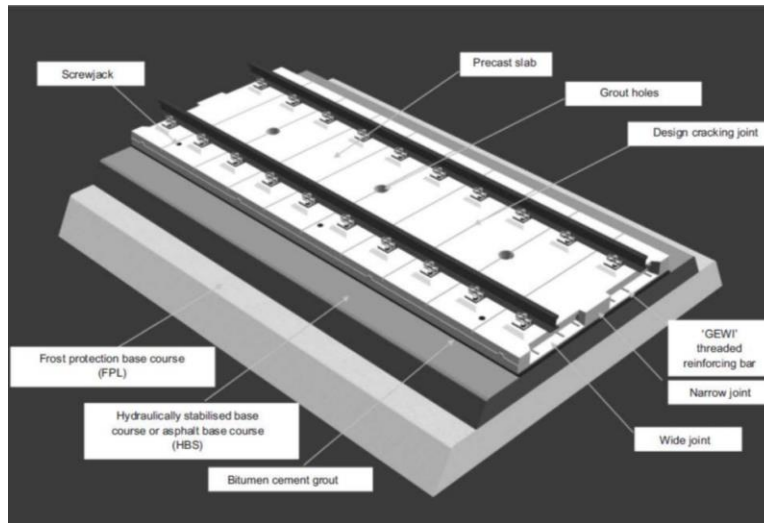
(g) Getrac A3 (Michas 2012)

Figure 2.5. Continued

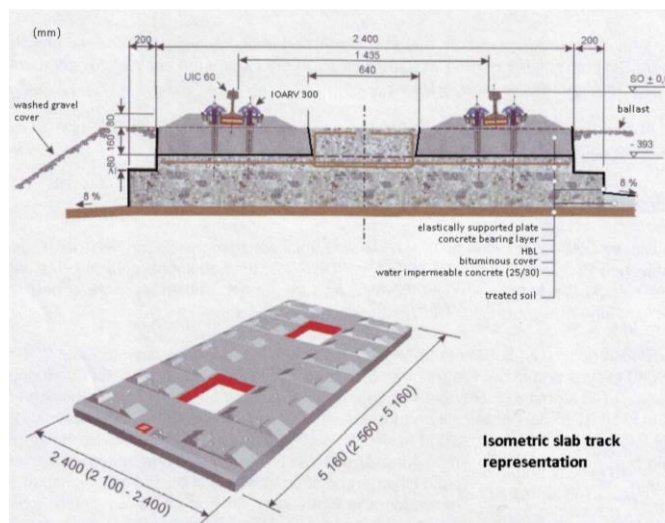


(a) Shinkansen (Bastin 2005)

Figure 2.6. Components of several discrete rail support systems in the subcategory prefabricated concrete slabs

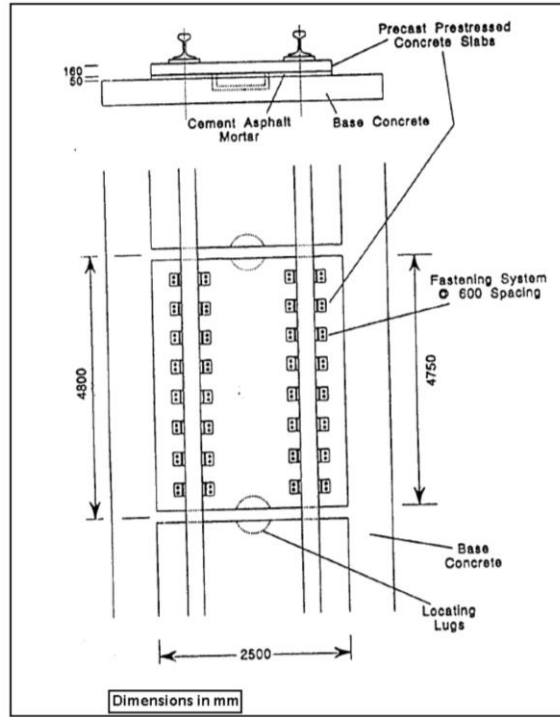


(d) Bögl (Bastin 2005)



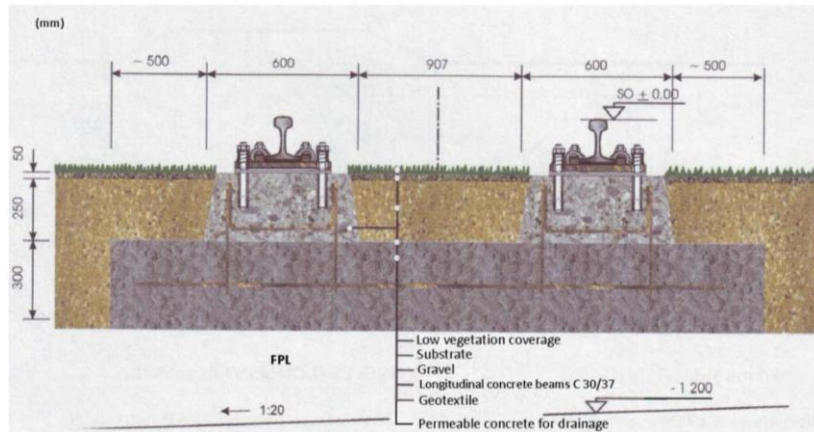
(c) ÖBB-Porr system (Darr and Fiebig 2006)

Figure 2.6. Continued



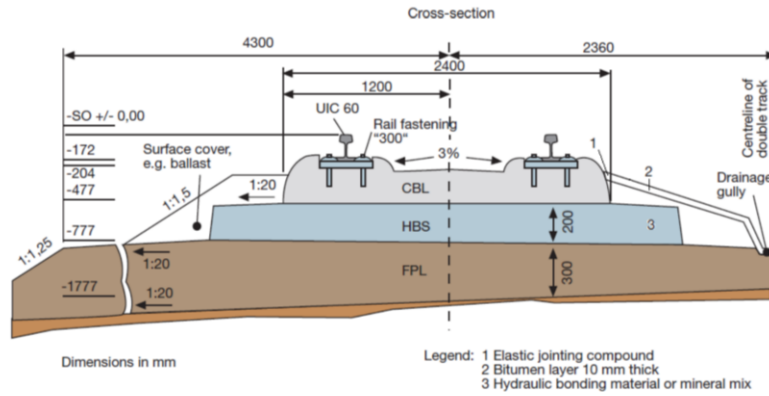
(d) IPA (Round 1993)

Figure 2.6. Continued

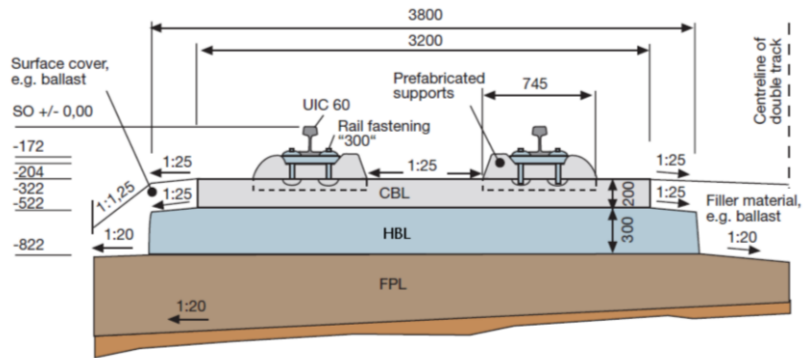


(a) Rasengleis, or Lawn track (Darr and Fiebig 2006)

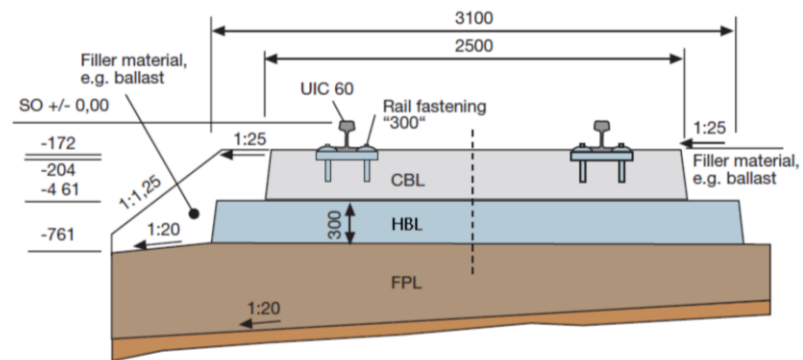
Figure 2.7. Components of several monolithic design, discrete rail support slab track systems



(b) FCC (Darr and Fiebig 2006)

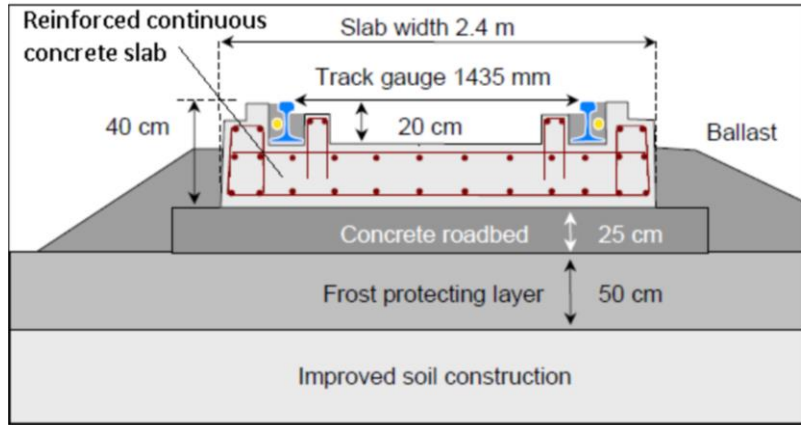


(b) Hochtief/SHRECK-MIEVES/LONGO (Darr and Fiebig 2006)

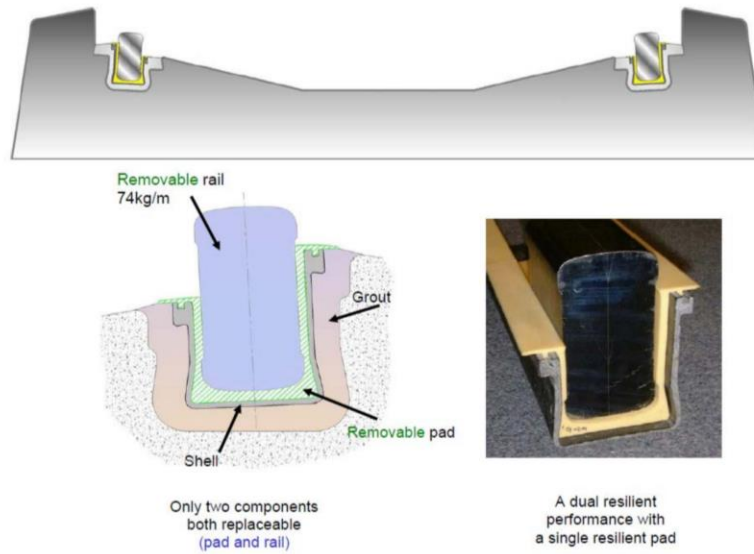


(c) BES (Darr and Fiebig, 2006)

Figure 2.7. Continued

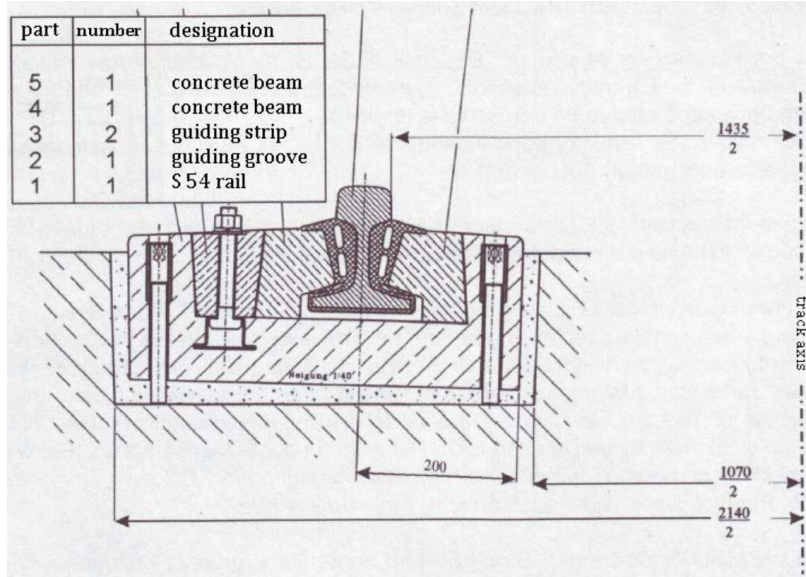


(a) INFUNDO (Esveld 1997)

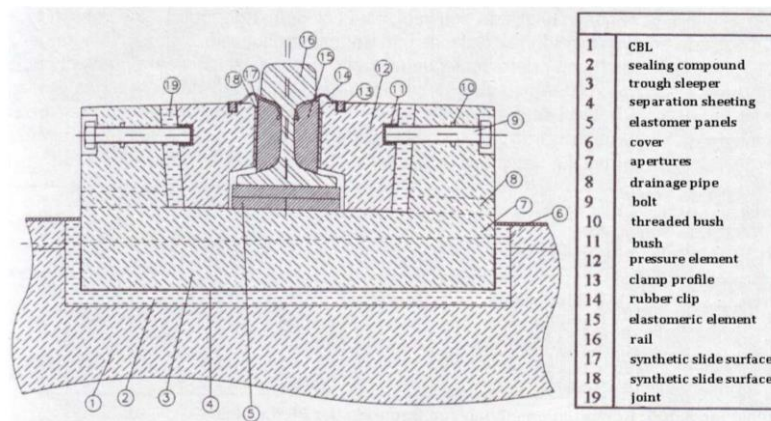


(b) BBERS (Penny 2009)

Figure 2.8. Components of 2 Continuous rail support systems, subcategory embedded rail structures



(a) SFF (Darr and Fiebig 2006, Lichtberger 2005)



(b) SAARGUMI (Darr and Fiebig 2006; Lichtberger 2005)

Figure 2.9. Components of 2 continuous rail support systems in the subcategory clamped rail structures

Table 2.2. Components of Ballasted and Slab Tracks (Michas 2012; Nigel and Franz 2001)

Component	Ballasted Track	Ballast-less Track
<i>Superstructure</i>	<ul style="list-style-type: none"> ▪ Rail ▪ Rail fastening ▪ Rail supported by sleeper: <ul style="list-style-type: none"> ○ Normal transverse beams ○ Innovative solution as frame or ladder ▪ Ballast 	<ul style="list-style-type: none"> ▪ Rail ▪ Rail fastening ▪ Rail supported by sleeper: <ul style="list-style-type: none"> ○ Discrete with sleeper or support points ○ Continuous support with embedded or clamped rails ▪ CSL or ASL ▪ HBL¹
<i>Substructure</i>	<ul style="list-style-type: none"> ▪ Upper, non-bonded, supportive layer, possibly as frost protection layer ▪ Lower non-bonded supportive layer: Earth works with compressed or improved embankment or cut formation ▪ Foundation possibly compressed 	<ul style="list-style-type: none"> ▪ Upper, non-bonded, supportive layer: frost protection layer ▪ Lower non-bonded supportive layer: Earth works with compressed or improved embankment or cut formation ▪ Foundation possibly compressed

¹ HBL: Hydraulically Bonded Layer

2.3.2 Track Stiffness

Track stiffness is a fundamental design parameter of tracks (Selig and Li 1994, Selig and Waters 1994, Berggren 2009). The standard definition is the vertical track load per unit length of rail per unit track deflection (Berggren 2009). This parameter plays an influential role in the bearing capacity of track, the dynamic behavior of operating trains,

track lifetime, and track geometry. High track stiffness leads to decreased track deflection and, consequently, helps reduce track deterioration. At the same time, high track stiffness results in increased dynamic interaction force between the wheels and rails as well as sleepers and ballast, and as a result, it causes fatigue of track and its components. Track irregularity or uneven vertical settlement is also the result of variation in train/track interaction force which happens due to changes in track stiffness (see section 5). Changes in track stiffness increase the vibration problems (see section 4).

Track stiffness is characterized by track modulus, which is an effective parameter for determining track quality (Arnold et al. 2006, Berggren 2009). All components of the track structure, both superstructure and substructure components, have an influence on the track modulus (Farritor 2006). Although much research and many publications on different methods of quantifying track stiffness have been produced since the early days of the railroad industry, a reliable method is still not available (Zarembski and Chorus 1980, Berggren 2009). In addition to a discussion of track modulus and its effect on track performance, one of railway researchers' major interests, different theoretical methods used to estimate track stiffness as well as techniques for measuring track stiffness will be reviewed in this section.

2.3.2.1 Theoretical Methods

A variety of theoretical methods including the beam on elastic foundation, deflection basin, and pyramid load distribution can be applied to assess the track modulus.

In this section, the most commonly used method for a quick estimate of track modulus, the beam on elastic foundation (BOEF) method, will be reviewed.

Winkler (1897) introduced the BOEF model, also known as the beam on spring method, and it is still one of the most common methods used to represent railway tracks today (Winkler 1867, Zarembski and Choros 1980, Hay 1982, Cai et al. 1994, Kerr 2002, Norman et al. 2004). In this model, the beam represents the rail, and the springs or elastic foundation represent all other track components including all substructure and superstructure components except for the rails (Iwnicki 2006). In this simplified model, the stiffness of the springs represents the track modulus (Hay 1982).

The beam on spring model is based on the differential Equation 2.1 which governs the static response of the beam (Nicks 2009).

$$EI \frac{d^4 y(x)}{dx^4} + uy(x) = q(x) \quad (2.1)$$

where EI is the vertical flexural rigidity of the beam (rail); $y(x)$ is the vertical deflection of the beam at position x away from the load; u is the track modulus (springs' stiffness); and $q(x)$ is the distributed load induced by train wheel loads on the beam (Cai et al. 1994). The solution to Equation 2.1 for a single point load (Figure 2.10) is obtained by the following equation (Hetényi 1946):

$$y(x) = \frac{P\beta}{2u} e^{-\beta x} (\cos \beta x + \sin \beta x) \quad (2.2)$$

where β is the damping factor given by Equation 2.3 (Hetényi 1946):

$$\beta = \sqrt[4]{\frac{u}{4EI}} \quad (2.3)$$

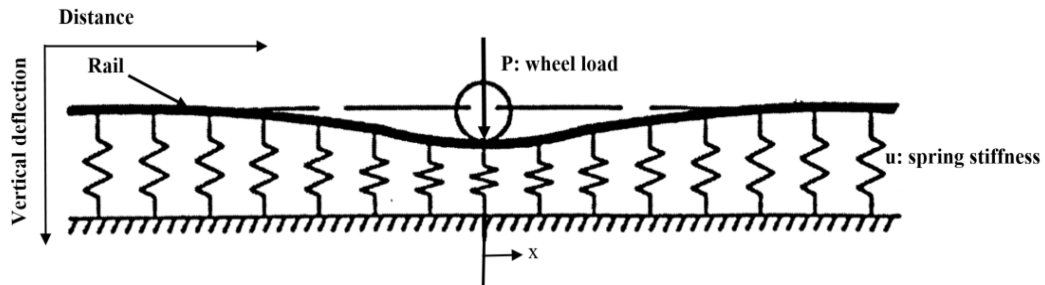


Figure 2.10. Track deflection under a single point load (wheel load) (Adapted Kerr 2000)

According to Equation 2.3, if the track deflection is known, the track modulus can be estimated with the following equation (Hetényi 1946):

$$u = \frac{1}{4} \sqrt[3]{\frac{P^4}{(EI)y_0^4}} \quad (2.4)$$

where y_0 is the maximum deflection at the point load position ($x = 0$).

2.3.2.2 Measurement Techniques

Regardless of what theoretical method is applied to calculate the track modulus, a track modulus estimate is not accurate enough. Variations in soil parameters, uneven construction impacts, loading history, geometric irregularities (Chang et al. 1980), the effects of freeze-thaw cycles (Cai et al. 1994), changes in soil water content, and so on create a situation in which too many variables interact, thus making estimates very imprecise.

Specifically, the BOEF model has another limitation: Deflection measured or calculated in this method is for a static load; however, static deflection is not actual when train speeds increase and approach the Rayleigh wave speed of the track/soil system (see section 4). Because the load is moving, particularly at higher speeds, deflection will be larger than what is measured assuming a static load (Timoshenko 1926). Track stiffness is a function of frequency. To investigate problems related to the bearing capacity of the subgrade and to ground vibrations in soft soil, measuring the track stiffness at appropriate frequencies is necessary. Therefore, measuring the track modulus at the actual moving load level seems to be necessary.

Two categories of methods are available to measure track modulus, standstill measurement and rolling measurement. In standstill methods, discrete intervals are applied for measurement; in rolling methods, track stiffness is measured continuously (Berggren 2009).

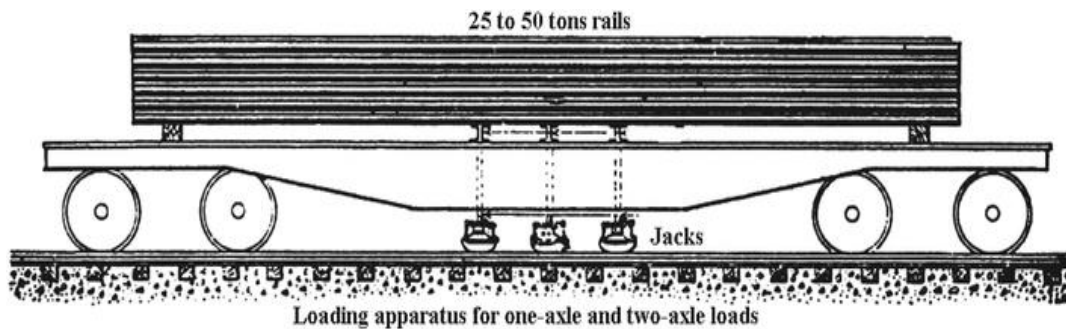
- *Standstill measurements*

Standstill measurement techniques are largely used for research purposes. In this section, the techniques simple instrumentation, the impact hammer, the falling weight deflectometer (FWD), and the track loading vehicle (TLV) are discussed.

In the simple instrumentation test, accelerometers or displacement transducers are placed on sleepers and/or rails at specific intervals. Track responses to passage of trains are then obtained as trains pass over the tracks. By knowing the train axle load, the track modulus can be calculated. To increase the accuracy, the actual dynamic load of train is measured using strain gauges on the rails or sleepers. The regular results from this method are presented in the form of measured load-deflection diagrams used for track modulus assessment (Berggren 2009). The traditional hydraulic jack-loading method is pictured in Figure 2.11. A certain force is applied to the rails while rail deflection is measured with a displacement meter. The tangent or secant modulus can then be obtained from force-displacement graphs (Wang et al. 2016).



(a) Jack-loading diagram and vertical rail displacement measurement (Wang et al. 2016)



(b) Track stiffness measurement (Kerr 2000)

Figure 2.11. General caption that explains how the two images are connected

In the impact hammer method, accelerometers set up on rails or sleepers are used to measure the track vibrations, and a force transducer on the hammerhead measures the impulse. From these measurements, the transfer function of the tracks can be obtained. A handheld hammer is used to hit the rail or sleeper, causing vibrations (Figure 2.12). Frequencies in the range of 50 to 1500 Hz are measured and recorded, and using the information obtained, a track modulus can be calculated. This device can be usefully applied to problems regarding noise, vibration, and wheel/rail interaction force because frequencies less than 50 Hz are not recorded and frequencies below 50 Hz do not affect

those 3 issues (Berggren 2009, Wang et al. 2016). However, this method is not suited for situations in which frequencies lower than 50 Hz must be measured.

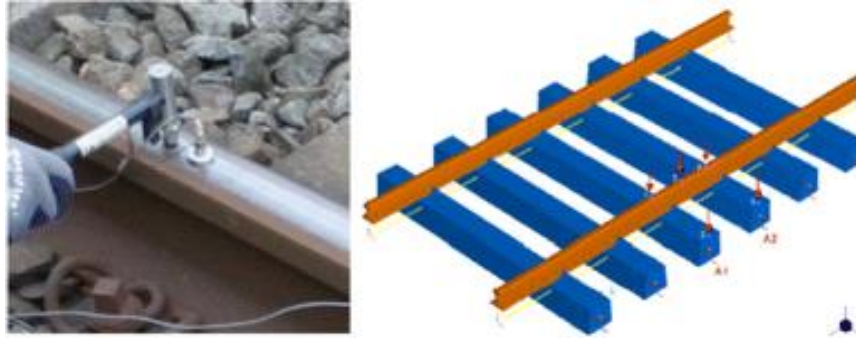


Figure 2.12. Impact hammer technique (Wang et al. 2016)

In the third technique, FWD, the vibration response of the track to a mass typically weighing 125 kN is measured by a load cell installed on the center of the plate while velocity transducers or geophones are used to assess the surface velocity at different distances (Figure 2.13) (Reddy et al. 2004, Berggren 2009, Wang et al. 2016). A transfer function is then applied to identify the track stiffness. This method is best suited for assessing the impact of running HST on tracks. In the UK, the method is designed to apply a loading pulse similar to that exerted by a single axle load of HST (Berggren 2009).

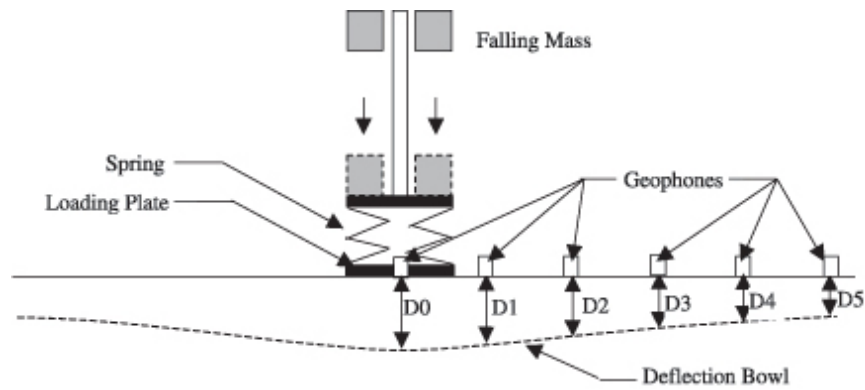
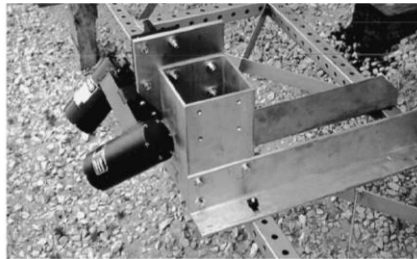


Figure 2.13. FWD technique (Reddy et al. 2004)

The TLV method was developed in the United States (US) at the Transportation Technology Center, Inc. (TTCI), a subsidiary of the American Association of Railroads (Figure 2.14) (Thompson et al. 2001, Thompson and Li 2002, Li et al. 2004a, Li et al. 2004b, Nicks 2009). This technique of estimating track modulus uses an instrumentation coach, a track loading vehicle designed especially for this test, an empty track car, a locomotive to move the TLV system, and a non-contact laser and camera system to measure the deflection (Wang et al. 2016).



(a) The track load vehicle developed by the Transportation Technology Center, Inc. (Nicks 2009)



(b) A laser and camera system being used in the track load vehicle technique (Li et al. 2004 a)

Figure 2.14. Components of the track load vehicle technique

To obtain a dynamic track modulus, two runs of the TLV system using different loads can be made. The loaded and unloaded profiles of the track (see Li et al. 2004a) are obtained for both runs. Then, using the laser and camera system, deflections for the 2 runs are measured. The dynamic track modulus can then be calculated using Equation 2.5 (Winkler model).

$$u = \frac{1}{4} \sqrt[3]{\frac{1}{EI} \left(\frac{P_1 - P_2}{y_1 - y_2} \right)^4} \quad (2.5)$$

where E is the rail modulus of elasticity; I is the moment inertia of the rail; P₁ and P₂ are the loads in the first and second runs, respectively; y₁ is the rail deflection due to P₁; and y₂ is the rail deflection due to P₂.

This method has both advantages and disadvantages. An advantage of this method is that a wider range of dynamic load and frequencies can be applied than can be used in the rolling measurement method which will be discussed below. On the other hand, it has some limitations, too; for example, the maximum train speed is 16.2 km/h (4.5 m/s) restricting the length of the track that can be measured in a reasonable amount of time. In addition, it is an expensive method due to the need of costly equipment and qualified personnel. Hence, usage of this method is limited to the railroad industries (Lu et al. 2007).

- *Rolling measurements*

While standstill measurement techniques are widely used in research, rolling or continuous measurement techniques have been used more in production measurements like maintenance purposes. A variety of rolling methods to measure track stiffness have been developed by several organizations (Berggren 2009, Wang et al. 2016). Some of these rolling measurement systems are summarized in this section.

The China Academy of Railway Science (CARS) can be considered one of the pioneers in developing a rolling method for measuring track modulus (Wangqing et al. 1997). The system designed by CARS is capable of traveling up to 60 km/h (16.66 m/s). To reduce the impact of track geometry irregularities on the track modulus assessment, a lightweight car weighing 40 kN is used in this system. A schematic view of Chinese track stiffness measurement technique is presented in Figure 2.15.

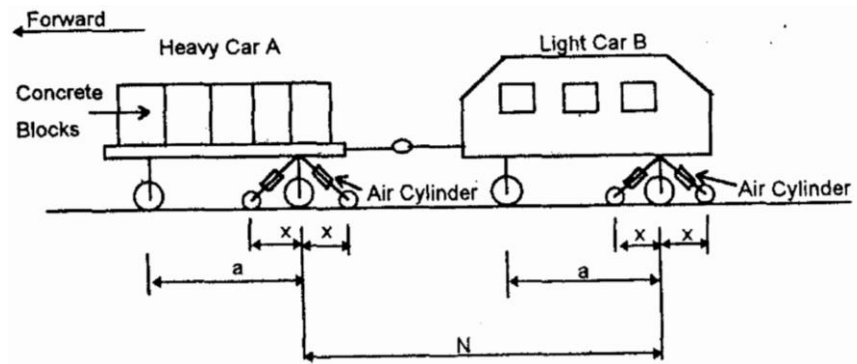


Figure 2.15. Schematic view of the rolling measurement method for track modulus developed by CARS (Wangqing et al. 1997)

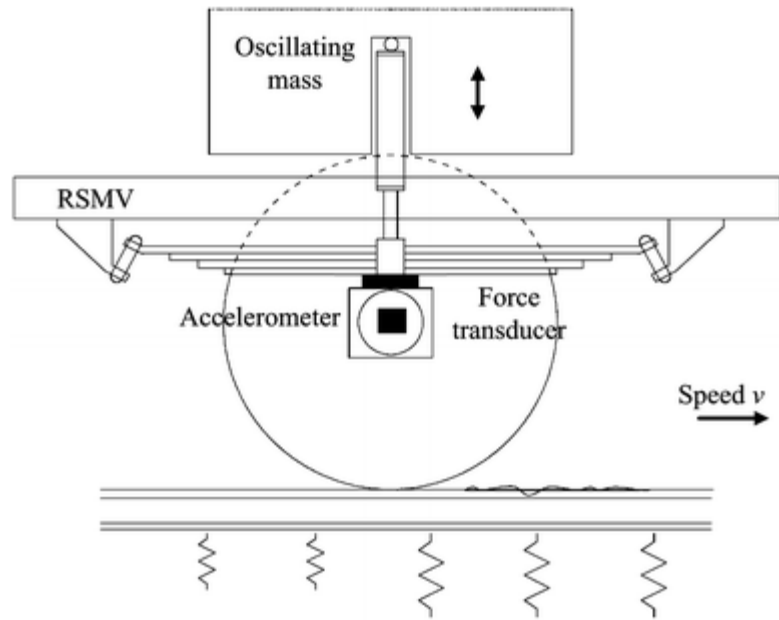
Banverket, the Swedish rail authority, developed a prototype trolley which could be used together with the Swedish TLV for rolling stiffness measurements (Berggren et al. 2002, Berggren et al. 2005, Berggren et al. 2005, Smekal et al. 2006, Berggren 2009). Subsequently, the Swedish university KTH Royal Institute of Technology developed a new device called the rolling stiffness measurement vehicle (RSMV), a two-axle freight wagon (Figure 2.16 (a)) more advanced than the Banverket prototype trolley. An RSMV can measure dynamic track stiffness of up to 50 Hz. The highest speed at which the track

modulus can be measured is 50 km/h (13.88 m/s). Track stiffness can be estimated from measured force using a force transducer and measured acceleration can be measured/estimated using an accelerometer (Figure 2.16 (b)).



(a) The KTH rolling stiffness measurement vehicle

Figure 2.16. KTH rolling measurement method for track modulus (Wang et al. 2016)

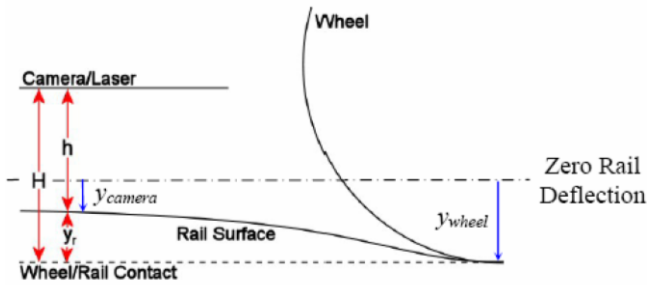


(b) Side view of measured principal of the KTH rolling stiffness measurement vehicle (RSMV)

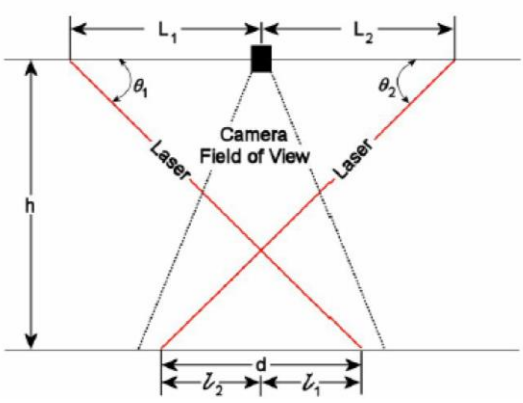
Figure 2.16. Continued

The University of Nebraska at Lincoln in the US has developed a continuous system of measuring track modulus. In this method, the relative deflection between a bogie and the rail is measured by means of a line-laser (Norman et al. 2003, McVey 2005). The relative deflection is measured by two lasers and a camera measuring the distance between the two lines called d (Figure 2.17). As the sensor moves along the rail surface, d changes; for instance, when the rail subsides into weak subgrade, d increases. The change in d is measured with camera representing the rail deflection. The Winkler model is used to relate the measured deflection to the track modulus. Track modulus measurement using technique is reliable because this technique is completely developed and its results

adequately verified. To check the quality of the track, using a reliable method to measure track modulus is essential.



(a) Principal of rail deflection measurement developed by UNL



(b) Sensor geometry of the University of Nebraska at Lincoln measurement system

Figure 2.17. Principal of rolling measurement system developed by UNL (Norman et al. 2004)

2.3.2.3 Effect of Track Components on Track Modulus

All substructural and superstructural components of the track are important in identifying the track modulus (Farritor 2006). Several studies investigating the effects of various track components on the track modulus have been done (Chang et al. 1980, Stewart and Selig 1982, Stewart 1985, Selig and Li 1994, Abu Sayeed and Shahin 2016). Although they show that all substructural and superstructural components of the track are important in identifying the track modulus, the results of these parametric studies indicate that the subgrade resilient modulus has the greatest impact on track modulus. In fact, as the subgrade modulus increases, track modulus increases (Figure 2.18) (Selig and Li 1994, Abu Sayeed and Shahin 2016). In addition to the subgrade modulus, the subgrade thickness has a strong influence on track modulus (Selig and Li 1994).

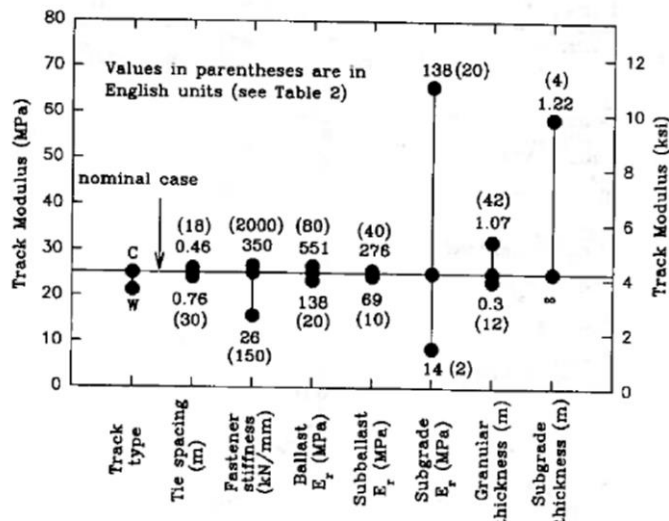


Figure 2.18. The effects of track components on track modulus (Selig and Waters 1994)

2.3.3 Track/Embankment Settlement

Track/embankment must be observed for settlement happening in two phases: immediate settlement and long-term settlement (Dahlberg 2001). Immediate settlement is defined as the static performance of the embankment and starts directly after tamping to adjusting the track position when an embankment is built (Dahlberg 2001). This settlement happens relatively fast and is due to ballast consolidation. The ballast consolidation, however, decreases over time (Sunaga 2001). In contrast to immediate settlement, Long-term settlement is slower, and it does not decrease with passing time (Sunaga 2001, Dahlberg 2001). Dahlberg (2001) believes that the relationship between settlement and time is almost linear. The long-term settlement occurs due to several basic mechanisms of ballast (granular soil) and subgrade (fine-grain soil) (Dahlberg 2001):

- Continued (after immediate settlement) ballast and subgrade compaction or grain rearrangement due to repeated train loading,
- Changing track level caused by sinking ballast in to underneath layers; indeed, this phenomenon happens due to subballast and subgrade material penetration into ballast voids.
- Particles break down causing volume reduction happening due to environmental events or repeated train load factor.
- After each loading-unloading cycle, very small portion of settlement remains unrecovered which is considered as inelastic permanent deformation of the track. This permanent deformation is a function of two factors: stress history and stress state. In case of HSR tracks, vibration caused by dynamic train loads increase the

permanent deformation increment remains in each cycle. Thus, in HSR tracks, the vibration induced by HST loading is required intensive observation and measurement to prevent ballast instability.

Track settlement is estimated using empirical models. Alva-Hurtado and Selig (1981) proposed one such empirical model which relates the total permanent strain in the granular soil layer (ballast) to the number of load cycles (N) (Nicks 2009). Alva-Hurtado and Selig's technique commonly used in the US is described in Equation 2.6.

$$\varepsilon_p = \varepsilon_1 [1 + c \log(N)] \quad (2.6)$$

where ε_p is the total permanent strain; ε_1 is the permanent strain after the first load cycle; C is a dimensionless constant controlling the rate of growth of deformation, typically ranging from 0.2 to 0.4 (Seilig and Waters 1994); and N is the number of load cycles. This method of calculating the permanent deformation response of track under repeated train loads is based on both the assumption of ballast densification and recovery on unloading ballast as well as the assumption that ballast starts in an uncompressed state (Alva-Hurtado and Selig 1981). This model, however, has several limitations as it considers neither the soil properties of the ballast and subgrade nor the stress level in the ballast layer. The factors taken into account are the number of load cycles and magnitude of the loads.

In developing a simple model to predict track deterioration, Shenton (1985) realized that the logarithmic settlement law could only be applied over a short period of time. Several factors affecting on the track deterioration including dynamic force, rail shape, sleeper spacing, ballast and subgrade types were considered. He suggested that the

logarithmic settlement law has the limitation as it can be applied reasonably over a short period of time. However, In fact, this law might considerably underestimate the settlement in the case of a large number of loading cycles. To obtain a better estimate for larger load cycles ($N > 10^6$), Shenton added the linear constant K_2 to the settlement law. Shenton's settlement equation is described in Equation 2.7.

$$y = k_1 N^{0.2} + K_2 N \quad (2.7)$$

where K_1 and K_2 are constants. Second term of this relationship is the linear term added to the settlement law only for $N > 10^6$.

2.4 Loading on Tracks

The most important factor influencing track design is the load acting on the track. Three different types of loads act on tracks: vertical, transversal, and longitudinal. However, in the current research study, only the vertical component of load is taken into account. The vertical load is sum of the static load which is the nominal train axle load, also called the wheel load and dynamic load. The dynamic load causes increase in track stress parameters due to 5 factors (Doyle 1980):

- track lateral bending
- eccentric vertical loading

- transfer of wheel load due to the rolling action of the train
- effect of train speed on the vertical wheel/rail interaction
- stiffness and geometrical irregularities and non-uniformities along track.

The effect of speed and irregularities are areas of focus in this research.

To estimate the dynamic vertical load, the dynamic vertical load is expressed as a function of the static wheel load Equation 2.8 (Doyle 1980, Banimahd 2008).

$$F_{dynamic} = (DAF)F_{static} \quad (2.8)$$

where $F_{dynamic}$ and F_{static} are the dynamic and static loads, respectively. To calculate the dynamic force using this equation, the static force is multiplied by a factor called the dynamic amplification factor (DAF). DAF is a dimensionless impact factor that is always greater than one. Several empirical formulas define DAF as a function of train speed. However, in these formulas, the effect of vertical track elasticity absorbing some of the impact on the rails was neglected. A list of different empirical models used to calculate DAF is in Tables 2.3. In Table 2.4, a comparison of the train/track parameters included in the DAF calculations is presented.

The American Railroad Engineering Association (AREA) proposed an equation to estimate DAF as a function of train speed (V_T) and wheel diameter (D) (AREA 1996):

$$DAF = 1 + 5.21 \frac{V_T(\frac{km}{h})}{D(mm)} \quad (2.9)$$

Equation 2.9 is very similar to one proposed earlier by Talbot (1918, 1920):

$$DAF=1+0.0062(V_T-8) \quad (2.10)$$

A third method of estimating the DAF is Eisenmann's (1972) statistical method (Eisenmann 1972) shown in Equations 2.11 and 2.12.

$$DAF = 1 + t\varphi \quad (V_T < 60 \text{ km/h}) \quad (2.11)$$

$$DAF = 1 + t\varphi \left(1 + \frac{V_T \left(\frac{km}{h}\right) - 60}{140}\right) \quad (60 \text{ km/h} \leq V_T \leq 200 \text{ km/h}) \quad (2.12)$$

where t is a multiplication factor which depends on the upper confidence limit (UCL), and φ is an empirical factor based on the track quality. The values for these 2 factors are given in Table 2.5. Based on the Eisenmann model, the higher the speed and the more track deteriorates, the higher the DAF.

Some researchers consider both factors, train speed and track/supporting stiffness to calculate DAF. Calrke (1957) developed the following equation for a wooden sleeper system (Banimahd 2008):

$$DAF = 1 + \frac{19.65 V}{D\sqrt{k}} \quad (2.12)$$

where k is the track modulus (MN/m/m).

Table 2.3. Summary of Models Used to Estimate the Dynamic Amplification Factor (DAF) (Adapted Doyle 1980)

No	Name of Model	Year First Published	DAF Formula ¹
1	AREA	1984	$1 + 5.21 \frac{V_T (\frac{km}{h})}{D(mm)}$
2	Talbot	1918 1920	$1 + 0.0062(V_T - 8)$
3	Eisenmann	1972	$1 + t\phi$ ($V_T < 60$ km/h) $1 + t\phi(1 + \frac{V_T (\frac{km}{h}) - 60}{140})$ ($60 \text{ km/h} \leq V_T \leq 200 \text{ km/h}$)
4	Clarke	1957	$1 + \frac{19.65 V_T}{D\sqrt{k}}$
5	Agarwal (Indian formula)	1974	$1 + \frac{V_T}{58.14\sqrt{k}}$
6	Schramm (German Formula)	1961	$1 + \frac{V_T^2}{3 \times 10^4}$ ($V_T \leq 100$ km/h) $1 + \frac{4.5V_T^2}{10^5} - \frac{1.5V_T^3}{10^7}$ ($V_T > 100$ km/h)
7	Lombard (South African formula)	1974	$1 + 4.92 \frac{V_T}{D}$
8	Prause et al. (WMATA ² formula)	1974	$(1 + 3.86 \times 10^{-5} V_T^2)^{0.67}$
9	British Railway ³	1970 1972 1974	$1 + \frac{8.784(\alpha_1 + \alpha_2)V_T}{F_{static}} \sqrt{\frac{D_j F_u}{g}}$

¹ where V_T = train speed (km/h), k = track modulus (MPa), D = wheel diameter (mm), $(\alpha_1 + \alpha_2)$ = total rail joint dip angle (radius), F_{static} = static wheel load (kN), D_j = track stiffness at joint (Kn/mm), F_u = unsprung weight at one wheel (kN), and g = gravitational constant = 9.8 m/s²

²WMATA: Washington Metropolitan Transit Authority

³Jenkins et al. (1974), Railway Gazette (1970),³and Koffmann (1972)

Table 2.4. Parameters Used in the Various DAF Formulas (Adapted Doyle 1980)

Model	Formula	Train factors						Track factors					
		Train speed	Wheel diameter	Static wheel load	Unsprung wheel mass	Center of gravity of train	Locomotive maintenance condition	Track Modulus	Track stiffness at joint	Track joint dip angle	Cant deficiency in curve	Curve radius	Track maintenance condition
AREA	$DAF = 1 + 5.21 \frac{V_T (\frac{km}{h})}{D(mm)}$												
Eisenmann	$DAF = 1 + t\phi$ ($V_T < 60$ km/h) $DAF = 1 + t\phi(1 + \frac{V_T (\frac{km}{h}) - 60}{140})$ ($60 \text{ km/h} \leq V_T \leq 200 \text{ km/h}$)												
ORE ¹	$DAF = 1 + \alpha^2 + \beta^2 + \gamma^2$												
BR ²	$DAF = 1 + \frac{8.784(\alpha_1 + \alpha_2)V_T}{F_{static}} \sqrt{\frac{D_j F_u}{g}}$												
IR ²	$DAF = 1 + \frac{V_T}{58.14\sqrt{k}}$												
German	$DAF = 1 + \frac{V_T^2}{3 \times 10^4}$ ($V_T \leq 100$ km/h) $DAF = 1 + \frac{4.5V_T^2}{10^5} - \frac{1.5V_T^3}{10^7}$ ($V_T > 100$ km/h)												
SAR ²	$DAF = 1 + 4.92 \frac{V_T}{D}$												
Clarke	$DAF = 1 + \frac{19.65 V_T}{D\sqrt{k}}$												
WMATA	$DAF = (1 + 3.86 \times 10^{-5} V_T^2)^{0.67}$												

¹ORE: Office of Research and Experiments of the International Union of Railway (1965)

² BR: British Railway, IR: Indian Railway, and SAR: South Africa Railway

Table 2.5. Values of t and φ for Eisenmann’s DAF Model (Adapted Esveld 2001)

Probability (%)	t	Application	Track Condition	φ
68.3	1	Contact stress, subgrade	Very good	0.1
95.4	2	Lateral load, ballast bed	Good	0.2
99.7	3	Rail stresses, fastenings, supports	Bad	0.3

A simple was developed to combine the effect of train speed, unsprung mass and track irregularities (Jenkins et al. 1974, Railway Gazette 1970, and Koffmann 1972). This model was proposed for a discrete irregularity like dipped rail joint (Doyle 1980). The DAF can be defined by following equation (Doyle 1980):

$$DAF = 1 + \frac{8.784(\alpha_1 + \alpha_2)V_T}{F_{static}} \sqrt{\frac{D_j F_u}{g}} \quad (2.13)$$

where $(\alpha_1 + \alpha_2)$ is total rail joint dip angle (radius); F_{static} is static wheel load (kN); D_j is track stiffness at joint (Kn/mm); F_u is unsprung weight at one wheel (kN); and g is gravitational constant (m/s^2). This model was developed for British main line condition. Figure 2.19 gives the dynamic wheel load due to train striking a dip rail joint at different speeds.

One of the most complete model to estimate DAF is the one proposed by ORE. This model is entirely based on track measurements (ORE 1965). DAF can be determined in terms of three dimensionless speed coefficients α' , β' , γ' as it comes in following equation (Doyle 1980):

$$DAF = 1 + \alpha' + \beta' + \gamma' \quad (2.14)$$

where α' and β' related to the mean value of the DAF and γ' is related to the standard deviation of the DAF. Different factors such as the level of the track, the suspension

system of the train, and train speed have strong impact on the coefficient α' . α' can be determined by the equation 2.15 (Doyle 1980):

$$\alpha' = 0.04\left(\frac{V_T}{100}\right) \quad (2.15)$$

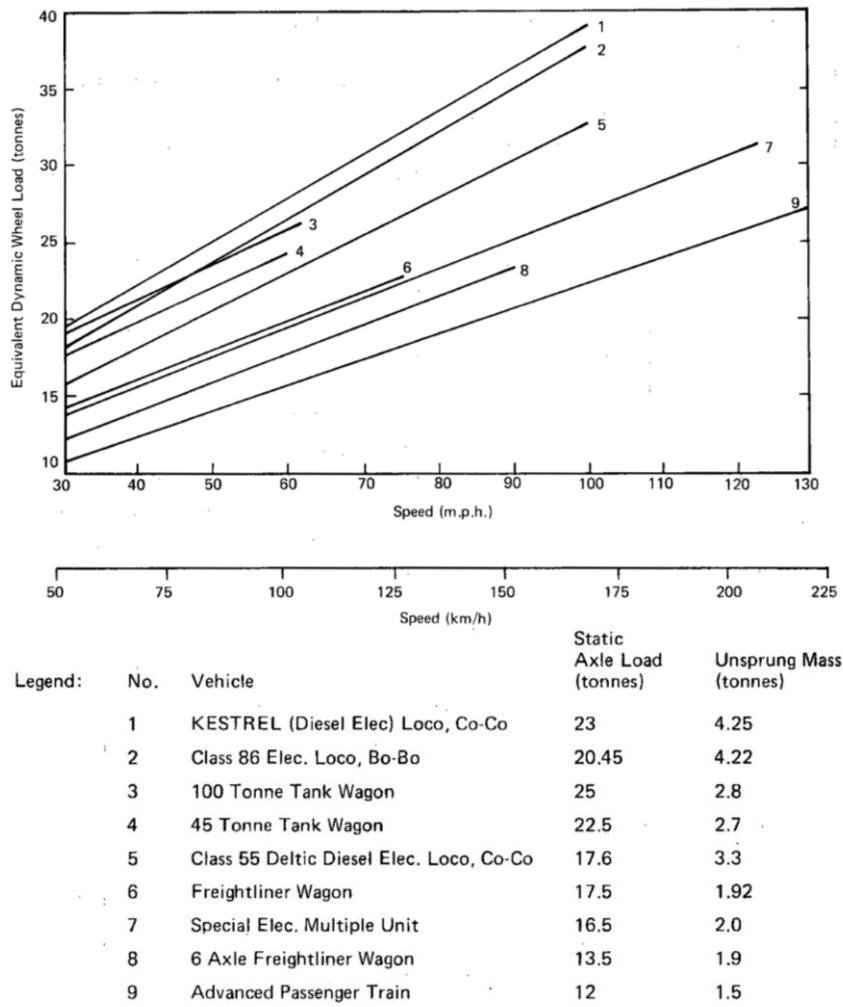


Figure 2.19. Dynamic wheel loads on BR as a function of train speed, static axle load, and unsprung masses (Railway Gazette 1970)

Variety of factors like train speed, track deficiency, and the center gravity of the train affecting the coefficient β' . This coefficient can be estimate by either the French (SNCF) equation (Equation 2.16) or the German (DB) formula (Equation 2.17) (Doyle 1980).

$$\beta' = \frac{2d.h}{g^2} \quad (2.16)$$

$$\beta' = \frac{V_T^2(2h+c)}{127Rg} - \frac{2c.h}{g^2} \quad (2.17)$$

where g is gauge width (m); h is height of the center of gravity of the train (m); d is suspension deficiency (m); R is radius of curve (m).

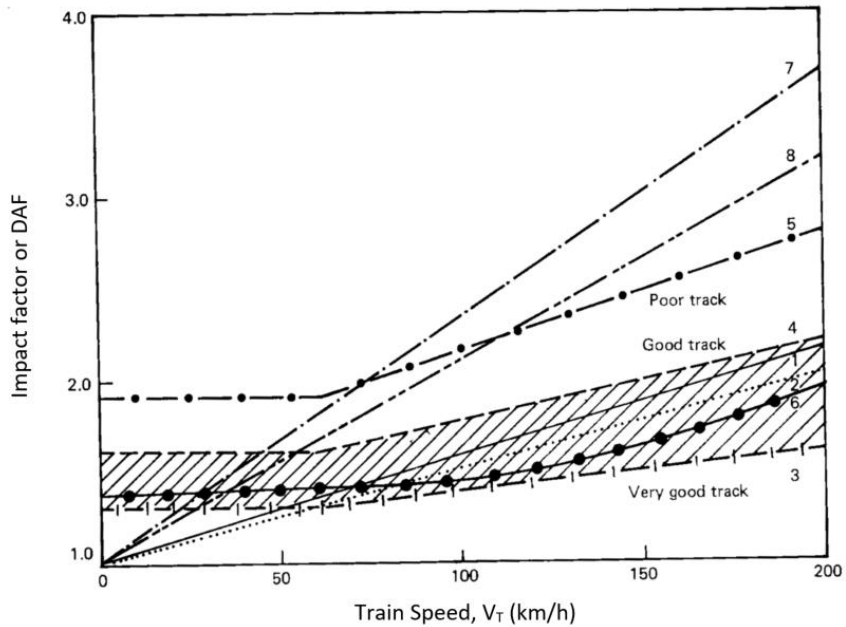
The coefficient γ' depends on different factors such as the train speed, the track age, the possibility of hanging sleeper, the train design, and the maintenance condition of the locomotive. Equation 2.18 was developed to estimate γ' unless the experimental data are available (Doyle 1980).

$$\gamma' = 0.1 + 0.017\left(\frac{V_T}{100}\right)^3 \quad (2.18)$$

Equation 2.18 can be used as a first approximation.

Figure 2.20 shows the comparison of the four main types of DAF formulas, AREA, Eisenmann, ORE, and BR. The envelope defined by Eisenmann's curve of DAF or impact factor for good to very good track conditions includes the AREA and ORE DAF curves which have been given for average track condition. In addition, DAF curve driven by

Eisenmann for poor track condition is nearly the same as DAF value given by BR formula for train hitting poorly maintained rail joint.



Legend:	No.	Formula	Remarks
	1	Area	Wheel diameter = 900 mm
	2	Area	Wheel diameter = 1000 mm
	3	Eisenmann	Very good track UCL = 99.9%
	4	Eisenmann	Good track UCL = 99.9%
	5	Eisenmann	Poor track UCL = 99.9%
	6	Ore	β' assumed = 0.20 $a_o = 1.5$, $b_o = 1.2$
	7	B.R.	Class 55 Deltic Diesel Elec. $P_s = 86.2$ kN $P_u = 65$ t
	8	B.R.	Kestrel Diesel Elec. $P_s = 112.7$ kN $P_u = 2.12$ t

Figure 2.20. The comparison of DAF formulas (Adapted Doyle 1980)

3 LONG-TERM MOISTURE SOFTENING OF COMPACTED EMBANKMENTS

3.1 Introduction

water content in soil and embankments is a fundamental factor in railway design. Moisture levels affect track stiffness, which is of key importance because of its strong impact on (1) the bearing capacity of the tracks, (2) the dynamic behavior of passing trains (i.e., higher stiffness means a reduction in the critical speed (V_C) that results in accelerated track deterioration), and (3) track deflection (i.e., higher track stiffness accelerates bump generation).

Seasonal variation of water content within compacted embankment layers and its impact on the soil modulus is a main concern for both railways (Selig and Li 1994, Berggren 2009, Sanchez et al. 2014, Cui 2014, Chen et al. 2014, Jiang et al. 2015, Bian et al. 2016) and highways (Aubeny & Lytton 2002, Aubeny and Lytton 2003, Salem 2005, Phan et al. 2008, Sawangsuriya 2009, Ng et al. 2013, Salour 2015). The variation of soil water content has a great impact on pavement and railway load capacity through soil modulus changes. Higher water content leads to a reduction in stiffness and subsequent loss of support, particularly during saturated conditions (Phan et al. 2008).

To improve understanding of the effects of seasonal moisture variation on compacted embankment stiffness, a laboratory study investigating the hydro-mechanical behavior of unsaturated soil was conducted. Any change in water content of unsaturated soil due to seasonal moisture variation is followed by a change in both water tension

between soil particles and soil stiffness. It was expected that there is a relationship between water tension and soil modulus. This research was conducted to assess the relationship between soil modulus as a mechanical property of soils and water tension between soil particles as a hydraulic property of soils. The final charts obtained from experimental study provide better understanding of unsaturated soil behavior during drying process.

3.2 Review of Previous Studies

The effects of soil moisture on rail subgrade properties along with the other main causes of subgrade problems will be reviewed here. As explained in section 2, vertical track stiffness is a basic parameter in track design and is a function of multiple parameters: the structural properties of the rails, rail pads, and sleepers as well as the properties of the ballast, subballast, and subgrade soil (Selig and Waters 1994, Berggren 2009, Nicks 2009). However, among all these factors influencing track stiffness, the most effective parameters for evaluating track stiffness are the subgrade soil properties (Selig and Waters 1994). Therefore, in this section, the subgrade problems and their main causes leading to frequent maintenance and in worst scenario subgrade failure, in addition to several influential concepts will be reviewed.

3.2.1 Subgrade Problems

The main problems leading to subgrade failure and/or high levels of required maintenance are progressive shear failure (Selig and Water 1994, Li and Selig 1995, Feng et al. 2001), excessive plastic deformation (Li and Selig 1995, Li and Selig 1998a, Li et al. 2012), and mud pumping (Saxena and Hsu 1986, Li and Selig 1995, Berggren 2009, Doung et al. 2014). To prevent these types of problems, a comprehensive understanding of the main causes of subgrade problems is necessary. Load factors, soil factors, and environmental factors are the most common causes of subgrade problems (Li and Selig 1995). When these factors act together, problems in the subgrade can develop. These causes of subgrade problems are described as follows (Li and Selig 1995):

- *Load factors:* As described in section 2, two types of loads act on tracks, static loads due to the weight of the construction materials themselves and repeated dynamic loads from passing trains. Repeated dynamic loads are the primary issue. –Of the repeated dynamic loads or traffic loads features magnitude of the dynamic wheel load and number of load cycles, the number of load cycles is more important because the subgrade behaves differently under a single load than repeated loads. This different behavior comes from the presence of fine-grained soils, such as silt and clay, in subgrade material. Such materials show a lower strength under repeated loads.
- *Soil factors:* Due to lower strength and permeability, fine-grained soil is major source of subgrade problems. Fine-grained soil strength is very sensitive to changes in soil water content, and rising soil water content in subgrade soil can

result in decreasing the strength and stiffness of material. Therefore, the performance of the subgrade is closely related to the type of soil used in the subgrade as well as to changes in soil water content.

- *Environmental factors:* Seasonal variations in water and temperatures can also affect subgrade performance. Rainfall or lack thereof, soil suction, and changes in groundwater levels can cause the subgrade to become saturated. Soil temperature is of concern because it can cause cycles of freezing and thawing which weaken the subgrade and the track materials.

Clearly, nearly all major problems regarding subgrade soil occur when the factors above act together, and most are related to high soil water content in fine-grained soil (Selig and Water 1994, Li and Selig 1995, Feng et al. 2001, Berggren 2009, Briaud 2013, Dounq et al. 2014, Chen et al. 2014; Weber et al. 2014).

These factors clearly interact. A summary of the subgrade problems and their causes is given in Table 3.1.

Table 3.1. Subgrade Problems, Their Causes, and Their Features (Adapted Li & Selig 1995)

Type	Causes	Features
<i>Progressive shear failure</i>	Repeated over-stressing	Squeezing near subgrade surface
	Fine-grained soils	Heaves in crib and/or shoulder
	High water content	Depression under ties
<i>Excessive plastic deformation (ballast pocket)</i>	Repeated loading	Differential subgrade settlement
	Soft or loose soils	Ballast pockets
<i>Subgrade attrition with mud pumping</i>	Repeated loading of subgrade by ballast	Muddy ballast Inadequate subballast
	Contact between ballast and subgrade	
	Clay rich rocks or soils	
	Water presence	
<i>Liquefaction</i>	Repeated loading	Large displacement
	Saturated silt and fine sands	More severe with vibration Can occur in subballast
<i>Massive shear failure (slope stability)</i>	Weight of train, track, and subgrade	High embankment and cut slope
	Inadequate soil strength	Often triggered by increased in water content
<i>Consolidation settlement</i>	Embankment weight Saturated fine-grained soils	Increased static soil stress as from newly constructed embankment
<i>Frost action (heave and softening)</i>	Periodic freezing temperature	Occur in winter/spring period Rough track surface
	Free water	
	Frost susceptible soils	
<i>Swelling/shrinkage</i>	Highly plastic soils	Rough track surface
	Changing water content	
<i>Slope erosion</i>	Running surface and subsurface water wind	Soil washed or blow away
<i>Soil collapse</i>	Water inundation of loose soil deposits	Ground settlement

Soil water is the main source of several subgrade problems. Thus, in this section, the main focus is the effects of soil moisture on the soil stiffness or particularly on soil modulus, specifically, the effects of various environmental conditions on subgrade performance; in fact, due to the soil softening caused by changes in soil water content, track stiffness can vary greatly, and this variation in track stiffness influences track

performance tremendously. The rest of the literature review focuses on the effects of changes in water content on the stiffness of fine-grained soils.

3.2.2 Effects of Water Content Factor on Fine-Grained Soil Stiffness

Several studies (Edil 1973, Edil and Krizek 1976, Mancuso et al. 2002, Costa et al. 2003, Inci et al. 2003, Khoury and Zaman 2004, Sawangsuriya et al. 2005, Berggren 2009, Sawangsuriya 2009, Doung et al. 2014, Chen et al. 2014, Weber et al. 2014) have addressed the effects of variation in environmental factors, particularly water content, on fine-grained soil stiffness (or modulus), which has the greatest impact on track and subgrade performance. As mentioned earlier in this section, a subgrade soil layer of fine-grained soil is strongly sensitive to changes in water. Therefore, understanding the mechanical and hydraulic behavior of fine-grained soil as water content varies is essential. Before reviewing the research regarding the hydro-mechanical behavior of fine-grained soil, some concepts should be explained more fully.

- *Water tension and suction*

The concept of water tension must be fully understood in order to understand the behavior of unsaturated soils in wet-dry cycles. Water tension is the tension in the water while suction is the potential that the water has to achieve a certain water tension. When the suction potential is fully realized, water tension will be equal to suction; otherwise, suction is higher than tension. Water tension and suction are caused by one of two things: the attraction of water molecules to the minerals in the soil particles (matric suction) or the attraction of distilled water to salty water (osmotic suction). Generally, osmotic suction is much smaller than matric suction. The sum of matric suction and osmotic suction equals the total suction. Values of total suction or water tension and water compression for a range of condition is given in Table 3.2.

Water can be in a state of either compression (pore pressure) or tension (suction). Normal water stress is considered negative when water is in tension and positive when water is in compression (Briaud 2013). The zones above ground water level (GWL) in a common case are shown in Figure 3.1. Some examples of water stress profiles under and above GWL are displayed in Figure 3.2 (Briaud 2013).

Table 3.2. Range of Water Tension and Water Compression for Different Conditions (Briaud 2013)

Water state	Examples	Water stress			Degree of saturation	Water content	Swell	Shrink
		pF	cm	kPa				
Tension ↑	Oven dry	7	-10^7	-10^6	0	0	Yes ↑ ↓ No ↓ Yes	No ↑ ↓ Yes
	Air dry	6	-10^6	-10^5				
	Shrinkage limit	4	-10^4	-10^3	Near 100 %	8 to 15 %		
	Swell limit	2	-10^2	-10^1		25 to 50 %		
		0	0	0	100 %			
Compression ↓	Large river		10^3	10^2			No	
	Deepest offshore platforms		10^5	10^4				
	Bottom of deepest ocean		10^9	10^8				

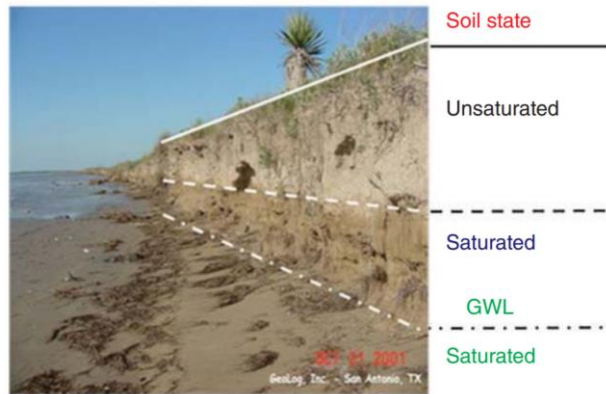


Figure 3.1. Soil state above ground water level (Briaud 2013)

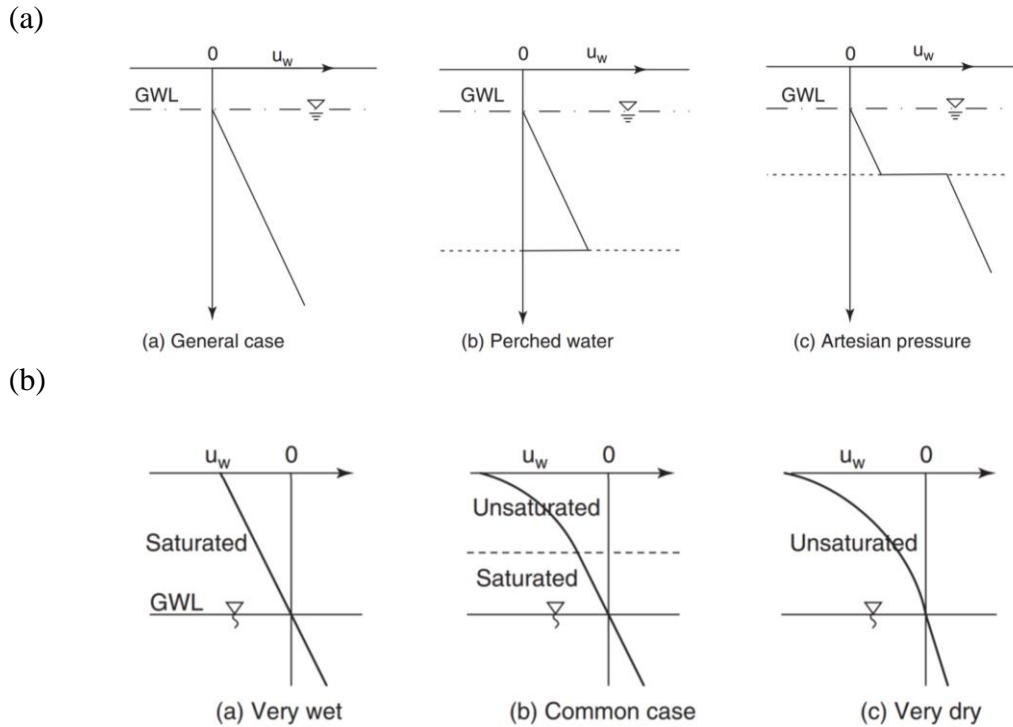


Figure 3.2. Examples of water normal stress (u_w) profile (a) below and (b) above ground water level (Briaud 2013)

- *Matric Suction*

Matric suction comes from the attraction between the water molecules and the minerals in soils. It is called capillary action if the mineral is silica. How to calculate the matric suction between two soil particles is shown in Figure 3.3. Between the GWL and the ground surface is a zone of subgrade soil that can be affected by the surface weather conditions. In this zone, the surface weather conditions can dry the soil by evaporating the water between the spherical soil particles. When the water is almost gone, the water is only found around the contact between the two particles (Figure 3.3). In this condition, the water is in tension (u_w), and the air is at atmospheric pressure (Briaud 2013). The matric

suction increases as the radius of the curvature of the meniscus forming at the surface of the soil-air interface decreases. When the vapor pressure in the water decreases, water pressure becomes more negative. Vapor pressure decreases as the degree of saturation decreases, i.e., as the soil becomes dryer. The radius of the curvature, and consequently, the matric suction, changes as the size of the soil pores varies due to soil particle size variation.

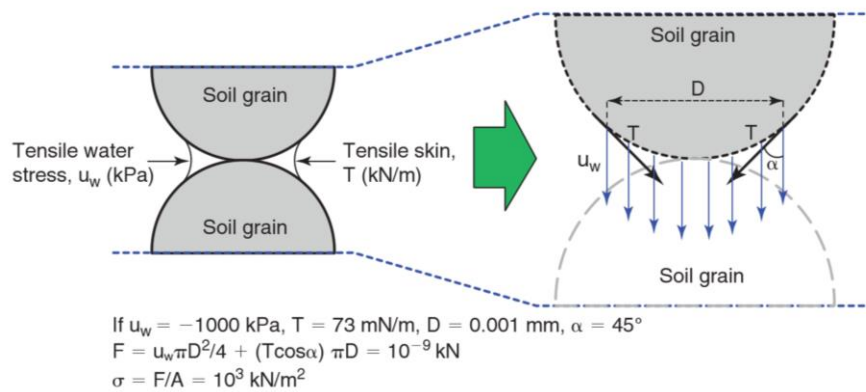


Figure 3.3. Water tension at the contact between two particles (Briaud

- *Osmotic Suction*

Osmotic suction is the attraction between water and salt in soil (Briaud 2013). Osmosis is the movement of water through a semipermeable membrane to a higher solutes concentration; therefore, a difference in elevation will be generated (Figure 3.4 (a)). A semipermeable membrane is selectively permeable, i.e., permeable only to certain molecules (Figure 3.4 (b)). Different factors including salt concentration and the type of the salt in the water influence the

osmotic suction. The higher the salt concentration is, the higher the potential for osmotic suction is (Briaud 2013). The various values of osmotic suction associated with different salt types and levels of salt concentration are presented in Table 3.3. If a soil contains dissolved salts, osmotic suction exists in this soil. This suction exists in potential, and it transfer to water tension if the salt concentration between two locations (Briaud 2013). Additionally, because osmotic suction depends only on the chemistry of the pore fluid, osmotic suction can exist in both saturated and unsaturated soils.

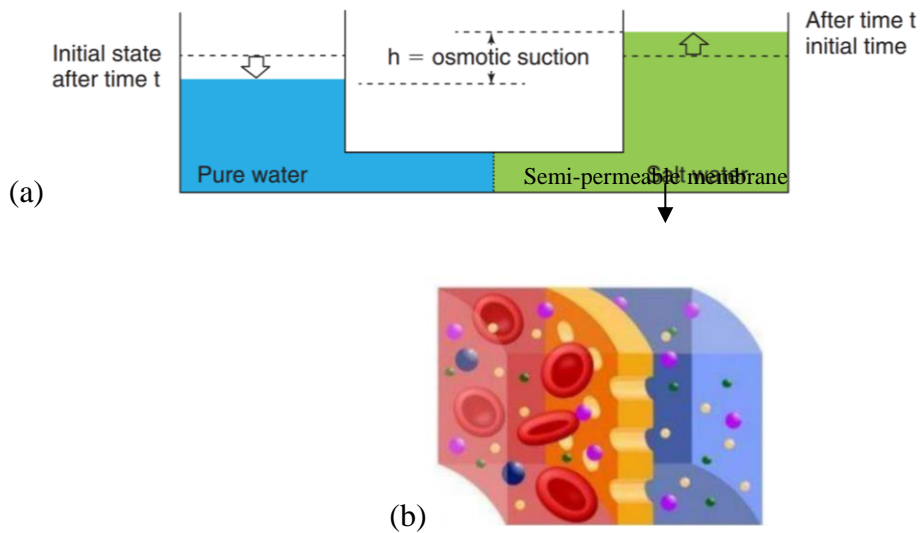


Figure 3.4. (a) osmotic suction experiment (Briaud 2013) (b) semi-permeable membrane

Table 3.3. Osmotic Suction with Various Salt Solutions at 25oC (Briaud 2013)

Osmotic Suction in kPa at 25°C							
Molality (mol/kg)	NaCl	KCl	NH ₄ Cl	Na ₂ SO ₄	CaCl ₂	Na ₂ S ₂ O ₃	MgCl ₂
0.001	5	5	5	7	7	7	7
0.002	10	10	10	14	14	14	14
0.005	24	24	24	34	34	34	35
0.010	48	48	48	67	67	67	68
0.020	95	95	95	129	132	130	133
0.050	234	233	233	306	320	310	324
0.100	463	460	460	585	633	597	643
0.200	916	905	905	1115	1274	1148	1303
0.300	1370	1348	1348	1620	1946	1682	2000
0.400	1824	1789	1789	2108	2652	2206	2739
0.500	2283	2231	2231	2582	3396	2722	3523
0.600	2746	2674	2671	3045	4181	3234	4357
0.700	3214	3116	3113	3498	5008	3744	5244
0.800	3685	3562	3558	3944	5880	4254	6186
0.900	4159	4007	4002	4384	6799	4767	7187
1.000	4641	4452	4447	4820	7767	5285	8249
1.200	5616	5354	5343	N/A	N/A	N/A	N/A
1.400	6615	6261	6247	N/A	N/A	N/A	N/A
1.500	N/A	N/A	N/A	6998	13391	7994	14554
1.600	7631	7179	7155	N/A	N/A	N/A	N/A
1.800	8683	8104	8076	N/A	N/A	N/A	N/A
2.000	9757	9043	9003	9306	20457	11021	22682
2.500	12556	11440	11366	11901	29115	14489	32776

*All suction values are in kPa.
(After Bulut et al. 2001)

- *Relationship between total suction and relative humidity*

Relative humidity (R_H) has a close relationship with total suction in soils. R_H is defined as the amount of water vapor present in air expressed as a percentage of the amount needed for saturation at the same temperature. In a sealed container with water, the humidity of the air inside will change until it comes to an equilibrium which depends on different factors such as pressure and the temperature inside the container. Typically, at 1 atmospheric pressure and a temperature of 25°C, if the air in the sealed container is dry, there is enough space in the air for water molecules to vaporize and become part of the air. This process will increase the relative humidity of the air until an equilibrium this closed system reaches equilibrium (Briaud 2013). According to the ideal gas law, the sum of all the partial pressures of the gas components in the air is equal to the air pressure:

$$p_{air} = \sum p_i \quad (3.1)$$

where p_{air} is air pressure, and p_i is the partial pressure of all gas components in the air, e.g., nitrogen, oxygen, and water. At any given R_H , the air has a corresponding partial water vapor pressure (p_{water}). For example, at 100% relative humidity, the water vapor pressure is called saturated water vapor pressure ($p_{water,sat}$) and is equal to 3.17 kPa at atmospheric pressure and 25°C. If the saturated water vapor pressure is known, the relationship between water vapor pressure and R_H can be defined by equation 3.2:

$$R_H = \frac{p_{water}}{p_{water,sat}} \quad (3.2)$$

Using Kelvin's equation, the relationship between the R_H of the air in the void of an unsaturated soil and suction potential (Ψ) can be obtained using equation 3.3 (Fredlund and Rahardjo 1993, Lu and Likos 2004):

$$\psi (Pa) = \frac{\rho_w RT}{M} \ln R_H \quad (3.3)$$

where ρ_w is mass density of water (1000 kg/m³), M is the molecular weight of water (0.01802 kg/mol), T is the absolute temperature in Kelvin, R is universal gas constant (8.3145 N m/mol K), and R_H is the relative humidity expressed as a ratio rather than a

percent (Briaud 2013). This suction potential in the void of the unsaturated soil can transfer into water tension:

$$u_w (Pa) = \frac{\rho_w RT}{M} \ln R_H \quad (3.4)$$

A simpler relationship can be defined between water tension and R_H if the same given constant values considered and at 25°C:

$$u_w (Pa) = 135000 \ln R_H \quad (3.5)$$

where R_H is taken as fraction.

- *Soil Water Retention Curve*

The soil water retention curve (SWRC) is a relationship between the water content of the soil and the water tension, or suction, in the soil pores. In fact, the SWRC shows the amount of water retained in a soil (expressed as either gravimetric or volumetric water content) under equilibrium at a given water tension stress or suction. Typically, determining accurate SWRC is not simple because water tension is more complicated to measure and the water tension or suction magnitude extends over wide range (-10 to -10^6 kPa) for the common range of water content (varies from 5% to 50%) in practical application (Tuller 2003, Briaud 2013). A study conducted by Garner (2002, unpublished) to show how the arithmetic value of suction varies a lot more than the water content

(Figure 3.5). Also, Garner (2002) has confirmed that the error band for identically prepared samples is much larger for the determination of suction in comparison to that for water content. The suction is often plotted on a logarithmic scale to approaching the error band of the log of the suction to the error band of water content.

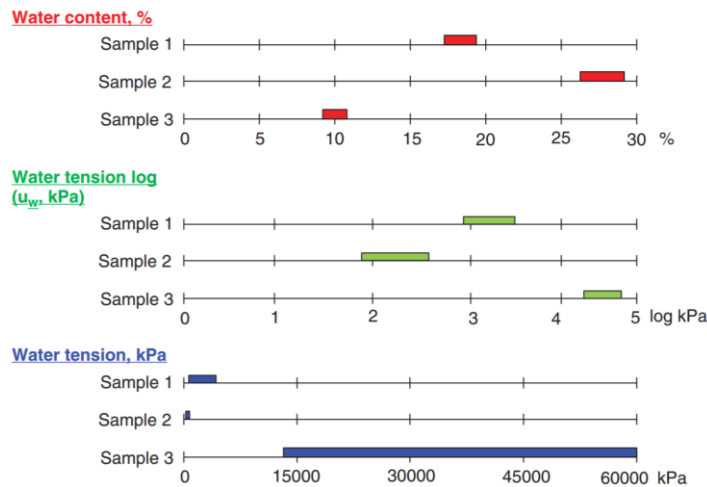


Figure 3.5. Error band for suction and water content (Briaud 2013)

In Figure 3.6, one example of SWRC is depicted, a semi-log plot. The gravimetric water content is on a natural scale; whereas, the water tension stress is on a logarithmic scale. Three different phases can be defined based on this graph. In the first phase (from A to B), the soil is saturated with increasing water tension. At point B, which is called the air entry value, the water content starts to decrease while the water tension increases. In first phase, water tension stress increases, and at a specific water tension stress (suction), called the air entry value (u_{wae}), air enters the soil pores. From this point, soil enters an unsaturated state.

In second phase (B to C), an almost a linear relationship between water content and the log of water tension in the soil exists. The water content can be defined by the following equation (Briaud 2013):

$$\Delta w = C_w \log \frac{u_w}{u_{wae}} \quad (3.6)$$

where Δw is the change in water content, C_w is the slope of the SWRC, u_w is the water tension, and u_{wae} is the air entry value of the water tension.

From point C to D, phase three, water tension continues to increase at a much higher rate compared to phase two while water content decreases.

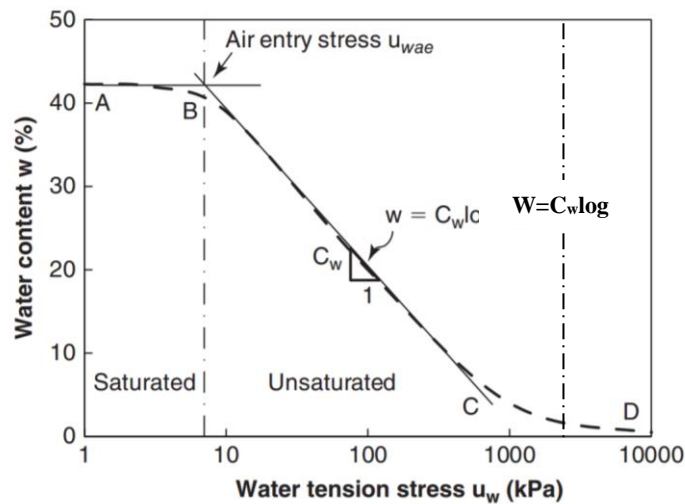


Figure 3.6. An example of a soil water retention curve (SWRC) (Briaud 2013)

The SWRC is characteristic for various types of soil and it is a hydraulic property of the soil depending on soil texture and structure (Tuller 2003, Briaud 2013). The SWRCs for different types of soils are different (Figure 3.7).

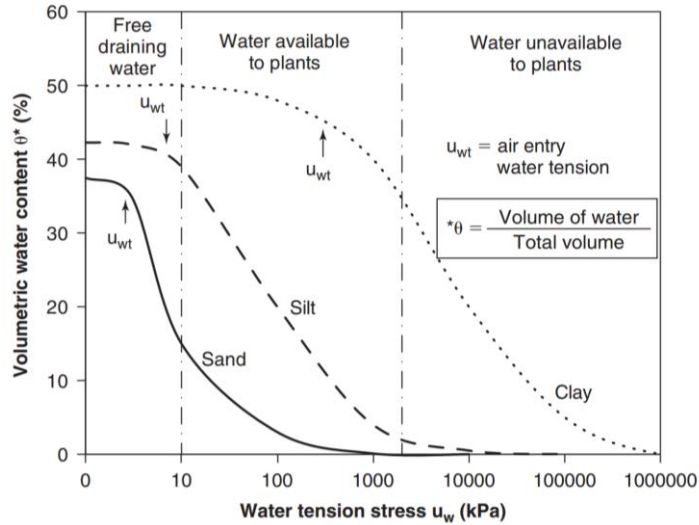


Figure 3.7. Soil water retention curves (SWRC) of different soil types (Briaud 2013)

3.2.3 Literature Review of the Effect of Water Content Variation on Soil

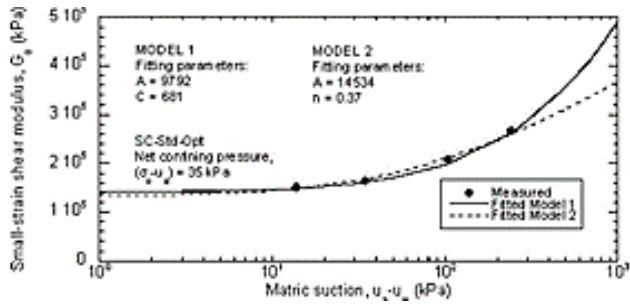
Softening

As mentioned earlier in this chapter, the subgrade consists of fine-grained soil whose modulus is strongly sensitive to the water content variation. Soil suction also plays a fundamental role in reflecting the modulus behavior of a soil (Edil 1973, Edil and Krizek 1976, Sawangsurinya 2009). Indeed, the subgrade is exposed to a change in water content

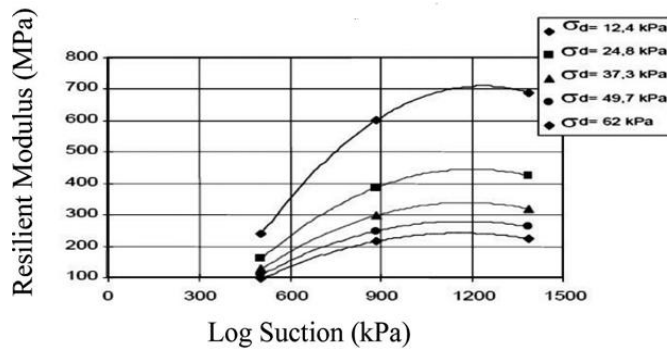
due to weather events such as heavy rainfall, floods, and drought; GWL variation; and weak drainage. These frequent dry-wet cycles impact the subgrade soil's mechanical behavior (Chen 2014 et al., Weber et al. 2014).

In the case of unsaturated soil, as the soil dries, it becomes stiffer due to increasing water tension between particles. The impact of water content and consequent suction change on the mechanical behavior of unsaturated soils has been investigated through a number of experimental studies. Such research has focused on the relationship of the suction to the soil modulus or the water content with modulus of soil (Fredlund et al. 1975, Fredlund et al. 1977, Edil and Motan 1979, Edil et al. 1981, Mancuso et al. 2002, Costa et al. 2003, Inci et al. 2003, Khoury and Zaman 2004, Sawangsuriya et al. 2005, Sawangsuriya 2009, Ng et al. 2012, Leal-Vaca, 2012, Briaud 2013, Cui 2014, Weber et al. 2014).

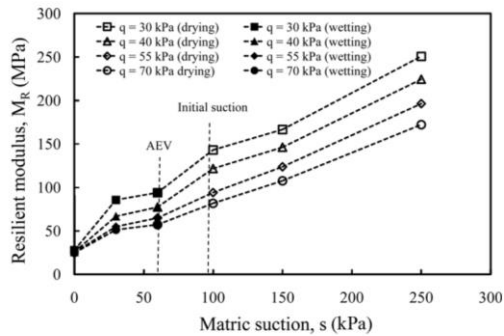
Models based on these experiments have indicated that a decrease in soil modulus can be seen as the water tension decreases and soil water content increases (Edil and Motan 1979, Edil et al. 1981, Mancuso et al. 2002, Costa et al. 2003, Khoury and Zaman 2004, Sawangsuriya et al. 2005, Sawangsuriya et al. 2009, Berggren 2009, Briaud 2013, Jiang et al. 2015, Bian et al. 2016). Some examples of these proposed model are given in Figure 3.8. Measured modulus – small-strain shear modulus or resilient modulus – depends on suction level (Edil et al. 1981, Ceratti et al. 2004, Sawangsuriya 2009, Ng et al. 2012, Weber et al. 2014). Almost all plots (Figure 3.8) show that the soil modulus increases significantly as suction increases (Edil et al. 1981, Ceratti et al. 2004, Sawangsuriya 2009, Ng et al. 2012, Weber et al. 2014). This could be due to the fact that as suction increases, the interparticle normal force increases; hence, the stiffness of the soil increases.



(a) Small-strain shear modulus vs. matric suction for the SC specimens with optimum compacted water content and subjected to a net confining pressure of 35 kPa (Sawangsurriya et al. 2009)

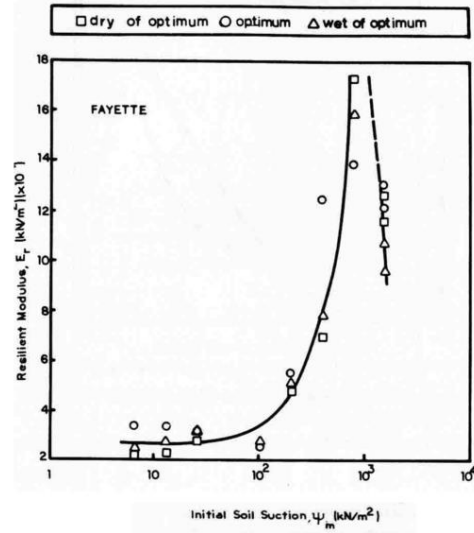


(b) resilient modulus- suction relationship (Ceratti et al. 2004)

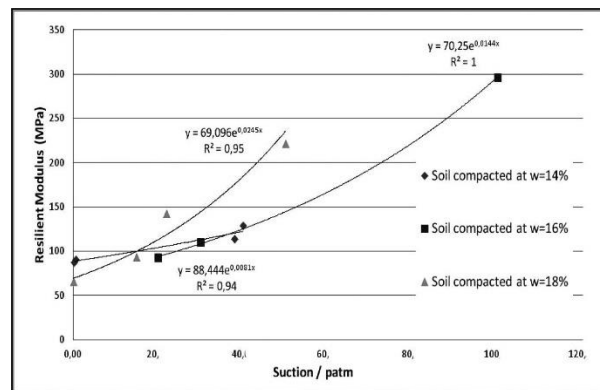


(c) resilient modulus- suction relationship (Ng et al. 2012)

Figure 3.8. Modulus –suction relationship



(d) resilient modulus- initial matric suction relationship (Edil et al. 1981)



(e) resilient modulus-suction relationship (suction is normalized by atmospheric pressure (p_{atm})) (Weber et al. 2014)

Figure 3.8. Continued

3.2.4 Soil Softening Consequences in Railroad Industry

Over time, soil softening due to water level rises in the soil can cause serious problems such as large track deflections that result in track irregularities (Banimahd 2008, Nicks 2009, Chen 2014, Bian 2016) and reduction of the critical speed (Madshus and Kaynia 2000).

3.2.4.1 Long-Term Response of HSR Track to Rising Water Levels

water content change in the subgrade of HSR has a strong impact on the cumulative settlement of the subgrade (Chen et al. 2014). This cumulative settlement over time will result in unacceptable irregularities in the form of bumps and/or dips along the HSR (Banimahd 2008, Nicks 2009, Chen 2014, Bian 2016). Train speeds are increasing worldwide, and as a consequence, track regularity is becoming even more important than before. As mentioned in section 2, vertical track stiffness is a key component in track regularity (Banimahd 2008, Berggren 2009, Nicks 2009).

In a worst-case scenario, a noticeable change in modulus can cause subgrade failure. Based on data released by the United States' Federal Railroad Administration (FRA), from 1995 to 2005, at least 861 railroad incidents worldwide were associated with weather conditions and the resulting change in modulus (Rossetti, 2007, Bian et al. 2016). An extensive, full-scale experimental study was conducted in China to check the effects of water level changes and, consequently, water content variation on cumulative

settlement of high-speed track subgrade (Chen et al. 2014, Bian et al. 2014a, Bian et al. 2014b, Jiang et al 2015, Bian et al., 2016). A schematic view of this experimental test set-up is shown in Figure 3.9. Water level is varied throughout the model's subsoil using a movable water storage tank connected to a network of branch tubes at the bottom of the subgrade with a main supply tube (Chen et al. 2014, Bian et al 2014a, Bian et al. 2016,). Subsoil, subgrade, and roadbed were made of silt, coarse sand, and graded gravel respectively. This model was used to investigate the performance of slab track system under train moving loads at various train speeds (5 to 360 km/h). Both the short-term dynamic responses and long-term accumulated settlement in two phases, before and after water level change were studied through this full-scale model testing (Chen et al. 2014, Jiang et al. 2015, Bian et al. 2016).

The accumulative settlement as a function of number of load cycles was measured at the surface of the track structure in two phases of tests as shown in Figure 3.10. The results showed that water level rising leads to considerable ascent in the accumulative settlement of subgrade.

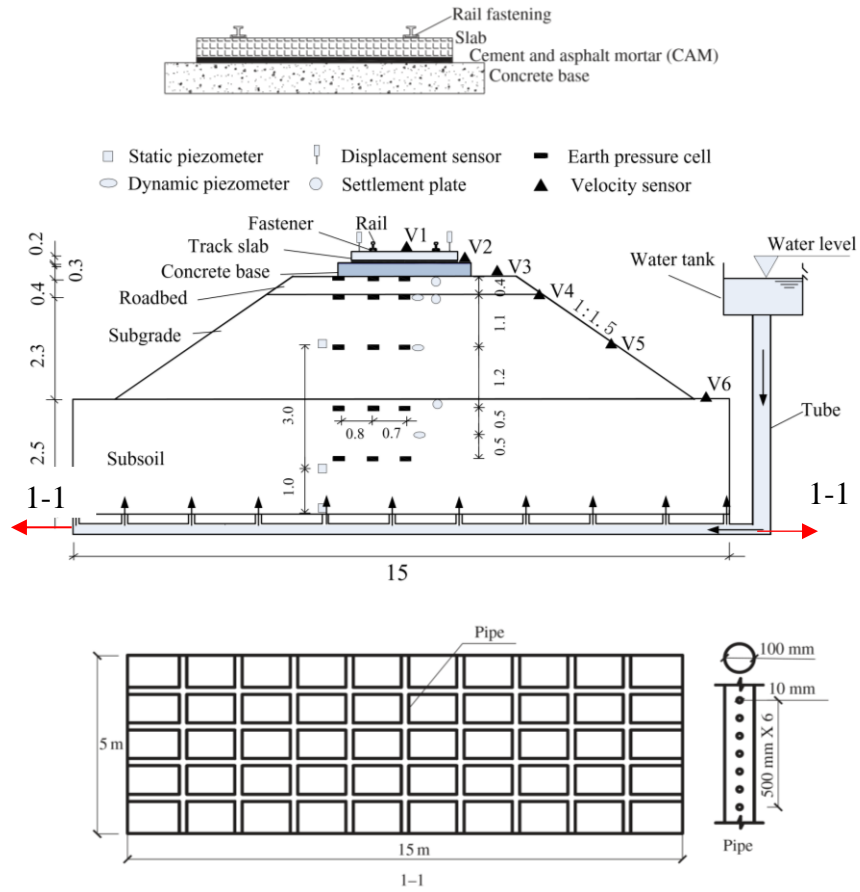


Figure 3.9. Schematics of (a) cross-sectional view of the full-scale model (b) top view of water control pipes (Chen et al. 2014; Jiang et al. 2015, Bian et al. 2016)

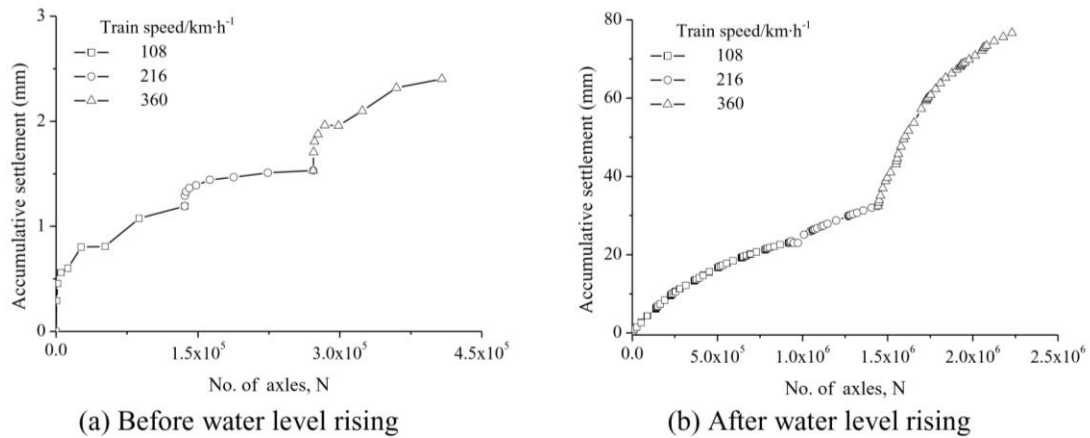


Figure 3.10. Accumulative settlement as a function of the number of train axle load passage (Bian et al. 2016)

3.2.4.2 Short-Term Response of HSR Track due to Rising Water Levels

Tests have also been done to study the short-term effects of higher water levels and water content in subgrade soils of HSR (Madshus and Kaynia 2000, Bian et al. 2016). The effects in the short term are more immediate and also dangerous; additionally, the short-term effects influence the situation in the longer term.

Madshus and Kaynia (2000) show that as the subgrade water content rises and the soil modulus decreases, the track stiffness decreases. Because the critical speed (V_C) is a function of the track stiffness, the lower the track stiffness the lower the critical speed. Therefore, when trains run on tracks in saturated soft soils, the train speed approaches the Rayleigh wave speed of the subgrade soil at lower speeds, resulting in high track vibrations at lower speeds (Madshus and Kaynia 2000).

Bian and colleagues similarly found that as the water level rises in the subgrade, the vibrations at subgrade and roadbed increase significantly by almost 35% and 107%, respectively (Bian et al. 2016). A plot of time history of vibration velocity at two locations, track slab and roadbed, before and after water level rising through compacted embankment is displayed in Figure 3.11. Maximum measured vibration velocities as a function of different train speeds at track structure and roadbed before and after water level rising are plotted in Figure 3.12. As shown in Figure 3.12, the vibration level increases as train speed and water level increases.

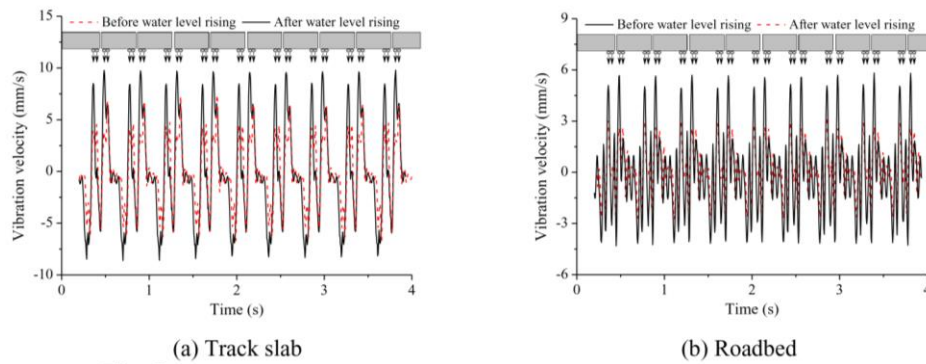


Figure 3.11. Measured time history of vibration velocity at track slab and roadbed at train speed of 216 km/h (before and after water level rising) (Bian et al. 2016)

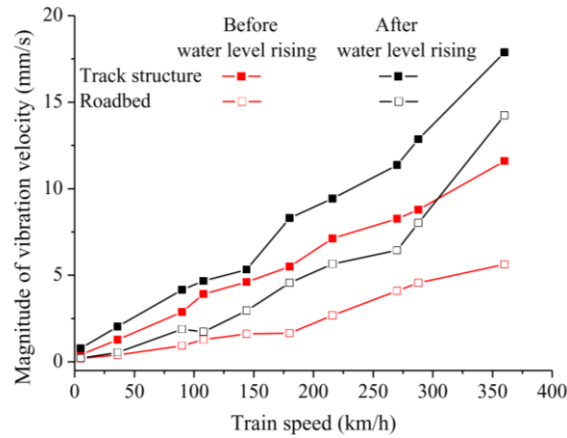


Figure 3.12. Maximum measured vibration velocity as a function of train speed at track slab and roadbed (before and after water level rising) (Bian et al. 2016)

3.2.4.3 Purpose of this Study

The current research aims to quantify the impact of water content changes caused by environmental events on porcelain clay, which is classified as a fine-grained soil modulus. To achieve this objective through laboratory testing, the effects of drying path on both the soil modulus and soil water tension were investigated. Thus, the rest of section 3 focuses on soil softening due to water content change. This process was simulated in the laboratory by measuring the soil modulus and water tension in a manmade porcelain clay for different water contents. In order to find the relationship between soil modulus and water tension, unconsolidated undrained (UU) triaxial tests, chilled-mirror psychrometer tests, and salt solution equilibrium (SSE) tests were conducted. Results obtained from these three types of tests will be combined to find the curve showing how the soil modulus changes with respect to water content and water tension changes.

3.3 Laboratory Tests

A laboratory study was performed to evaluate the effect of the moisture content change (drying path) in the soft, fine-grained soil. A fine-grained soil whose stiffness is extremely sensitive to the varied moisture content was selected for the experimental study. The experimental program included three different series of laboratory tests: UU triaxial tests followed by chilled-mirror psychrometer tests (WP4) and, lastly, SSE tests. The UU triaxial tests were carried out on the clayey soil with different water contents to study the influence of the drying process on the Young modulus of the soil. This soil parameter as a mechanical property of the soil is considered an influential parameter controlling deflection of the clayey soils. The results obtained from the UU triaxial tests will be used to assess the relationship between soil modulus and soil moisture content. The WP4 and SSE tests are used to evaluate how the moisture content of the soil impacts the water tension between soil particles. The results of the WP4 and SSE test will be plotted as an SWRC, and a graph will be created to show how the soil modulus behavior changes as the suction, or water tension, between soil particles changes.

3.3.1 Unconsolidated Undrained Triaxial Test

The UU triaxial test (ASTM D5311) is an unconfined compression test that uses a chosen confining pressure on the sample before compression occurs (Figure 3.13).

Generally, almost all triaxial tests include two phases: a consolidation phase followed by a shearing phase. In the first phase, the sample is brought to the desired stress state that the sample would face in the field at project situation. The cell pressure is gradually increased up to the chosen confining pressure. This confining pressure is applied all over the sample equally and is the representative of minor principal stress σ_3 . In fact, this pressure confines the sample hydrostatically. As the test enters the second phase, the shear phase, the vertical load Q is applied on top of the sample. As Q is gradually increased, the vertical stress, the major principal stress σ_1 , increases.

$$\sigma_1 = \sigma_3 + \frac{Q}{A} \tag{3.7}$$

where σ_3 is the confining pressure, Q is the vertical load, and A is the cross-section of the sample.

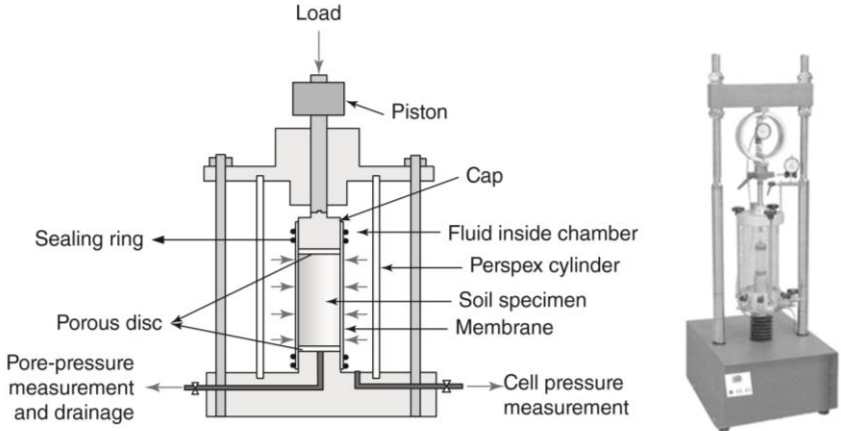


Figure 3.13. Unconsolidated undrained (UU) triaxial test set-up (Briaud 2013)

Due to the various possible combinations of drainage, type, and sequence of stress applications, different types of triaxial tests exist.

1. Unconsolidated undrained (UU) triaxial test: In a UU triaxial test, drainage is not allowed in either the consolidation nor the shear phase.
2. Consolidated undrained (CU) triaxial test: Here drainage is allowed during consolidation phase (but not in second, undrained phase).
3. Consolidated drained (CD) triaxial test: In this test, drainage is allowed in both phases.

Among these three types of triaxial tests, UU triaxial tests are the most common because they are the simplest and fastest. It was chosen because it is a reliable and accurate enough to determine the Young modulus of the fine-grained soil in this research study (Briaud 2013). The results of UU triaxial tests are presented in the form of a stress-strain plot that typically relates the deviatoric stress ($\sigma_1 - \sigma_3$) to the vertical strain ($\varepsilon = \Delta h/h$) where Δh is the change in height of the sample and h is the initial height of the sample. A deformation modulus E can be determined by applying the elasticity equation:

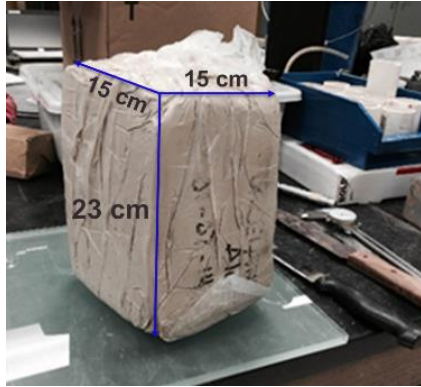
$$E = \frac{\sigma_1 - 2\nu\sigma_3}{\varepsilon_1} \quad (3.8)$$

where σ_1 is the major principal stress, σ_3 is the minor principal stress, ν is Poisson ratio, and ε_1 is the vertical strain.

3.3.1.1 Material and Specimen Preparation Method

The soil sample used in the laboratory studies was a block of porcelain clay with the dimensions 15cm×15cm×23cm (6in×6in×9in) that was well protected from moisture loss. The specimens were prepared for the UU triaxial tests as follows (Figure 3.14):

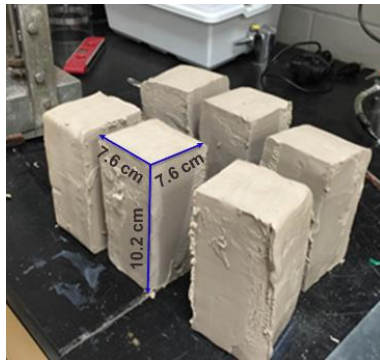
1. Each soil block was cut into twelve blocks with the dimensions of 7.62 cm×7.62 cm×10.16 cm (3in×3in×4in) as precisely as possible. Six were used in the UU triaxial tests, and the six remaining blocks were used in the SSE tests.
2. Using a trimming device, six specimens were trimmed into cylinders with a diameter of 3.81 cm (1.5 in) and a height of 7.62 cm (3.0 in) (ASTM D2850). The samples used for the UU triaxial tests require a height two times the diameter to ensure that the oblique shear plane that typically develops during failure in compression can propagate through the entire sample without intersecting the top or bottom platen (Briaud 2013). The trimmed specimen must be slightly taller than the final desired height to cut the bottom and top of specimen before final measurement recorded before running the UU triaxial test.
3. Each specimen was well protected to avoid loss of moisture. After trimming each to the proper cylindrical shape and size, they were placed in an air-tight container. All the specimens were assumed to have the same moisture content when the first test was initiated ($t_0 = 0$).



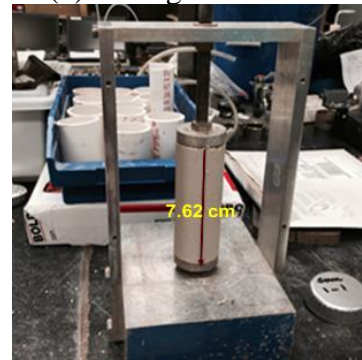
(a) block of porcelain clay



(b) cutting a soil block



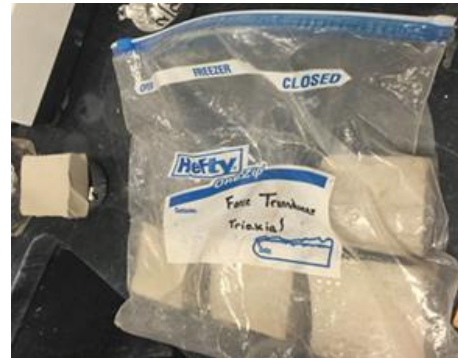
(c) six smaller blocks for the UU triaxial tests



(d) trimming the six smaller blocks to the required cylindrical shape and size



(e) protecting samples from moisture loss in a properly sealed, air-tight container

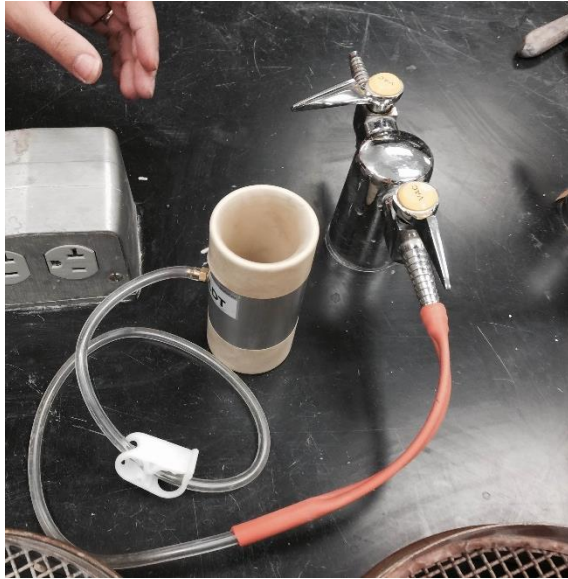


(f) the blocks used for the SSE tests cut into cubes and stored in a properly sealed, air-tight container

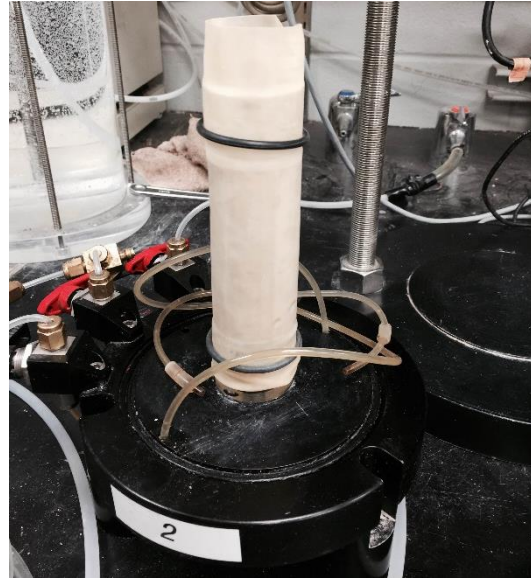
Figure 3.14. The process of creating the samples for the unconsolidated undrained (UU) triaxial tests

To start each UU triaxial test, necessary measurements must be taken; these include the wet weight of the sample, its height and diameter, and the thickness of the membrane. Then, is placed in the membrane. To do so, researchers followed these steps (see Figure 3.15):

1. First, one plastic cap was placed on the top and one on the bottom of the specimen.
2. Two o-rings were fitted near the middle of the membrane stretcher. The membrane was put inside the stretcher and folded back at two ends. Then a vacuum was applied to the stretcher.
3. The membrane stretcher was lowered over the sample until properly centered. Then the vacuum was released, and the membrane was allowed to adhere to the specimen.
4. Two more o-rings were rolled down the samples and placed at mid-height of the caps. The membrane was then folded down over the o-rings.



(a) Putting membrane inside the stretcher



(b) Prepared sample for UU triaxial test

Figure 3.15. Membrane fitting

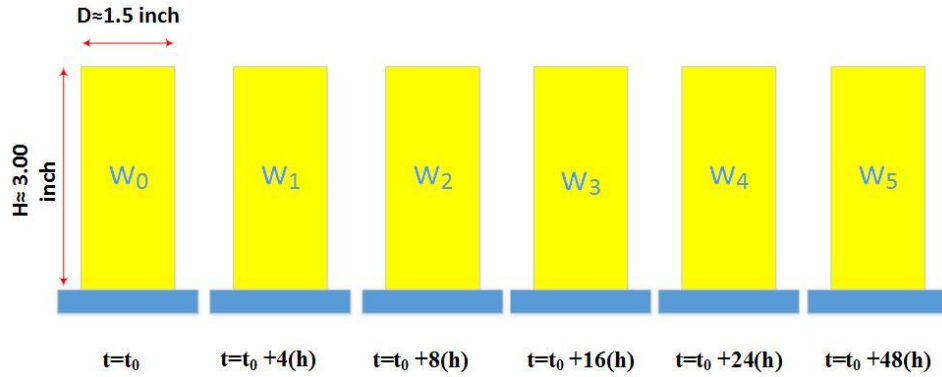
3.3.2 Test Procedures

Before unwrapping the samples, the triaxial cell was assembled. In the UU triaxial test, six specimens with different moisture content were required to calculate the effect of changes in soil moisture content on the soil Young modulus. To achieve this, all of the prepared specimens were unwrapped at the same time and put on top of the sieves to air dry as uniformly as possible (Figure 3.16).

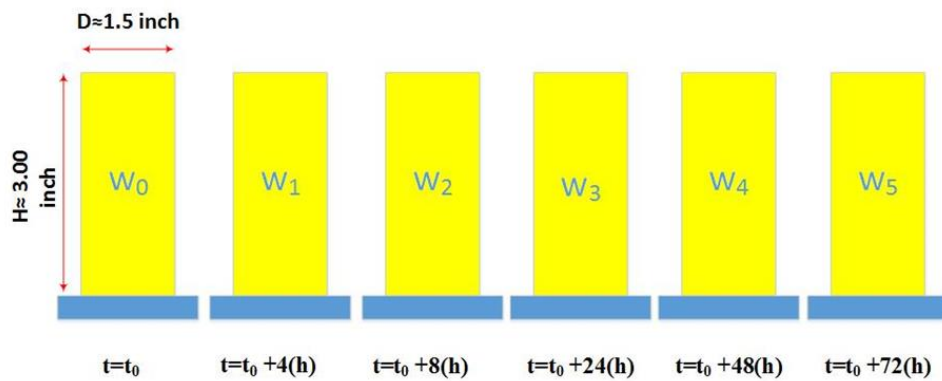


Figure 3.16. Six samples on top of the sieves to air dry uniformly

Drying times to produce uniformly varied moisture contents were chosen by trial and error (Figure 3.17). The first series of drying times tested was 0 hour (h), 4 h, 8 h, 16 h, 24 h, and 48 h. However, the first series of tests was not able to answer the research question because the samples were not dry enough; soil must be almost dry at the final drying time step. The second interval times were chosen based on the experience we obtained from the first series of tests. It was estimated that we need more time to have almost dried soil the second series of drying intervals were longer (Figure 3.17).



(a) Series 1 time interval



(b) Series 2 time interval

Figure 3.17. Two different series of time intervals leading to have soil specimens with different water content ranges

As previously described, each specimen was encased in a plastic membrane and placed in a triaxial cell for running the UU triaxial test. The piston was aligned with the top of the cap. The cell was then placed in a loading frame and the cell was filled with water. The rod in the piston was set so that it rested on the top cap in the correct position. After waiting 10 minutes (min.) waiting to reach equilibrium, the desired confined pressure was then applied as a vertical load at a strain rate of approximately 1% per min. until soil failure was reached. This represents the shearing phase of the UU triaxial test.

The computer took continuous Readings at intervals of 6 seconds and when the axial strain reached 15%, the test ended. One of the failed UU triaxial test samples is shown in Fig. 3.18. For each selected drying time, a total of six UU triaxial tests were performed to collect sufficient data which will be presented in section 3.4.1 for a graph that shows the key role of the change in soil moisture content on the soil modulus behavior as a mechanical property of soil. All the UU triaxial tests were followed by a WP4 test, which is explained later in this section. At the end, to calculate the water content of each sample, was put in the oven. Drying takes at least 12 hours in a standard oven (ASTM D 2216).

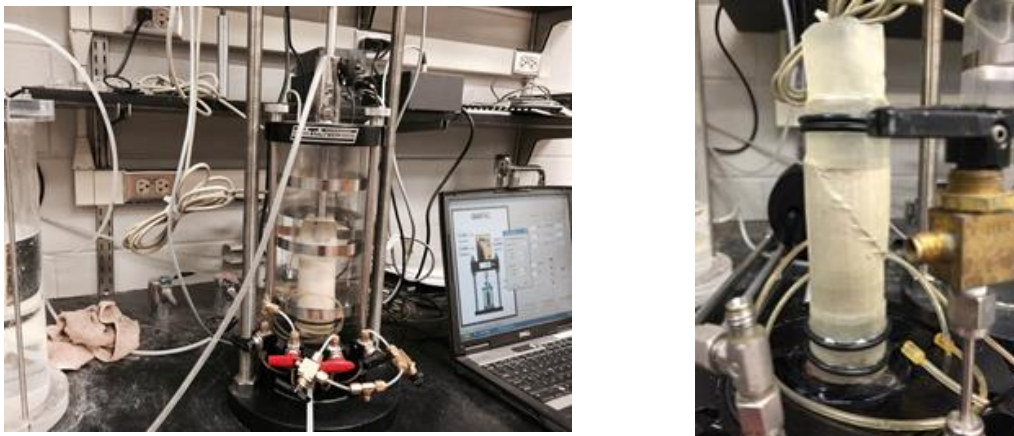


Figure 3.18. A photo summary of the UU triaxial test procedure and failure plane

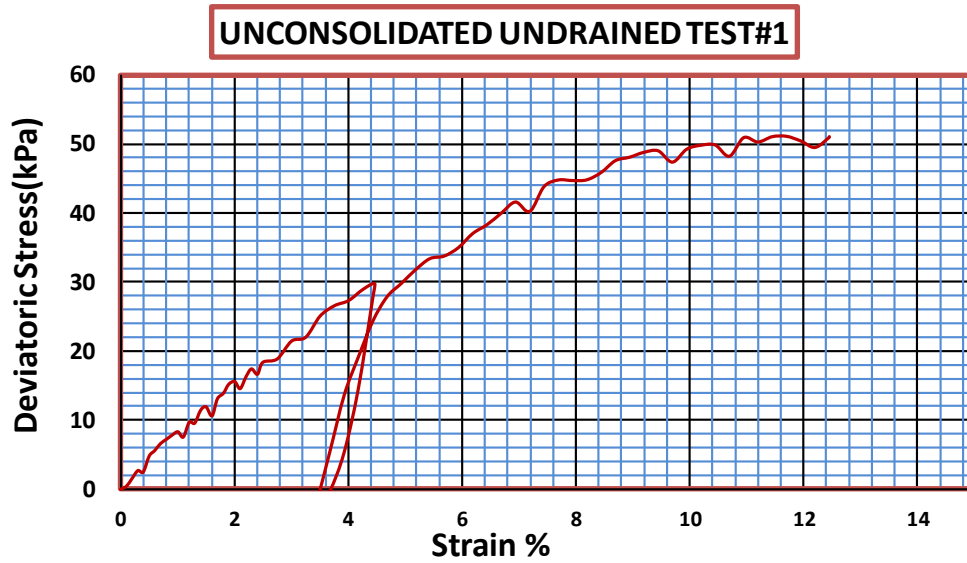
3.3.3 Data Processing

3.3.3.1 Unconsolidated Undrained Triaxial Test

The stress-strain curves obtained from the triaxial tests must be corrected for calculating the Young modulus. Using recorded Q applied to the sample during UU triaxial test, the deviatoric stress can be calculated using Equation 3.7. The assumption is made that volume does not change and the sample is axially deformed during the test; thus, the area of the cross-section of the specimen must be corrected due to cross-sectional area changes as the strain increases. The following formula was used to correct for this deformation:

$$A = \frac{A_0}{(1-\varepsilon)} \quad (3.9)$$

where A_0 is the initial cross-sectional area obtained from measuring sample dimension, and ε is vertical strain. After calculating deviatoric stress-strain (Equation 3.7), the stress-strain curve was plotted (Figure 3.19). Figure 3.19 also shows how the secant Young modulus of the sample was calculated using Equation 3.8.



(a) The stress-strain curve obtained from the UU triaxial test after correction

$$E = \frac{\sigma_1 - 2\nu\sigma_3}{\epsilon_1}$$

ϵ_1	$\sigma_1 - \sigma_3$ (kPa)	σ_3 (kPa)	σ_1 (kPa)	ν	E (kPa)
0.01	8.328	32.612	40.940	0.45	1158.908

(b) Using UU triaxial test stress-strain curve for Young modulus calculation

Figure 3.19. UU triaxial test data processing

In addition to Young modulus, the water content of the sample had to be estimated for each sample. The mass water content of the sample can be calculated from following equation:

$$w(\%) = \frac{M_{cws} - M_{cs}}{M_{cs} - M_c} \times 100 = \frac{M_w}{M_s} \times 100 \quad (3.5)$$

where w is mass water content in percent (%); M_{cws} is the mass of the container plus the wet specimen; M_{cs} is the mass of the container plus the oven dried specimen; M_c is the

mass of the container alone; M_w is the mass of the water; and M_s is the mass of the solid particles in the specimen. One example of the measured data required to calculate the stress-strain curve correction and the water content is in Tables 3.4 and 3.5.

After the UU triaxial test, each sample was cut into smaller pieces for the WP4 test. At least 6 small samples along the height of each sample were required to run WP4 tests and calculate the average value of suction along each sample. To calculate the post-WP4 test water content, again, all the six specimens in addition to remaining soils from each UU test were put in the oven to dry.

Table 3.4. Sample Information

Test series#1 at t=0				
Test No:1		TRIAXIAL DATA SHEET - UU		
Test Date: Nov. 16, 2014				
1.Sample Information				
<i>Soil Type</i>	Parcelin Clay		<i>Height (cm)</i>	7.991
			<i>Diameter (cm)</i>	3.670
2.Water Content				
<i>Before Test</i>			<i>After Test</i>	
	<i>Wet</i>	<i>Dry</i>	Table (b)	
<i>Container (g)</i>	1.50	1.50		
<i>Container + Soil (g)</i>	29.04	23.40		
<i>Soil(g)</i>	27.54	21.90		
Initial Water Content (%)		25.753	Final water content (%)	26.096

Table 3.5. Water Content Calculation

Water content After Test#1 at t=0						
Sample	Container (g)	Container + soil (wet) (g)	Soil (wet) (g)	Container + soil (dry) (g)	Soil(dry) (g)	Final water content (%)
1.1	1.50	9.43	7.93	7.80	6.30	25.873
1.2	1.50	10.71	9.21	8.85	7.35	25.306
1.3	1.50	14.21	12.71	11.56	10.06	26.342
1.4	1.50	14.39	12.89	11.75	10.25	25.756
1.5	1.50	11.10	9.60	9.06	7.56	26.984
1.6	1.50	11.59	10.09	9.46	7.96	26.759
Remain	23.70	132.34	108.64	110.16	86.46	25.653
Average water content (%)						26.096

3.3.3.2 Chilled-Mirror Psychrometer Test

To evaluate the total suction of the soil samples, each UU triaxial test was followed by a WP4 test (ASTM 6836). WP4 is the name of the device used to run the chilled-mirror psychrometer test. The test is an easy and fast way to accurately measure the suction (Briaud 2013). To run the test, the soil sample is placed in a round, plastic sample cup which is then set in a lexan sample drawer. and the drawer is inserted into a small chamber which is sealed off from the outside air by turning the knob (Figure 3.20). Depending on the size of the sample and how wet the sample is, 5 to 30 min. WP4 tests measure the relative humidity of the specimen above a sample in a closed chamber and then calculate the suction (Briaud 2013). As shown in Figure 3.20(b), a mirror is inside the sealed chamber and a thermoelectric cooler accurately controls its temperature, which enables this calculation (Alessio Ferrar et al. 2014). The air in the sealed chamber comes to relative

humidity equilibrium with the air in the soil sample. The reason this equilibrium occurs was explained in section 3.2.2. Then the mirror is chilled down to the point where dew forms on the mirror. The temperatures of the mirror and the soil at this point are recorded. The relative humidity in the soil is the calculated from the difference in temperature between the mirror at the dew point and the soil. Finally, by knowing the relative humidity, the water tension or suction can be estimates with equation 3.5.

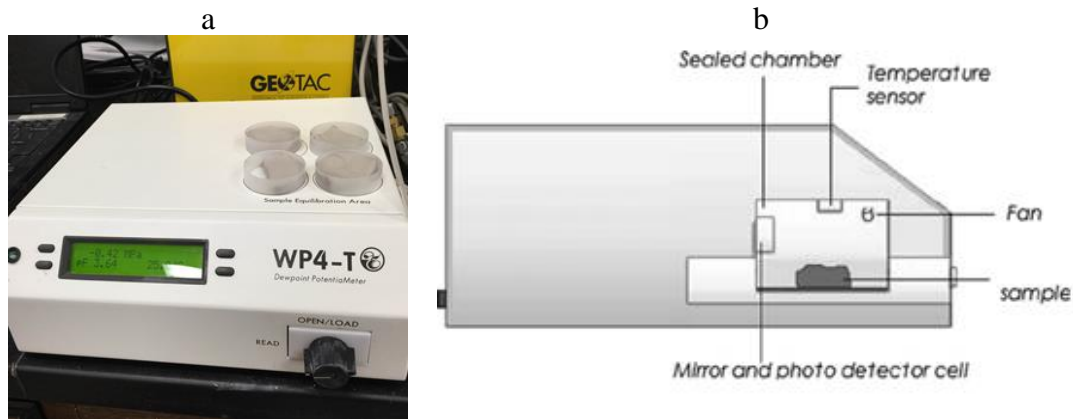


Figure 3.20. (a) a WP4 device; (b) a schematic representative of the inside of a WP4 device (Leong et al. 2003)

In this study, after each UU triaxial test, the soil sample was extruded from the plastic membrane and six small pieces of the soil were taken from each cylindrical sample and used in the WP4 tests. Thus, 6 samples were used to calculate the average value of suction in each of the six soil specimens. To estimate the suction as accurately as possible properly, preventing any change in the moisture content of the samples during the UU triaxial test and while extruding the sample from the UU triaxial chamber was crucial.

The WP4 device was set up at least 6 hours before the test. When the soil sample is inserted into device, the values for suction and temperature were displayed on a small digital window on the device as equilibrium was reached (Figure 3.20 (a)). The average of the suction values for all the samples was considered the suction for that soil specimen. To find the moisture content of each sub-specimen, each must be weighed and dried in an oven following the WP4 tests. By completing all six UU triaxial tests followed by the WP4 tests, the average value of suction and water content of the soil was obtained. In Tables 3.6 and 3.7, one example of the results is given. The outcomes of all six tests were used to evaluate the relationship between suction and soil moisture content in an SWRC plot (see section 3.4.2).

Table 3.6. WP4 Results for Suction

Table (a) Test Series #1 at t = 0				
Sample	U(MPa)	w (%)	U(pf)	T(°C)
1	0.42	25.873	3.64	25
2	0.53	25.306	3.74	25
3	0.27	26.342	3.45	25
4	0.33	25.756	3.53	25
5	0.44	26.984	3.66	25
6	0.59	26.759	3.79	24.9
Average suction (MPa)			0.430	
Average water content (%)			26.170	

Table 3.7. Water Content Calculation

Table (b) Water Content after Test#1 at t = 0						
Sampl e	Containe r (g)	Container + soil (wet) (g)	Soil (wet) (g)	Container + soil (dry) (g)	Soil (dry) (g)	Final water conten t (%)
1	1.5	9.43	7.93	7.80	6.30	25.873
2	1.5	10.71	9.21	8.85	7.35	25.306
3	1.5	14.21	12.71	11.56	10.06	26.342
4	1.5	14.39	12.89	11.75	10.25	25.756
5	1.5	11.10	9.60	9.06	7.56	26.984
6	1.5	11.59	10.09	9.46	7.96	26.759

3.3.3.3 Salt Solution Equilibrium Test

The SSE test measures suction using the osmotic suction in a salt solution. Osmotic suction comes from the tendency of a water molecule to be attracted to a salt molecule. The apparatus used in this test is a closed chamber called a desiccator in which the salt solution is at the bottom and the soil sample at the top (Figure 3.21). In this closed system, a certain relative humidity is generated in the air above the chamber. The higher the salt concentration is in the salt solution, the lower the relative humidity generated above the salt solution in the chamber will be.

Before the test, the soil was dried so that the ambient relative humidity and the water tension in the soil sample could reach equilibrium. At the point of equilibrium, the suction was calculated from the relative humidity in the chamber. The relative humidity depends on two factors: the salt concentration in the solution and the type of the salt used to make the solution (Briaud 2013).

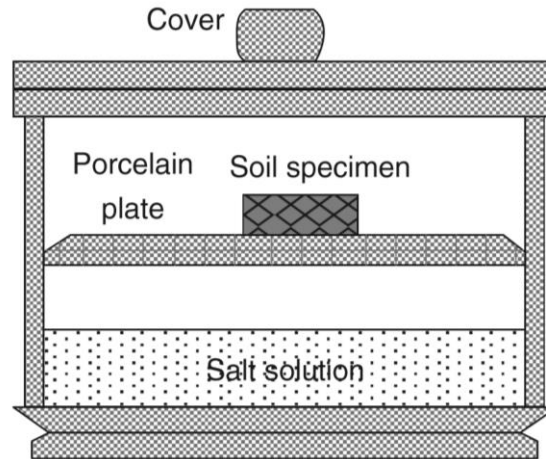


Figure 3.21. Schematic cross-sectional view of the salt solution equilibrium (SSE) container (Briaud 2013)

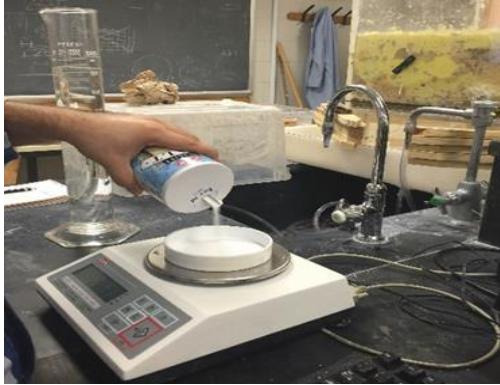
The remains from the porcelain clay blocks used for the UU triaxial tests were used to perform SSE tests (Figure 3.14(f)). Six different soil specimens from each triaxial cylinder were used. First, they were weighed, and then based on the range of suction in the soil required to draw the soil water retention curve, salt type and concentration were chosen (Table 3.3). In this study, the salt used was sodium chloride (NaCl) at different concentration (Table 3.8).

Table 3.8. Salt Solution Equilibrium Test Parameters

Sample #	Molarity (mol/kg)-NaCl	Suction (kPa) at 25°C	m ₀ * (g)
1	0.002	10	175.840
2	0.020	95	181.530
3	0.100	463	139.760
4	0.300	1370	137.230
5	1.400	6615	180.980
6	2.500	12556	202.550

*m₀ is the initial wet weight of each sample

Once the parameters of the salt solutions had been determined, all six specimens were put in different desiccators with different salt solution concentrations (Figure 3.22). To check for equilibrium, the weight of the soil was recorded (Briaud, 2013). The first data were collected after one month because the soil was not expected to come to equilibrium before one month. Thereafter, every 5 days, the samples were checked. As the change in soil weight decreased, the time interval between each record was decreased because equilibrium was closer. When the soil weight stopped changing, equilibrium had been reached. The final weight was recorded as the wet weight of the soil, after which the soil was dried an oven, allowing researchers to estimate the water content of each specimen. The results of this test provided the data required for drawing the SWRC (see section3.4.3).



(a) weighing the salt to make solution with specific concentration



(c) mixing predefined amounts (g) of water and salt to have solutions with exact salt concentrations



(c) put the soil sample inside the closed chamber and wait for equilibrium



(d) weighing the soil to check when equilibrium had been reached

Figure 3.22. Preparing samples and the salt solution to run the SSE tests

3.4 Test Results and Discussion

To determine the influence of water content change on the soil modulus and suction between soil particle in unsaturated state, an experimental study was conducted as it has been explained in detail earlier in section 3.3. In this section, the results of these tests including UU tests, WP4 tests, and SSE tests are presented and discussed.

3.4.1 Unconsolidated Undrained Triaxial Test Results

The relationship between the Young modulus and the gravimetric water content of the porcelain clay specimens were calculated from the data collected in the UU triaxial tests. As mentioned in section 3.3.1.2, tests were conducted using two different time series, which achieved a relatively wide range of water contents, from 2.620% to 25.786%. The Young modulus as a function of water content is illustrated in Figure 3.23. In general, in drying paths, the Young modulus increased as the water content decreased for the range of water contents measured in this study. The Young modulus of soil increased at a lower rate when water content was $\geq 20\%$. Likewise, as water content decreased, the Young modulus increased at a much higher rate.

To explain this phenomenon and why soil becomes stiffer as it dries, the hydro-mechanical behavior of the soil needed to be investigated. As mentioned earlier in this chapter, in the case of unsaturated soils, the suction between soil particles plays an influential role in mechanical behavior of the soils. Therefore, WP4 tests and SSE tests were chosen to get a better understanding of the coupled hydromechanical behavior of unsaturated soils.

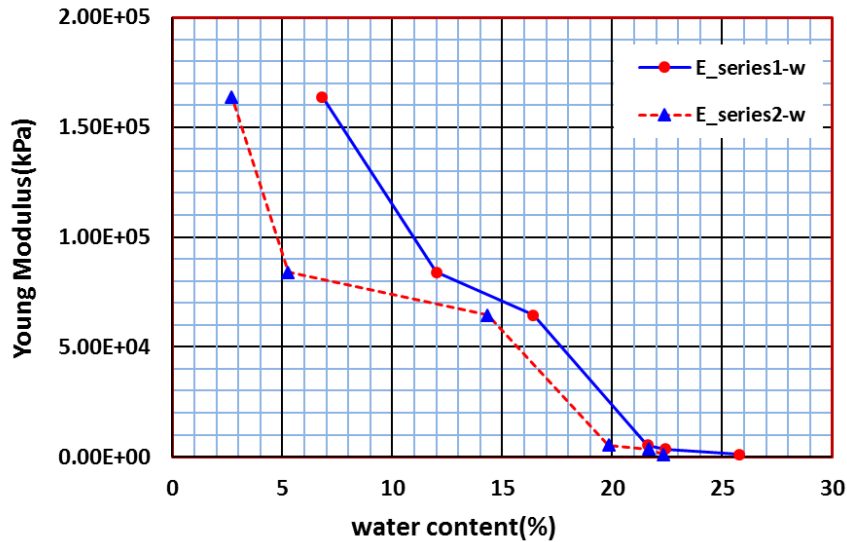


Figure 3.23. The relationship between water content and Young’s soil modulus

3.4.2 Chilled-Mirror Psychrometers Test Results

The results of the WP4 tests show that as soil became drier, meaning that the water content decreased, the suction between particles increased (Figure 3.24). Additionally, the SWRC in Figure 3.24 shows that with water content higher than 20%, the soil remained in a nearly saturated state (phase one of SWRC); therefore, changes in suction were not noticeable. But as soil became drier ($w < 20\%$) and entered phase two of SWRC, a sharp increase in suction between particles occurred. This change in suction strongly influenced the mechanical behavior of the soil. To better understand the impact on the mechanical behavior, the results obtained from the WP4 tests and the UU triaxial tests were combined to obtain the graph showed in Figure 3.25. This graph displays the relationship found between soil modulus and suction. As can be seen, the Young modulus of the soil

increased significantly as suction increased, but the slope of this increase was not constant. Apparently, when the first test was initiated, the soil specimen was in an almost saturated state. In first phase, as the soil becomes drier, changes in suction and resulting changes in the soil modulus are not significant (Briaud 2013). However, as the sample passed from a state of saturated soil to an unsaturated -state phase two of SWRC- the water stress can be significantly negative. In this case that the water stress becomes negative, it can contribute considerably to increase effective stress between the soil particles and also soil modulus.

As mentioned in section 3.2.2, the SWRC is a characteristic curve considered a property of the specific soil (Briaud 2013). Therefore, a unique graph was expected for SWRC (Figure 3.24). However, due to some experimental problems, there is a gap between the two graphs obtained from the two different test series. One important factor when testing unsaturated soil is preventing as much moisture loss as possible. However, in case of very wet specimens, the WP4 device took at least 30 min. to reach equilibrium and record the suction. The length of time it took the test to run resulted in some water content loss. As seen in Table 3.6, the range of change of suction among the six samples was relatively high, which was due to unavoidable moisture loss. Moreover, this technique of estimating suction cannot be used for wide ranges of suction (Table 3.9). Reading of very wet sample (1000 kPa) will have an increasing and unacceptable percentage of error. Furthermore, at high suction (>8000 kPa), the temperature differences between saturated vapor pressure and the vapor pressure of the specimen become extremely small (WP4 manual). Therefore, this method of measuring suction is not suited for drawing an accurate SWRC if wide range of suction are required to be estimated. In spite of these drawbacks, because the tests were performed on the same specimens used for the UU triaxial tests and

because it is a fast test in comparison to the SSE test, the WP4 test was chosen to investigate the relationship between suction and soil modulus. The results obtained from the WP4 tests were compared to the SSE tests, which were used to measure suction.

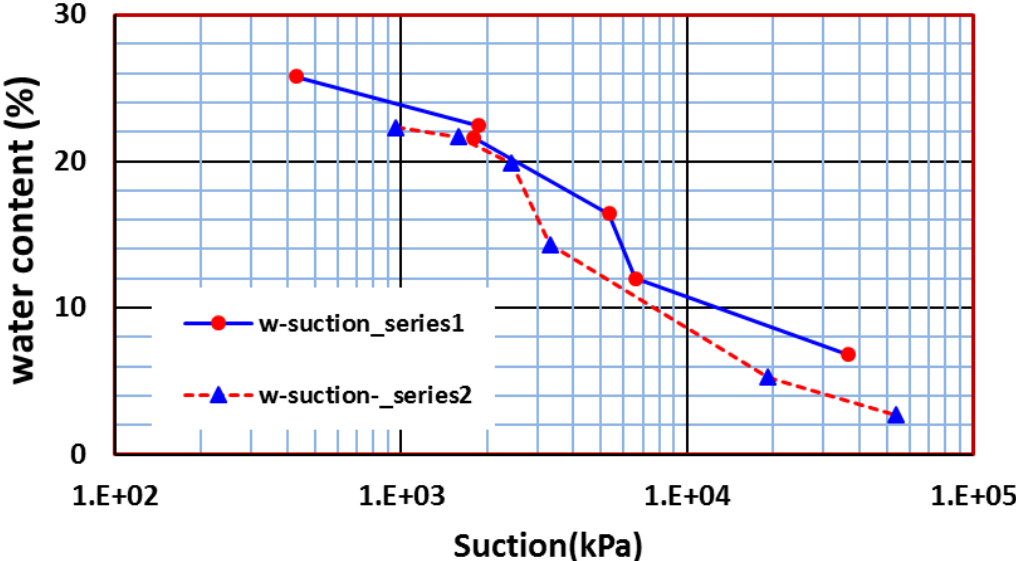


Figure 3.24. Soil water retention curves obtained from WP4 tests

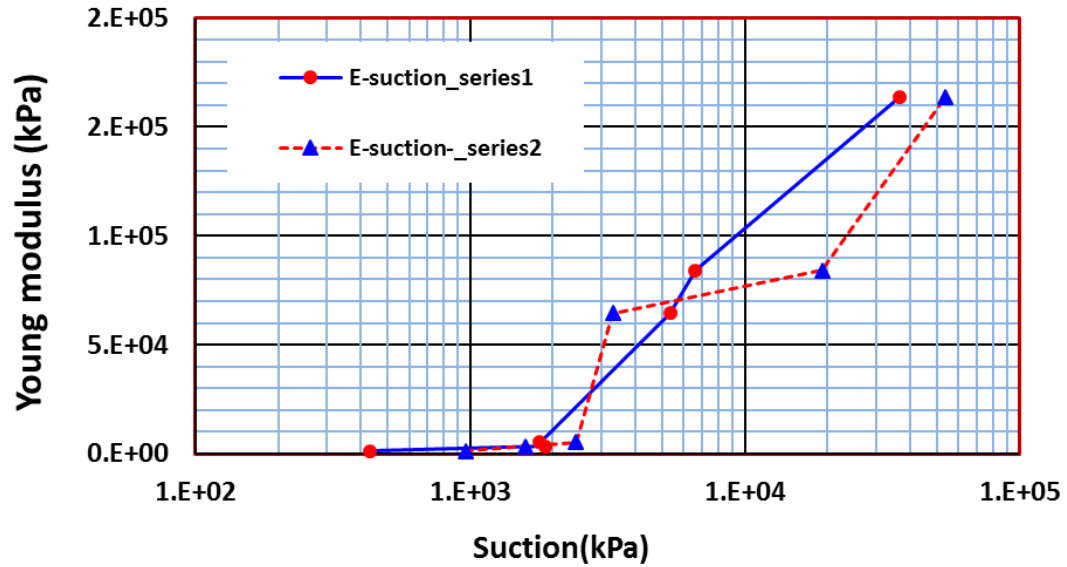


Figure 3.25. Young's soil modulus vs. suction

Table 3.9. Different Techniques for Measuring Suction or Water Tension (Briaud 2013)

Device or Method	Water Tension or Suction	Range (kPa)	Natural or SWRC*	Time Required	Comments	ASTM
Filter paper	Total	Entire range	Natural	1 to 2 weeks	May measure matric suction if in good contact	D5298
Thermocouple psychrometer	Total	100 to 8000	Natural	1 to 2 hours	Constant environment required	E337
Chilled mirror psychrometer	Total	1000 to 8000	Natural	10 minutes	Scatter at suction values less than 1000 kPa	D6836
Tensiometer	Matric	0 to 90	Natural	10 minutes	Difficulties with cavitation and diffusion through ceramic cup	D3404
Pressure plate	Matric	0 to 1500	Natural or SWRC*	1 to 5 days	Difficulties with pressures higher than 1500 kPa	D6836
Salt solution	Total	Entire range	SWRC*	1 to 2 weeks	Mainly used for calibrating other devices	None

3.4.3 Salt Solution Equilibrium Test Results

The SSE test is the proper method of measuring suction over a wide range, and it is the most suitable method for drawing an accurate SWRC (Briaud 2013) (see Table 3.9). Therefore, in this study, in addition to using the WP4 test results to construct an SWRC for the samples, the results of the SSE tests were used for the same purpose. Thus, the results obtained from the SSE tests were compared to those from the WP4 tests. As mentioned in section 3.3.3, samples in the SSE tests take a long time to reach equilibrium. A summary of results of weighing samples to check if they reached their equilibrium are given in Figure 3.26. This figure shows that the first sample to reach equilibrium was sample 1 and that took almost 3 months.

Before running the SSE tests, all six samples were assumed to have the same water content. During the process of reaching equilibrium, all the samples become drier (drying path). Sample 1 reached its equilibrium first since less soil moisture needed to evaporate for it to reach equilibrium. In fact, the lower the target suction chosen for each sample (according to Table 3.8), the less moisture required to evaporate for the sample to reach equilibrium; thus, samples with lower target suction reached equilibrium in a shorter time.

After 3 months, the test was stopped because it was taking too long to reach the equilibrium, and a mathematical analysis was adopted to calculate the wet weight of the samples at equilibrium. In fact, the asymptotic value of each graph shown in Figure 3.26 was calculated. The calculation to estimate the asymptotic value of each graph, which is the ratio of the wet weight of the sample at equilibrium to its own initial wet weight, is

shown in Figure 3.27. The final results of this asymptotic calculation are presented in Table 3.10.

The results obtained from the SSE tests were used to draw the SWRCs in Figure 3.28. As mentioned in section 3.4.2, the SWRC was expected to be unique because it is a characteristic curve. Due to the fact that the WP4 test results are valid only for a limited range of suction and that water content was lost during WP4 testing, the SWRC obtained from the SSE tests was considered more reliable than the one obtained from the WP4 tests. In Figure 3.28, the results from the SSE tests at one month and at two months are shown. Clearly, the match between SWRCs constructed by the two types of tests was better earlier, before the samples reached equilibrium. Thus, even though it takes much more time to reach equilibrium using the SSE test, the SWRC from the SSE test was more accurate than the SWRC obtained by the WP4 test.

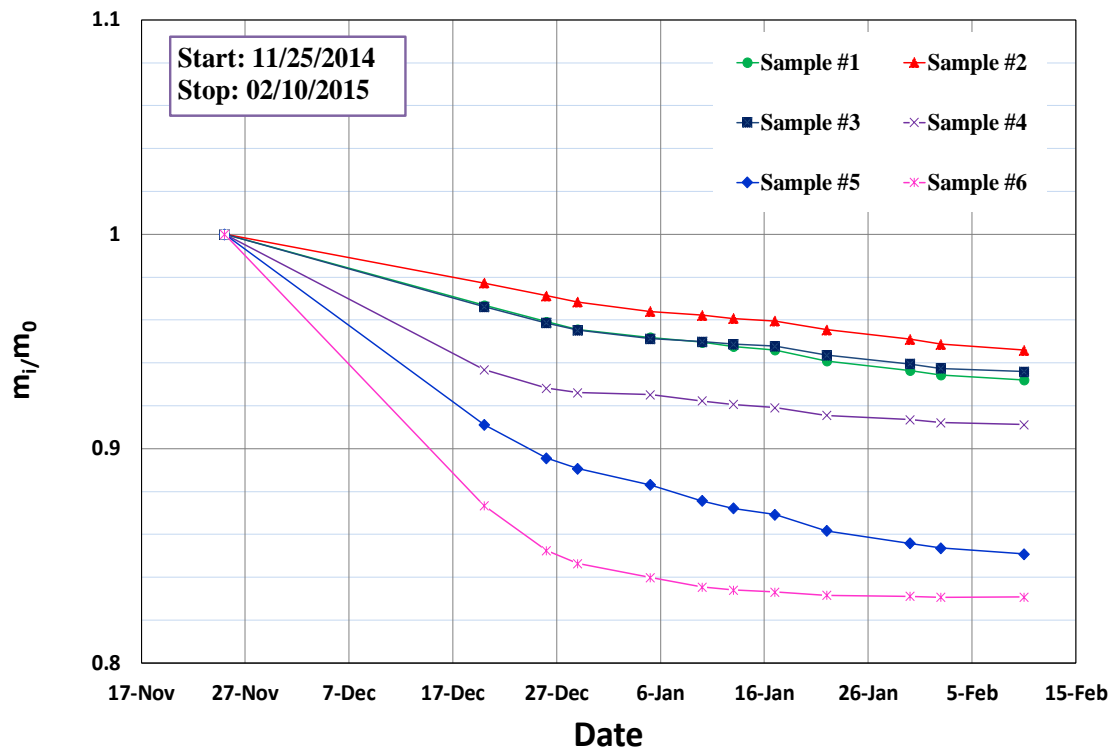


Figure 3.26. Raw data obtained from the salt solution equilibrium (SSE) tests

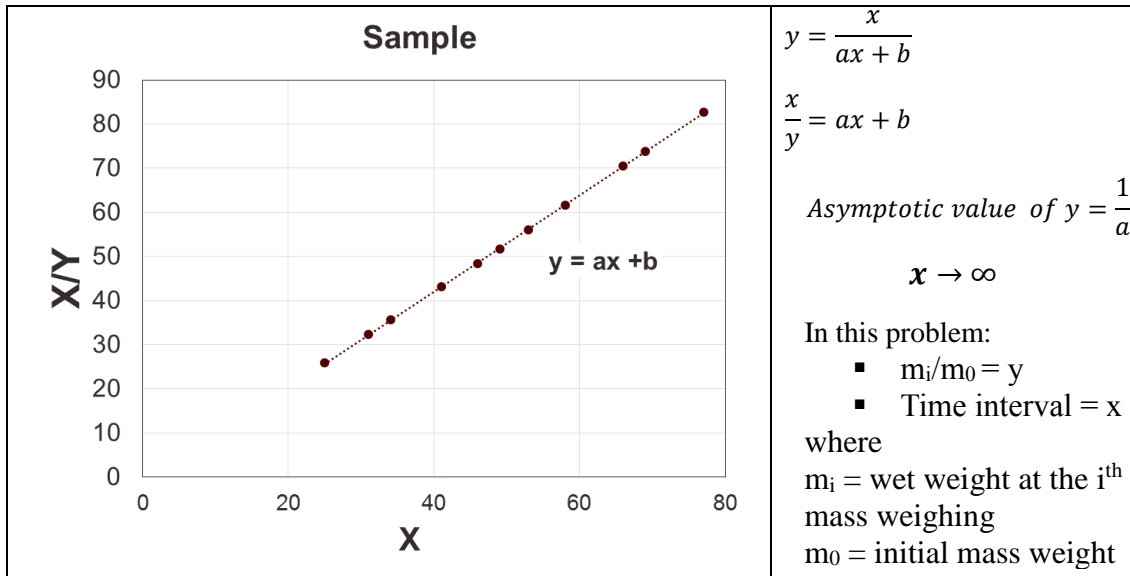


Figure 3.27. Calculation of the asymptotic value of Y

Table 3.10. Results of the Salt Solution Equilibrium Tests

Calculating the Asymptotic Values						
Sample	m_i/m_0	m_0 (gr)	$m_i = m_{\text{wet}}$ (gr)	m_{dry} (gr)	w (%)	$u_w = s^*$ (kPa)
1	0.928	175.840	165.277	138.85	19.03	10
2	0.943	181.530	171.222	145.650	17.56	95
3	0.933	139.760	130.349	112.04	16.34	463
4	0.908	137.230	124.596	109.99	13.28	1370
5	0.843	180.980	152.533	144.51	5.55	6615
6	0.824	202.550	166.831	162.01	2.98	12556

*s is suction

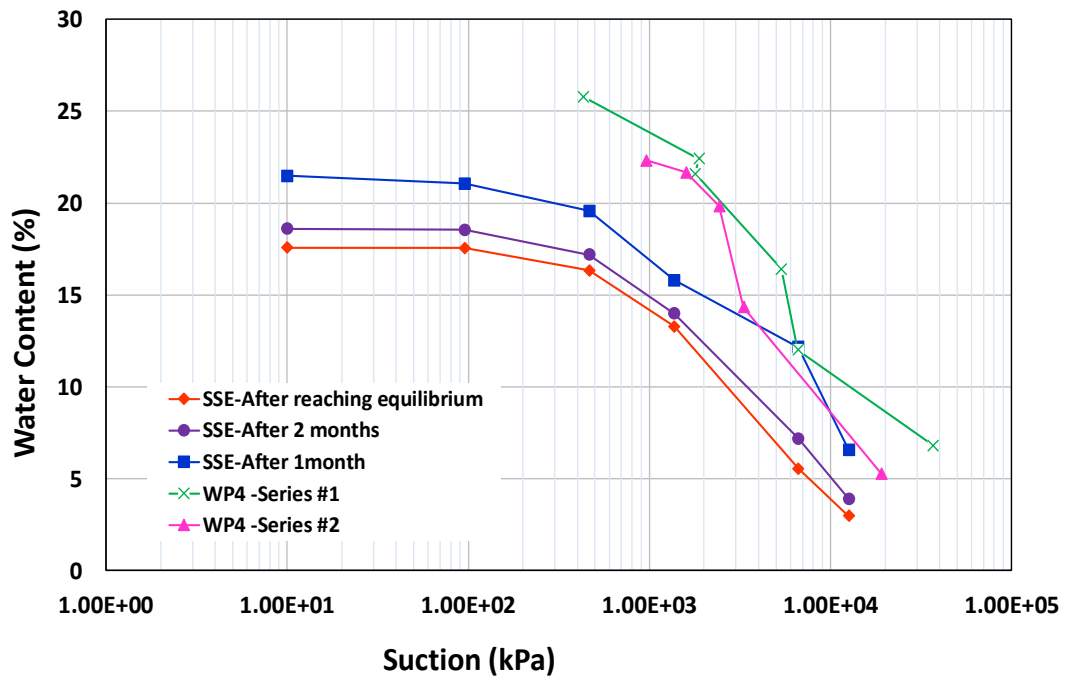


Figure 3.28. Comparison of Soil Water Retention Curve calculated using different methods

3.5 Design Solutions

The presence of water and cyclic loading due to passing HST are two influential factors that play an important role in accelerating railroad deterioration. Through this experimental study, it was demonstrated that very small increases in the water content of fine-grained soil resulted in significant reduction in the soil modulus as a mechanical parameter of soil under the conditions tested in this experiment. Therefore, increasing the water content of sub-structural layers of railways may lead to considerable decreases in the bearing capacity, accelerated soil deterioration, large permanent deformations, and

other major safety issues. Thus, designing an effective and efficient drainage system which helps maintain low levels of subgrade moisture is key to decreasing the risk of failure as well as maintenance costs (Ferreira and Teixeira 2011).

3.5.1 Sources of Moisture in Tracks

To make a wise decision and design suitable drainage systems, knowing which sources of water lead to changes in the soil water content of the sub-structural layers is essential. The main sources of moisture in the subgrade can be divided into three categories (Figure 3.29) (Li et al. 2016):

1. *Direct water:* This source of water is in the form of local snow and rainfall. Depending on the place and time of a year, the amount of this type of water can vary widely.
2. *Runoff water:* This category includes the rain and snow melt flowing from higher ground to the tracks. The rainfall intensity and the surface area of the contributing drainage basin are two factors playing an important role in the amount of runoff moisture affecting the tracks.
3. *Ground water:* Ground water can flow upward into the track substructure from below due to either capillary or pressure gradient. Ground water exists within the subsurface, and saturates all soil/rock pores.

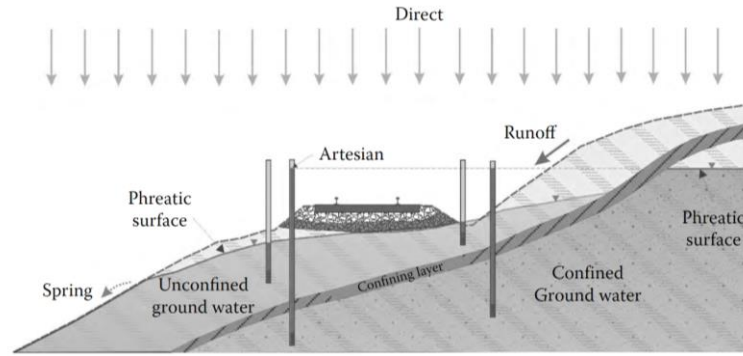


Figure 3.29. Sources of moisture in train tracks (Li et al. 2016)

3.5.2 Track Drainage

Track drainage includes interception, collection, and disposal of water from surface or subsurface of the track. It can be achieved using natural features of a landscape or artificially through installing suitable external and/or internal drainage systems (Figure 3.30) (Prajapati 2017, Li et al. 2016, CE 2303 Railway Engineering). Different factors such as ballast contamination, subballast gradation, slope of subgrade surface, ditch or pipe depth, longitudinal slope and expected rainfall characteristics should be considered before designing drainage systems. In this section, the different drainage materials and drainage designs will be discussed.

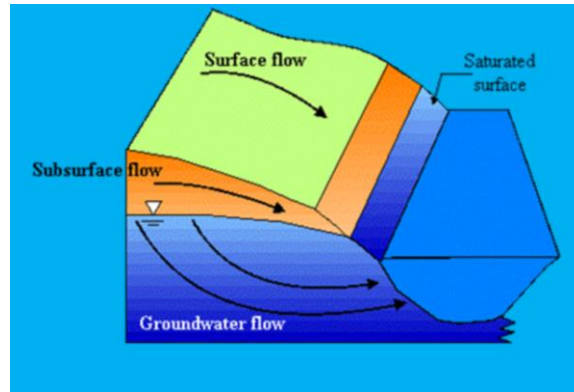


Figure 3.30. A schematic view of surface and subsurface flow (CE 2303 Railway Engineering)

3.5.2.1 Drainage Materials

Different types of materials can be applied for various drainage design methods such as pipes of various materials, graded aggregates, geosynthetics, and hot mixed asphalt (HMA) (Li et al. 2016).

Pipes can be used to convey water longitudinally along tracks and laterally under tracks. Two types of pipes are used in drainage systems, perforated pipes containing slots or holes allowing ingress of water and nonperforated pipes for conveying water.

Graded aggregate is also used in drainage systems. In fact, the most effective and economical subsurface drainage material is coarse aggregate with high permeability. To have an effectively permeable aggregate, the type of material and its gradation are two considerations should be taken into account during the process of designing drainage systems. One example of the grain size distribution of typical aggregate drain material in compare to a common sandy subgrade soil is displayed in Figure 3.31. One problem

should be avoided where this type of material used is migration of fine-grained soils from adjacent soil layers into the void space of the aggregate layer.

Geosynthetics are a family of products including geotextiles, geogrid, geomembranes, geocells, and geocomposites manufactured from synthetic polymer. These products have a wide range of application in railway engineering. Among all types of geosynthetic products, geomembranes, also called geosynthetic lines, are used to create an impermeable layer. This material can be used to prevent the filtration of water from the track surface into the sub-structural layers, consequently minimizing softening of the subgrade due to changes in soil water content (Figure 3.32). Geomembranes can be used to raise the drainage surface within the track substructure to provide an effective gravity drainage away from the tracks (Figure 3.32). Geotextile is a permeable geosynthetic that can provide filtration and separation between different graded layers. Geotextile allows water to escape from the fine-grained layer but does not permit small particles to pass into the voids of the coarse-grained layers.

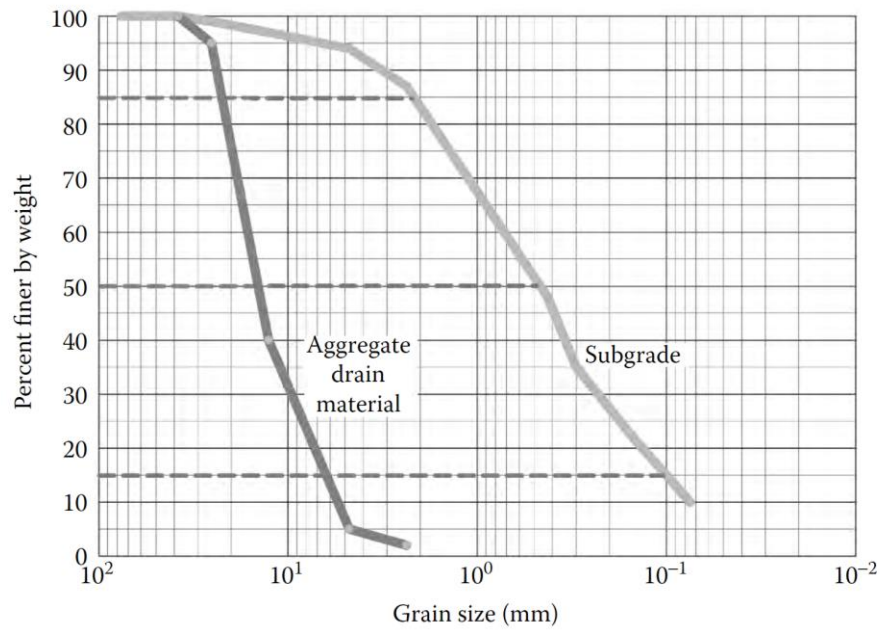


Figure 3.31. Grain size distribution plots of typical aggregate drain material and common sandy subgrade (Li et al. 2016)

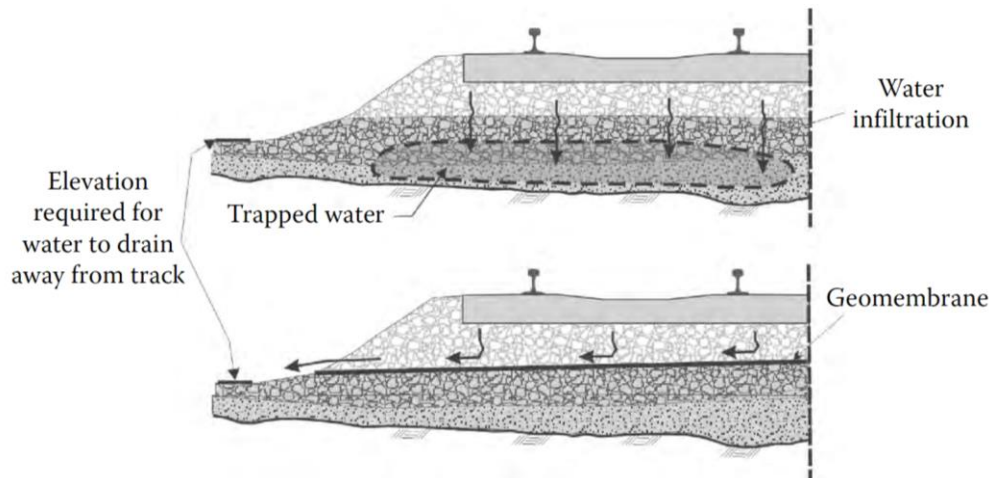


Figure 3.32. Geomembrane used to raise drainage surface within substructure (Li et al. 2016)

HMA is an impermeable material that can provide improved shedding of water from above thereby reducing access of water to the fine-grained layers whose mechanical properties depend on water content. The application of HMA is similar to that of geomembrane which is raising the drainage surface within the track substructure (Figure 3.33). One potential problem regarding using HMA and geomembrane is the possibility of trapping excess water beneath the impermeable layer. This could result in softening of subgrade soils under the impermeable layer (LoPresti and Li 2005) and loss of soil strength due to pore water pressure build-up under the impermeable layer. Therefore, in case water gets trapped under an impermeable layer, creating a proper drainage layer beneath the impermeable layer for water escape laterally seems to be essential (Li et al. 2016).

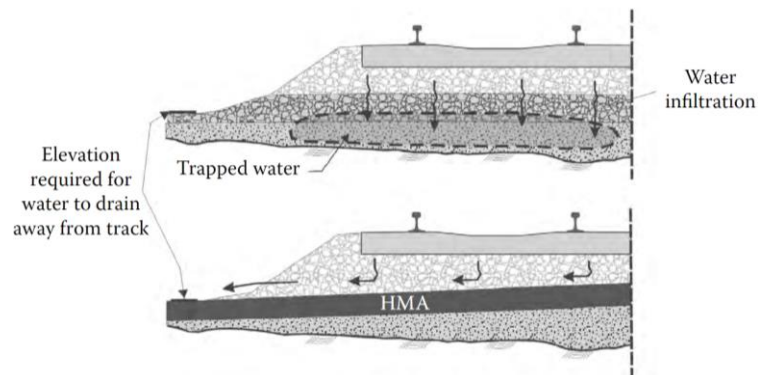


Figure 3.33. Using hot mixed asphalt (HMA) to raise drainage surface within track substructure (Li et al. 2016)

3.5.2.2 Drainage Design

A well-designed track drainage system is defined as a system that ensures no water penetrates the tracks substructures or superstructures at either surface or subsurface levels. Track drainage design includes two phases: surface, or external, track drainage and subsurface, also called internal, track drainage.

In phase 1, surface water due to rain, snow, or adjacent areas must be drained off by designing and installing a suitable and effective surface drainage system. The two main goals of designing a surface track drainage system are to minimize the access of water to the track while removing water from the track itself (Li et al. 2016). A well-designed surface track drainage includes side drains and cross-drains to collect the surface water and dispose of it in the nearest streams or other natural waterways (Li et al. 2016). One example of an effective surface drainage design is illustrated in Figure 3.34.

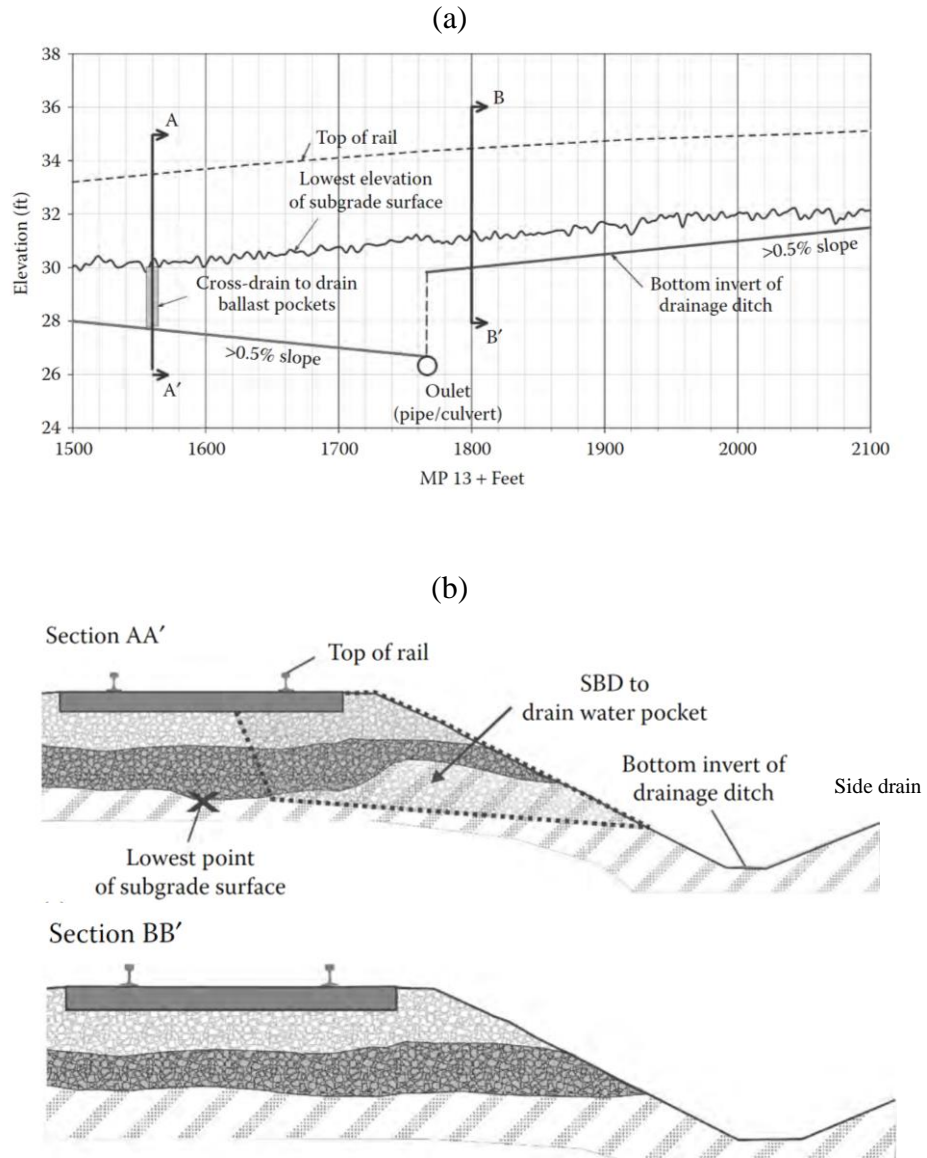


Figure 3.34. Example of surface drainage system design (a) plan (b) cross-sectional view (Li et al. 2016)

Sand piles, meaning a series of holes filled with clean sand, can be used for the removal of surface water from embankments. As shown in Figure 3.35, holes of 0.3 m in diameter and 1.8 to 3.0 m deep are constructed between the two track rails and in the

embankments on the sides of the rails. The main functions of the sand piles are to support the track, provide mechanical support to the subgrade by compacting the soil, and improve the drainage of the subgrade by providing vertical drainage by capillary rise of water to the surface and evaporation.

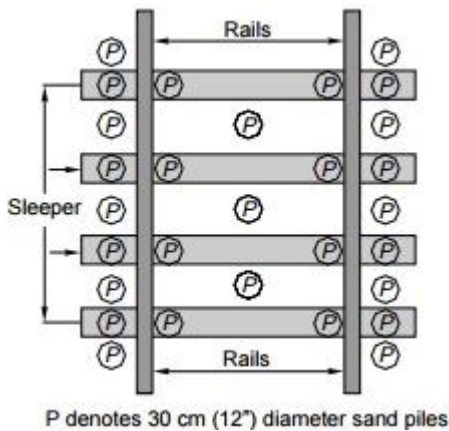


Figure 3.35. An external drainage system using sand piles

Phase 2 focuses on minimizing variations in water content of sub-structural layers by designing a suitable subsurface (internal) drainage system. The main factors that cause changes in moisture content in sub-structural layers of the tracks are (a) movement of water due to capillary action, (b) seepage water from adjacent area, (c) rising of ground water level, and (d) penetration of surface water.

The main goal of designing subsurface or internal track drainage systems is to provide ballast with enough lateral drainage to let water to escape and prevent saturation. A highly permeable ballast is the key element in order to have an effective and well-

designed internal drain. Component of a suitable internal track drainage is illustrated in Figure 3.36 (Li et al. 2016). An effective and sufficient drainage cannot simply be achieved by excavating a cross trench and allowing water out of the tracks but is reliant on providing a free drainage base as shown in Figure 3.37.

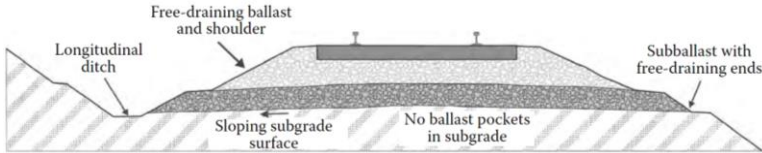


Figure 3.36. Cross-sectional view of an ideal track for good subsurface drainage (Li et al. 2016)

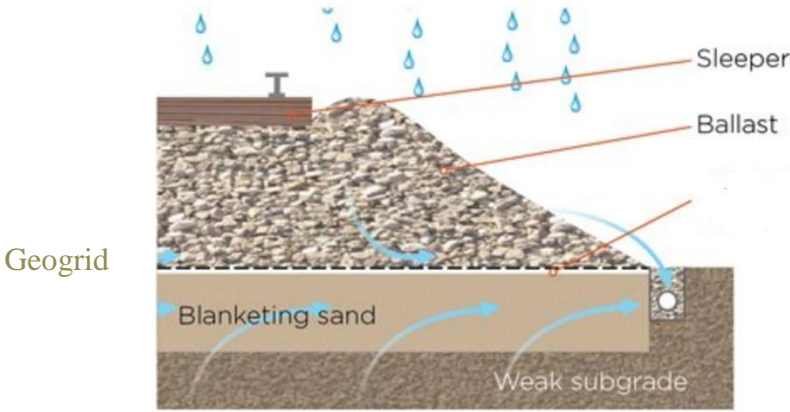


Figure 3.37. Ground water removal and capillary protection of railways ballast

Here are some two characteristics of internal drainage systems that can improve the overall effectiveness of the systems. First, using geosynthetic products properly can provide appropriate internal drainage (Figure 3.37). Additionally, an inverted filter with a blanket of adequate thickness comprised of non-cohesive materials placed between the ballast and the weak formation can work to cut off the capillary layer, state the function of cutting off the capillary layer. The blanket material should be well graded, starting with fine mesh at the bottom and increasing upward to a size slightly smaller than stone ballast at the top (Figure 3.38).

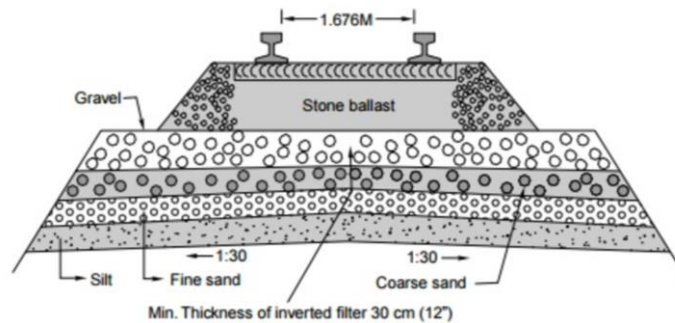


Figure 3.38. An inverted filter

3.6 Conclusions and Recommendations

While designing a new HSR, an important criterion of track stiffness is tolerable rail deflection. However, during a railway's service life, parameters such as weather conditions and poor drainage can seriously affect track stiffness and speed up track deterioration. Subsoil modulus significantly impacts track stiffness; therefore, any change in subsoil modulus can change track stiffness, resulting in large, unexpected track deflection.

This experimental study was conducted to provide a clearer understanding of the effects of changing moisture content on the subsoil modulus. The study showed that the Young modulus of porcelain clay, a fine-grained soil, is very sensitive to changes in soil moisture content; wetting the subgrade was shown to cause loss of track stiffness. Such wetting occurs via capillary action as the water is attracted upward into the dry embankment. The loss of subgrade stiffness induced both an increase in track deterioration due to a larger dynamic effect of running HST and uneven settlement of the embankments along with associated roughness of the train ride.

Appropriate measures need to be taken to prevent rises in subgrade water levels. The aim of this study was to investigate the hydromechanical behavior of porcelain clay as an example of fine-grained soils. The outcomes of these experiments included graphs help railway designers and engineers monitor track deterioration and better understand embankment softening due to changes in moisture in embankments over time. The outcomes of these experimental analyses can be summarized as follow:

1. The UU triaxial tests showed that the Young modulus significantly increased as the water content decreased when soil samples were in an unsaturated state.
2. As expected, as the soil became drier, the suction between soil particle increased, particularly when the soil was in an unsaturated state.
3. Combining the results obtained from the UU triaxial tests and the WP4 tests confirmed that the considerable increase in the Young modulus of soil was due to large suction between soil particles. The results confirmed the idea that in unsaturated soils, the suction played an important role in the mechanical behavior of soil.
4. SWRCs drawn using the WP4 and SSE tests showed that as soil became drier, suction between particles increased. This suction increase was significant when soil was in an unsaturated state. In unsaturated soils, the suction played an important role in the mechanical behavior of the soil.
 - a. Although a unique SWRC was expected for each method of measuring suction, measuring suction is very complicated and this parameter varied across an extremely wide range. Assuming the range of suction in a problem is known, different methods can be applied to measure suction depending on what is appropriate for the situation. The SSE tests is one of the most accurate for measuring suction when a wide range is present (Briaud 2013); this test also provides more accurate data for drawing SWRC (Briaud 2013). However, combining the results obtained from the UU triaxial tests and the SSE tests was not easy. Thus, although the WP4 test was not the ideal technique for measuring suction, it was chosen

because this method can be used following UU triaxial tests and conducted on the same samples used in the UU triaxial tests. Therefore, it was easier to predict the hydromechanical behavior of soil by conducting UU triaxial tests followed by WP4 tests.

In addition to the results directly obtained from experimental study, this study shows that because increasing water content in the substructure can cause a series of problems, appropriately designed drainage is of vital importance. As with all substructures, drainage should be designed and constructed properly when building the track. Although this study provides researchers with some useful data regarding unsaturated soil and its behavior during drying process, more experimental studies are required to complete our understanding of the issues and propose appropriate safety guidelines.

4 BREAKING THE RAYLEIGH WAVE BARRIER

4.1 Introduction

In this section, the geodynamic challenges regarding breaking the Rayleigh wave barrier and its consequences will be addressed. In fact, this problem in high-speed and high axle load railways is met with as train speed approaches an apparent critical value, which is assessed by the Rayleigh wave propagation speeds on soft ground. In fact, running high-speed trains accompanied with large vibration in the track/ground system resulting in considerable track displacement, with train derailment as the worst-case scenario. Consequently, this large dynamic response of high-speed tracks leads to comfort and safety issues as well as increased maintenance costs. In this section, a numerical study of the performance of HSRs as a function of train speed will be presented. In the current study, a sophisticated four-dimensional finite element model (4-D FEM) of train/track/embankment was developed to investigate the performance of HSR as a function of train speed. Field measurements performed in Sweden and full-scale laboratory model testing conducted in China were utilized to verify the reliability of the numerical model to reproduce the dynamic response of the track, embankment, and underlying soils under the train loads. The verified model was used to carry out the parametric studies. Through parametric studies, the effect of different ground stiffness, embankment stiffness, and embankment thickness on the critical speed were investigated. The results of parametric studies led to a proposed design procedure in the form of some guideline charts, which are presented in this section.

4.2 Background

This section focuses on the problem of large vibration induced in the soil by operating HSTs. Some fundamental concepts, such as sources of vibration in HSRs, wave propagation in soil skeleton, ground Mach, and critical speed will be reviewed in the following sections.

4.2.1 Source of Vibration in High-Speed Railways

The problem of train induced track/ground vibration can be divided into three parts: source, medium, and objects. There are many sources of vibration caused by moving trains (Table 4.1), consisting of train, track, pads, ties, and other railway structures (Göran Holm et al. 2002). The medium is the soil, which is typically layered and inhomogeneous. Buildings, humans, tracks, and all structures belonging to the railway can be considered as objects. In this research, our object is railway structures.

The main source of train induced ground vibration is the behavior of the moving vehicle, with its engine and cars exciting the track system and soil. Among all those sources presented in Table 4.1, the most influential factors determining the wave properties and affecting the track structural responses induced by the moving trains are the axle configuration (including axle load and spacing of the wheel axles) and train speed (Banimahd 2008, Göran Holm et al. 2002). Our main concern in this research; however,

is the impact of train speed on the track dynamic responses. This factor was chosen because the interaction of the railway structure with the surrounding soil will generate considerable displacement of the railway structures as train speed approaches the critical speed where resonance occurs.

Table 4.1. Different Sources of Track/Ground Vibration Induced by HST (Hall 2000)

<p>Stress waves induced by the track structural response</p> <ul style="list-style-type: none"> ▪ Axle weight ▪ Spacing of wheel axles ▪ Speed of train
<p>Vibration sources at wheel-rail interface</p> <ul style="list-style-type: none"> ▪ Unsteady riding of the vehicle (bouncing, rolling, pitching) ▪ Dynamic properties of the vehicle bogie ▪ Wheel defects (eccentricity, imbalance, flats) ▪ Misalignment of motors ▪ Acceleration and deceleration of train
<p>Discontinuity on the track</p> <ul style="list-style-type: none"> ▪ Rail defects (unevenness, waviness) ▪ Spacing and interval of rail joints ▪ Switches ▪ Curves and tilting track (centrifugal forces)
<p>Variable support</p> <ul style="list-style-type: none"> ▪ Geometry, stiffness, and spacing of ties (sleepers) ▪ Geometry, stiffness, and heterogeneity of the ballast ▪ Geometry and stiffness of the ground

4.2.2 Wave Propagation in Soil Skeleton

The source and the medium (the soil around the source) interact dynamically (Göran Holm et al. 2002). If the source generating the ground vibration is considered to be constant, geometry and stiffness of the medium (surrounding soil) have significant

impact on the degree to which the ground vibration will spread. Therefore, it is important to study this source/medium (train/track/ground) interaction. There are three different stress waves with different propagation speeds that can be induced in the soil medium (Figure 4.1) (Kramer 1996, Towhata 2008, Briaud 2013,):

1. *Compression wave (P wave)*: Body waves propagating throughout the soil mass.

The wave speed depends on material properties of the medium through which the wave propagates. The P wave speed (V_P) can be estimate with Equation 4.1:

$$V_P = \sqrt{\frac{M}{\rho}} = \sqrt{\frac{K + \frac{4}{3}G}{\rho}} = \sqrt{\frac{E}{\rho} \frac{(1-\nu)}{(1+\nu)(1-2\nu)}} \quad (4.1)$$

where ρ is the mass density; ν is Poisson ratio; M, K, G, and E are the constrained, bulk, shear, and Young's Modulus, respectively. It should be noted that in soil mediums, the soil modulus value depends on the strain level corresponding to the particle motion during the wave propagation (Briaud 2013).

2. *Shear wave (S wave)*: Body waves propagating throughout the soil mass. The speed of a shear wave (V_s), which less than P wave speed ($V_s \sim 0.6 V_P$), can be calculated by using Equation 4.2.

$$V_P = \sqrt{\frac{G}{\rho}} \quad (4.2)$$

3. *Rayleigh wave*: Surface wave propagating along the ground surface; it is much slower than body waves ($V_R \sim 0.9 V_s$) but propagates further than body waves due to its large amplitude, large wave length, and long duration (Briaud 2013). Rayleigh wave speed can be estimate with following equation.

$$V_R \cong V_s \frac{0.87+1.12\nu}{1+\nu} \quad (4.3)$$

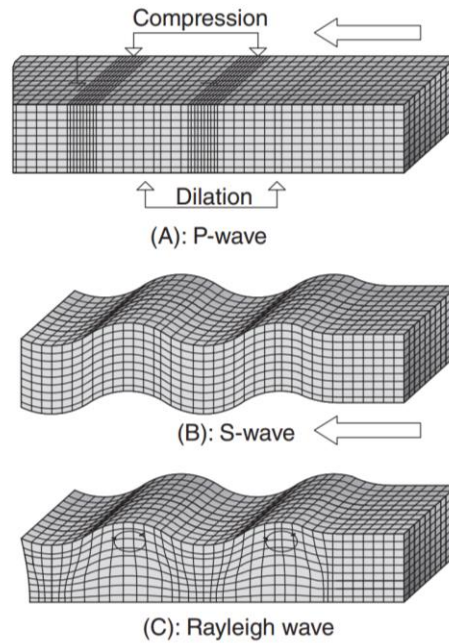


Figure 4.1. Different waves propagating in soil skeleton (Briaud 2013)

The wave types and the magnitude of the excitation are two factors that have great influence on the ground-born energy distribution (Banimahd 2008). In cases of localized excitation on the surface of a relatively small area, the Rayleigh waves will be dominant,

but if the excitation area is large, the body waves will carry most of the energy. The former cases occur with railway tracks where the Rayleigh waves are dominant (Banimahd 2008). More than half (67%) of the energy from a circular disk oscillating vertically on the surface of an isotropic homogenous half-space is carried by Rayleigh waves, and the rest of the energy is propagated as S waves and P waves (Miller and Pursey 1954).

4.2.3 Critical Speed and Ground Mach 1.0

When a train passes the threshold of the equivalent Rayleigh wave speed of the medium through which the waves induced by the train propagate, it is subjected to the same phenomenon as an airplane going through the sound barrier (Figure 4.2). This speed at which the maximum track deformation or resonance occurs is called critical speed (V_C). The Rayleigh wave barrier must be defined because when train speed approaches this barrier, it causes large track displacement that may lead to safety and comfort issues. This threshold speed or critical speed is also known as Ground Mach 1.0 (GM 1.0) (Bian et al. 2008, Lefeuvre-Mesgouez and Mesgouez 2008, Woodward et al. 2013). The Ground Mach (GM) is defined like the Mach number (M) in aerospace engineering (Figure 4.3):

$$M = \frac{V_A}{V_S} \quad (M=1.0 \text{ when } V_A=V_S) \quad (4.4)$$

$$GM = \frac{V_T}{V_R} \quad (GM=1.0 \text{ when } V_T=V_R=V_C) \quad (4.5)$$

where V_A , V_S , V_T , V_R , and V_C are airplane, sound, train, Rayleigh wave and critical speed, respectively. Results obtained from numerical simulations (Bian et al. 2008, Lefeuvre-Mesgouez and Mesgouez 2008, Woodward et al. 2013, Tafti et al. 2017) show that the displacement contour shape is symmetrical and exactly under the moving load when a single load moves with subcritical speed (subsonic conditions), $V_T < V_R$ or $GM < 1.0$. As the train speed approaches or passes the Rayleigh wave speed of the track/ground system, $V_T \geq V_R$ or $GM \geq 1.0$ (supersonic conditions), the Ground Mach cone forms, and the bulb of displacement contours lags behind the train wheels. The cone tip angle, which becomes steeper as train speed increases, can be calculated using following Equation 4.6.

$$\alpha = \sin^{-1} \frac{1}{GM} \quad (4.6)$$

where α is the actual angle of the Ground Mach cone (Figure 4.3).

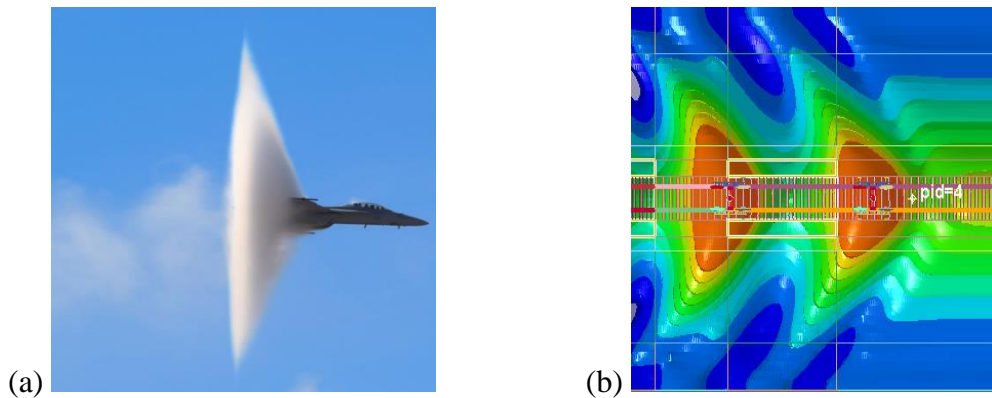


Figure 4.2. Passing (a) the sound barrier ($M > 1.0$) and (b) the Rayleigh wave barrier ($GM > 1.0$)

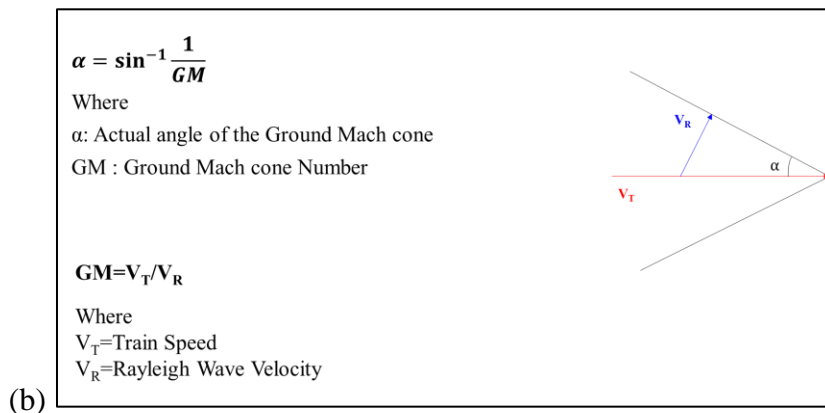
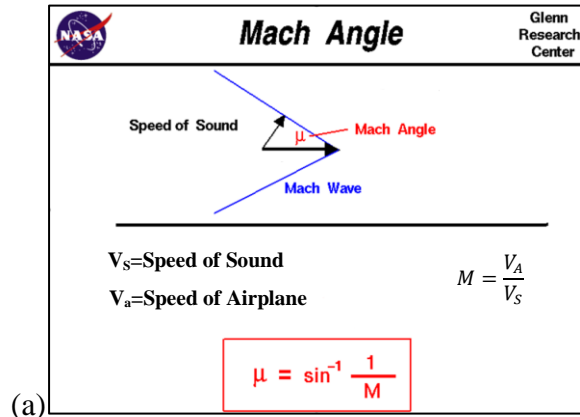


Figure 4.3. Calculation of (a) the Mach number and Mach angle; (b) the Ground Mach Cone number and Mach Cone Angle (Adapted Woodward 2013)

4.3 Review of Previous Studies

Aspects of breaking the Rayleigh wave barrier are really only important in cases of HSTs, not for regular passenger and freight trains that never reach the Rayleigh wave barrier. As mentioned in section 2, according to different codes, various minimum train speeds are considered to define a railway line as HSR. Based on the world speed survey published in Railway Gazette International, trains operating at more than 150 km/h (42 m/s) are put in this category (Takagi 2005). In some countries such as Japan and France,

train speeds exceed 300 km/h (83 m/s) (Takagi 2005). Therefore, the typical speed of current HSTs is between 150 km/h (42 m/s) and 300 km/h (and 83 m/s). We anticipate that HSTs in the near future will reach speeds up to 400 km/h (110 m/s); therefore, in the current study, train speed equal to 400 km/h (110 m/s) was considered as the train speed target value. In HSR systems, Rayleigh waves range from 144 km/h (40 m/s) in very soft soils (Madshus et al. 2004, Woldrigh and New 1999) to 1800 km/h (500 m/s) in very stiff soils (Briaud 2013). Clearly, the problem of large dynamic displacement at critical speed is most acute when HSTs travel over soft to medium soils. This subject has been investigated through several numerical (Kaynia et al. 2000, Kaynia and Madshus 2001, Madshus et al. 2004, Banimahd 2008, Bian et al. 2008, Lefeuve-Mesgouez and Mesgouez 2008, Woodward et al. 2013, Bian et al. 2014, Tafti et al. 2017) and experimental (De Nie 1948, 1949a and 1949b, Fortin 1982, Sunaga et al. 1990, Hunt 1994, Woldright and New 1999, Adolfsson et al. 1999, Mudshus and Kaynia 2000, Kaynia et al. 2000, Bian et al. 2014) studies. According to the fifth International Workshop on Railway Noise (IWRN) in Voss, Norway, in 1995, about 25% of the research on noise problems of high speed railways dealt with ground vibration of HSR traffic (Madshus and Kaynia 2000). Several studies have focused primarily on critical speed issues, track structure durability, and the vibro-environmental issues (Kaynia et al. 2000, Madshus et al. 2004, Banimahd 2008, Bian et al. 2014). In this section, the past studies will be reviewed.

4.3.1 Experimental Evidence

The experimental evidence of the effect of train speed on vertical track/ground displacement will be reviewed in two following sections: Field or in-situ tests and laboratory full-scale tests.

4.3.1.1 Field Observations

To assess the track displacement as a function of the train speed, several measurements have been conducted since 1938 (De Nie 1948, 1949a and 1949b, Fortin 1982, Sunaga et al. 1990, Hunt 1994, Woldright and New 1999, Adolfsson et al. 1999, Mudshus and Kaynia 2000, Kaynia et al. 2000). In this section, some of these studies will be described.

- *Netherlands (1938)*

The earliest evidence of the dynamic effect of increased train speed on track/ground displacement, particularly where a poor geotechnical subgrade condition exists, was observed by De Nie (1938) (Woldright and New 1999). This measurement of the rail displacement as a function of train speed was carried out in the Netherlands from 1938 to 1940 on the Oudewater to Gouda line due to observation of a very frequent need of maintenance in this area (De Nie 1948, 1949a and 1949b). De Nie stated in a report (unpublished manuscript, undated, approximately 1949b found in old archives of Dutch

railways cited from Woldright and New 1999) that rail displacement is a function of different factors: axle load, thickness of the embankment fill, the elastic properties of the sub-soil, damping in the system, and train speed. He believes that at a certain speed, resonance happens. The maximum dynamic displacement, which occurs at critical speed, is considerably larger than the static displacement due to only train axle loads. He also mentioned that this phenomenon results in the need for excessive maintenance to fix the large displacement of the track/ground, so that speed reduction or any countermeasures reducing the dynamic effect of running HST seems essential.

- *Japan (1990)*

A series of measurements in conventional lines having a shallow embankment (embankment thickness less than 3 m) overlying soft soils and in the Shinkansen lines were conducted to investigate the relationship between train speed and track displacement (Sunaga et al. 1990). The vibrations induced by running HST at different speeds were measured by accelerometers installed near the edge of railway ballast as shown in Figure 4.4 (a). The results of these tests at increasing train speeds are given in Figure 4.4 (b), which shows the relationship between train speed and vertical displacement of the roadbed for two cases where the embankment is constructed on top of very soft ($q_c=260\text{kPa}$ where q_c is CPT test value) and hard ($q_c=15\text{MPa}$) soils. As can be seen in Figure 4.4 (b), with hard soil, vertical displacements are almost constant as train speed increases; however, for soft soils, the vertical displacements tend to depend on the train speed. The magnitude of the vertical displacement in soft soil is much larger than for hard soil.

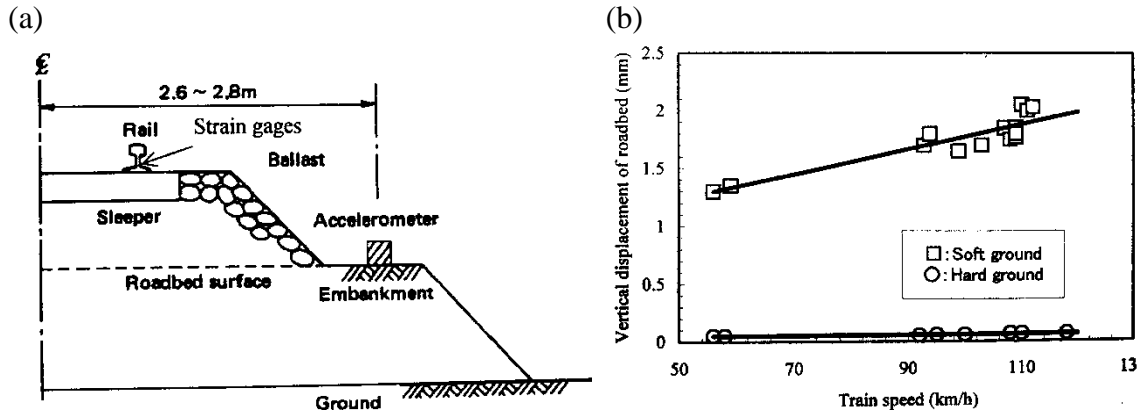
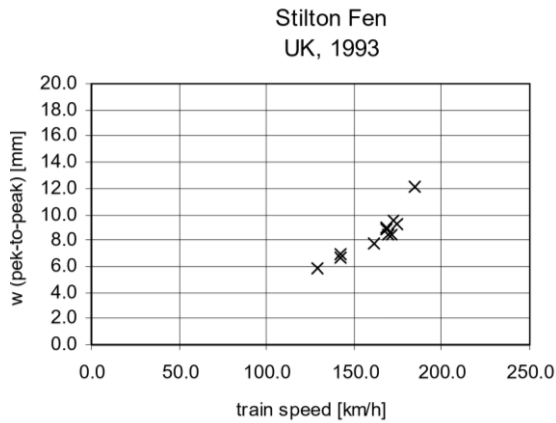


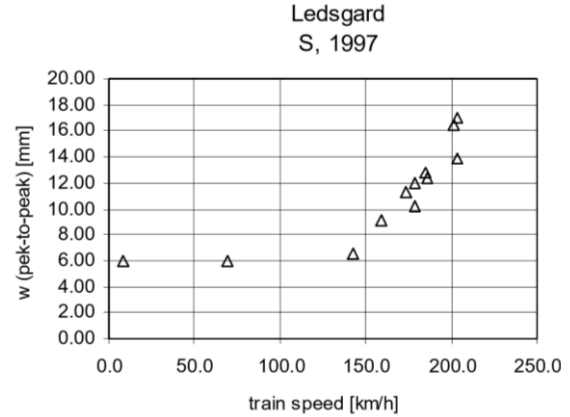
Figure 4.4. (a) Cross sectional view of the real in-situ test in Japan; (b) Vertical displacement of roadbed vs. train speed (Sunaga et al. 1990)

UK (1993)

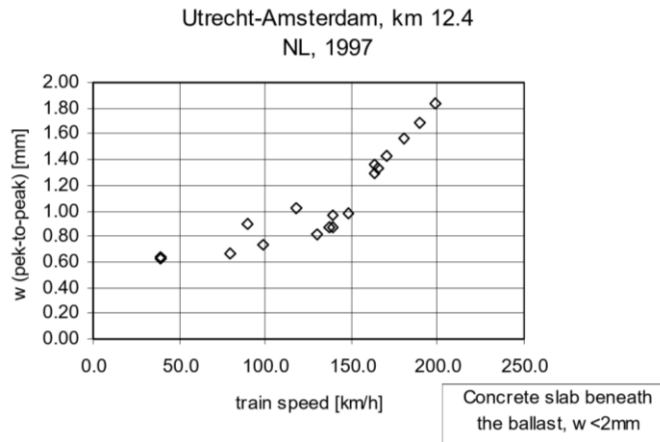
Another example of real-site measurement of vertical displacement as a function of train speed (up to 180 km/h) was conducted over an embankment constructed on a very soft soil at Stilton Fen in the UK in 1993 (Figure 4.5 (a)) (Woldright and New 1999). Figure 4.5 (a) shows peak-to-peak track displacement measured as a function of train speed. The static and maximum dynamic displacements (peak-to-peak) on the ballast were measured at approximately 5 mm and 12 mm, respectively. This indicates that a significant increase in track displacement was observed with increasing speed. The maximum dynamic displacement observed in this site is about three times larger than the static displacement. This figure illustrates that the ballast displacement significantly increases with train speed. In this case study, embankment was constructed on the layered soil with a very soft layer of silty clay.



(a) Stilton Fen (UK)



(b) Ledsgard (Sweden)



(c) Utrecht-Amsterdam (Netherlands)

Figure 4.5. Peak-to-peak displacement of ballast as a function of train speed (Woldright and New 1999)

- *Sweden (1997)*

A speed reduction of the Swedish X2000 high-speed train (from 180 km/h to 160 km/h) on the Göteborg-Malmö line was ordered due to the large track deformation observed in 1997. After this order, the Swedish Rail administration started an extensive

research program into this high-speed line to solve the problem (Madshus 1998, Adolfsson et al. 1999, Madshus and Kaynia 2000, Kaynia et al. 2000). In a different area in Sweden, increasing train speed from 140 km/h to 200 km/h had resulted in unacceptable and large track displacement due to constructing on an embankment on soft clays. In this R&D project supported by the Swedish Rail Administration, different useful parameters such as vertical track displacement, pore pressure, particle acceleration, and particle velocity were measured for a wide range of train speeds (up to 204 km/h). This measurement was recorded on the ground surface as well as in the soil (Adolfsson et al. 1999). The relationship between track displacement (peak-to-peak) and train speed is illustrated in Figure 4.5 (b). The data obtained from this measurement were used for FEM verification.

- *Netherlands (1997)*

Existing track between Amsterdam and Utrecht is built on very shallow embankments (about 2 m of sand fill) constructed over 6 m soft clay and peat layers. In-situ tests supported by the Dutch Rail Administration were performed to investigate potential problems regarding the plan for upgrading train speed to 160 km/h and higher. The Dutch tests were conducted with a French TGV in 1997. One example of the test results given at km 12.4 on the Amsterdam-Utrecht line is shown in Figure 4.5 (c) (Woldright and New 1999).

Figure 4.5 (a), (b), and (c) show the same relationship between peak-to-peak track displacement and train speed. In all these in-situ tests, the maximum speed has not been reached since the range of train speed was not wide enough. However, the dynamic effect

of operating HST on the conventional railway lines is obvious. The ratio of the maximum dynamic displacement over static displacement of the track is between 2.0 and 3.0 (Figure 4.6). This large displacement should be avoided by reducing the train speed or using countermeasures to increase the critical speed of the track/ground system.

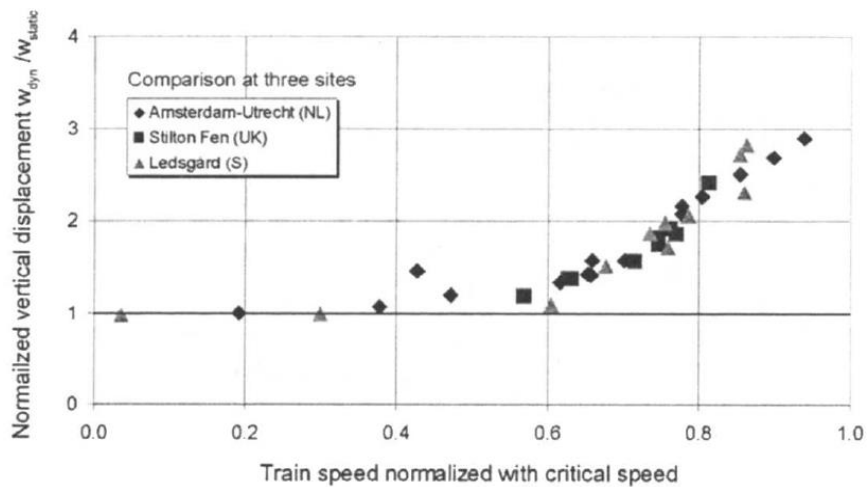


Figure 4.6. Normalized peak-to-peak vertical track displacement as a function of normalized train speed (Madshus et al. 2004)

4.3.1.2 Laboratory Experiments

A full-scale laboratory model can be used as a helpful and effective alternative to the field measurements to study the dynamic behavior of track/ground systems under the dynamic moving load of HSTs. Some examples of these laboratory studies will be presented in this section.

- *China (2013)*

In China, a full-scale laboratory test (with a portion of realistic track identical to the HSRs in China) provided valuable data to better understand the effects of train speed on the dynamic responses of track/soil structures (Chen et al. 2013, Jiang et al. 2014, Bian et al. 2014). To assess the reliability of the full-scale model, the geometry of the track/ground system construction procedure and the mechanical properties of the track/ground system were almost identical to the section of Wu-Guang HSRs in China where the field measurement had been conducted. This model showed that the vibrations induced in the soil/track structures have an increasing tendency as train speed increases (Figure 4.7). The full-scale model was developed to simulate the effect of trains moving loads at a wide range of speeds up to 360 km/h on the dynamic performance of the geotechnical infrastructures in HSRs. In fact, this study aimed to represent how a well-designed embankment can effectively decrease the vibration intensity transmitted to the subgrade soil. Full details of this test will be provided later in this section. The experimental results obtained from this test were used to verify the reliability of the FEM developed through current numerical studies.

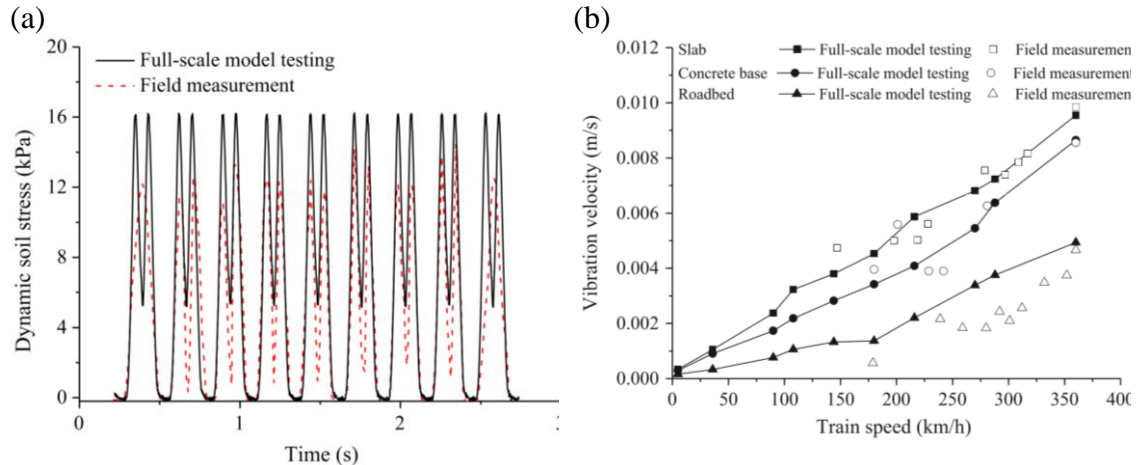


Figure 4.7. Model verification of (a) dynamic vertical stress-time in roadbed at train speed equal to 330 km/h and (b) vibration velocity vs. train speed (Bian et al. 2014)

- *Heriot-Watt University (UK)*

A full-scale laboratory Geopavement and Accelerated Fatigue Testing (GRAFT) facility at Heriot-Watt University (Figure 4.8) was developed to facilitate testing of ballast reinforcement products and assess their effects on track/ground settlement and track stiffness under real conditions (Kennedy 2011). In this experimental practice, to consider the effect of train speed on the track responses, different ranges of the loading frequencies were applied in GRAFT. The loading frequency applied represents repeated quasi-static single wheel loading; indeed, this loading frequency is from a typical low to medium train speed. In order to simulate the dynamic track responses at higher speed, the load should be increased in GRAFT according to the dynamic amplification factor (DAF) empirical equations given in section 2. However, in research studies conducted by Justin Kennedy (2011), the effect of high speed on soft soils was not investigated. Through this study, the impact of different factors such as subgrade modulus number of cycles and axle load on

track performance was investigated. In addition, various types of geosynthetic products were applied to quantify how effective they would be to reduce track settlement and increase track stiffness.



Figure 4.8. GRAFT facilities (Kennedy 2011)

4.3.2 Numerical Simulations

The problem of passing the threshold critical speed and its consequences, such as accelerating HSR track deterioration, have been studied through a large number of analytical and numerical simulations (Sheng et al. 1999, Kaynia et al. 2000, Madshus and Kaynia 2000, Madshus and Kaynia 2001, Madshus et al. 2004, Hendry 2007, Banimahd 2008, Bian et al. 2008, Lefeuve-Mesgouez and Mesgouez 2008, Woodward et al. 2012, Woodward et al. 2013, Jiang et al. 2015, Abu Sayed and Shahin 2016). Results from numerical analyses have indicated that a large dynamic amplification appears in the vertical dynamic movement of the HSR as the train speed approaches the Rayleigh wave

speed. This high level of vibration in the high-speed track can cause rapid deterioration of the track structures and possible derailment in the worst-case scenario (Banimahd, 2008). The Rayleigh wave speed, mentioned above, refers to the equivalent Rayleigh wave speed of the rail/embankment/ground systems. This threshold speed is called the critical speed and is known as Ground Mach 1.0 or GM 1.0 (Bian et al. 2008, G. Lefeuvre-Mesgouez and Mesgouez 2008, Woodward et al. 2013, Tafti et al. 2017). A study of track responses through different field measurement and numerical simulations reveals that below a certain train speed (about 50% of critical speed), no wave propagates through the soil skeleton; consequently, the displacement field is almost the same as the static displacement field under the train due its self-weight (Figure 4.9 (a)), and it moves with the train (Madshus and Kaynia 2000, Madshus and Kaynia 2001, Madshus et al. 2004, Banimahd 2008, Bian et al. 2008, Abu Sayed and Shahin 2016). The direction of the displacement in this train speed zone is always downwards (Figure 4.9 (b)). This train speed is called the cut-off speed and this zone of train speed (below about 50% of critical speed) is considered as the quasi-static zone (Madshus and Kaynia 2000, Madshus and Kaynia 2001, Madshus et al. 2004). As illustrated in Figure 4.9 (b), a symmetric displacement pattern can be observed in time if the load pattern is symmetric. On the other hand, as a train passes cut-off speed, the displacement magnitude will start increasing with the speed due to waves being generated and propagated through the soil skeleton (Madshus and Kaynia 2000). However, the rate of increase is not considerable until train speed reaches about 70% of critical speed. Therefore, this zone of speed ($0.5V_C < V_T < 0.7V_C$) can be considered as a quasi-static zone too. For higher train speeds (about $V_T > 0.7V_C$), different displacement patterns appear. They are in both directions:

upwards and downwards as shown in Figure 4.9 (c) which includes the time history of the displacements along the track, including a non-symmetric pattern in time.

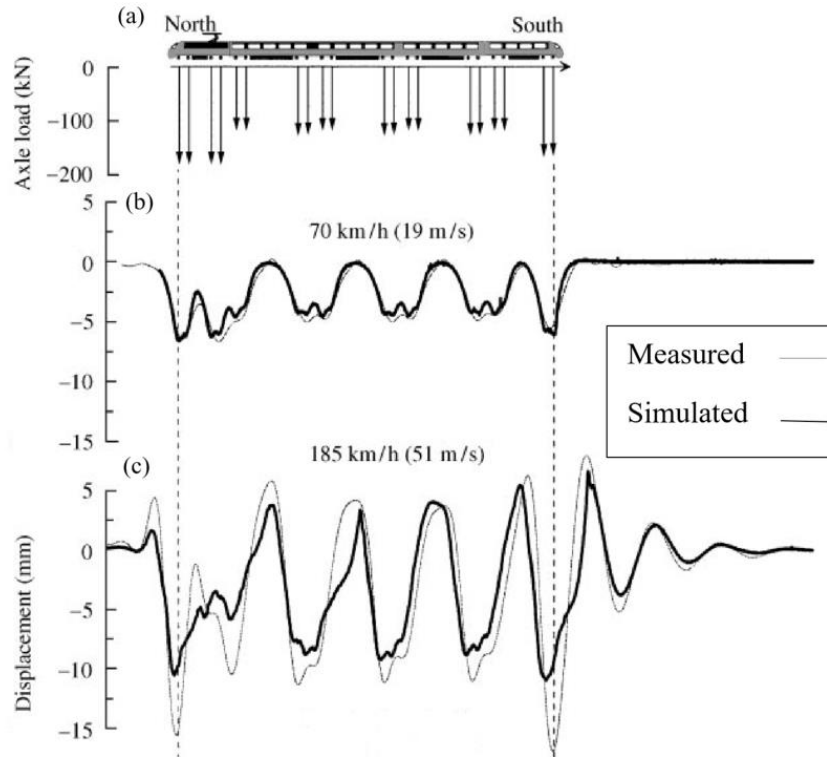


Figure 4.9. (a) Train configuration and its axle loads in measured and simulated vertical track displacement at (b) cut-off train speed and (c) speed close to critical speed (Madshus and Kaynia 2000)

A summary of maximum track displacement at different train speeds is displayed in Figure 4.10, which plots the amplitude of dynamic embankment displacement as a function of train speed. At the Ledsgard site, cut-off speed is almost equal to 70 km/h below which the amplitude of dynamic embankment displacement is almost zero since there is no wave propagation through soil. As soon as a train passes this speed limit,

Rayleigh waves start to generate, and their dynamic amplification increases gradually until train speed reaches the speed of 150 km/h, at which point the dynamic amplification increase becomes much more pronounced with train speed increase. According to the results obtained numerically, at this site the critical speed, which causes the maximum track displacement, is close to 235 km/h (Madshus and Kaynia 2000, Madshus and Kaynia 2001). As a train passes the critical speed, the amplitude of the track displacement decreases as train speed increases (Figure 4.10).

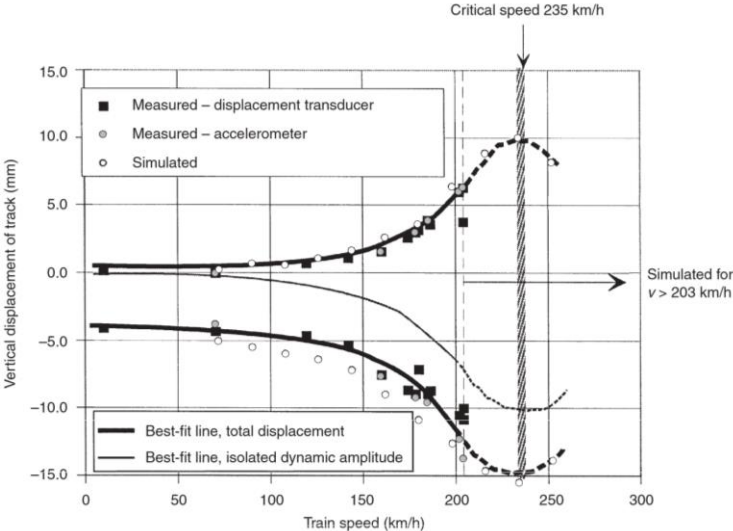


Figure 4.10. Measured and simulated peak vertical track displacement amplitude vs. train speed (Madshus and Kaynia 2001)

4.3.3 Purpose of this Study

A reliable Estimate of the critical speed has been always one of researcher's primary concern. In cases of very shallow embankment, the critical speed is almost equal to the soft subsoil Rayleigh wave speed (Sunaga 1990, Madshus et al 2004). At the Ledsgard site, the track is constructed on a shallow embankment (embankment thickness less than 1m) on top of a soft soil; however, in this case study, the subsoil is a layered soil with different Rayleigh wave speeds (Figure 4.11). In such a complex case study, it is not simple to estimate the critical speed. To provide safe and comfortable rides by HSTs, it is essential to precisely model the complex track/embankment/ground system to estimate the track responses to critical speed (Krylov 1994, Madshus and Kaynia 2000, Kaynia and Madshus 2001, Madshus et al. 2004, Woodward et al. 2012, Woodward et al. 2013, Tafti et al. 2017).

Because measurement data on the behavior of the HSR tracks as train speed approaches or passes the critical speed are limited, a numerical simulation verified with real field data can be a good substitute to investigate different cases with any complexities. The specific area that will be addressed in the current study is the problem of critical speed, including potential derailment when HSTs break the Rayleigh wave barrier when traveling 400 km/h (110 m/s) and higher. In this section, the complex 4-D FEM of train/tracks/embankment will be fully explained. Then field measurements performed in Sweden and full-scale laboratory model testing conducted in China will be utilized to verify the reliability of the numerical model to reproduce the dynamic response of the track, embankment, and underlying soils. Some effective countermeasures used all over

the world will be reviewed in this section before proposing any recommendation to mitigate the effects of breaking the Rayleigh wave barrier. A design procedure of HSRs is proposed based on the results obtained from these parametric studies. The results of the parametric studies are presented in the form of some guideline charts which can be used in the HSR design procedure. Finally, conclusion and recommendations will be presented at the end of this section.

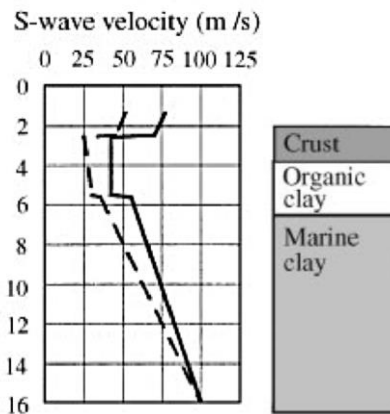


Figure 4.11. S-wave speed vs. depth at Ledsgard site (Sweden) (Madshus and Kaynia 2000)

4.4 Computer Model: LS-DYNA

There are numerous computer models used to investigate the dynamic effect of running HSTs on track structures (Madshus et al. 2004, Banimahd 2008, Nicks 2009). Depending on the area of interest, one of two types of models can be used: a vehicle dynamic model or a track model. The vehicle models such as NUCARS, VAMPIRE,

GENSYS, SIMPACK, and ADAMS/Rail-MEDYNA include a well-developed vehicle model and simple track structure model (Nicks 2009). On the other hand, track models such as ILLITRACK, GEOTRACK and KENTRACK are comprised of complex track structure models but have a very simple vehicle model (Nicks 2009).

LS-DYNA, developed by Livermore Software Technology Corp (LSTC), is a general purpose implicit and explicit finite element program with a wide range of applications to analyze nonlinear structure responses. It can be used to model different engineering problems consisting of crashworthiness, occupant protection, metal forming, product testing, drop testing, high-speed impact, seismic structural design and so on. In railway industries, this software has been used to model crash impacts and carry out dynamic analysis of bridges. Among all models mentioned above, LS-DYNA has the benefit of a well-developed modeling of both vehicle and track structure which enables it to analyze the effect of breaking the Rayleigh wave barrier on the dynamic track motion. It also was used to simulate the problem of bump along HSR, which will be presented in section 5. This software was used for numerical simulation in this research study because of previous success with this package (Nicks 2009). Nicks (2009) performed several LS-DYNA simulations on train/track systems to model the bump at the end of railway bridges. It was a successful experiment in numerical modeling of the train/track systems; therefore, in this study, LS-DYNA was selected for numerical simulations.

4.5 Development of Four-Dimensional Finite Element Model: Numerical Simulation

Numerical models aim to simulate the responses of the train/track systems at high train speeds. For this purpose, as mentioned in section 4.4, the powerful numerical software LS-DYNA has been used to model the components involved and to simulate the dynamic motion.

Our model components included the train, the track, the embankment, and the natural soil on which the embankment was placed. In this section, different aspects of the 4-D FEM that was used for numerical simulation in this research study will be illustrated in term of representation of the train/track model configurations, their material properties, and boundary conditions. Model verification will be presented too.

4.5.1 Track/Embankment/Soil Model Description

The rail and ties were modeled as solid elements, and rail was attached to the model of the railroad ties. The railroad ties were spaced at 0.7 m from center to center and had dimensions of 0.3 m x 0.2 m x 2.4 m. Two models of embankments for ballasted and slab track were modeled in the same way as the site condition in Ledsgard in Sweden and as the China full-scale test. Both ballasted track and slab track were modeled. The ballasted track embankment included ballast or embankment and layered natural subgrade while the

slab track embankment was comprised of track slab, concrete base, roadbed, subgrade, and natural subsoil. These two models will be described completely in section 4.5.5. The embankment used for parametric studies included two layers, one of ballast and the other of natural subgrade comprising different sublayers. Figure 4.12 displays a cross section and side view of the model that was used in the parametric studies. Solid elements were used to model embankment/soil. The ballast thickness varied from 1 m to 10 m, and the model depth was extended to 20 m to avoid boundary condition effects, i.e., wave reflection. In this research, only one-half of the full model was simulated because the mesh was symmetrical from the track centerline. The embankment and track were 352.3 m long to ensure that the whole train could run until a steady state situation was reached and that the effects of the boundary conditions were avoided (Figure 4.13). Figure 4.13 also illustrates the run time of the train (T) which can be defined as

$$T(s)=L(m)/V_T(m/s) \quad (4.7)$$

where L is length of the train model; V_T is train speed which is varied in different case studies.

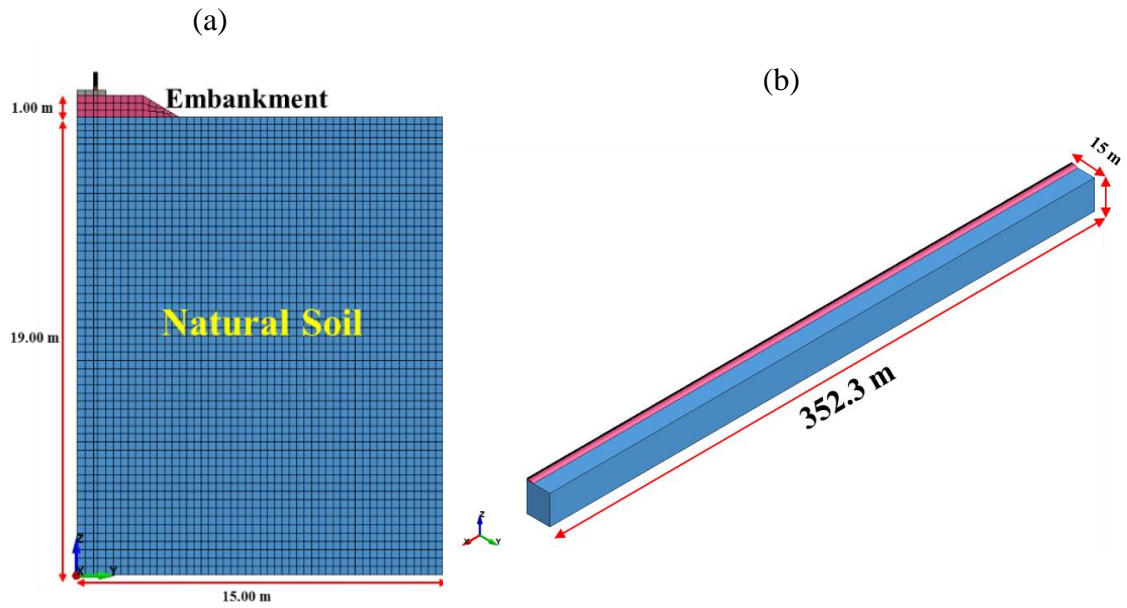


Figure 4.12. (a) Cross section and (b) side view of the finite element model

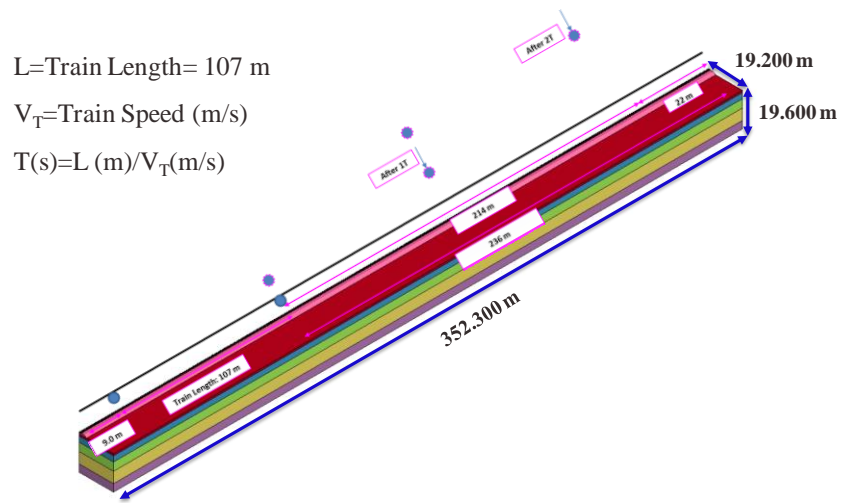
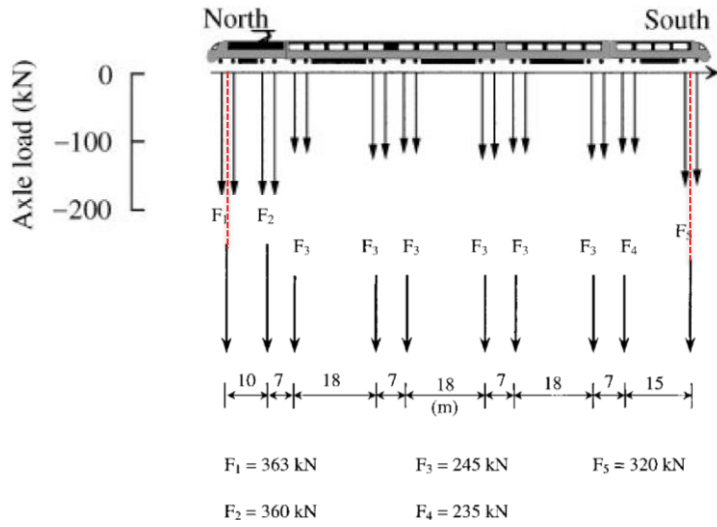


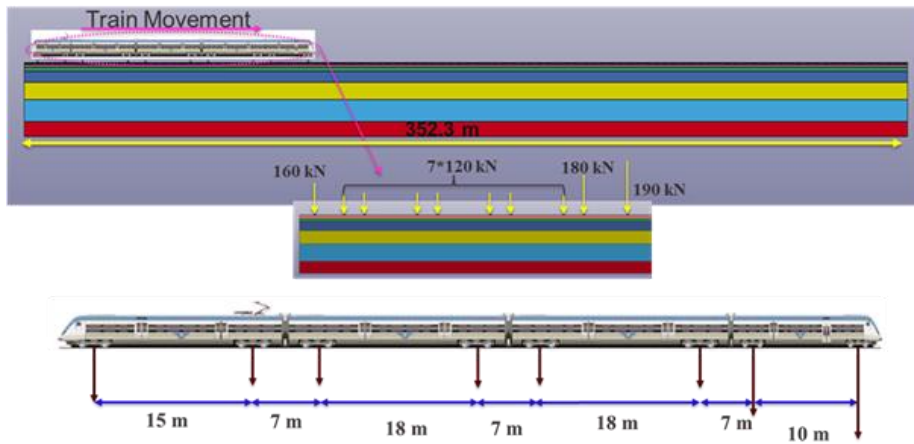
Figure 4.13. Train run time calculation

4.5.2 Train Model Configuration

The train was modeled as a series of train wheels with a concentrated load at the center of the wheel moving at a constant speed. The wheel section was modeled to be solid. Two types of trains were modeled for two case studies, Sweden and China. The first one, which was used for parametric studies and model verification versus field measurements obtained from the Ledsgard site, was modeled after the X2000 train for trainload and dimensions (Figure 4.14) (Kaynia et al. 2000). To simplify the train model, the two axle loads on each side of each bogie were combined into one concentrated load at the centerline of a bogie. The second one, which was used for verifying the model against data given by full-scale model testing in China, was a CRH2-type HST with an axle load of 140 kN as modeled numerically in LS-DYNA (Figure 4.15).

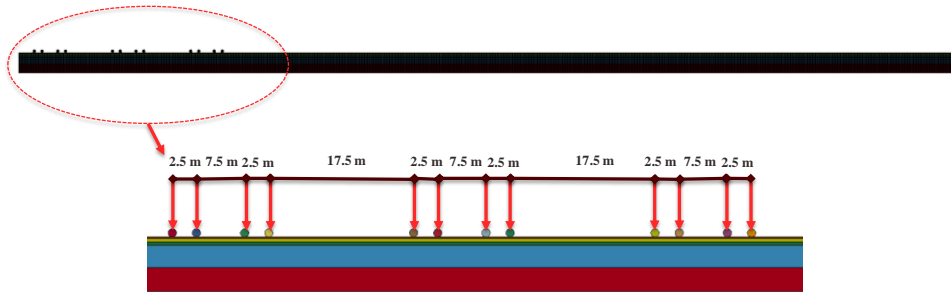
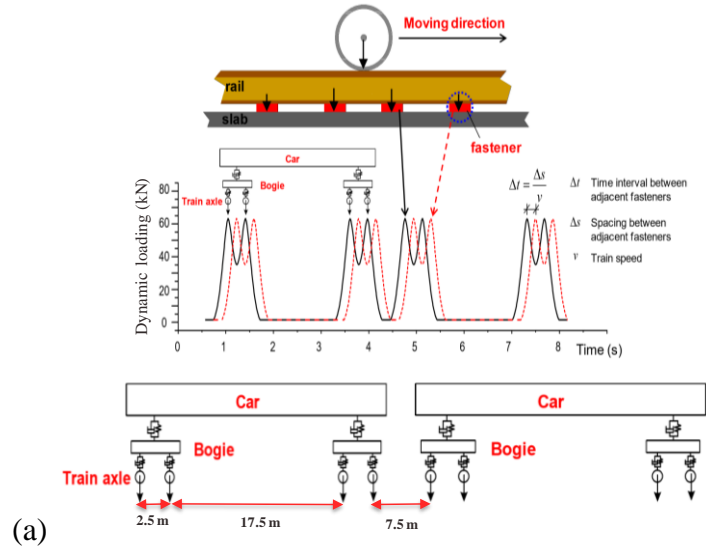


(a)



(b)

Figure 4.14. X2000 specification (load and dimension) (a) Adapted Kaynia et al. (2000) and Madshus and Kaynia (2000) and (b) as used in the current numerical simulation



(a)

(b)

Figure 4.15. CRH2 specification (load and dimension) (a) Adapted Chen et al. (2014) and (b) as used in the current numerical simulation

In the LS-DYNA FEM, a surface-to-surface contact was defined between the outer surface of the wheel and the top surface of the rail with a friction based on a Coulomb formulation (Hallquist 2006). The static and dynamic friction coefficients were considered to be 0.4 and 0.35, respectively. The outer elements of the wheels and the top outer elements of the rail were considered as the slave and master surfaces, respectively (Figure 4.16). A penalty algorithm applied to define the contact between the wheel/rail surfaces

will place normal interface springs between the contact surface and penetrating nodes as the slave nodes penetrate the master nodes (Hallquist 2006).

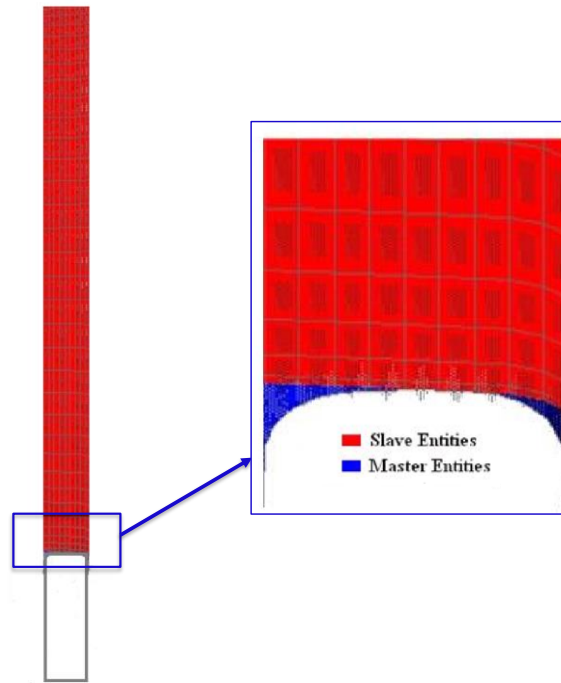


Figure 4.16. Wheel/rail contact surface (Adapted Nicks 2009)

4.5.3 Material Properties

All elements of rail and ties were modeled with elastic material properties. The rail and the railroad ties were modeled with steel and concrete material properties, respectively (Table 4.2). The wheel materials were modeled with rigid material properties (steel) (Table 4.2). The material properties for rail, ties, and wheels were constant for all case

studies. However, the material properties of embankment/soil were varied and will be given in each related section. The big concern in soil modeling is the effect of soil nonlinearity on the critical speed. In the following section, this issue will be discussed.

Table 4.2. Elastic Material Properties of Rail, Ties and Train Wheels

Section	Elasticity Modulus (E) MPa	Poisson's Ratio (ν)	Unit Weight (ρ) kg/m³
<i>Rail</i>	210e3	0.25	7897
<i>Ties</i>	20e3	0.3	1000
<i>Train Wheels</i>	210e3	0.25	7897

In soil material modeling, the big question is whether the non-linearity needs to be considered regarding dynamic responses of the HSR tracks or not. While soil is not perfectly elastic, under small strain conditions, soil layers can be assumed to be elastic materials. However, permanent deformation of the track due to running HSTs cannot be estimated with this elastic model. Through a numerical study by Abu Saeed et al. (2016), the influence of nonlinearity of track materials on the critical speed was investigated with two material models under consideration. In Model 1, a linear elastic model was applied to model subgrade and ballast materials, while in Model 2, the ballast and subgrade materials were represented by the elastoplastic Mohr-Coulomb (MC) and hyperbolic Duncan-Chang (DC) constitutive models, respectively. Results obtained from these two scenarios are given in Figure 4.17. According to the outcomes of this research study, the effect of nonlinearity of soil materials on the critical speed estimate is insignificant;

however, considering nonlinearity of soil materials resulted in somewhat higher downward track displacement magnitudes (Figure 4.17).

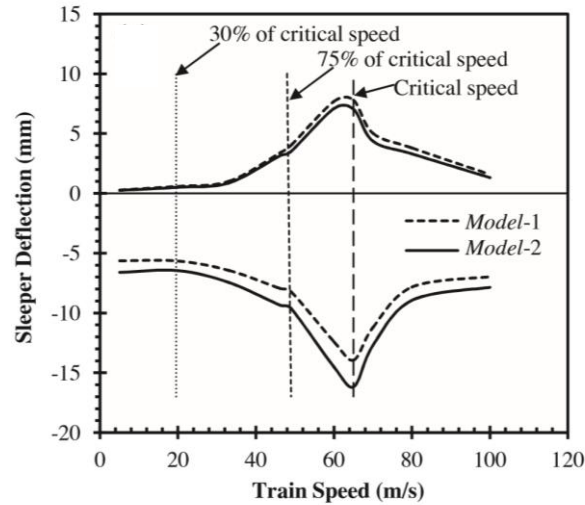


Figure 4.17. The effect of nonlinearity on the critical speed (Abu Saeed et al. 2016)

Banimahd (2008) also conducted a numerical simulation in which the effect of nonlinearity of soil materials was investigated. In accordance with the results obtained through this study, for low to medium train speeds, the soil nonlinearity has negligible impact on the track displacement while an increase can be seen in track displacement as train speed approaches the critical speed (Figure 4.18). However, this research did not find that considering nonlinearity had any effect on the critical speed.

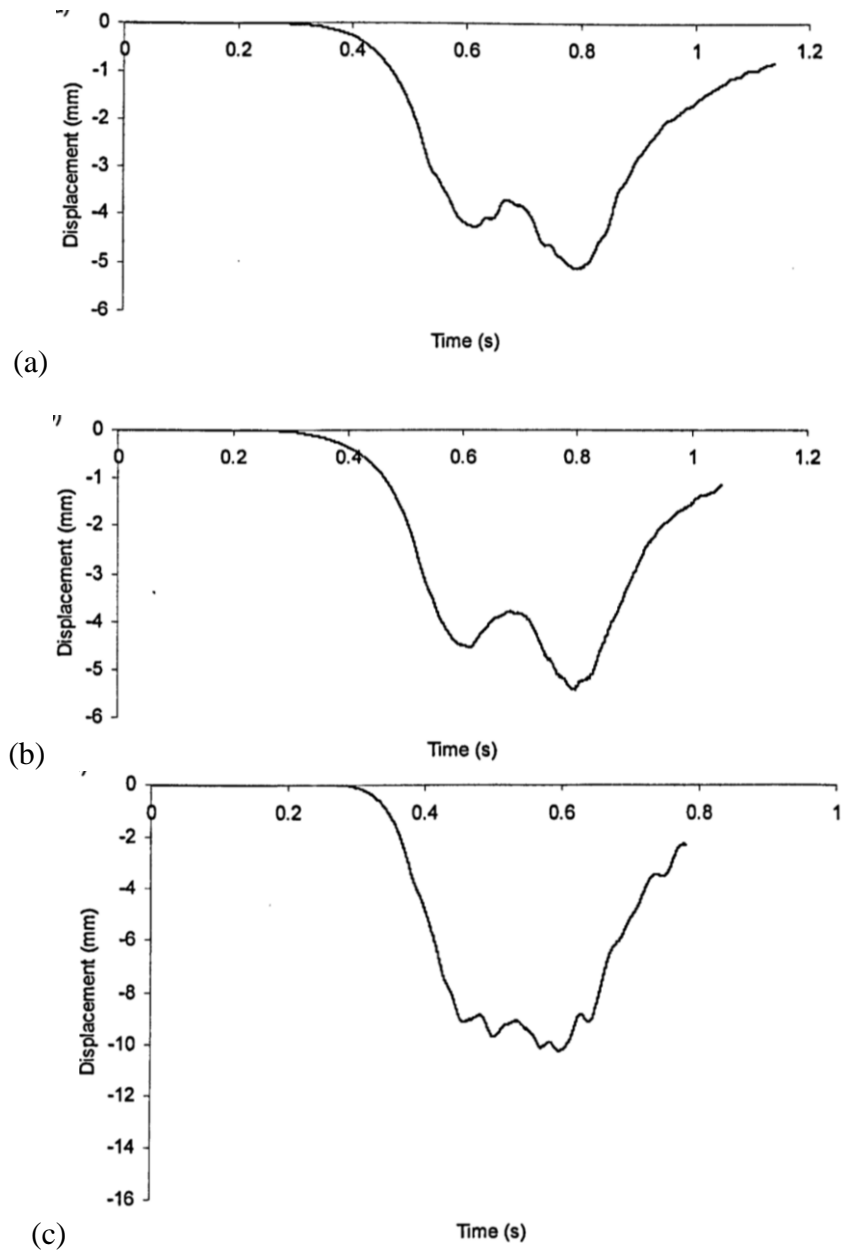


Figure 4.18. Ballast vertical displacement under train load (a) at train speed of 50 m/s and linear ballast, (b) at train speed of 50 m/s and nonlinear ballast, (c) at train speed of 70 m/s and linear ballast, and (d) at train speed of 70 m/s and nonlinear ballast

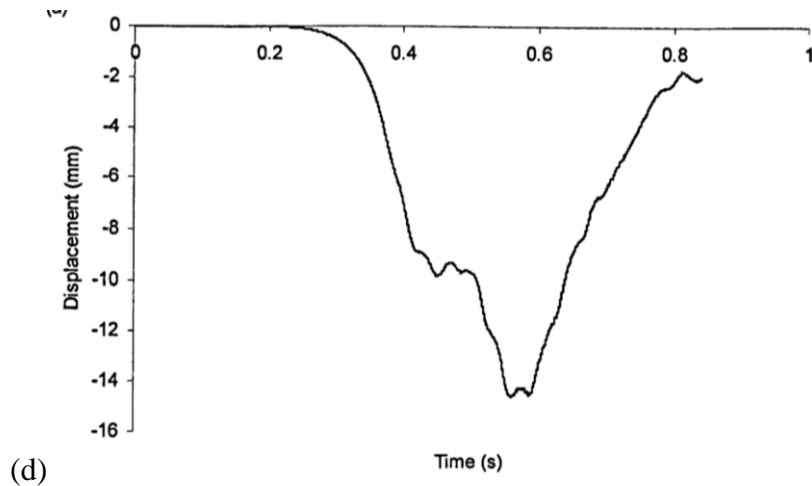


Figure 4.18. Continued

The analysis of measured data obtained from Sweden field tests and lab test results has revealed that the dynamic track displacement induced by HSTs is too high to consider the linear soil behavior (Madshus and Kaynia 2000) (Figure 4.19). Madshus and Kaynia, in their projects, used an “equivalent linear” approach (Madshus and Kaynia 2000, Madshus and Kaynia 2001). In this approach, for higher strain range where the nonlinear behavior of soil materials appears, the real hysteretic behavior of soil is approximated by less secant shear modulus and more hysteretic damping compared to the values estimated for much lower strains. In this method, a dynamic triaxial laboratory test is needed to determine the modulus reduction and damping increase as a function of the strain levels (Figure 4.19). Based on the strain estimated from measured displacements due to passage of HSTs, these curves can be used to estimate the real modulus and damping. Figure 4.19 (b) shows the triaxial test results of organic clay from the Ledsgard site (Madshus and Kaynia 2001). In this research, the results of these studies from the Ledsgard site were

used to assess the reliability of the model. In a literature review, there was no research found that considered nonlinearity of the soil as having considerable impact on the critical speed. Therefore, in this study, to look at the problem in a simple fashion, the linear soil model was assumed, which is a reasonable assumption since our emphasis is on the critical speed, not permanent displacement of the track.

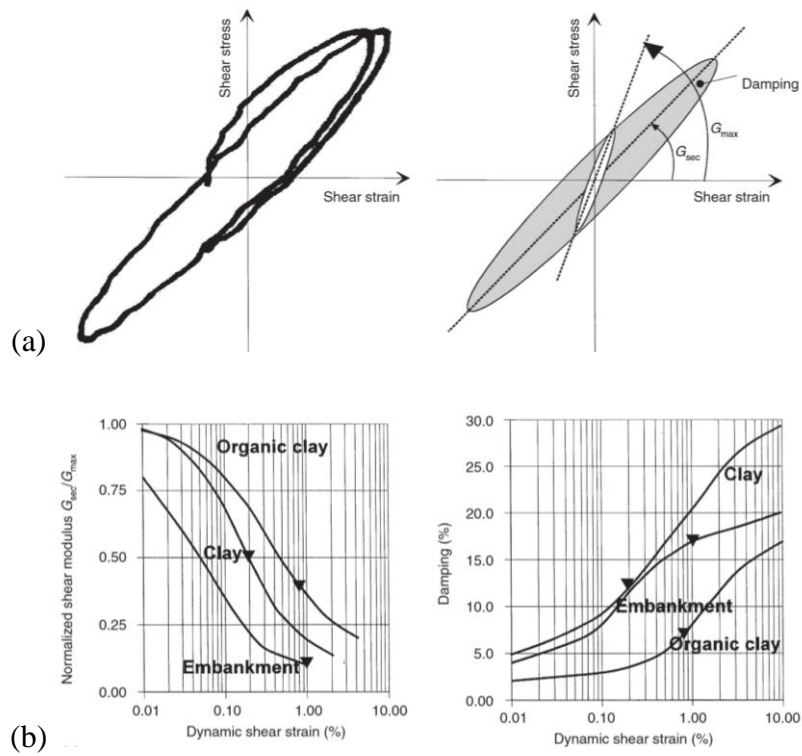
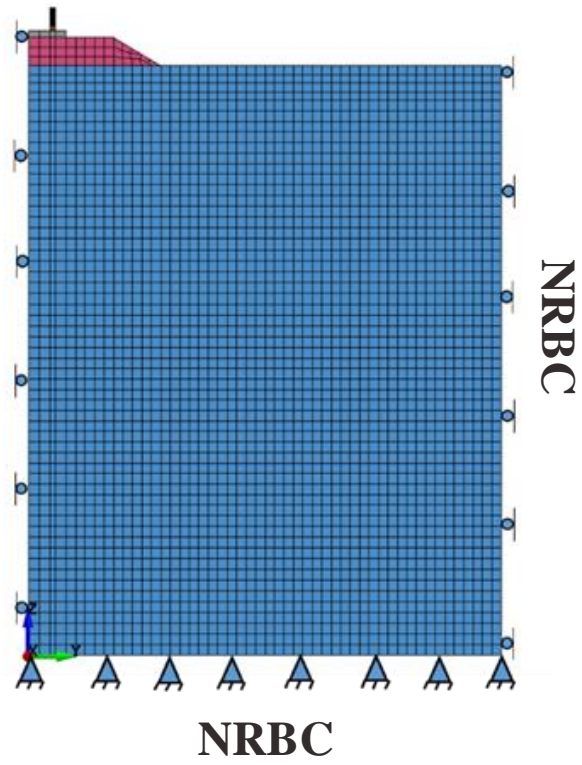


Figure 4.19. Equivalent linear approach: (a) Hysteretic, nonlinear response of soil; (b) modulus degradation and damping curves of organic clay from the Ledsgard site (Sweden) (Madshus and Kaynia 2000)

4.5.4 Boundary Conditions

In a dynamic finite element simulation, due to the presence of stress wave and wave reflection, defining suitable boundary conditions is complicated. The stress wave propagated from its source will experience radiation or geometric damping as it is propagated to the far field. The problem is that if the far field is not modeled as far as required, the wave energy will be reflected back at boundary conditions into the finite element mesh, resulting in an incorrect dynamic response. To prevent these phenomena from happening, the wave energy should be absorbed at the boundary or the model should be long enough. As mentioned earlier in section 4.5.1, the model was long enough in three directions to avoid boundary condition effects. Also, in LS-DYNA, a non-reflecting boundary condition- (NRBC) has been applied in all three directions. The boundary conditions imposed on the model (Figure 4.20) are comprised of (1) roller supports on the sides of the embankment model, which allow vertical motion and (2) pin supports at the bottom of the embankment model to restrict both horizontal and vertical movements. The pin supports used at the bottom of the model were used to simulate a bedrock location. It should be noted that at centerline, only the horizontal motion in y-direction is restricted.

(a)



(b)

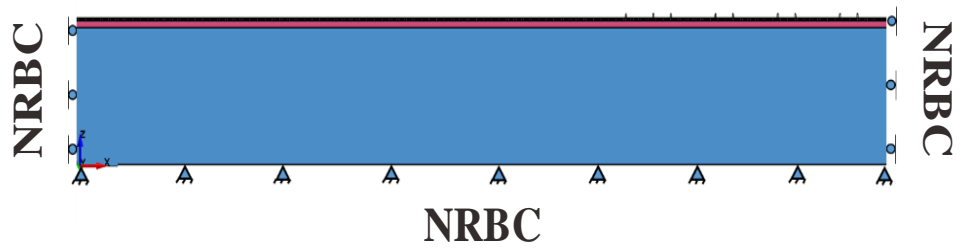


Figure 4.20. Boundary conditions: (a) cross section (b) side view

4.5.5 Model Verification

Before relying on the FEM to investigate the effect of different parameters on the critical speed (conducting parametric studies), results obtained from numerical simulation must be compared to the measured data obtained from field or full-scale laboratory tests. In this research, this is accomplished by choosing two case studies: measurement from the Ledsgard site in Sweden (Adolfsson 1999) and full-scale laboratory model testing in China (Bian et al. 2014), for model validation.

4.5.5.1 HST on Soft Soil: Measurements in Sweden

In 1996, a very high level of vibration was observed by the Swedish National Rail Administration (Banverket) on the Swedish west coastline south of Gothenburg as train speed increased from 140 km/h (39 m/s) to 200 km/h (56 m/s) in different areas along the train line. In these specific areas, the track was located on a low embankment with a height of less than 1 m. Track and embankment was placed on a layer of soft clay. As the acceleration amplitudes induced by X2000, the Swedish HST, were much higher than the amplitudes from freight trains, experts concluded that this high level of vibration was due to the “critical speed,” referring to speeds above the Rayleigh wave speed of the soil profile. To analyze and solve this problem, one which speeds up track degradation, Banverket initiated a research and development project to measure vertical displacements, pore pressure, particle acceleration, and particle velocity for different train speeds of up to 204 km/h (57 m/s). Extensive field measurements on train vehicle and track responses

including measured vertical displacements of the track were used in this study to evaluate the reliability of the numerical simulations.

The site chosen for the measurements was located at Ledsgard, Sweden, 25 km south of Gothenburg. A cross section view of the embankment, where the measurements were obtained and used in this study for model verification, is shown in Figure 4.21 (a). The finite element model in this part of the study was almost identical to a section of the Ledsgard site in Sweden (Figure 4.21 (b)). An X2000 train including an engine and four cars with the axle load varying from 120 kN to 190 kN was used to run the tests (see Figure 4.14). The train speeds varied from 10 km/h (3 m/s) to 204 km/h (57 m/s).

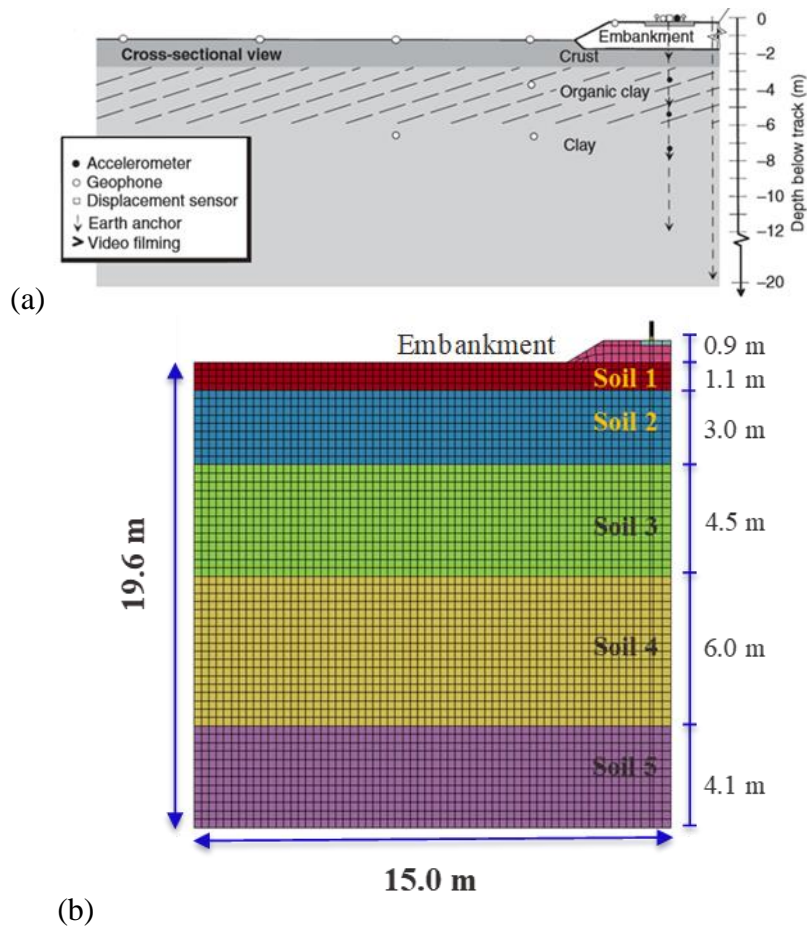
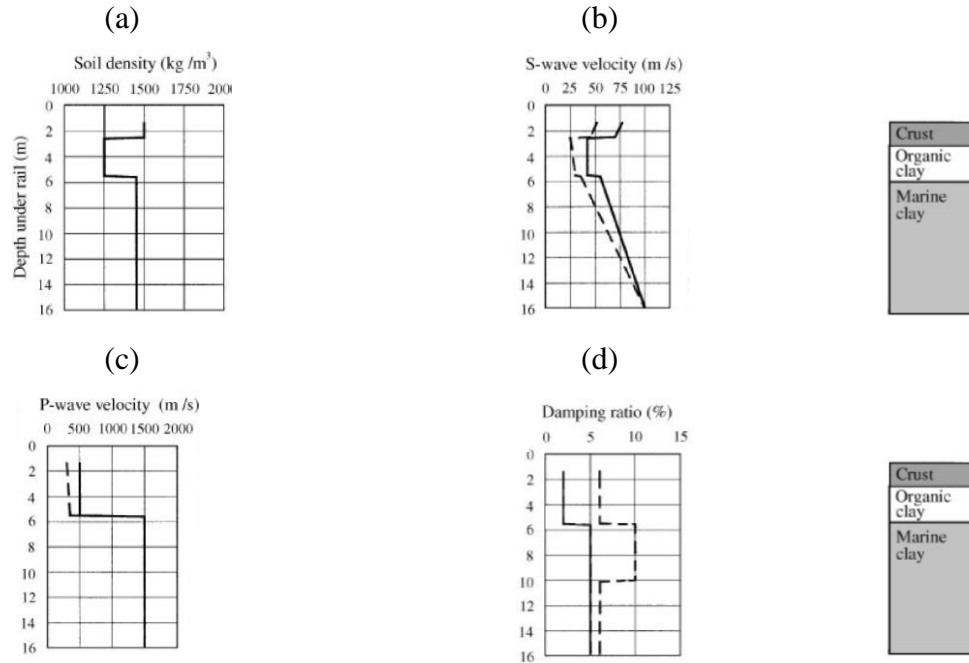


Figure 4.21. (a) A cross section of the embankment at the Ledsgard, Sweden, site (Madshus and Kaynia 2001) (b) The embankment cross section for the numerical simulation

The soil properties of embankment and soil layering materials at the Ledsgard site were obtained from the site investigation (Figure 4.22) (Adolfsson 1999, Madshus and Kaynia 2000, Kaynia et al. 2000, Madshus and Kaynia 2001, Madshus et al. 2004). Figure 4.22 (b) illustrates the measured wave velocities of different soil layers under the embankment, which were obtained through cross-hole and down-hole (seismic CPT) tests (Madshus et al. 2004). There is a gyttja (organic) soft soil with 3 m thickness and

approximately 162 km/h (45 m/s) shear wave speed. The shear wave speed in the soil under the embankment is not constant (Figure 4.22 (b)). In addition to site investigation to map the properties of the embankment/soil materials at the Ledsgard site, dynamic triaxial tests were performed on undisturbed samples obtained from the site to plot the modulus degradation and damping curves, which were applied with an equivalent elastic method (Figure 4.19). The soil characteristics for the two train speeds of 70 km/h (19.44 m/s) and 200 km/h (55.56 m/s) are summarized in Table 4.3 (Kaynia et al. 2000). These soil parameters presented in Table 4.22 were obtained from an equivalent linear approach as explained in section 4.53 (see Figure 4.19). The boundary conditions are defined in the same way as mentioned in Section 4.5.4.



_____ small strain (initial values)
 ----- large strain (values according for nonlinearity used in “equivalent linear” approach)

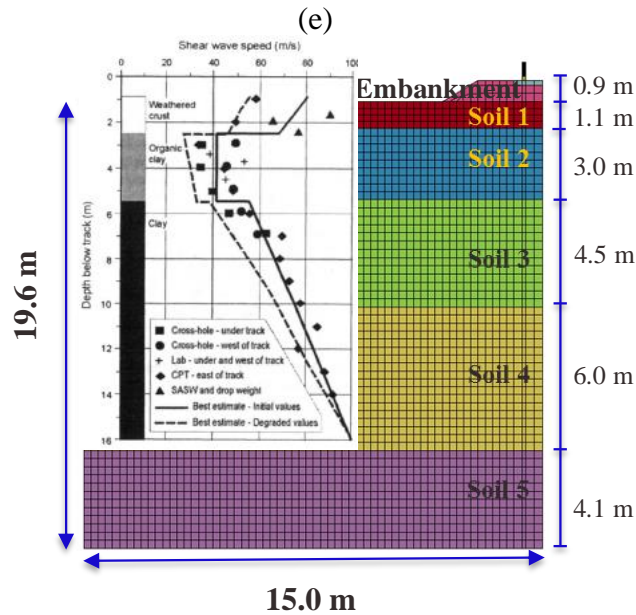


Figure 4.22. (a) to (d) Dynamic soil properties of the embankment/soil vs. depth for Ledsgard site (Sweden) (Madshus and Kaynia 2000), and (e) material properties adopted for FEM

Table 4.3 . Embankment/Soil Parameters for Train Speeds of 200 and 70 km/h (Adapted Kaynia et al. 2000)

<i>Soil Properties ($V_T=200$ km/h)</i>						
<i>Soil Layer#</i>	V_R (km/h)	ρ (kg/m ³)	ν	V_s (m/s)	$G(N/mm^2)$	$E(N/mm^2)$
<i>1</i>	216	1500	0.45	63.32	6.01	17.44
<i>2</i>	111	1260	0.45	32.71	1.35	3.91
<i>3</i>	198	1480	0.45	58.04	4.97	14.41
<i>4</i>	288	1480	0.45	84.43	10.51	30.49
<i>5</i>	360	2000	0.45	105.53	22.27	64.59
<i>Embankment</i>	540	2000	0.35	162.06	55.40	120.00
<i>Soil Properties ($V_T=70$ km/h)</i>						
<i>1</i>	247	1500	0.45	72.30	6.01	17.44
<i>2</i>	140	1260	0.45	41.20	1.35	3.91
<i>3</i>	221	1480	0.45	64.90	4.97	14.41
<i>4</i>	297	1480	0.45	87.00	10.51	30.49
<i>5</i>	360	2000	0.45	105.53	22.27	64.59
<i>Embankment</i>	540	2000	0.35	162.06	55.40	120.00

The measurements, including the time histories of the recorded vertical track displacement for train speeds of 70 and 185 km/h in addition to the maximum track displacement under the train load as a function of train speed, were used to verify the numerical model. Figure 4.23 illustrates the model validation results, and shows that the time history of the simulated vertical track displacements agreed well with the time history of field measured vertical track displacements. Figure 4.23 (a) illustrates the subsonic condition when the train speed is much less than the critical speed, which is equal to approximately 234 km/h (65 m/s). The displacements are quasi-static, downward, and a mirror image of the train axle loads. However, at higher train speeds (Figure 4.23 (b)) that

approach the critical speed, the displacements are not only in the downward direction. The displacement pattern changes from a symmetrical shape in time to a tail of free oscillations which follow the train. Figure 4.24 (a) displays a summary of the downward displacement peaks as a function of train speeds. It shows that the well-developed finite element model can effectively reproduce the essential feature of the HSR track/embankment/soil responses. The maximum speed reached during field testing was 202 km/h; however, the trend shows that this is not yet the critical speed at which resonance happens, and this plot indicates that the track displacement can increase more with increased train speed. Numerical simulation done by Madshus and Kaynia (2000 and 2001) showed that the maximum dynamic displacement of the track occurred at a speed of 235 km/h, which can be considered as the critical speed. The same results were obtained from current simulations (Figure 4.24 (a)). Figure 4.24 (b) shows the comparison between measurements taken at different sites (Woldringh and New 1999) and predicted track displacement. Prediction agrees well with measurements (Figure 4.24 (b)).

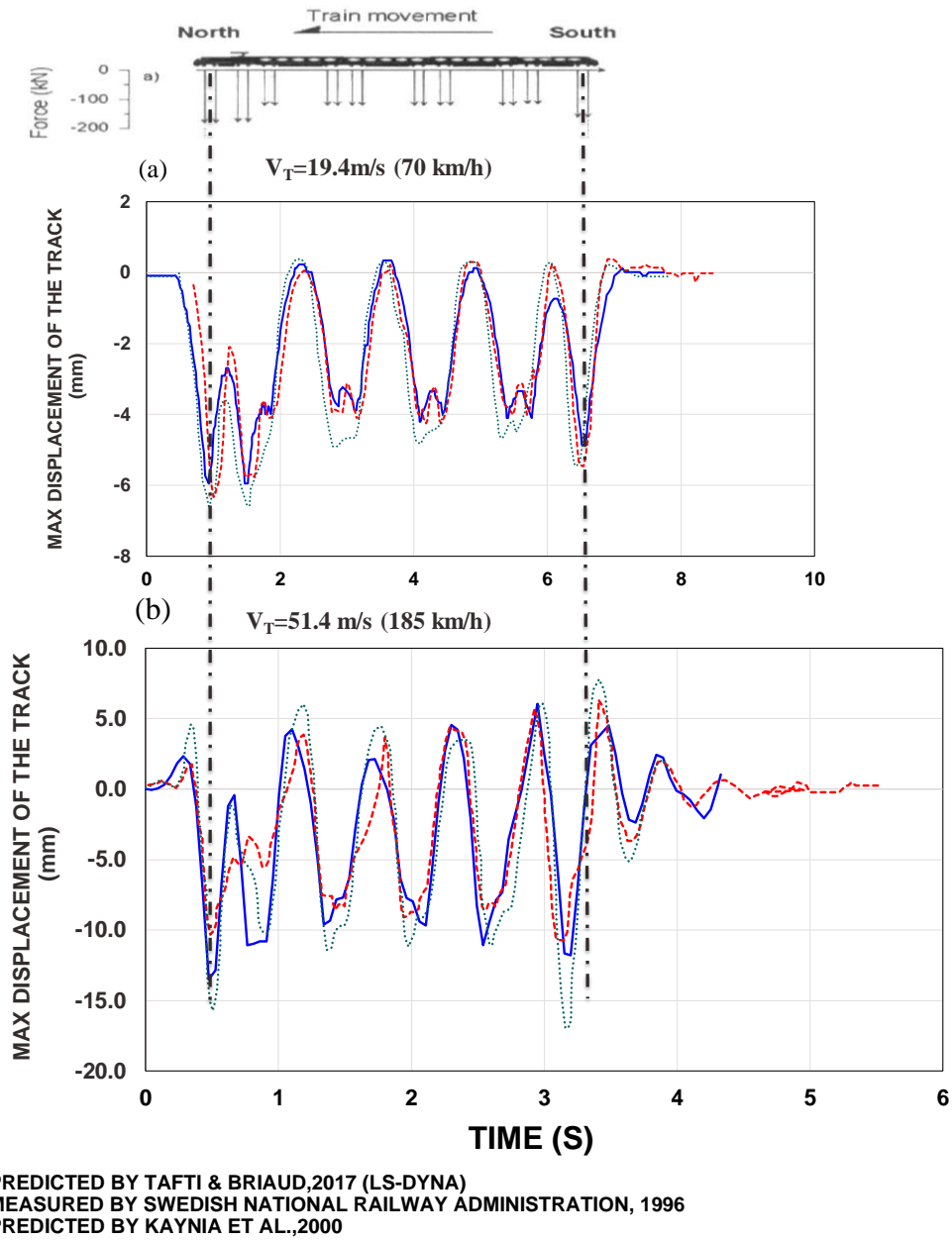
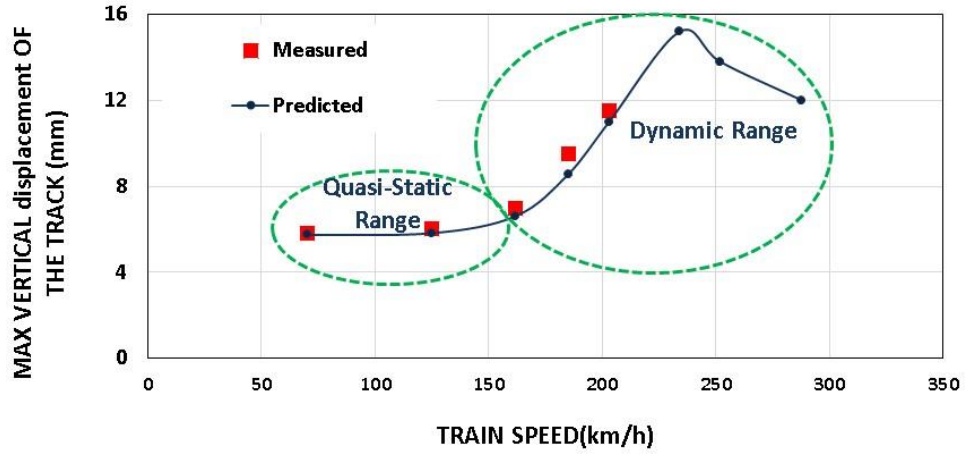
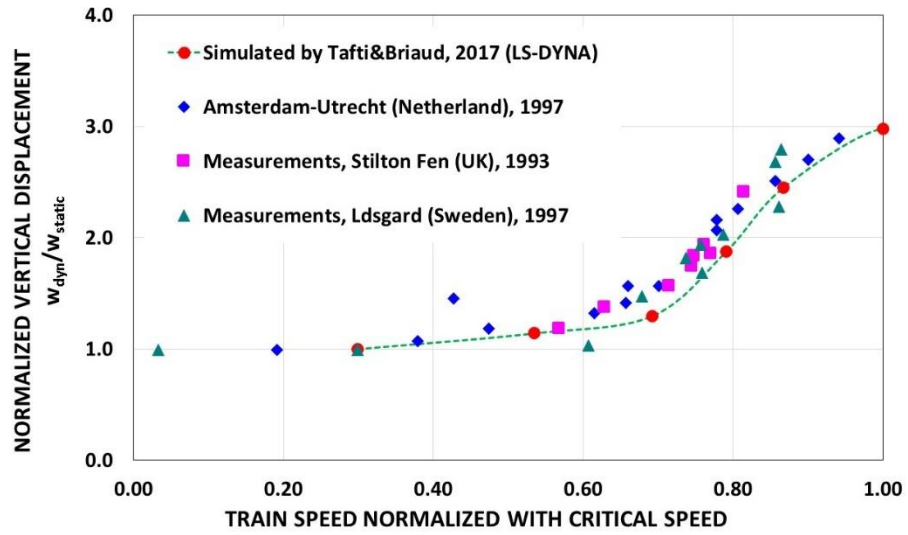


Figure 4.23. Time history of the vertical track displacement at train speeds of (a) 70 km/h and (b) 185 km/h



(a)



(b)

Figure 4.24. (a) Peak track displacement amplitudes as a function of train speeds and (b) Normalized track displacement vs. normalized train speed: measured and simulated

4.5.5.2 Full-Scale Model Testing on a Slab Track in China

In this full-scale laboratory study, a portion of a full-scale HSR slab track was built in a steel box as shown in Figure 4.25 (a). The full-scale model was identical to a section of the Wu-Guang HSR where field measurements exist that can verify the model. Geometry of the model is shown in Figure 4.25 (a) and (c). To hold the physical model, a steel box with inner dimensions of 15 m long, 5 m wide, and 6 m high was used (Figure 4.25 (a)). The track structures included double rails, fasteners, a track slab, a layer of CAM and a concrete base (Figure 4.25). The substructures were comprised of a layer of 0.4 m thick gravel as the roadbed to support the concrete slab, a layer of 2.3 m thick granular soil as the subgrade under the roadbed, and the underlying natural subsoil which was composed of silty soil. The geometry of the finite element model is illustrated in Figure 4.25 (b) and (d). The FEM includes rail, concrete slab, roadbed, subgrade, and subsoil (Figure 4.25 (d)). The FEM is long enough ($L=100$ m) to run the full length of the CRH2 train (Figure 4.25 (b)).

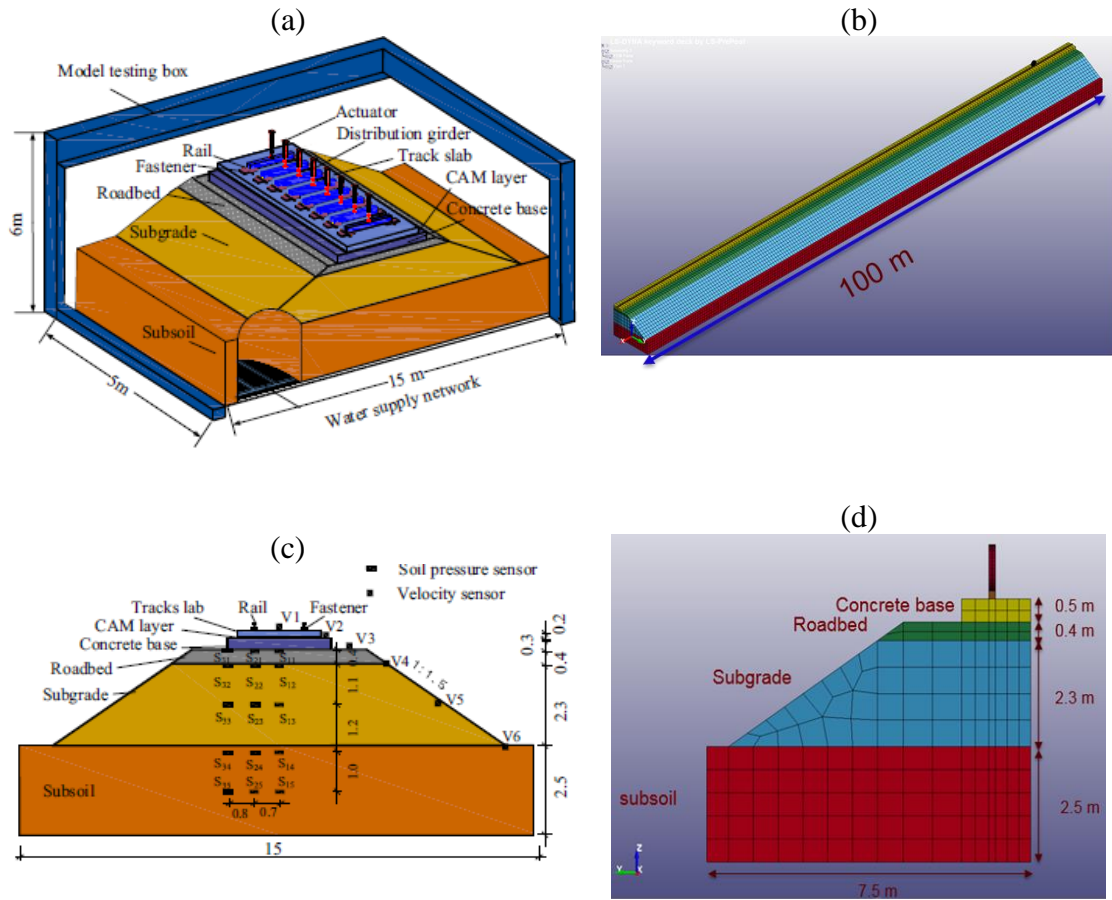


Figure 4.25. Side views of (a) the full-scale experimental study of slab track in China (Bian et al. 2014) and (b) the finite element model in LS-DYNA, and cross section views of (c) the full-scale experimental study of slab track in China (Bian et al. 2014) and (d) the finite element model in LS-DYNA

In this study, a series of dynamic vertical loads output from actuators were applied to simulate the train moving loads (Figure 4.26). Figure 4.26 shows the details of the developed sequential loading device in the laboratory (Bian et al. 2014). The CRH2-type HST with an axle load of 140 kN was modeled numerically in LS-DYNA (see Figure 4.15). The train speeds used in our numerical modeling varied from 180 km/h (50 m/s) to

360 km/h (100 m/s). This range is exactly the same as the one used in the laboratory model (Bian et al. 2014).

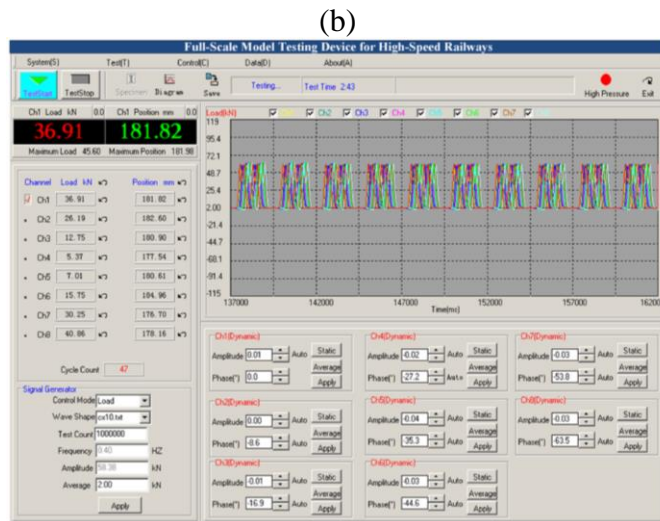
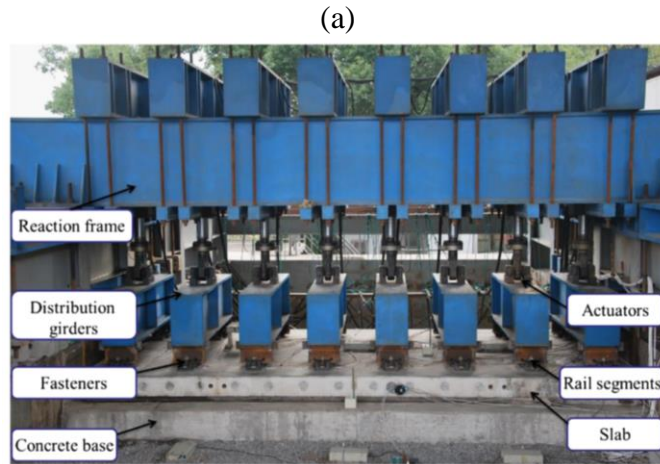


Figure 4.26. (a) The sequential loading system components and (b) the loading program (Bian et al. 2014)

The results of the plate load tests for the deformation modulus E_{v1} and E_{v2} are given in Figure 4.27, which is a typical plot of loading-unloading-reloading for the

deformation modulus of subgrade and roadbed (Bian et al. 2014). The results of plate load tests for the deformation modulus of the subgrade and roadbed (Figure 4.27). The track/soil material properties for finite element modeling were derived from outcomes of the plate load tests and parameters summarized in Tables 4.4 and 4.5 (Bian et al. 2014) are presented in Table 4.6.

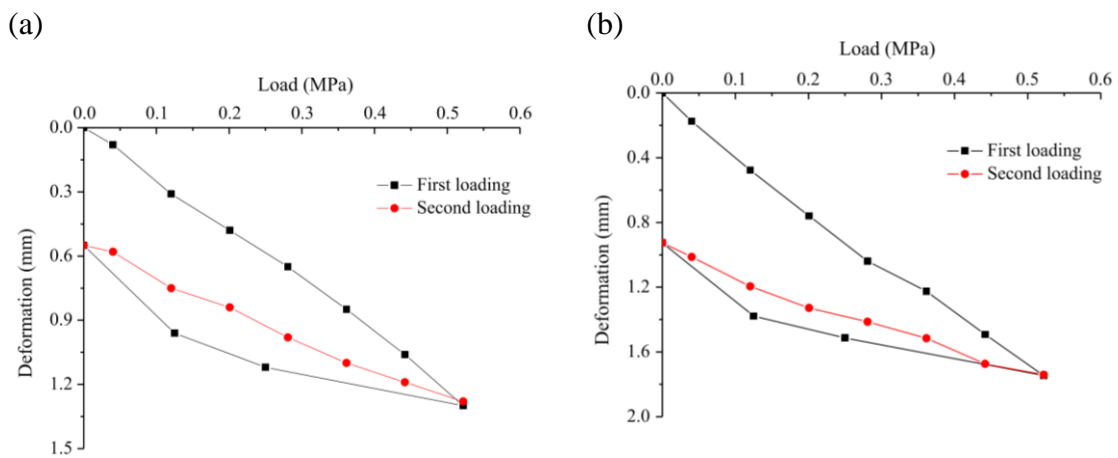


Figure 4.27. The plate load test results for the deformation modulus: (a) subgrade, (b) roadbed (Bian et al. 2014)

Table 4.4. Physical Properties of Subgrade and Subsoil (Bian et al. 2014)

Filling materials	Specific gravity	Maximum dry density (g/cm ³)	Minimum dry density (g/cm ³)	Liquid limit (%)	Plastic limit (%)	Plastic index
Granular soil	2.66	2.11	1.62	na	na	na
Silty soil	2.67	1.62	na	35	24	9

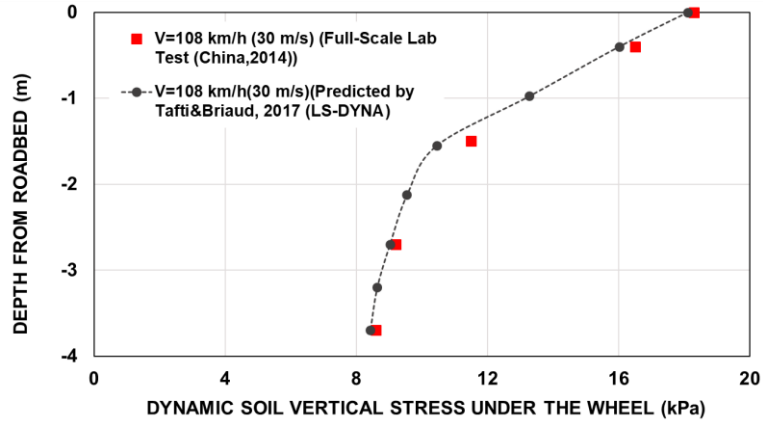
Table 4.5. Materials Results of the Plate Load Tests for The Deformation

Location	LS-1*	LS-2	LS-3	LS-4	LR-1**	LR-2	LR-3
σ_{max} (MPa)	0.52	0.52	0.52	0.52	0.52	0.52	0.52
E_{v1} (E_{v2}) (MPa)	92(157)	79(144)	82(143)	67(151)	73(134)	69(147)	76(160)
E_{v2}/E_{v1}	1.7	1.8	1.7	2.3	1.8	2.1	2.1
E_{38} (MPa)	149	133	134	136	126	136	136
σ_s (MPa)	0.38	0.45	0.48	0.50	0.39	0.37	0.34
k_{30} (MPa/m)	306	360	382	402	309	296	272
K	0.95	0.96	0.97	0.96	0.97	0.97	0.98

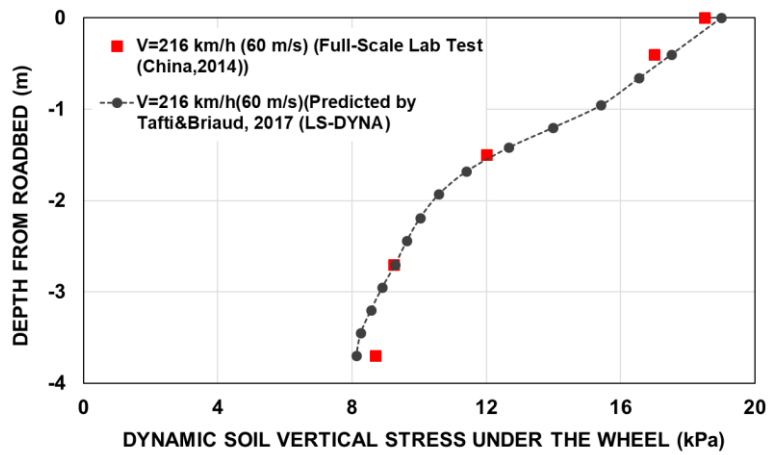
Table 4.6. Material Properties of The Different Sections Used in FEM

Sections	Young Modulus (MPa)	Poisson Ratio, ν	Density, ρ (kg/m^3)
<i>Subsoil</i>	38	0.35	1.620e3
<i>Subgrade</i>	144	0.35	2.110e3
<i>Roadbed</i>	147	0.35	2.110e3
<i>Concrete base</i>	2e4	0.15	2.403e3
<i>Rail</i>	2.1e5	0.28	7.850e3
<i>Wheel</i>	2.1e5	0.28	7.85e3

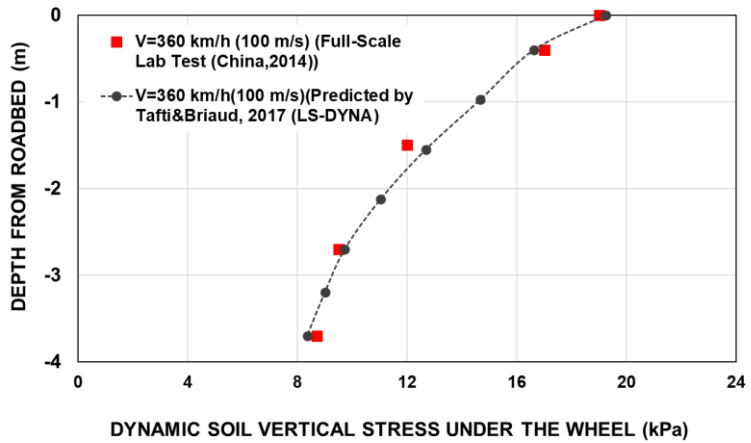
The numerical results from the dynamic responses of the track and underlying soil were compared to those obtained from full-scale model testing. Figure 4.28 illustrates the distribution of the dynamic soil stress versus depth for three different train speeds: 108, 216, and 360 km/h. This comparison between full-scale laboratory tests and simulation confirmed the reliability of the FEM. Figure 4.28 shows that the dynamic soil stresses decreased much faster along shallower depths (< 1.5 m) than greater depths. This is most likely because of Rayleigh wave propagation. As mentioned earlier in this section, Rayleigh waves propagate further in shallower depths than in deeper ones. Therefore, the greatest impact of wave propagation can be experienced by shallower depths.



(a)



(b)



(c)

Figure 4.28. Dynamic soil stress distribution along the depth from roadbed surface at different train speeds of (a) 108 km/h; (b) 216 km/h; (c) 360 km/h

4.6 Ground Mach 1.0 Problem

The numerical simulation results show that in cases of shallow embankment on top of soft ground, the maximum displacement found at the critical speed is about 3 times larger than the static value found at low speeds. This is attributed to a resonance phenomenon between the riding vibrations created by the train and the natural frequency of the soil mass. As mentioned in Section 4.2.3, the shape of deformation, which is very similar to a cone, is called the Mach cone, and the ratio of the train speed to the Rayleigh wave speed is called the Ground Mach number or GM (Woodward 2013) (see Figure 4.3). Figure 4.29 illustrates the effect of train speed on developing the Ground Mach cone. When train speed is less than the critical speed, i.e., at subsonic speeds, the ground vibrations due to the train load are limited to a local area (Figure 4.29 (a)). The distribution of ground deformation under the moving load is almost symmetrical about the load distribution geometry for subsonic speeds ($V_T < V_R$). As train speed approaches critical speed, the Mach effects can be seen clearly. As train speed passes the critical speed and enters the supersonic range, the ground deformation will take on a boomer appearance (Figure 4.29 (b)). Ground deformation at the rear of the moving load becomes very significant, while in front of the load position, it becomes smaller (Figure 4.29 (b)).

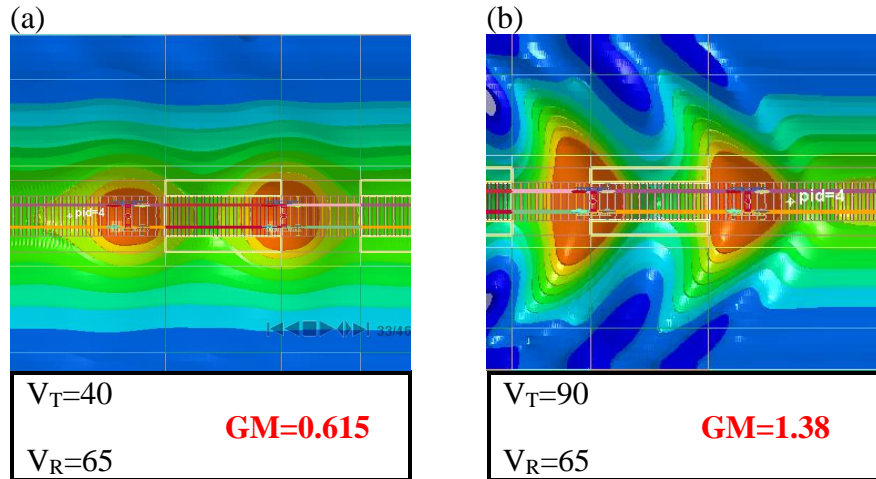


Figure 4.29. Ground deformation (Top View) (a) at subsonic train speed and (b) at supersonic train speed

As with Figure 4.29 (a), the track displacement contour has a symmetrical shape for a subsonic train speed ($V_T < V_R$). In contrast, as train speed passes the threshold speed of critical speed (at supersonic speed: $V_T > V_R$), the Ground Mach cone appears, resulting in unstable ground responses (Figure 4.29 (b)). Figure 4.30 shows the cross-sectional view of the bulb of deformation at subsonic, critical, and supersonic train speeds. The Mach Cone angle is displayed in this figure in addition to the schematic view of the bulb of deformation under the moving loads (train wheels) at different train speeds. The higher the train speed, the more acute the Mach Cone angle will be (Figure 4.30). Calculating GM value to investigate the behavior of the track/ ground components is one essential. Later in this section, GM will be used to define the safe zone of speed that is far enough from critical speed. In fact, the calculation of this parameter is required during parametric studies when trying to predict which parameters have great impacts on track displacement

mitigation strategies. All mitigation strategies are aimed at modifying the track critical speed.

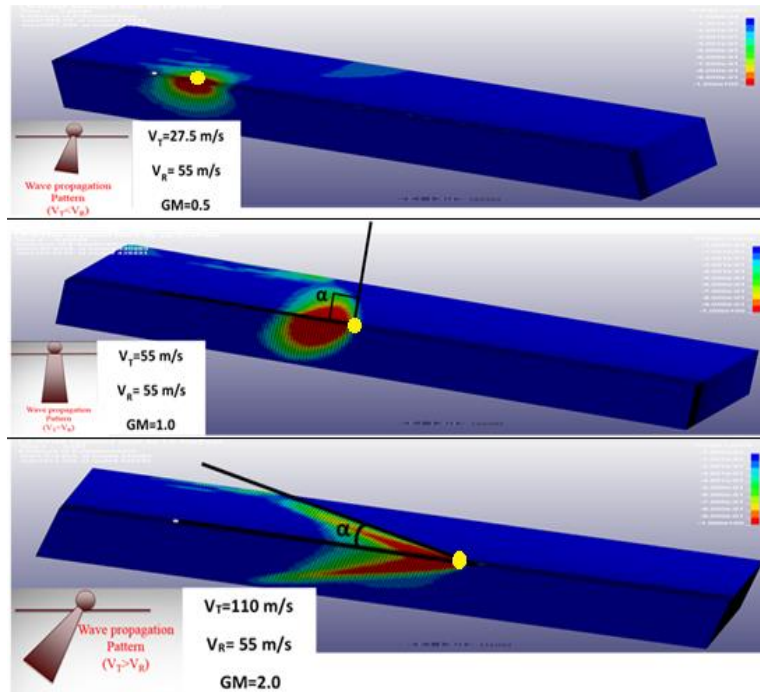


Figure 4.30. Effect of train speed on the development of the GM cone

4.7 Parametric Studies

This parametric study was aimed at assessing the effect of different components of train/track on the problem of breaking the Rayleigh wave barrier and critical speed, which is an influential parameter for HSR embankment design. The verified FEM was

used to conduct this parametric study. Figure 4.31 shows the cross-sectional view of the reference case. In this parametric study, an X2000 train (see Figure 4.14) with the same axle load and bogie/wheel distance was used. One very influential parameter in HSR track/embankment/ground performance is train speed, which was chosen as the first parameter to for the parametric study.

In addition to train speed, the effect of different embankment/ground components on critical speed of track/embankment/ground was determined through this parametric study. On this account, three parameters were considered: embankment modulus (E_e), embankment thickness (H_e), and subgrade modulus (E_s). These three parameters were selected because the most effective design methods for modifying critical speed are based on strengthening the subgrade or stiffening the embankment (discussed later in this section). This parametric study revealed how effective these parameters are on critical speed modification. To simplify the model and assess the effects of the parameters, the subsoil and embankment were considered to be homogeneous. In the parametric study, again only one-half of the full model was simulated because of symmetrical mesh from the track centerline. The same track material properties (see Table 4.2) and boundary conditions (see Figure 4.20) as explained in section 4.5.3 and 4.5.4, respectively, were modelled. The embankment/ ground model dimensions for each case study are different. They will be illustrated in subsequent sections.

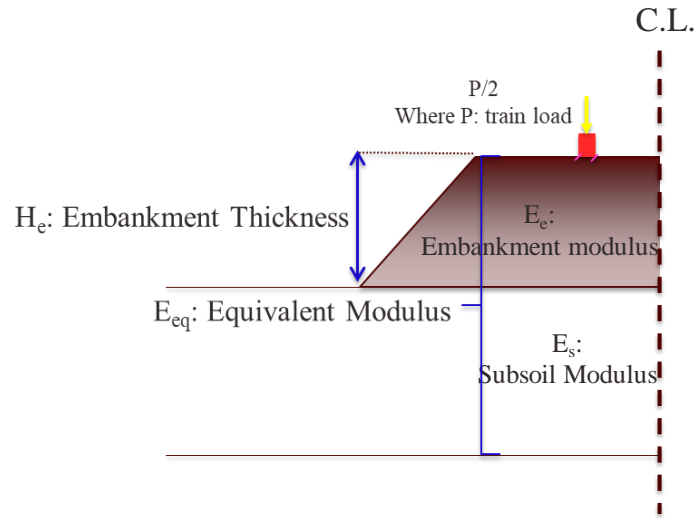


Figure 4.31. Cross sectional view of the finite element model used in the parametric study

4.7.1 Effect of Train Speed on Track Dynamic Responses

The results of numerous studies regarding breaking Rayleigh wave barrier have been confirmed that track/embankment/ground experience the high level of vibration at train speed close to critical speed ($V_T \geq (0.6 \text{ to } 0.7) V_R$). This dynamic response of track/embankment/ground leads to comfort and safety issues for passengers and required frequent maintenance. Therefore, due to the importance of this parameter on the track/embankment/ground system performance, in this section, the FEM was applied to perform a parametric study investigating the effect of speed on track response. The reference case model configuration is illustrated in Figure 4.32. Material properties are given in Table 4.7. In this table, the Rayleigh wave speeds of the soil layers (embankment and subgrade) as estimated by Equation 4.3 were given. The aim of this section is to show

how the critical speed of the track/embankment/ground system (called equivalent Rayleigh wave speed of the track/embankment/ground system) can be obtained from the simulation, which will be used later in subsequent sections. Before investigating the best design method to modify critical speed, it is essential to know how this parameter can be estimated for complex systems including track components, embankment, and subsoil.

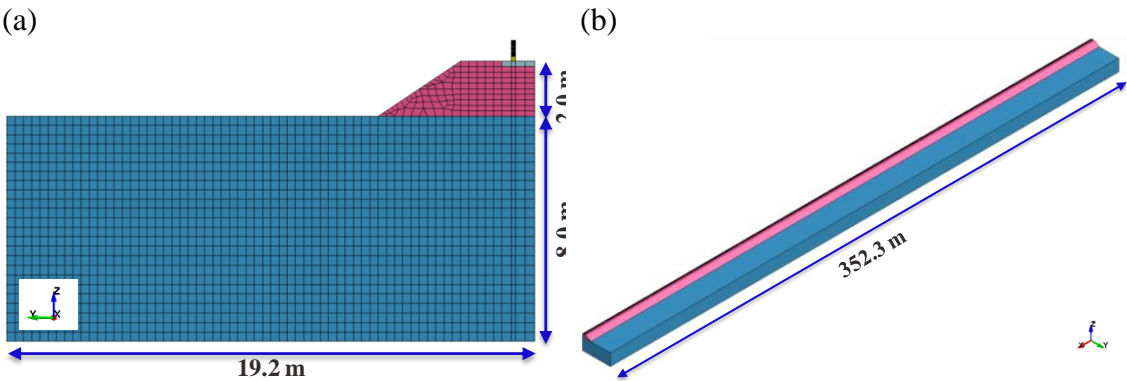


Figure 4.32. FEM dimension used for simulation: (a) cross-section view, (b) side view

Table 4.7. Material Properties of Track/Embankment/Ground System

<i>Section</i>	Elasticity Modulus(E) MPa	Poisson’s Ratio (ν)	Unit Weight (ρ) kg/m³	Rayleigh Wave Speed, V_R (km/h)
<i>Rail</i>	210000.00	0.25	7897	-
<i>Ties</i>	20000.00	0.30	1000	-
<i>Train Wheels</i>	210000.00	0.25	7897	-
<i>Embankment</i>	150.00	0.35	2000	561
<i>Subgrade</i>	6.51	0.45	1260	144

The only parameter that was varied in this part of the study was train speed. The train speed range should be large enough to determine when exactly the resonance (the maximum track displacement) occurs. A wide range of train speeds from 18 km/h (5 m/s) to 720 km/h (150 m/s) was selected to perform the parametric study for the case study explained in this section. Several simulations were performed to study the track dynamic responses due to running an X2000 train under different train speeds. Figure 4.33 depicts examples of time histories of vertical track displacement at four different train speeds: $V_T=108$ km/h (30 m/s), 180 km/h (50 m/s), 252 km/h (70 m/s), and 324 km/h (90 m/s). Significant increase in track displacement can be seen with train speed increase up to a train speed of 252 km/h (70 m/s). In addition to the displacement amplitude increase with train speed, the pattern of the track responses becomes more asymmetrical as train speed increases. Figure 4.34 shows the displacement contours at different train speeds. At low speed ($V_T=108$ m/s: $V_T < 0.5V_C$), as expected, the displacement pattern is almost symmetric, the displacement field moves with the moving loads of the train, and every wheel has its own footprint (Figure 4.34 (a) and 4.35 (a)). In fact, the displacement pattern is the same as the static displacement pattern. As mention before, this range of train speeds at which no dynamic effect of running HSTs can be experienced by track/embankment/ground system is called the “quasi-static” range (Figure 4.36). In this range of train speed, the dynamic amplitudes of the track displacements are almost zero (Figure 4.36). As train speed passes the threshold speed of $0.7 V_C$ (in this case: $V_T=180$ km/h), dynamic effects of operating HSTs becomes much more considerable. As the train speed increases at this range of train speed up to the critical speed ($0.7 V_C < V_T < V_C$), the displacement field moves with the moving load but its shape is not symmetrical anymore

(Figure 4.34 (b) and (c) and Figure 4.35 (b) and (c)). The dynamic amplitude of the track displacement increases up to critical speed at which the maximum track dynamic amplitude can be observed (Figure 4.36). As train speed passes the critical speed (in this case: $V_T > 252$ km/h), as with Figure 4.34 and 4.35 (d), the train is moving ahead of the displacement contours, showing that the train goes faster than the embankment/subgrade Rayleigh wave. The Mach cone shape appears clearly in this train speed range ($V_T > V_C$) (Figure 4.34 and 4.35 (d)). Figure 4.35 illustrates the summary of the track responses as a function of train speed.

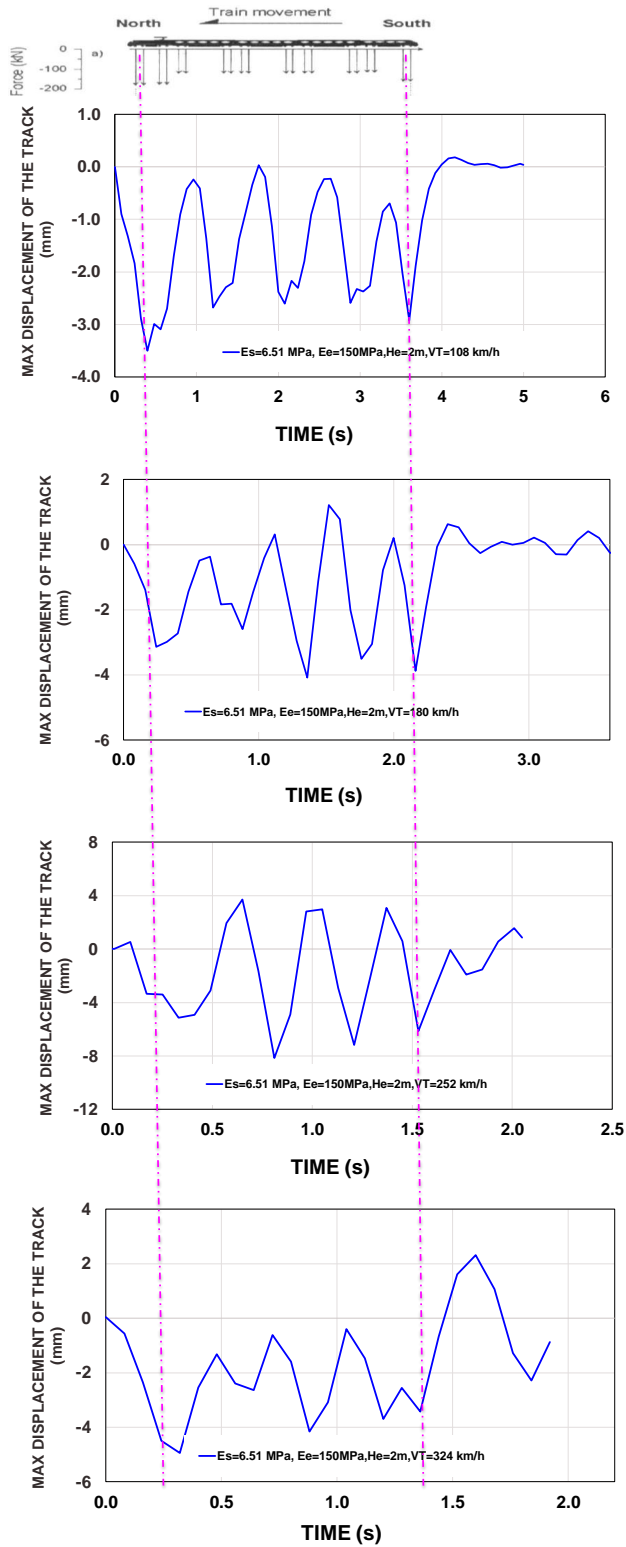


Figure 4.33. Predicted vertical track displacement at different train speeds

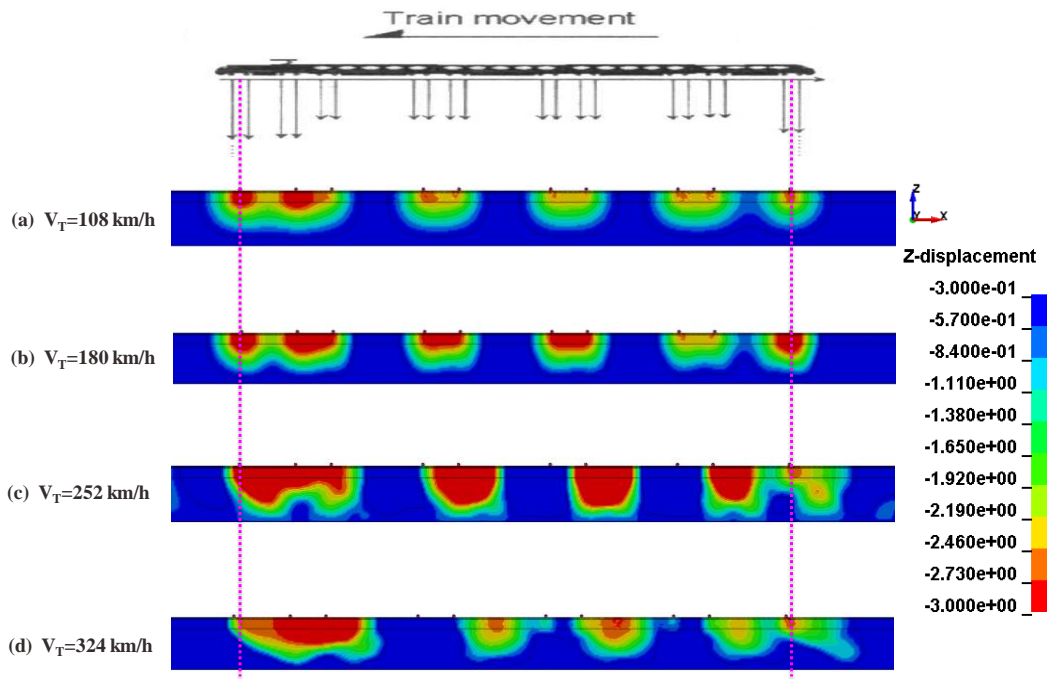


Figure 4.34. Cross-section view of track displacement contour at different train speeds: (a) $V_T=108$ km/h ($GM=0.43$), (b) $V_T=180$ km/h ($GM=0.71$), (c) $V_T=252$ km/h ($GM=1.0$), and (d) $V_T=324$ km/h ($GM=1.29$)

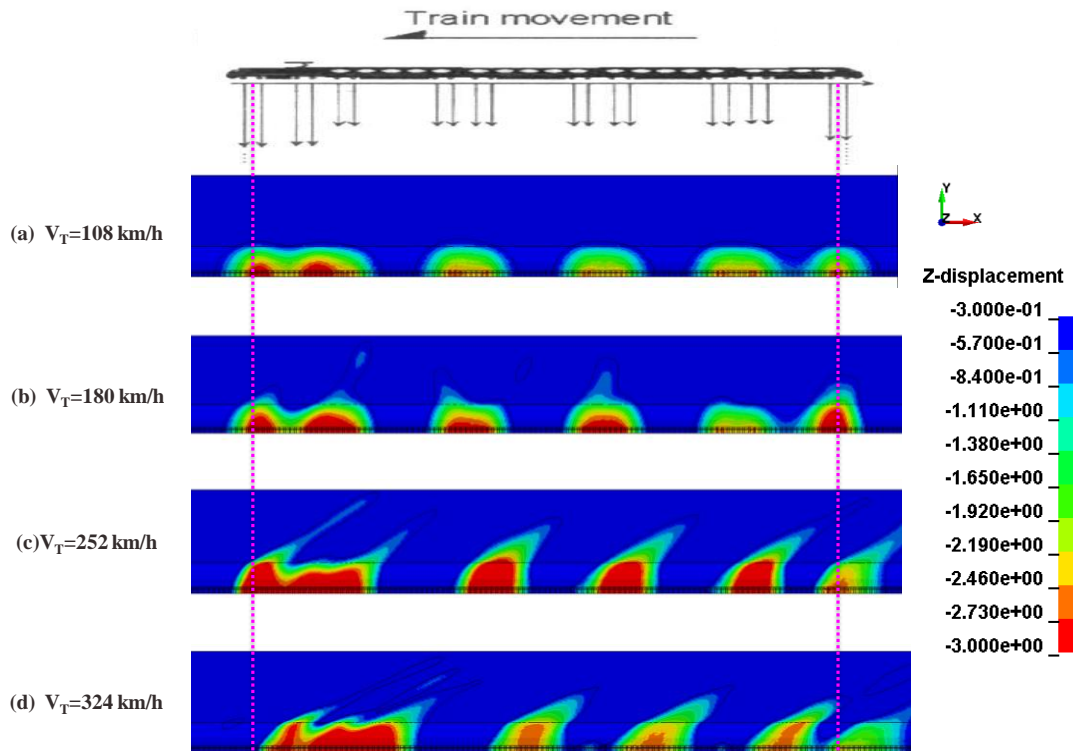


Figure 4.35. Plan view of track displacement contour at different train speeds: (a) $V_T=108$ km/h ($GM=0.43$), (b) $V_T=180$ km/h ($GM=0.71$), (c) $V_T=252$ km/h ($GM=1.0$), and (d) $V_T=324$ km/h ($GM=1.29$)

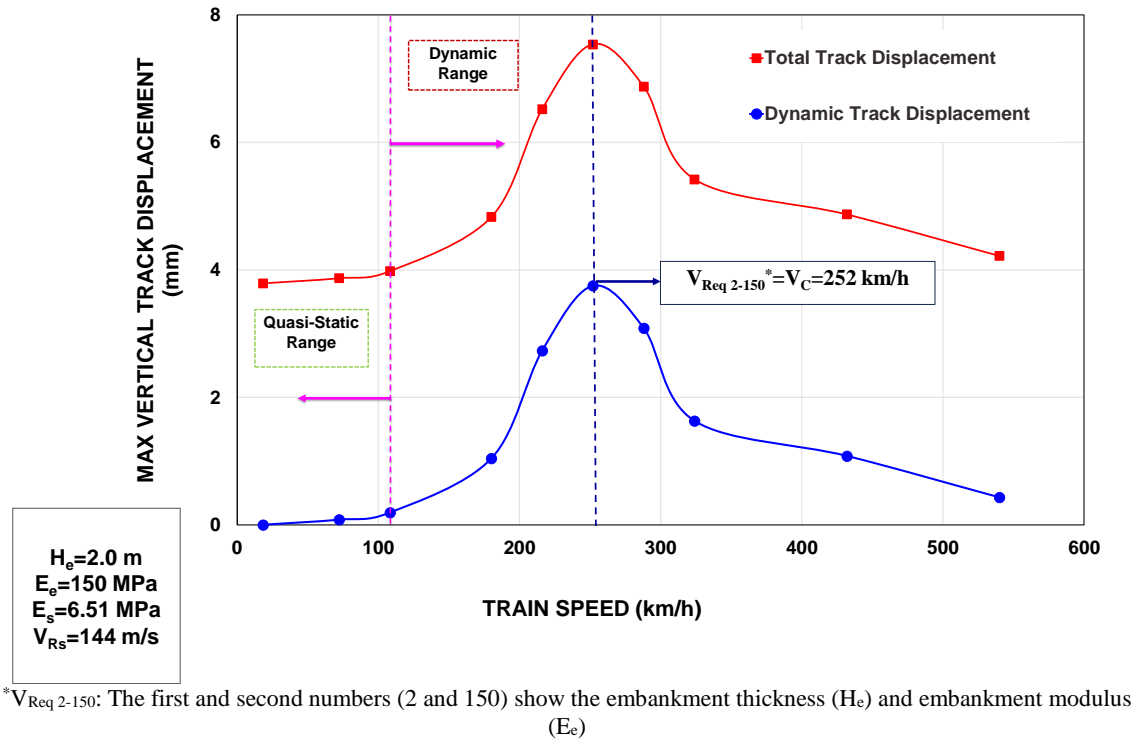


Figure 4.36. Predicted peak vertical track displacement vs. train speed

In this case study, the critical speed is equal to 252 km/h which is not close to the subgrade Rayleigh wave speed. It was mentioned earlier that in case of shallow embankment ($H_e < 1\text{m}$), the critical speed is almost equal to subgrade Rayleigh wave, which is equal to 144 km/h in this case study. However, in this case, the embankment height was 2 m, which was deep enough to increase the critical speed (from 144 km/h to 252 km/h). In fact, this higher critical speed can be reached as a result of stiffening the embankment by increasing its height. In such cases in which the embankment has a large effect on the critical speed, the critical speed will be equal to an equivalent Rayleigh wave speed (V_{Req}) of the whole system, not only the subgrade. In total, 10 different cases with

different train speeds were simulated to obtain the equivalent Rayleigh wave speed (or critical speed) of the track/embankment/subgrade system ($V_{Req}=V_C$), which was 1.75 times greater than the subgrade Rayleigh wave speed ($V_{R(s)}$). Figure 4.37 shows the normalized vertical track displacement as a function of normalized train speed, which is equal to the GM. GM is defined as the ratio of train speed to the equivalent Rayleigh wave speed of track/embankment/ground system. As illustrated in Figure 4.37, at GM 1.0, the maximum dynamic track displacement which is almost twice as high as the static one was predicted. Different measurements (Figure 4.24) show that in cases of shallow embankments ($H_e < 1\text{m}$) on top of soft soil, the ratio of the maximum track displacement at critical speed over the static track displacement is almost equal to three. The results confirmed that when the higher embankments were used, this ratio decreases. This shows that using higher embankments has two advantages: increasing the critical speed and decreasing the track displacement. The effects of this parameter (embankment height: H_e) will be determined in the next section.

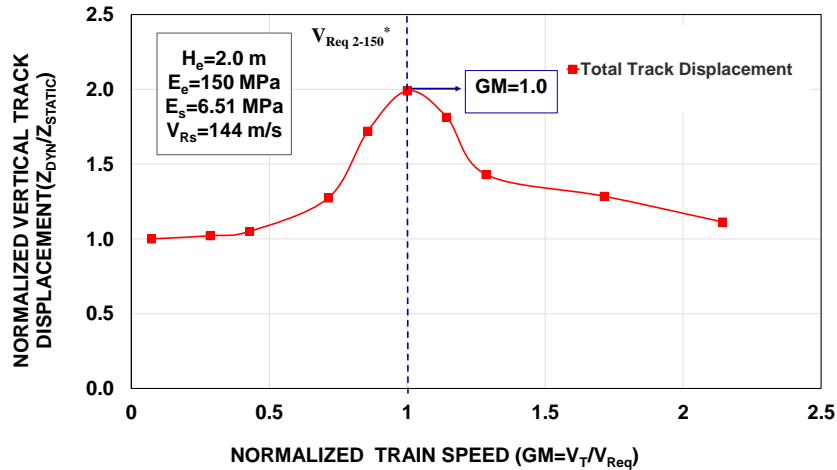


Figure 4.37. Simulated normalized track displacement vs. normalized train speed or Ground Mach number (GM)

4.7.2 Effect of Embankment Thickness on Critical Speed

The effect of embankment thickness or embankment depth (H_e) on the critical speed of track/embankment/subgrade systems is investigated in this section. The height of the embankment with a constant modulus of 150 MPa changes from 0 to 8 m. Also, the modulus of the subsoil is considered to be constant ($E_s=6.51$ MPa). The same material properties as given in Table 4.6 were used in the FEM for determining the influence of embankment thickness on critical speed. The geometry of the FEM is given in Figure 4.38. As mentioned earlier, estimating the critical speed in such a complex track/embankment/subgrade system is not easy. In the current study, these complex systems were modeled in LS-DYNA, and the results obtained from simulations were used to estimate the critical speed as accurate as possible. The steps followed to find the critical

speed of each case study with constant embankment thickness (H_e =constant) are summarized below:

1. The FEM with constant H_e was run for different train speeds. It should be noted that the train speed range should be wide enough to see when the resonance occurs.
2. The time histories of vertical displacement of the track at different train speeds obtained from the FEM simulations were used to find the maximum vertical track displacement at each train speed.
3. Then, the maximum track displacements as a function of train speed were plotted.
4. The train speed at which the maximum track displacement happened was considered as the critical speed (or equivalent Rayleigh wave speeds of embankment/subgrade system).

In this study, to estimate the critical speed of each case study with constant H_e , each case was run for at least 10 different train speeds. In total, 50 different simulations were conducted to determine the critical speed of 8 cases with different embankment thicknesses.

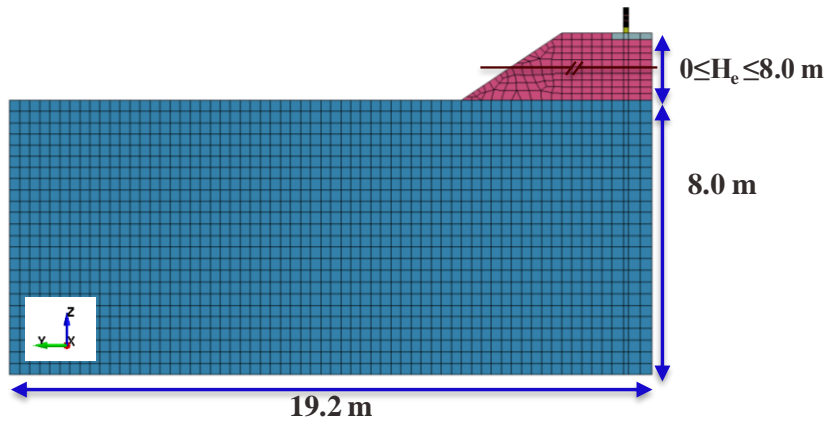


Figure 4.38. The geometry of the FEM used in section 4.7.2

Figures 4.39 to 4.41 show the time history of the track vertical displacement for different cases with different embankment thicknesses (H_e) of 0 to 8 m at various train speeds: 108, 216, and 324 km/h. These figures illustrate the effect of embankment thickness on track dynamic responses. At the low train speed of 108 km/h (30 m/s), an almost symmetrical displacement pattern can be seen; however, in comparison to the track on the higher embankment, a track on a shallower embankment results in significantly more displacement. At a higher speed ($V_T=216$ km/h (60 m/s)), the case with no embankment shows the asymmetrical displacement pattern, which means in this case, the train speed passes the threshold critical speed. At the highest train speed of 324 km/h (90 m/s), two cases ($H_e=0$ and 2 m) show the asymmetrical pattern.

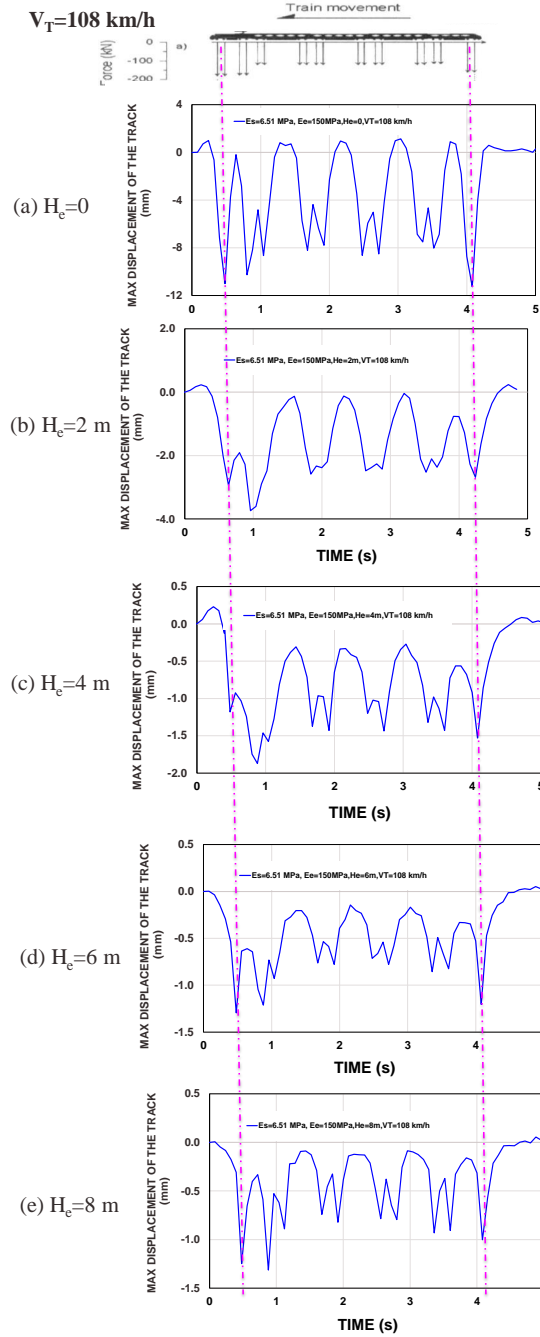


Figure 4.39. Predicted vertical track displacement time history at $VT=108 \text{ km/h}$ with (a) $H_e=0$ ($GM=0.75$), (b) $H_e=2 \text{ m}$ ($GM=0.43$), (c) $H_e=4 \text{ m}$ ($GM=0.27$), (d) $H_e=6 \text{ m}$ ($GM=0.25$), (e) $H_e=8 \text{ m}$ ($GM=0.20$)

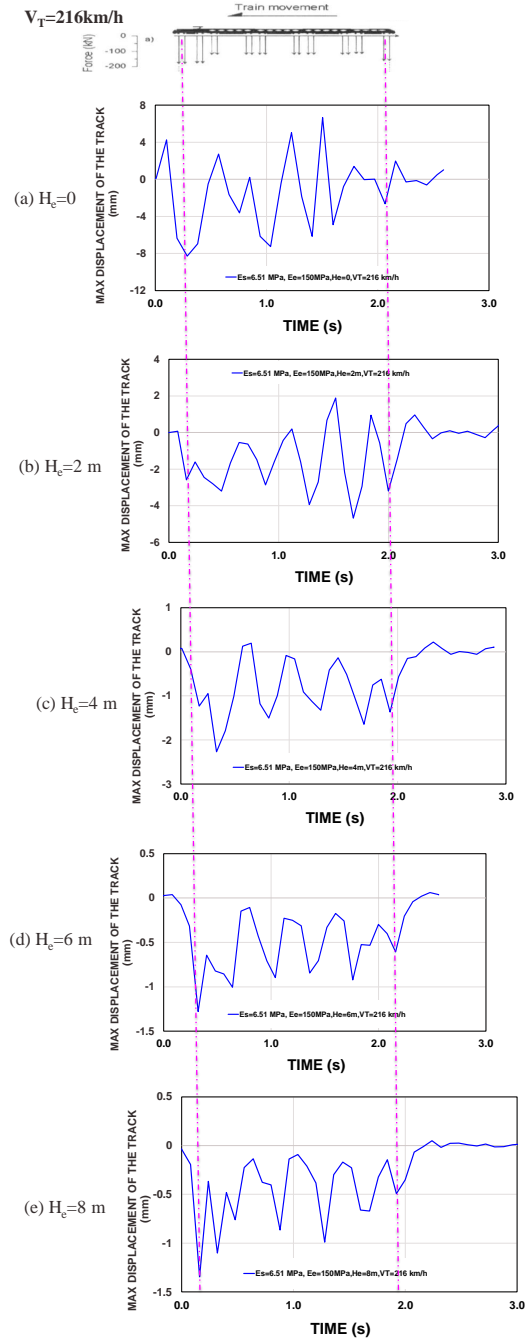


Figure 4.40. Predicted vertical track displacement time history at $V_T=216\text{ km/h}$ with (a) $H_e=0$ ($GM=0.75$), (b) $H_e=2\text{ m}$ ($GM=0.43$), (c) $H_e=4\text{ m}$ ($GM=0.27$), (d) $H_e=6\text{ m}$ ($GM=0.25$), (e) $H_e=8\text{ m}$ ($GM=0.20$)

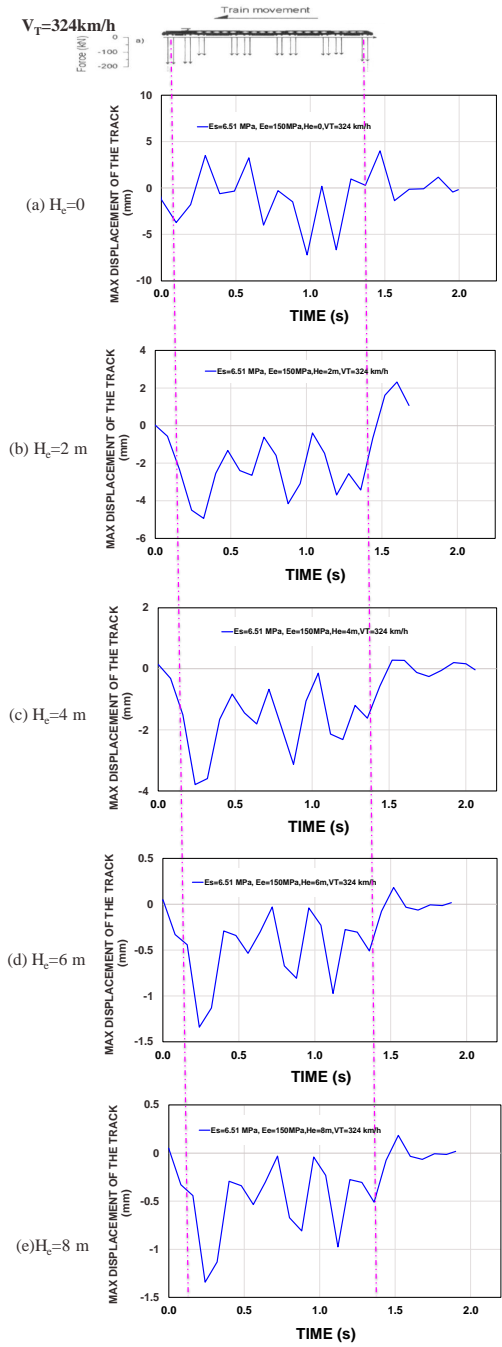


Figure 4.41. Predicted vertical track displacement time history at VT=324 km/h with (a) He=0 (GM=0.75), (b) He=2 m (GM=0.43), (c) He=4 m (GM=0.27), (d) He=6 m (GM=0.25), (e) He=8 m (GM=0.20)

To illustrate the impact of embankment thickness on track performance at different train speeds, the cross-section view of the displacement contours of track/embankment/ground FEM are depicted in Figures 4.42 to 4.44. Figures 4.45 to 4.47 show the plan view of the displacement contour of the model. At the lowest train speed ($V_T=108$ km/h), as with Figures 4.42 and 4.45, the same pattern (almost symmetrical pattern) can be observed for all five cases ($0 \leq H_e \leq 8$ m). The vertical displacement is induced almost directly beneath the train wheels' positions, and there is a small wave propagation to the surrounding ground. The amplitudes of the displacements, however, are not the same. At the same train speed, as the H_e increases, the predicted vertical displacement decreases, and also the zone of influence, which is defined as the depth at which the downward movement of the soil is equal to 10% of the downward movement at the surface (Briaud 2013), below the axle loads decreases. This shows that with a thicker embankment at a constant train speed, in addition to reducing the amplitude of the track displacement, the depth to which the downward movement of the soil extends considerably decreases. At higher speeds ($V_T=216$ and 324 km/h), there is the same relationship between H_e and model displacement as the one observed at the train speed of 108. Moreover, the model indicates that depth of influence increases with shallower embankments (Figure 4.43, 4.44, 4.46, and 4.47). On the contrary, the displacement patterns are not the same for all cases. As Figures 4.43 (a), 4.44 (a) and (b), 4.46 (a), and 4.47 (a) and (b) illustrate, the train goes faster than the equivalent Rayleigh wave speed of the track/embankment/subgrade system ($V_T > V_{Req}$; $GM > 1.0$). On the other hand, in the other cases, the critical speeds have not been reached yet. To understand the phenomena better, the critical speeds for all cases were assessed. A summary of the maximum track vertical displacements as a function of

embankment thicknesses for three different train speeds ($V_T=108, 216, 324$ km/h) is plotted and shown in Figure 4.48. As mentioned earlier in this section, the maximum track displacements significantly decreased as modeled embankment thickness increased.

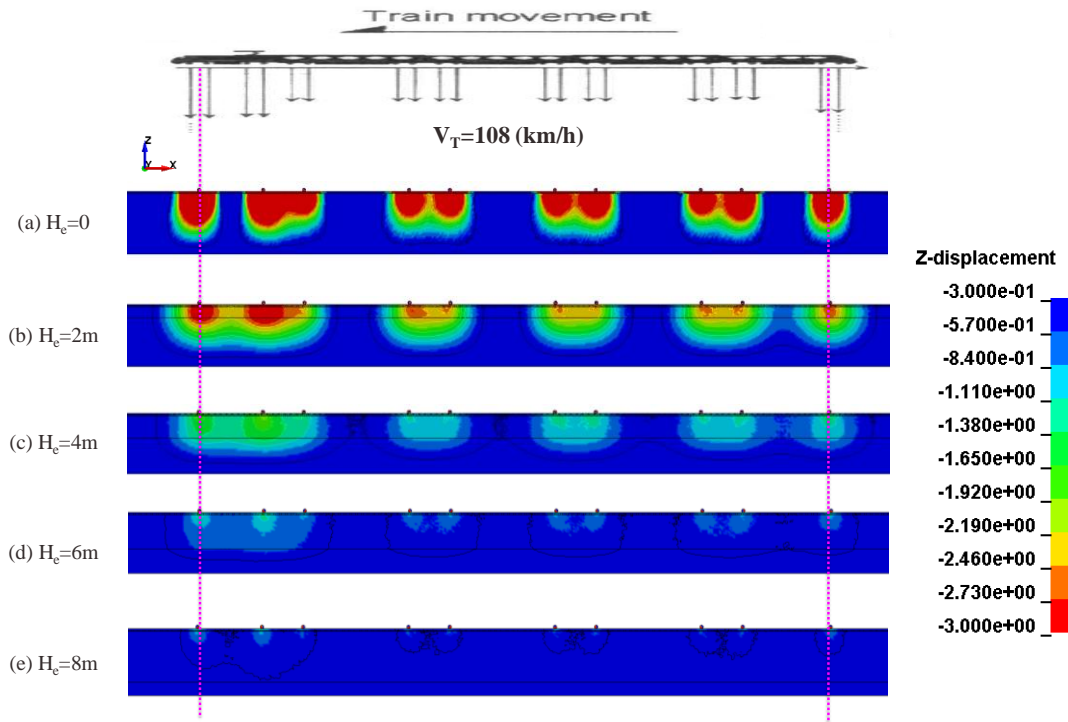


Figure 4.42. Cross-section view of track displacement contour at train speed of 108 km/h with (a) $H_c=0$ ($GM=0.75$), (b) $H_c=2$ m ($GM=0.43$), (c) $H_c=4$ m ($GM=0.27$), (d) $H_c=6$ m ($GM=0.25$), (e) $H_c=8$ m ($GM=0.20$)

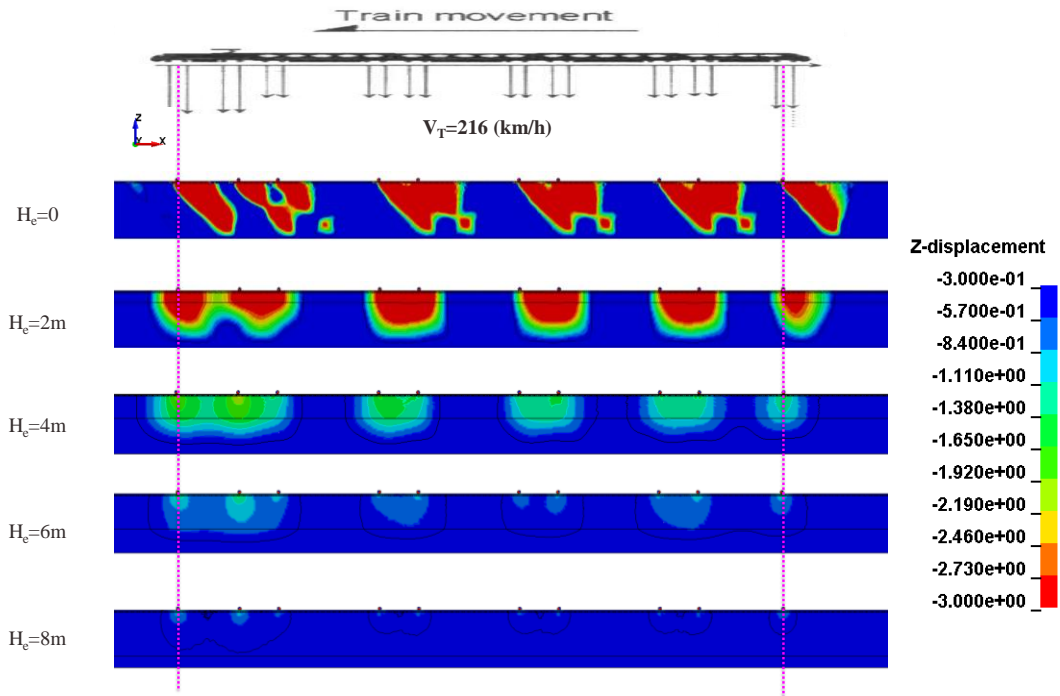


Figure 4.43. Cross-section view of track displacement contour at train speed of 216 km/h with (a) $H_e=0$ (GM=0.75), (b) $H_e=2$ m (GM=0.43), (c) $H_e=4$ m (GM=0.27), (d) $H_e=6$ m (GM=0.25), (e) $H_e=8$ m (GM=0.20)

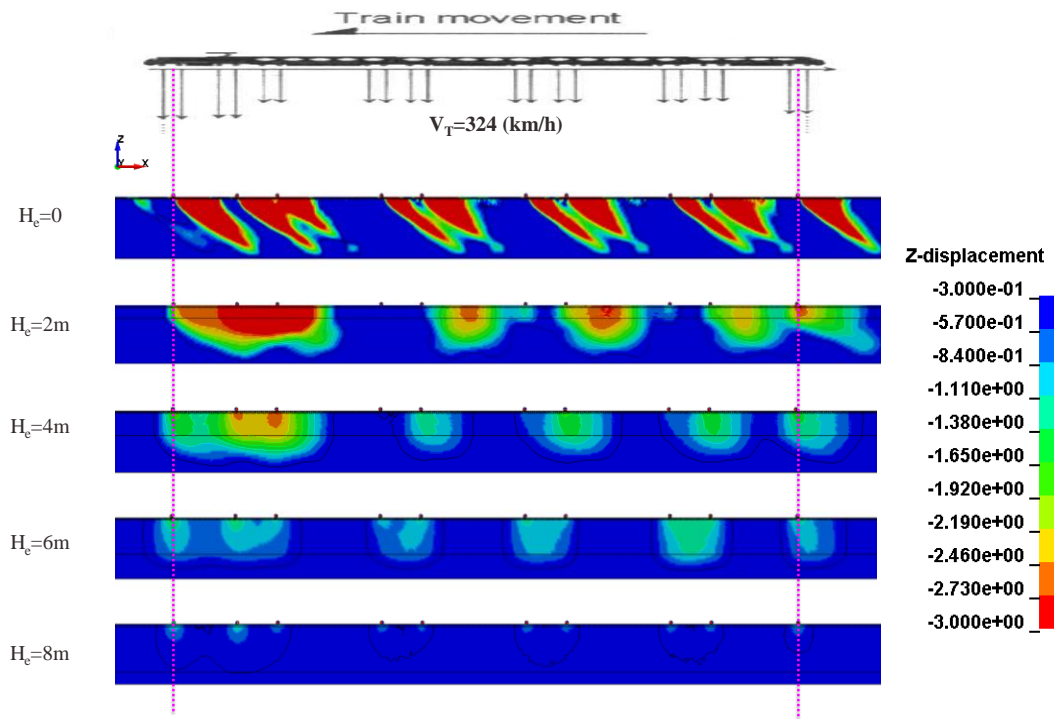


Figure 4.44. Cross-section view of track displacement contour at train speed of 324 km/h with (a) $H_c=0$ (GM=0.75), (b) $H_c=2$ m (GM=0.43), (c) $H_c=4$ m (GM=0.27), (d) $H_c=6$ m (GM=0.25), (e) $H_c=8$ m (GM=0.20)

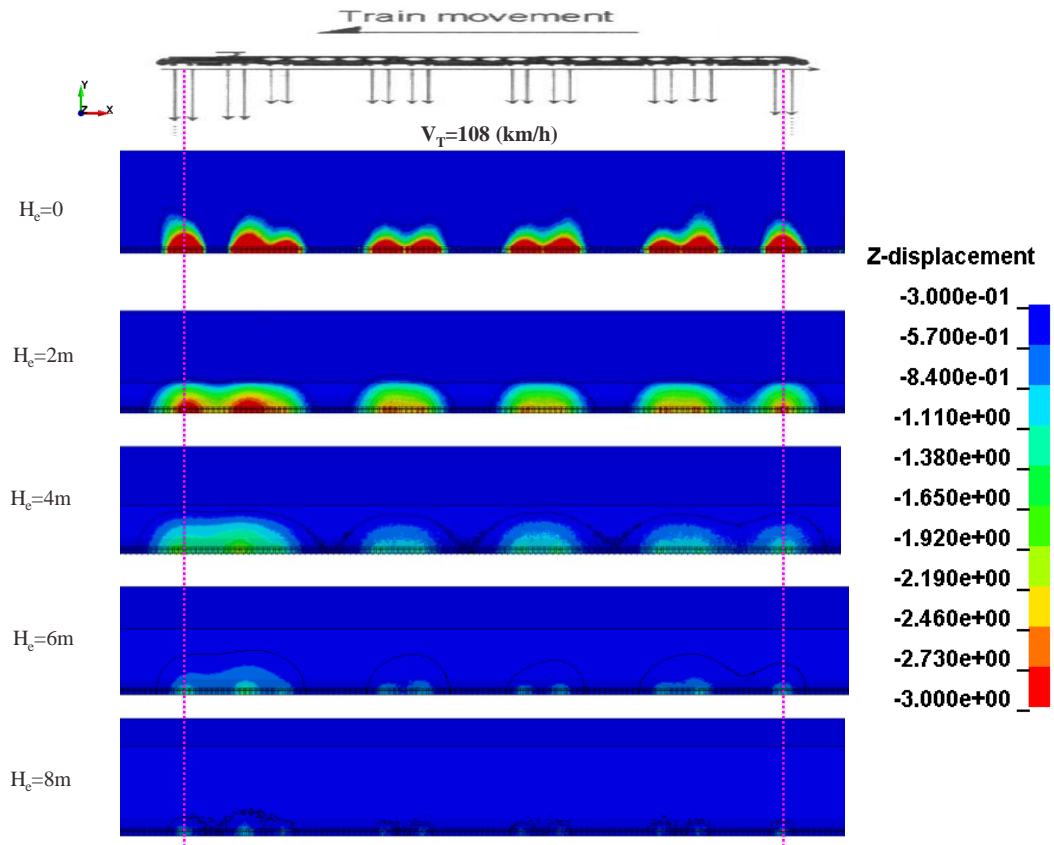


Figure 4.45. Plan view of track displacement contour at train speed of 108 km/h with (a) $H_e=0$ ($GM=0.75$), (b) $H_e=2$ m ($GM=0.43$), (c) $H_e=4$ m ($GM=0.27$), (d) $H_e=6$ m ($GM=0.25$), (e) $H_e=8$ m ($GM=0.20$)

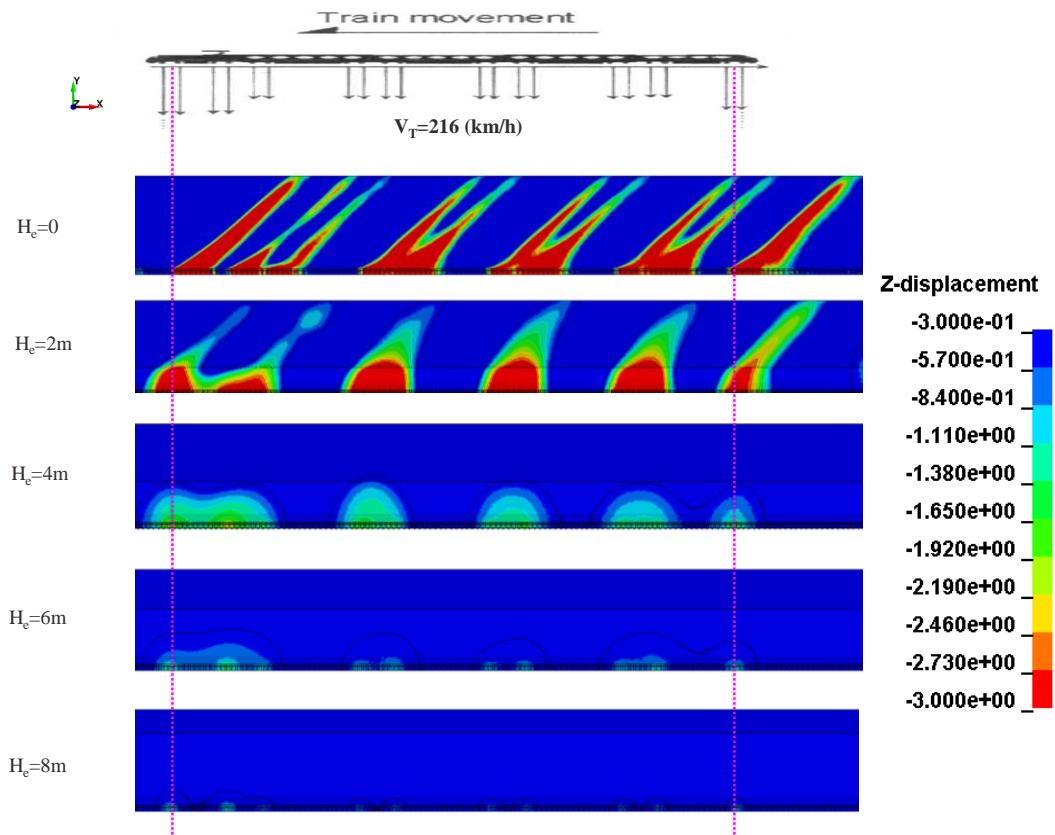


Figure 4.46. Plan view of track displacement contour at train speed of 216 km/h with (a) $H_c=0$ (GM=0.75), (b) $H_c=2$ m (GM=0.43), (c) $H_c=4$ m (GM=0.27), (d) $H_c=6$ m (GM=0.25), (e) $H_c=8$ m (GM=0.20)

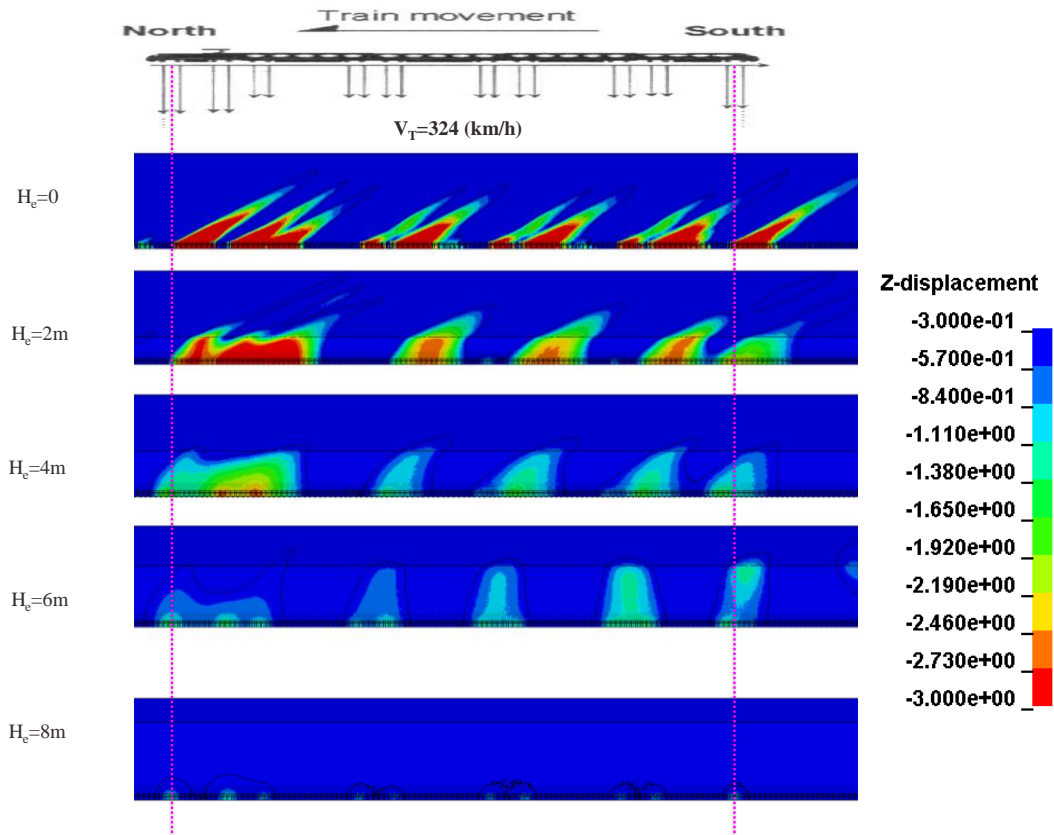
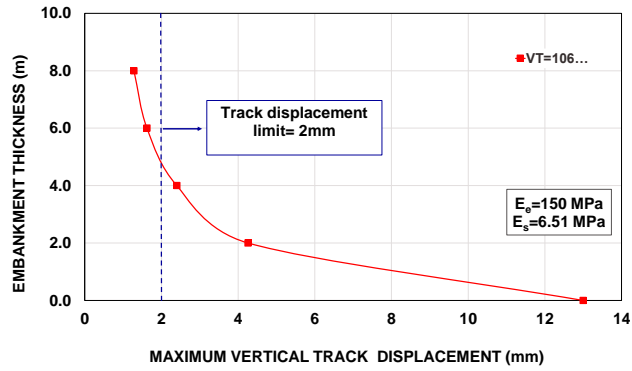
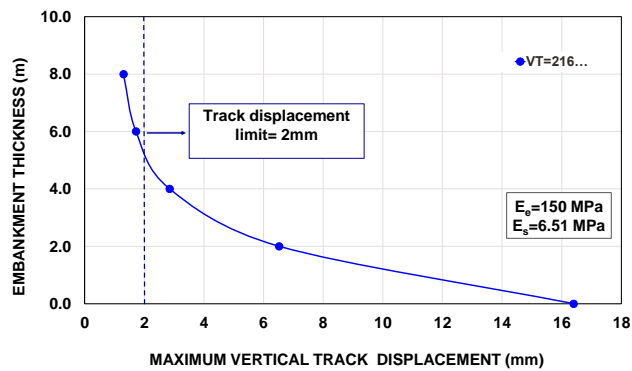


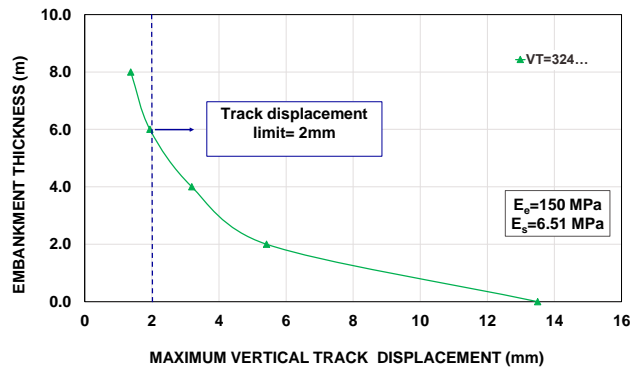
Figure 4.47. Plan view of track displacement contour at train speed of 324 km/h with (a) $H_c=0$ ($GM=0.75$), (b) $H_c=2$ m ($GM=0.43$), (c) $H_c=4$ m ($GM=0.27$), (d) $H_c=6$ m ($GM=0.25$), (e) $H_c=8$ m ($GM=0.20$)



(a)



(b)



(c)

Figure 4.48. Maximum track vertical displacement vs embankment thickness (H_e) at train speed of (a) 108 km/h (b) 216 km/h, and (c) 324 km/h

The maximum track displacements as a function of train speeds for all 5 different cases with different embankment thickness (0 to 8 m) are shown in Figures 4.49 (a) to

4.49 (e). Using these plots shown in Figures 4.49 (a) to 4.49 (e), the critical speeds (or equivalent Rayleigh wave speeds of embankment/subgrade systems) estimated in the same way as discussed earlier in this section and summarized in Table 4.8.

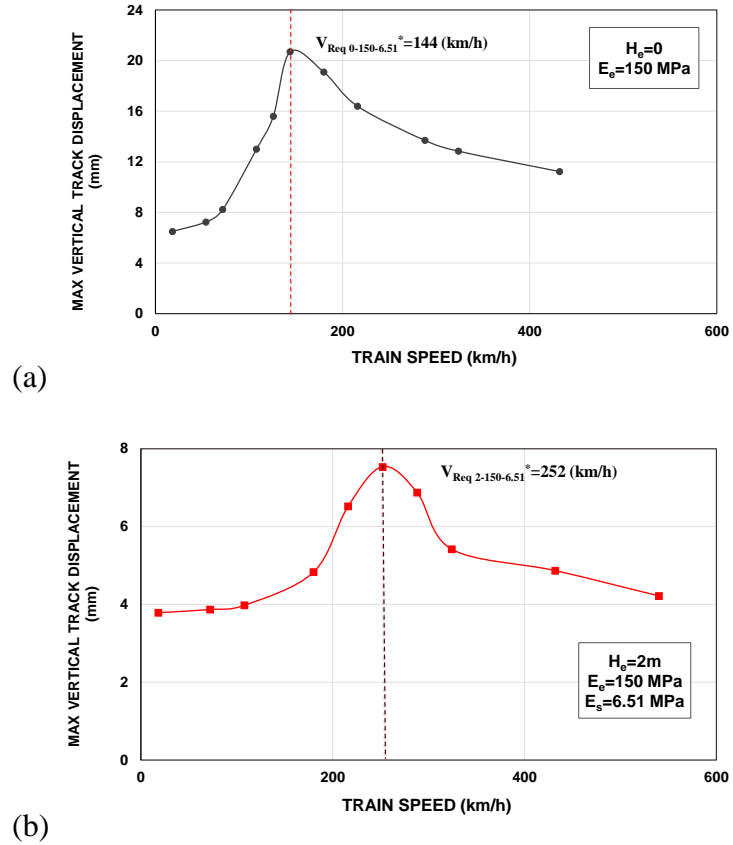
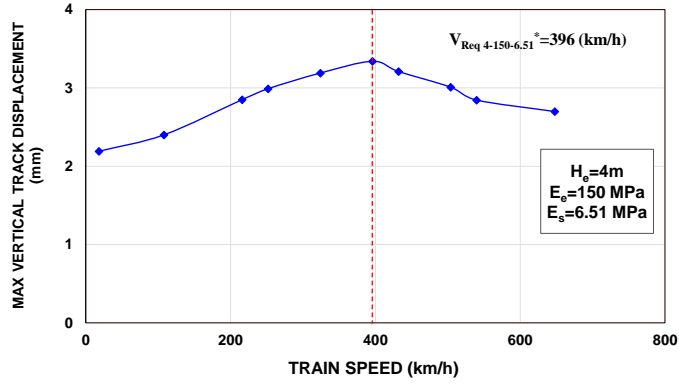
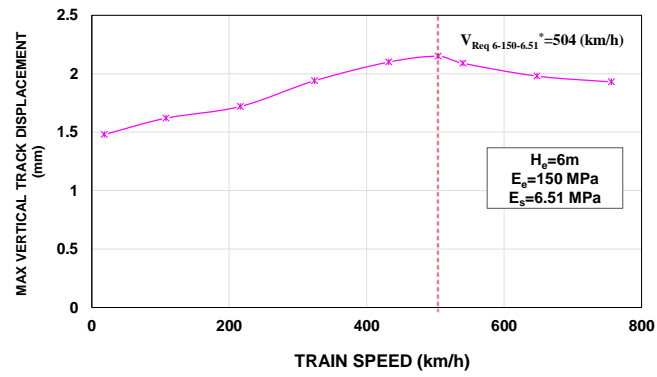


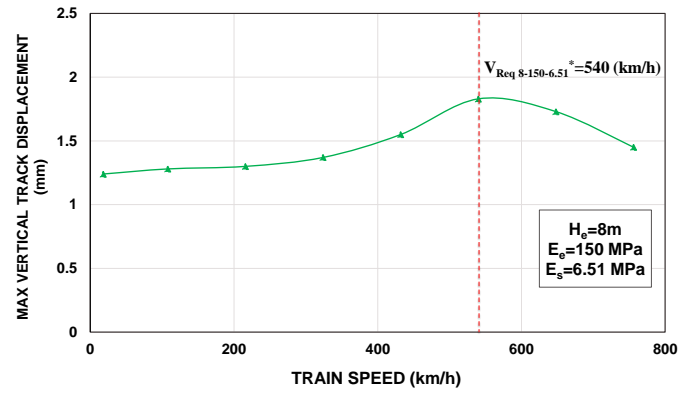
Figure 4.49. Predicted peak vertical track displacement vs. train speed for different case studies: (a) No embankment, (b) He=2 m, (c) He=4 m, (d) He=6 m, and (e) He=8 m



(c)



(c)



(e)

* $V_{\text{Req } H_e-E_e-E_s}$: The subscript numbers are for embankment thickness (H_e), embankment modulus (E_e), and subgrade modulus (E_s).

Figure 4.49. Continued

Table 4.8. Effect of Embankment Thickness (H_e) on the Critical Speed or the Equivalent Rayleigh Wave Speed (V_{Req}) of Track/Embankment/Ground System

<i>Case No</i>	Embankment thickness (H_e) (m)	V_C or V_{Req} (km/h)	Maximum vertical track displacement at critical speed (mm)
1	0	144	20.7
2	2	252	7.54
3	4	396	3.34
4	6	504	2.15
5	8	561	1.83

Figure 4.50 shows a summary of all plots of the maximum track displacements as they relate to train speed for all cases (with embankment thickness ranging from 0 to 8 m). The critical speed increases with embankment thickness up to the Rayleigh wave speed of the embankment ($V_{Re}=561$ km/h). The Rayleigh wave speed of the embankment in this case was calculated using Equation 4.3. It is given in Table 4.7.

Rayleigh waves are categorized as surface waves whose depth of propagation is shallow. Therefore, when the embankment is deep enough, embankment layer would be the predominant layer to determine the Rayleigh wave speed of the whole system. In other words, in cases with a deep enough embankment, the subgrade would not be affected by the wave induced by operating HSTs. As mentioned in section 4.7.1, increasing the height of embankment results in increasing critical speed and decreasing the maximum track displacement (Table 4.8).

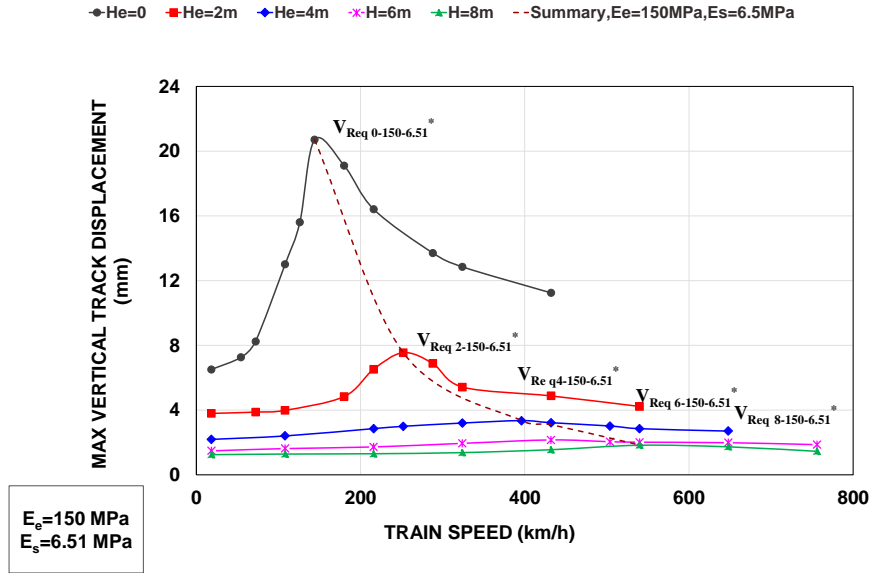


Figure 4.50. Summary of the predicted peak vertical track displacement vs. train speed for different case studies ($H_e=0$ to 8 m)

Figure 4.51(a) depicts that in addition to the maximum track displacement, the ratio between dynamic track displacement over static track displacement considerably decreases as the height of embankment increases. Compared to the case without embankment ($H_e=0$), the normalized track displacement decreases approximately 60% when there is a 2 m embankment on top of the subgrade. Figure 4.51 (b) shows how this ratio changes with embankment thickness. As it is obvious in this figure, the normalized track displacement at critical speed decreases with embankment thickness but not with a uniform slope. In cases of very shallow to medium embankment ($1\text{ m} < H_e < 4\text{ m}$), very small changes in embankment thickness result in considerable critical speed modification and huge decreases in maximum dynamic track displacement; on the other hand, in cases of deep enough embankment, the change in maximum normalized track displacement

becomes moderate. For instance, when embankment thickness changes from 4 m to 6 m, the maximum normalized track displacement changes only by 4%. Compared to the 60% decrease, the maximum normalized track displacement when H_e increases from 0 to 2 m, this change (4%) when H_e increases from 4 m to 6 m is not noticeable. It can be concluded that a 4 m to 6 m embankment can be effectively used to modify critical speed and reduce the dynamic effect of HSTs on track performance.

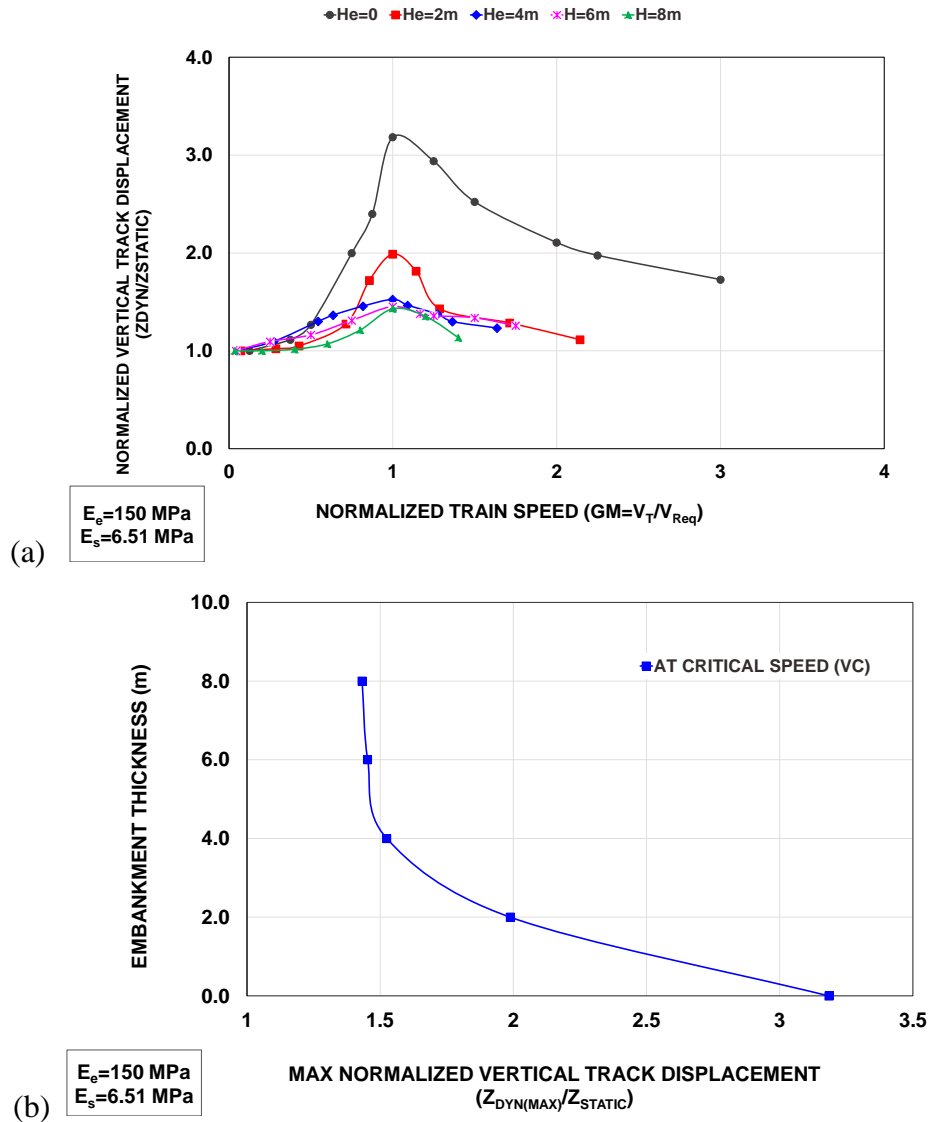


Figure 4.51. Effect of embankment thickness on simulated normalized track displacement: (a) normalized track displacement vs. normalized train speed or ground Mach number (GM), (b) normalized track displacement vs. embankment thickness

The main goal of this part of the study was to determine the effect of embankment thickness on the critical speed. Figure 4.52 shows the final results, including the plot of critical speeds as functions of embankment thicknesses. The plot of embankment thickness versus critical speed obtained for different case studies shows the same results as the one

obtained for maximum normalized track displacements. Obviously, the effect of embankment thickness on critical speed is greater with a higher rate of increase when H_e is less than 6 m, compared to higher embankments ($H_e \geq 6$ m). It can be concluded that a 4 to 6 m embankment thickness is thick enough for critical speed modification and dynamic track displacement reduction.

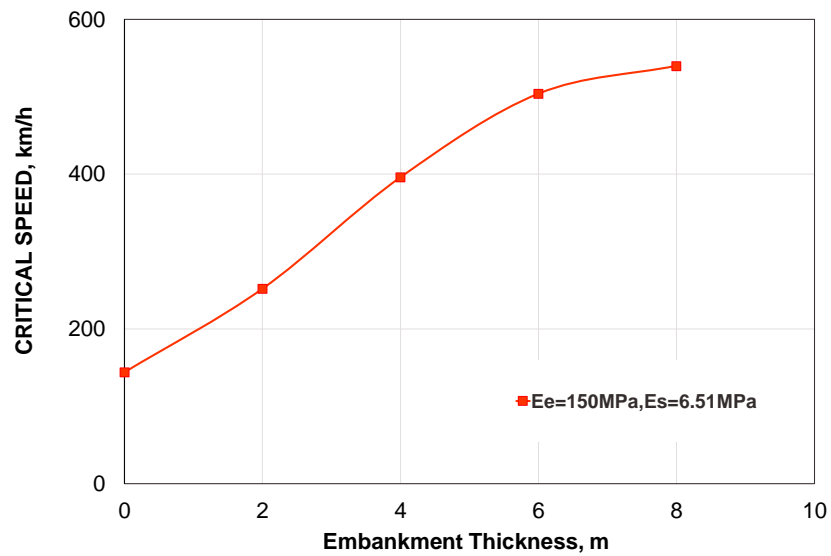


Figure 4.52. Effect of embankment thicknesses on critical speed

4.7.3 Embankment Modulus Effect

The second parameter playing an important role in critical speed of the track/embankment/ground systems is the embankment stiffness. In this research, the embankment modulus as an influential parameter of soil stiffness was chosen to perform the parametric studies. Indeed, the main objective of this part of parametric study was to evaluate the effect of embankment modulus on critical speed of the whole system. Several simulations were conducted to investigate track response under different train speed and considering different embankment conditions in terms of embankment modulus. The FEM used to conduct parametric study is the same one used in section 4.7.1. The height of embankment is considered to be constant ($H_e=2$ m). The material properties are the same as given in Table 4.7. The only difference is the modulus of embankment, which is not constant in this part of the study. A reasonable range of soil modulus was selected to perform the parametric study (Table 4.9).

Table 4.9. Material Properties of Embankment

<i>Case No</i>	Elasticity Modulus(E) MPa	Poisson's Ratio (ν)	Unit Weight (ρ) kg/m³	Rayleigh Wave Speed, V_R (km/h)
1	100	0.35	2000	458
2	150	0.35	2000	561
3	200	0.35	2000	648
4	250	0.35	2000	721
5	300	0.35	2000	793

Figures 4.53 to 4.55 depict a typical simulated track response under three different train speeds ($V_T = 108, 252, \text{ and } 396 \text{ km/h}$). These figures compare the track performance through showing the time histories of the track displacement under different embankment conditions ($100 \text{ MPa} \leq E_e \leq 300 \text{ MPa}$). In these figures, a considerable increase in track displacement is clearly seen as train speed increases. However, the amplitude of the track displacement increases slowly as embankment modulus decreases. Compared to significant changes in track displacement amplitude with changes in embankment thickness (Figure 4.48), the amplitude of the track displacements did not change noticeably when embankment modulus changes.

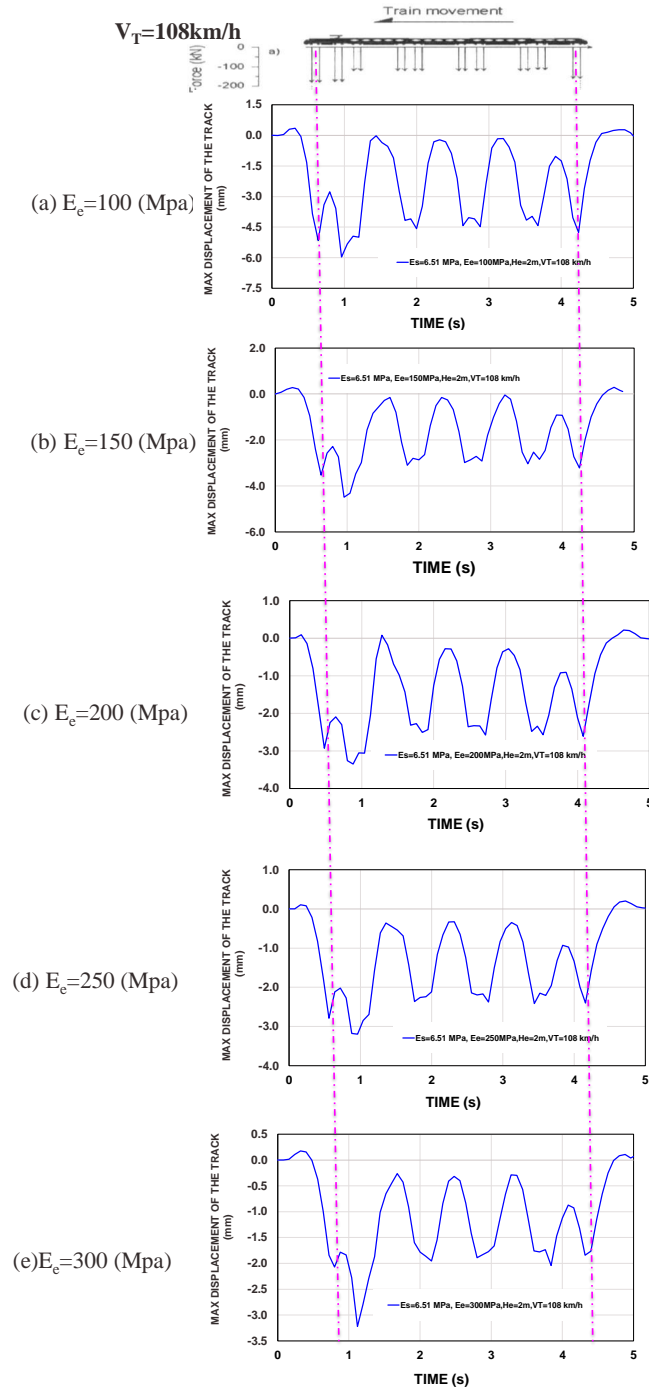


Figure 4.53. Effect of E_e on simulated vertical track displacement amplitude at $V_T=108$ km/h

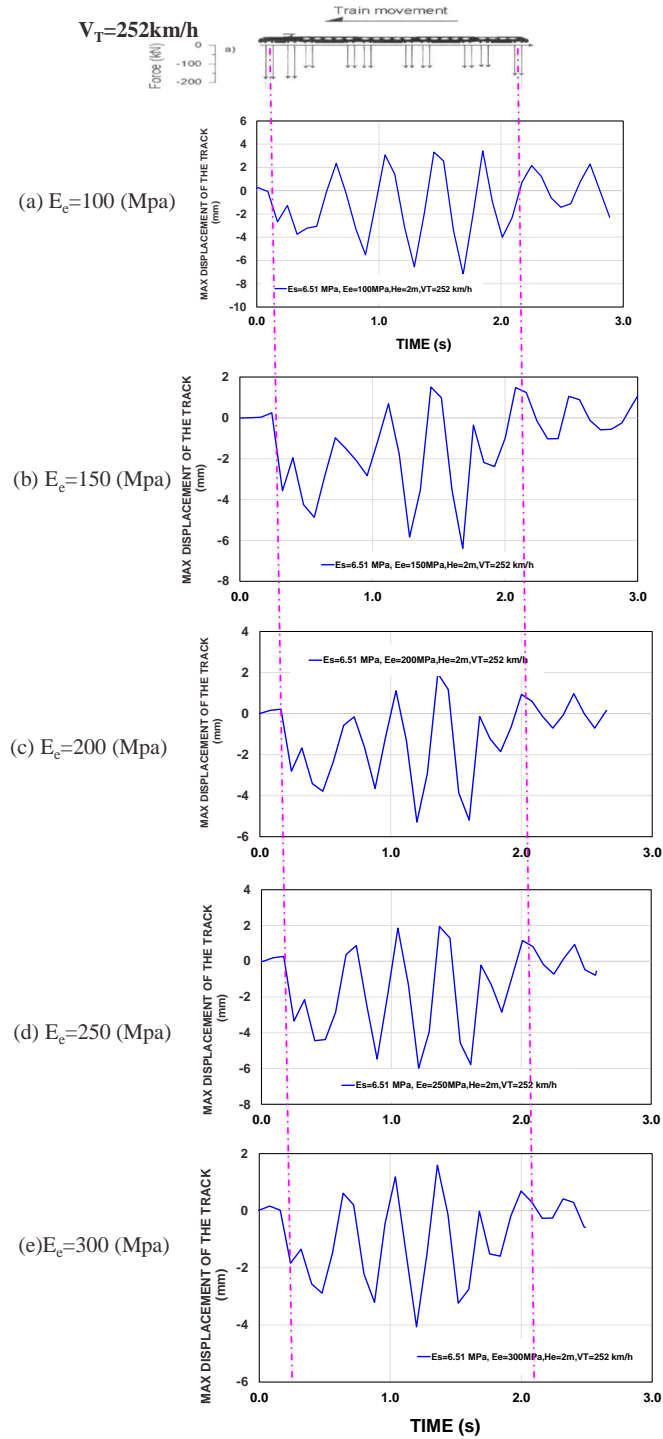


Figure 4.54. Effect of E_e on simulated vertical track displacement amplitude at $V_T=252$ km/h

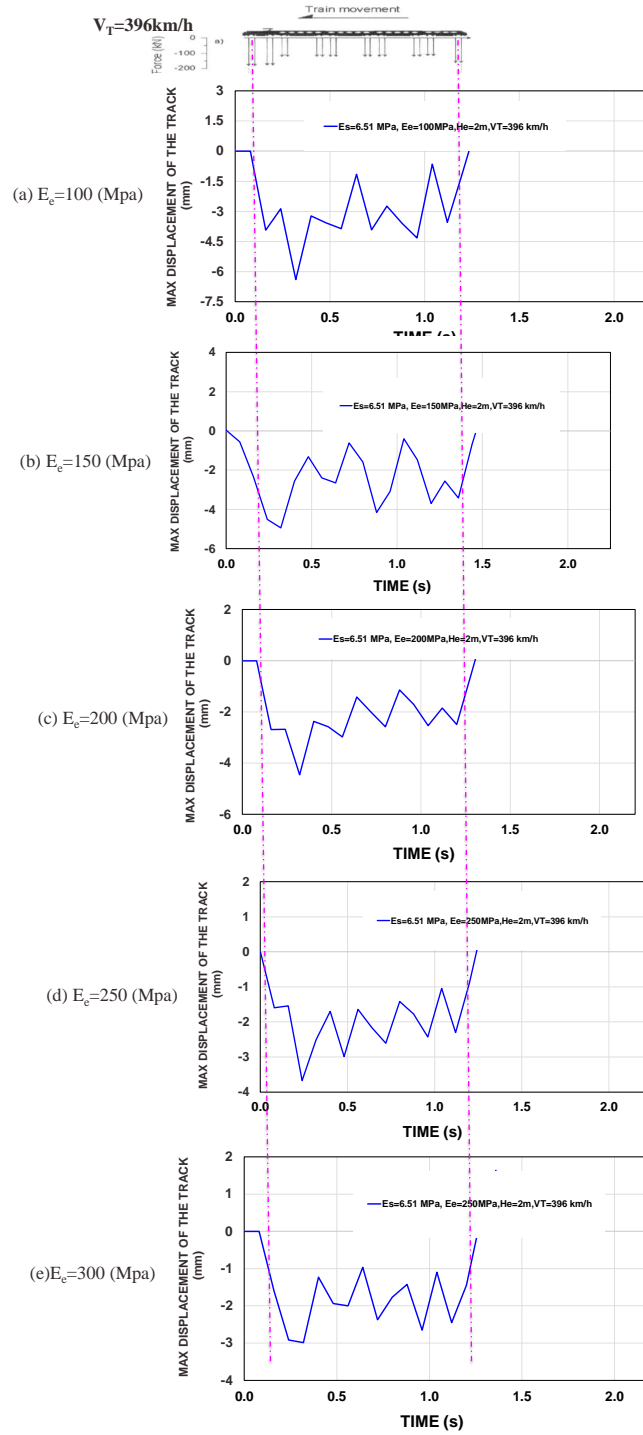


Figure 4.55. Effect of E_e on simulated vertical track displacement amplitude at $V_T=396$ km/h

The cross-section and plan views of the bulb of deformation along depth for all 5 cases at three different train speeds are given in Figures 4.56 to 4.58 and Figures 4.59 to 4.61, respectively. As it is obvious from these figures, at 108 km/h, all cases show the quasi-static condition with an almost symmetrical bulb of deformation under the moving load. At this train speed, the GM for all cases is less than 1.0 (subsonic situation). However, at train speed 252 km/h and 396 km/h, dynamic effects are obvious.

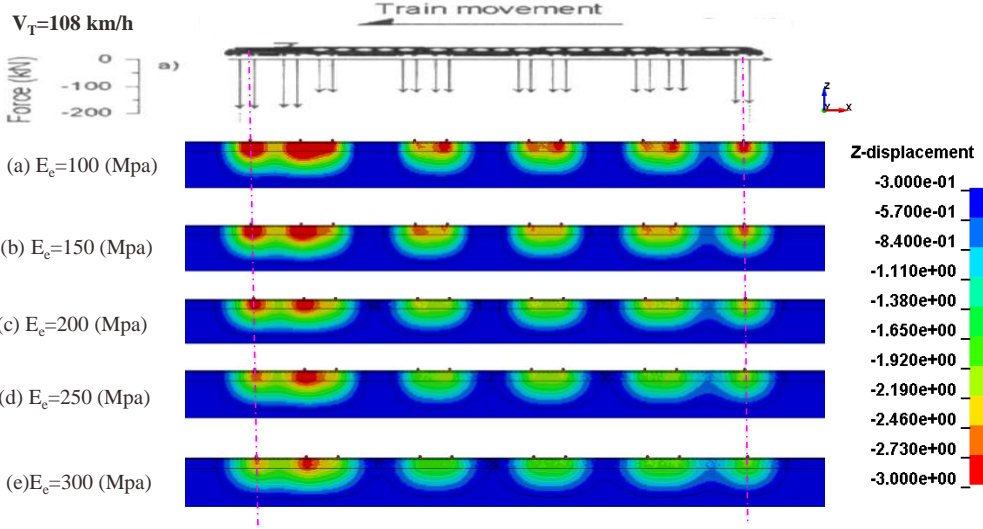


Figure 4.56. Cross-section view of track displacement contour at train speed of 108 km/h under different embankment conditions (different embankment modulus)

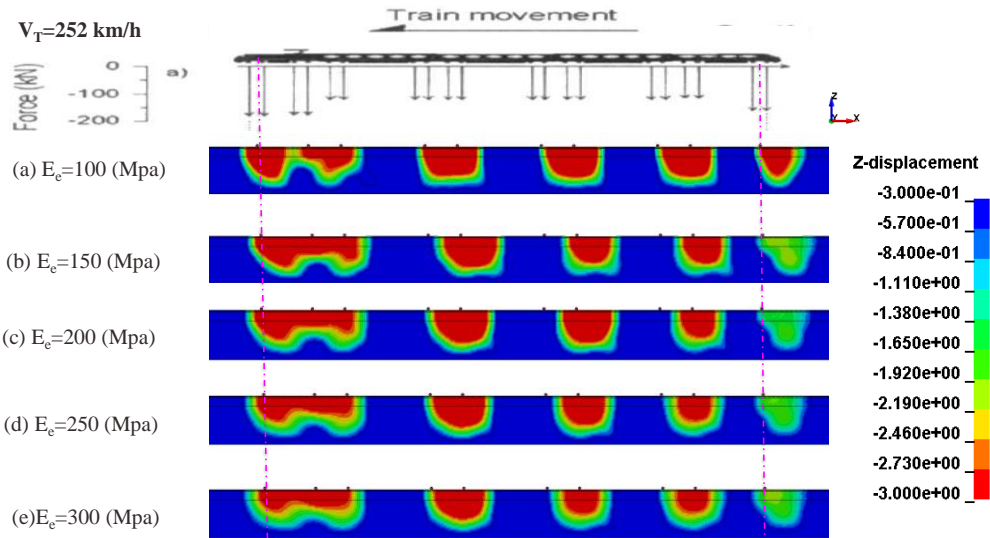


Figure 4.57. Figure 4.57. Cross-section view of track displacement contour at train speed of 252 km/h under different embankment conditions (different embankment modulus)

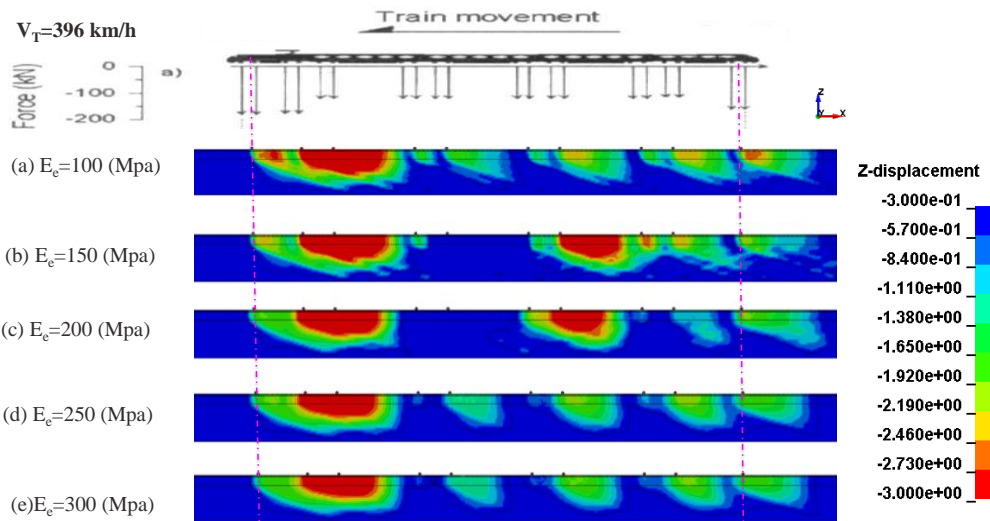


Figure 4.58. Cross-section view of track displacement contour at train speed of 396 km/h under different embankment conditions (different embankment modulus)

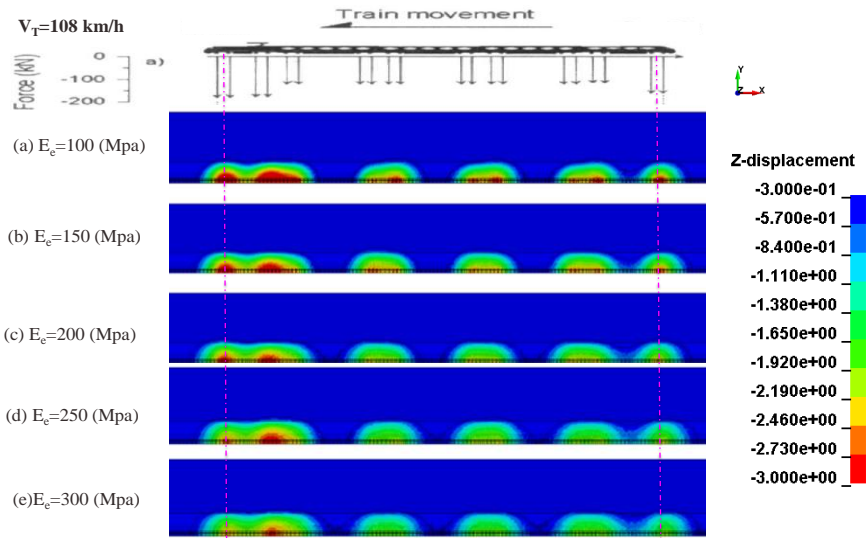


Figure 4.59. Plan view of track displacement contour at train speed of 108 km/h under different embankment conditions (different embankment modulus)

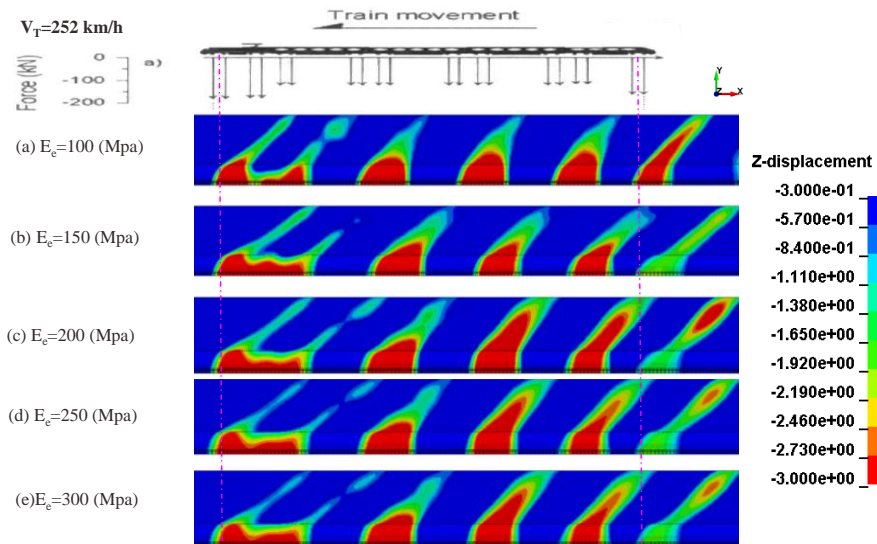


Figure 4.60. Plan view of track displacement contour at train speed of 252 km/h under different embankment conditions (different embankment modulus)

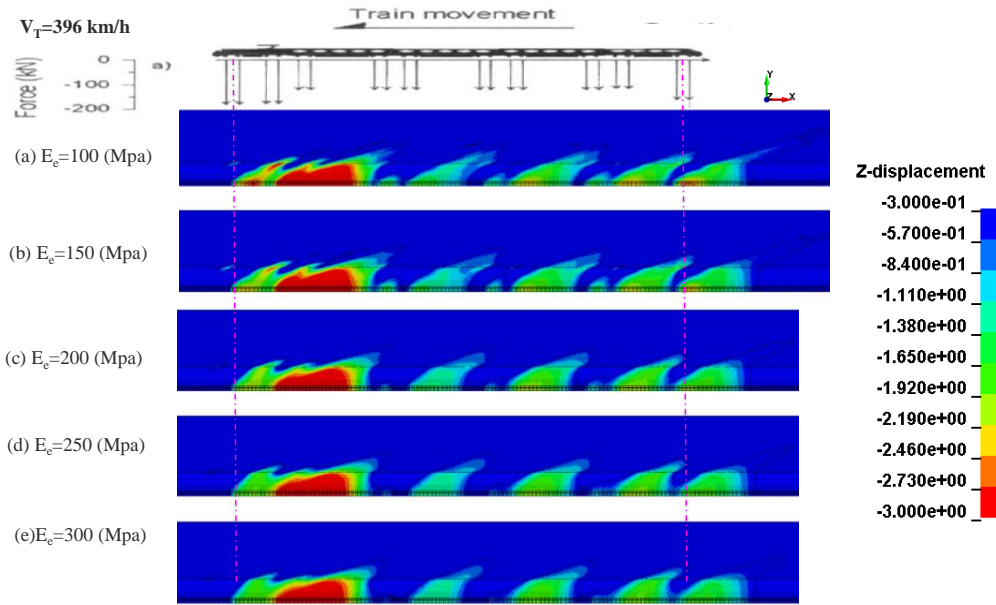
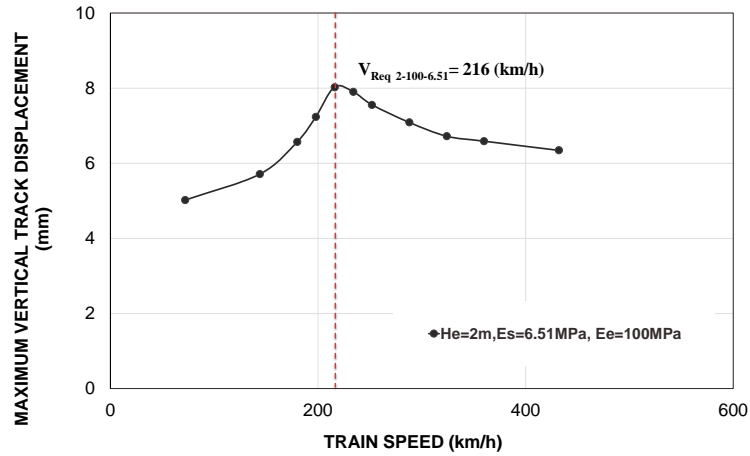


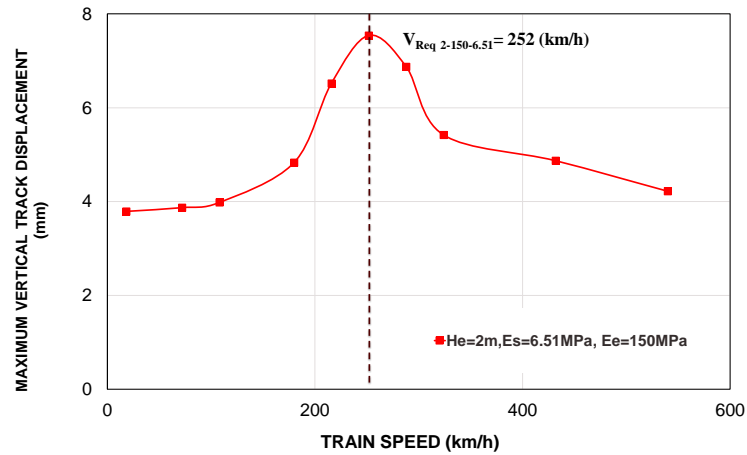
Figure 4.61. Plan view of track displacement contour at train speed of 396 km/h under different embankment conditions (different embankment modulus)

To find the relationship between critical speed and embankment modulus, estimating critical speeds for all cases with different embankment moduli is necessary. Critical speeds are estimated in the same way that was mentioned in section 4.7.2. In total, 50 different cases with different train speeds and embankment moduli were modeled and simulated to estimate the critical speeds. The results of these simulations are shown in Figure 4.62. Using these plots (Figure 4.62), the critical speeds at which resonance occurs can be estimated as summarized in Table 4.10. Figure 4.63 shows the critical speed change insignificantly as embankment modulus changes. These simulations confirmed that in cases of shallow embankments ($H_e \leq 2\text{m}$), the embankment modulus does not have a great impact on critical speed modification. In other words, when track is constructed on top of a shallow embankment, subgrade stiffness is the predominant parameter having the

greatest impact on the critical speed of the track/embankment /subgrade system (Shahu et al. 1999, Ebersson et al. 1993, Banimahd 2008).

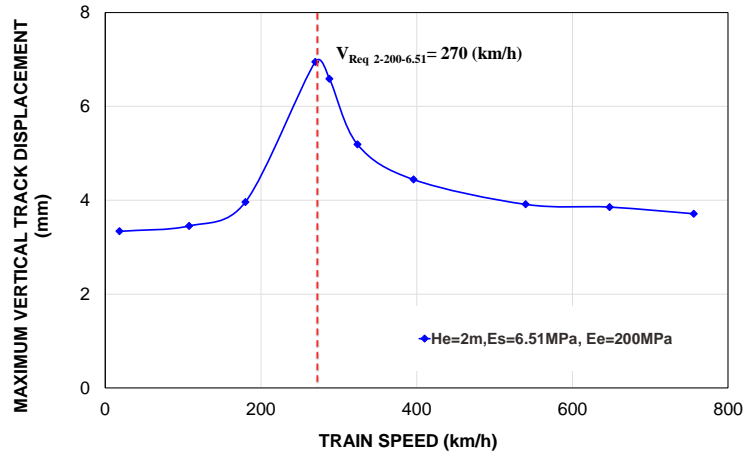


(a)

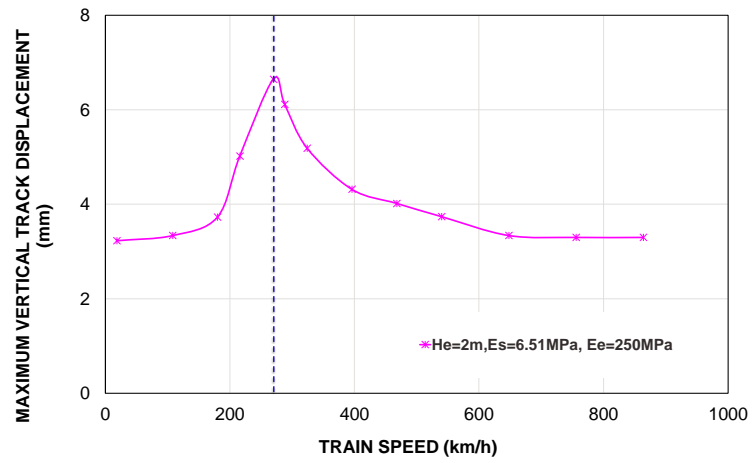


(b)

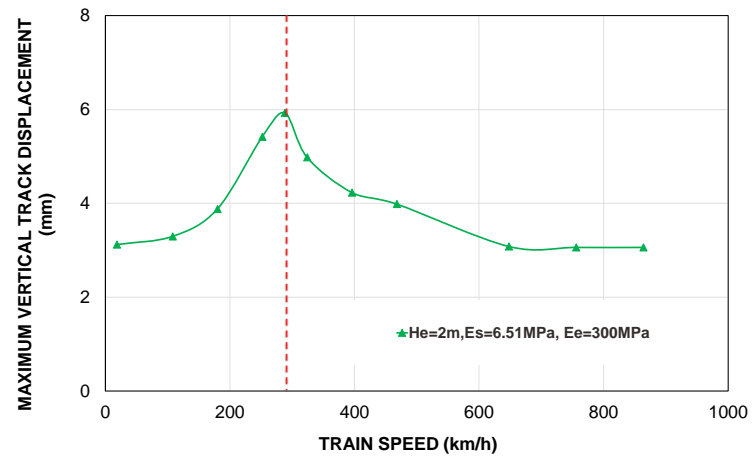
Figure 4.62. Maximum vertical track displacement vs. train speeds (a) $E_e = 100 \text{ MPa}$, (b) $E_e = 150 \text{ MPa}$, (c) $E_e = 200 \text{ MPa}$, (d) $E_e = 250 \text{ MPa}$, (e) $E_e = 300 \text{ MPa}$, (f) summary of all cases



(c)



(d)



(e)

Figure 4.62. Continued

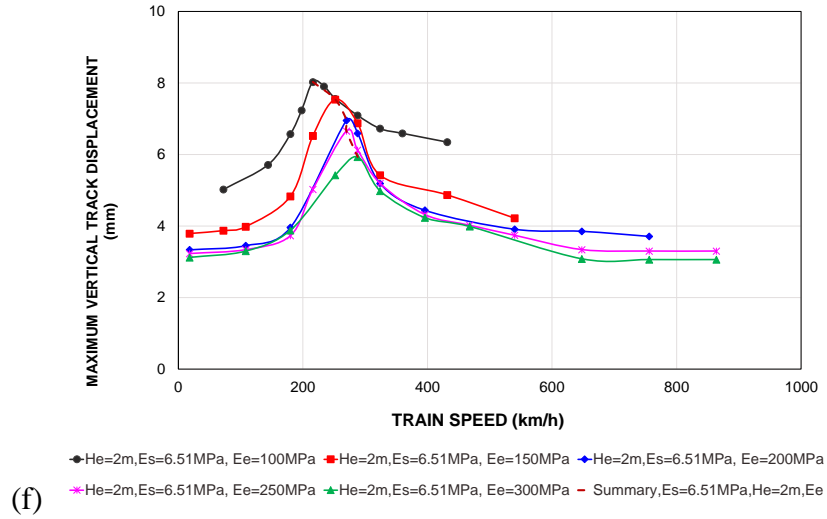


Figure 4.62. Continued

Table 4.10. Embankment Modulus (E_e) Effect on the Equivalent Rayleigh Wave Speed (V_{Req}) of Track/Embankment/Ground Systems (Embankment Thickness (H_e)=2.0 m)

Case No.	Embankment Modulus (E_e) (MPa)	V_{Req} (km/h)	Maximum vertical track displacement at critical speed (mm)
1	100	216	9.24
2	150	252	7.54
3	200	270	6.95
4	250	270	6.27
5	300	288	5.93

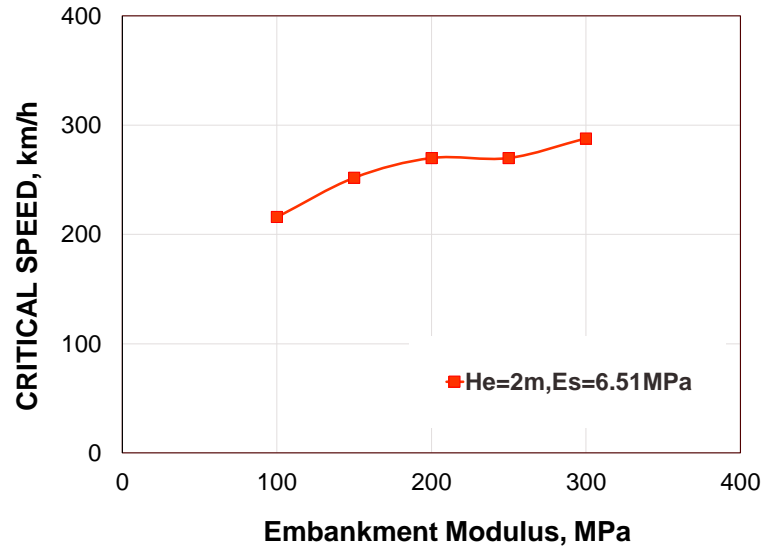
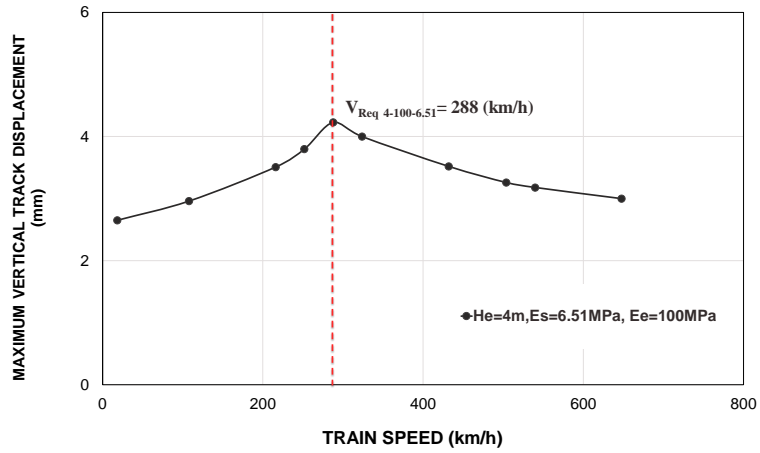
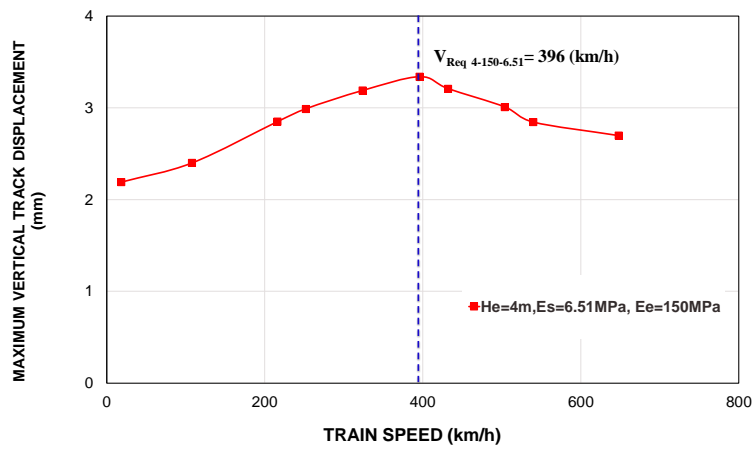


Figure 4.63. Effect of embankment moduli on critical speed

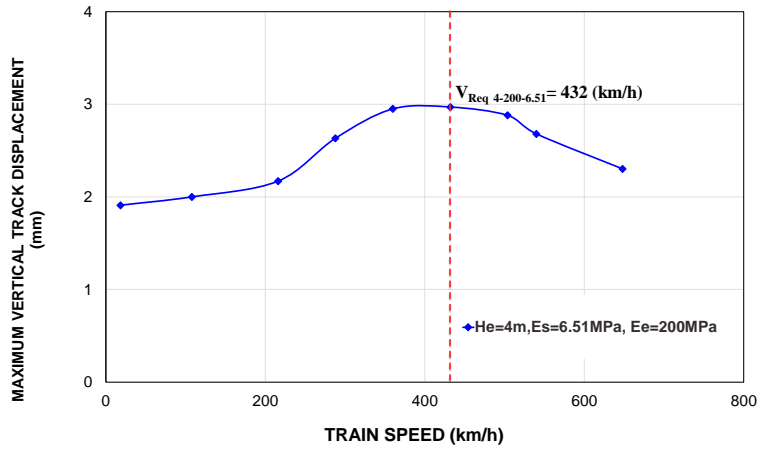
Yet, in cases of higher embankment ($H_e > 2.0\text{m}$), the embankment becomes a more influential parameter, playing an important role in critical speed modification. To investigate the effect of embankment modulus on critical speed in case of high enough embankment, all the parametric studies ($100 \text{ MPa} \leq E_e \leq 300 \text{ MPa}$) were repeated for the case with $H_e = 4.0 \text{ m}$. Using the plots shown in Figure 4.64, the critical speeds for these cases were assessed. A summary of the critical speeds for all different cases with constant H_e ($H_e = 4.0 \text{ m}$) and varied embankment modulus is presented in Table 4.11. Figure 4.65 depicts that when there is a thick enough embankment ($H_e = 4.0 \text{ m}$) under the track, the embankment modulus is a more important factor in critical speed compared to cases with a shallow embankment ($H_e = 2.0\text{m}$).



(a)



(b)



(c)

Figure 4.64. Maximum vertical track displacement vs. train speeds (a) $E_e = 100 \text{ MPa}$, (b) $E_e = 150 \text{ MPa}$, (c) $E_e = 200 \text{ MPa}$, (d) $E_e = 250 \text{ MPa}$, (e) $E_e = 300 \text{ MPa}$, (f) summary of all cases

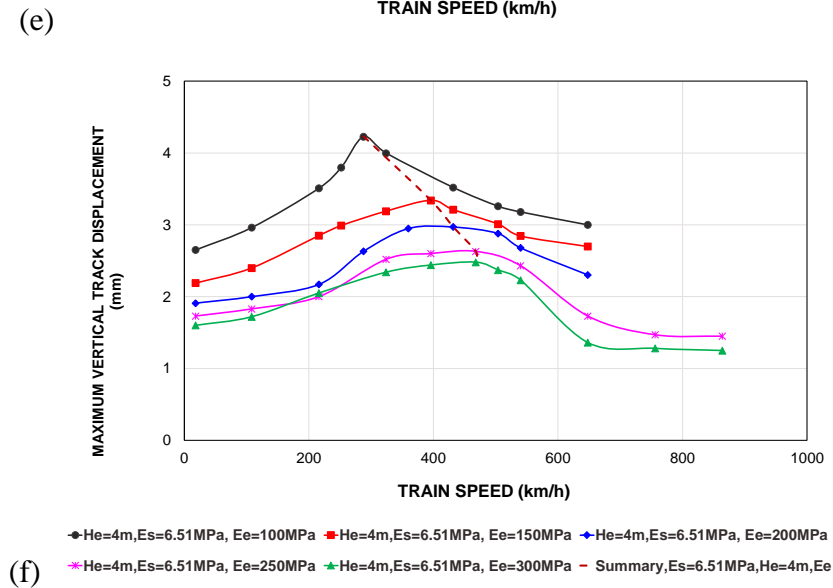
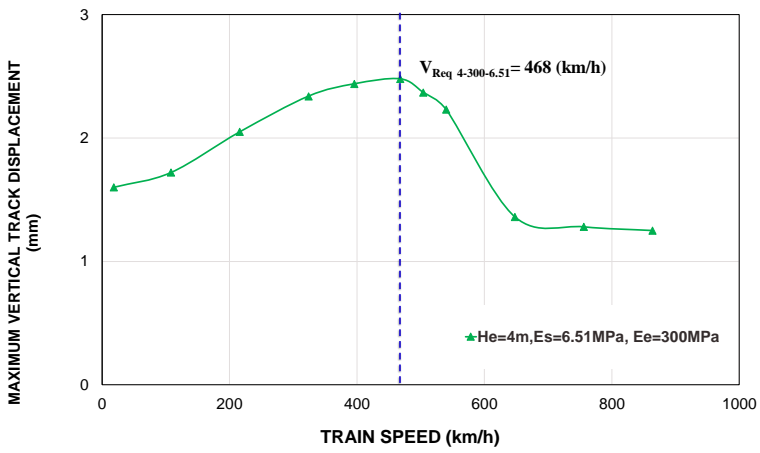
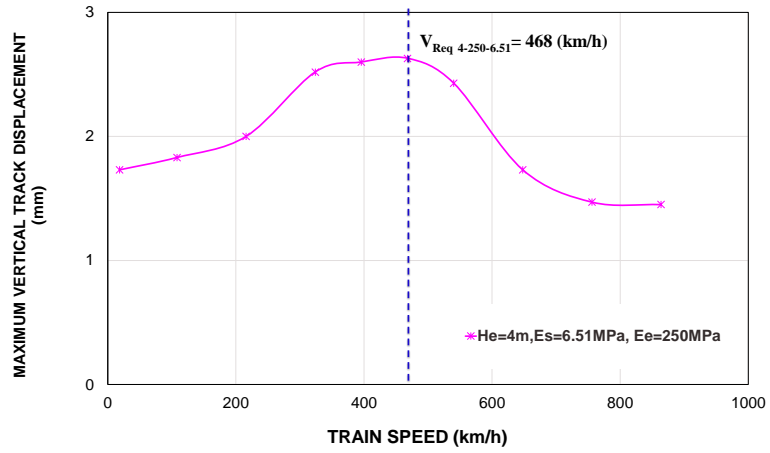


Figure 4.64. Continued

Table 4.11. Embankment Modulus (E_e) Effect on the Equivalent Rayleigh Wave Speed (V_{Req}) of track/embankment/Ground Systems (Embankment Thickness (H_e)=4.0m)

Case No	Embankment Modulus (E_e) (MPa)	V_{Req} (km/h)	Maximum vertical track displacement at critical speed (mm)
1	100	288	4.23
2	150	396	3.34
3	200	432	2.97
4	250	468	2.63
5	300	468	2.48

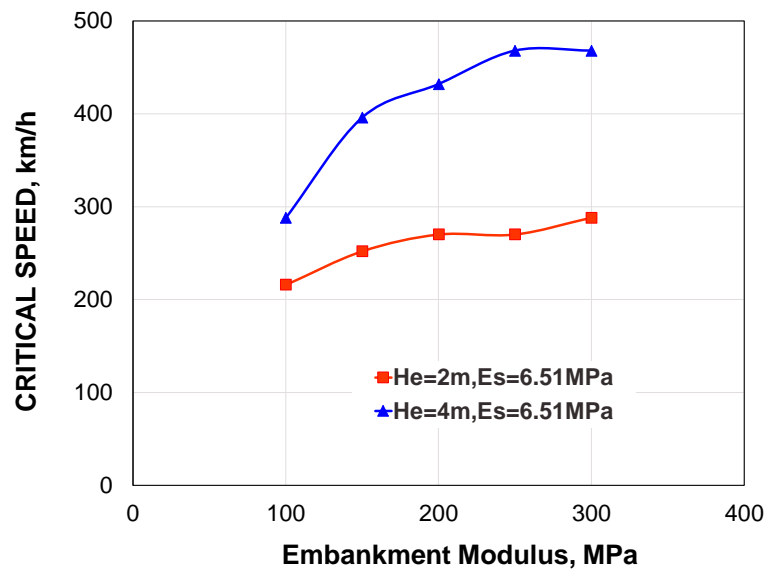


Figure 4.65. Effect of embankment moduli on critical speed ($H_e=2.0$ and 4.0 m)

It was shown that using shallow embankment made of soil materials with low ranges of modulus, embankment modulus has minor effect on critical speed modification. Because constructing deep enough embankment or preparing soils with high enough modulus to avoid passing Rayleigh wave barrier is not an applicable countermeasure in

some railway lines, through an additional simulation, shallow layer of embankment made of concrete was modeled too. Indeed, through this part of study it was shown that if the extremely stiff material, such as concrete, is modeled as embankment layers, it can be influentially useful to modify the critical speed. Results of these simulation are plotted in Figure 4.66. These results confirmed that the embankment moduli should be changed approximately in order of 10 to be considered as an effective parameter influencing the critical speeds. Figure 4.66 shows that when embankment modulus increases by 200 times, the critical speed increases by 3.2 times. Moreover, the model indicates that maximum track displacement decreases drastically when concrete material is used as an embankment layer instead of soil with $E_e=100$ MPa. The ratio of maximum dynamic track displacement over the static displacement also considerably decreases when concrete is modelled instead of a layer of soil. Kaynia and Madshus (2001) show that one effective method to modify critical speed is to use a 0.4 m thick concrete slab under the embankment. In section 4.10, a variety of design methods will be reviewed.

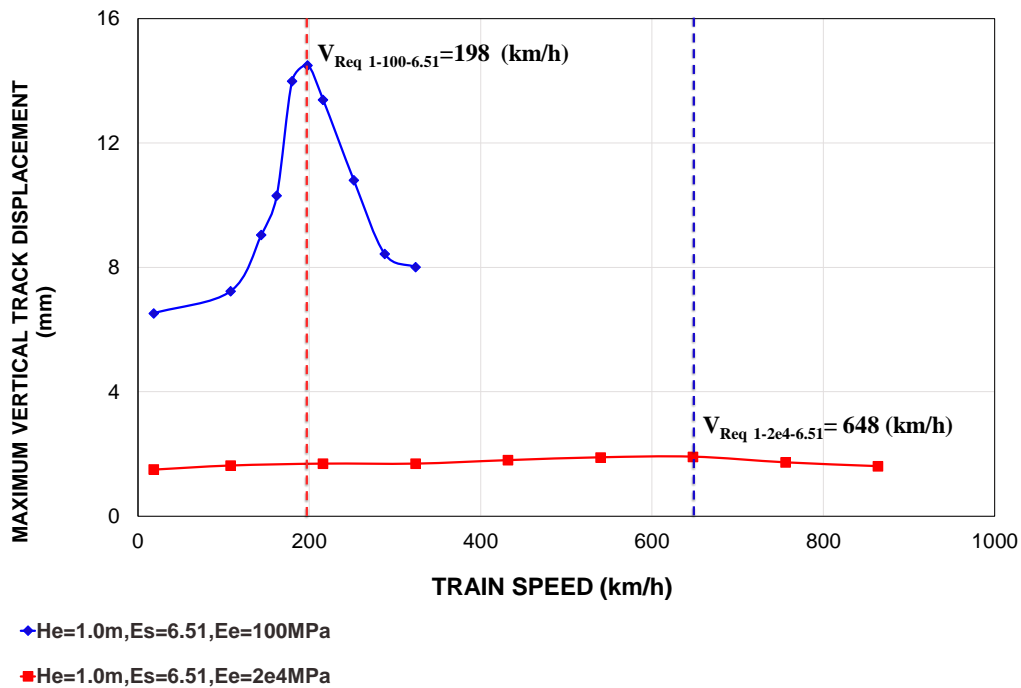


Figure 4.66. Maximum vertical track displacement vs. train speed

4.7.4 Subgrade Modulus Effect

As mentioned earlier in this section, particularly when the track is constructed on a shallow embankment, the subgrade stiffness under the embankment plays a crucial role in determining the critical speed of the track/embankment/ground system; indeed, the ground or subgrade properties directly affect the critical speed magnitude (Equation 4.1 to 4.3). Therefore, one effective mitigating practice for cases where embankment overlays very soft soil with low Rayleigh wave speed is to stiffen the subsoil. There are different methods used to increase the stiffness of the subgrade or the foundation under the

embankment, which will be discussed in section 4.10. In this section, the effect of subgrade modulus as an effective parameter in subgrade stiffness will be investigated.

In order to conduct the parametric study, the worst scenario which includes a track directly located on top of the subgrade without any embankment layer will be studied. The subgrade modulus will be changed within an applicable range of soil moduli (Table 4.12).

The finite element model configuration is illustrated in Figure 4.67. The material properties of the track (rail and ties) and train (wheels) are the same as the ones given in Table 4.7.

Table 4.12. Subgrade Material Properties

<i>Case No.</i>	Elasticity Modulus (E) MPa	Poisson's Ratio (ν)	Unit Weight (ρ) kg/m³	Rayleigh Wave Speed, V_R (km/h)
1	6.51	0.45	1260	144
2	14.65	0.45	1260	216
3	26.10	0.45	1260	288
4	41.00	0.45	1260	360

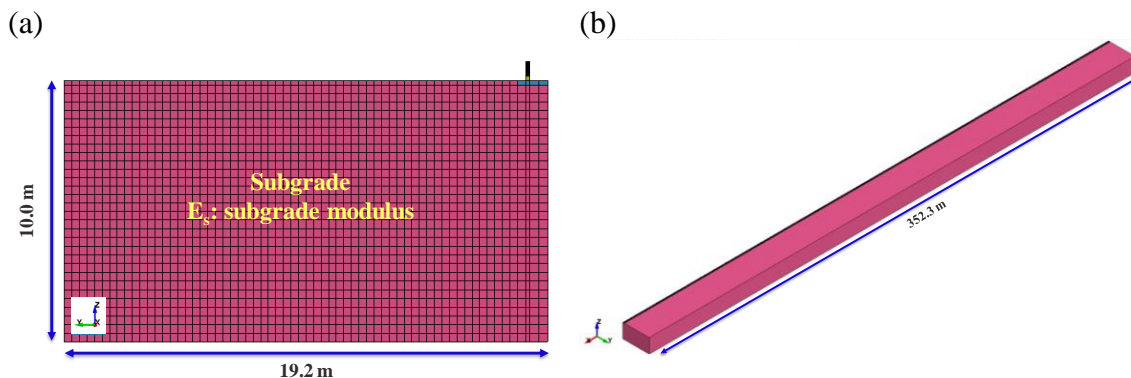


Figure 4.67. Finite element model dimension used for parametric study (assessing the effect of subgrade modulus on the critical speed) (a) cross-section view (b) side view

Figures 4.68 to 4.70 show the time history of the vertical track displacement for different subgrade conditions ($E_s = 6.51, 14.65, 26.10$ and 41.00 MPa) at three different train speeds, namely 108, 216, and 324 km/h. As with Figure 4.68, the displacement pattern is almost symmetrical, which means there is no dynamic effect of operating HSTs along the track. However, in terms of displacement magnitude, there are considerable differences between different cases. For example, in comparison to the track modelled on the softest subgrade ($E_s = 6.51$ MPa), the track on top of the stiff subgrade ($E_s = 41$ MPa) results in 4 times higher track displacement at a train speed of 108 km/h, at which the train did not run close to or faster than the Rayleigh wave speed of the subgrade soil. At a train speed of 216 km/h, however, two cases ($E_s = 6.51$ and 14.65 MPa) show asymmetrical displacement patterns, which means the train passes critical speed. All cases except for the case with the railway system on top of the stiffest subgrade ($E_s = 41$ MPa) show the same asymmetrical displacement pattern at a train speed of 324 km/h. This means that at this train speed, in all three cases ($E_s = 6.51, 14.65,$ and 26.1 MPa), the train goes faster than the Rayleigh wave speed of the subgrade. Figures 4.71 to 4.76 depict the displacement contour along the model depth in both a cross-section view and a plan view. The results show that stiffening the subgrade can have a great impact on critical speed. The displacement amplitude difference between different cases become more considerable as train speed becomes higher.

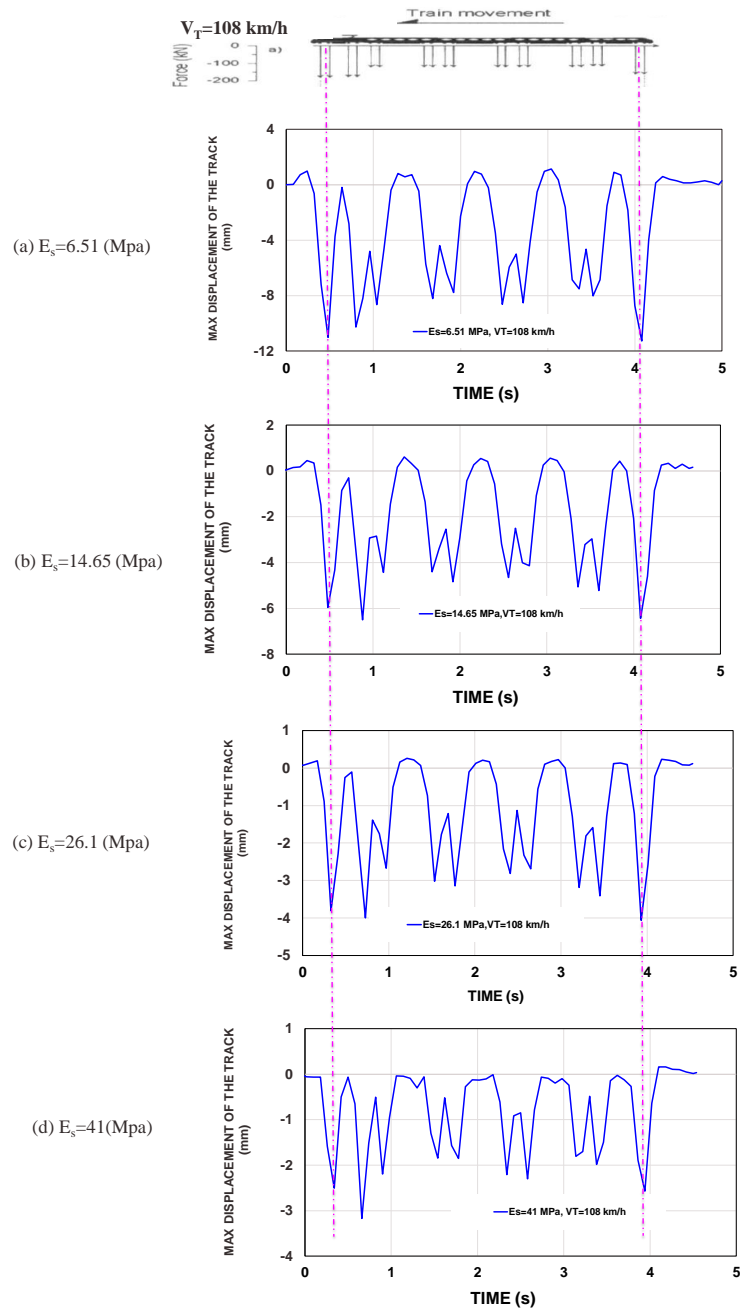


Figure 4.68. Effect of E_s on simulated vertical track displacement amplitude at $V_T = 108$ km/h

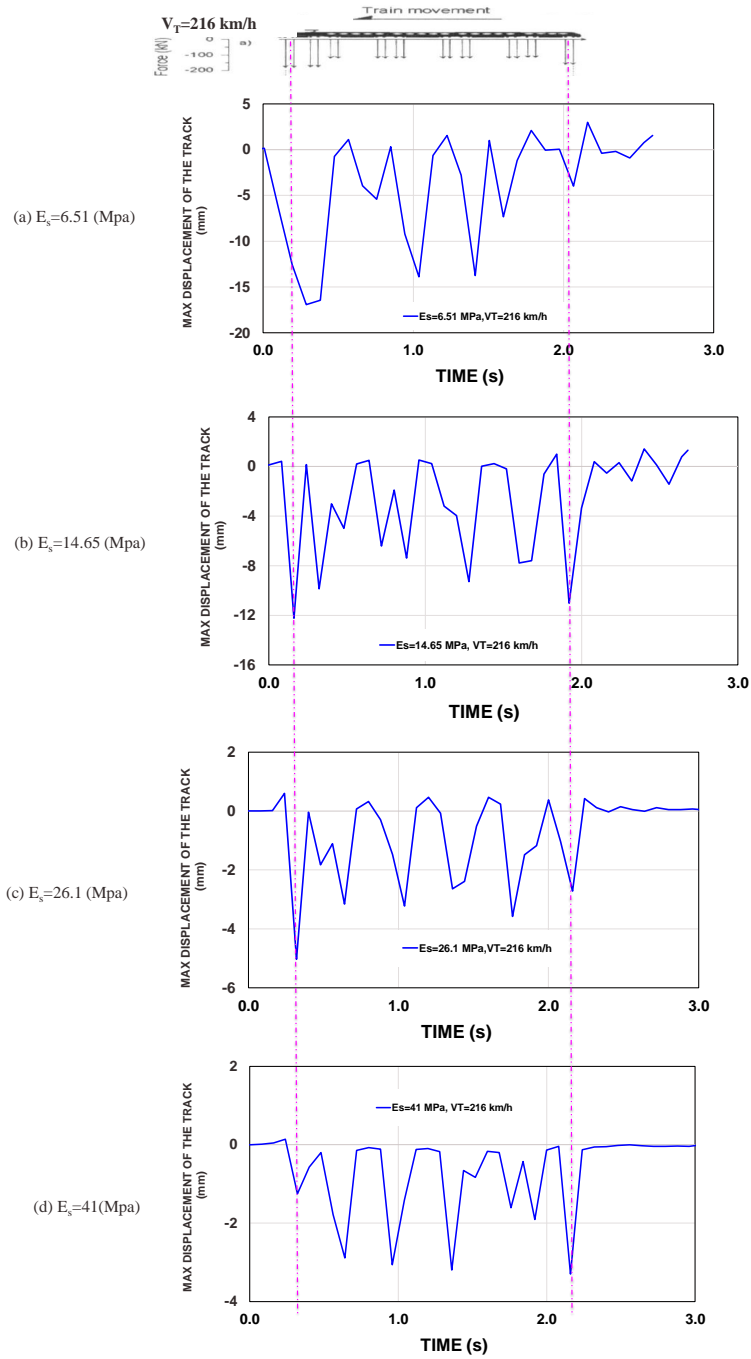


Figure 4.69. Effect of E_s on simulated vertical track displacement amplitude at $V_T=216$ km/h

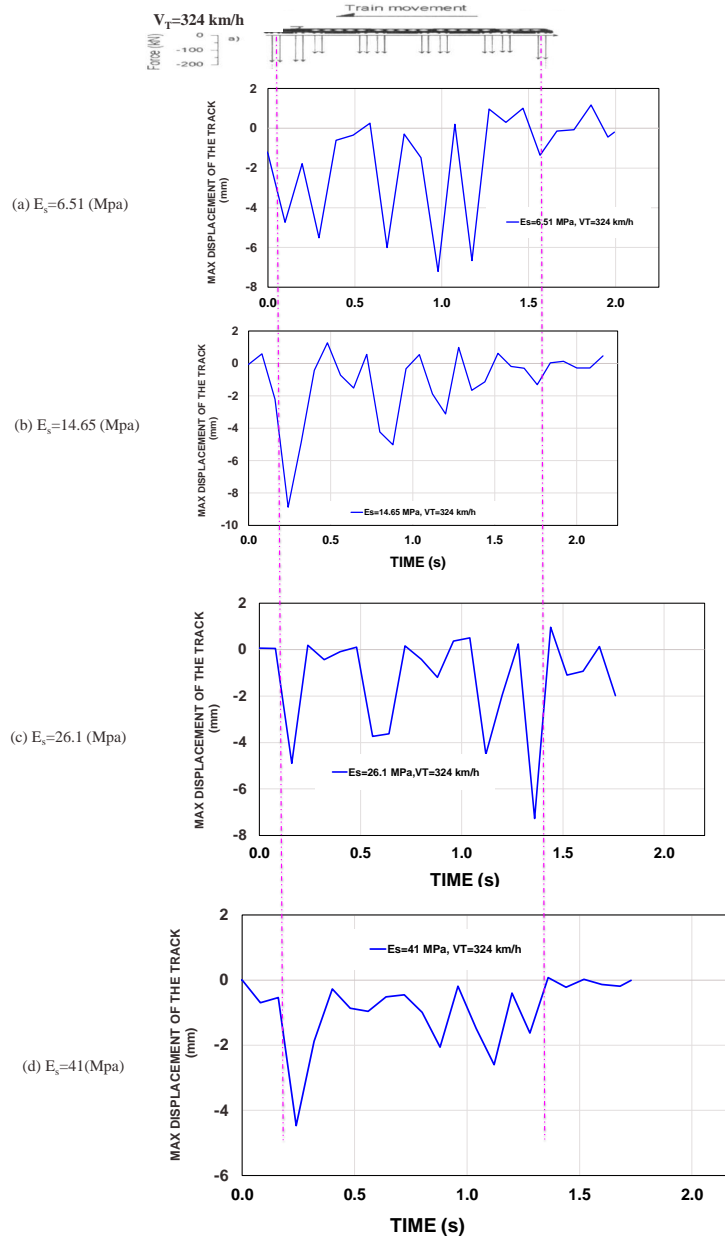


Figure 4.70. Effect of E_s on simulated vertical track displacement amplitude at $V_T=324$ km/h

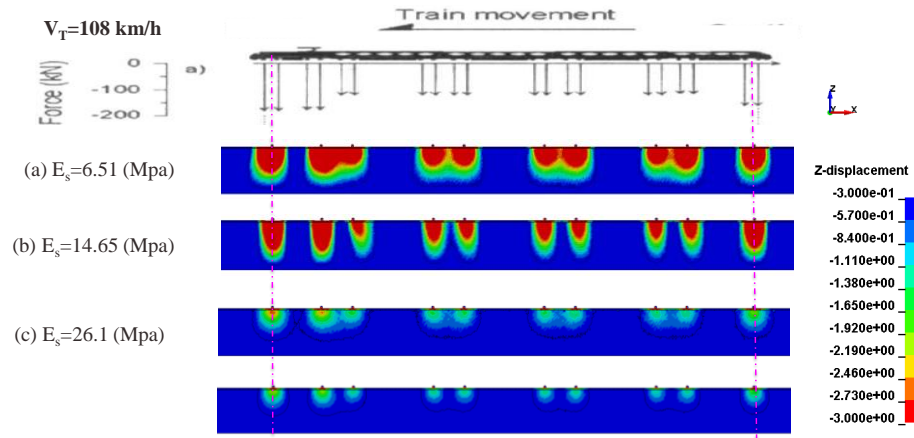


Figure 4.71. Cross-section view of track displacement contour at 108 km/h under different embankment conditions (different subgrade modulus)

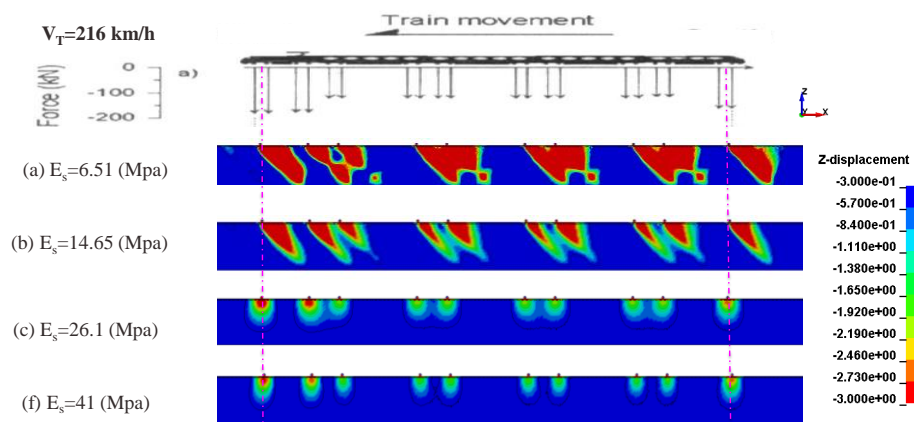


Figure 4.72. Cross-section view of track displacement contour at 216 km/h under different embankment conditions (different subgrade modulus)

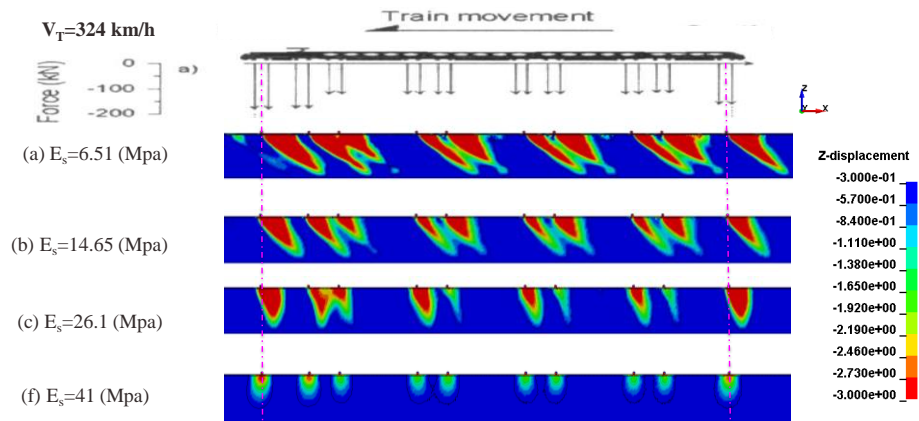


Figure 4.73. Cross-section view of track displacement contour at 324 km/h under different embankment conditions (different subgrade modulus)

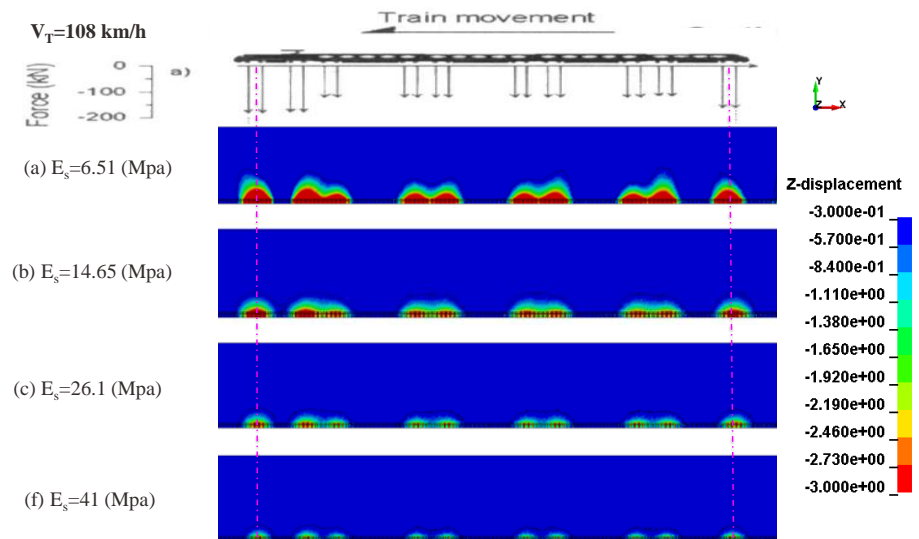


Figure 4.74. Plan view of track displacement contour at 108 km/h under different embankment conditions (different subgrade modulus)

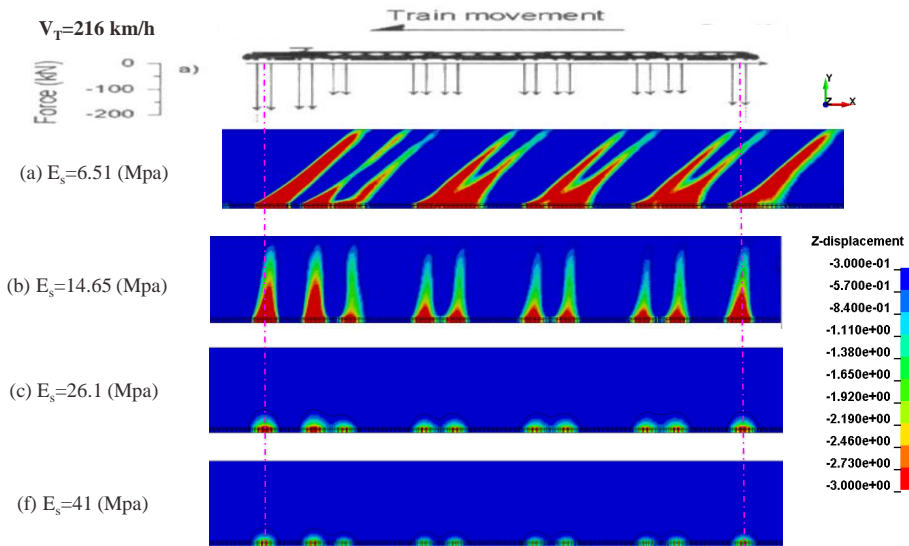


Figure 4.75. Plan view of track displacement contour at 216 km/h under different embankment conditions (different subgrade modulus)

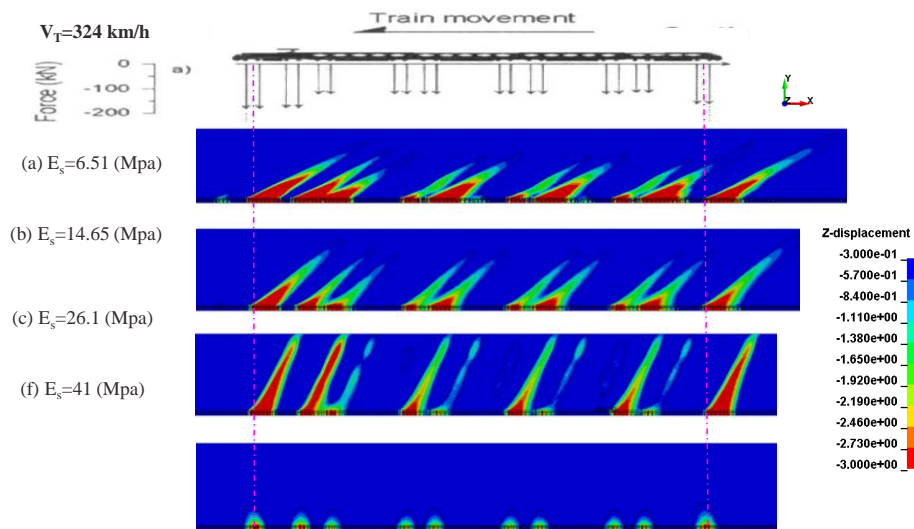
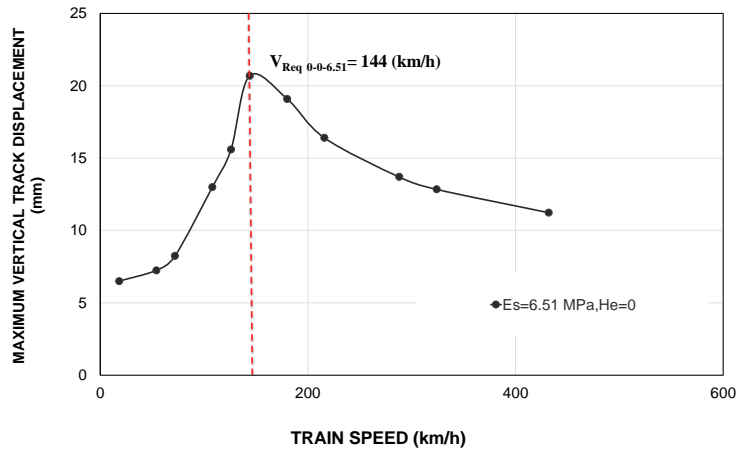


Figure 4.76. Plan view of track displacement contour at 324 km/h under different embankment conditions (different subgrade modulus)

In such a simple case where there is only a one-layer subgrade without embankment, the critical speed of the whole system can be directly estimated by Equation 2.3 and substituting the subgrade properties in this equation:

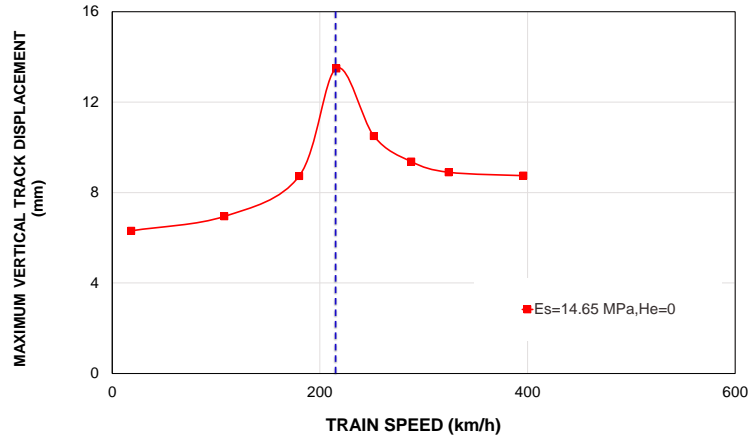
$$V_{Req} = V_{R(s)} = \sqrt{\frac{E_s}{2\rho_s(1+\nu_s)} \frac{0.87+1.12\nu_s}{1+\nu_s}} \quad (4.8)$$

where V_{Req} is equivalent Rayleigh wave speed of the track/embankment/ground system, $V_{R(s)}$ is subgrade Rayleigh wave speed, E_s is subgrade modulus, ν_s is Poisson ratio of the subgrade, and ρ_s is mass density of the subgrade. In these simple cases, the critical speeds obtained from finite element simulations (Figure 4.77) are the same as the ones obtained using Equation 4.8.

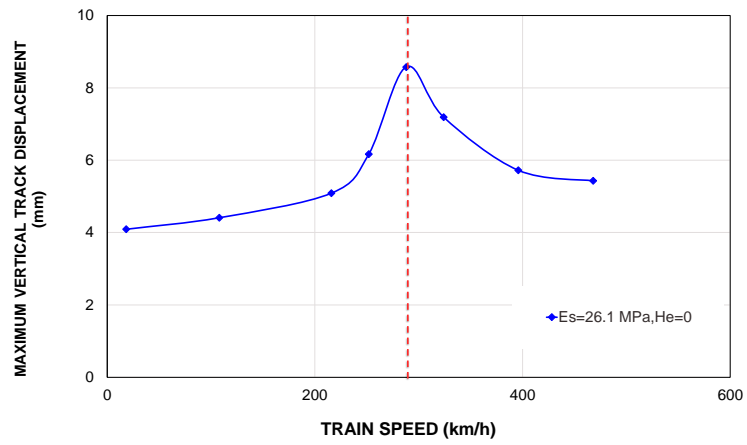


(a)

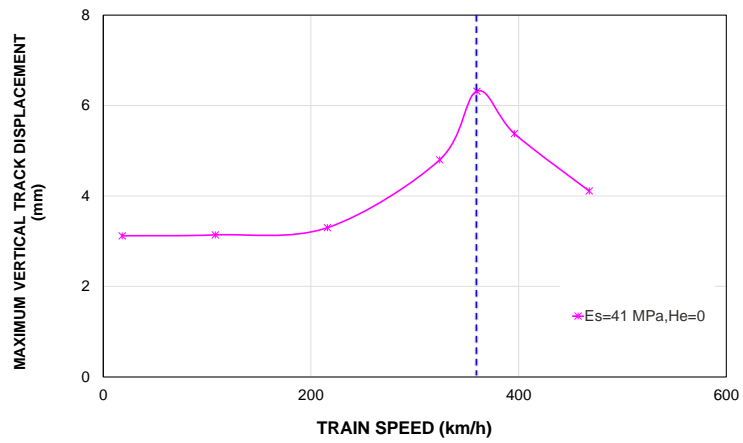
Figure 4.77. Maximum vertical track displacement vs. train speeds (a) $E_s=6.51\ MPa$, (b) $E_s=14.65\ MPa$, (c) $E_s=26.1\ MPa$, (d) $E_s=41\ MPa$, (e) summary of all cases



(b)

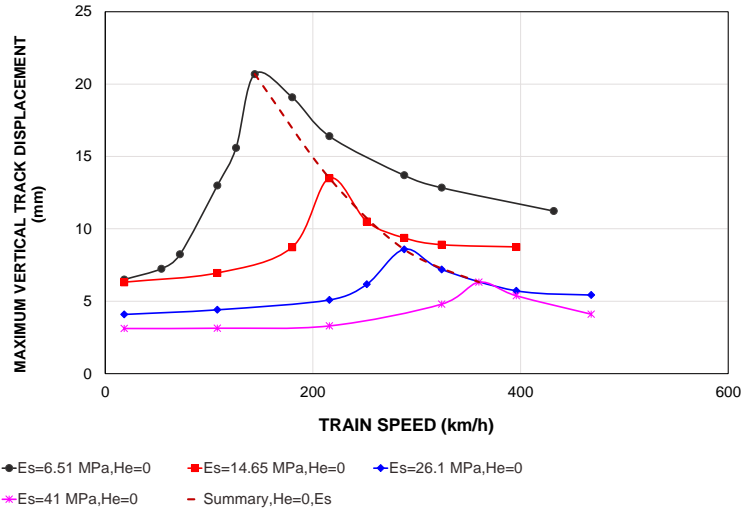


(c)



(d)

Figure 4.77. Continued



(e)

Figure 4.77. Continued

A summary of the results obtained from this parametric study is illustrated in Figure 4.78. Comparing Figure 4.63 and Figure 4.78, the effect of the embankment modulus on the critical speed is seen to be limited, but subgrade modulus is an influential parameter on modifying critical speed. It can be concluded that, one practical solution is to increase the stiffness and shear wave speed of the soil mass under the embankment by means of different methods that will be discussed in section 4.10. In this section, the main object was to show how effective these methods can be to modify shear wave speed or Rayleigh wave speed of the whole system.

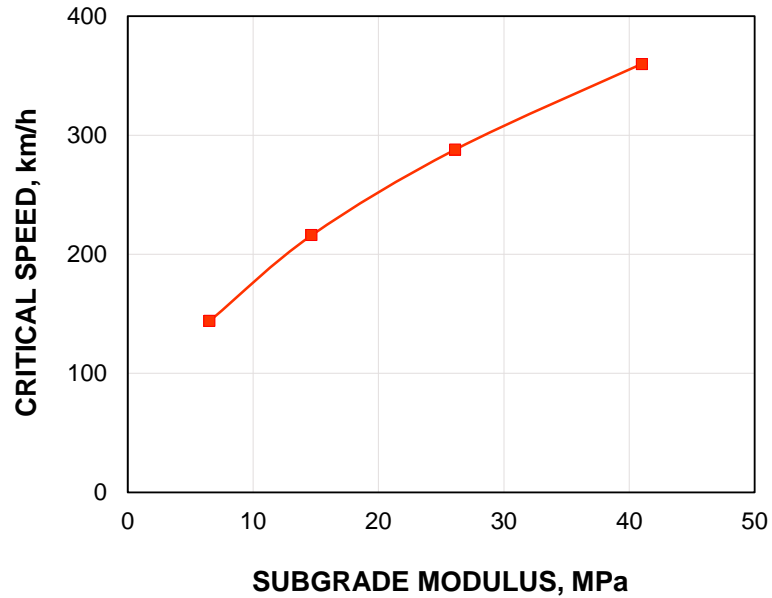


Figure 4.78. Effect of subgrade moduli on critical speed ($H_e=0$)

A combination of all these parameters was used to perform an extensive parametric study to propose some guideline charts which can help railway engineers to choose the best technique to modify critical speed so that resonance does not occur. The results of this parametric study will be given in the next section.

4.8 Proposed Guideline Charts

The main goal of conducting parametric studies was to create several guideline charts to help railway engineers have safer embankment designs without any risk of breaking the Rayleigh wave barrier, with the accompanying consequences. Indeed, the

results of this study will show target values for subgrade modulus, embankment modulus and embankment height so that the train speed is kept in a safe zone. It should be noted that this safe zone of speed must be defined as well. Different zones of train speed will be defined later in this section. This section both comprises the results of the parametric studies and defines the threshold values.

4.8.1 Parametric Study Results

The matrix cases that were selected to cover a reasonable range of embankment heights (H_e), embankment modulus (E_e), and subsoil modulus (E_s) to modify the critical speed are given in Table 4.13. The reason that these parameters were chosen in order to propose guideline charts was that the most effective design solutions have been aimed at modifying critical speed through either strengthening the subgrade under the embankment or stiffening the embankment by constructing deep and stiff enough embankment. Other material properties such as Poisson Ratio and soil unit weight are the same as the ones presented in Table 4.7. The FEM was fully described in section 4.7 (Figure 4.31).

Table 4.13. Matrix Cases Selected for Proposed Guideline Charts

Case No.	Subgrade Modulus, E_s (MPa)	Embankment Modulus, E_e (MPa)	Embankment Height, H_e (m)
1	6.51	150	2.0
2			4.0
3			6.0
4			8.0
5	6.51	200	2.0
6			4.0
7			6.0
8			8.0
9	6.51	250	2.0
10			4.0
11			6.0
12			8.0
13	6.51	300	2.0
14			4.0
15			6.0
16			8.0
17	6.51	2e4 (Concrete)	0.5
18			1.0
19	14.65	150	2.0
20			4.0
21			6.0
22			8.0
23	14.65	200	2.0
24			4.0
25			6.0
26			8.0
27	14.65	250	2.0
28			4.0
29			6.0
30			8.0
31	14.65	300	2.0
32			4.0
33			6.0
34			8.0
35	14.65	2e4 (Concrete)	0.5
36			1.0
37	26.1	150	2.0
38			4.0

Table 4.13. Continued

Case No.	Subgrade Modulus, E_s (MPa)	Embankment Modulus, E_e (MPa)	Embankment Height, H_e (m)
39			6.0
40			8.0
41			2.0
42			4.0
43	26.1	200	6.0
44			8.0
45			2.0
46	26.1	250	4.0
47			6.0
48			8.0
49			2.0
50	26.1	300	4.0
51			6.0
52			8.0
53	26.1	2e4 (Concrete)	0.5
54			1.0
55			2.0
56	41.0	150	4.0
57			6.0
58			8.0
59			2.0
60	41.0	200	4.0
61			6.0
62			8.0
63			2.0
64	41.0	250	4.0
65			6.0
66			8.0
67			2.0
68	41.0	300	4.0
69			6.0
70			8.0
71	41.0	2e4 (Concrete)	0.5
72			1.0
73	6.51	-	0.0
74	14.65	-	0.0
75	26.1	-	0.0
76	41	-	0.0

Table 44.13. Continued

Case No.	Subgrade Modulus, E_s (MPa)	Embankment Modulus, E_e (MPa)	Embankment Height, H_e (m)
77	6.51	100	2.0
78			4.0
79			6.0
80			8.0
81	14.65	100	2.0
82			4.0
83			6.0
84			8.0
85	26.1	100	2.0
86			4.0
87			6.0
88			8.0
89	6.51	100	10.0
90			12.0
91	14.65	100	10.0
92			12.0
93	26.1	100	10.0
94			12.0

In sections 4.7.1 to 4.7.4, how influential the parameters including train speed (V_T), embankment height (H_e), embankment modulus (E_e), and subgrade modulus (E_s) are on the critical speed (V_C) was explained. The method discussed in section 4.7.2 was used to estimate the critical speed for each case study. The final results of numerical analyses for all 94 cases are illustrated in Figures 4.79 to 4.84. In total, more than 2000 simulations were conducted to assess the critical speeds. In all cases, as embankment thickness increases, the track displacement decreases significantly; this difference can be most clearly seen when embankment thickness increases between 0 and 4 m. For example, when embankment thickness increases from 0 to 2 m, the track displacement decreases by 2 times. The results have confirmed that a well-designed embankment with proper stiffness

and thickness can effectively be used to prevent large displacement. This results in lower costs of maintenance and higher levels of passenger safety and comfort. In addition to low track displacement as a result of embankment design, the critical speed increases considerably with embankment thickness, embankment modulus, and subgrade modulus. Indeed, combining these three factors can have a great impact on modifying critical speeds of the whole system in addition to decreasing the track displacement.

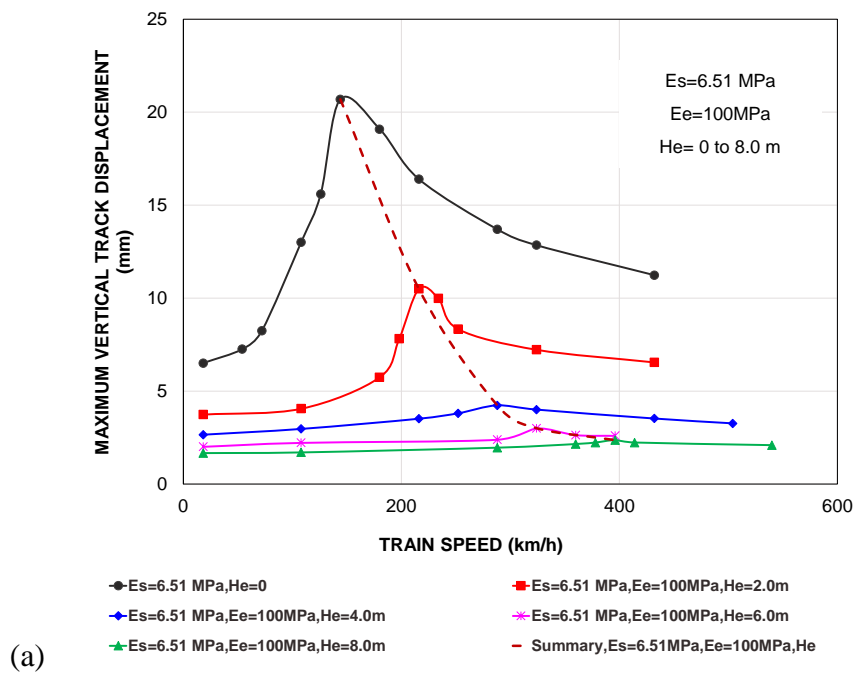
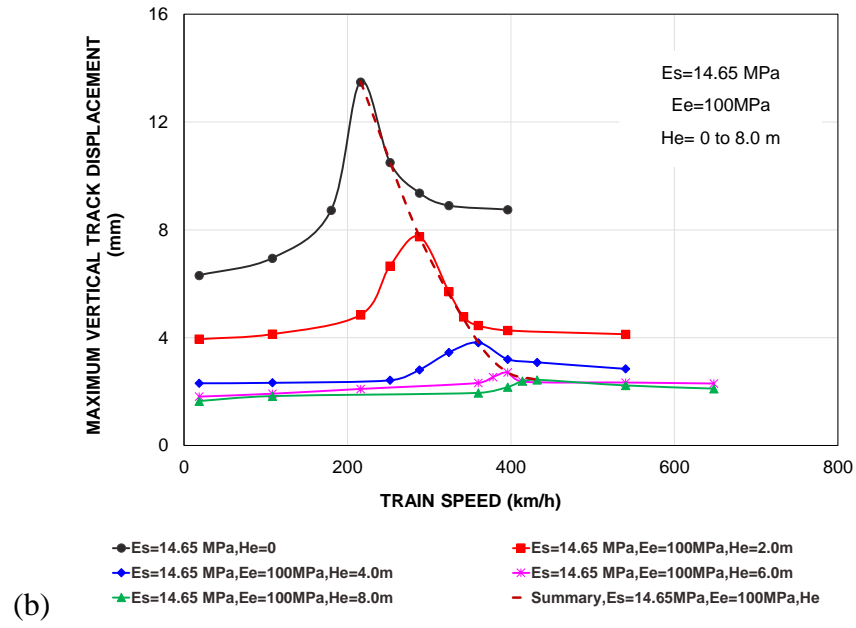
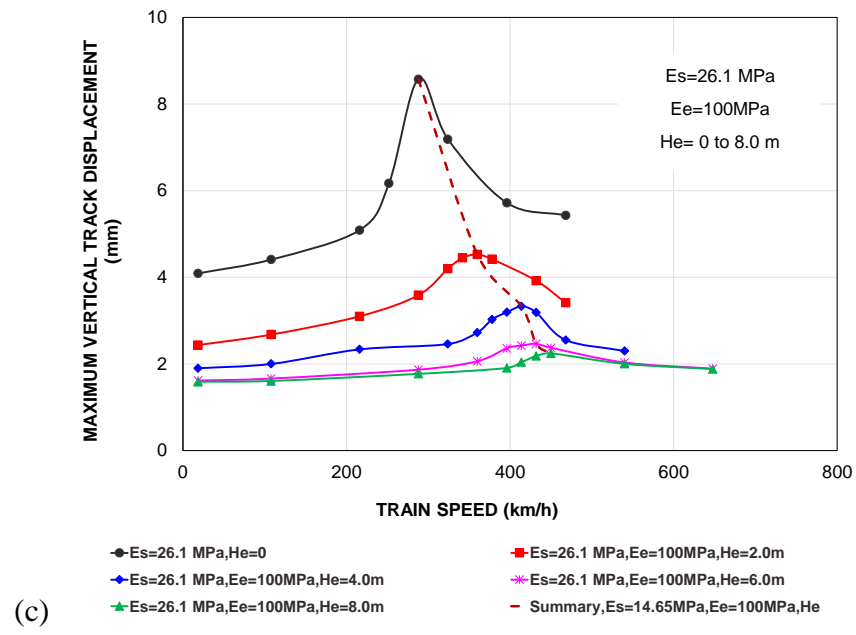


Figure 4.79. Maximum vertical track displacement vs. train speeds with embankment modulus $E_e=100$ MPa, different embankment heights ($0 \leq H_e \leq 8.0$ m) at (a) $E_s=6.51$ MPa, (b) $E_s=14.65$ MPa, and (c) $E_s=26.1$ MPa



(b)



(c)

Figure 4.79. Continued

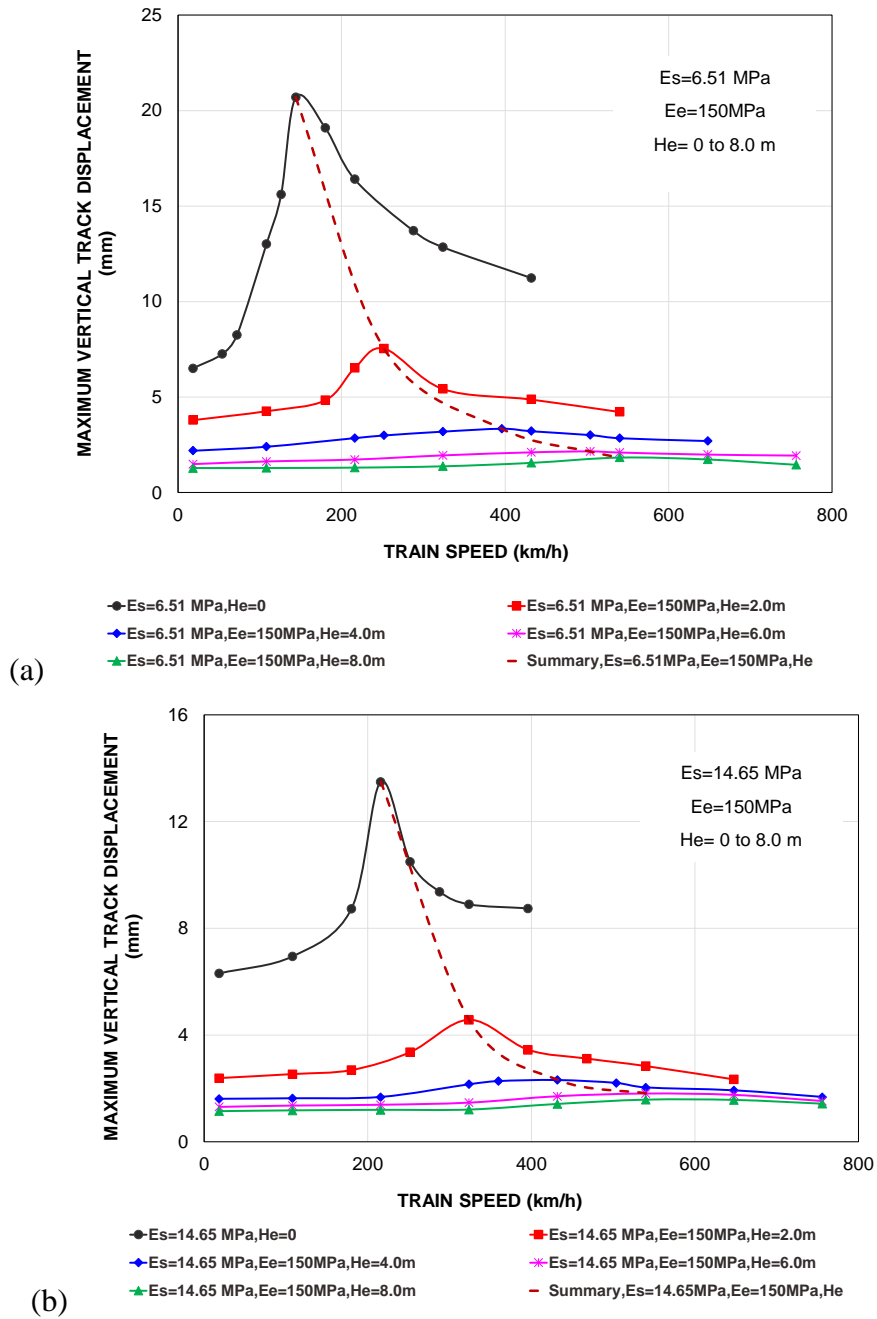
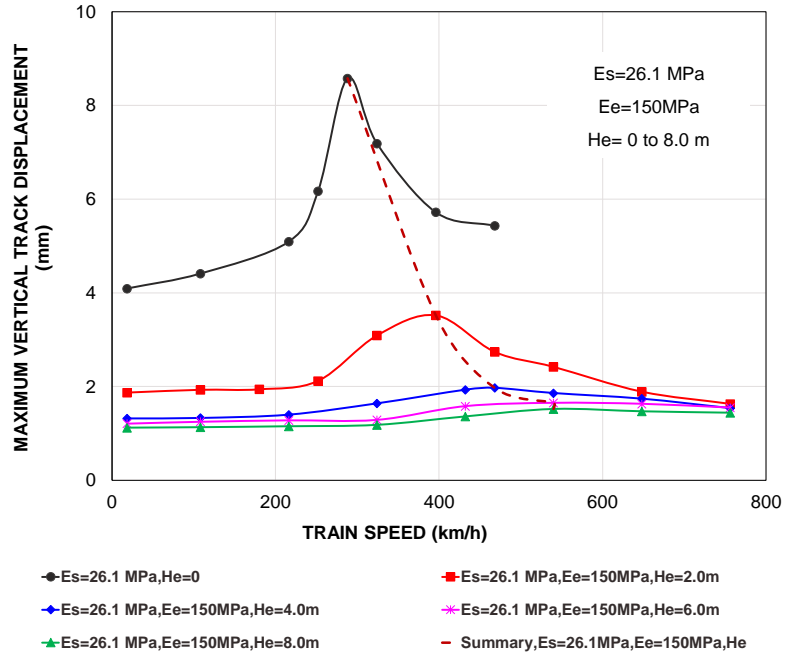
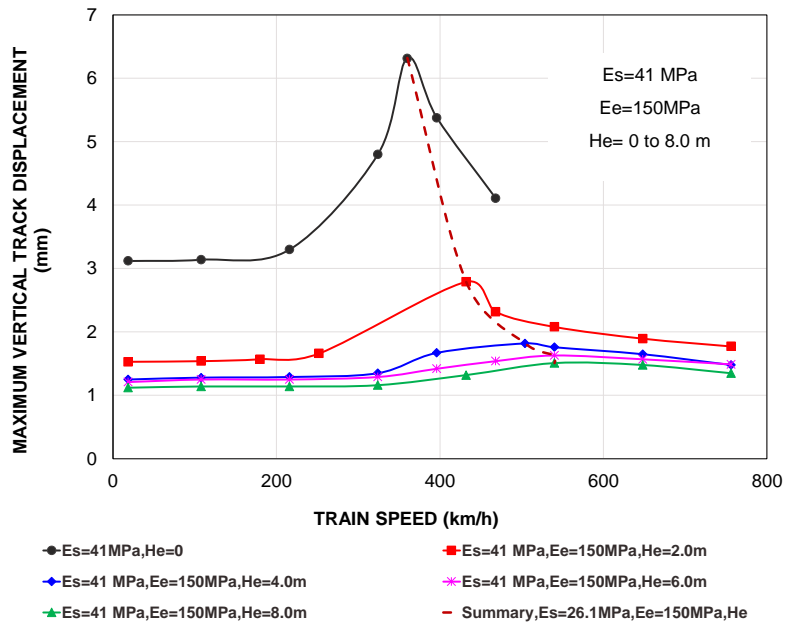


Figure 4.80. Maximum vertical track displacement vs. train speeds with embankment modulus $E_e=150$ MPa, different embankment heights ($0 \leq H_e \leq 8.0$ m) at (a) $E_s=6.51$ MPa, (b) $E_s=14.65$ MPa, (c) $E_s=26.1$ MPa, (d) $E_s=41$ MPa



(c)



(d)

Figure 4.80. Continued

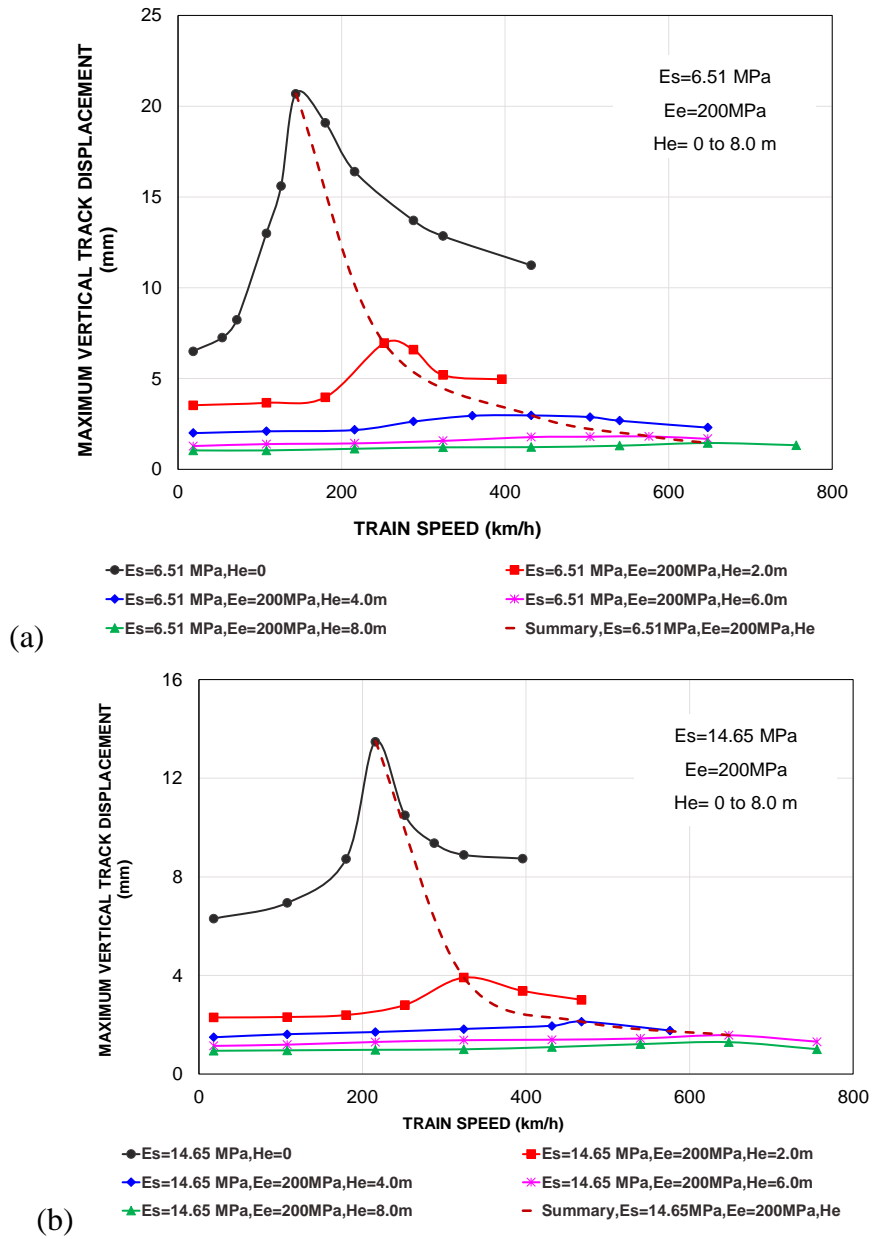
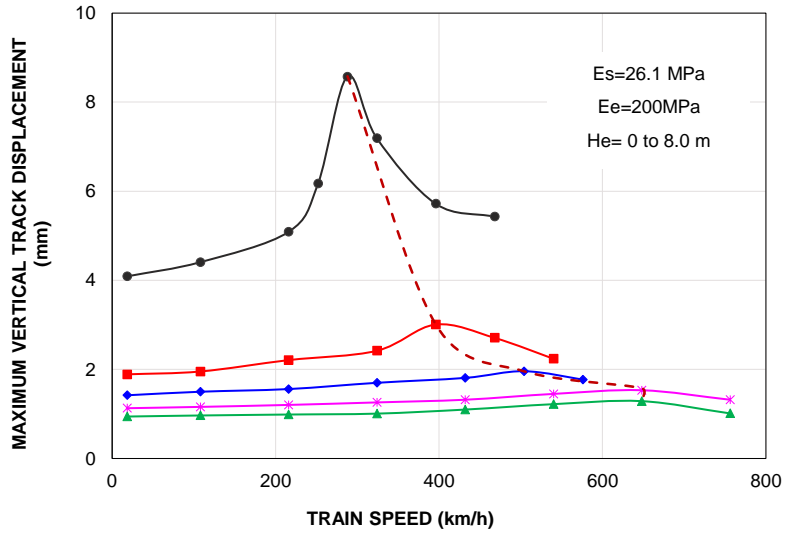
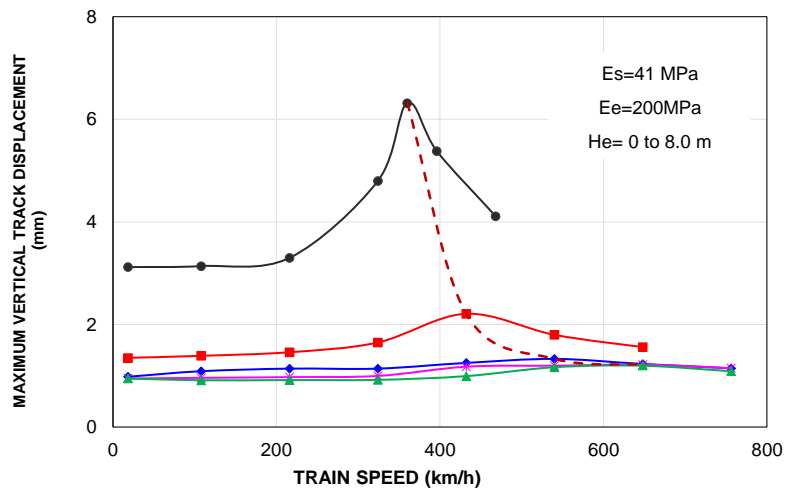


Figure 4.81. Maximum vertical track displacement vs. train speeds with embankment modulus $E_e=200$ MPa, different embankment heights ($0 \leq H_e \leq 8.0$ m) at (a) $E_s=6.51$ MPa, (b) $E_s=14.65$ MPa, (c) $E_s=26.1$ MPa, (d) $E_s=41$ MPa



(c)



(d)

Figure 4.81. Continued

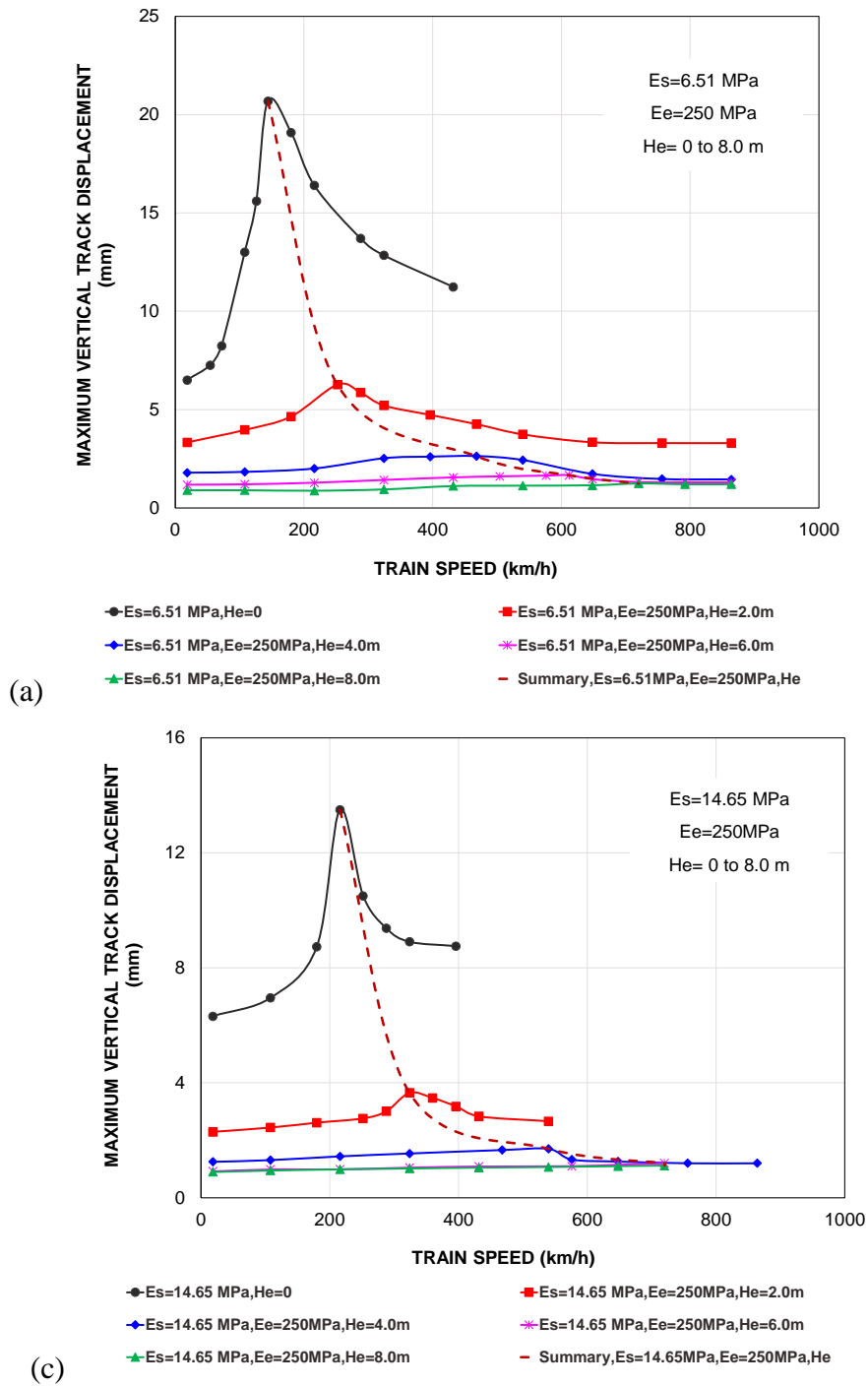
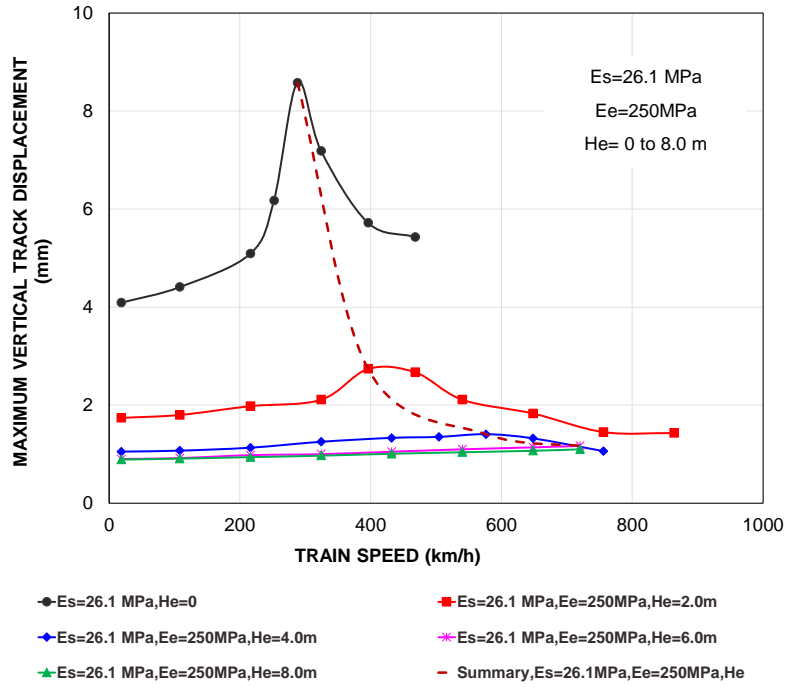
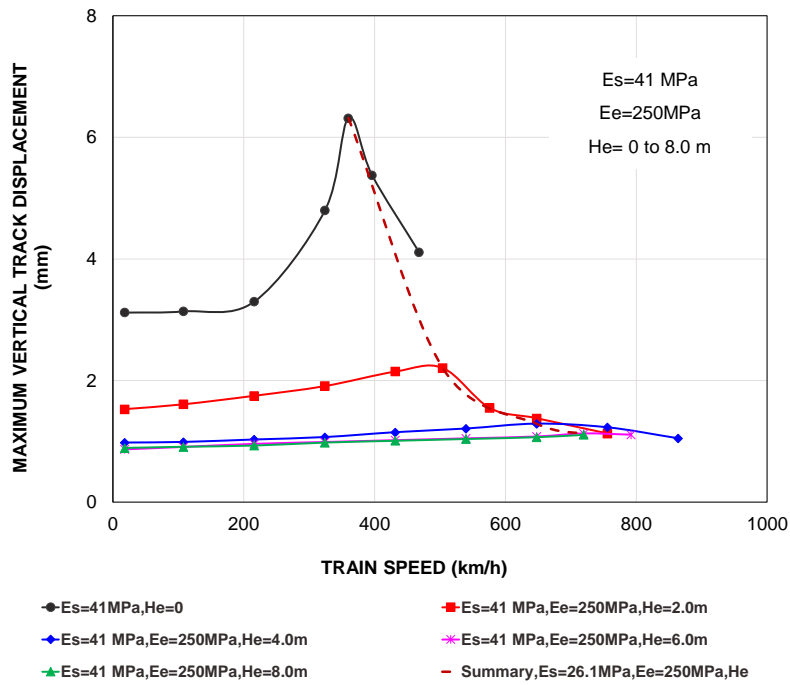


Figure 4.82. Maximum vertical track displacement vs. train speeds with embankment modulus $E_e=250$ MPa, different embankment heights ($0 \leq H_e \leq 8.0$ m) at (a) $E_s=6.51$ MPa, (b) $E_s=14.65$ MPa, (c) $E_s=26.1$ MPa, (d) $E_s=41$ MPa



(c)



(d)

Figure 4.82. Continued

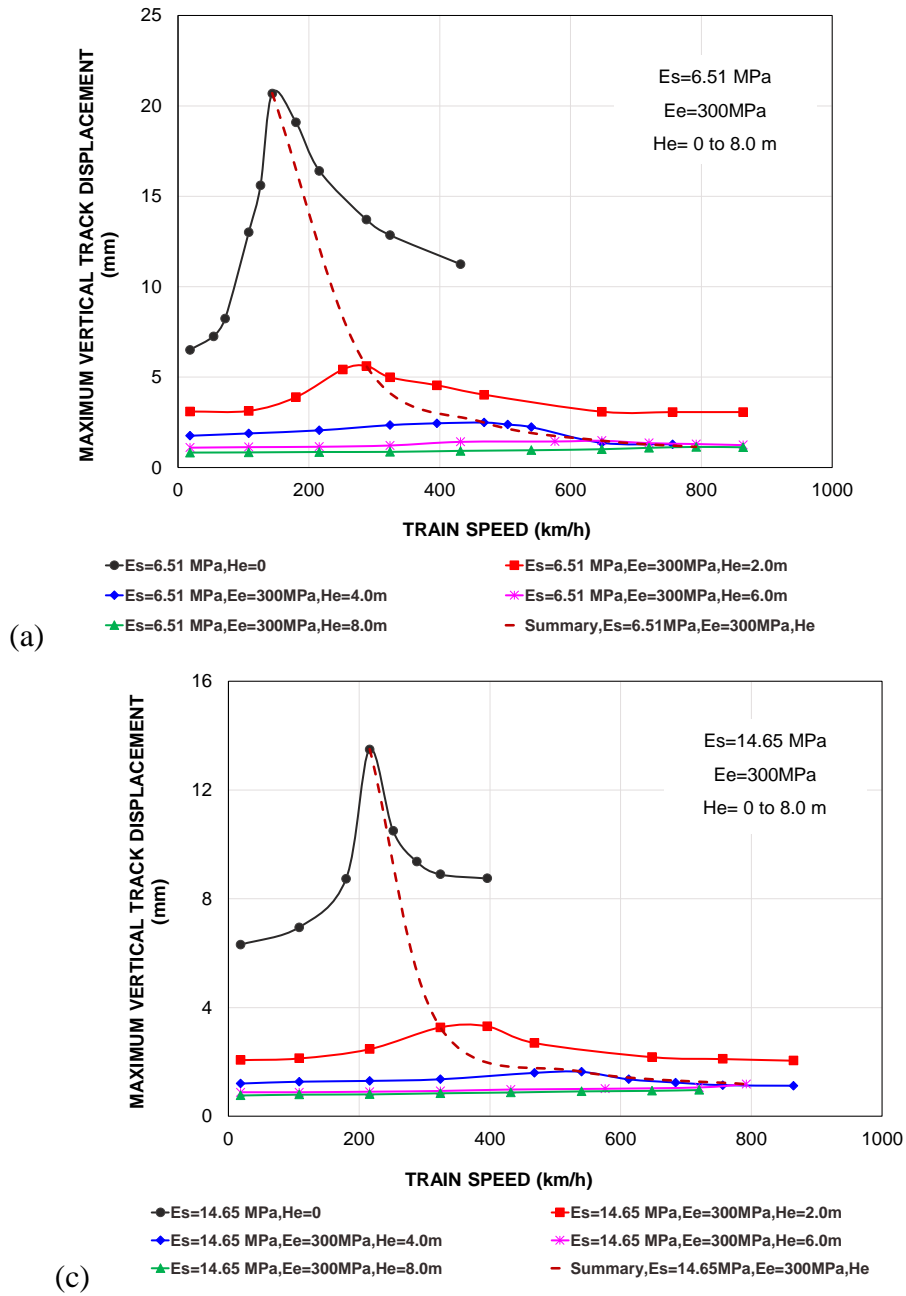


Figure 4.83. Maximum vertical track displacement vs. train speeds with embankment modulus $E_e=300$ MPa, different embankment heights ($0 \leq H_e \leq 8.0$ m) at (a) $E_s=6.51$ MPa, (b) $E_s=14.65$ MPa, (c) $E_s=26.1$ MPa, (d) $E_s=41$ MPa

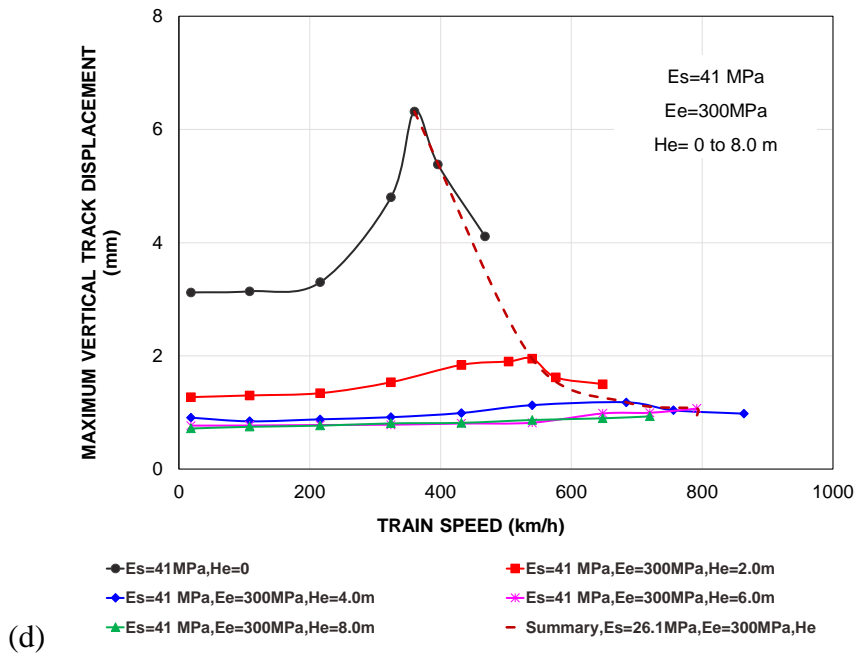
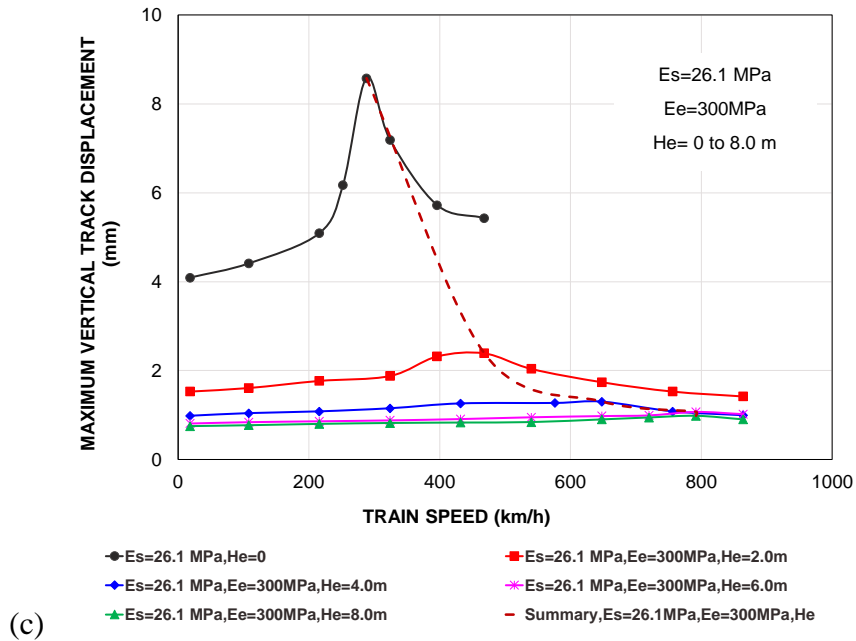


Figure 4.83. Continued

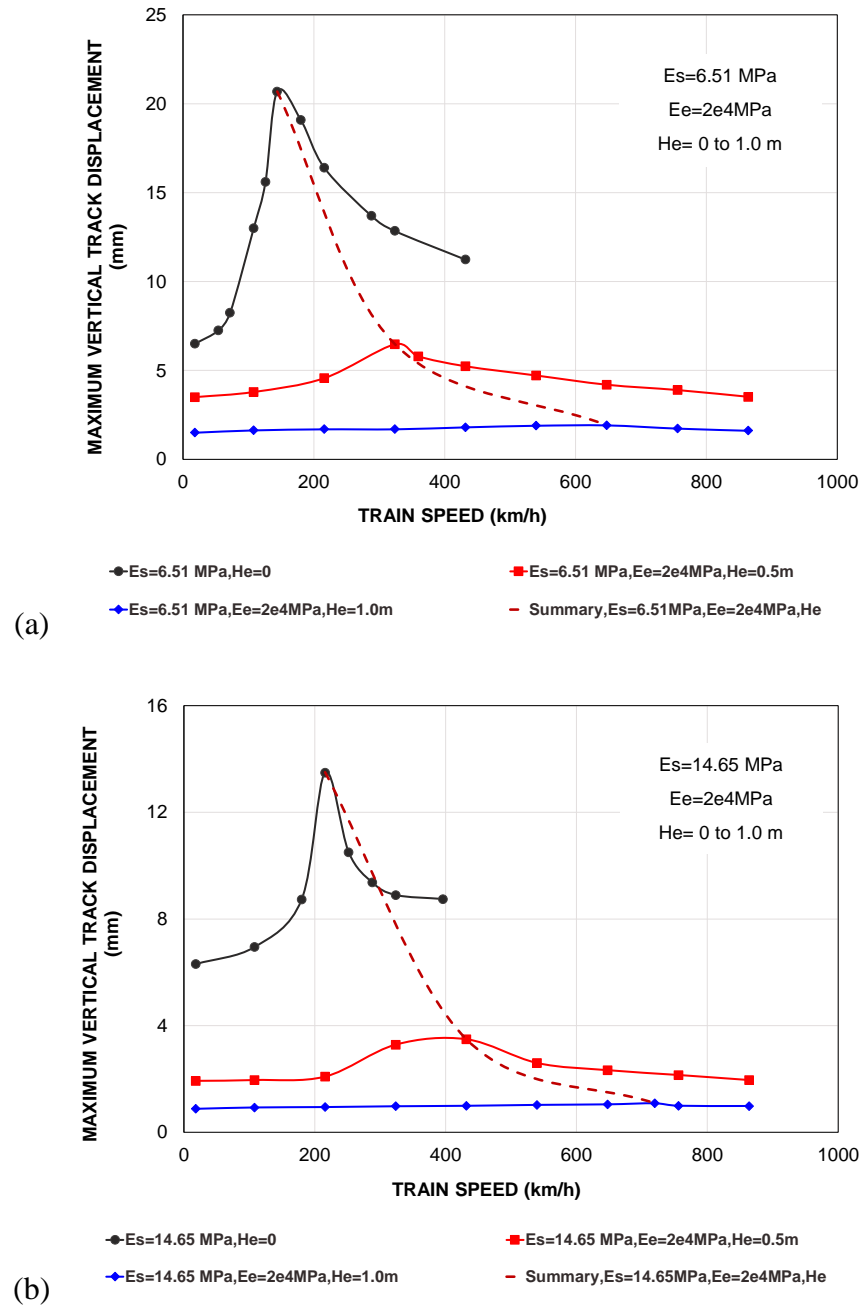
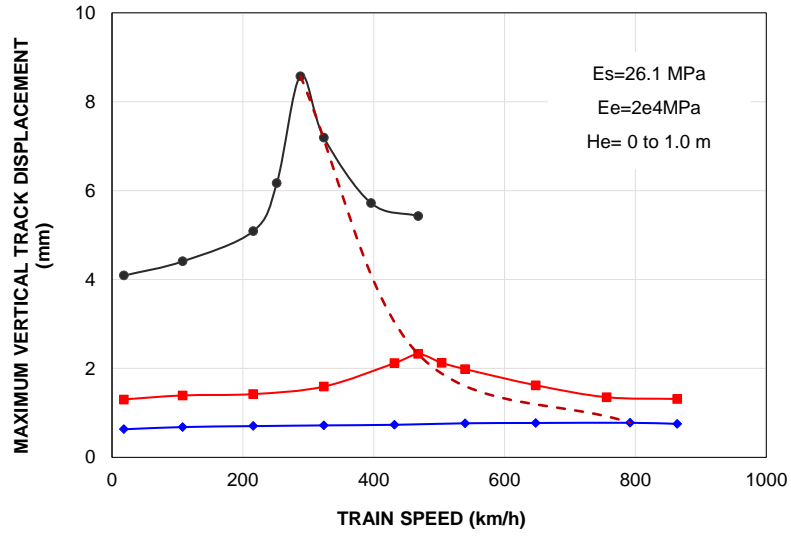
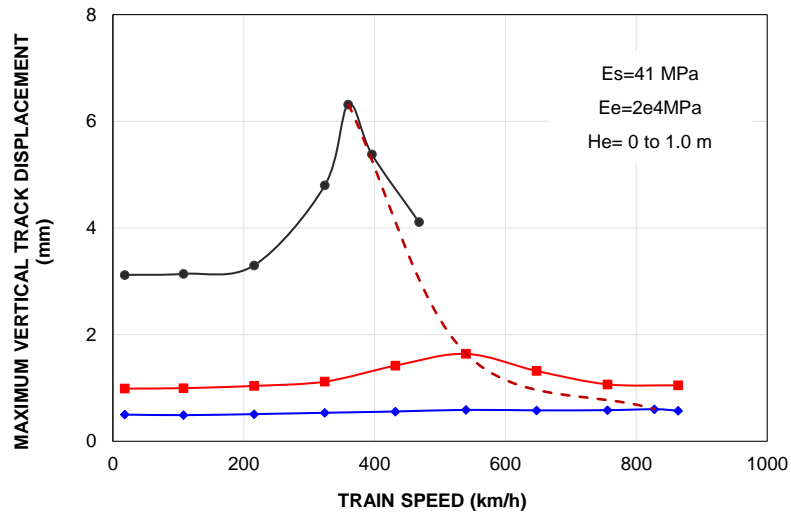


Figure 4.84. Maximum vertical track displacement vs. train speeds with embankment modulus $E_e=2e4$ MPa (Concrete slab), different embankment heights ($0 \leq H_e \leq 1.0$ m) at (a) $E_s=6.51$ MPa, (b) $E_s=14.65$ MPa, (c) $E_s=26.1$ MPa, (d) $E_s=41$ MPa



(c)



(d)

Figure 4.84. Continued

The results of simulations for all 94 cases are summarized and shown in Figure 4.85. Figure 4.85 (a) to (f) depicts the relationship between critical speed (V_C) and three influential design parameters: embankment height (H_e), embankment modulus (E_e) and subgrade modulus (E_s). Almost the same trend can be seen in each case. Three phases are obvious in almost all graphs. At the beginning, there is a sharp slope where embankment thickness is less than 4 m. In this phase, both embankment soil layer and subgrade soil layer have impacts on the critical speed of the whole system, but not with equal impact. When there is no embankment ($H_e=0$), as mentioned earlier in section 4.7.4, the critical speed is equal to the Rayleigh wave speed of the subgrade (Equation 4.8). However, as embankments with specific thickness H_e are modelled under the track, the embankment layer also plays an important role in estimating the critical speed of the whole system. This role becomes more predominant as embankment height increases up to $H_e=4.0$ m. After that, in phase two, the slope of the graphs becomes lower up to the embankment thickness at which the subgrade properties do not have any effect on estimating critical speed. In this phase, as embankment thickness increases, embankment layer becomes more predominate in defining the critical speed than the subgrade layer. In phase three the slope of the graph becomes zero, which means there is no change of critical speed with embankment height. This happens because the only soil property that is important to determining the critical speed is the embankment layer property. In fact, if the embankment is high enough, the critical speed will be equal to the Rayleigh wave speed of embankment. In such a case with high enough embankment, the critical speed can be defined as

$$V_{Req} = V_{R(e)} = \sqrt{\frac{E_e}{2\rho_e(1+\nu_e)} \frac{0.87+1.12\nu_e}{1+\nu_e}} \quad (4.9)$$

where $V_{R(e)}$ is embankment Rayleigh wave speed, E_e is embankment modulus, ρ_e is embankment unit weight, and ν_e is embankment Poisson ratio. Figure 4.85 (f) obviously depicts only the first phase, since a very shallow concrete slab was modeled in this case study. However, it is shown that this very shallow concrete slab can effectively modify the critical speed, which was our main objective.

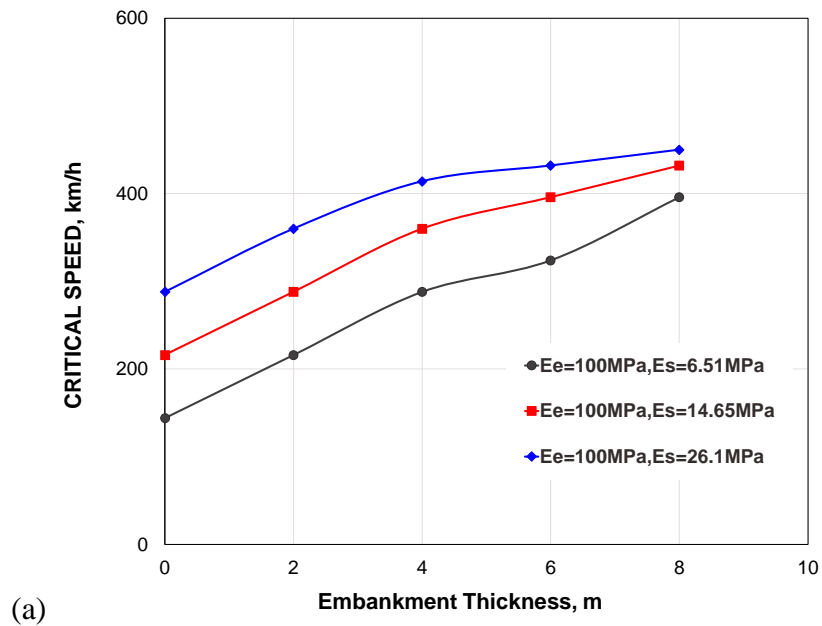


Figure 4.85. Effect of embankment thicknesses (H_e), embankment moduli (E_e) and subgrade moduli (E_s) on the critical speeds (V_C) (a) $E_e=100$ MPa (b) $E_e=150$ MPa, (c) $E_e=200$ MPa, (d) $E_e=250$ MPa, (e) $E_e=300$ MPa, and (f) $E_e=2e4$ MPa (Concrete slab)

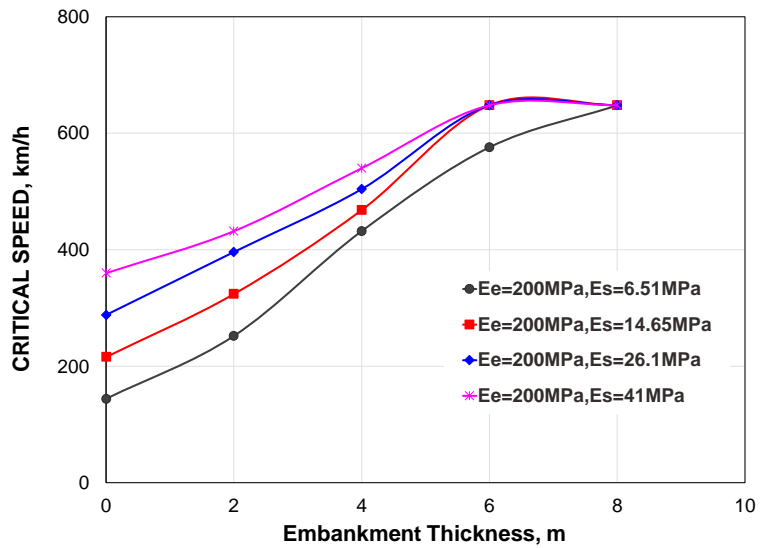
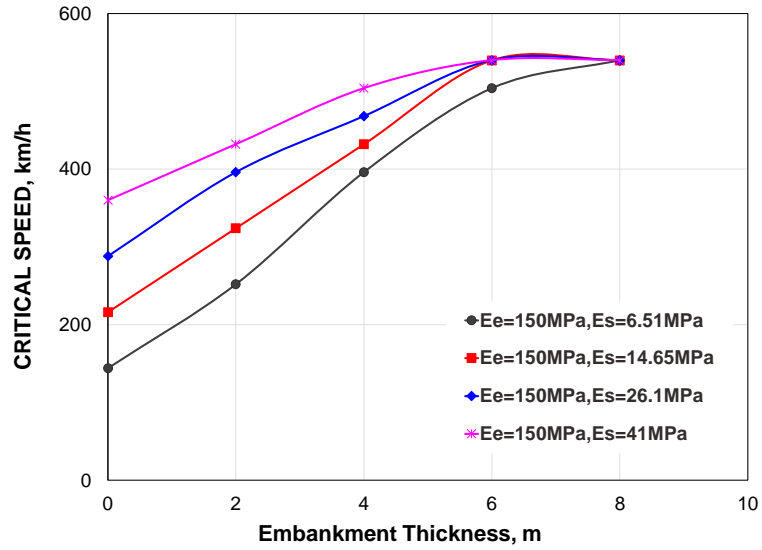


Figure 4.85. Continued

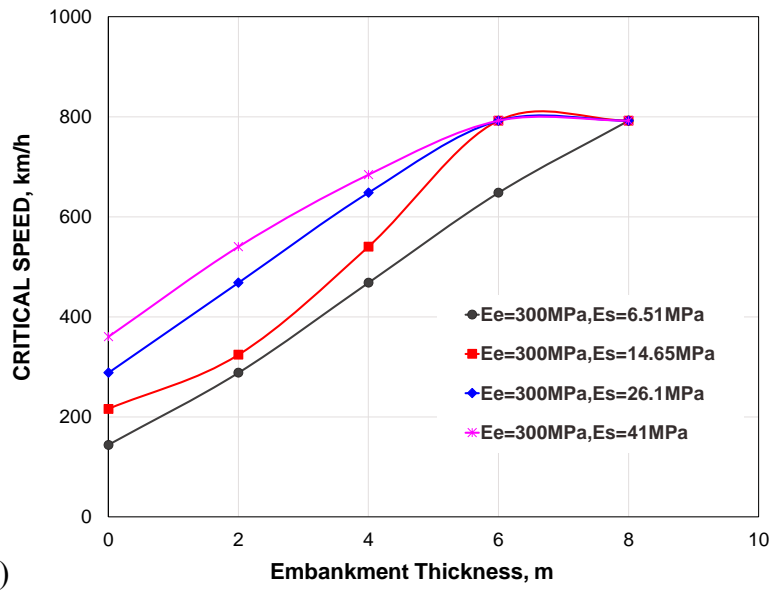
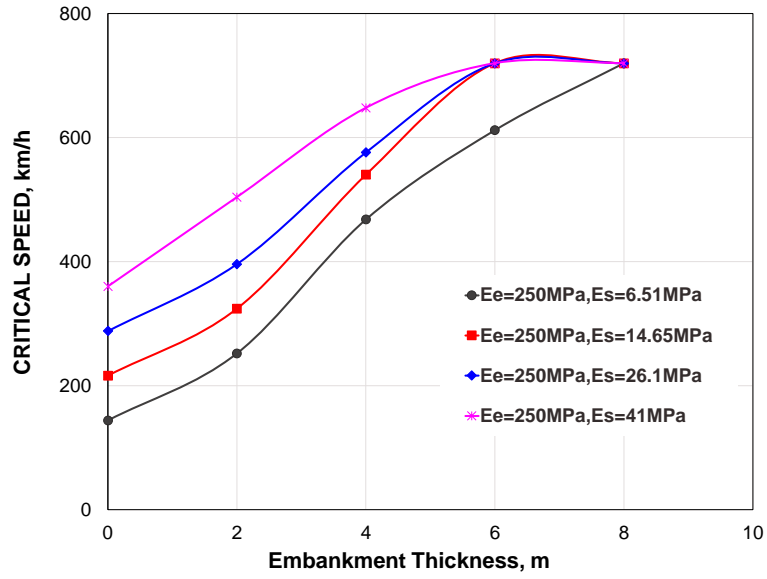


Figure 4.85. Continued

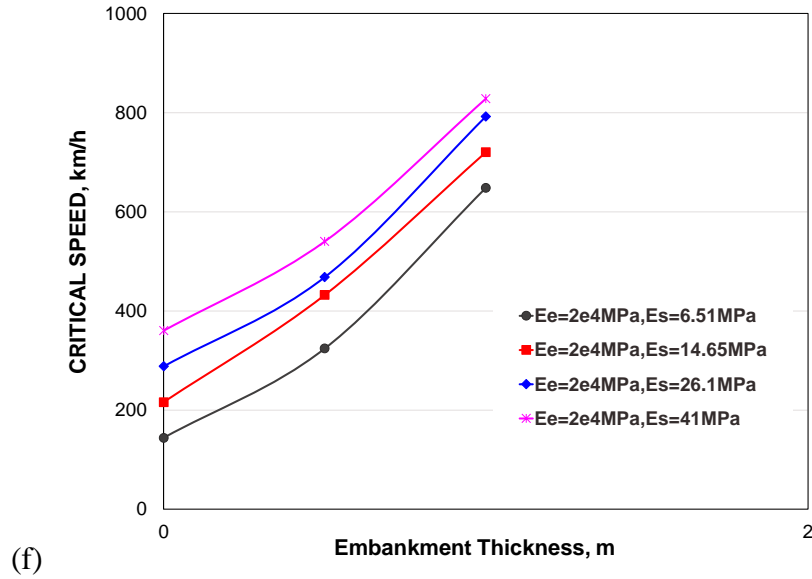


Figure 4.85. Continued

4.8.2 The Threshold Value

In order to have a safe design that avoids dynamic vibration when running HSTs, the threshold values must be defined. The GM number of the system should be limited to the threshold range where the dynamic effect of Rayleigh wave propagation is not noticeable. It was shown earlier how maximum track displacement is a function of train speed (Figure 4.36). Different train speed zones are defined below (and in Figure 4.86):

Zone I: Obviously, track displacement increases significantly as train speeds reach the velocity called the cut-off speed (Madshus and Kaynia 2000). Below the cut-off speed, where GM is less than 0.5 ($V_T \leq 0.5 V_{Req}$), no waves are generated. Above this speed, waves are generated and amplified rapidly as train speed increases. In fact, the track displacement appears to be quasi-static when trains run below the cut-off speed. In the speed zone below

the cut-off speed, the corresponding stress is in static equilibrium with the train load. This speed zone is called Zone I. This speed zone, at which there are no effects of wave propagation and the track displacement is almost equal to the static displacement due to train self-weight, is called the first safe train speed zone.

Zone II: When trains run faster than the cut-off speed ($0.5 V_{Req} < V_T \leq 0.7 V_{Req}$ or $0.5 < GM \leq 0.7$), the dynamic effect can be seen clearly. In Zone II, which is above the cut-off speed, a dynamic displacement associated with Rayleigh wave generation in the HSR system can be seen. Although some dynamic effects of Rayleigh wave propagation can be seen in this zone, this zone will be considered as a safe zone since displacement of the track cannot cause big problems.

Zone III: In the third speed zone, Zone III, the train speed approaches and reaches the critical speed, $0.7 V_{Req} < V_T \leq V_{Req}$. In this zone, the dynamic amplification reaches its maximum; as a result, the maximum track displacement at critical speed can be seen.

Zone IV: Above the critical speed ($V_T > V_{Req}$ or $GM > 1.0$), track displacement decreases as train speed increases; this is defined as Zone IV.

These speed zones are defined based on ranges of GM values. The threshold was defined as the GM value for the track/embankment/ground system for which the train remains in the safe zones (Zones I, II). Therefore, the threshold value for GM can be defined as 0.7 (Madshus et al. 2004, Banimahd 2008, Woodward et al. 2013). There is a controversial discussion about whether we can consider Zone IV as a safe zone. If we want to consider it as a safe zone, we need to define the second threshold value at which there is not a significant sign of dynamic effects of wave.

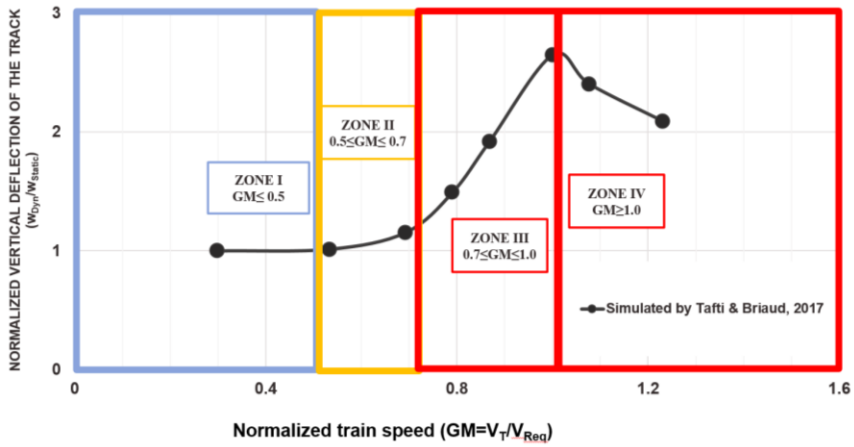


Figure 4.86. Definitions of different speed zones

Conventionally, to decrease the GM, the train speed was reduced in specific areas where the dynamic effect of Rayleigh wave propagation led to unexpected track displacement. However, this method is not acceptable in the long run because being fast is one of the primary goals of running HSTs. Another way to decrease GM is to increase V_{Req} of the track/soil system. The first recommendation to do so is to design a higher and stiffer embankment. As pointed out in this section, shallow embankments do not have a big impact on the Rayleigh wave value of the track/soil system. In this study, we showed how the stiffer and higher embankments can effectively change the Rayleigh wave speed of the whole system. The second effective way to increase the Rayleigh wave speed of the system is to increase the subgrade stiffness and consequently the Rayleigh wave of the subgrade. These design methods will be discussed in more detail in section 4.10. Figure 4.85 depicts the results of the parametric studies in terms of critical speed. However, as mentioned at the beginning of this section, GM is the most suitable parameter that can be

used to define the safe train speed zone. Based on Equation 4.5, to assess the GM, two parameters (train speed and critical speed) should be defined for all 94 cases presented in Table 4.14. Train speed is considered to be a constant value for each HSR line. Based on the literature review given in section 2 (section 2.1), train speed in this study is equal to 396 km/h (110 m/s), which is high enough in compare to the current HSTs operating in existing high-speed lines. The critical speeds for all 94 cases were obtained and presented in section 4.8.1. The proposed guideline charts considering the threshold speed defined in this section are illustrated in Figure 4.87. Also, all the results of parametric studies are summarized in Table 4.13. It should be mentioned that these charts would be applicable if the target train speed is 396 km/h or less. But in case of train speed higher than 396 km/h the general graphs shown in Figure 4.85 would be applicable. It is very simple to generate the guideline charts like the one illustrated in Figure 4.87 whenever the target value for train speed is determined. In final analyses, the proposed charts given in Figure 4.86 in general and 4.87 for specific high-speed lines where the train speed is equal to 396 km/h or less can be used to design safe track/embankment/ground systems whose GM values do not exceed the threshold value.

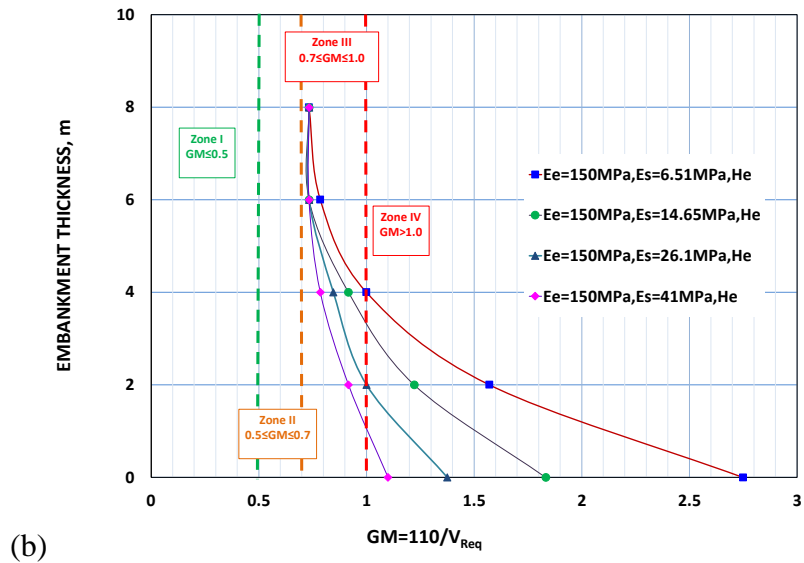
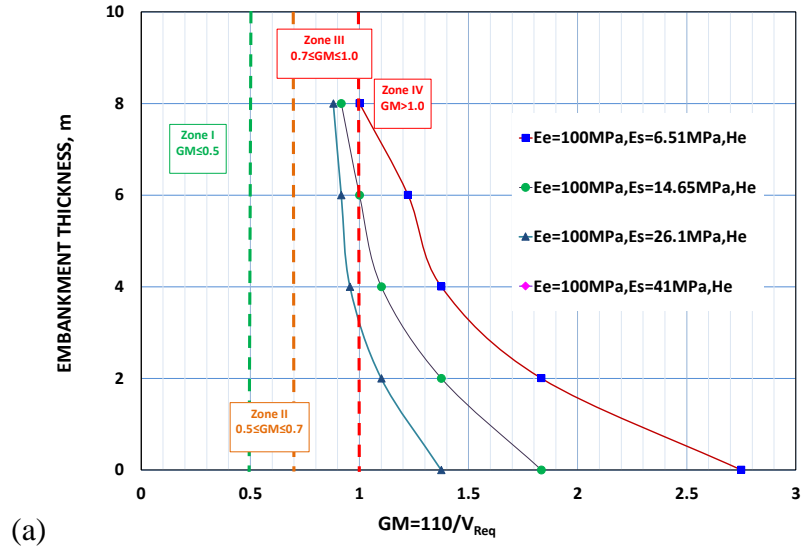
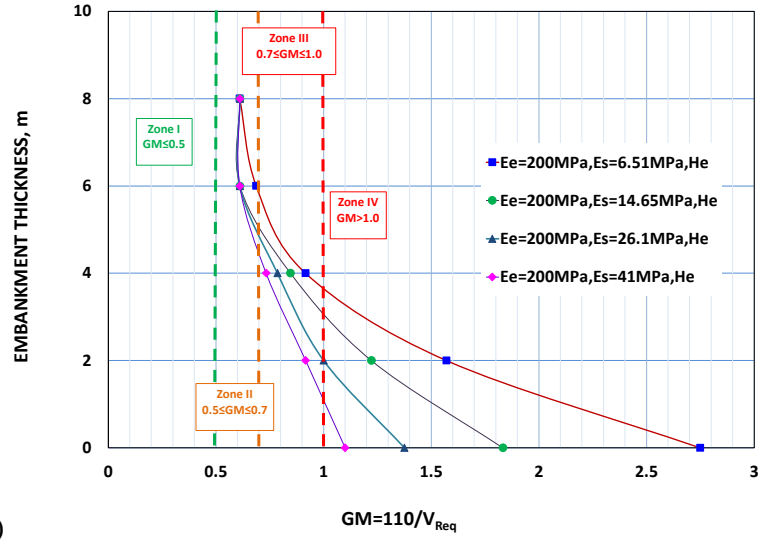
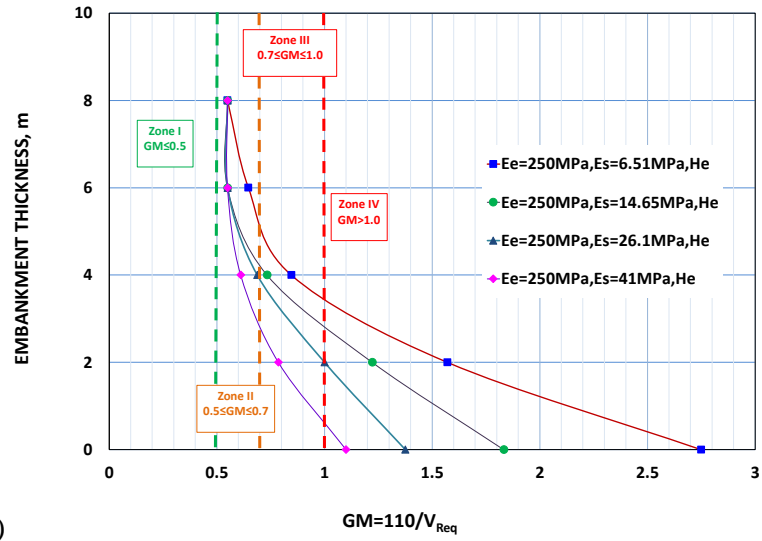


Figure 4.87. Effect of embankment heights (H_e), embankment modulus (E_e) and subgrade modulus (E_s) on the Ground Mach (GM) (a) $E_e=100$ MPa (b) $E_e=150$ MPa, (c) $E_e=200$ MPa, (d) $E_e=250$ MPa, (e) $E_e=300$ MPa, and (f) $E_e=2e4$ MPa (Concrete slab)

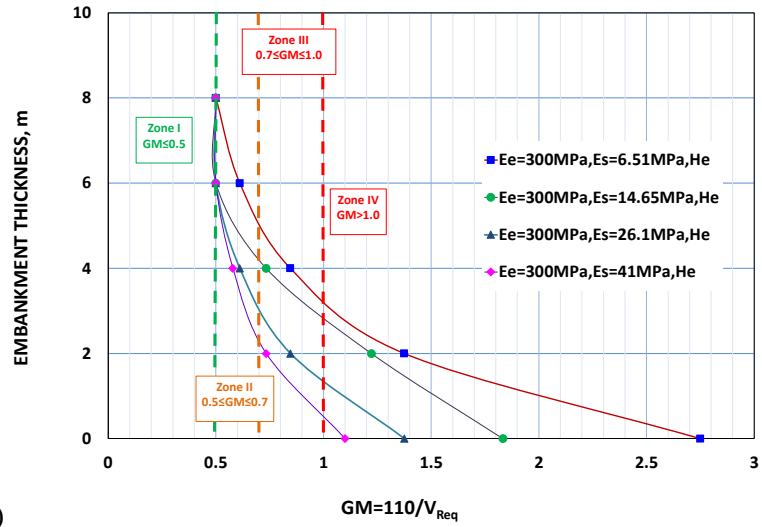


(c)

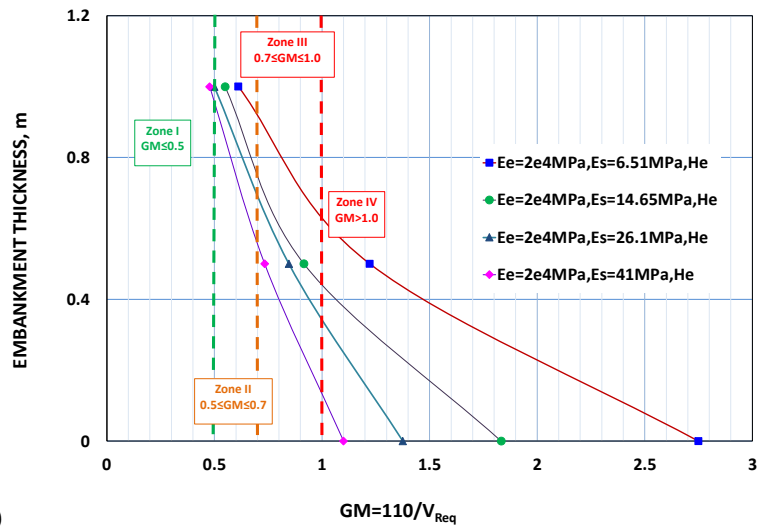


(d)

Figure 4.87. Continued



(e)



(f)

Figure 4.87. Continued

Table 4.14. Summary of the Parametric Studies' Results

Case No	E_s (MPa)	E_c (MPa)	H_c (m)	V_{Req} (km/h)	$GM = \frac{396}{V_{Req}}$	Max. Track Displacement (Δ)(mm)	$GM \leq 0.7$	$\Delta \leq 2mm$
1	6.51	150	2.0	252	1.571	7.54	No	No
2			4.0	396	1	3.34	No	No
3			6.0	504	0.786	2.15	No	No
4			8.0	540	0.733	1.83	No	Yes
5	6.51	200	2.0	252	1.571	6.95	No	No
6			4.0	432	0.917	2.97	No	No
7			6.0	576	0.688	1.82	Yes	Yes
8			8.0	648	0.611	1.45	Yes	Yes
9	6.51	250	2.0	252	1.571	6.27	No	No
10			4.0	468	0.846	2.63	No	No
11			6.0	612	0.647	1.66	Yes	Yes
12			8.0	720	0.55	1.24	Yes	Yes
13	6.51	300	2.0	288	1.375	5.61	No	No
14			4.0	468	0.846	2.48	No	No
15			6.0	648	0.611	1.48	Yes	Yes
16			8.0	792	0.5	1.14	Yes	Yes
17	6.51	2e4 (Concrete)	0.5	324	1.222	6.47	No	No
18			1.0	648	0.611	1.91	Yes	Yes
19	14.65	150	2.0	324	1.222	4.57	No	No
20			4.0	432	0.917	2.32	No	No
21			6.0	540	0.733	1.81	No	Yes
22			8.0	540	0.733	1.58	No	Yes
23	14.65	200	2.0	324	1.222	3.92	No	No
24			4.0	468	0.846	2.13	No	No
25			6.0	648	0.611	1.58	Yes	Yes
26			8.0	648	0.611	1.3	Yes	Yes
27	14.65	250	2.0	324	1.222	3.65	No	No
28			4.0	540	0.733	1.7	No	Yes
29			6.0	720	0.55	1.2	Yes	Yes
30			8.0	720	0.55	1.12	Yes	Yes
31	14.65	300	2.0	324	1.222	3.27	No	No
32			4.0	540	0.733	1.64	No	Yes
33			6.0	792	0.5	1.18	Yes	Yes
34			8.0	792	0.5	1.03	Yes	Yes
35	14.65	2e4 (Concrete)	0.5	432	0.917	3.49	No	No
36			1.0	720	0.55	1.09	Yes	Yes
37	26.1	150	2.0	396	1	3.52	No	No
38			4.0	468	0.846	1.97	No	Yes
39			6.0	540	0.733	1.65	No	Yes
40			8.0	540	0.733	1.52	No	Yes
41	26.1	200	2.0	396	1	3.01	No	No
42			4.0	504	0.786	1.96	No	Yes
43			6.0	648	0.611	1.58	Yes	Yes
44			8.0	648	0.611	1.3	Yes	Yes
45	26.1	250	2.0	396	1	2.74	No	No
46			4.0	576	0.688	1.41	Yes	Yes
47			6.0	720	0.55	1.17	Yes	Yes
48			8.0	720	0.55	1.1	Yes	Yes
49	26.1	300	2.0	468	0.846	2.39	No	No
50			4.0	648	0.611	1.3	Yes	Yes

Table 4.14. Continued

Case No	E _s (MPa)	E _c (MPa)	H _c (m)	V _{Req} (km/h)	GM= 396/V _{Req}	Max. Track Displacement (Δ)(mm)	GM ≤ 0.7	Δ ≤ 2mm
51	26.1	2e4 (Concrete)	6.0	792	0.5	1.07	Yes	Yes
52			8.0	792	0.5	0.98	Yes	Yes
53			0.5	468	0.846	2.324	No	No
54			1.0	792	0.5	0.777	Yes	Yes
55	41.0	150	2.0	432	0.917	2.79	No	No
56			4.0	504	0.786	1.82	No	Yes
57			6.0	540	0.733	1.63	No	Yes
58			8.0	540	0.733	1.51	No	Yes
59	41.0	200	2.0	432	0.917	2.21	No	No
60			4.0	540	0.733	1.33	No	Yes
61			6.0	648	0.611	1.22	Yes	Yes
62			8.0	648	0.611	1.2	Yes	Yes
63	41.0	250	2.0	504	0.786	2.21	No	No
64			4.0	648	0.611	1.29	Yes	Yes
65			6.0	720	0.55	1.13	Yes	Yes
66			8.0	720	0.55	1.11	Yes	Yes
67	41.0	300	2.0	540	0.733	1.95	No	Yes
68			4.0	684	0.579	1.18	Yes	Yes
69			6.0	792	0.5	1.07	Yes	Yes
70			8.0	792	0.5	0.95	Yes	Yes
71	41.0	2e4 (Concrete)	0.5	540	0.733	1.64	No	Yes
72			1.0	828	0.478	0.601	Yes	Yes
73	6.51	-	0.0	144	2.750	20.7	No	No
74	14.65	-	0.0	216	1.833	13.5	No	No
75	26.1	-	0.0	288	1.375	8.58	No	No
76	41	-	0.0	360	1.100	6.32	No	No
77	6.51	100	2.0	216	1.833	10.5	No	No
78			4.0	288	1.375	4.23	No	No
79			6.0	324	1.222	3	No	No
80			8.0	396	1	2.36	No	No
81	14.65	100	2.0	288	1.375	7.75	No	No
82			4.0	360	1.1	3.82	No	No
83			6.0	396	1	2.71	No	No
84			8.0	432	0.917	2.44	No	No
85	26.1	100	2.0	360	1.1	4.53	No	No
86			4.0	414	0.957	3.33	No	No
87			6.0	432	0.917	2.46	No	No
88			8.0	450	0.88	2.243	No	No

It should be mentioned that to have a safe and comfortable ride, the track displacement should be limited to 2 mm. In fact, the track/embankment/subgrade system should be designed such that both critical speed and track displacement should be limited to the threshold values specified in the codes (for example: EURO code, SNCF, Chinese

Railway practice and so on). Based on these guideline charts, a design procedure was proposed which will be discussed in the next section.

4.9 Proposed Design Procedure

The design of the track/embankment/subgrade system has been mainly based on empirical or semi-empirical methods. It should be noted that most of the guidelines followed for track/embankment/ground design did not consider the effect of train speed as an influential factor in their design procedures. The American Railway Engineering Association (AREMA 1996) proposed several empirical equations to estimate the suitable track bed depth so that the allowable bearing capacity of the subgrade and vertical stress applied on the ballast should be considered. However, these oversimplified equations did not reflect the repeated dynamic loading, train speed, traffic types, varying subgrade conditions and so on. Table 4.15 shows a comparison of different codes and available track design procedures (Burrow et al. 2007). Banimahd (2008) proposed another design procedure reflecting the effect of train speed. In his research, 70% of the track critical speed was treated as the speed limit. In case the train speed is required to exceed the speed limit, the subgrade should be improved (Banimahd 2008, NR Code 039). Figure 4.88 shows the proposed design procedure by Banimahd (2008). This design procedure was proposed to fulfill two main goals including decreasing both the deterioration of the subgrade and the level of the maintenance required for ballast.

Table 4.15. Comparison of Different Codes and Design Procedures (Banimahd 2008)

Factors	Li and Selig (1998a and b)	UIC¹ 719 R	British Rail	NR² code 039	WJRC³
Static axle load	Via GEOTRACK ⁴	Yes	From an elastic model	No-but 25.4 T axle load limit on UK network	No
Sleeper type, length, and spacing	Via GEOTRACK	Yes	No difference in stress found for sleeper spacings of 630-790 mm	No	No
Rail section	Via GEOTRACK	No	No	No	No
Train speed	By using DAF (Dynamic Amplification Factor)	Yes	No	Via minimum requirement for the dynamic sleeper support stiffness	Crude variation, Shinkansen has greater depth than commuter lines
Annual tonnage	Yes	Yes	Could be incorporated using DAF	No	For commuter lines only
Cumulative tonnage	From annual tonnage multiplied by the design life	No	No	No	No
Subgrade condition	Charts are provided for different subgrade type in terms of the resilient modulus and soil strength	Yes	Using a threshold stress for the material in question		Bearing capacity of subgrade assumed to be 288 kPa otherwise ground improvement must be carried out

¹The International Union for Railways (1994)

²The Network Rail code of practice (2005)

³West Japan Railway Standards (WJRC, 2002a and b)

⁴use of computer model developed by Chang et al. (1980) including an analytical approach and employed a static multi layered elastic model (Li and Selig 1998a and b)

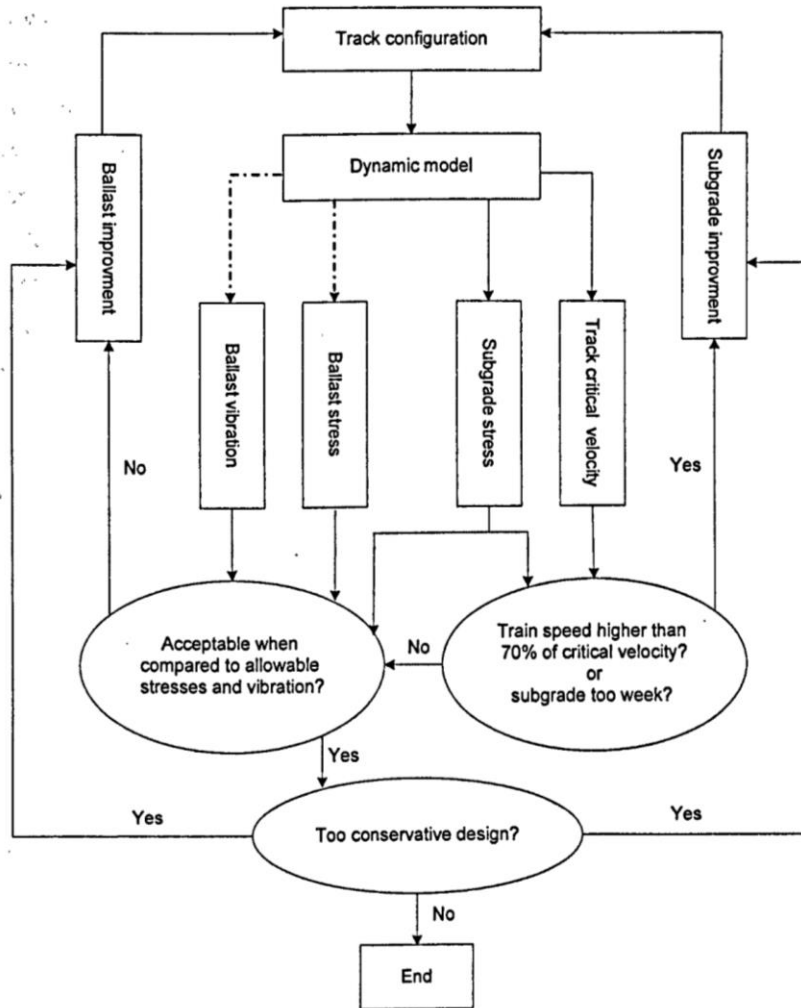


Figure 4.88. Proposed design procedure of HSR track based on the 3-D FEM (Banimahd 2008)

The current proposed design procedure considers two main criteria: to limit both train speed and maximum track displacement. The results obtained from the 4-D FEMs were used to propose this design procedure. This recommended procedure includes two main steps (Figure 4.89) for designing HSR track/embankment/ground systems, which will be described here in more depth:

Step 1. Define the GM number of the subgrade soil: As mentioned earlier in this section, with no embankment or shallow embankment (height of embankment less than 1 m), the critical speed of the track/soil system (V_C) is very close to the Rayleigh wave speed of the subgrade ($V_{R(s)}$). As a result, initially it can be assumed that the only elements required to assess the Rayleigh wave speed of the track/soil system are the subgrade soil data, specifically the Young modulus (E_s), the Poisson ratio (ν_s), and the soil density (ρ_s). The Rayleigh wave speed of the subgrade soil can be evaluated with Equation (4.8).

In order to assess the GM number, two pieces of information are needed (Equation 4.5). In addition to the critical speed, which is related to the soil parameters, the train speed (V_T) is also required.

Step 2. Define speed zone based on threshold value: The threshold values to limit train speed and reduce maximum track displacement were defined in section 4.8.2. Two limits are necessary to be checked: The GM value obtained from step one should not exceed 0.7 and track vertical displacement should not be greater than 2.0 mm. In case, either of these criteria are not satisfied, the embankment design is required in order to increase the critical speed (decrease the GM value) and/or decrease the maximum track displacement. To choose suitable values for parameters including embankment height, embankment modulus, and subgrade modulus, the proposed guideline charts presented in section 4.8 can be applied. In fact, these charts help engineers to select the target values for these design parameters. Then, selecting a proper design technique will be essential to achieving these target values for design parameters. These design methods will be discussed in more detail in the subsequent section.

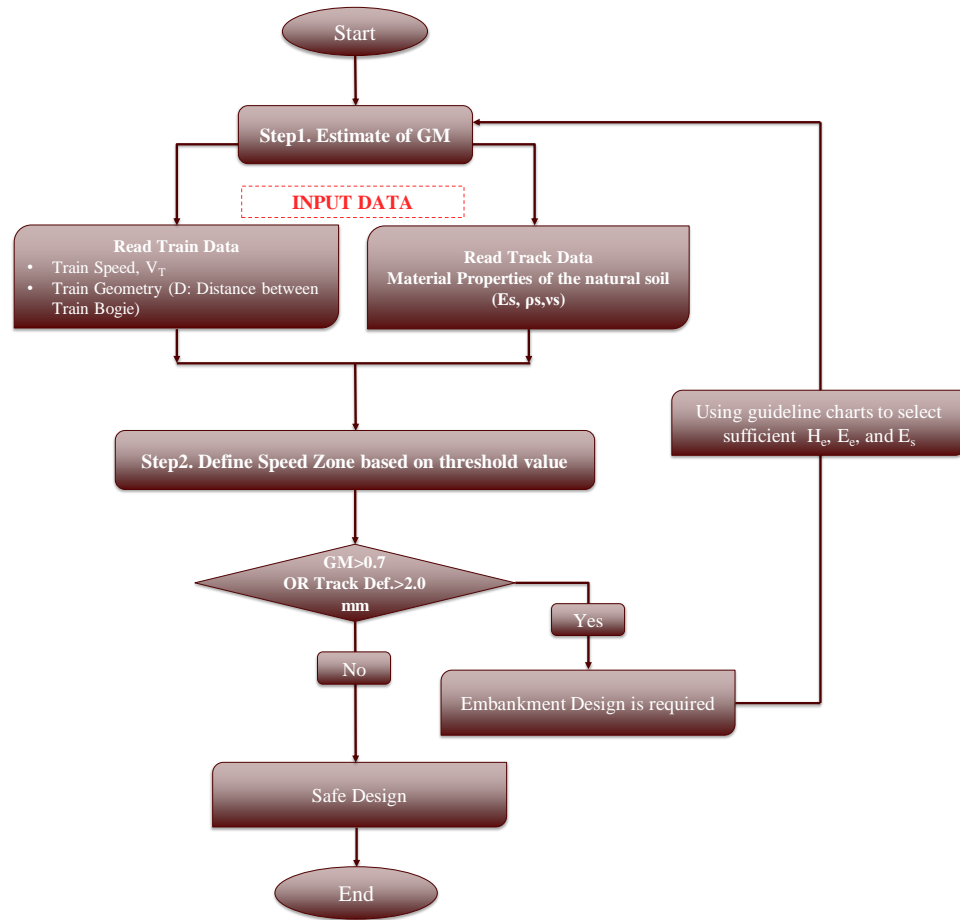


Figure 4.89. Flowcharts of design procedure

4.10 Design Solutions

The main objective of different design strategies is to protect the soil layer from degradation due to the high level of vibration induced by HSTs. Either a new HSR line, which has no possibility to avoid crossing over soft areas on a conventional track structure without the critical speed being exceeded, or an existing line which has a very low critical speed, are required to apply an effective design method to increase the critical speed of

the track/embankment/ground system (Woldringh and New 1999, Madshus and Kaynia 2001, Madshus et al. 2004, Woodward et al. 2012). The proper solution to this problem must increase the critical speed of the track/embankment/ground system to at least 1.5 to 1.7 times greater than the operational train speed or $GM < 0.6$ to 0.7 (Woldringh and New 1999, Banimahd 2008). Almost all design methods solve the problem of breaking the Rayleigh wave barrier by either strengthening the soft ground under the embankment or stiffening the embankment (Madshus and Kaynia 2001, Madshus et al. 2004, Hendry 2007, Banimahd 2008).

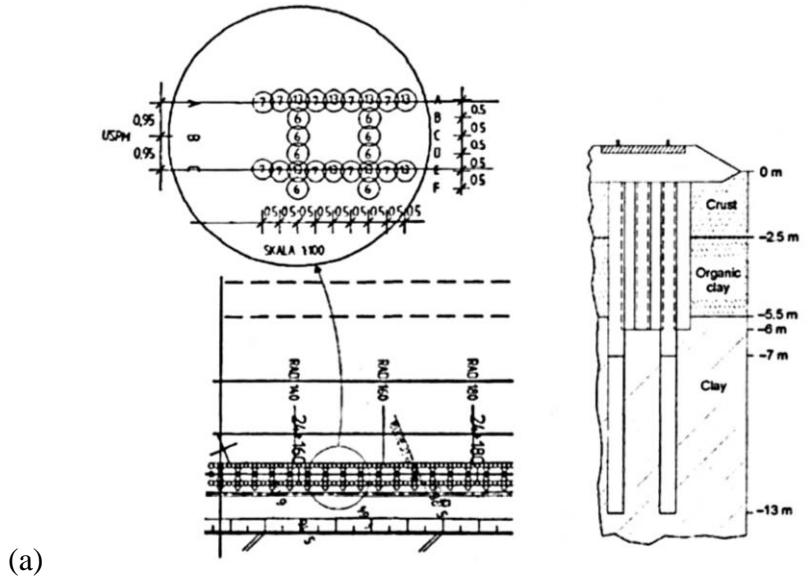
4.10.1 Strengthening of the Ground Techniques

Improving soil underneath of the embankments can be easily achieved as part of the foundation work for new lines, but it is not easy to apply as a retrofitting method under existing lines (Madshus et al. 2004). The following techniques can be used to strengthen the ground:

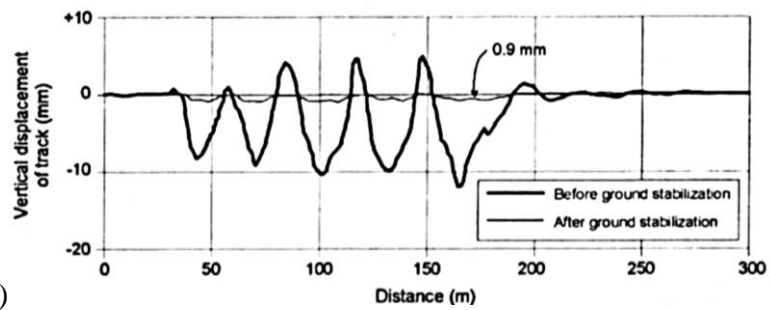
- Use of lime-cement piles (Carlsten and Extrom 1997, Halkola 1999, Madshus and Kaynia 2001, Smekal and Berggren 2002 Madshus et al. 2004)
- Jet-piles (Bell 1993, Burke 2000, Sonderman and Toth 2000, Madshus et al 2004)
- Dip-mix methods (Terashi 1997, Holm et al. 2002, Madshus et al. 2004)
- Using geotextile (Woldringh and New 1999)

- Horizontal confinement of the foundation material in the case of deep foundation ($H_s \geq 10\text{m}$)

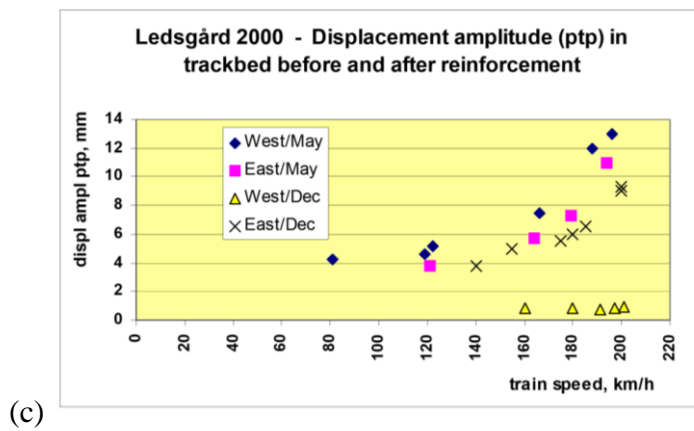
In Sweden at the Ledsgard site, lime-cement piles for ground improvement were used to modify the critical speed. For this site, with soft soil underneath a shallow embankment, the ground was improved by lime-cement piles with diameter of 600 mm, 6 to 13 m deep installed in a ladder-grid (Smekal and Berggren 2002, Madshus et al. 2004) (Figure 4.90 (a)). The measured vertical track displacement before and after ground improvement is shown in Figure 4.90 (b). This method was very effective at increasing the Rayleigh wave speed of the ground; on the other hand, this is not an applicable method for this existing line because added weight could result in excessive settlement or a bearing capacity problem (Madshus et al. 2004). As can be seen in Figure 4.90 (c), ground improvement reduced the high level of vibration experienced by the track and soil under the track. This project took three months to complete (May to July 2000). By means of a dry dip mixed method (DMM) the track displacement was reduced by a factor of approximately 5 at lower train speeds (quasi-static zone) and 15 at higher train speeds (dynamic zone). The total cost for this project was estimated at about 5.1 million Swedish Krona (SEK) (about 0.56 million USD). The cost distribution for this project including the cost for dry DMM (dip mixing method) and soil improvement is shown in Figure 4.91, which reveals that the cost of this soil improvement method is a minor part of the total cost (Holm et al. 2002).



(a)



(b)



(c)

Figure 4.90. (a) lime-cement column method for soil stabilization, (b) measured track displacement before and after soil improvement at train speed between 190 and 200 km/h (Madshus et al. 2004), (c) peak-to-peak track displacement before (May) and after (December)

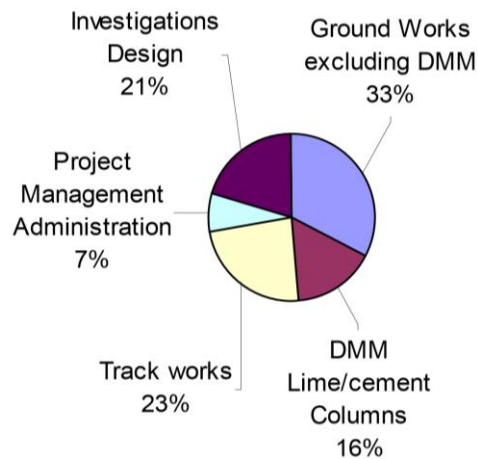


Figure 4.91. Cost distribution of countermeasure (Holm et al. 2002)

4.10.2 Stiffening of the Embankment Techniques

The following techniques can be used to increase the stiffness of the embankment:

- Inserting a concrete slab under the embankment (Madshus and Kaynia 2001)
- Replacing the embankment with a concrete box girder (Madshus and Kaynia 2001)
- Ensuring that the embankment has a good quality of fill (sand) with a minimum embankment thickness of 5 m ($H_e \geq 5$ m) (Rehfield 1994)
- Using slab tracks (Hillig 1996, De Nie 1948, 1949a and b)
- To avoid soft foundation, using track beds supported on piled concrete foundation or low viaducts, which is really expensive but is a well-understood and risk-free method

- Application of in-situ polyurethane polymers, termed XiTRACK in the UK (Woodward et al. 2012)
- Application of geogrid (Hendry 2007)

The effectiveness of the two methods (installing concrete slab under the embankment and installing a concrete box girder) used for embankment stiffening were simulated and presented in Figure 4.92 (Madshus and Kaynia 2001). In this figure, these two design approaches were compared to the lime-cement approach used for soil improvement. This figure reveals that using embankment stiffening methods leads to higher track/embankment/ground stiffness, resulting in lower track displacement and higher critical speed. The results of this simulation showed that using a 0.4 m thick concrete slab under the embankment (medium stiffness $EI=800$ MN) and a 1.2 m high concrete box girder (high stiffness $EI=4000$ MN) decreased the dynamic displacement of the track by about 25% and 50%, respectively, at a train speed of 108 km/h; while at 216 km/h, track displacement was reduced by 40% for a medium stiffness embankment and 75% for a high stiffness embankment (Madshus and Kaynia 2001).

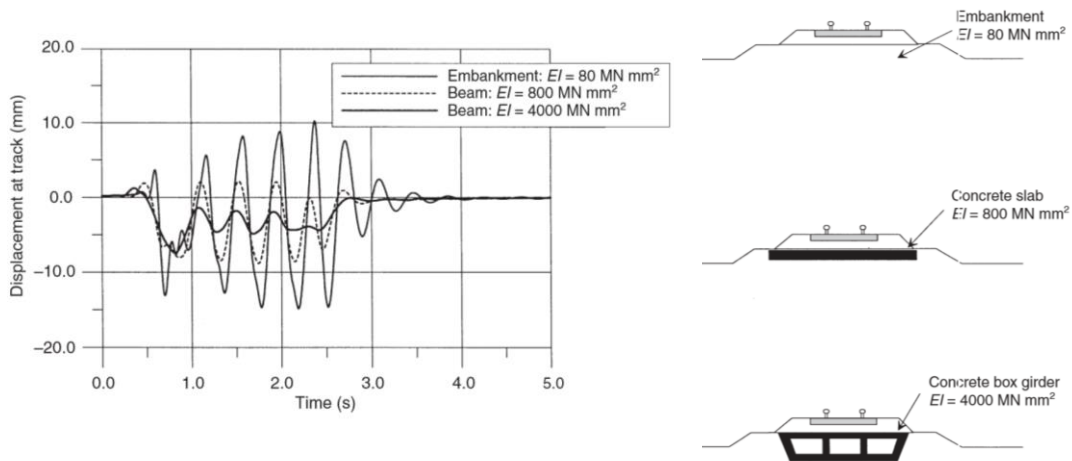


Figure 4.92. Simulated effect of countermeasures (Kaynia et al. 2001)

Another method used to increase ballast stiffness and strength is the application of polymer XiTRACK to the ballast surface, as shown in Figure 4.93 (Woodward et al. 2012). Woodward et al. (2012) believe that improving the ballast stiffness could reduce the ballast vibration effects, which would greatly decrease the frequency of track maintenance required. This method (3D polymer reinforcement of the track ballast) can be effectively applied to strengthen the ballast and consequently increase the track/ground system stiffness.

(a)



(b)

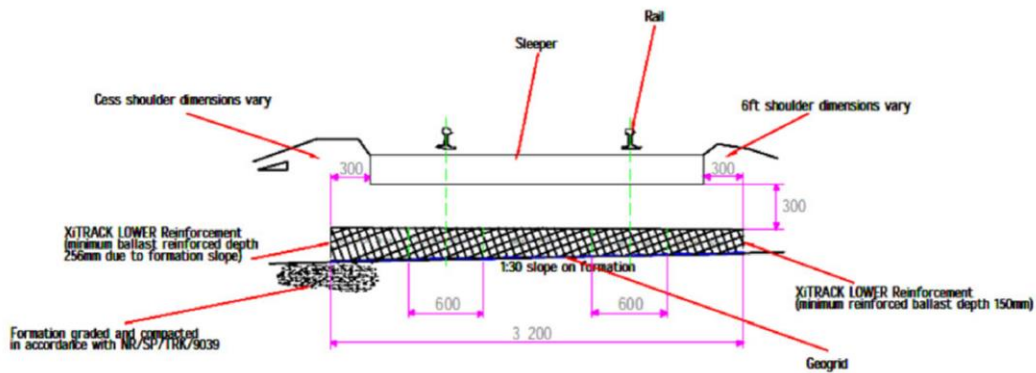


Figure 4.93. (a) Application of the polymer XiTRACK to the ballast surface, (b) schematic cross-sectional view of the XiTRACK polyurethane reinforcement used at Manningtree North Junction UK (Woodward et al. 2012)

Predicted critical speeds for different methods used to enhance the HSR embankment dynamic performance are given in Table 4.16. These results were obtained from full-scale tests on 5 embankments with 80-120 m lengths and 1-5 m heights (Woldring and New 1999). Code HW1 (HW stands for Hoeksche Waard, the name of the polder where the test site was located) to HW5 are the codes used for different test case studies. As with Table 4.16, the continuous support provided to the embankment by the FMI wall (HW3) foundation is the most effective method among all others. A mixture

of these three methods, which means a wall-type linear foundation under the granular embankment reinforced with geotextile with a continuous form of concrete slab rail support, can be a proper method to increase the critical speed and reduce the dynamic effect of running HSTs. Woldringh and New (1999) believed that this method can be more cost-effective compared to the conventional concrete piled slab or low viaduct solutions.

Table 4.16. Predicted Critical Speed of Embankment/Subsoil System (Woldringh and New 1999)

Embankment	Code	Critical velocity km/h
Reference (example)	Case A	206
Anhydrite-cement mixed columns,	HW2	440
FMI 'walls',	HW3	500
Sand filled geotextile columns,	HW4	360

4.11 Conclusions and Recommendations

As pointed out in this section, results from instrumented tests performed on HSR on soft soil at different sites and associated numerical analyses indicate that a large dynamic amplification appears in the vertical dynamic movement as train speed approaches the threshold speed. This threshold speed is called the critical speed and is known as Ground Mach 1.0 (GM 1.0). The critical speed is almost equal to the Rayleigh wave speed of the ground if the track is constructed on top of very shallow and soft embankment. However, through parametric study, it is shown that the critical speed is not exactly equal to the subgrade Rayleigh wave speed when a deep and stiff embankment is

designed under the HSR tracks. This Rayleigh wave speed is called the equivalent Rayleigh wave speed of the rail/embankment/ground systems. In this research, the numerical simulations, calibrated to the measurements from a soft soil site in Sweden (Adolfsson 1999) and full-scale test in China (Bian et al. 2014), showed that the maximum displacement of the rail occurs at the critical speed and is about three times larger than the static displacement when track is modeled on top of a very shallow embankment and very soft ground. This displacement raises concerns about high maintenance cost, uncomfortable rides, and possible derailment. Different thresholds to maintain safety were defined in this section. Using the threshold values for GM and maximum track displacement, safer embankments can be designed. In the case that GM is higher than 0.7 – the zone in which the dynamic effect of Rayleigh wave propagation becomes worse – the conclusion is that GM should decrease. Conventionally, to decrease the GM, the train speed is reduced in specific areas where the dynamic effect of Rayleigh wave propagation leads to unexpected track displacement. However, this method is not optimal because being fast is one of the primary goals of running HSTs. The second way to decrease GM is to increase V_R or V_{Req} of the track/soil system. The first recommendation is to design a higher and stiffer embankment. As pointed out in this section, a lower embankment does not have a big impact on the Rayleigh wave value of the track/soil system. Within this project, a parametric study was performed to determine sufficient height and stiffness of embankments to raise the equivalent Rayleigh wave of the track/soil system above the top speed of the train to avoid the maximum track displacement that occurs near the critical speed. Indeed, one mitigation strategy is to put a higher and stiffer embankment on top of the subgrade. This stiffens the whole track/embankment/soil system, which increases the

equivalent Rayleigh Wave speed of the whole system. In this study, the outcome of the parametric study showed that the stiffer and higher embankment can effectively increase the Rayleigh wave speed of the whole system. Another recommendation to avoid the resonance effect on the soil is to stiffen the ground. This study showed how these two remedies can lead to safer designs of HSRs. The results of an extensive parametric study were presented in the form of guideline charts, which will give railroad designers a way to choose the height and stiffness of the embankment given a natural soil stiffness to prevent any resonance effect on the track/embankment/soil system. A design procedure was proposed to help railway engineers have a clearer view of how they can apply the guideline charts to have safer design.

5 BUMPS IN HIGH-SPEED RAILS

5.1 Introduction

There are different sources resulting in various types of track irregularities including non-homogenous properties of the ballast and subgrade soil, rail defects, joints, welds, and transition zones near bridges and tunnels (Banimahd 2008).

The transition zone between compacted soil embankments and bridge abutments resting on deep foundations is a major source of track bumps. This irregularity is due to the difference in stiffness between the two rolling surfaces (Davis and Plotkin 2009) that leads to a dynamic oscillation of the train wheels and to a cyclic variation of the contact force between the wheels and the rail. This dynamic effect can result in accelerating deterioration of the track near bridges. Indeed, a track modulus differential alone—without bump modeling—at a location near a bridge increases the impact force. The problem of bumps at bridges due to this transition is not only a major concern of the railway industry (Davis et al. 2003, Davis and Li 2006, Li et al. 2003, Li and Davis 2005, Plotkin et al. 2006), but the highway sector has a similar problem (Wahls 1990, Stark et al. 1995, Briaud et al. 1997, Long et al. 1998, Seo et al. 2002, Dupont and Allen 2002, Seo 2005).

These additional forces acting on train-track interface result in the formation of a bump or dip in the track. This dynamic effect becomes more intense as these irregularities, bump or dip, present in the track profile (Plotkin et al. 2006, Banimahd 2008, Nicks 2009, Davis and Plotkin 2009). The dynamic loads caused by increased differential settlement, bumps or dips, can increase to approximately 1.5 to 3 times the static load (Davis et al.

2003). In addition, an HST can intensify the impact loads due to the higher train speeds (Banimahd 2008, Nicks 2009).

The problem of irregularity along railway tracks is a concern for both freight and public transportation. The main problem associated with freight tracks is the maintenance cost to repair the irregularities generated along the railway lines due to high impact load, especially at the transition zones. On the other hand, for public transportation, the main concern is the train body acceleration, which can affect the quality of the ride.

In the present chapter, the train/track interaction problem, especially at either end of bridge transition zones, will be addressed. Different parameters such as train speed, Type of irregularity, a wide range of bump sizes, and subgrade modulus will be explored. All of these parameters play important roles in defining tolerable irregularity bump size, which will be investigated through an extensive parametric study. A well-developed 4-D FEM is used. This model includes a verified coupled train/track/soil model to investigate the problem of different types of irregularity along HSRs. The problem of stiffness transition between track on top of embankment and a track on top of bridge abutment (non-faulted track) will be discussed, in addition to the presence of various types of irregularities along HSRs (faulted tracks). To assess the allowable irregularity size, two criteria will be considered: the allowable or tolerable wheel/rail force and train body acceleration. The tolerable values for these criteria are defined in order to give passengers a safe and comfortable ride and decrease the cost and frequency of maintenance. The final results will be presented in the form of applicable guideline charts.

5.2 Causes Involved in Development of the Irregularities

Different types of irregularities are generated as a result of a repeated process. This process starts with differential settlement in the transition zone due to difference in stiffness between the compacted soil embankment and the bridge that typically rests on deep foundations. This differential settlement causes irregularity in general to increase, which can lead to increased interaction force between wheel and rail. This high impact force will accelerate track degradation, leading to a larger irregularity size. Figure 5.1 illustrates different factors causing irregularity initiation and extension. The most important factors contributing to irregularity development include different track moduli at transition zones, quality of approach fill, impact load, ballast material, drainage, damping abutment type, bridge joint, traffic conditions, and quality of construction (Nicks 2009).

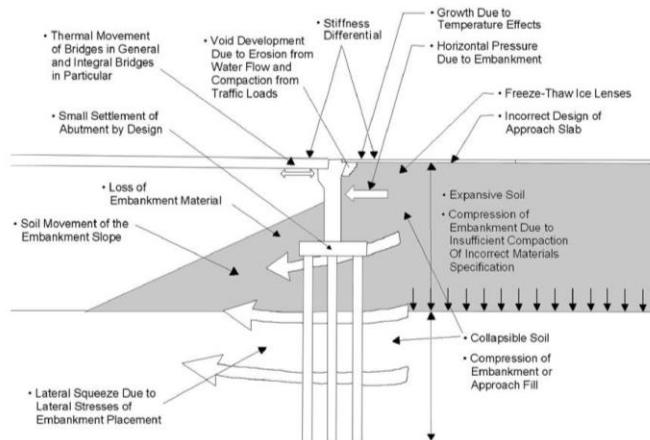


Figure 5.1. Different aspects contributing to irregularity formation along highway or railway lines (Briaud et al. 1997)

5.2.1 Differential Modulus

Among all these factors, the most common and influential factor contributing to irregularity generation is the abrupt change in the vertical track stiffness between the approach embankment with low track modulus and the bridge on top of an almost rigid base (Davis and Plotkin 2009, Read et al. 1994, Ebersohn and Selig. 1994). It was mentioned earlier in section 3 that the vertical stiffness plays an important role in track settlement; therefore, the abrupt change in the vertical track stiffness results in differential settlement or irregularities. The track modulus value for the stiff bridges can be twice as big as the track modulus for the approaching compacted embankment (Plotkin et al. 2006). Several studies (Plotkin et al. 2006, Davis and Plotkin 2009, Banimahd 2008, Nicks 2009, Briaud et al. 2017) have shown that the stiffness differential does not have a significant effect on the dynamic impact load by itself; however, the differential settlement developed because of modulus differential will eventually result in amplifying the interaction force between wheel and rail at transitions near bridges. This may be correct in cases of regular trains travelling at lower speed. However, Banimahd (2008) showed that even when there is no irregularity along the railway, with only modulus differential at higher train speeds (for example $V_T=252$ km/h) there are considerable dynamic impact loads (Figure 5.2). As with Figure 5.2., at higher train speeds, the differential moduli can have a greater impact on the interaction force between wheel and rail. Although these impact loads or interaction forces between rail and wheel do not exceed the allowable value, compared to low speeds, impact load generated due to high speeds causes rapid track deterioration. The strong

effect of differential modulus on the impact dynamic load will be addressed later in this chapter.

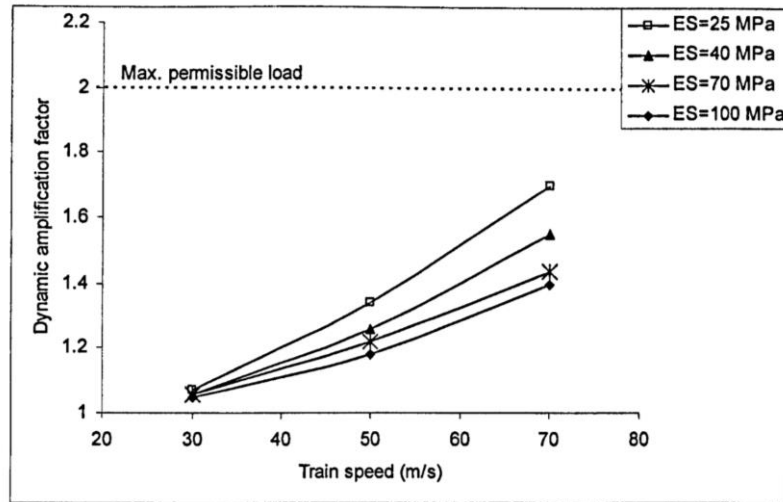


Figure 5.2. Dynamic amplification factor of wheel/rail interaction force at different train speeds (VT=108, 180, 252 km/h) for different subgrade conditions (Es= 25 to 100 MPa) (Banimahd 2008)

The main concern, however, regarding differential modulus is the resulting differential settlement. as mentioned earlier, this differential settlement leads to increased differential settlement at the transition zone, which results in amplifying the interaction force between rail and wheel (Davis et al. 2003, Banimahd 2008, Nicks 2009) (Figure 5.3). Figure 5.3 shows that as the approaching embankment becomes stiffer, less differential settlement is developed. Davis et al. (2003) showed that this differential settlement can cause a dynamic impact load 1.5 to 3 times bigger than the static load. This high impact load will speed up track degradation and cause even more settlement.

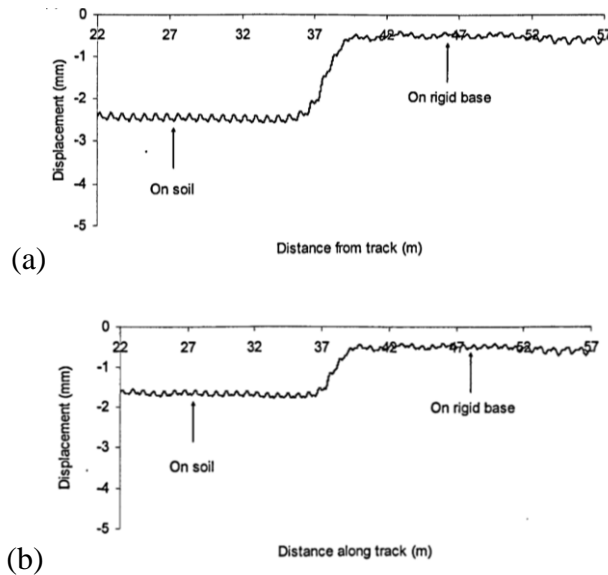


Figure 5.3. Track displacement with non-faulted transition at a train speed of 252 km/h for (a) $E_s=40$ MPa (b) $E_s=100$ MPa (Banimahd 2008)

5.2.2 Quality of Approach Fill or Subgrade

The second parameter that has a strong impact on the degradation of the approach embankment geometry is the quality of the approach fill and subgrade materials. Poor quality material (low subgrade modulus) can cause differential settlement. Using rock, gravel, and sand deposits (with higher modulus) can effectively decrease the long-term settlement effects experienced by the approach embankment because these materials fully compress immediately after loads are applied (Briaud et al. 1997, Li et al. 2003). On the other hand, highly compressible clays or silts are considered as unfavorable materials for fill at transition zones near the bridges (Li et al. 2003). Because clayey soils are very

sensitive to changes in water level (section 3), when they are the only choice for fill material, well-designed drainage must be ensured.

5.2.3 Wheel/Rail Interaction Force

The interaction force between wheel and rail is considered as the one effective cause of irregularity generation, and it becomes more severe as the irregularity size increases. This force results from any wheel or rail defect. In other words, if there is a smooth interface between wheel and rail, the dynamic loads will not increase (Frederick and Round 1985). Nevertheless, most of the time this is not the case. As a result of differential modulus and differential settlement, impact loads occur.

5.3 Different Types of Irregularities

Different types of irregularities along railway lines can be classified as track geometry degradation problems (Banimahd 2008, Nicks 2009). Figure 5.4 depicts two typical forms of irregularities (bump and dip) that occur at transition zones near the bridges at the interface between the approach compacted embankment and the bridge structure. Nicks (2009) used this definition of irregularities in her work. Approaching the bridge, compacted embankments are made of compressible fill material (with low soil modulus)

while the bridges are constructed on top of a deep foundation (an almost rigid base). Due to this differential modulus, under the same loading (train body load), the approach embankment will settle more than the bridge structure (Figure 5.3). As a result of this differential settlement, a bump will form. In addition, dips form because of localized settlement on the approach embankment (Nicks 2009). As any type of irregularity (bump or dip) develops along the railway track, the impact force will increase as mentioned in section 5.1.1. This leads to more degradation and, consequently, bigger irregularity formation.

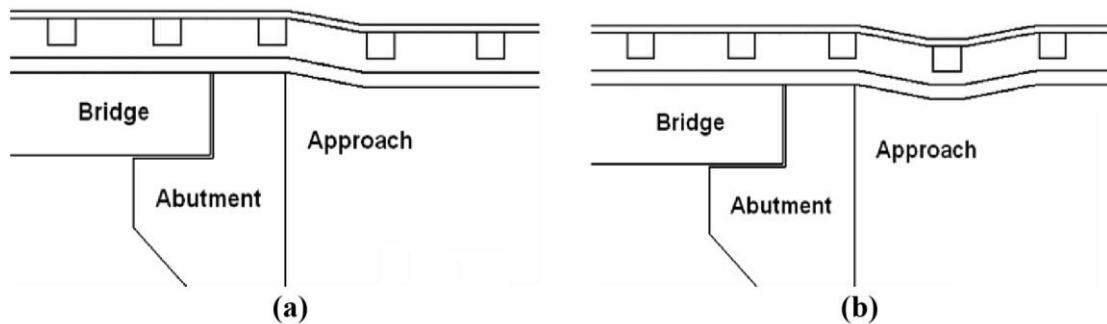


Figure 5.4. Schematic view of different types of irregularities: (a) a bump, (b) a dip at the transition zone near bridges (Nicks 2009)

To define types of irregularity and irregularity sizes, the track differential settlement, for example, occurring near the bridges at transition zones must be evaluated. Figure 5.5 illustrates the results of an investigation conducted by Hunt (1997). In this investigation, a single force was applied to the track at different positions along the track and corresponding deflections were predicted. In this study, the bending stiffness of the

beam was held constant while the track modulus was linearly changed across the 2-meter transition zone. As mentioned before, repeating this process causes the differential settlement to increase, as shown in Figure 5.6 (Hunt 1997).

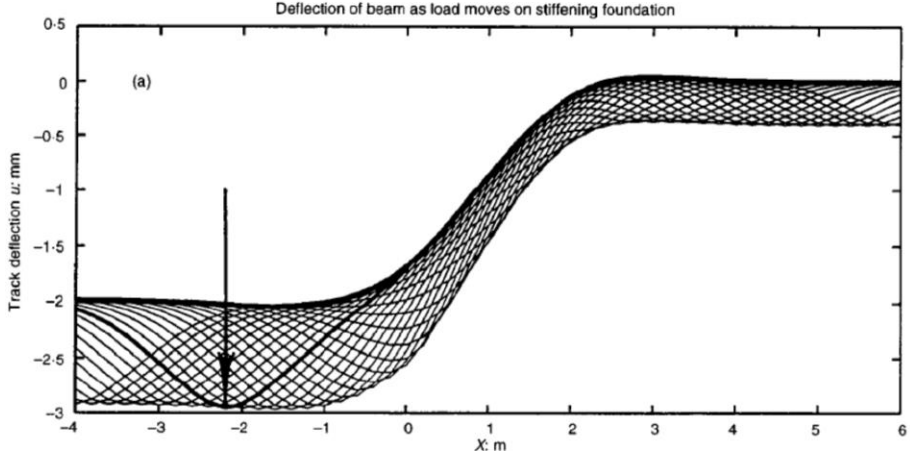


Figure 5.5. Static beam deflection as loads move along the track with variable track modulus (Hunt 1997)

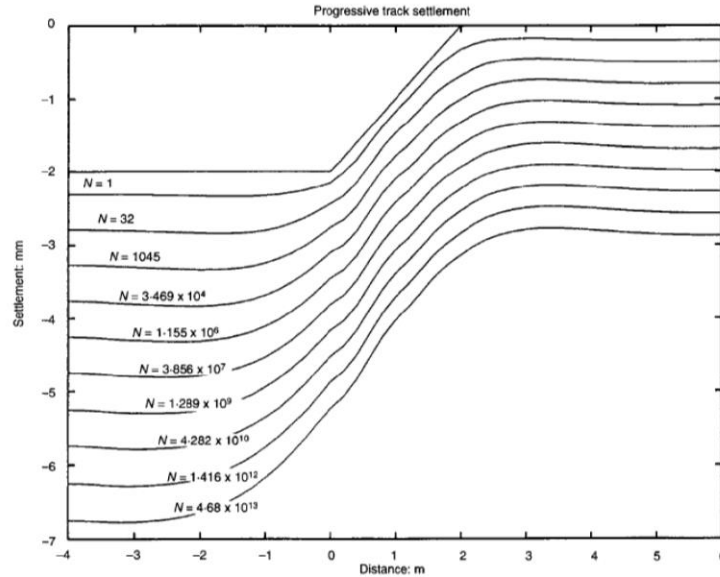


Figure 5.6. Differential settlement along the track at the transition zone for different numbers of load cycles (Hunt 1997)

Banimahd and Woodward (2007) and Banimahd (2008) estimated the track deflection at the transition zone without any irregularity modeling (see Figure 5.3). The results agreed with the outcome obtained from the Hunt (1997) study. In general, the track deflection with larger amplitude started to decrease almost linearly on the soft side (compacted embankment fills with low soil modulus) of the transition zone up to the stiff side (bridge) where the minimum track deflection can be seen. This profile can be used to define the irregularity type called bump. The deflection profile at the transition zone can be quantified by two variables: transition (bump) length (L) and differential deflection (h) (Figure 5.7). Banimahd used a transition curve from the soft to the stiff base. To model the transition curve bump from the soft soil to the rigid base of a bridge, the following equations were used (Schooleman, 1996):

$$\begin{cases} z(y) = R_{vert} \left(1 - \sin \left(\arccos \left(\frac{y}{R_{vert}} \right) \right) \right) & y \leq \frac{L}{2} \\ z(y) = \frac{L^2}{4R_{vert}} - R_{vert} \left(1 - \sin \left(\arccos \left(\frac{L-y}{R_{vert}} \right) \right) \right) & y > \frac{L}{2} \end{cases} \quad (5.1)$$

where y is the distance along the track in the transition zone, L is the deflection spanning length (Figure 5.8), and R_{vert} is the vertical radius which is calculated from the following equation:

$$R_{vert} = \frac{L^2}{4\Delta h} \quad (5.2)$$

where Δh is the deflection difference between the track on the soft soil and the bridge (Figure 5.8).

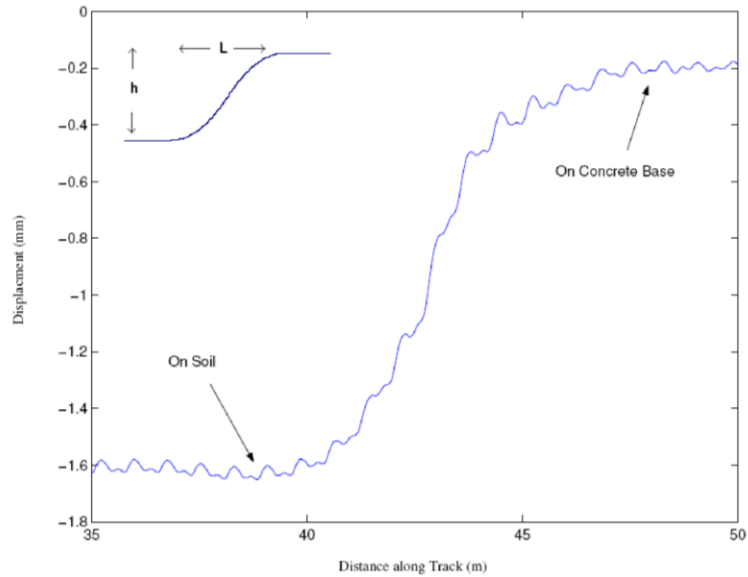


Figure 5.7. Differential rail deflection at the transition zone under moving load (Banimahd and Woodward 2007)

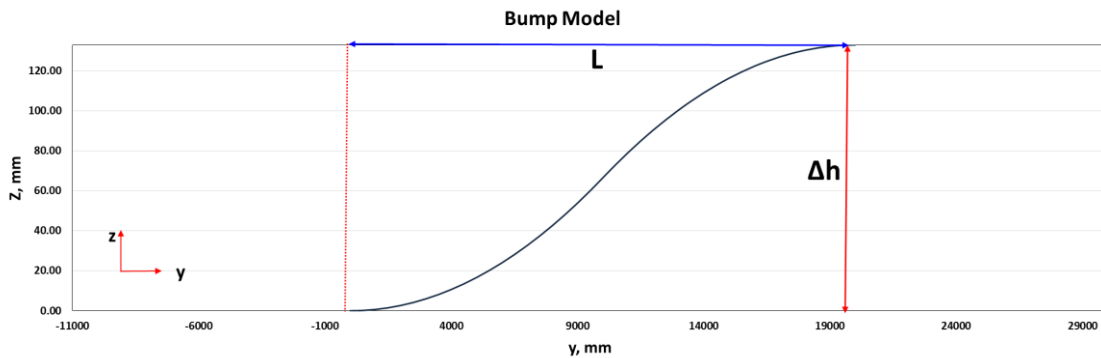


Figure 5.8. Bump model in transition zone used by Banimahd (2008)

Zai et al. (2001) investigated the wheel/rail interaction force due to existence of track irregularities by applying a theoretical model using computer software called VICT. As with Figure 5.9, the bump (irregularity type used by Zai et al. (2001)) model includes two variables, namely the length of the transition (L) and the bump angle (α).

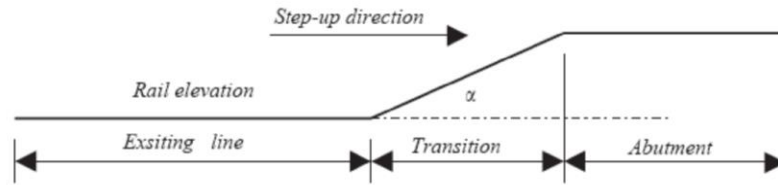


Figure 5.9. Bump profile at transition zone (Lei and Mao 2004)

Banimahd and Woodward (2007) also looked at the faulted transition due to voided sleeper causing a dip along the HSR under the moving loads. The variables used to define the dip size are shown in Figure 5.10. These variables include the dip length and void height (h). However, in this study the only variable was void height, and the dip length was considered to be constant ($L= 1$ m).

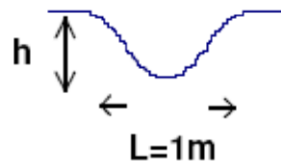










Figure 5.10. Dip profile (Adapted Banimahd and Woodward 2007)

In addition to bump and dip, two types of irregularities that are very common near bridges at transition zones, a summary of other types of irregularities along modern railways are presented in Table 5.1. It should be noted that any abnormality along the track can cause dynamic impact force, leading to increased rates of differential settlement.

Table 5.1. Different Types of Irregularities along Railway Lines (Steffens 2005)

Irregularity	Equation	Shape
No irregularity	Nil	
Wheel flat	$f(x) = \frac{d}{2} \left(1 - \cos \frac{2\pi x}{L} \right)$	
Sinusoidal corrugation	$f(x) = \frac{d}{2} \left(\sin \frac{2\pi x}{L} \right)$	
Dipped joint	$f(x) = \frac{d}{2} \left(1 \pm \cos \frac{\pi x}{L} \right)$	
Hollow weld	$f(x) = \frac{d}{2} \left(1 - \cos \frac{2\pi x}{L} \right)$	
Humped weld	$f(x) = -\frac{d}{2} \left(1 - \cos \frac{2\pi x}{L} \right)$	
Arbitrary wheel surface profile	x and y coordinates must be defined	
Arbitrary rail surface profile	x and y coordinates must be defined	

Note that $f(x)$, shape function of the irregularity; x , current coordinate on the rail; d , depth of the irregularity; and L , total length of the irregularity.

5.4 Track Response Criteria

Two response components are of interest in this study: wheel/rail interaction force and train body acceleration. As mentioned in section 5.1, the wheel/rail interaction force should be limited, or safety problems will result. If impact force exceeds the allowable value, it results in bigger differential settlement leading to high maintenance cost or, in the worst-case scenario, derailment. However, the threshold values should be established for the second response component, train body acceleration, in order to provide a smooth and comfortable ride for passengers. In this section, different codes and recommendations will be reviewed to define the proper threshold values for these two response components.

5.4.1 Wheel/Rail Forces

The limit proposed for impact force or wheel/rail interaction force is for the dynamic amplification factor (DAF), which is defined as the ratio of the maximum dynamic wheel/rail reaction force to the static load on the wheel. If this factor exceeds the permissible value, it results in accelerating deterioration of the track and the soil below. Banimahd (2008) used the criteria proposed by Esveld (2001). A limit value of wheel load equal to 170 kN was recommended by Esveld (2001). Considering the wheel load to be equal to 8.2 T, which was according to the static load of the train that Banimahd (2008) used in his work, then the $DAF=2.0$ seemed to be the maximum permissible value established for DAF on the track at the transition location.

Using a track settlement model that was developed by TTCI (Transportation Technology Center, Inc), a linear relationship was seen between the rate of settlement increase due to increase in load (Davis et al. 2007). Plotkin and Davis (2008) believes that the load felt under the track must increase by 50% in order to have a 25% increase in differential track settlement rate. In other words, to see a noticeable track differential settlement, DAF should be 1.5 or higher ($DAF \geq 1.5$).

Based on AS 1085.14 (Australia Standard Series AS1085), a code provided for Prestressed Concrete Sleeper, the combined design load factor (including quasi-static and dynamic loads) should not be less than 2.5 times the static load (Steffens 2005, Remennikov and Kaewunruen 2007). The typical values of quasi-static loads are around 1.4 to 1.6 times the static wheel load. The dynamic loading due to high-frequency effects of wheel/rail interaction is 1.5 times the static wheel load. The combination of these two

loads is considered as a design load, which is 2.5 times or greater than the static load (Remennikov and Kaewunruen 2007). A summary of all codes and recommendation for limit values for DAF are given in Table 5.2.

Table 5.2. Dynamic Amplification Factor Threshold Limit Values

<i>Parameter</i>	Value	Reference
<i>DAF</i> ¹	1.50	Plotkin and Davis 2008
<i>DAF</i>	2.00	Banimahd 2008
<i>DAF</i>	2.50	Majka 2009 (based on EN1991-2 Recommendation)
<i>DAF</i>	1.50	AS 1085.14

¹DAF: Dynamic Amplification Factor

5.4.2 Train Body Acceleration

Another track response criterion which is considered as a representative of the passenger comfort level and our interest in this study is the maximum permissible vertical train body acceleration (a_{max}). Like for DAF, many different values have been recommended by codes and researchers. Among all of these values, SNCF (the national railway of France) considered a very restrictive value of 0.05 g as the limit value for train body acceleration (Grandil and Ramodence 1990). Eurocode (European Committee for Standardization 1995) suggested a maximum value of 0.1 g for maximum permissible vertical train body acceleration. Considering the riding quality criteria according to Chinese Railway practice, Lei and Mao (2004) recommended an a_{max} equal to 0.2 g. Zai

et al. (2001) also proposed a 1.25 m/s^2 (0.12 g) value for a_{\max} . A summary of all these criteria for a_{\max} can be seen in Table 5.3.

Table 5.3. Threshold Limit Values for Vertical Train Body Acceleration

<i>Parameter</i>	Value	Reference
$a_{\max}^1 (g^2)$	0.10	Eurocode (European Committee for Standardization 1995)
$a_{\max} (g)$	0.12	Zhai et al. 2001
$a_{\max} (g)$	0.20	Mao 2004 (based on Chinese railway practice)
$a_{\max} (g)$	0.05	SNCF 1990 (the national railway of France)

¹ a_{\max} : Maximum permissible vertical train body acceleration

² $g = 9.81 \text{ m/s}^2$

5.5 Review of Previous Studies

According to Banimahd (2008), when considering train/track interaction during track design, two main phenomena must be taken into account:

1. How the train/track geometrical and mechanical properties change the train/track interaction forces
2. How the track design can effectively change train and passenger safety and passenger comfort.

The first one will be reviewed in this section. In section 5.9, we will review different design methodologies and their effects on the safety and comfort of passengers on trains.

Any type of geometric irregularity causes severe dynamic disturbances at the wheel/rail contact surface. As a result of the irregular interface between wheel and rail in either form (see section 5.3), high interaction forces between rail and wheel are produced. This large impact force can be considered as one of the main causes of train/track/soil components deterioration. It should be noted that the initiation and development of any type of wheel/track irregularity occurs as a consequence of intense interaction force; moreover, these irregularities lead to increased intensity of the dynamic impact force between rail and wheel. Therefore, it can be concluded that these two factors, irregularities existence and interaction force intensity, are being the cause of the other (Banimahd 2008). Dynamic problems associated with the train/track interaction along HSR lines can be categorized into four major classes (Zhai et al. 2001):

1. High train speeds cause impact and vibration on turnout structures. When trains operate at high speeds over the fixed frog, which is a rail discontinuity in fixed noses, the impact force between wheels and noses becomes more severe, resulting in shortened life of turnout structures.
2. The short-wave length irregularity on the welded rail joints results in large wheel/rail interaction force, particularly at high speeds.
3. The most important problem lies in the transition zones near bridges and tunnels. This type is considered as a form of structural irregularity. When HSTs pass the transition zones, the dynamic load will fluctuate, and the train will experience a high level of vibration. This vibration, which can be felt by passengers, results in both decreased comfort level and increased deterioration rate of track geometry. This is our primary concern in the current study.

4. The last problem is associated with wheel defects or existence of a wheel flat. The periodic interaction produced by wheel flats adversely affects the geometry and necessitates maintenance of railway lines.

Among all sources causing train excitation and, consequently, interaction force between wheel and track, stiffness variation throughout the track is the most common source (Banimahd 2008) and is our primary interest in the current study. Stiffness variation can be caused by either the discrete support of sleepers or variation in substructure stiffness. As mentioned in section 5.3, the first cause, discrete support of sleepers, results in developing dip, and the second cause, variation in substructure stiffness, results in bump initiation. There are two main and common sources resulting in stiffness variation along the railway lines: ballast depth variation and localized dirty ballast. Ballast particle abrasion and/or mud pumping can lead to localized dirty ballast. Excess pore pressure will generate and increase as a result of blocking the ballast voids with dirt (fine particles). This phenomenon of excess pore pressure increase decreases the soil stiffness and strength of the ballast. Due to this stiffness variation, the dynamic interaction load fluctuation will increase, which results in differential settlement formation. In final analysis, stiffness variation reduces the operational efficiency in terms of passenger comfort level, and, in worse scenarios, at high train speeds this phenomenon could lead to safety issues and train derailments (Clark et al. 2002).

Some research has focused on track stiffness variation or track modulus issues (Hunt and Newland 1996, Clark et al. 2002, Lei and Mao 2004, Sasaoka and Davis 2005, Plotkin et al. 2006, Li and Davis 2007, Namura and Suzuki 2007, Banimahd 2008, Ribeiro

et al. 2008, Davis and Plotkin 2009). The TLV outcomes from a bridge site near Marysville, Kansas showed that the bridge stiffness is noticeably higher than the stiffness of the approach embankment (Li and Davis 2007). However, there is no result of measured wheel/rail interaction force from this stiffness variation at the transition zone. Davis and Plotkin (2009), using FRA's research car T-16 near the bridges at the location outside of Baltimore, MD, presented an actual force measurement. This measurement data showed that crossing the stiffness variation alone does not induced any considerable dynamic interaction force. Plotkin et al. (2006) stated that the dynamic amplification factor produced by a stiffness variation alone is less than 10%. They showed that stiffness variation with the presence of irregularity increases the DAF (DAF= 1.5 to 3). As mentioned in section 5.2.1, Banimahd (2008) looked at the dynamic analysis of transition zones for high speed railway lines through a finite element modeling. The outcome obtained from simulations indicated that the effect of stiffness variation on the DAF can become more significant as the train speed increases (see Figure 5.2). Therefore, train speed can be considered as an influential factor affecting the DAF where there is stiffness variation alone. However, the range of train speed that Banimahd (2008) considered in his research study was not high enough. According to the literature review given in section 2, these days train speeds reach 350 km/h and even more. The maximum train speed in Banimahd's work is 252 km/h. In our study, trains reached a maximum speed of 720 km/h. Riberio et al. (2008) also simulated the dynamic behavior of the high-speed tracks with modeling stiffness change alone, without any imposed irregularity. These simulations including a 2-D track model and a 3-D track model using ANSYS and LS-DYNA,

respectively. The result of this study showed that a stiffness variation alone along the track produces an interaction force between rail and wheels.

The other issue is that the force on the front wheel is not equal to the one experienced by back wheels (Frederick and Round 1985, Zarembaski 1989, Riberio et al. 2008). Frederick and Round (1985) confirmed through several actual force measurements that the leading axle of the bogie induced lower impact forces than the trailing axle. They also indicated that while the peak force on the front axles is independent from the train speed, there is a linear relationship between train speed and the peak force on the back axles. On the other hand, Frederick (1978) believed that dynamic forces, regardless of the track profile, are a function of mass times the square of the velocity (mv^2).

Although the model of the transition zone alone without irregularity can particularly affect the DAF at high train speeds, the stiffness variation has a great impact on the differential settlement initiation and development along the track at transition zones (Hunt and Newland 1996, Hunt 1997, Banimahd 2008, Nicks 2009). This differential settlement is followed by an intense increase in DAF too. Indeed, it should be noted that the interaction force intensity is not only dependent on the characteristics of the train and of the track substructure and superstructures components but also the irregularity types and sizes (Jenkins et al. 1974, Zhai et al. 2001, Lei and Mao 2004, Banimahd and Woodward 2007, Banimahd 2008, Plotkin and Davis 2009, Nicks 2009). Zhai et al. (2001) used a theoretical model which is simulated with VICT, a computer software, to assess the effect of track irregularity (in the form of bump as presented in Figure 5.9) on the wheel/rail interaction force. As mentioned in section 5.3, their bump model includes two variables, namely bump angle (α) and bump length (L). The results of this study showed a linear relationship

between interaction force and bump angle (α). Leo and Mao's study included simulating the effect of both faulted, with irregularity model, and non-faulted, with stiffness variation model alone, transition zones. The bump model that was used in these simulations is illustrated in Figure 5.9. The results agreed with the findings of Sasaoka and Davis (2005), Plotkin et al. (2006) and Plotkin and Davis (2009), indicating that stiffness variation alone is not an influential factor on the DAF. On the other hand, they found that bump angle (α) and train speed (V) plays an important role in interaction force between wheel/rail (Figure 5.11). As with Figure 5.11, at higher train speed ($V=350$ km/h), the wheel/rail force for very steep bump ($\alpha=0.012$) was 5 times larger than for the no bump case.

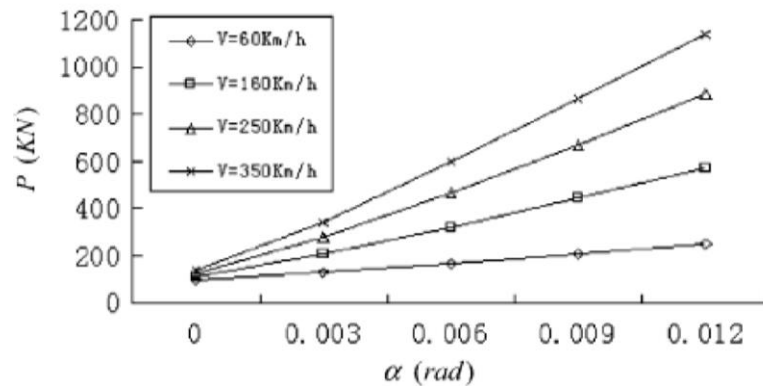


Figure 5.11. Maximum vertical wheel/rail interaction forces as a function of bump angles at different train speeds (Lei and Mao 2004)

Woodward and Banimahd (2007) and Banimahd (2008) looked at effects of different bump (Figure 5.12) and dip (Figure 5.13) sizes and train speeds on the track responses using 3-D FEM. Figure 5.12 depicts that at each train speed, for given differential settlement, the DAF increases as the deflection spanning length (L) becomes shorter. In fact, for a given differential settlement, the bump angle increases as L

decreases. Therefore, the results obtained from this study agreed well with the finding of Leo and Mao (2004). In total, the results showed a linear relationship between L and DAF with negative slope and h and DAF with positive slope. The effect of train speed is also can be clearly seen in Figure 5.12.

Increasing the train speed was also found to increase the DAF. Woodward and Banimahd (2007) used the same model to look at the effect of dip sizes as well as train speeds on the DAF (Figure 5.13). As it is obvious in Figure 5.13, DAF increases as train speed and/or the dip height (h) increases. Banimahd (2008) used two criteria, namely maximum permissible load and maximum permissible train body acceleration, to define the tolerable bump/dip size in this study. Although it was a valuable research study in its time, the main limitation of this study is the range of train speeds. Banimahd's research studies (2008) are limited to only three speeds: 108, 180, and 252 km/h (30, 50, and 70 m/s) as mentioned earlier in this section. Thus, according to the current operational train speeds, the role of train speed in impact force was not fully considered in these studies.

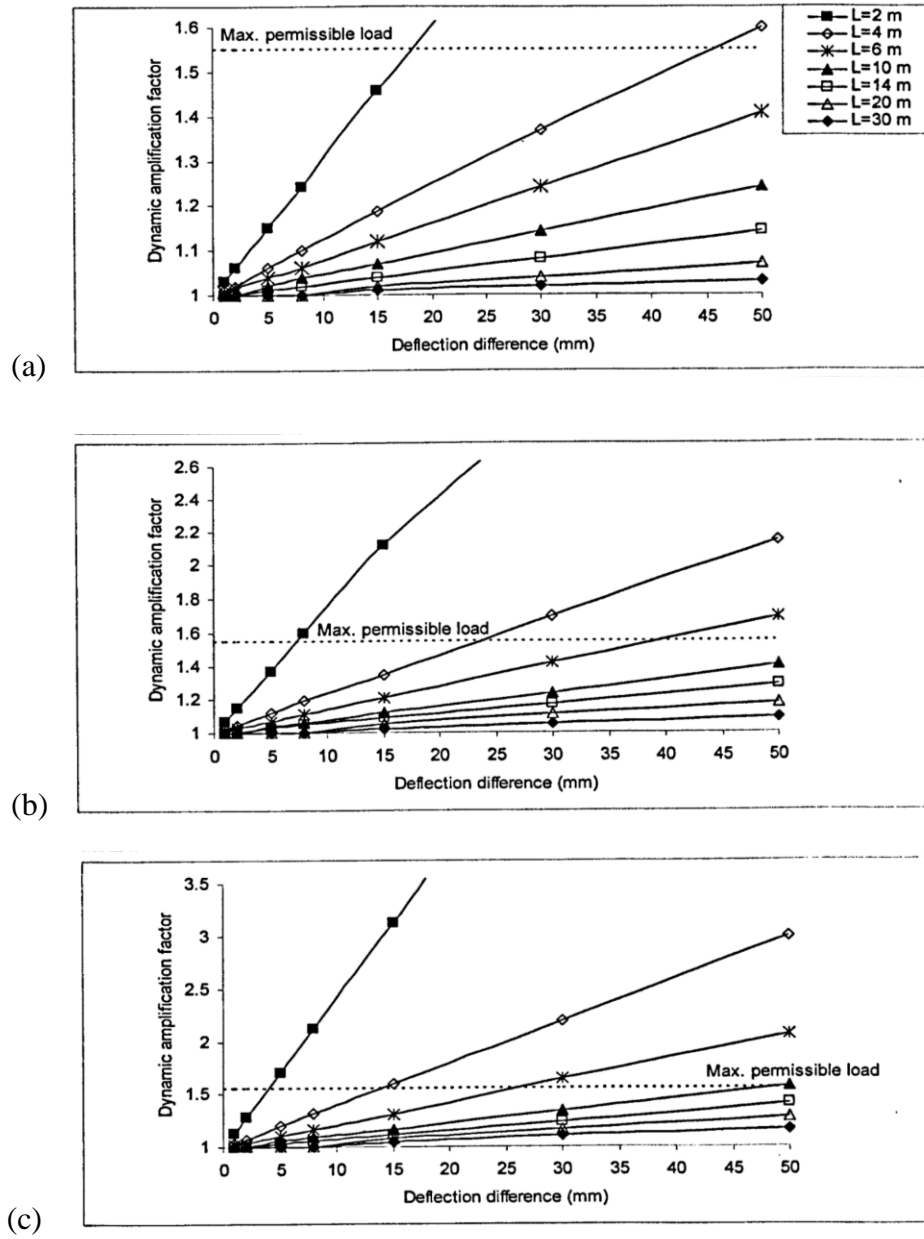


Figure 5.12. Effect of bump variables (L and h) on the DAF at train speed (a) 108 km/h, (b) 180 km/h, and (c) 252 km/h (Banimahd 2008)

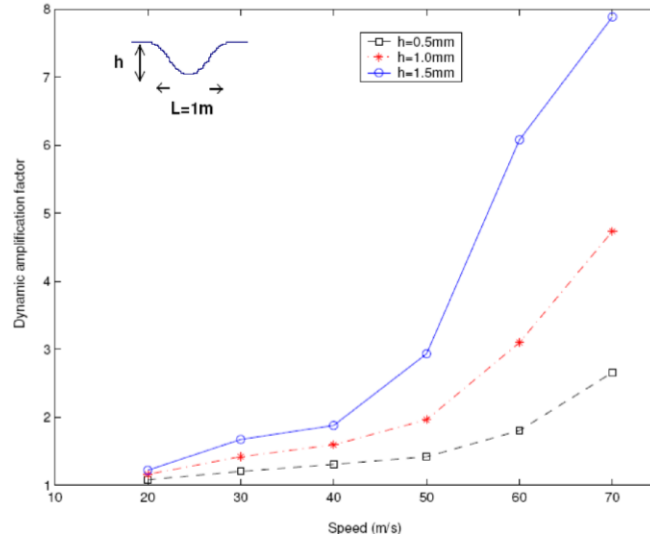


Figure 5.13. Effect of dip height (h) and train speeds on the DAF (Woodward and Banimahd 2007)

Another invaluable study to determine the tolerable bump/dip for passenger safety at the ends of bridges was conducted by Nicks (2009). Using LS-DNA, she performed an extensive parametric study looking at the effects of different train/track/soil factors including train direction, train speed, bump/dip size, approach embankment soil modulus, approach tie and bridge tie material, bridge deck type, ballast thickness, and approach tie length on the train/track/soil responses comprising the impact force intensity, track deflection, ballast and subgrade pressure. Figure 5.14 shows the effect of train speed on the tolerable bump/dip size considering the maximum permissible load is twice as much as the static load ($DAF=2.0$). As with Figure 5.14, Nicks (2009) ran her numerical model only for low train speeds ($V_T < 45 \text{ m/s} = 160 \text{ km/h}$). Thus, like Banimahd (2008), a proper range for train speed according to different codes was not fully considered in her studies. In addition, since an important parameter used to characterize track quality is the vertical

track modulus (Farritor 2006), the current study will include the effects of changes in vertical track modulus on the track responses in both cases, i.e., with a bump present and without a bump. In addition, she just considered two types of irregularities in her study, whereas the current study looked at various types of irregularities. Moreover, in her work, because her focus was on the freight railway lines, she did not consider the maximum train body acceleration for passenger comfort. Therefore, this study will address the effects of a wide range of train speeds ($18 \leq V_T \leq 720$ (km/h)), different subgrade conditions considering a wide range of subgrade modulus values ($10 \leq E_s \leq 100$ MPa), various types of irregularities including drop, rise, bump, and dip, which will be defined later in section 5.6.2, and a wide range of irregularity sizes ($0.000625 \leq \alpha \leq 0.01$) on the DAF and maximum vertical train body acceleration (a_{\max}) as safety and comfort criteria. Finally, the results of the entire parametric study will be presented in the form of guideline charts showing the tolerable irregularity size according to two different criteria, i.e., DAF and a_{\max} .

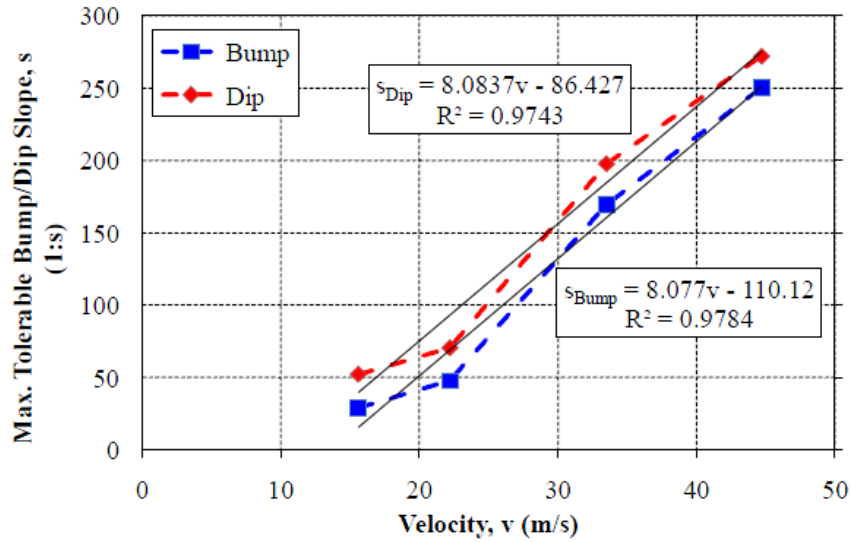


Figure 5.14. Tolerable bump/dip size vs. train speed based on permissible DAF of 2.0 (Nicks 2009)

5.6 Development of Four-Dimensional Finite Element Model: Numerical Simulation

To arrive at a suitable and applicable mitigation and design method to overcome the problem of bump and other types of irregularities along HSR lines, the transition zone where the risk of irregularity initiation and development is high must be modeled as correctly and precisely as possible. This model should comprise track components, the multilayered embankment and natural soil under the embankment, track geometrical irregularities, and train/track interaction. Several models based on the spring-beam type or 2-D and 3-D finite element models have been proposed to model the transition zone

and irregularities along railway lines (Esveld 1997, Suiker and Esveld 1997, Zhai and True 1999, Lei and Mao 2004, Woodward and Banimahd 2007, Banimahd 2008, Nicks 2009). In the present study, the transition mechanism is investigated using LS-DYNA to develop a 4-D train/track FEM. This model includes track, train, and geometrical irregularities to assess the effect of irregularity and stiffness variation at transition zones on the train/track dynamic responses. In this section, all components of the well-developed FEM will be given. Two existing numerical models (Banimahd 2008, Nicks 2009) were used to verify the model reliability (given in section 5.6.6). In the next section (section 5.7), results of an extensive parametric study using this verified 4-D FEM will be presented. The outcome of the current study was used to propose some guideline charts showing the tolerable bump size to meet safety and comfort criteria.

5.6.1 Track Model Configurations

A 4-D model of a plain track on subgrade was simulated in LS-DYNA to evaluate the response of the coupled train/track system at speeds of up to 720 km/h (200 m/s) for both faulted tracks and non-faulted tracks. The track and subgrade meshing layout were similar to that applied in the previous problem of breaking the Rayleigh wave barrier (section 4). The track model configuration is given in Figure 5.15. Because the mesh was symmetrical from the track centerline, only one-half of the full model was simulated. As mentioned earlier in this section, this study included two phases. In the first phase, the track without any type of irregularity will be modeled as shown in Figure 5.15 to assess

the effect of stiffness variation on the track responses, while in the second phase, to investigate the effect of different types of irregularities with various sizes on the track responses, the irregularity was modeled along the track. The second model including irregularities will be explained more in-depth in section 5.7. Different types of irregularities and their variables will be defined in section 5.6.2. The model dimension, however, used for two phases is the same as the one shown in Figure 5.15. A very low ballast 300 mm deep and with the properties presented in Table 5.3 is placed on top of the subgrade. The material properties for track components, ballast and subgrade are given in Table 5.4. Like the model used in section 4, the track components including ties and rail were modeled as solid elements with elastic material properties at transition zones (Table 5.4). Track components on top of the bridges were modeled with rigid material properties. The track was attached to the railroad ties. The rail and ties were modelled with steel and concrete material, respectively. Ties were spaced at 0.7 m from center to center with dimensions of 0.3 m x 0.2 m x 2.4 m. The subgrade moduli, depending on case study, varied from 10 MPa to 100 MPa (Table 5.4). Two existing numerical models (Banimahd 2008, Nicks 2009) were used to verify the model reliability (section 5.6.6).

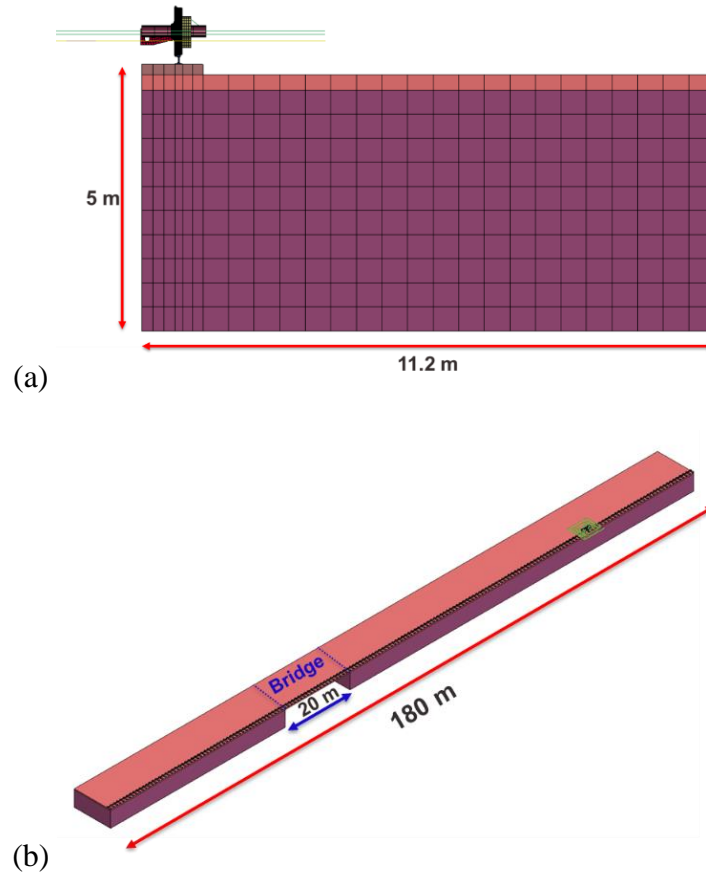


Figure 5.15. (a) Cross section and (b) side view of the finite element model

Table 5.4. Track/Soil Properties

<i>Section</i>	Elasticity Modulus (E_s) MPa	Poisson's Ratio (ν_s)	Unit Weight (ρ_s) kg/m³
<i>Subgrade</i>	5 to 120	0.35	1260
<i>Ballast</i>	120	0.35	1260
<i>Rail</i>	210000	0.25	7897
<i>Ties</i>	20000	0.3	1000

5.6.2 Irregularity Model

In addition to stiffness variation at transition zones, in the second phase of the parametric study, different types of irregularities need to be modeled. Modeling an irregularity includes a track geometry change in the form of any type of irregularity defined in Table 5.5. with different sizes in the FEM and changes in variables. In the present study, the effects of both variables, namely irregularity length (L) and irregularity height (h), on the train/track responses were investigated. Table 5.6 shows the range of irregularity variables. In this study, size of irregularity is defined with the following equation:

$$s = \frac{L}{h} \quad (5.3)$$

where s is irregularity size, L is irregularity length, and h is irregularity height (Table 5.5).

Table 5.5. Irregularity Profile

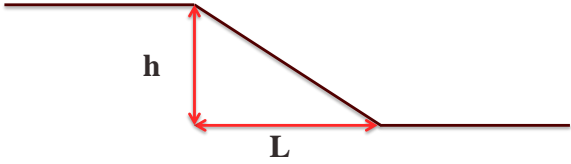
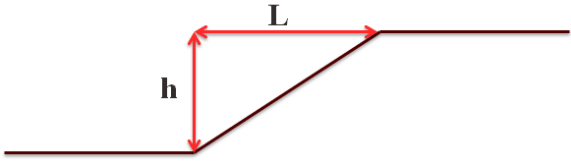
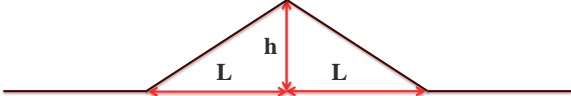
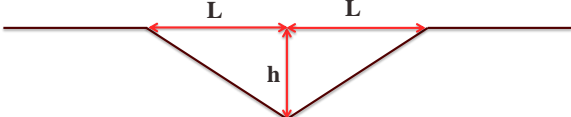
Irregularity type	Variables
<i>Drop</i>	
<i>Rise</i>	
<i>Bump</i>	
<i>Dip</i>	

Table 5.6. Irregularity Size

L,m	h,mm	S=L/h
6	60	100
	30	200
	15	400
	7.5	800
	3.75	1600
12	120	100
	60	200
	30	400
	15	800
	7.5	1600

5.6.3 Train Model Configuration

In this study, one-fourth of a train car, meaning one bogie, including the suspension system represented by springs and dampers, was modeled. A schematic model of the bogie is shown in Figure 5.16. However, to simplify the train model, the equivalent spring stiffness (K_{eq}) and damper coefficient (C_{eq}) of primary and secondary suspension systems were considered when modeling the train suspension system (Figure 5.17). The HST suspension system specifications are presented in Table 5.7. It should be noted that in order to limit the bolster horizontal motion (backward and forward), two very stiff horizontal side springs were modelled. The bolster was connected to the side frame by

means of these horizontal side springs. These springs did not have a noticeable weight. The spring stiffness assigned to these two horizontal springs is $5 \times 10^9 \text{ N/m}$ ($K_{ss}=5 \times 10^9$). In fact, these springs are representative of the friction wedges which were used to constrain the bolster within the side frame. In this simple model where the vehicle dynamics are not our primary concern, the friction wedges can be modeled by these two very stiff horizontal springs.

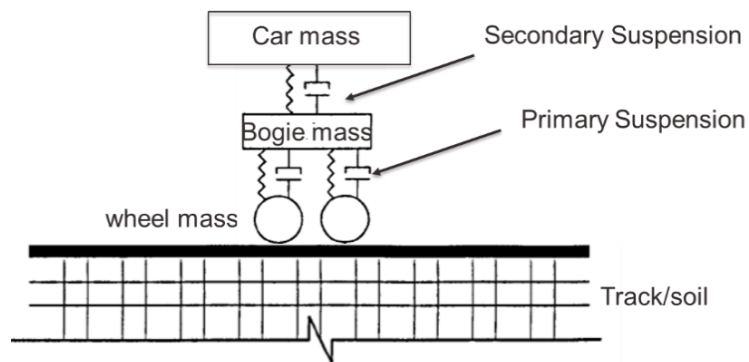


Figure 5.16. Schematic view of the bogie with its suspension system

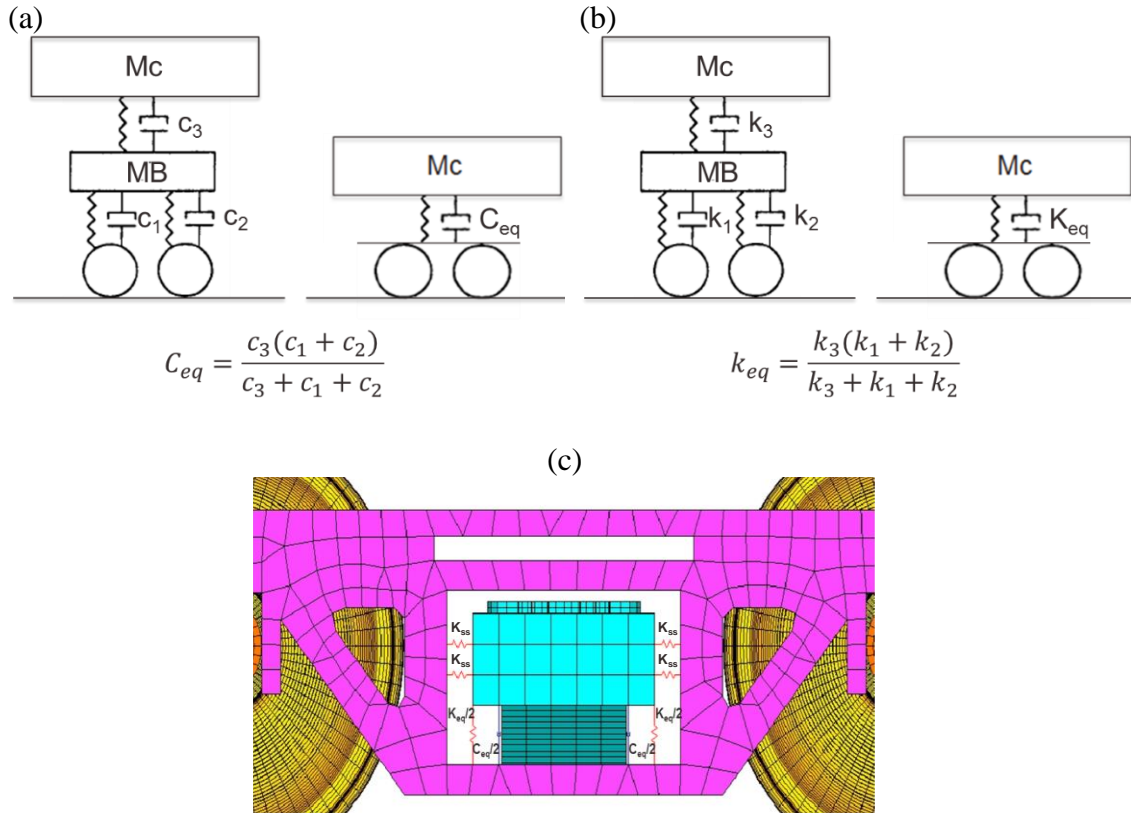


Figure 5.17. (a) Equivalent damper coefficient, (b) spring constant, and (c) side view of the finite element model of the train suspension system

Table 5.7. HST Specifications (Train Model: X2000)

<i>Parameter</i>	<i>Value</i> (metric tons)	<i>Parameter</i>	<i>Value</i>	
M_{car}	55.08	<i>Primary Suspension</i>	k_1, k_2 (kN/m)	3280
			c_1, c_2 (kNs/m)	90
M_{bogie}	3.26	<i>Secondary Suspension</i>	k_3 (kN/m)	1310
			c_3 (kNs/m)	30
<i>Axle Load</i>	17.40	<i>Equivalent suspension</i>	K_{eq} (kN/m)	1090
			C_{eq} (kNs/m)	26

A bogie with the same dimensions as the one Nicks (2009) used in her simulations was used in this train model (Figure 5.18). All material and section properties for the parts of the bogie were assumed to be rigid or solid (Table 5.8) except for the springs and dampers. Material properties of the wheels and axle components were considered to be like steel material properties as presented in Table 5.8. Based on the size of the other components including the side frame, bolster, and car mass components, the unit weight of the materials was assumed according to their real weight (Table 5.8). The total weight of the whole bogie was considered to be approximately 585 kN. Therefore, the total weight per each wheel would be 146.2 kN. However, in this study, one half of the full bogie was modeled because the mesh was symmetrical from the track centerline. A proper boundary condition was considered for the nodes located at the centerlines. Although one-half of the bogie was used in simulation, the static load of each wheel does not change.

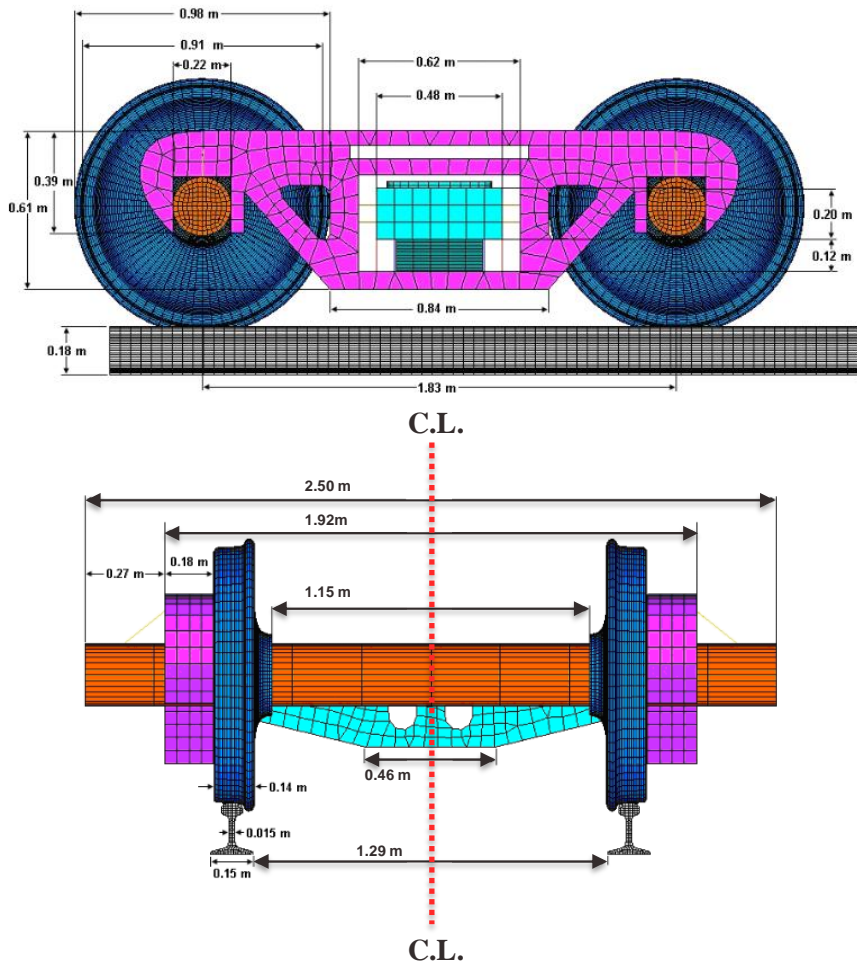


Figure 5.18. Train dimensions (Nicks, 2009)

Table 5.8. Material Properties of Different Parts of the Bogie

<i>Parts</i>	Material Property	Elasticity Modulus (E) MPa	Poisson's Ratio (ν)	Unit Weight (ρ) kg/m³
<i>Wheel</i>	Rigid	2e5	0.28	7850
<i>Axle</i>	Rigid	2e5	0.28	7850
<i>Side Frame</i>	Rigid	2e5	0.28	3816
<i>Bolster</i>	Rigid	2e5	0.28	2897
<i>Car Mass</i>	Rigid	2e5	0.28	2.2e7

5.6.4 Train/Track Contact

To model the wheel/rail interaction, there are different types of models with different levels of complexity and applications used in the various studies (Steenbergen 2006, Sun and Dhanasekar 2002, Banimahd 2008, Nicks 2009). Banimahd (2008) applied a continuous single point contact as shown schematically in Figure 5.19. A non-linear Hertzian spring permitting the separation of the wheel and rail is considered. The interaction force can be obtained from Hertzian theory.

A “Surface-To-Surface” contact defined in LS-DYNA was the type of contact considered between the outer surfaces of the wheel and tracks (Figure 5.20). In the present study, the same type of contact was modeled between wheel and rail. The outer, elastic elements of the wheel were defined as the slave surface while the top, outer elastic elements of the rail include the master surface. A penalty algorithm will place a normal interface spring between the contact surface and penetrating nodes if the slave nodes penetrate the master nodes (Hallquist 2006). In LS-DYNA, based on the Coulomb formula, friction is assessed. A value of 0.4 and 0.35 were given for the static and the dynamic coefficients of friction, respectively (Nicks 2009).

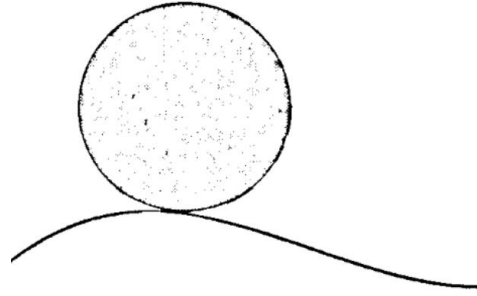


Figure 5.19. Continuous single-point contact (Banimahd 2008)

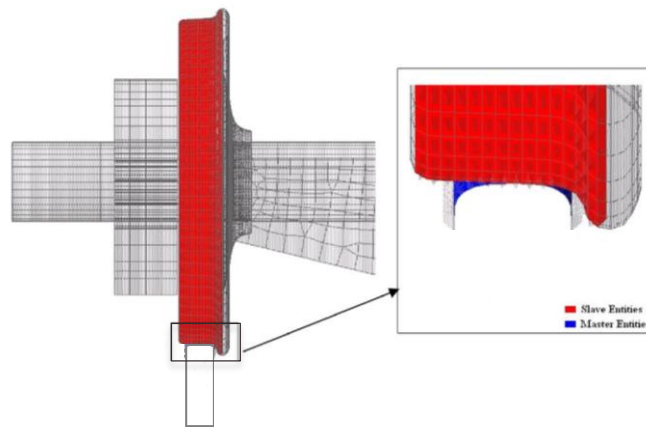


Figure 5.20. Contact between the wheel and the rail (Adapted Nicks 2009)

Newton's second law of motion ($F = \Sigma ma$) was applied to assess the vertical wheel/rail interaction force. To determine the wheel/rail forces, the acceleration time histories of all bogie components including the front (A_F) and back (A_B) wheels, the right (S_R) and the left (S_L) side frames, and the car body (C) were used (Figure 5.21). The normal force (N) between wheel and rail can be obtained by solving the following equation:

$$F = \sum_{i=1:N} m_i a_i \quad (5.4)$$

where m is the mass of each component, a is the acceleration of the components and N is the total number of the components. It is assumed that the normal force and the friction force between wheel and rail are the same, which means that the reaction force does not capture the rolling and rocking forces. It should be noted that in LS-DYNA, the “rcforce” is considered as the reaction force result between wheel and rail.

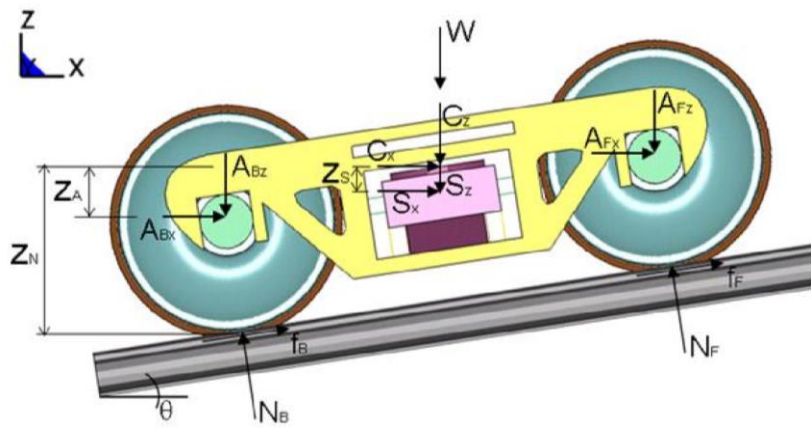


Figure 5.21. Free body diagram of forces acting on the bogie model (Nicks 2009)

5.6.5 Boundary Condition

The boundary conditions applied for this model included (1) roller supports on the side of the track/ballast/subgrade model allowing vertical motion and (2) pin supports at the bottom of the subgrade and bridge to restrict both horizontal and vertical motion. The pin supports were applied to simulate a bedrock location. The pin supports were used

under the bridge because it is assumed that the bridge was located on top of a rigid base. In addition to these two boundary conditions, at the centerline, the horizontal movement in the y-direction for both track and train was restricted. As mentioned earlier, this is because the study considers one-half of the model due to symmetrical mesh. Figure 5.22 shows the boundary conditions imposed in the finite element model.

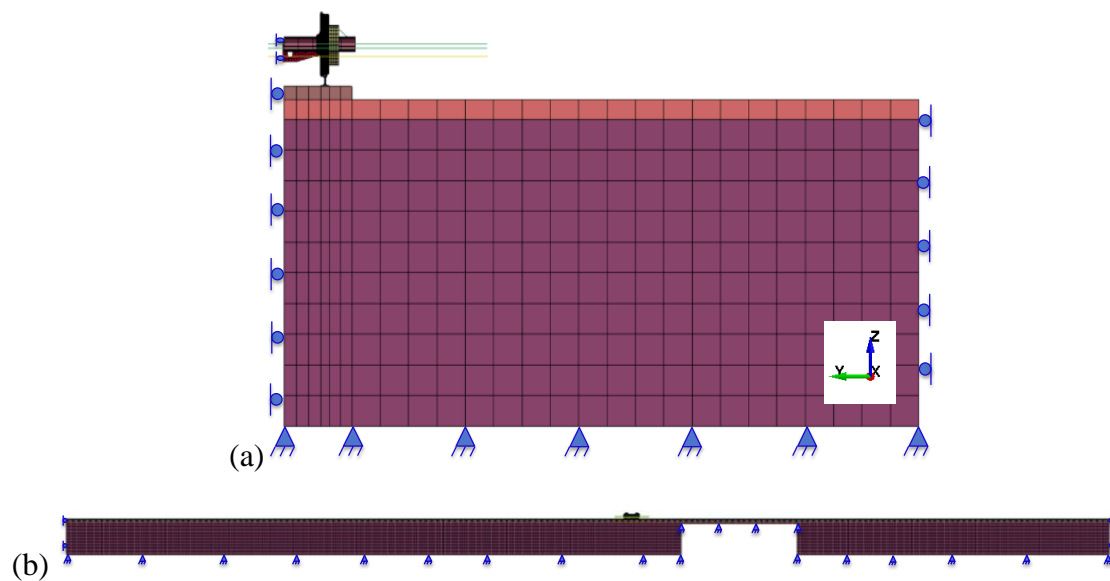


Figure 5.22. Boundary conditions: (a) cross-section and (b) side view

5.6.6 Model Verification

Model validation is required before relying on the model to simulate the problem of irregularity along HSR lines. In this study, two existing finite element models were used to verify the reliability of the current finite element model. The first one is the model used by Nicks (2009) to assess the problem of the bump at the end of railway bridges. She

compared the track static deflection to the analytical solution. In this section, it was shown that the results obtained from the current simulation agreed well with the outcomes of these existing valuable numerical simulations.

5.6.6.1 Banimahd's Model

Banimahd used a finite element model to simulate both the train responses to the bump model as described in section 5.2.3 (Equation 5.1, Figure 5.8) and the deflection difference induced in a transition zone due to stiffness variation. Using this coupled train/track model, the current finite element model was verified.

- *Train Model*

The train suspension system specifications adopted for Banimahd's model were according to Lei and Noda (2002) (Table 5.9). Figure 5.23 illustrates different components of a bogie including the suspension system. A bogie is comprised of mass of wheels (m_w), car mass (m_c), and mass of other bogie components (m_b). The suspension system included primary and secondary springs with spring stiffness labeled as K_b and K_c , respectively. Similarly, the primary and secondary damper coefficients are called C_b and C_c , respectively. In the current study, however, an equivalent spring and damper was modeled. In the same way as explained in section 5.6.3, an equivalent spring stiffness (K_{eq}) and damper coefficient (C_{eq}) of primary and secondary suspension systems were calculated (Table 5.9). L_b and L_c are depicted in Figure 5.23. $2L_b$ and $2L_c$ are the distance between the centers of wheels connected to a bogie and the distance between the centerline of two

bogies of the same coach, respectively. As mentioned in section 5.6.3, the unit weight of the material of each bogie component was assumed according to their real weight (Table 5.9) and their size. The axle load associated with all bogie components and car body mass is 17.4 tons (174 kN) and the wheel load is 8.7 tons (87 kN). To determine the interaction force between wheel and rail, a “Surface-To-Surface” contact between the outer surfaces of the wheel and track was assumed, as explained in section 5.6.4 (Figure 5.20).

Table 5.9. Train Specifications

<i>Parameter</i>	Value	<i>Parameter</i>	Value
<i>Axle Load (metric tons)</i>	17.4	<i>K_b (kN/m)</i>	3.28e3
<i>M_w (metric tons)</i>	1	<i>K_c (kN/m)</i>	1.31e3
<i>M_b (metric tons)</i>	3.26	<i>K_{eq} (kN/m)</i>	1.09e3
<i>M_c (metric tons)</i>	55.08	<i>C_b (kNs/m)</i>	90
<i>L_b</i>	1.3	<i>C_c (kNs/m)</i>	30
<i>L_c</i>	5.15	<i>C_{eq} (kNs/m)</i>	26

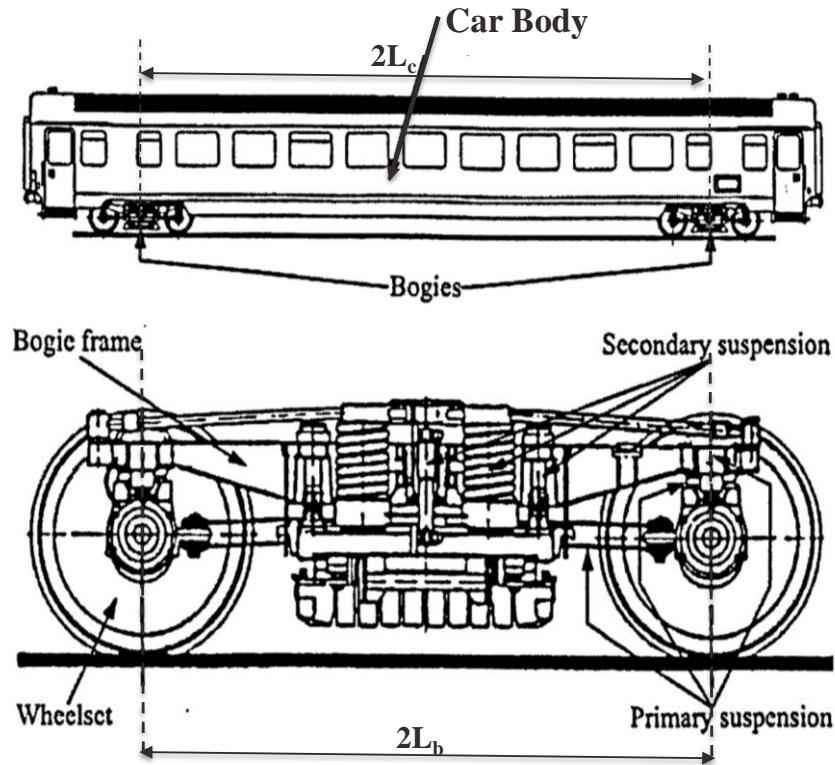


Figure 5.23. Train body and bogie components (Popp et al. 1999)

- *Track Model with Irregularity*

The same track model on subgrade as explained in section 5.6.1 was simulated in LS-DYNA to assess the model reliability. The material properties for the track are presented in Table 5.4. A very shallow ballast (ballast thickness equal to 300 mm) with Young modulus (E_b) of 120 MPa, unit weight (ρ_b) of 2000 kg/m³, and Poisson ratio (ν_b) of 0.35 was modeled on top of a subgrade with Young modulus (E_s) of 100 MPa, unit weight (ρ_s) of 2000 kg/m³, and Poisson ratio (ν_s) of 0.45 (Figure 5.15). The boundary conditions were defined the same as fully described in section 5.6.5, the boundary conditions were defined (Figure 5.22). Total length of the bridge was 20 m, and it was

located on top of a rigid base (Figure 5.15). Irregularities in the forms of rises of various sizes were modeled along the track using Equations 5.1 and 5.2 (Figure 5.24). The rise length (L) is assumed to be constant ($L=6$ m). The rise height changes from 15 mm to 60 mm ($S=120, 200,$ and 400).

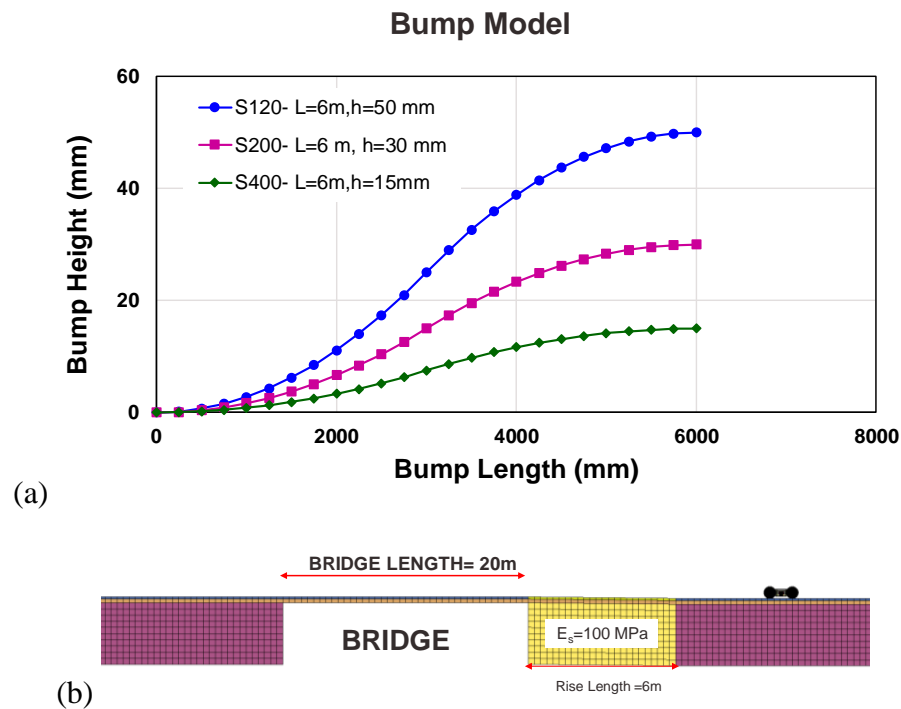


Figure 5.24. (a) Rise profile (b) the finite element model of rise along track

- *Model Validation Results*

The DAF as a function of irregularity size was plotted as shown in Figure 5.25. Good agreement is seen between the present finite element model and Banimahd’s finite element model. As expected, the DAF increases as train speeds increase. This validated

model was used to perform a parametric study. As mentioned earlier in this section, Banimahd’s study covered only three different train speeds ($V_T=108, 180,$ and 252 km/h) which are not high enough to reflect current operational HSTs.

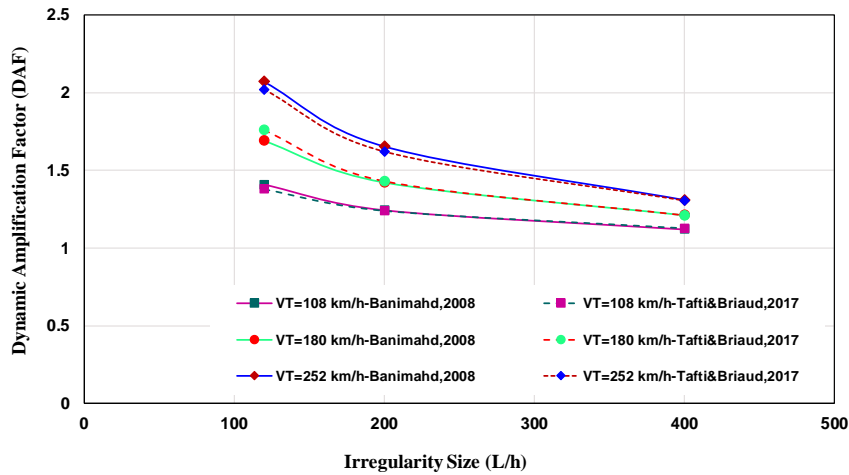


Figure 5.25. Model verification result: Dynamic Amplification Factor (DAF) vs. Irregularity Size

5.6.6.2 Nicks’ Model

The second model used for model verification was from Nicks (2009). Nicks performed an extensive finite element simulation to determine the allowable bump/dip size. The model configuration followed by the results of model validation will be presented in this section.

- *Train/track Model Configuration*

The train model used in this part of the study has the same dimensions as shown in Figure 5.18. The suspension system properties including damper and spring specifications are given in Table 5.10. In addition to train suspension system specifications, the weights of different bogie components were presented in Table 5.10. Track was modeled in the same way as explained in section 5.6.1. A 300-mm ballast with Young modulus (E_b) of 120 MPa, unit weight (ρ_b) of 2000 kg/m³, and Poisson ratio (ν_b) of 0.35 was modeled on top of a subgrade with Young modulus (E_s) of 25 MPa, unit weight (ρ_s) of 2000 kg/m³, and Poisson ratio (ν_s) of 0.45 (Figure 5.15). The boundary conditions defined in section 5.6.5 were imposed into the model. Rises of different sizes as shown in Figure 5.26 were modeled along the track. There is a linear relationship between rise height and rise length with the slope equal to 1/S. A rise length of 6 m with different rise heights ranging from 24 to 60 mm were considered as the rise variables. The rise coordinates shown in Figure 5.26 were used to model the rise along the track. It should be noted that Nicks called this irregularity a bump, but in the current study this type of irregularity was defined as a rise (Table 5.5).

Table 5.10. Train Specifications

<i>Parameter</i>	<i>Value</i>	<i>Parameter</i>	<i>Value</i>
<i>Axle Load (kN)</i>	292.393	Bolster Weight (kN)	4.5619
<i>Wheel Weight (kN)</i>	3.5575	Car Mass (kN)	541.9494
<i>Side Frame Weight (kN)</i>	4.3892	<i>K (kN/m)</i>	2.26e3
<i>Axle Weight (kN)</i>	7.6328	<i>C (kNs/m)</i>	25

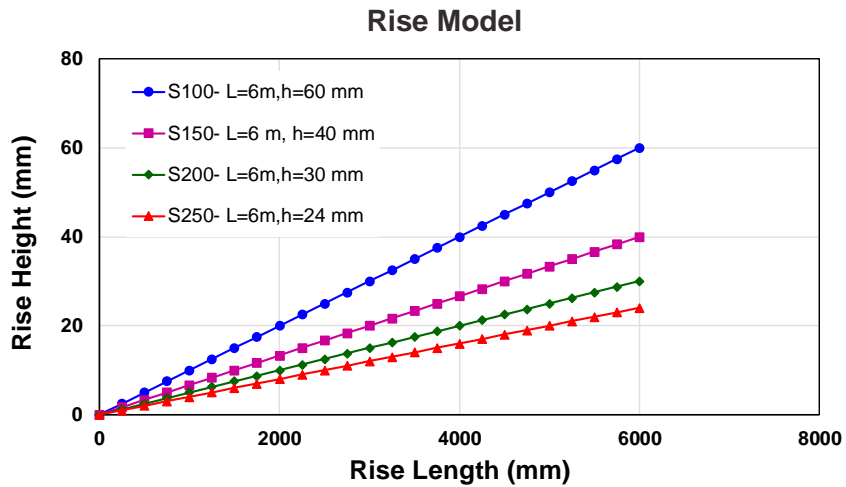


Figure 5.26. Rise profile

- *Model Validation Results*

To evaluate the reliability of the model, the dynamic amplification factors versus rise sizes were plotted for three different train speeds ($V_T = 80.64, 127.8, 160.92$ km/h). Figure 5.27 depicts the comparison results, showing that the present model agreed well with the Nicks model. Figure 5.27 shows that the same relationship between DAF and irregularity size exists as shown in Figure 5.25. Also, DAF increases as the train speed increases. However, it is obvious that the range of train speed in Nicks’s parametric study is for regular trains, not HSTs. As mentioned earlier, it is a great work, but our main concern is to find the tolerable irregularity size at a reasonable range of train speeds for HSR lines based on the definition provided in section 2. This model was used to verify the finite element model, and the verified model was applied to perform the parametric study.

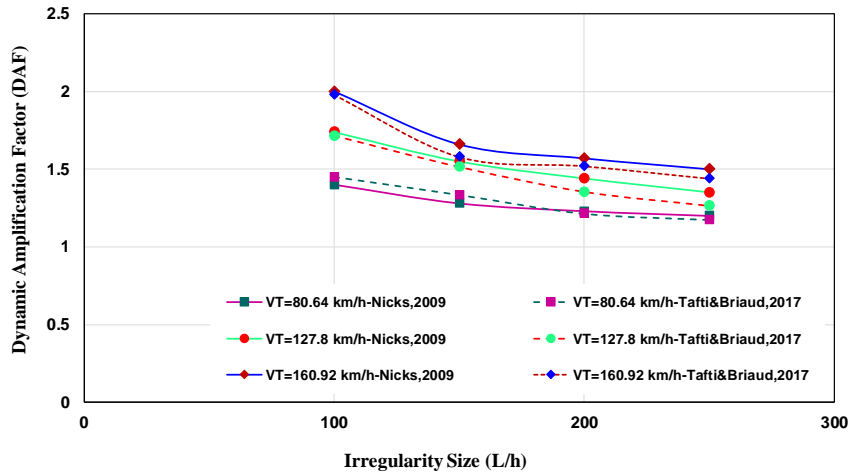


Figure 5.27. Model verification result: Dynamic Amplification Factor (DAF) vs. Irregularity Size

5.7 Parametric Studies

A parametric study was performed to determine the effect of different components on the irregularity problem along HSR lines. As mentioned earlier in this section, the parametric study was conducted in two phases: non-faulted and faulted transition. In the first phase (non-faulted transition), there is no irregularity modeled along the HSR lines. The developed and verified train/track 4-D FEM was employed to study the effect of stiffness variation in the transition zone. The influence of various components including train speed (V_T) and subgrade modulus (E_S) were assessed through this phase of the present parametric study. In the second phase, different types of irregularities with varied sizes were introduced along the HSR lines at transition zones. This part of the study determines the impact of different parameters such as train speed, subgrade modulus,

irregularity size, and irregularity type. The reference train/track model was fully explained in section 5.6.1 and 5.6.3. The train speed and subgrade modulus are the parameters that change in the parametric study, and will be defined for each case. The train/track contact and boundary conditions are the ones defined in section 5.6.4 and 5.6.5. In phase two, the irregularity models defined in section 5.6.2 with different sizes along the HSR lines will be employed. The results of the parametric study include the wheel/rail interaction force, vertical train body acceleration, track deflection, and dynamic amplification factor (DAF) for different cases. In the next sections, two phases of the parametric study and their results will be presented.

5.7.1 Non-Faulted Transition

A 4-D FEM (fully explained in section 5.6) is used in this phase to study the effect of stiffness variation at transition zones, for example, near the bridges. In this section, it was assumed that no geometrical irregularity existed along the HSR lines. The stiffness changes near the bridges between track on top of the compacted embankment with different subgrade stiffness (E_s) and track on top of the bridge abutment which was considered as a rigid base were the main concern of this part of the study. Train speed and subgrade modulus are two parameters whose influence on the train/track responses were determined.

5.7.1.1 Train Speed Effect

The train speed (V_T) varied from 18 to 720 km/h (5 to 200 m/s). This range of train speed was chosen based on the literature review given in chapter section 2. The subgrade modulus is equal to 20 MPa in this case study. According to the following equation, it was expected that train speed plays an important role on producing a higher dynamic amplification factor (DAF). The kinematic energy of a bogie (E) can be obtained by using following equation:

$$E = \frac{1}{2} m V_T^2 \quad (5.5)$$

where m is the mass of the bogie and V_T is train speed. It can be concluded that as train speed increases the kinematic energy will increase too. This higher kinematic energy can result in higher DAF and train body acceleration. This phenomenon will be addressed in this section. Typical track displacements in the vicinity of the transition zone for three different train speeds (144, 288, and 432 km/h) are displayed in Figure 5.28. As expected, due to significant stiffness changes between track on top of the embankment and track on top of the rigid base (bridge), a considerable difference can be seen between displacement induced in the track on soil and track on a bridge. As with Figure 5.28, this difference between track displacements becomes higher as train speed increases.

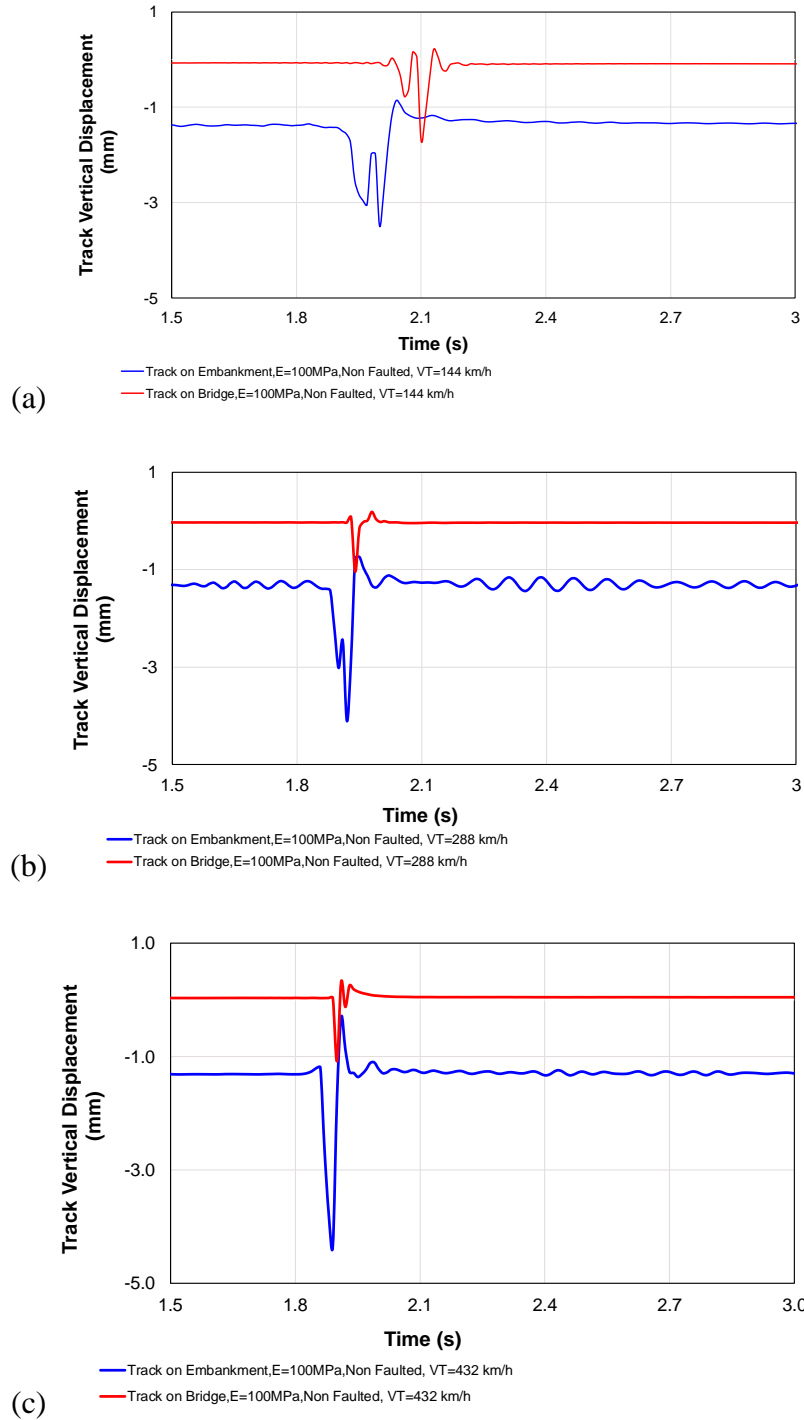


Figure 5.28. Track displacement under the moving load on embankment and bridge sides of the transition at (a) VT=144 km/h, (b) VT=288 km/h, (c) VT=432 km/h

Figures 5.29 to 5.31 illustrate some of the results for wheel/rail interaction force, vertical train body acceleration, and track deflection for train speeds of 144, 288, and 432 km/h. The mechanism of amplification of wheel/rail interaction force which was obtained from the developed 4-D FEM are shown. Figure 5.29 shows that the higher the train speed is, the more wheel/rail interaction force amplification can be seen. In addition, as train speed increases, the train body excitation becomes more significant (Figure 5.30). Increase in the train body acceleration at transition zones, such as near bridges, results in passenger comfort issues. The most important piece of information from this part of the study is related to the track differential displacement near the bridge. As with Figure 5.31, displacement starts to change in the vicinity of a non-faulted transition zone. The results showed that the stiffness variation, for example, near the bridges lead to initiate irregularity development. Also, this differential settlement at transition zones becomes more severe as train speed increases (Figure 5.31).

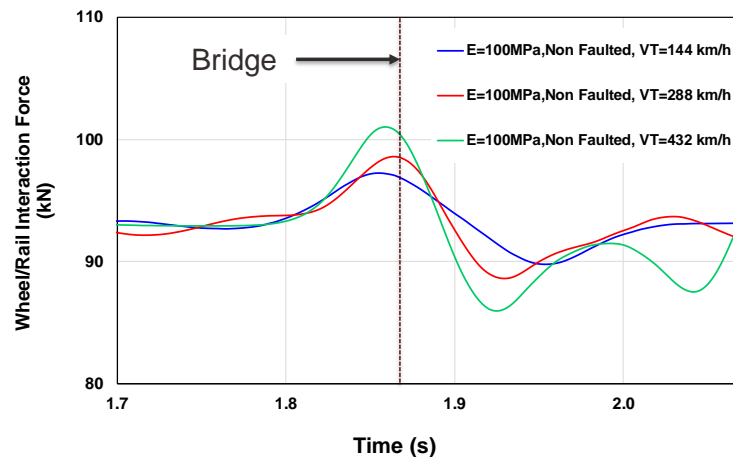


Figure 5.29. Effect of train speed (VT) on wheel/rail interaction force

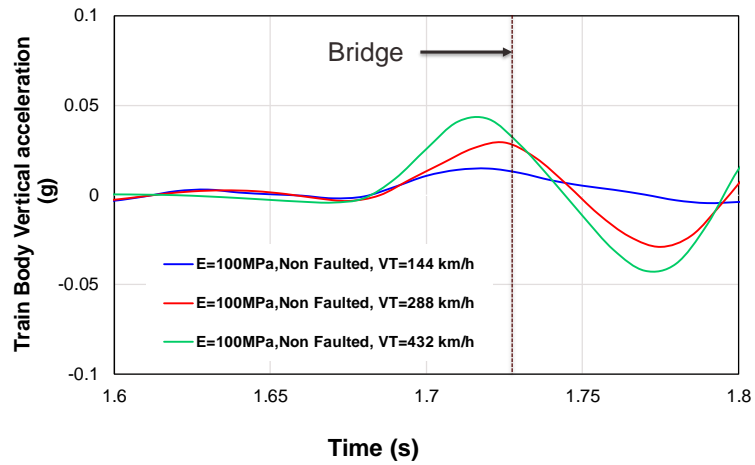


Figure 5.30. Effect of train speed (VT) on train body vertical acceleration

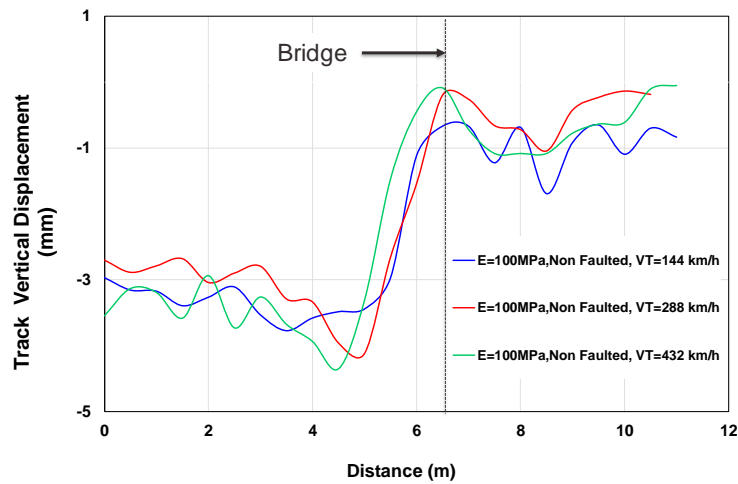


Figure 5.31. Effect of train speed (VT) on track vertical displacement

A summary was compiled of the complete set of results for all train speeds ranging from 18 to 720 km/h. Dynamic amplification factors (DAF) and maximum train body accelerations (a_{\max}) as a function of train speeds are plotted in Figures 5.32 and 5.33,

respectively. As train speed increases, DAF and a_{max} increase; however, in this case on which a stiff embankment was modeled, very moderate change can be seen. Therefore, in the next section the effects of both parameters (subgrade modulus (E_s) and train speed (V_T)) will be addressed.

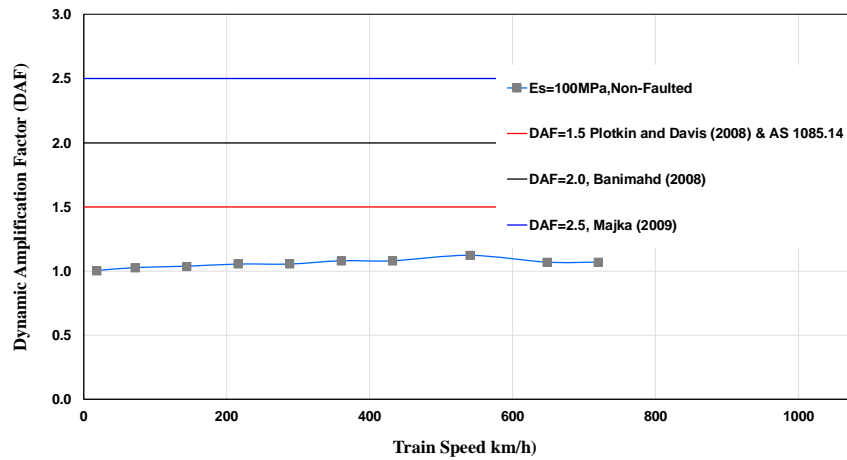


Figure 5.32. Dynamic amplification factor (DAF) vs. train speed (VT)

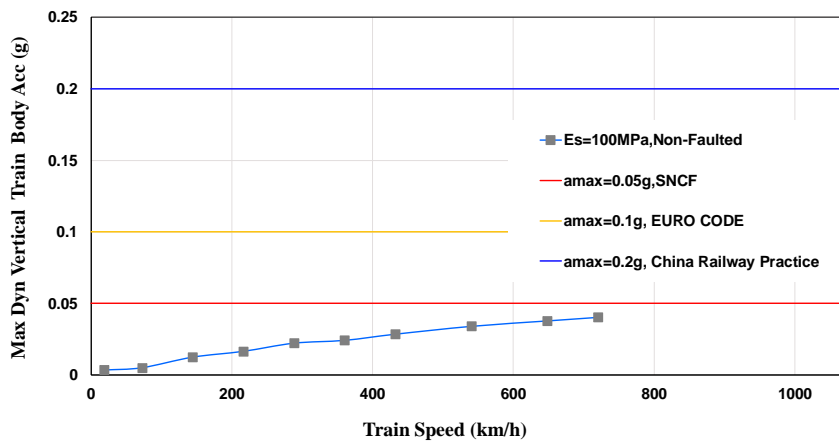


Figure 5.33. Maximum dynamic vertical train body acceleration(a_{max}) vs. train speed (VT)

5.7.1.2 Subgrade Modulus Effect

In this section, the effects of subgrade modulus alone as well as subgrade modulus combined with train speed on train/track responses due to stiffness variation in the vicinity of the transition zone (near the bridge) will be discussed. The subgrade modulus was changed from 10 MPa (representative of a very soft soil) to 100 MPa for very stiff soil. The full sets of results including track vertical displacement, wheel/rail interaction force, and train body acceleration for different soil modulus ($E_s = 10, 20, 80, 100$ MPa) are illustrated in Figures 5.34 to 5.37. Figure 5.34 depicts the effect of subgrade modulus on the difference between track displacement located on compacted embankment and bridge. Indeed, the differential settlement can be obtained from track displacement on top of an embankment subtracted from track displacement on top of a bridge. It is obvious that at a constant train speed ($V_T = 360$ km/h), as subgrade modulus increases, the differential settlement decreases. Figure 4.35 shows a summary of the differential settlement near the bridge as a function of subgrade modulus. A big gap can be seen between the differential settlement observed in the vicinity of the transition zone when a very soft soil with $E_s = 10$ MPa was modeled in compare to modeling very stiff soil with $E_s = 100$ MPa. As subgrade modulus increases by 10 times, the differential settlement becomes 7.5 times higher. Figure 4.35 depicts that the modulus variation in the vicinity of the transition zone plays an important role in irregularity development. The differential settlement initiates and expands at a higher rate as the difference between soil modulus and bridge modulus increases. Huge differences also can be seen in wheel/rail interaction force and train body acceleration on soft soil vs. stiff soil (Figures 5.36 and 5.37). Even though there is no

irregularity modeled along the rail, considerable wheel/rail interaction force is induced when track is placed on top of soft soil with $E_s=10$ or 20 MPa (Figure 5.36). This force becomes much less as the soil becomes stiffer ($E_s \geq 80$ MPa). As mentioned earlier in this chapter, this wheel/rail interaction force is considered as an influential parameter that accelerates irregularity formation. The results showed that stiff soil in the transition zone can effectively reduce the interaction force and consequently the differential settlement developed as a result of this interaction force. As stated before, train body acceleration is an important part of the analysis to check the level of passenger comfort. Figure 5.37 shows that the subgrade modulus in the vicinity of the transition zone has a great impact on the maximum train body acceleration occurring near the bridge. When subgrades become 10 times softer, the maximum train body acceleration increases by 2 times.

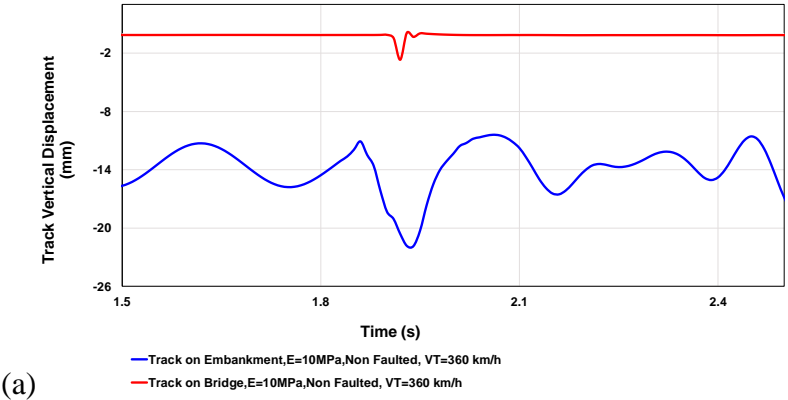


Figure 5.34. Track displacement under the moving load on embankment and bridge sides of the transition at VT=360 km/h, (a) $E_s=10$ MPa, (b) $E_s=20$ MPa, (c) $E_s=80$ MPa, (d) $E_s=100$ MPa

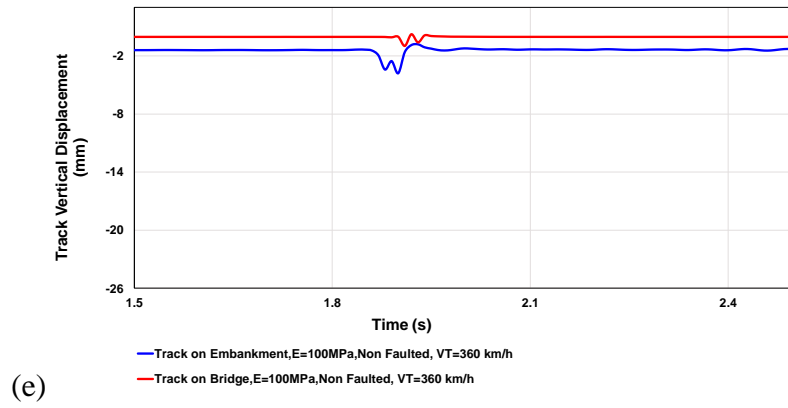
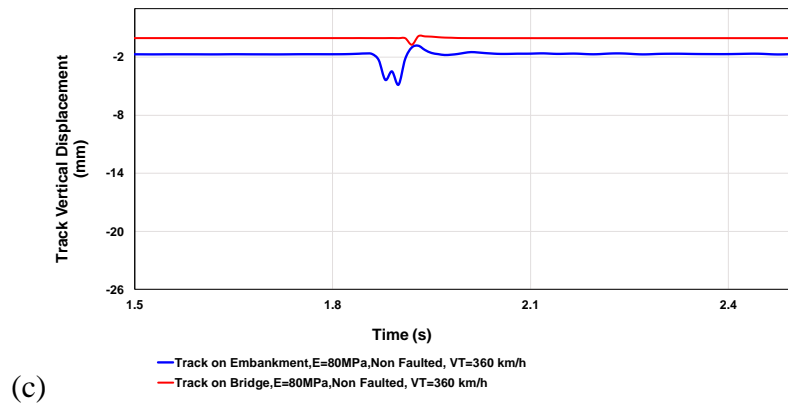
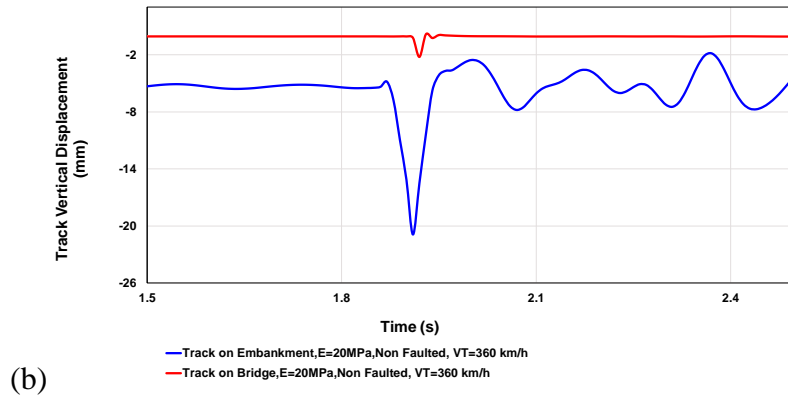


Figure 5.34. Continued

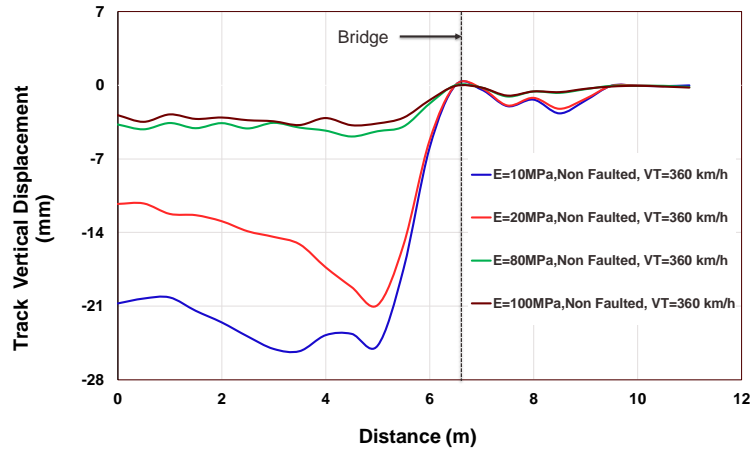


Figure 5.35. Effect of subgrade modulus (E_s) on track vertical displacement in the vicinity of a non-faulted transition zone

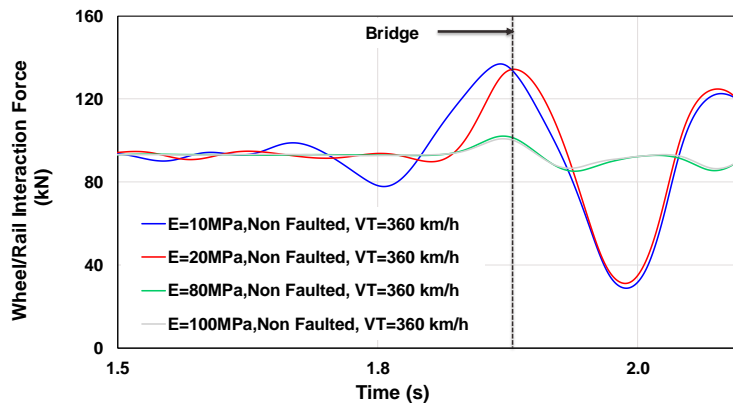


Figure 5.36. Effect of subgrade modulus (E_s) on wheel/rail interaction force

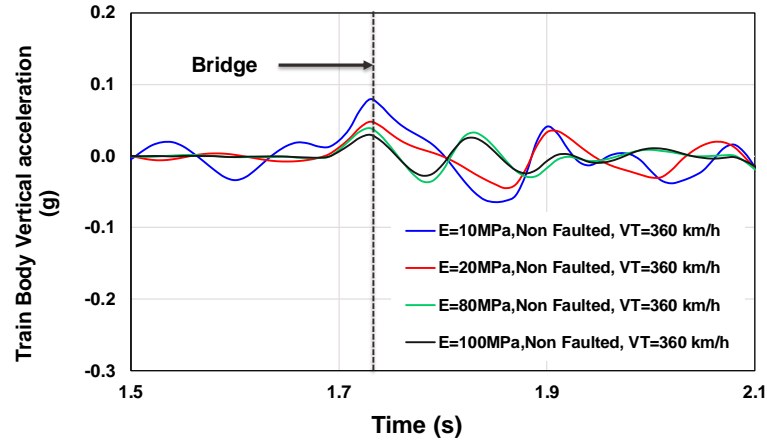


Figure 5.37. Effect of subgrade modulus (E_s) on train body vertical acceleration

A summary of all results considering the effects of both parameters (train speed and subgrade modulus) are plotted in Figures 5.38 and 5.39. Train speed is seen to have a significant impact on DAF and a_{\max} near the bridge when the subgrade modulus is as low as 10 or 20 MPa. These plots showed that although no irregularity exists along the railway line, a considerable interaction force and train body acceleration can be induced at very high train speeds if the track was constructed on top of a very soft soil.

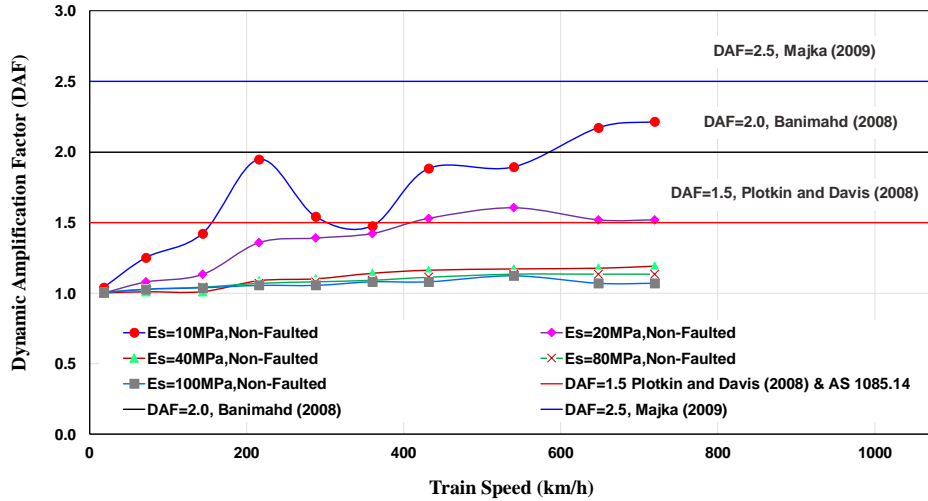


Figure 5.38. Effect of subgrade (E_s) and train speed (V_T) on dynamic amplification factor (DAF)

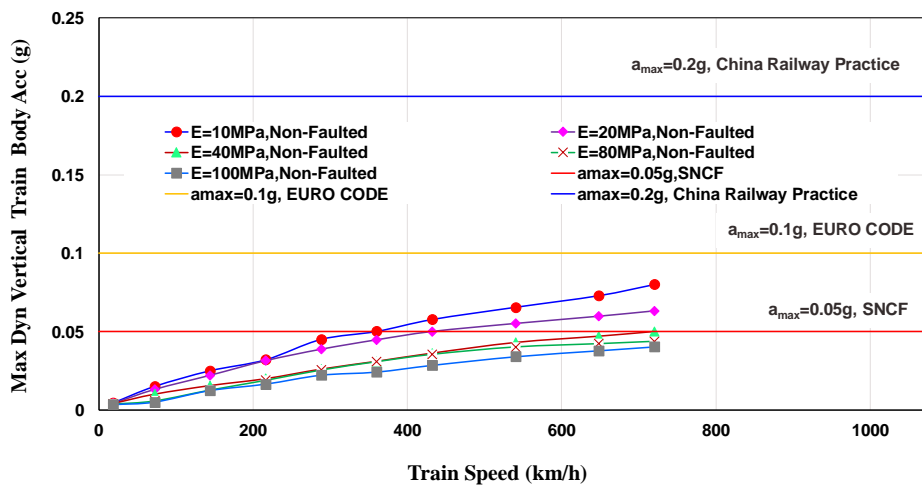


Figure 5.39. Effect of subgrade (E_s) and train speed (V_T) on maximum train body acceleration (a_{max})

5.7.2 Faulted Transition

In second phase of the parametric study, in addition to stiffness variation in the vicinity of the transition zone, different types of irregularities as defined in section 5.6.2 (Table 5.5) with different irregularity sizes (Table 5.6) were modeled. The primary concern of this study was the effect of train speed on the train/track responses, and this will be addressed through this parametric study. In addition to train speed, the other influential parameters evaluated here were irregularity type, irregularity size, and subgrade modulus.

5.7.2.1 Train Speed Effect

In this study, our primary focus was on the effects of train speed on the train/track/soil responses. The verified 4-D FEM of coupled train/track, as fully explained in section 5.6, was used to perform this part of the parametric study. The train and its suspension system were described in section 5.6.3. The type of irregularity modeled along the railway line was rise with irregularity size (s) equal to 400. Rise length was 12 m and rise height was 30 mm. The subgrade modulus is 100 MPa. The only variable is train speed ($18\text{km/h} \leq V_T \leq 720 \text{ km/h}$). In these simulations, the truck is moving from the approach embankment onto the bridge at different train speeds (V_T).

The resulting track displacement, vertical train body acceleration, and wheel/rail interaction forces are shown in Figures 5.40, 5.41, and 5.42, respectively. It should be

noted that in these figures, the direction of train motion is from left (the approach) to right (the bridge). Figure 5.40(a) illustrates the effect of train speed on the track displacement along the track. To see the effect of train speed (V_T) on track displacement clearly, the absolute displacement without considering the track profile along the irregularity was shown in Figure 5.40(b). Obviously, as train speed increases the track displacement increases. Also, as a train approaches the bridge, in the vicinity of the transition zone, the track displacement decreases gradually. The track displacement increased approximately 1.75 times when train speed increased from 72 km/h to 432 km/h. The reason is postulated as follows: This phenomenon could occur because as train speed increases and passes the quasi-static train speed zone, track and soil under the track will experience a large deflection due to wave propagation. This was fully explained earlier in section 4. Also, If the soil is more compressible, the settlement of the track in the embankment zone is larger, and thus a bigger irregularity is created when coming onto the bridge.

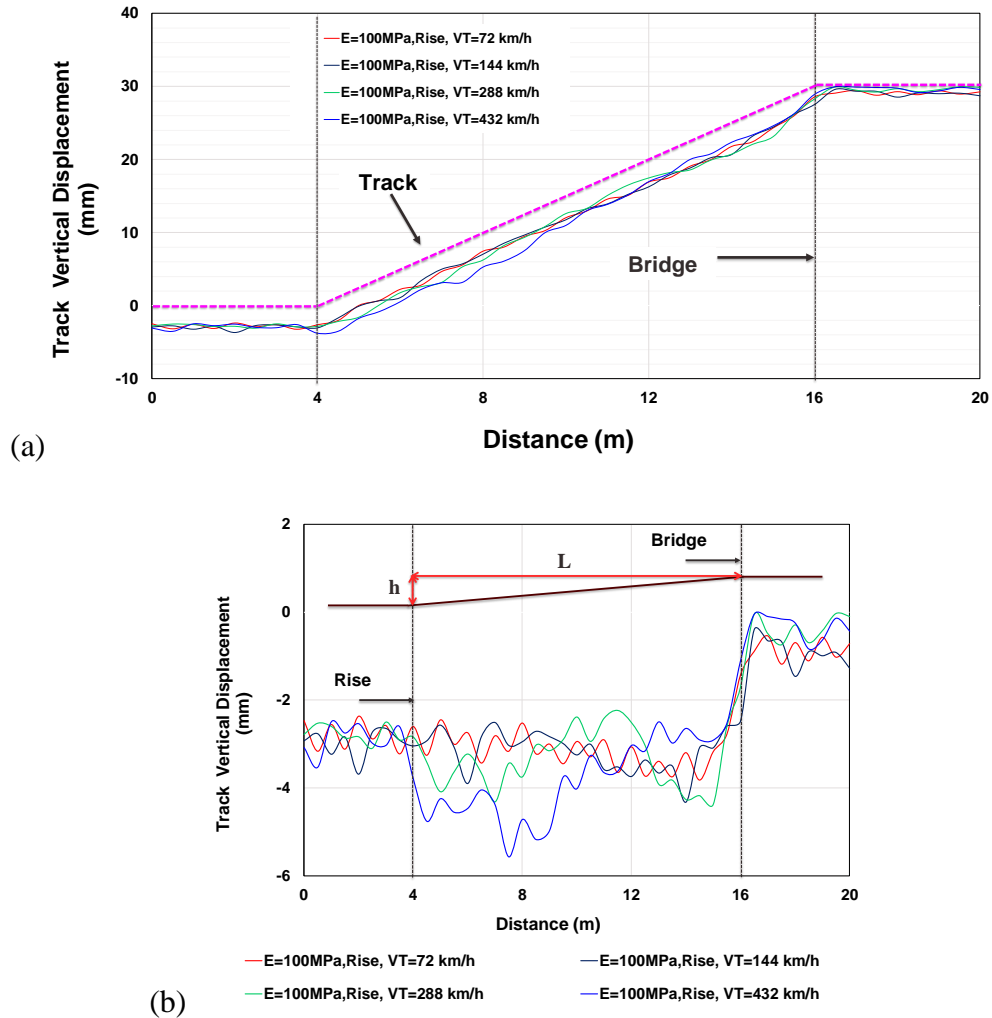


Figure 5.40. Track displacement along track as a function of train speed, (b) zoom on track displacement along irregularity (rise)

Train body acceleration and wheel/rail interaction force along the track near the bridge were plotted for four different train speeds ($V_T = 72, 144, 288, 432$ km/h) in Figures 5.41 and 5.42, respectively. The first impact seen in these figures represents the train wheels hitting the rise, and the second impact force is due to the abrupt change in track modulus near the bridge. The maximum value for vertical train body acceleration and

wheel/rail interaction force occurs almost at the beginning of the irregularity. As train speed increases, both vertical train body acceleration and wheel/rail interaction force increases (as expected). A full set of results, including dynamic amplification factor and maximum train body acceleration as a function of train speed for a wide range of train speeds ($18 \leq V_T \leq 720$), are displayed in Figures 5.43 and 5.44.

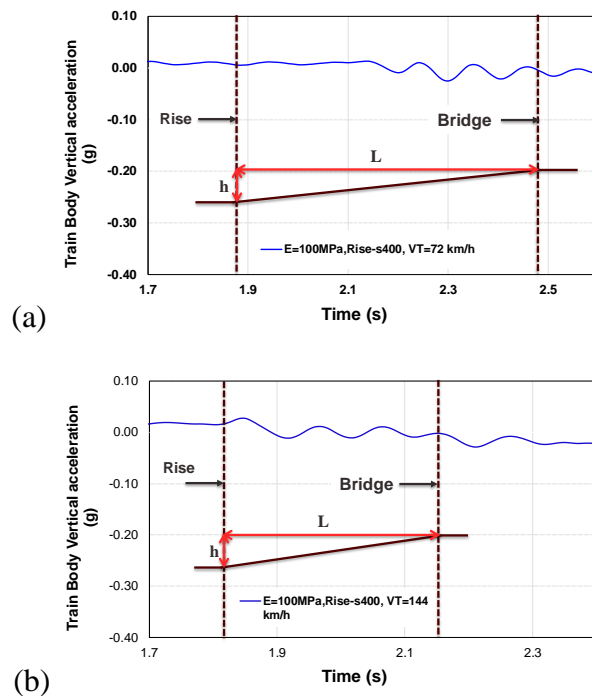


Figure 5.41. Effect of train speed on train body acceleration at (a) $V_T=72$ km/h, (b) $V_T=144$ km/h, (c) $V_T=288$ km/h, (d) $V_T=432$ km/h

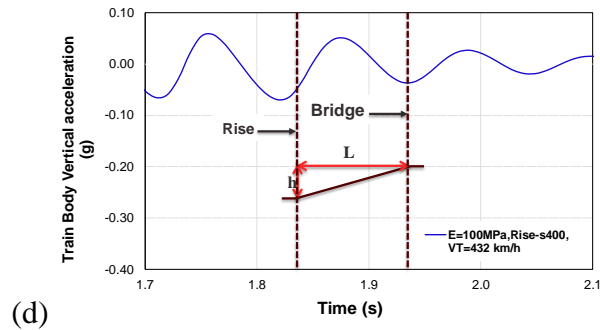
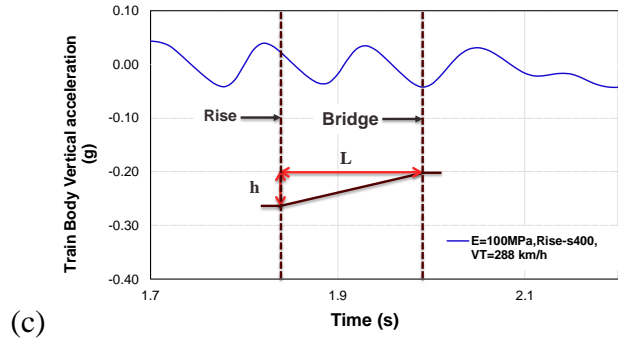


Figure 5.41. Continued

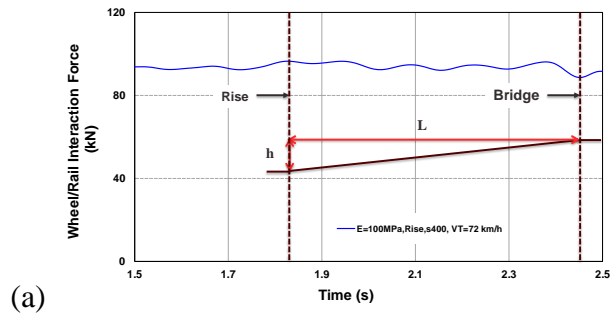


Figure 5.42. Effect of train speed on wheel/rail interaction force at (a) VT=72 km/h, (b) VT=144 km/h, (c) VT=288 km/h, (d) VT=432 km/h

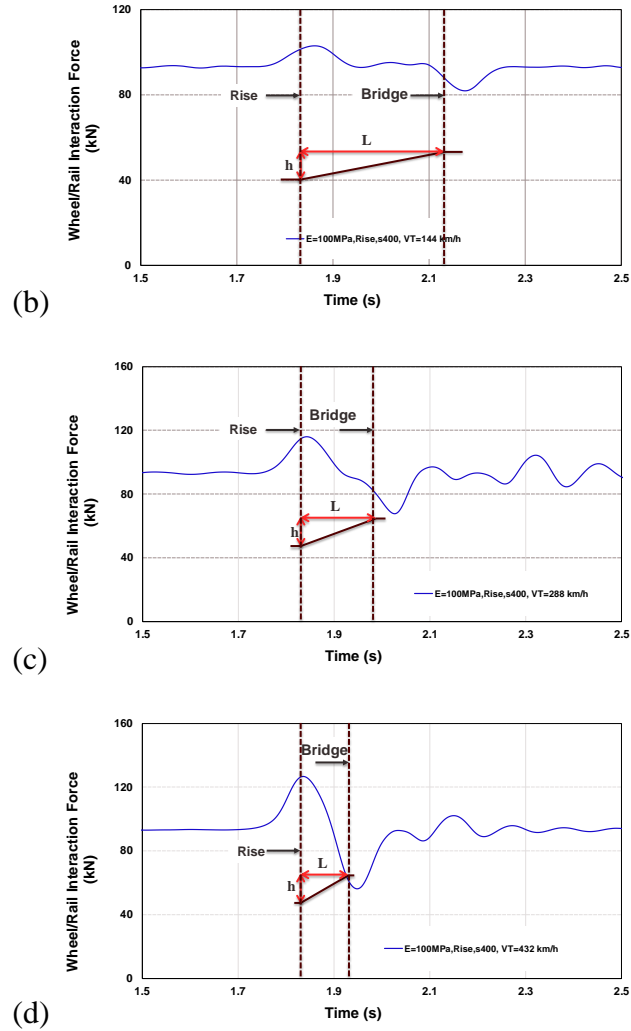


Figure 5.42. Continued

This phenomenon becomes much more severe when an irregularity exists in addition to modulus changes near the bridges. Figures 5.43 and 5.44 also illustrate the comparison between two models: with irregularity and without irregularity along the HSR line. Comparing the results of first phase (non-faulted track) to the results of second phase (faulted track) shows that in addition to train speed, irregularity plays an important role in

train/track responses. The effect of irregularity sizes and types will be addressed in the next section. It should be noted that the difference between the results for two cases (faulted and non-faulted track) increases as train speed increases. For example, a stiffness variation along with a 1:400 rise in the track produced approximately a 22% increase in the load when train speed is 432 km/h. At a higher train speed (VT=720 km/h) the load increases by 48% when both stiffness change and rise exist along the track compared to when there is only a track stiffness change along the track in the vicinity of transition zones. The same result can be seen when the maximum train body acceleration for two cases, faulted and non-faulted track, are compared. At 720 km/h, the maximum train body acceleration for stiffness change along with a 1:400 rise in the track is almost 4.43 times greater than the case where there was only stiffness change (non-faulted track).

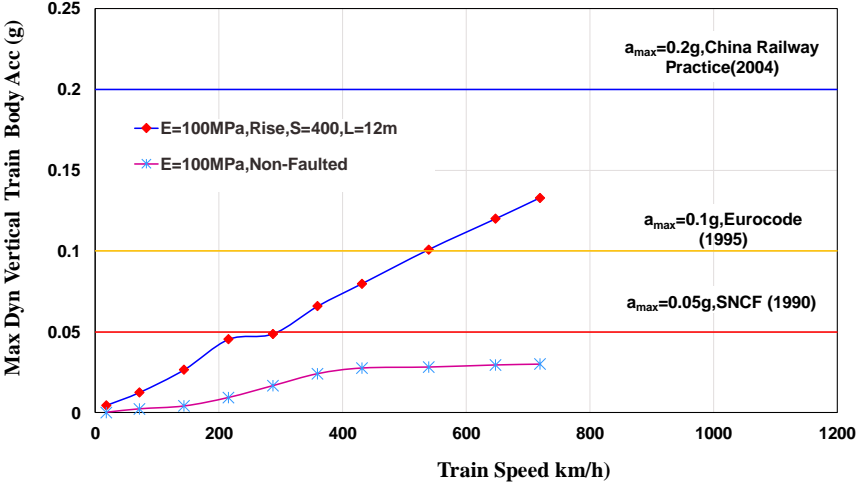


Figure 5.43. Maximum train body acceleration vs. train speed

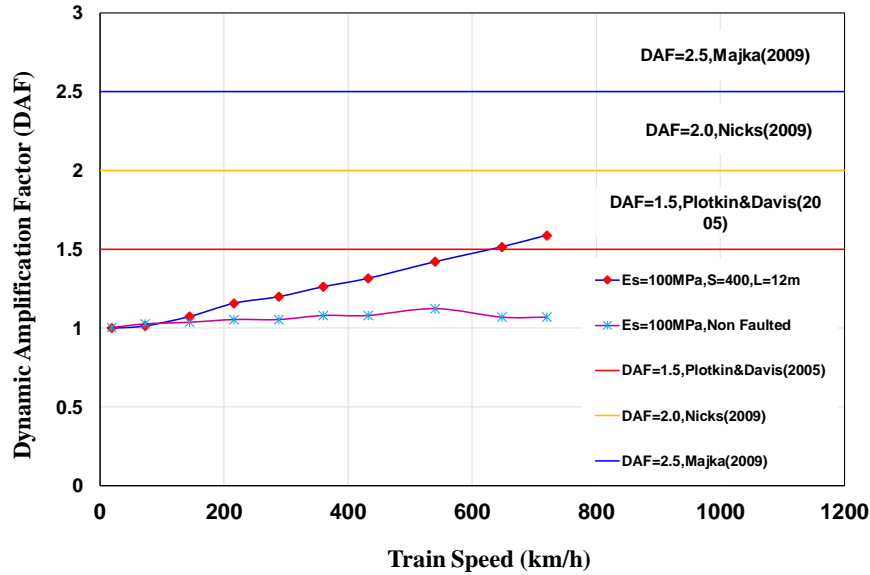


Figure 5.44. Dynamic amplification factor (DAF) vs. train speed

5.7.2.2 Irregularity Size Effect

According to Equation 5.3, irregularity size is defined with two variables (irregularity length and irregularity height) that may have impacts on the train/track responses. In this study, the effect of both variables on the dynamic amplification factor and maximum train body acceleration were investigated. To evaluate the influence of irregularity size, the same model as explained in section 5.7.2.1 was used to perform the study. Table 5.6 shows how two variables were selected to have a wide range of irregularity sizes. To compare the effect of irregularity size, other parameters like irregularity type, train speed, and subgrade modulus were assumed to be constant; i.e., irregularity type: rise, $V_T=360$ km/h, and $E_s=100$ MPa. The effect of irregularity size on the train/track responses was assessed first by keeping the length (L) of the rise the same

($L=12$ m) and varying the height (h) to reach the desired rise size (Table 5.6). It was expected that the train track responses including track deflection, wheel/rail interaction force, and maximum train body acceleration become more severe with a steeper irregularity slope (lower irregularity size) than a shallow irregularity slope.

A set of plots for track displacements, vertical train body accelerations, and wheel/rail interaction forces for each rise size at a train speed of 360 km/h are presented in Figures 5.45 to 5.47. Figure 5.45 (a) illustrates the track deflection along the track profile. As with Figure 5.45 (a), as rise size increases (lower rise slope), the track displacement decreases as it was expected before. In Figure 5.45 (b), the track displacement along the rise is displayed in detail. The track displacement near the bridges is noticeably less than track displacement on the compacted embankment. Particularly, the track displacements at the beginning of the rise length to mid length are much more significant than the track displacement on the compacted embankment near the bridge. This difference between track displacement at different locations along the rise length is more severe when the rise slope increases. The same trend can be followed in Figures 5.46 and 5.47, showing the vertical train body accelerations and wheel/rail interaction forces as functions of rise size. It was mentioned in section 5.7.2.1 that particularly for steeper irregularities, the maximum force and train body acceleration occurring along the irregularity length are caused by the geometry change, not by the track modulus differential in the vicinity of the transition zone.

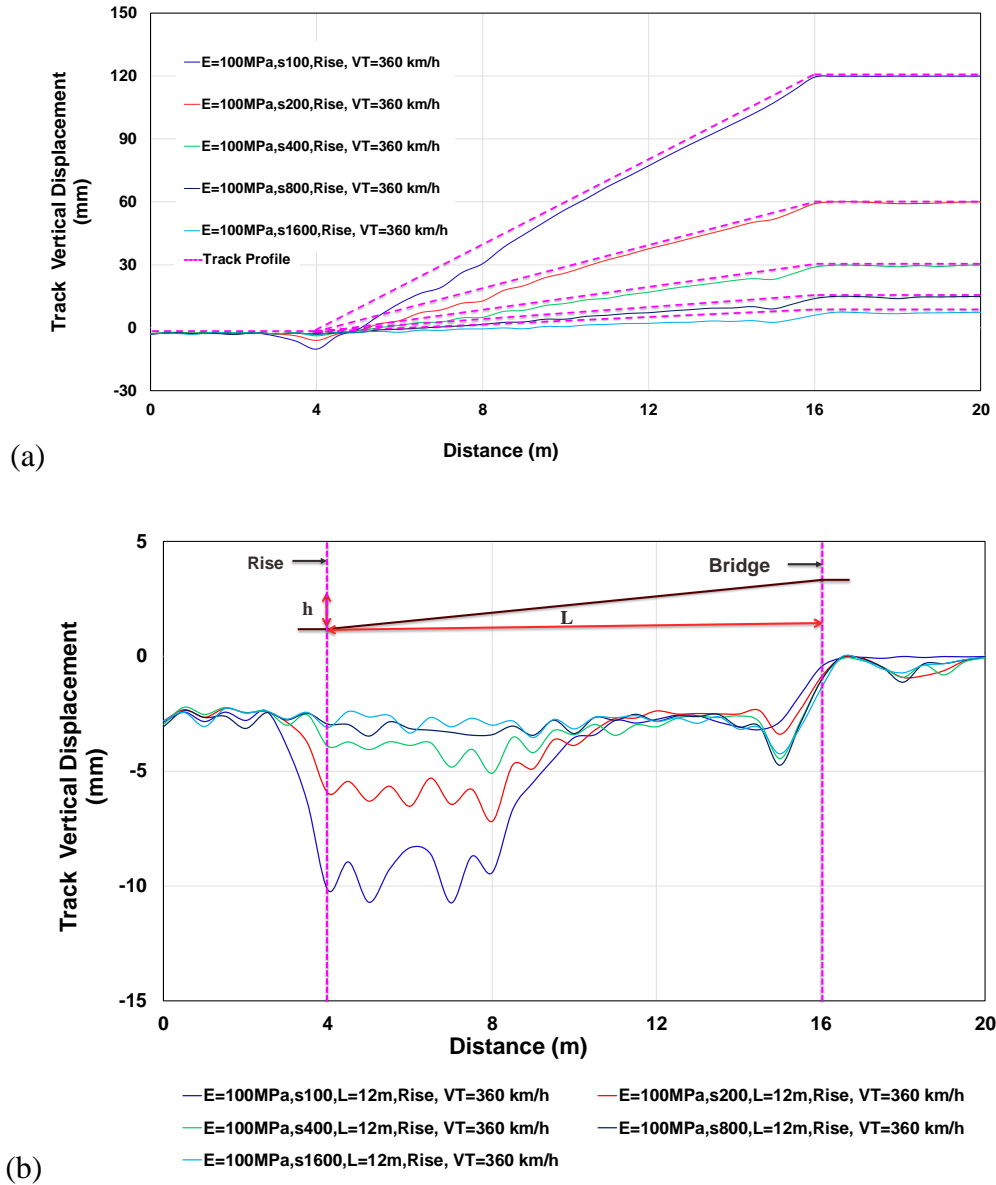


Figure 5.45. Track displacement comparison for different irregularity (rise) sizes of equal length ($L=12$ m) (a) along the track profile, (b) zoom on displacement along irregularity length

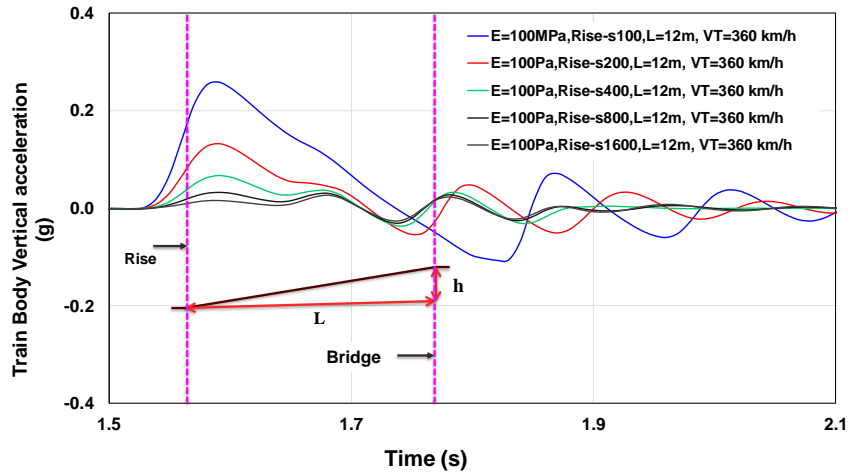


Figure 5.46. Train body acceleration comparison for different irregularity (rise) sizes of equal length ($L=12\text{ m}$)

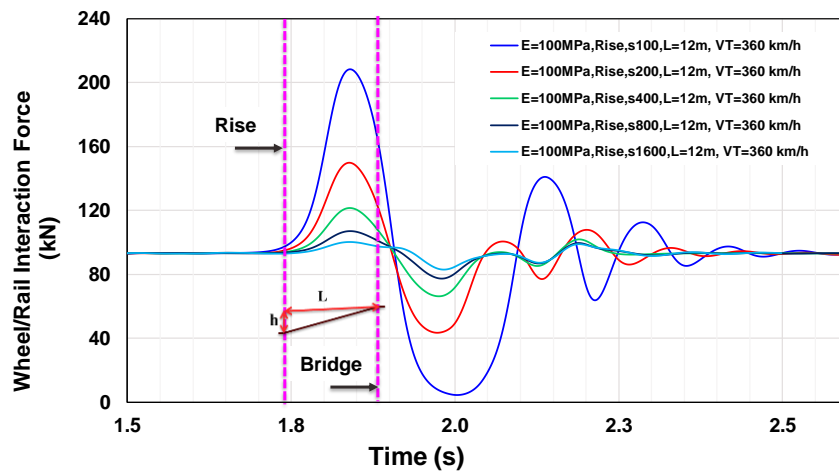


Figure 5.47. Wheel/rail interaction force comparison for different irregularity (rise) sizes of equal length ($L=12\text{ m}$)

The results for the a_{\max} and DAF for different rise sizes with equal length at different train speeds are summarized in Figures 5.48 and 5.49, respectively. As mentioned earlier, the a_{\max} and DAF increase as the rise slope increases (and the rise size decreases). In other words, considering an equal rise length ($L=12\text{ m}$), the higher rise height results in

higher train/track responses. Also, it can be clearly seen that with the increase in train speed, the train/track responses increase considerably.

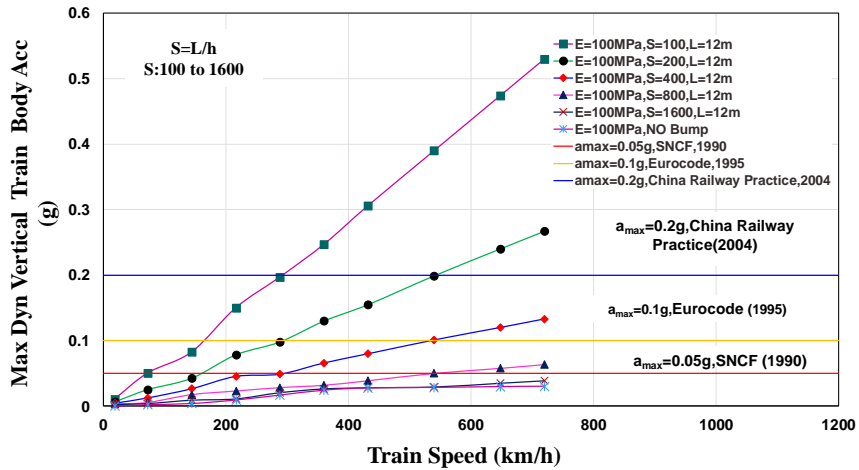


Figure 5.48. Maximum train body acceleration vs. train speed comparison for various rise sizes of equal rise length (L=12 m)

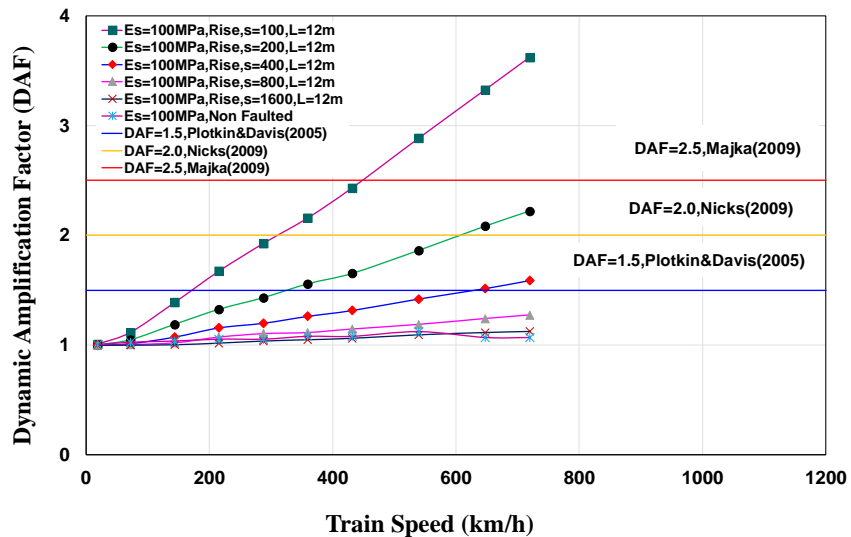


Figure 5.49. Dynamic amplification factor (DAF) vs. train speed comparison for various rise sizes of equal rise length (L=12 m)

As mentioned at the beginning of this section, in the current study the effect of the parameters irregularity length (L) and irregularity height (h) on the track responses were investigated. To check the effect of irregularity size, the same model used to determine the effect of irregularity height was applied. The length of irregularity was changed to check the influence of L on the a_{\max} and DAF for different rise sizes (Figure 5.50). a_{\max} and DAF obtained from simulations with different rise sizes are shown in Figures 5.51 and 5.52, respectively. The results illustrate that the DAF and a_{\max} increase as the irregularity size increases; however, the effect of the irregularity length on the DAF is negligible. It can be observed that an increase in the deflection spanning length (irregularity length) results in a decrease in the transition DAF and a_{\max} for a given deflection difference (irregularity height) and train speed. This change, however, is not significant compared to the effect of irregularity height and train speed. Indeed, the height and length of the irregularity are not as important as the overall slope (Nicks 2009).

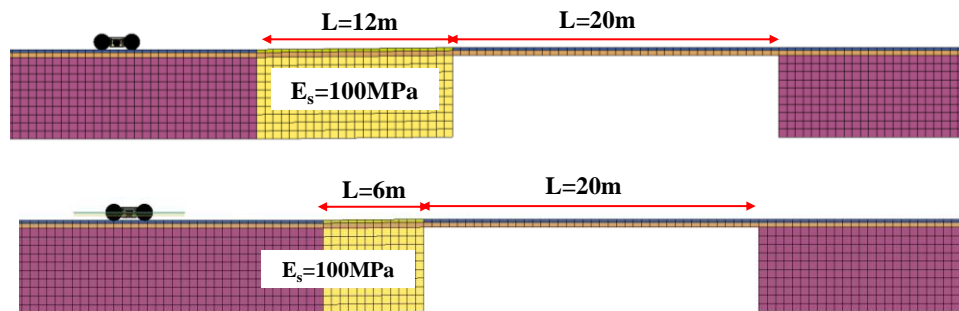


Figure 5.50. Cross-section view of the FEM used to assess the effect of irregularity length (L)

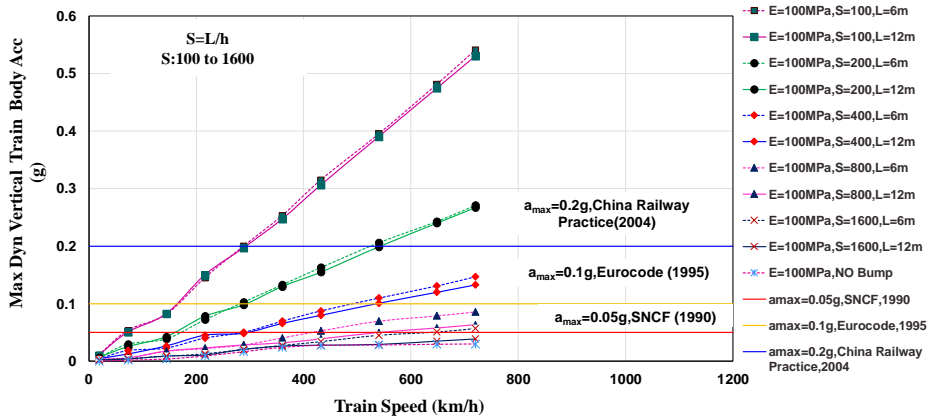


Figure 5.51. Maximum train body acceleration vs. train speed comparison for various rise sizes (effect of bump length (L) and bump height (h))

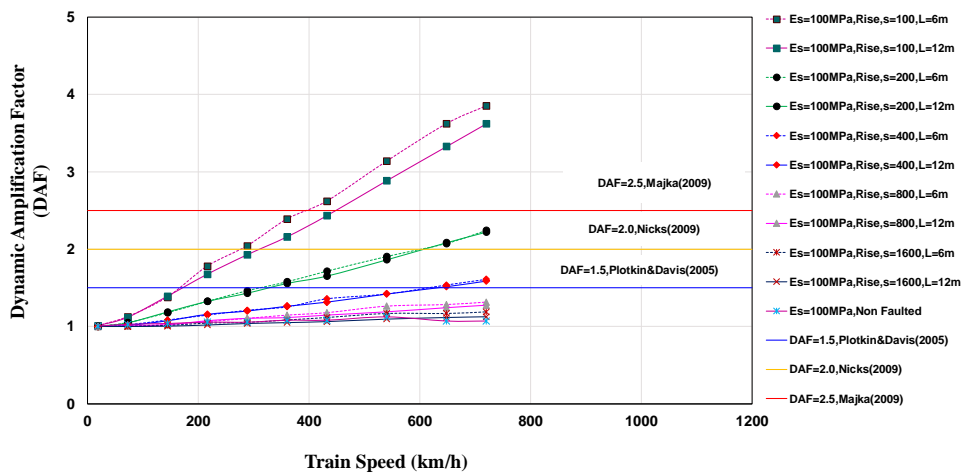


Figure 5.52. Dynamic amplification factor (DAF) vs. train speed comparison for various rise sizes (effect of bump length (L) and bump height (h))

5.7.2.3 Irregularity Type Effect

Different types of irregularities that may occur along railway lines (Table 5.5) were modeled in LS-DYNA. Cross-sectional views of four different finite element models of irregularities along high-speed railway lines are shown in Figure 5.53. First, to investigate

the effect of irregularity shape on the track/train responses, other parameters including train speed, subgrade modulus, and irregularity size were considered to stay constant ($V_T=360$ km/h, $E_S=100$ MPa, and $s=400$). The resultant track displacement, vertical train body acceleration, and wheel/rail interaction force obtained from the simulations are plotted in Figures 5.54, 5.55, and 5.56, respectively.

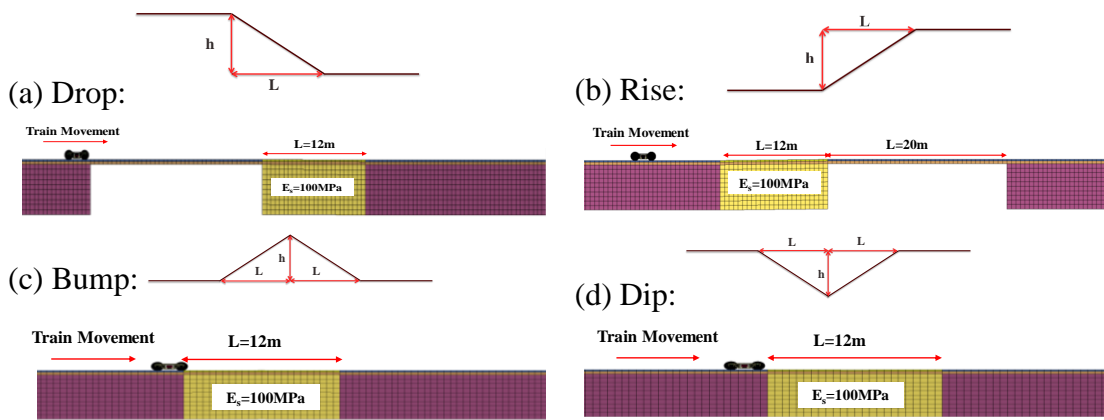


Figure 5.53. Cross-section view of the FEMs used to assess the effect of irregularity Types (a) Drop, (b) Rise, (c) Bump, (d) Dip

As with Figure 5.54, the patterns of displacements along the track profile with various types of irregularities are different. It seems that the displacement pattern of track with rise mirrors the displacement pattern of track with drop (Figure 5.54 (a) and (b)). The maximum track displacement values are almost the same for these two cases, and maximum displacement occurs at the beginning of the rise and the end of the drop profile. As seen in Figure 5.54 (c) and (d), the same mirror displacement pattern can be seen for dip and bump along the track. It is interesting to note that for bump, the track displacement

actually decreases dramatically at the drop slop of the bump very close to the end of the bump. This becomes more severe when the irregularity slope and train speed increase where the track displacement goes to zero. This occurs because there is not full contact between the train and the track at this location, which could pose a serious danger. The same phenomenon happens for dip but at a different location: at the drop slope of the dip very close to the beginning of the dip. Indeed, the track displacements for bump and dip are very similar to the combination of drop and rise slopes together.

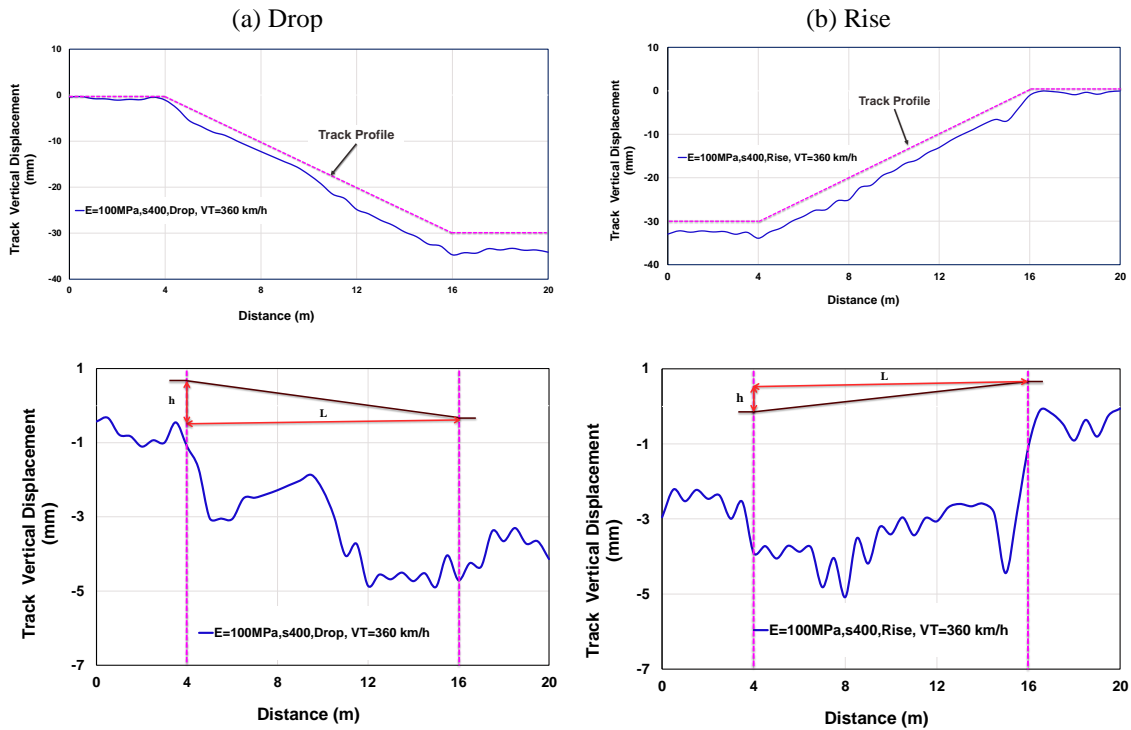


Figure 5.54. Track displacement comparison for different irregularity types of equal irregularity size ($s=400$) at train speed of 360 km/h (a) Drop, (b) Rise, (c) Bump, (d) Dip

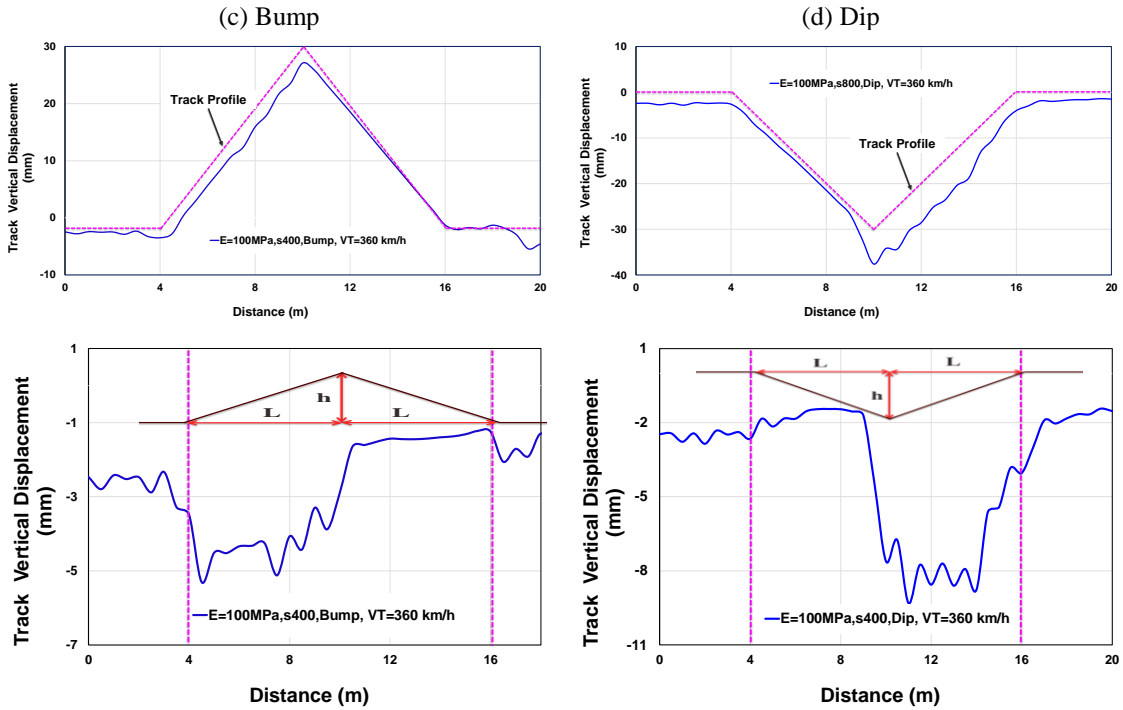
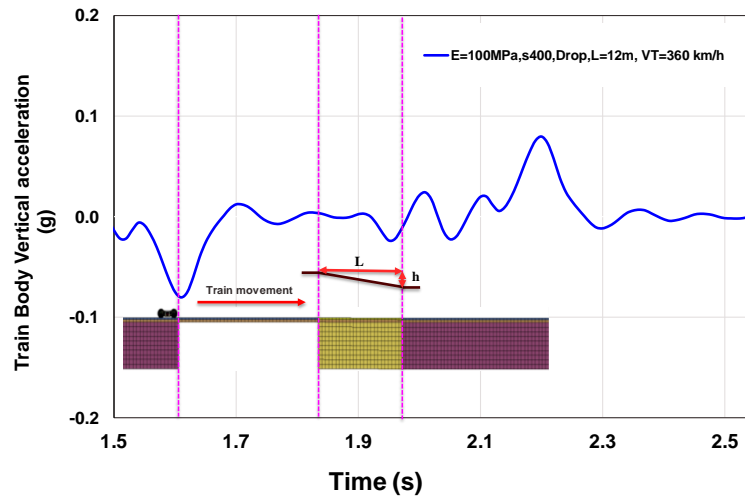


Figure 5.54. Continued

Figure 5.55 and 5.56 illustrate the comparison of train body acceleration and wheel/rail interaction force along the irregularity profile for various irregularity shapes. It was not easy to find a clear pattern for these two parameters versus irregularity shapes. At high speeds like 360 km/h, it was much more difficult to understand the obvious pattern for train body acceleration and wheel/rail interaction force, particularly for dip and drop shapes where at some point the wheel/rail contact force becomes zero when there is not full contact between wheel and rail.

(a) Drop



(b) Rise

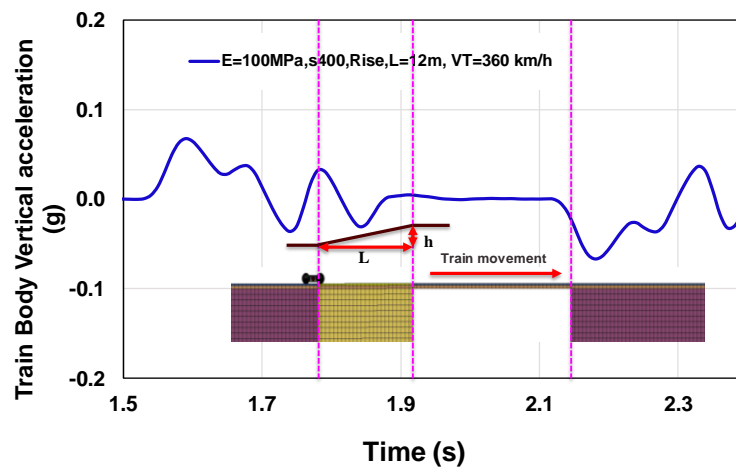
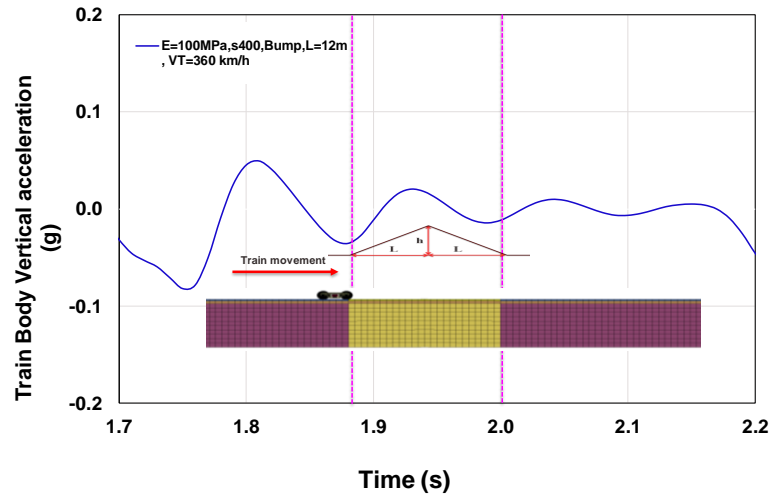


Figure 5.55. Vertical train body acceleration comparison for different irregularity types of equal irregularity size ($s=400$) at train speed of 360 km/h (a) Drop, (b) Rise, (c) Bump, (d) Dip

(c) Bump



(d) Dip

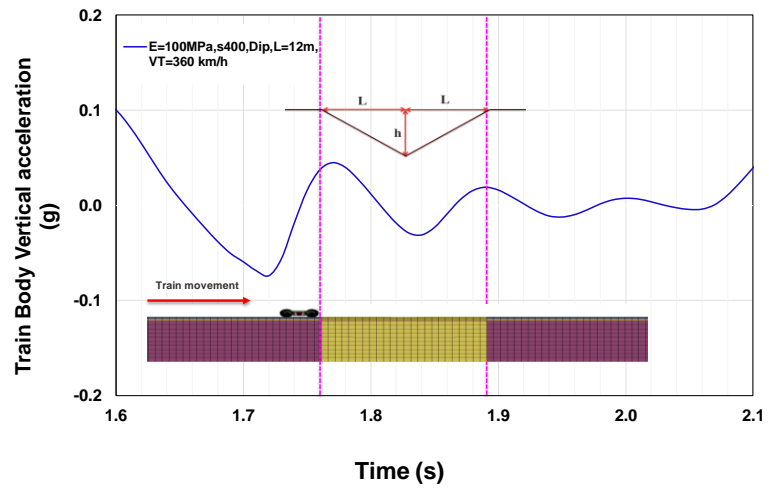
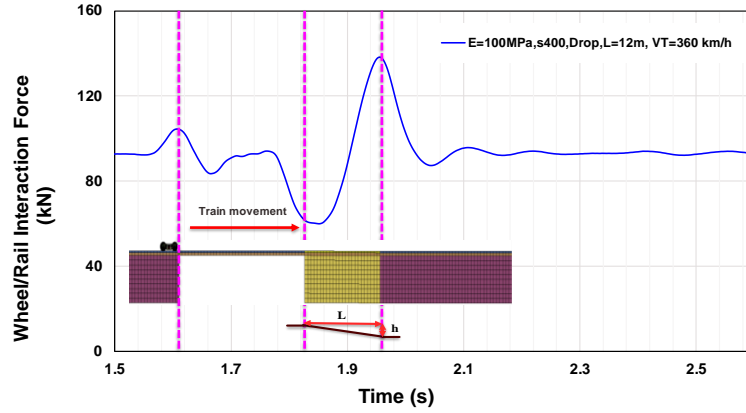
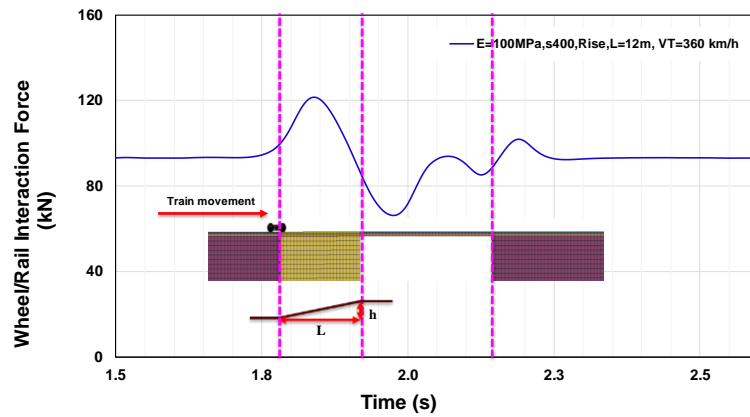


Figure 5.55. Continued

(a) Drop



(b) Rise



(c) Bump

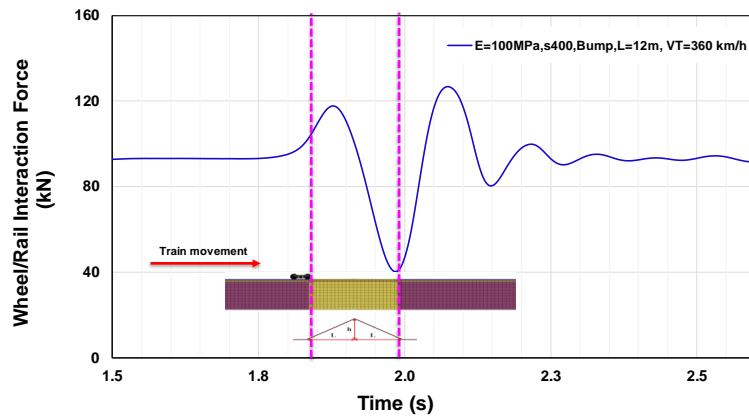


Figure 5.56. Wheel/rail interaction force comparison for different irregularity types of equal irregularity size ($s=400$) at train speed of 360 km/h (a) Drop, (b) Rise, (c) Bump, (d) Dip

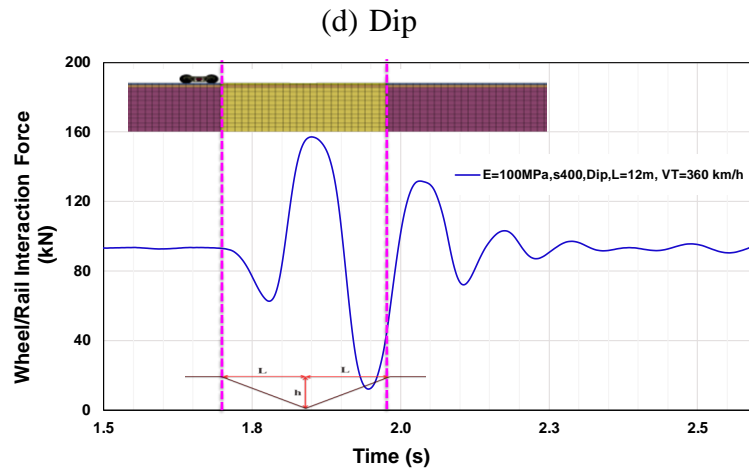


Figure 5.56. Continued

To have a better understanding, the a_{\max} and DAF for different irregularity types at various train speeds are summarized in Figures 5.57 and 5.58, respectively. Compared to the cases with non-faulted track and stiffness variation at transition, the a_{\max} and DAF are considerably higher. At lower train speeds, irregularity shape does not have a noticeable effect on the train/track responses. However, at higher train speeds, differences in irregularity shape have significant impacts on the resultant a_{\max} and DAF. Figures 5.59 and 5.60 show the a_{\max} and DAF as functions of train speed for different irregularity sizes and shapes. It can be seen clearly that the irregularity size and train speed have more considerable impact than irregularity type on the train/track responses. A summary of the tolerable irregularity size considering two criteria, DAF and a_{\max} , will be presented in section 5.8.

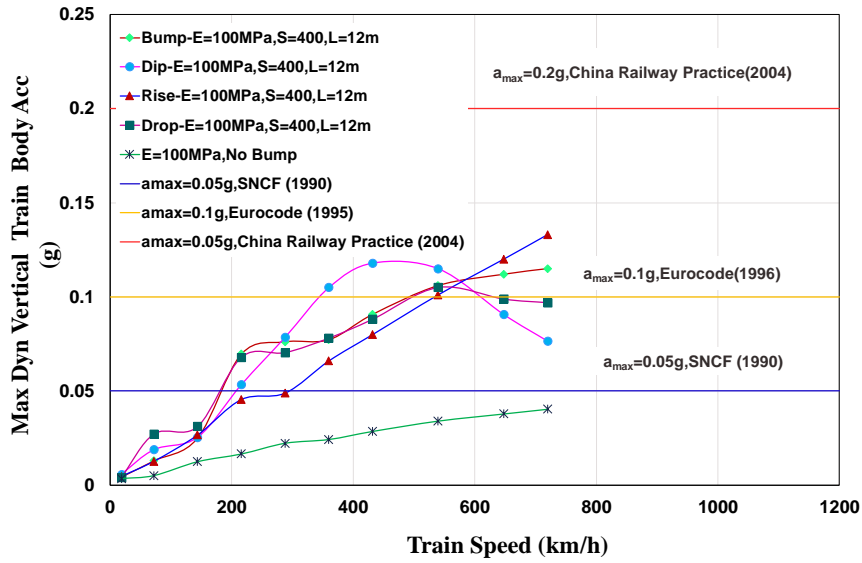


Figure 5.57. Maximum train body acceleration vs. train speed comparison for various irregularity types

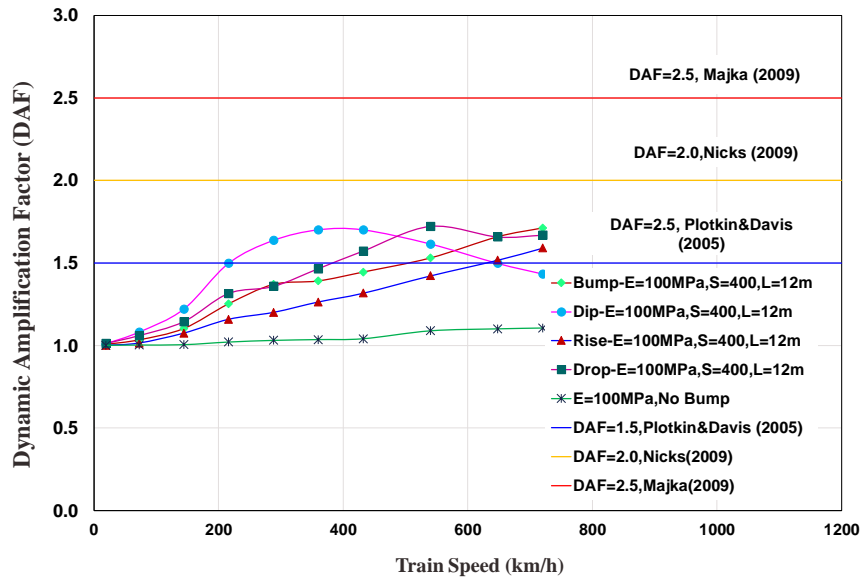


Figure 5.58. Dynamic amplification factor (DAF) vs. train speed comparison for various irregularity types

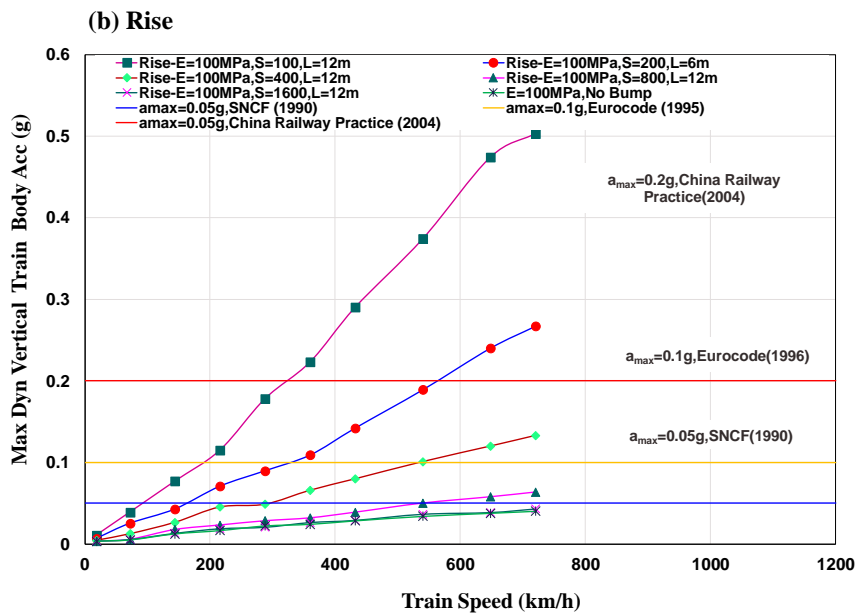
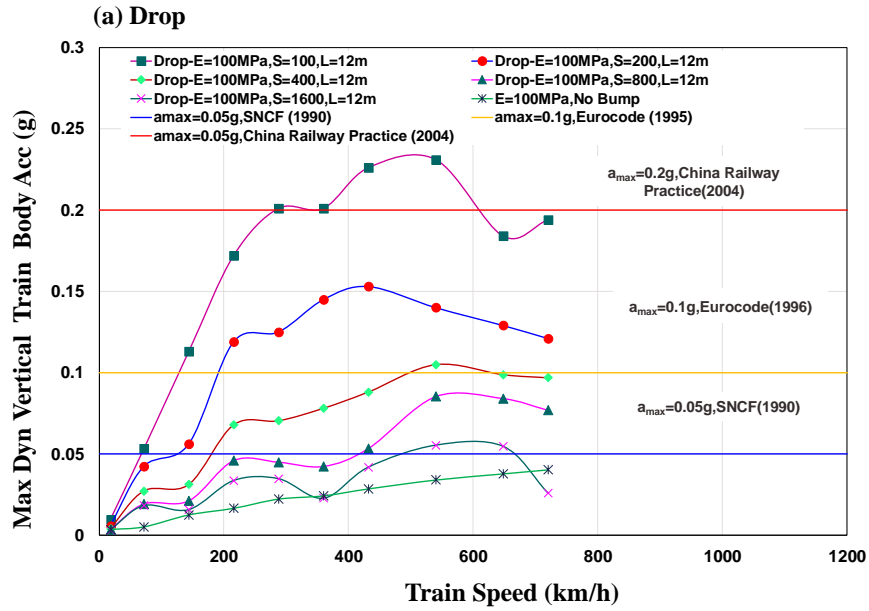


Figure 5.59. Maximum train body acceleration vs. train speed comparison for various irregularity types and irregularity sizes (a) Drop, (b) Rise, (c) Bump, (d) Dip

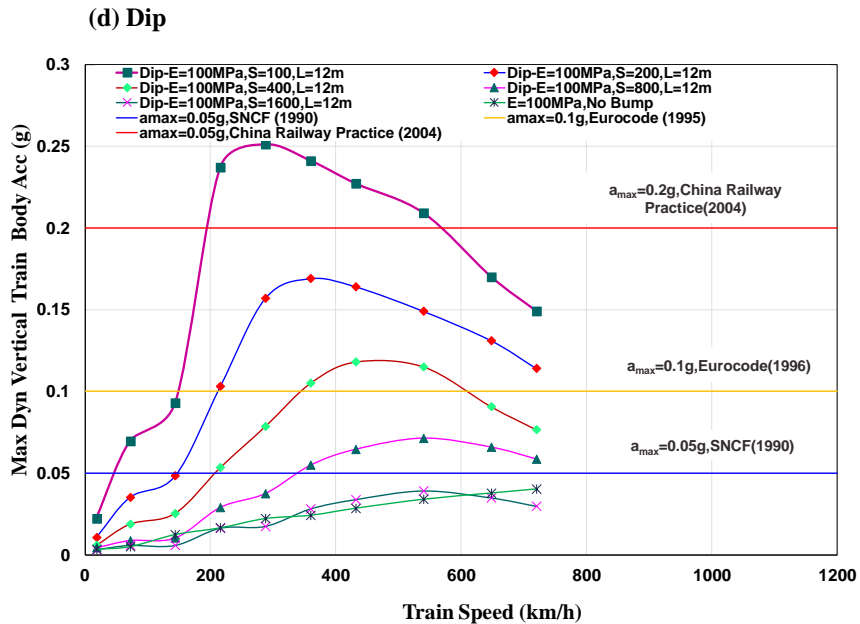
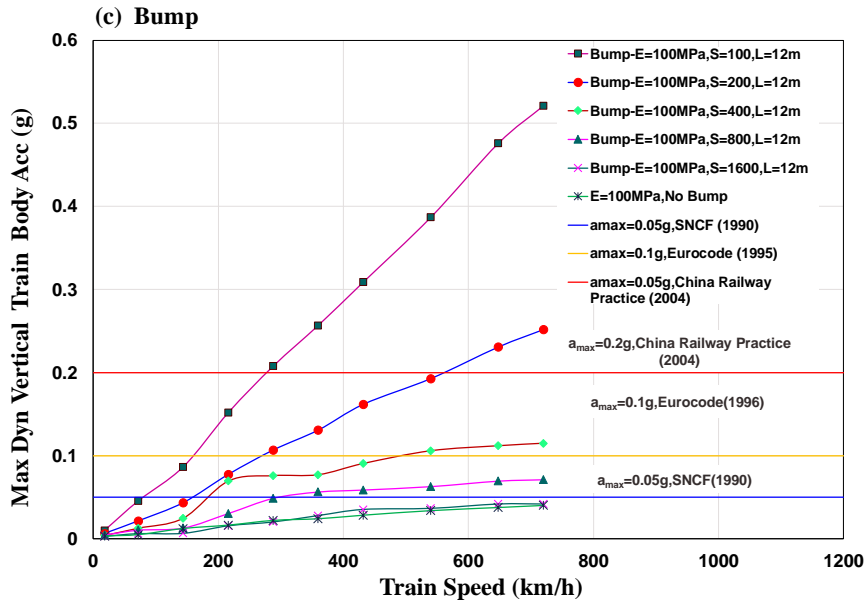


Figure 5.59. Continued

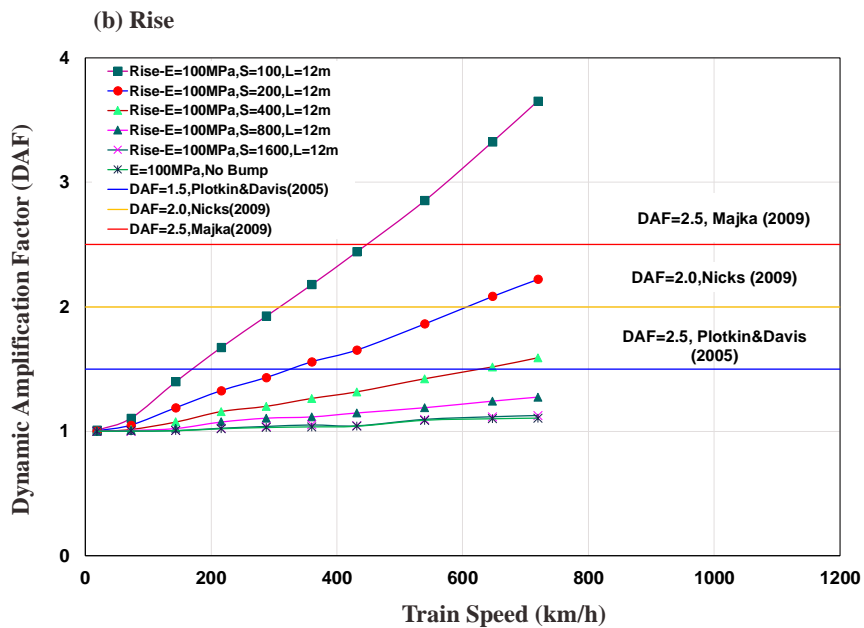
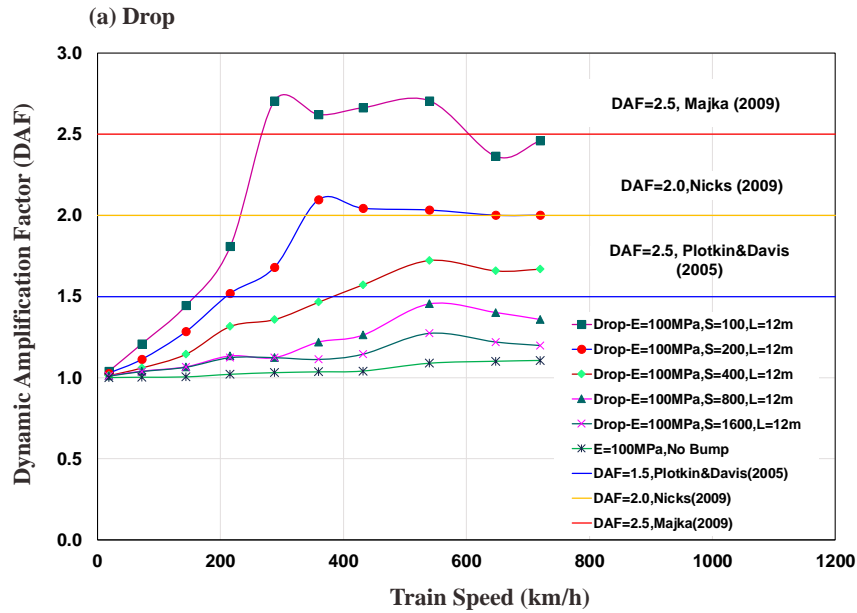


Figure 5.60. Dynamic amplification factor (DAF) vs. train speed comparison for various irregularity types and irregularity sizes (a) Drop, (b) Rise, (c) Bump, (d) Dip

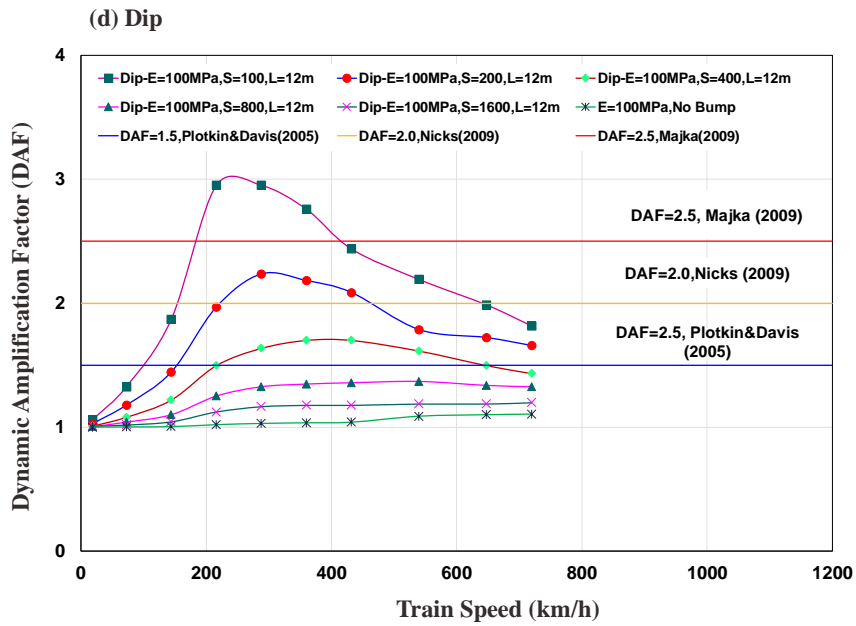
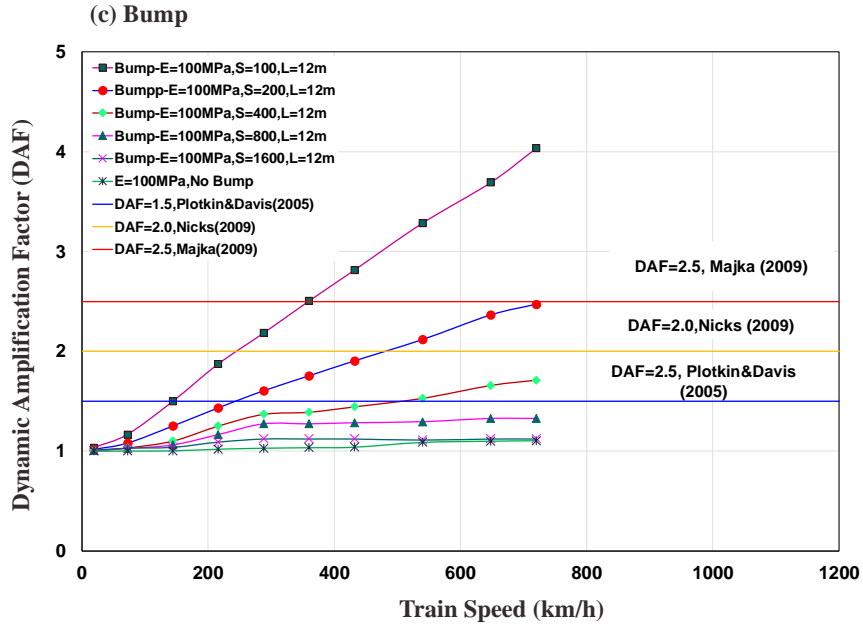
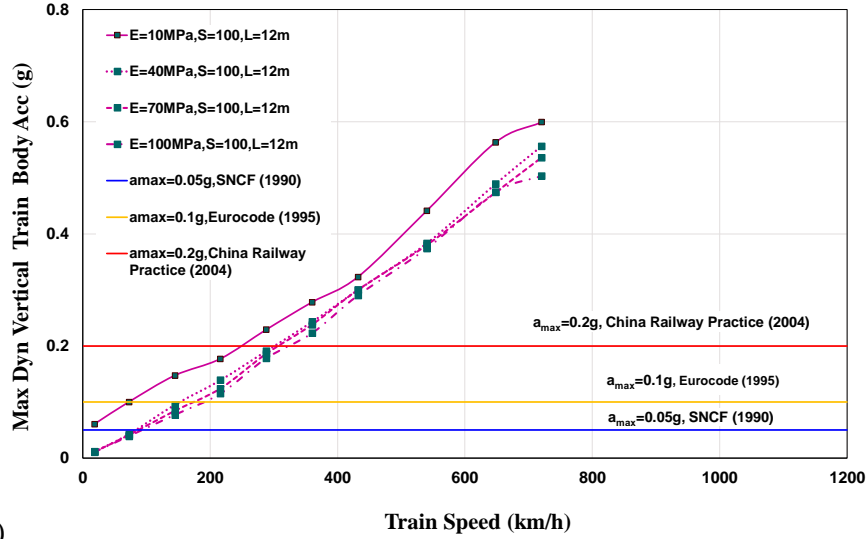


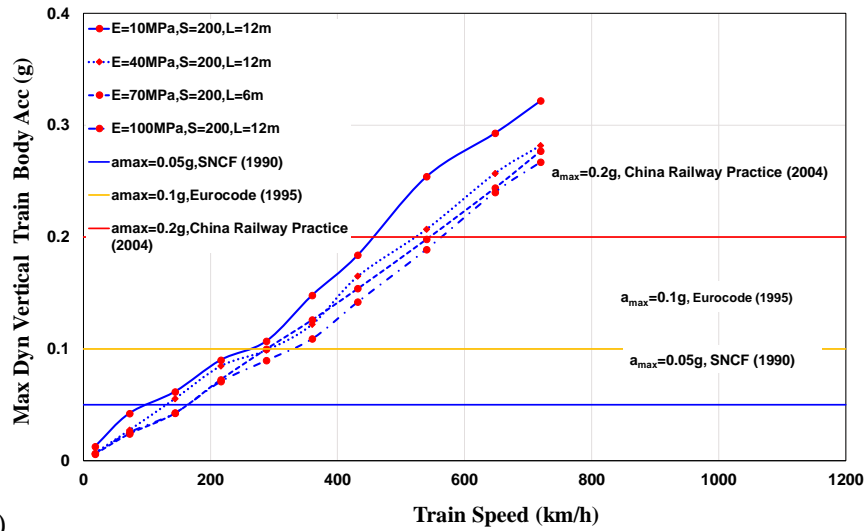
Figure 5.60. Continued

5.7.2.4 Subgrade/Fill Modulus Effect

It was mentioned that the modulus of the subgrade and embankment, if it is thick enough, has a dominant influence on the track modulus (Selig and Li 1994). In section 5.7.1.2 described how changing the soil modulus has an impact on the train/track responses when there is no irregularity along the HSR. The effect of subgrade modulus can be much more significant on the train/track responses for faulted tracks. In this section, the effect of subgrade modulus variation when an irregularity is modeled will be addressed. In this case study, subgrade moduli of 10 MPa, 40 MPa, 70 MPa, and 100 MPa were evaluated for various rise sizes with an equal rise length of 12 m. The train speed varies from 18 km/h to 720 km/h. A summary of results including maximum train body acceleration and dynamic amplification versus train speeds for different rise sizes obtained from 200 simulations are shown in Figures 5.61 and 5.62, respectively. As with Figure 5.61 and 5.62, the maximum train body acceleration and wheel/rail impact due to the subgrade modulus variation is much stronger for a soft soil with a low modulus than for a stiff soil; on the other hand, these plots illustrate that the rise in general irregularity size plays a more crucial role than changes in subgrade modulus. The results also show that reducing the track modulus differential between the approach embankment and bridge will lead to less impact forces and maximum train body acceleration.

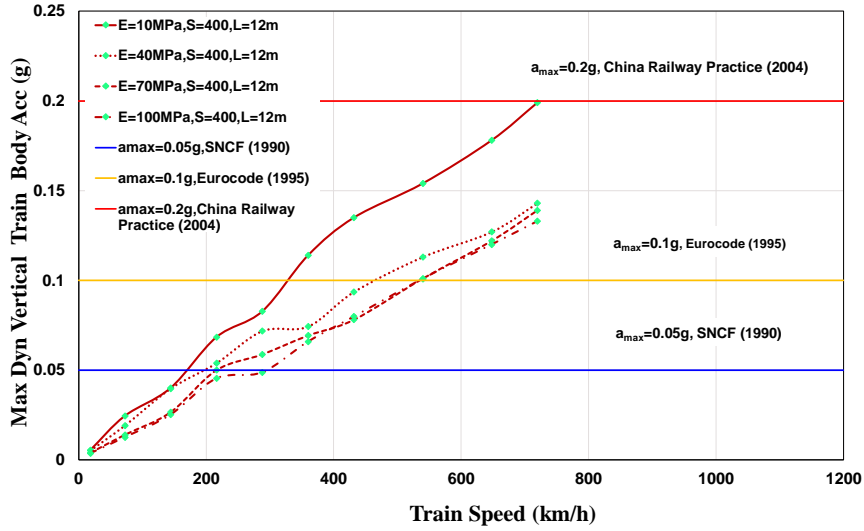


(a)

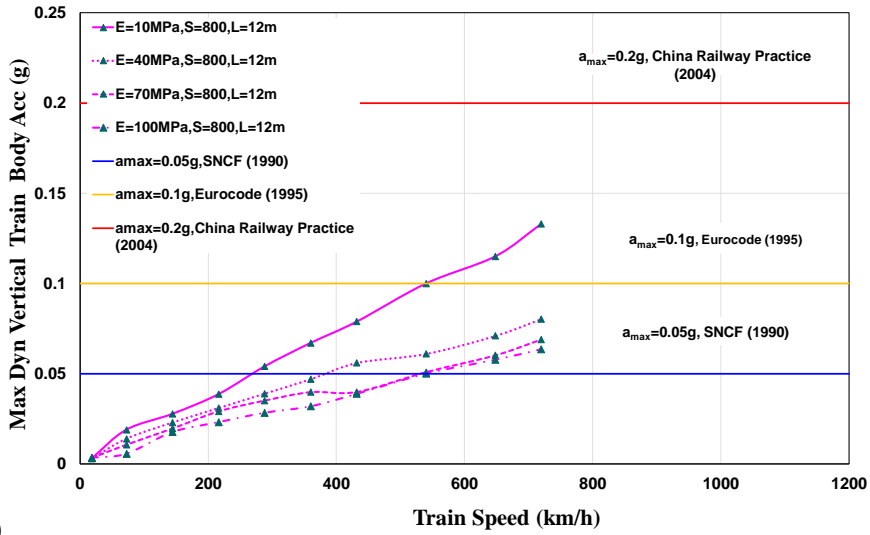


(b)

Figure 5.61. Maximum train body acceleration vs. train speed comparison for subgrade modulus changes and various irregularity sizes (a) $s=100$, (b) $s=200$, (c) $s=400$, (d) $s=800$, (e) $s=1600$



(c)



(d)

Figure 5.61. Continued

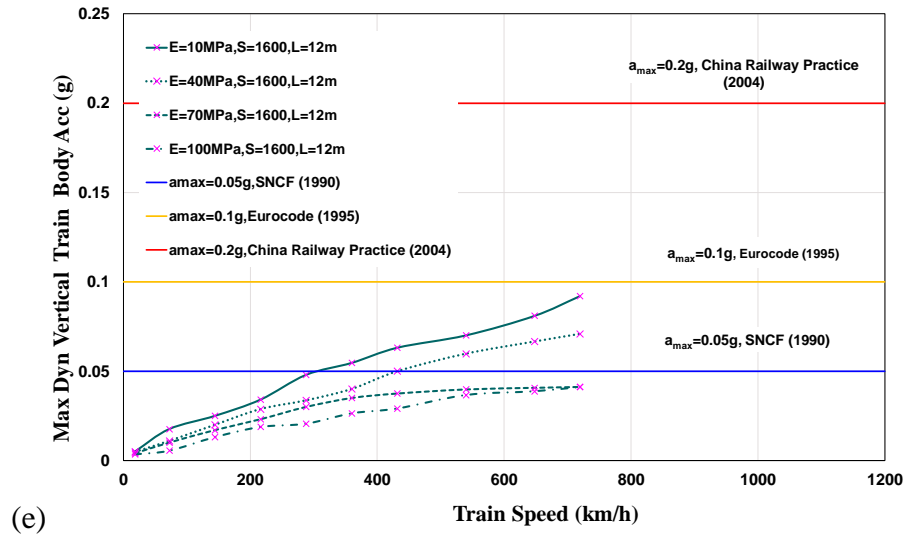


Figure 5.61. Continued

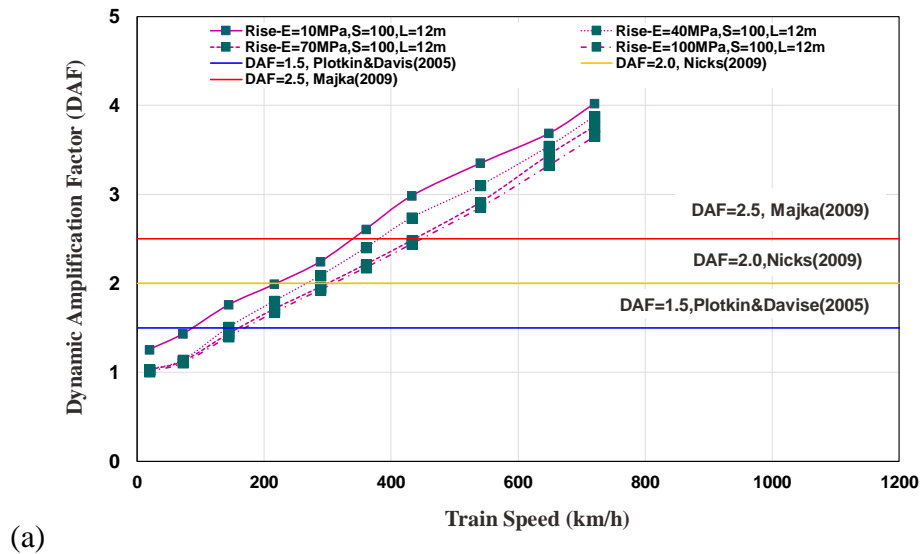
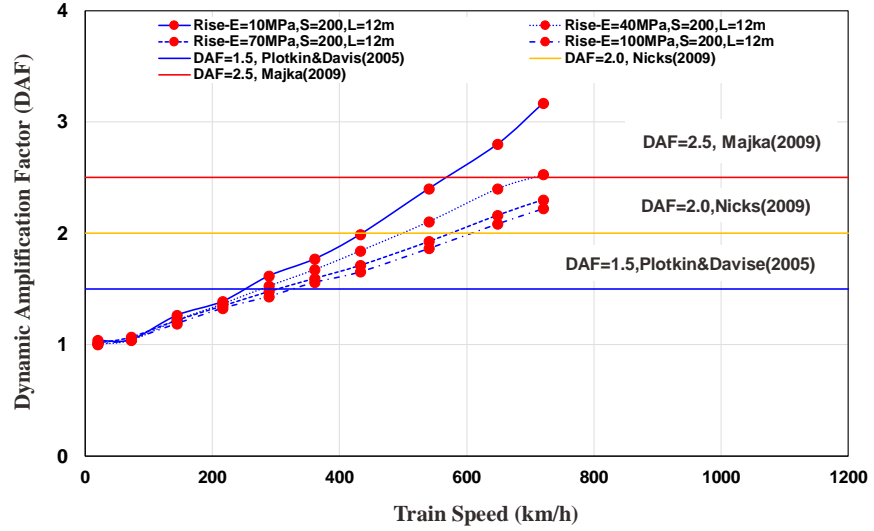
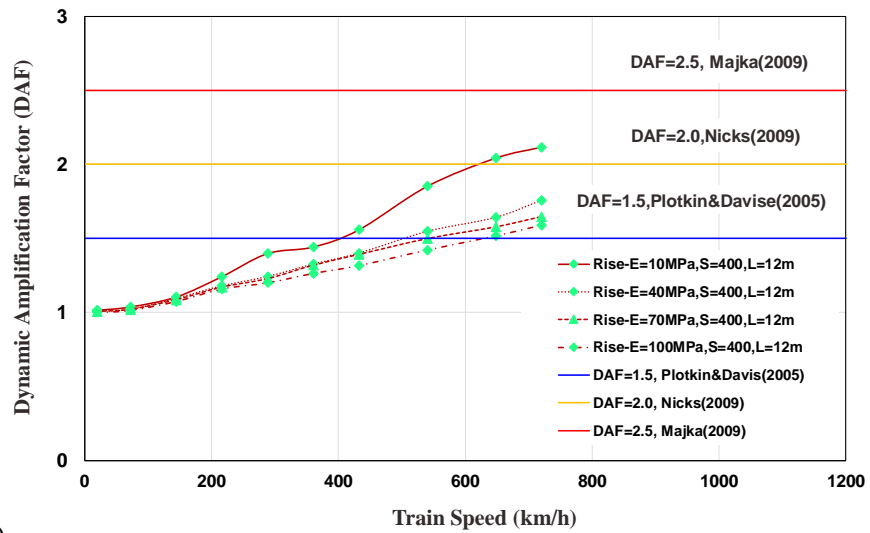


Figure 5.62. Dynamic amplification factor vs. train speed comparison for subgrade modulus changes and various irregularity sizes (a) $s=100$, (b) $s=200$, (c) $s=400$, (d) $s=800$, (e) $s=1600$

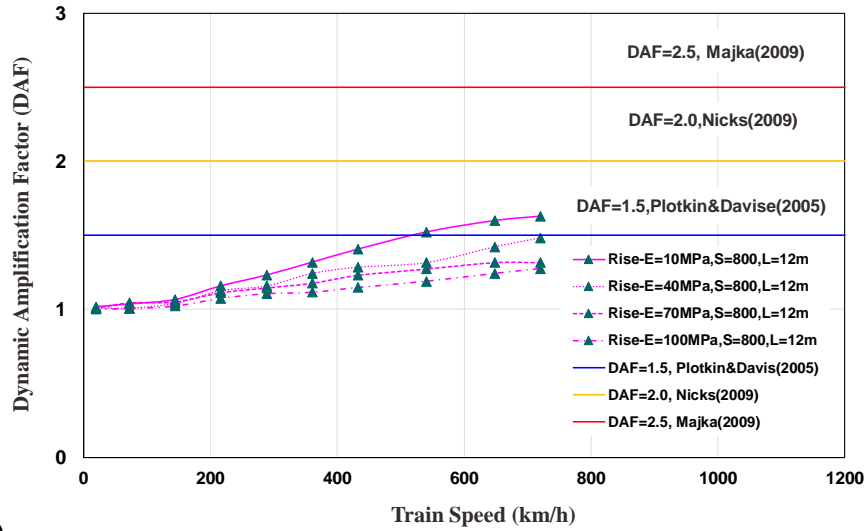


(b)

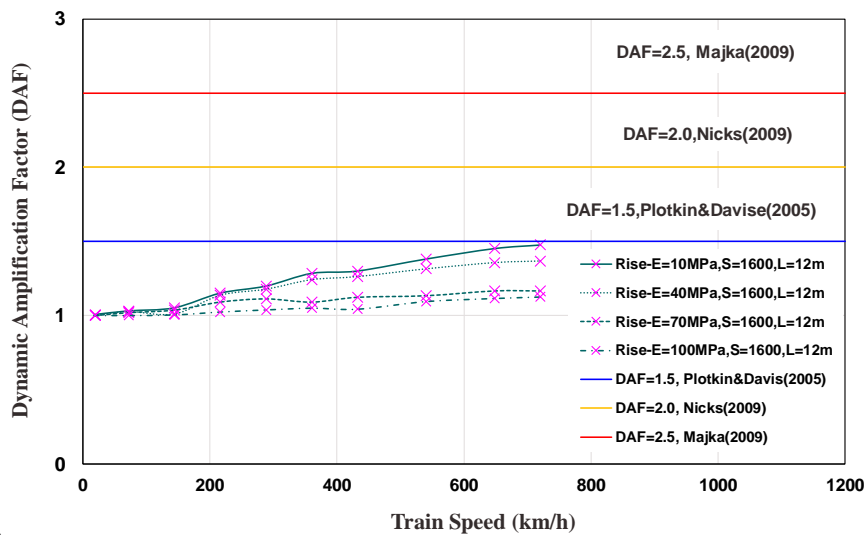


(c)

Figure 5.62. Continued



(d)



(e)

Figure 5.62. Continued

5.8 Proposed Guideline Charts

Through an extensive parametric study, some well-tested guideline charts of permissible irregularity sizes were established for HSR consultants, designers, and engineers to provide the passengers with safe, comfortable, and fast rides. The main goal of these charts is to define tolerable irregularity size for HSR lines, keeping the vertical acceleration of the train car body and dynamic amplification factor below chosen threshold values. A summary of the proposed design procedure is illustrated in Figure 5.62.

This flowchart presented in Figure 5.63 includes two main steps. In similar situations, instead of performing numerical simulations to estimate the train/track responses, the guideline charts shown in Figures 5.59 to 5.62 can be used. To define whether the size of an irregularity is tolerable or not, the threshold values for DAF and a_{\max} should be defined. As mentioned earlier in this section, there are already different codes and recommendations that define these values (Table 5.2). In the guideline charts derived from current study, different values are considered. A complete recording of DAF and a_{\max} for all cases in the parametric study are presented in Table 5.11. Considering the limitations of DAF and a_{\max} , all the cases defined in Table 5.12 are evaluated based on different values given in Table 5.2. Table 5.12 can be used by railway engineers to define the tolerable irregularity for similar cases they are faced with.

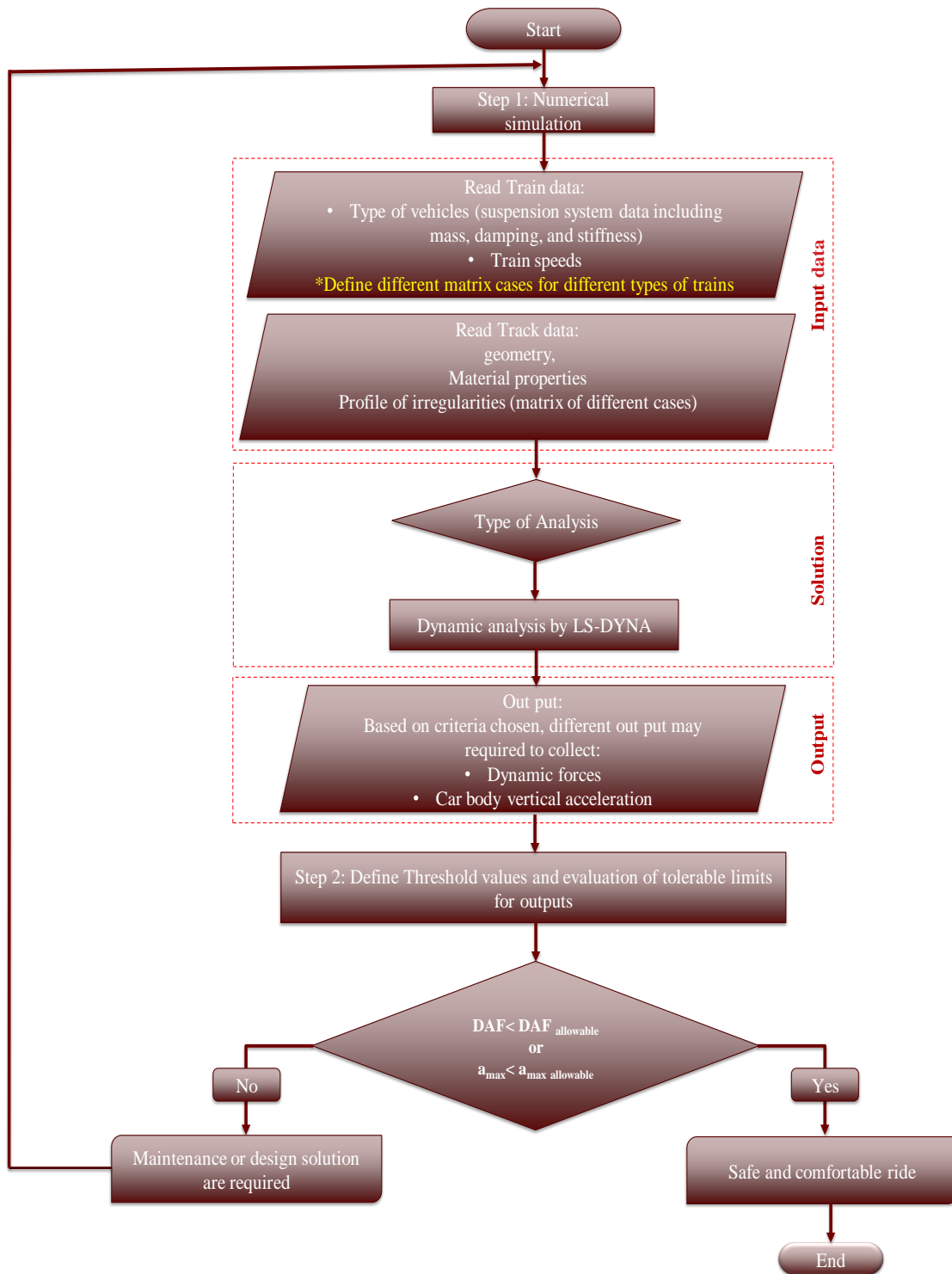


Figure 5.63. Flowchart of proposed design procedure

Table 5.11. Parametric Study Summary

Case	E_s (MPa)	V_T (km/h)	Irregularity Type	$s=L/h$	L (m)	DAF	a_{max} (g)
1	100	18	Bump	100	12	1.033	0.0103
2		72				1.166	0.0458
3		144				1.497	0.0868
4		216				1.872	0.152
5		288				2.182	0.208
6		360				2.503	0.257
7		432				2.813	0.309
8		540				3.283	0.387
9		648				3.69	0.476
10		720				4.032	0.521
11	100	18	Bump	200	12	1.017	0.00652
12		72				1.080	0.0216
13		144				1.251	0.0436
14		216				1.433	0.0776
15		288				1.604	0.107
16		360				1.754	0.131
17		432				1.904	0.162
18		540				2.118	0.193
19		648				2.364	0.231
20		720				2.471	0.252
21	100	18	Bump	400	12	1.005	0.00416
22		72				1.033	0.0129
23		144				1.102	0.025
24		216				1.251	0.0696
25		288				1.369	0.0761
26		360				1.390	0.0772
27		432				1.444	0.0907
28		540				1.529	0.106
29		648				1.658	0.112
30		720				1.711	0.115
31	100	18	Bump	800	12	1.005	0.00471
32		72				1.029	0.0105
33		144				1.063	0.0131
34		216				1.166	0.0306
35		288				1.273	0.0489
36		360				1.273	0.0565
37		432				1.283	0.0589
38		540				1.294	0.063
39		648				1.326	0.0696
40		720				1.326	0.0713
41	100	18	Bump	1600	12	1.006	0.00316
42		72				1.029	0.00637

Table 5.11. Continued

Case	E_s (MPa)	V_T (km/h)	Irregularity Type	$s=L/h$	L (m)	DAF	a_{max} (g)
43	100	144	Bump	1600	1	1.037	0.00679
44		216				1.091	0.0158
45		288				1.123	0.0204
46		360				1.123	0.0281
47		432				1.0123	0.0354
48		540				1.112	0.0367
49		648				1.123	0.0419
50		720				1.123	0.0419
51	100	18	Dip	100	12	1.061	0.0222
52		72				1.326	0.0696
53		144				1.872	0.0929
54		216				2.952	0.237
55		288				2.952	0.251
56		360				2.759	0.241
57		432				2.439	0.227
58		540				2.193	0.209
59		648				1.987	0.17
60		720				1.818	0.149
61	100	18	Dip	200	12	1.027	0.0105
62		72				1.176	0.0352
63		144				1.444	0.0483
64		216				1.968	0.103
65		288				2.235	0.157
66		360				2.182	0.169
67		432				2.086	0.164
68		540				1.786	0.149
69		648				1.722	0.131
70		720				1.658	0.114
71	100	18	Dip	400	12	1.009	0.0057
72		72				1.080	0.0188
73		144				1.219	0.0254
74		216				1.497	0.0534
75		288				1.636	0.0786
76		360				1.701	0.105
77		432				1.701	0.118
78		540				1.615	0.115
79		648				1.497	0.0906
80		720				1.433	0.0765
81	100	18	Dip	800	12	1.005	0.00428
82		72				1.042	0.00876
83		144				1.102	0.0103
84		216				1.251	0.029
85		288				1.326	0.0375
86		360				1.348	0.0548
87		432				1.358	0.0645

Table 5.11. Continued

Case	E_s (MPa)	V_T (km/h)	Irregularity Type	$s=L/h$	L (m)	DAF	a_{max} (g)
88	100	540	Dip	800	12	1.369	0.0713
89		648				1.337	0.0658
90		720				1.326	0.0586
91	100	18	Dip	1600	12	1.009	0.00313
92		72				1.018	0.00572
93		144				1.044	0.00574
94		216				1.123	0.0163
95		288				1.166	0.0174
96		360				1.176	0.0281
97		432				1.176	0.0338
98		540				1.187	0.0391
99		648				1.187	0.0348
100		720				1.198	0.0297
101	100	18	Rise	100	12	1.008	0.0106
102		72				1.105	0.039
103		144				1.4	0.077
104		216				1.674	0.115
105		288				1.926	0.178
106		360				2.178	0.223
107		432				2.442	0.29
108		540				2.853	0.374
109		648				3.326	0.474
110		720				3.653	0.503
111	100	18	Rise	200	12	1.002	0.0066
112		72				1.048	0.0253
113		144				1.189	0.0428
114		216				1.326	0.0708
115		288				1.432	0.0897
116		360				1.558	0.109
117		432				1.653	0.142
118		540				1.863	0.189
119		648				2.084	0.24
120		720				2.221	0.267
121	100	18	Rise	400	12	1	0.00455
122		72				1.014	0.0126
123		144				1.074	0.0266
124		216				1.158	0.0454
125		288				1.2	0.0488
126		360				1.263	0.0659
127		432				1.316	0.0799
128		540				1.421	0.101
129		648				1.516	0.12
130		720				1.589	0.133
131	100	18	Rise	800	12	1	0.00344
132		72				1.006	0.00567

Table 5.11. Continued

Case	E_s (MPa)	V_T (km/h)	Irregularity Type	$s=L/h$	L (m)	DAF	a_{max} (g)
133	100	144	Rise	800	12	1.022	0.0177
134		216				1.074	0.0232
135		288				1.105	0.0284
136		360				1.115	0.032
137		432				1.147	0.0389
138		540				1.189	0.0501
139		648				1.242	0.0578
140		720				1.274	0.0636
141		100				18	Rise
142	72		1	0.00564			
143	144		1.004	0.0132			
144	216		1.0237	0.0189			
145	288		1.038	0.0207			
146	360		1.05	0.0265			
147	432		1.043	0.0292			
148	540		1.095	0.0367			
149	648		1.116	0.0388			
150	720		1.126	0.0432			
151	100		18	Rise	100	6	
152		72	1.0126				0.0535
153		144	1.379				0.0815
154		216	1.779				0.145
155		288	2.042				0.2
156		360	2.389				0.253
157		432	2.621				0.315
158		540	3.137				0.395
159		648	3.621				0.481
160		720	3.853				0.541
161	100	18	Rise	200	6	1.002	0.00625
162		72				1.053	0.03
163		144				1.179	0.039
164		216				1.326	0.0724
165		288				1.463	0.103
166		360				1.579	0.133
167		432				1.716	0.163
168		540				1.905	0.206
169		648				2.074	0.243
170		720				2.242	0.271
171	100	18	Rise	400	6	1.0	0.00421
172		72				1.022	0.0189
173		144				1.084	0.0232
174		216				1.147	0.0406
175		288				1.21	0.0505
176		360				1.253	0.0699
177		432				1.358	0.0877

Table 5.11. Continued

Case	E_s (MPa)	V_T (km/h)	Irregularity Type	$s=L/h$	L (m)	DAF	a_{max} (g)
178	100	540	Rise	400	6	1.421	0.11
179		648				1.537	0.131
180		720				1.61	0.147
181	100	18	Rise	800	6	1.0	0.00313
182		72				1.006	0.00578
183		144				1.028	0.0178
184		216				1.063	0.022
185		288				1.105	0.0282
186		360				1.147	0.0406
187		432				1.179	0.053
188		540				1.263	0.0698
189		648				1.284	0.0791
190		720				1.316	0.0861
191		100				18	Rise
192	72		1.003	0.00457			
193	144		1.014	0.00875			
194	216		1.044	0.0128			
195	288		1.053	0.0207			
196	360		1.084	0.0275			
197	432		1.116	0.0342			
198	540		1.168	0.0453			
199	648		1.168	0.051			
200	720		1.189	0.0572			
201	100		18	Drop	100	12	
202		72	1.209				0.0532
203		144	1.444				0.113
204		216	1.807				0.172
205		288	2.706				0.201
206		360	2.62				0.201
207		432	2.663				0.226
208		540	2.706				0.231
209		648	2.364				0.184
210		720	2.460				0.194
211		100	18				Drop
212	72		1.112	0.0423			
213	144		1.283	0.0561			
214	216		1.519	0.119			
215	288		1.679	0.125			
216	360		2.096	0.145			
217	432		2.043	0.153			
218	540		2.032	0.14			
219	648		2.0	0.129			
220	720		2.0	0.121			
221	100		18	Drop	400	12	
222		72	1.06				0.0272

Table 5.11. Continued

Case	E_s (MPa)	V_T (km/h)	Irregularity Type	$s=L/h$	L (m)	DAF	a_{max} (g)
223	100	144	Drop	400	12	1.144	0.0312
224		216				1.316	0.0679
225		288				1.358	0.0704
226		360				1.465	0.0781
227		432				1.572	0.0881
228		540				1.722	0.105
229		648				1.658	0.0988
230		720				1.668	0.0969
231		100				18	Drop
232	72		1.040	0.0192			
233	144		1.066	0.0211			
234	216		1.134	0.0459			
235	288		1.123	0.0449			
236	360		1.219	0.0423			
237	432		1.262	0.0533			
238	540		1.455	0.0853			
239	648		1.401	0.0841			
240	720		1.358	0.0769			
241	100	18	Drop	1600	12	1.009	0.0032
242		72				1.037	0.0182
243		144				1.064	0.0157
244		216				1.123	0.0336
245		288				1.123	0.0347
246		360				1.112	0.0227
247		432				1.144	0.0418
248		540				1.273	0.0553
249		648				1.219	0.0546
250		720				1.198	0.0259
251	70	18	Rise	100	12	1.026	0.0109
252		72				1.123	0.0407
253		144				1.433	0.0839
254		216				1.711	0.124
255		288				1.957	0.186
256		360				2.214	0.238
257		432				2.481	0.3
258		540				2.909	0.38
259		648				3.444	0.474
260		720				3.765	0.536
261	70	18	Rise	200	12	1.014	0.00603
262		72				1.068	0.0241
263		144				1.219	0.0425
264		216				1.348	0.0726
265		288				1.476	0.1
266		360				1.594	0.126
267		432				1.711	0.154

Table 5.11. Continued

Case	E_s (MPa)	V_T (km/h)	Irregularity Type	$s=L/h$	L (m)	DAF	a_{max} (g)
268	70	540	Rise	200	12	1.925	0.198
269		648				2.160	0.244
270		720				2.299	0.277
271	70	18	Rise	400	12	1.005	0.00398
272		72				1.020	0.014
273		144				1.085	0.0266
274		216				1.170	0.05
275		288				1.227	0.0588
276		360				1.318	0.0693
277		432				1.391	0.0781
278		540				1.498	0.101
279		648				1.578	0.122
280		720				1.647	0.139
281		70				18	Rise
282	72		1.044	0.0106			
283	144		1.050	0.0196			
284	216		1.112	0.0291			
285	288		1.144	0.0351			
286	360		1.176	0.0398			
287	432		1.230	0.0399			
288	540		1.273	0.0509			
289	648		1.316	0.0602			
290	720		1.316	0.069			
291	70		18	Rise	1600	12	
292		72	1.020				0.01
293		144	1.037				0.017
294		216	1.091				0.0231
295		288	1.112				0.03
296		360	1.091				0.035
297		432	1.123				0.0375
298		540	1.134				0.0398
299		648	1.166				0.0407
300		720	1.166				0.0412
301		40	18				Rise
302	72		1.137	0.0425			
303	144		1.505	0.0948			
304	216		1.800	0.139			
305	288		2.084	0.191			
306	360		2.400	0.243			
307	432		2.737	0.3			
308	540		3.102	0.383			
309	648		3.541	0.189			
310	720		3.878	0.556			
311	40		18	Rise	200	12	
312		72	1.041				0.0274

Table 5.11. Continued

Case	E_s (MPa)	V_T (km/h)	Irregularity Type	$s=L/h$	L (m)	DAF	a_{max} (g)
313	40	144	Rise	200	12	1.221	0.0556
314		216				1.368	0.0847
315		288				1.526	0.0989
316		360				1.674	0.122
317		432				1.842	0.165
318		540				2.105	0.207
319		648				2.400	0.257
320		720				2.526	0.282
321		40				18	Rise
322	72		1.020	0.0191			
323	144		1.095	0.0397			
324	216		1.179	0.0539			
325	288		1.242	0.0718			
326	360		1.326	0.0743			
327	432		1.400	0.0936			
328	540		1.547	0.113			
329	648		1.642	0.127			
330	720		1.758	0.143			
331	40	18	Rise	800	12	1.009	0.003
332		72				1.009	0.014
333		144				1.040	0.023
334		216				1.126	0.031
335		288				1.158	0.039
336		360				1.242	0.047
337		432				1.284	0.056
338		540				1.315	0.061
339		648				1.421	0.071
340		720				1.482	0.0803
341	40	18	Rise	1600	12	1.0	0.00487
342		72				1.027	0.011
343		144				1.011	0.02
344		216				1.137	0.0288
345		288				1.178	0.0337
346		360				1.242	0.0401
347		432				1.263	0.05
348		540				1.315	0.0598
349		648				1.357	0.0666
350		720				1.368	0.0709
351	10	18	Rise	100	12	1.253	0.0604
352		72				1.432	0.0998
353		144				1.758	0.147
354		216				1.989	0.177
355		288				2.242	0.229
356		360				2.608	0.278
357		432				2.982	0.323

Table 5.11. Continued

Case	E_s (MPa)	V_T (km/h)	Irregularity Type	$s=L/h$	L (m)	DAF	a_{max} (g)
358	10	540	Rise	100	12	3.348	0.441
359		648				3.684	0.563
360		720				4.021	0.599
361	10	18	Rise	200	12	1.038	0.0126
362		72				1.045	0.0423
363		144				1.263	0.0618
364		216				1.389	0.0901
365		288				1.615	0.107
366		360				1.768	0.148
367		432				1.989	.184
368		540				2.400	0.254
369		648				2.8	0.293
370		720				3.168	0.322
371		10				18	Rise
372	72		1.038	0.0245			
373	144		1.105	0.0401			
374	216		1.242	0.0684			
375	288		1.398	0.0828			
376	360		1.442	0.114			
377	432		1.558	0.135			
378	540		1.852	0.154			
379	648		2.042	0.178			
380	720		2.116	0.199			
381	10		18	Rise	800	12	
382		72	1.035				0.019
383		144	1.065				0.0278
384		216	1.157				0.0387
385		288	1.230				0.0541
386		360	1.317				0.0671
387		432	1.405				0.0789
388		540	1.521				0.1
389		648	1.598				0.115
390		720	1.628				0.133
391		10	18				Rise
392	72		1.030	0.0176			
393	144		1.051	0.025			
394	216		1.150	0.0341			
395	288		1.198	0.048			
396	360		1.284	0.0547			
397	432		1.300	0.0632			
398	540		1.381	0.0701			
399	648		1.452	0.081			
400	720		1.476	0.0921			
401	100		18	No Irregularity	-	-	
402		72	1.027				0.005

Table 5.11. Continued

Case	E_s (MPa)	V_T (km/h)	Irregularity Type	$s=L/h$	L (m)	DAF	a_{max} (g)
403	100	144	No Irregularity	-	-	1.037	0.0124
404		216				1.055	0.0165
405		288				1.055	0.0222
406		360				1.080	0.0242
407		432				1.080	0.0285
408		540				1.123	0.034
409		648				1.070	0.0378
410		720				1.070	0.0403
411		80				18	No Irregularity
412	72		1.029	0.00579			
413	144		1.0428	0.0127			
414	216		1.0700	0.0189			
415	288		1.0800	0.0255			
416	360		1.091	0.0308			
417	432		1.112	0.0355			
418	540		1.134	0.0402			
419	648		1.135	0.0423			
420	720		1.135	0.0438			
421	70	18	No Irregularity	-	-	1.002	0.00384
422		72				1.030	0.00739
423		144				1.0723	0.0155
424		216				1.0966	0.0233
425		288				1.156	0.030
426		360				1.208	0.0312
427		432				1.213	0.0298
428		540				1.300	0.0400
429		648				1.308	0.0453
430		720				1.301	0.0477
431	40	18	No Irregularity	-	-	1.004	0.004
432		72				1.0085	0.01
433		144				1.009	0.0155
434		216				1.087	0.0199
435		288				1.10	0.026
436		360				1.139	0.031
437		432				1.161	0.0362
438		540				1.170	0.043
439		648				1.175	0.047
440		720				1.190	0.05
441	20	18	No Irregularity	-	-	1.002	0.0041
442		72				1.080	0.0131
443		144				1.134	0.0221
444		216				1.358	0.0314
445		288				1.390	0.0387
446		360				1.422	0.0447

Table 5.11. Continued

Case	E_s (MPa)	V_T (km/h)	Irregularity Type	$s=L/h$	L (m)	DAF	a_{max} (g)
447	20	432	No Irregularity	-	-	1.529	0.05
448		540				1.604	0.0551
449		648				1.519	0.0597
450		720				1.519	0.0631
451	10	18	No Irregularity	-	-	1.040	0.00441
452		72				1.251	0.015
453		144				1.422	0.025
454		216				1.947	0.032
455		288				1.540	0.045
456		360				1.476	0.0501
457		432				1.882	0.0577
458		540				1.893	0.0655
459		648				2.171	0.0729
460		720				2.214	0.08
461	5	18	No Irregularity	-	-	1.102	0.00531
462		72				1.380	0.0181
463		144				1.701	0.0289
464		216				1.850	0.0329
465		288				1.880	0.0466
466		360				1.910	0.0511
467		432				2.050	0.0601
468		540				2.106	0.0789
469		648				2.221	0.0821
470		720				2.587	0.0850

Table 5.12. Evaluation of Tolerable Limits for Different Cases

Case	DAF			a _{max} (g)		
	≤1.5	≤2.0	≤2.5	≤0.05	≤0.10	≤0.20
1	Yes	Yes	Yes	Yes	Yes	Yes
2	Yes	Yes	Yes	Yes	Yes	Yes
3	Yes	Yes	Yes	No	Yes	Yes
4	No	Yes	Yes	No	No	Yes
5	No	No	Yes	No	No	No
6	No	No	No	No	No	No
7	No	No	No	No	No	No
8	No	No	No	No	No	No
9	No	No	No	No	No	No
10	No	No	No	No	No	No
11	Yes	Yes	Yes	Yes	Yes	Yes
12	Yes	Yes	Yes	Yes	Yes	Yes
13	Yes	Yes	Yes	Yes	Yes	Yes
14	Yes	Yes	Yes	No	Yes	Yes
15	No	Yes	Yes	No	No	Yes
16	No	Yes	Yes	No	No	Yes
17	No	Yes	Yes	No	No	Yes
18	No	No	Yes	No	No	Yes
19	No	No	Yes	No	No	No
20	No	No	Yes	No	No	No
21	Yes	Yes	Yes	Yes	Yes	Yes
22	Yes	Yes	Yes	Yes	Yes	Yes
23	Yes	Yes	Yes	Yes	Yes	Yes
24	Yes	Yes	Yes	No	Yes	Yes
25	Yes	Yes	Yes	No	Yes	Yes
26	Yes	Yes	Yes	No	Yes	Yes
27	Yes	Yes	Yes	No	Yes	Yes
28	No	Yes	Yes	No	No	Yes
29	No	Yes	Yes	No	No	Yes
30	No	Yes	Yes	No	No	Yes
31	Yes	Yes	Yes	Yes	Yes	Yes
32	Yes	Yes	Yes	Yes	Yes	Yes
33	Yes	Yes	Yes	Yes	Yes	Yes
34	Yes	Yes	Yes	Yes	Yes	Yes
35	Yes	Yes	Yes	Yes	Yes	Yes
36	Yes	Yes	Yes	No	Yes	Yes
37	Yes	Yes	Yes	No	Yes	Yes
38	Yes	Yes	Yes	No	Yes	Yes
39	Yes	Yes	Yes	No	Yes	Yes
40	Yes	Yes	Yes	No	Yes	Yes
41	Yes	Yes	Yes	Yes	Yes	Yes
42	Yes	Yes	Yes	Yes	Yes	Yes

Table 5.12. Continued

Case	DAF			a_{max} (g)		
	≤ 1.5	≤ 2.0	≤ 2.5	≤ 0.05	≤ 0.10	≤ 0.20
43	Yes	Yes	Yes	Yes	Yes	Yes
44	Yes	Yes	Yes	Yes	Yes	Yes
45	Yes	Yes	Yes	Yes	Yes	Yes
46	Yes	Yes	Yes	Yes	Yes	Yes
47	Yes	Yes	Yes	Yes	Yes	Yes
48	Yes	Yes	Yes	Yes	Yes	Yes
49	Yes	Yes	Yes	Yes	Yes	Yes
50	Yes	Yes	Yes	Yes	Yes	Yes
51	Yes	Yes	Yes	Yes	Yes	Yes
52	Yes	Yes	Yes	No	Yes	Yes
53	No	Yes	Yes	No	Yes	Yes
54	No	No	No	No	No	No
55	No	No	No	No	No	No
56	No	No	No	No	No	No
57	No	No	Yes	No	No	No
58	No	No	Yes	No	No	No
59	No	Yes	Yes	No	No	Yes
60	No	Yes	Yes	No	No	Yes
61	Yes	Yes	Yes	Yes	Yes	Yes
62	Yes	Yes	Yes	Yes	Yes	Yes
63	Yes	Yes	Yes	Yes	Yes	Yes
64	No	Yes	Yes	No	No	Yes
65	No	No	Yes	No	No	Yes
66	No	No	Yes	No	No	Yes
67	No	No	Yes	No	No	Yes
68	No	Yes	Yes	No	No	Yes
69	No	Yes	Yes	No	No	Yes
70	No	Yes	Yes	No	No	Yes
71	Yes	Yes	Yes	Yes	Yes	Yes
72	Yes	Yes	Yes	Yes	Yes	Yes
73	Yes	Yes	Yes	Yes	Yes	Yes
74	Yes	Yes	Yes	No	Yes	Yes
75	No	Yes	Yes	No	Yes	Yes
76	No	Yes	Yes	No	No	Yes
77	No	Yes	Yes	No	No	Yes
78	No	Yes	Yes	No	No	Yes
79	Yes	Yes	Yes	No	Yes	Yes
80	Yes	Yes	Yes	No	Yes	Yes
81	Yes	Yes	Yes	Yes	Yes	Yes
82	Yes	Yes	Yes	Yes	Yes	Yes
83	Yes	Yes	Yes	Yes	Yes	Yes
84	Yes	Yes	Yes	Yes	Yes	Yes

Table 5.12. Continued

Case	DAF			a_{max} (g)		
	≤ 1.5	≤ 2.0	≤ 2.5	≤ 0.05	≤ 0.10	≤ 0.20
85	Yes	Yes	Yes	Yes	Yes	Yes
86	Yes	Yes	Yes	No	Yes	Yes
87	Yes	Yes	Yes	No	Yes	Yes
88	Yes	Yes	Yes	No	Yes	Yes
89	Yes	Yes	Yes	No	Yes	Yes
90	Yes	Yes	Yes	No	Yes	Yes
91	Yes	Yes	Yes	Yes	Yes	Yes
92	Yes	Yes	Yes	Yes	Yes	Yes
93	Yes	Yes	Yes	Yes	Yes	Yes
94	Yes	Yes	Yes	Yes	Yes	Yes
95	Yes	Yes	Yes	Yes	Yes	Yes
96	Yes	Yes	Yes	Yes	Yes	Yes
97	Yes	Yes	Yes	Yes	Yes	Yes
98	Yes	Yes	Yes	Yes	Yes	Yes
99	Yes	Yes	Yes	Yes	Yes	Yes
100	Yes	Yes	Yes	Yes	Yes	Yes
101	Yes	Yes	Yes	Yes	Yes	Yes
102	Yes	Yes	Yes	Yes	Yes	Yes
103	Yes	Yes	Yes	No	Yes	Yes
104	No	Yes	Yes	No	No	Yes
105	No	No	Yes	No	No	Yes
106	No	No	Yes	No	No	No
107	No	No	Yes	No	No	No
108	No	No	No	No	No	No
109	No	No	No	No	No	No
110	No	No	No	No	No	No
111	Yes	Yes	Yes	Yes	Yes	Yes
112	Yes	Yes	Yes	Yes	Yes	Yes
113	Yes	Yes	Yes	Yes	Yes	Yes
114	Yes	Yes	Yes	No	Yes	Yes
115	Yes	Yes	Yes	No	Yes	Yes
116	No	Yes	Yes	No	No	Yes
117	No	Yes	Yes	No	No	Yes
118	No	Yes	Yes	No	No	Yes
119	No	No	Yes	No	No	No
120	No	No	Yes	No	No	No
121	Yes	Yes	Yes	Yes	Yes	Yes
122	Yes	Yes	Yes	Yes	Yes	Yes
123	Yes	Yes	Yes	Yes	Yes	Yes
124	Yes	Yes	Yes	Yes	Yes	Yes
125	Yes	Yes	Yes	Yes	Yes	Yes
126	Yes	Yes	Yes	No	Yes	Yes

Table 5.12. Continued

Case	DAF			a _{max} (g)		
	≤1.5	≤2.0	≤2.5	≤0.05	≤0.10	≤0.20
127	Yes	Yes	Yes	No	Yes	Yes
128	Yes	Yes	Yes	No	No	Yes
129	No	Yes	Yes	No	No	Yes
130	No	Yes	Yes	No	No	Yes
131	Yes	Yes	Yes	Yes	Yes	Yes
132	Yes	Yes	Yes	Yes	Yes	Yes
133	Yes	Yes	Yes	Yes	Yes	Yes
134	Yes	Yes	Yes	Yes	Yes	Yes
135	Yes	Yes	Yes	Yes	Yes	Yes
136	Yes	Yes	Yes	Yes	Yes	Yes
137	Yes	Yes	Yes	Yes	Yes	Yes
138	Yes	Yes	Yes	No	Yes	Yes
139	Yes	Yes	Yes	No	Yes	Yes
140	Yes	Yes	Yes	No	Yes	Yes
141	Yes	Yes	Yes	Yes	Yes	Yes
142	Yes	Yes	Yes	Yes	Yes	Yes
143	Yes	Yes	Yes	Yes	Yes	Yes
144	Yes	Yes	Yes	Yes	Yes	Yes
145	Yes	Yes	Yes	Yes	Yes	Yes
146	Yes	Yes	Yes	Yes	Yes	Yes
147	Yes	Yes	Yes	Yes	Yes	Yes
148	Yes	Yes	Yes	Yes	Yes	Yes
149	Yes	Yes	Yes	Yes	Yes	Yes
150	Yes	Yes	Yes	Yes	Yes	Yes
151	Yes	Yes	Yes	Yes	Yes	Yes
152	Yes	Yes	Yes	No	Yes	Yes
153	Yes	Yes	Yes	No	Yes	Yes
154	No	Yes	Yes	No	No	Yes
155	No	No	Yes	No	No	Yes
156	No	No	Yes	No	No	No
157	No	No	No	No	No	No
158	No	No	No	No	No	No
159	No	No	No	No	No	No
160	No	No	No	No	No	No
161	Yes	Yes	Yes	Yes	Yes	Yes
162	Yes	Yes	Yes	Yes	Yes	Yes
163	Yes	Yes	Yes	Yes	Yes	Yes
164	Yes	Yes	Yes	No	Yes	Yes
165	Yes	Yes	Yes	No	No	Yes
166	No	Yes	Yes	No	No	Yes
167	No	Yes	Yes	No	No	Yes
168	No	Yes	Yes	No	No	No

Table 5.12. Continued

Case	DAF			a _{max} (g)		
	≤1.5	≤2.0	≤2.5	≤0.05	≤0.10	≤0.20
169	No	No	Yes	No	No	No
170	No	No	Yes	No	No	No
171	Yes	Yes	Yes	Yes	Yes	Yes
172	Yes	Yes	Yes	Yes	Yes	Yes
173	Yes	Yes	Yes	Yes	Yes	Yes
174	Yes	Yes	Yes	Yes	Yes	Yes
175	Yes	Yes	Yes	No	Yes	Yes
176	Yes	Yes	Yes	No	Yes	Yes
177	Yes	Yes	Yes	No	Yes	Yes
178	Yes	Yes	Yes	No	No	Yes
179	No	Yes	Yes	No	No	Yes
180	No	Yes	Yes	No	No	Yes
181	Yes	Yes	Yes	Yes	Yes	Yes
182	Yes	Yes	Yes	Yes	Yes	Yes
183	Yes	Yes	Yes	Yes	Yes	Yes
184	Yes	Yes	Yes	Yes	Yes	Yes
185	Yes	Yes	Yes	Yes	Yes	Yes
186	Yes	Yes	Yes	Yes	Yes	Yes
187	Yes	Yes	Yes	No	Yes	Yes
188	Yes	Yes	Yes	No	Yes	Yes
189	Yes	Yes	Yes	No	Yes	Yes
190	Yes	Yes	Yes	No	Yes	Yes
191	Yes	Yes	Yes	Yes	Yes	Yes
192	Yes	Yes	Yes	Yes	Yes	Yes
193	Yes	Yes	Yes	Yes	Yes	Yes
194	Yes	Yes	Yes	Yes	Yes	Yes
195	Yes	Yes	Yes	Yes	Yes	Yes
196	Yes	Yes	Yes	Yes	Yes	Yes
197	Yes	Yes	Yes	Yes	Yes	Yes
198	Yes	Yes	Yes	Yes	Yes	Yes
199	Yes	Yes	Yes	No	Yes	Yes
200	Yes	Yes	Yes	No	Yes	Yes
201	Yes	Yes	Yes	Yes	Yes	Yes
202	Yes	Yes	Yes	No	Yes	Yes
203	Yes	Yes	Yes	No	No	Yes
204	No	Yes	Yes	No	No	Yes
205	No	No	No	No	No	No
206	No	No	No	No	No	No
207	No	No	No	No	No	No
208	No	No	No	No	No	No
209	No	No	Yes	No	No	Yes
210	No	No	Yes	No	No	Yes

Table 5.12. Continued

Case	DAF			a_{max} (g)		
	≤ 1.5	≤ 2.0	≤ 2.5	≤ 0.05	≤ 0.10	≤ 0.20
211	Yes	Yes	Yes	Yes	Yes	Yes
212	Yes	Yes	Yes	Yes	Yes	Yes
213	Yes	Yes	Yes	No	Yes	Yes
214	No	Yes	Yes	No	No	Yes
215	No	Yes	Yes	No	No	Yes
216	No	No	Yes	No	No	Yes
217	No	No	Yes	No	No	Yes
218	No	No	Yes	No	No	Yes
219	No	Yes	Yes	No	No	Yes
220	No	Yes	Yes	No	No	Yes
221	Yes	Yes	Yes	Yes	Yes	Yes
222	Yes	Yes	Yes	Yes	Yes	Yes
223	Yes	Yes	Yes	Yes	Yes	Yes
224	Yes	Yes	Yes	No	Yes	Yes
225	Yes	Yes	Yes	No	Yes	Yes
226	Yes	Yes	Yes	No	Yes	Yes
227	No	Yes	Yes	No	Yes	Yes
228	No	Yes	Yes	No	No	Yes
229	No	Yes	Yes	No	Yes	Yes
230	No	Yes	Yes	No	Yes	Yes
231	Yes	Yes	Yes	Yes	Yes	Yes
232	Yes	Yes	Yes	Yes	Yes	Yes
233	Yes	Yes	Yes	Yes	Yes	Yes
234	Yes	Yes	Yes	Yes	Yes	Yes
235	Yes	Yes	Yes	Yes	Yes	Yes
236	Yes	Yes	Yes	Yes	Yes	Yes
237	Yes	Yes	Yes	No	Yes	Yes
238	Yes	Yes	Yes	No	Yes	Yes
239	Yes	Yes	Yes	No	Yes	Yes
240	Yes	Yes	Yes	No	Yes	Yes
241	Yes	Yes	Yes	Yes	Yes	Yes
242	Yes	Yes	Yes	Yes	Yes	Yes
243	Yes	Yes	Yes	Yes	Yes	Yes
244	Yes	Yes	Yes	Yes	Yes	Yes
245	Yes	Yes	Yes	Yes	Yes	Yes
246	Yes	Yes	Yes	Yes	Yes	Yes
247	Yes	Yes	Yes	Yes	Yes	Yes
248	Yes	Yes	Yes	No	Yes	Yes
249	Yes	Yes	Yes	No	Yes	Yes
250	Yes	Yes	Yes	Yes	Yes	Yes
251	Yes	Yes	Yes	Yes	Yes	Yes
252	Yes	Yes	Yes	Yes	Yes	Yes

Table 5.12. Continued

Case	DAF			a _{max} (g)		
	≤1.5	≤2.0	≤2.5	≤0.05	≤0.10	≤0.20
253	Yes	Yes	Yes	No	Yes	Yes
254	No	Yes	Yes	No	No	Yes
255	No	Yes	Yes	No	No	Yes
256	No	No	Yes	No	No	No
257	No	No	Yes	No	No	No
258	No	No	No	No	No	No
259	No	No	No	No	No	No
260	No	No	No	No	No	No
261	Yes	Yes	Yes	Yes	Yes	Yes
262	Yes	Yes	Yes	Yes	Yes	Yes
263	Yes	Yes	Yes	Yes	Yes	Yes
264	Yes	Yes	Yes	No	Yes	Yes
265	Yes	Yes	Yes	No	Yes	Yes
266	No	Yes	Yes	No	No	Yes
267	No	Yes	Yes	No	No	Yes
268	No	Yes	Yes	No	No	Yes
269	No	No	Yes	No	No	No
270	No	No	Yes	No	No	No
271	Yes	Yes	Yes	Yes	Yes	Yes
272	Yes	Yes	Yes	Yes	Yes	Yes
273	Yes	Yes	Yes	Yes	Yes	Yes
274	Yes	Yes	Yes	Yes	Yes	Yes
275	Yes	Yes	Yes	No	Yes	Yes
276	Yes	Yes	Yes	No	Yes	Yes
277	Yes	Yes	Yes	No	Yes	Yes
278	Yes	Yes	Yes	No	No	Yes
279	No	Yes	Yes	No	No	Yes
280	No	Yes	Yes	No	No	Yes
281	Yes	Yes	Yes	Yes	Yes	Yes
282	Yes	Yes	Yes	Yes	Yes	Yes
283	Yes	Yes	Yes	Yes	Yes	Yes
284	Yes	Yes	Yes	Yes	Yes	Yes
285	Yes	Yes	Yes	Yes	Yes	Yes
286	Yes	Yes	Yes	Yes	Yes	Yes
287	Yes	Yes	Yes	Yes	Yes	Yes
288	Yes	Yes	Yes	No	Yes	Yes
289	Yes	Yes	Yes	No	Yes	Yes
290	Yes	Yes	Yes	No	Yes	Yes
291	Yes	Yes	Yes	Yes	Yes	Yes
292	Yes	Yes	Yes	Yes	Yes	Yes
293	Yes	Yes	Yes	Yes	Yes	Yes
294	Yes	Yes	Yes	Yes	Yes	Yes

Table 5.12. Continued

Case	DAF			a _{max} (g)		
	≤1.5	≤2.0	≤2.5	≤0.05	≤0.10	≤0.20
295	Yes	Yes	Yes	Yes	Yes	Yes
296	Yes	Yes	Yes	Yes	Yes	Yes
297	Yes	Yes	Yes	Yes	Yes	Yes
298	Yes	Yes	Yes	Yes	Yes	Yes
299	Yes	Yes	Yes	Yes	Yes	Yes
300	Yes	Yes	Yes	Yes	Yes	Yes
301	Yes	Yes	Yes	Yes	Yes	Yes
302	Yes	Yes	Yes	Yes	Yes	Yes
303	No	Yes	Yes	No	Yes	Yes
304	No	Yes	Yes	No	No	Yes
305	No	No	Yes	No	No	Yes
306	No	No	Yes	No	No	No
307	No	No	No	No	No	No
308	No	No	No	No	No	No
309	No	No	No	No	No	Yes
310	No	No	No	No	No	No
311	Yes	Yes	Yes	Yes	Yes	Yes
312	Yes	Yes	Yes	Yes	Yes	Yes
313	Yes	Yes	Yes	No	Yes	Yes
314	Yes	Yes	Yes	No	Yes	Yes
315	No	Yes	Yes	No	Yes	Yes
316	No	Yes	Yes	No	No	Yes
317	No	Yes	Yes	No	No	Yes
318	No	No	Yes	No	No	No
319	No	No	Yes	No	No	No
320	No	No	No	No	No	No
321	Yes	Yes	Yes	Yes	Yes	Yes
322	Yes	Yes	Yes	Yes	Yes	Yes
323	Yes	Yes	Yes	Yes	Yes	Yes
324	Yes	Yes	Yes	No	Yes	Yes
325	Yes	Yes	Yes	No	Yes	Yes
326	Yes	Yes	Yes	No	Yes	Yes
327	Yes	Yes	Yes	No	Yes	Yes
328	No	Yes	Yes	No	No	Yes
329	No	Yes	Yes	No	No	Yes
330	No	Yes	Yes	No	No	Yes
331	Yes	Yes	Yes	Yes	Yes	Yes
332	Yes	Yes	Yes	Yes	Yes	Yes
333	Yes	Yes	Yes	Yes	Yes	Yes
334	Yes	Yes	Yes	Yes	Yes	Yes
335	Yes	Yes	Yes	Yes	Yes	Yes
336	Yes	Yes	Yes	Yes	Yes	Yes

Table 5.12. Continued

Case	DAF			a _{max} (g)		
	≤1.5	≤2.0	≤2.5	≤0.05	≤0.10	≤0.20
337	Yes	Yes	Yes	No	Yes	Yes
338	Yes	Yes	Yes	No	Yes	Yes
339	Yes	Yes	Yes	No	Yes	Yes
340	Yes	Yes	Yes	No	Yes	Yes
341	Yes	Yes	Yes	Yes	Yes	Yes
342	Yes	Yes	Yes	Yes	Yes	Yes
343	Yes	Yes	Yes	Yes	Yes	Yes
344	Yes	Yes	Yes	Yes	Yes	Yes
345	Yes	Yes	Yes	Yes	Yes	Yes
346	Yes	Yes	Yes	Yes	Yes	Yes
347	Yes	Yes	Yes	No	Yes	Yes
348	Yes	Yes	Yes	No	Yes	Yes
349	Yes	Yes	Yes	No	Yes	Yes
350	Yes	Yes	Yes	No	Yes	Yes
351	Yes	Yes	Yes	No	Yes	Yes
352	Yes	Yes	Yes	No	Yes	Yes
353	No	Yes	Yes	No	No	Yes
354	No	Yes	Yes	No	No	Yes
355	No	No	Yes	No	No	No
356	No	No	No	No	No	No
357	No	No	No	No	No	No
358	No	No	No	No	No	No
359	No	No	No	No	No	No
360	No	No	No	No	No	No
361	Yes	Yes	Yes	Yes	Yes	Yes
362	Yes	Yes	Yes	Yes	Yes	Yes
363	Yes	Yes	Yes	No	Yes	Yes
364	Yes	Yes	Yes	No	Yes	Yes
365	No	Yes	Yes	No	No	Yes
366	No	Yes	Yes	No	No	Yes
367	No	Yes	Yes	No	No	Yes
368	No	No	Yes	No	No	No
369	No	No	No	No	No	No
370	No	No	No	No	No	No
371	Yes	Yes	Yes	Yes	Yes	Yes
372	Yes	Yes	Yes	Yes	Yes	Yes
373	Yes	Yes	Yes	Yes	Yes	Yes
374	Yes	Yes	Yes	No	Yes	Yes
375	Yes	Yes	Yes	No	Yes	Yes
376	Yes	Yes	Yes	No	No	Yes
377	No	Yes	Yes	No	No	Yes
378	No	Yes	Yes	No	No	Yes

Table 5.12. Continued

Case	DAF			a _{max} (g)		
	≤1.5	≤2.0	≤2.5	≤0.05	≤0.10	≤0.20
379	No	Yes	Yes	No	No	Yes
380	No	No	Yes	No	No	Yes
381	Yes	Yes	Yes	Yes	Yes	Yes
382	Yes	Yes	Yes	Yes	Yes	Yes
383	Yes	Yes	Yes	Yes	Yes	Yes
384	Yes	Yes	Yes	Yes	Yes	Yes
385	Yes	Yes	Yes	No	Yes	Yes
386	Yes	Yes	Yes	No	Yes	Yes
387	Yes	Yes	Yes	No	Yes	Yes
388	No	Yes	Yes	No	Yes	Yes
389	No	Yes	Yes	No	No	Yes
390	No	Yes	Yes	No	No	Yes
391	Yes	Yes	Yes	Yes	Yes	Yes
392	Yes	Yes	Yes	Yes	Yes	Yes
393	Yes	Yes	Yes	Yes	Yes	Yes
394	Yes	Yes	Yes	Yes	Yes	Yes
395	Yes	Yes	Yes	Yes	Yes	Yes
396	Yes	Yes	Yes	No	Yes	Yes
397	Yes	Yes	Yes	No	Yes	Yes
398	Yes	Yes	Yes	No	Yes	Yes
399	Yes	Yes	Yes	No	Yes	Yes
400	Yes	Yes	Yes	No	Yes	Yes
401	Yes	Yes	Yes	Yes	Yes	Yes
402	Yes	Yes	Yes	Yes	Yes	Yes
403	Yes	Yes	Yes	Yes	Yes	Yes
404	Yes	Yes	Yes	Yes	Yes	Yes
405	Yes	Yes	Yes	Yes	Yes	Yes
406	Yes	Yes	Yes	Yes	Yes	Yes
407	Yes	Yes	Yes	Yes	Yes	Yes
408	Yes	Yes	Yes	Yes	Yes	Yes
409	Yes	Yes	Yes	Yes	Yes	Yes
410	Yes	Yes	Yes	Yes	Yes	Yes
411	Yes	Yes	Yes	Yes	Yes	Yes
412	Yes	Yes	Yes	Yes	Yes	Yes
413	Yes	Yes	Yes	Yes	Yes	Yes
414	Yes	Yes	Yes	Yes	Yes	Yes
415	Yes	Yes	Yes	Yes	Yes	Yes
416	Yes	Yes	Yes	Yes	Yes	Yes
417	Yes	Yes	Yes	Yes	Yes	Yes
418	Yes	Yes	Yes	Yes	Yes	Yes
419	Yes	Yes	Yes	Yes	Yes	Yes
420	Yes	Yes	Yes	Yes	Yes	Yes

Table 5.12. Continued

Case	DAF			a _{max} (g)		
	≤1.5	≤2.0	≤2.5	≤0.05	≤0.10	≤0.20
421	Yes	Yes	Yes	Yes	Yes	Yes
422	Yes	Yes	Yes	Yes	Yes	Yes
423	Yes	Yes	Yes	Yes	Yes	Yes
424	Yes	Yes	Yes	Yes	Yes	Yes
425	Yes	Yes	Yes	Yes	Yes	Yes
426	Yes	Yes	Yes	Yes	Yes	Yes
427	Yes	Yes	Yes	Yes	Yes	Yes
428	Yes	Yes	Yes	Yes	Yes	Yes
429	Yes	Yes	Yes	Yes	Yes	Yes
430	Yes	Yes	Yes	Yes	Yes	Yes
431	Yes	Yes	Yes	Yes	Yes	Yes
432	Yes	Yes	Yes	Yes	Yes	Yes
433	Yes	Yes	Yes	Yes	Yes	Yes
434	Yes	Yes	Yes	Yes	Yes	Yes
435	Yes	Yes	Yes	Yes	Yes	Yes
436	Yes	Yes	Yes	Yes	Yes	Yes
437	Yes	Yes	Yes	Yes	Yes	Yes
438	Yes	Yes	Yes	Yes	Yes	Yes
439	Yes	Yes	Yes	Yes	Yes	Yes
440	Yes	Yes	Yes	No	Yes	Yes
441	Yes	Yes	Yes	Yes	Yes	Yes
442	Yes	Yes	Yes	Yes	Yes	Yes
443	Yes	Yes	Yes	Yes	Yes	Yes
444	Yes	Yes	Yes	Yes	Yes	Yes
445	Yes	Yes	Yes	Yes	Yes	Yes
446	Yes	Yes	Yes	Yes	Yes	Yes
447	No	Yes	Yes	No	Yes	Yes
448	No	Yes	Yes	No	Yes	Yes
449	No	Yes	Yes	No	Yes	Yes
450	No	Yes	Yes	No	Yes	Yes
451	Yes	Yes	Yes	Yes	Yes	Yes
452	Yes	Yes	Yes	Yes	Yes	Yes
453	Yes	Yes	Yes	Yes	Yes	Yes
454	No	Yes	Yes	Yes	Yes	Yes
455	No	Yes	Yes	Yes	Yes	Yes
456	Yes	Yes	Yes	No	Yes	Yes
457	No	Yes	Yes	No	Yes	Yes
458	No	Yes	Yes	No	Yes	Yes
459	No	No	Yes	No	Yes	Yes
460	No	No	Yes	No	Yes	Yes
461	Yes	Yes	Yes	Yes	Yes	Yes
462	Yes	Yes	Yes	Yes	Yes	Yes

Table 5.12. Continued

Case	DAF			a_{max} (g)		
	≤ 1.5	≤ 2.0	≤ 2.5	≤ 0.05	≤ 0.10	≤ 0.20
463	No	Yes	Yes	Yes	Yes	Yes
464	No	Yes	Yes	Yes	Yes	Yes
465	No	Yes	Yes	Yes	Yes	Yes
466	No	Yes	Yes	Yes	Yes	Yes
467	No	No	Yes	No	Yes	Yes
468	No	No	Yes	No	Yes	Yes
469	No	No	Yes	No	Yes	Yes
470	No	No	Yes	No	Yes	Yes

5.9 Design Solutions

There are various techniques for new bridge construction to mitigate the problem of irregularity formation, particularly in the vicinity of the transition zone. Mitigation methods have widely varied for both highways and railways. In this section, mitigation practices used in the past to prevent any types of irregularities from developing at transition zones along railway lines will be thoroughly reviewed. These methods are based on different approaches including reducing the settlement of the approach structure, minimizing the stiffness variation in the vicinity of the transition zones by either reducing the stiffness of the stiffer side or increasing the stiffness of the approaching embankment, increasing damping, and reducing ballast wear and movement (Banimahd 2008, Nicks 2009). Indeed, in designing transitions, the main consideration was to ensure either that the same vertical displacement occurs in both the stiff and soft side or at least that the differential settlement should not change rapidly (Kerr and Moroney 1993). Site

dependent factors dictate the types of solutions that should be chosen to reduce the problem of irregularity formation near the transitions.

As mentioned in this section, in the vicinity of the transition zones, the track stiffness increases from the approach compacted embankment to the bridge structure constructed on top of the rigid base. This differential track stiffness is known as the primary cause of track degradation or irregularity initiation. Minimizing the track stiffness change at transition zones can be achieved by either gradually increasing the stiffness on the approach embankment or decreasing the stiffness on the stiff side (Nicks 2009).

5.9.1 Stiffer Approach Structures

Approach slabs, oversized sleepers in the softer side, using geotextile or hot mixed asphalt (HMA) between ballast and subgrade, and using extra rails between or outside of the running rails are different solutions that can be applied to produce a stiffer track in the approach structures.

Placing extra rails attached to the sleepers developed by the German federal railway for ICE high-speed lines increases the bending stiffness of the rail on the approach structures (Banimahd 2008). Cantilevered or floating approach slabs with the fixed end supported by the rigid bridge structure and the free end supported by the subgrade, which have been used especially in the UK, are known as a mitigation method to improve the stiffness of the track on the softer side (Briaud et al. 1997, Hoppe 1999, Woodward et al.

2005, Nicks 2009). The main aim of constructing approach slabs is to provide a ramp for decreasing the differential settlement (Hoppe 1999). According to Briaud et al. (1997), the allowable slope for the angled slabs is less than 1:200 for highways. This limit for slope has not yet been defined precisely for railways. The main drawback of using approach slab is its maintenance costs.

As mentioned earlier in this section, another solution to improve the stiffness of the track on the softer side is to use oversized sleepers (Li et al. 2003). Increasing the length of the sleepers in the transition zone reduces the amount of differential settlement between approach and bridge structures. In fact, the length of the sleepers impacts the surface area over which the load is transmitted to the ballast. In addition to enlarging the length of the sleepers, increasing the sleepers' width and decreasing the sleepers' spacing can be used to stiffen the approach structure (Grissom 2005).

Nicks (2009) also proposed a new solution for approach embankments with soft subgrades at existing bridges to reduce the settlement on the approach structures in addition to minimizing the track stiffness variation in the vicinity of the transition zones. This valuable study included a full-scale field testing and numerical simulations of the proposed method. This method included installing varying-length steel bars between the sleepers into the subgrade as shown in Figure 5.64. These bars were used to increase the stiffness of the track on the soft side. In order to prevent any interference with future ballast tamping, these pile-like elements are installed directly underneath the ballast.

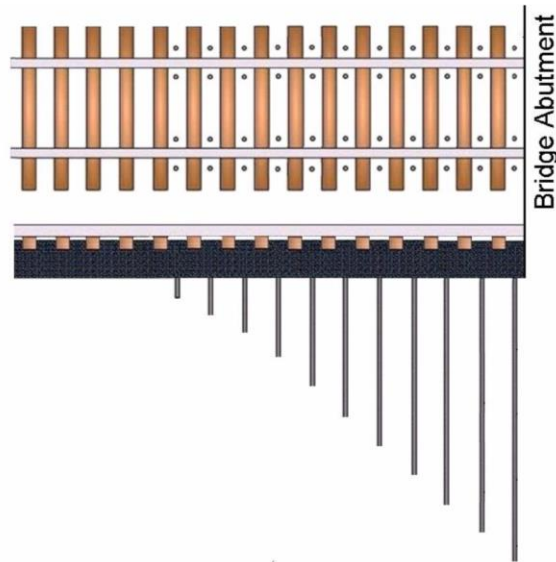


Figure 5.64. Schematic plan and cross-section view of the proposed solution by Nicks (2009)

5.9.2 Reduce Stiffness on Bridges

One of the most common and cost-effective techniques used to soften the stiffer side is to install elastic pads or mats, typically made of rubber or polyurethane (Li et al. 2003). They can easily be installed in a short time. There are four different types of placement of pads and mats including rail seat pads, sleeper plate pads, under sleeper pads, and ballast mats. These pads can also help with damping. All types of these installation pads and mats work to dissipate track loadings and vibrations. Depending on where in the track structure damping is required, pads can be installed between rails and the sleeper (rail seat pads), directly under the sleeper (sleeper plate pads), underneath the sleeper above the ballast (under sleeper pads), or under the ballast section (ballast mats).

5.10 Conclusions and Recommendations

In this section, the effects on train/track interaction responses of track modulus change along HSRs in transition zones at the bridge approach location, both for non-faulted and faulted tracks were numerically modeled. A verified 4-D FEM developed in LS-DYNA was used to conduct an extensive parametric study that resulted in proposing well-tested guideline charts that can be used to define tolerable irregularity size for different scenarios. This study includes two phases: modeling only the stiffness variation along the HSR lines without any irregularity along the track, and modeling different types of irregularities along high-speed tracks considering a wide range of irregularity sizes.

The results obtained from the first phase show that in the presence of no track faults, change of stiffness itself does not cause major problems when trains operate at low and medium speeds; even at high-speed train range, stiffness variation alone is not a major factor causing high train/track interaction responses. However, this factor (stiffness variation) can lead to initiating differential settlement in the vicinity of the transition zone, causing higher impact force and accelerating degradation of track and layers below. Indeed, the presence of any type of differential settlement called an irregularity along high-speed tracks can speed up deterioration of the railway track geometry as the result of significant increase in the dynamic wheel/rail interaction force. In this phase of the parametric study, it was clearly observed that the increase in train speed (V_T) and also the presence of a very soft layer under the track (soft subgrade with low modulus (E_s)) can increase both the interaction force affecting accelerating geometry deterioration and the train car body acceleration, affecting passenger comfort adversely.

Moreover, in phase two, the train/track dynamic responses due to the presence of different types and sizes of irregularities at different train speeds were investigated. It was shown that the train/track mechanism in the vicinity of the transition zone is mainly caused by the interaction responses of the train wheels as well as irregularities existing along the track in the transitions. The current parametric study was conducted to evaluate the effect of different parameters such as irregularity type, irregularity size including two variables (length and height), train speed, and subgrade modulus on the wheel/rail interaction force as well as maximum vertical train body acceleration. The results obtained from the parametric study show that among all parameters, train speed and irregularity size are most influential on the train/track responses. The subgrade modulus has the least effect on the train/track responses. It was also seen that although the irregularity height (deflection difference between softer and stiffer sides) has considerable impact on the train/track interaction responses, the effect of irregularity length variation on the wheel/rail interaction force and maximum train body acceleration is negligible. It was also confirmed that for a given irregularity length, the greater the irregularity height, the higher the interaction force and train body acceleration are at a constant train speed.

As mentioned earlier in this section, the primary goal of this research was to establish some well-tested guidelines of tolerable irregularity sizes for HSR consultants, designers, and engineers. Tolerable irregularity sizes for different high speeds at different soil moduli, presented in the form of charts and tables, were proposed. The train/track interaction responses were evaluated, keeping the dynamic amplification factor and maximum train body acceleration below the threshold values defined by different codes and research. Finally, different transition design techniques were reviewed in this section.

6 CONCLUSIONS AND RECOMMENDATIONS

6.1 Conclusions

In recent decades, the high demand for a safe and fast ride has caused rapid growth of HST lines. For example, in the United States, California is planning a HST line to link San Diego, Los Angeles, San Francisco, and Sacramento. The project is estimated at 68.4 billion US dollars (USD) for 1300 kilometers of rail, about 53 million USD per kilometer. The outcome of the current study can help railway designers to create safe and comfortable HSRs. This research was conducted to investigate three main geotechnical issues: the influence of rising groundwater levels on track stiffness, Rayleigh wave propagation effects, and the interaction problems of train/track interaction in transition zones, i.e., the stiffness variation and irregularity problems. In this research, a series of 4-D finite element models were developed to assess HSR system dynamic responses in specific situations. Data from field measurements and full-scale laboratory models were used to calibrate the 4-D FEMs. Extensive numerical analyses resulted in some proposed guidelines.

These guidelines are presented in charts that provide the data necessary for the design of safe embankments for HSTs. In addition, to minimize/eliminate an uncomfortable ride, defining tolerable irregularity size for HSR lines is important. In fact, by knowing the acceptable irregularity sizes for specific conditions, engineers can make better decisions regarding maintenance. Thus, creating graphs that show the irregularity size as a function of train speed was one of the goals of this work. Creating said graphs required establishing tolerability criteria for the interactions between train and rails

including maximum dynamic load, maximum train body acceleration, and more. Finally, a laboratory test was conducted to give the designer a better view of soil softening due to water level rising. The major findings of this research are summarized in this section.

6.1.1 Long-Term Moisture Softening of Compacted Embankments

Reviewing past studies reveals that vertical track stiffness is known as an important parameter for track design and track maintenance management. However, track stiffness can be varied during its service life due to the interaction between the environment, the natural soils and the embankment. It happens because poor drainage or weather conditions lead to changes in the soil water content, resulting in soil softening. Indeed, over time, water level variation in the compacted embankment and subsoil under the embankment can cause moisture softening of the embankment, leading to track stiffness variation. It was clear that subsoil modulus plays an important role in track stiffness, and any change in subsoil or natural soil modulus can effectively change track stiffness. It should be mentioned that the soil softening due to water level variation can cause serious problems such as large track deflection, accelerating track irregularity development and its consequences, reducing the critical speed, and so on. Because track stiffness has a strong impact on rail deflection, any change in subgrade modulus resulting in track stiffness variation can speed up track deterioration, leading to high maintenance costs or derailment in the worst scenario. Therefore, it is really important to have a clear understanding of the

effects wetting and drying cycles on the soil modulus and consequently on the track stiffness as an influential factor in track design. The current research has addressed the problem of soil softening due to water level variation through an extensive experimental study. This experimental research study was conducted to investigate the hydro-mechanical behavior of porcelain clay. Porcelain clay was chosen because fine-grained soils are more sensitive to moisture content change than to coarse-grained soils. A change in soil moisture content due to severe weather conditions like heavy rainfall, flood and drought, ground water level variation, or weak drainage is followed by a change in water tension between soil particles because the subgrade soil is considered unsaturated soil. As a result, changes in subgrade moisture levels can influence soil modulus greatly, and thus, in section 3, our main focus was on this major problem: long-term moisture softening of compacted embankments. As mentioned earlier, a laboratory study was performed to evaluate the effect of the ground water level rising in the soft, fine-grained soil. The experimental program included three different series of laboratory tests: unconsolidated undrained (UU) triaxial tests followed by chilled-mirror psychrometer tests (WP4) and salt solution equilibrium (SSE) tests. The major outcomes of these three sets of laboratory tests are listed below:

- The first set of experiments were the UU triaxial tests on the porcelain clay with different water contents to study the effect of the drying process on the Young modulus of the clayey soil. It should be noted that the Young modulus as a mechanical property of the soil was considered as one influential factor controlling deflection of the clayey soils. The primary goal of this set of

laboratory tests was to apply the outcomes of these tests to evaluate the relationship between soil modulus and soil moisture content. The results obtained from UU triaxial tests using the same samples under the same conditions except for their water content reveal that when soil samples are in the unsaturated situation, water content variation has a strong impact on the soil modulus changes. The soil modulus significantly increases as water content decreases. The plot of Young modulus of porcelain clay versus water content showed that soil modulus increases with water content decrease but not at the same rate. In order to explain the reason for these phenomena, hydro-mechanical behavior of unsaturated soil should be investigated. Due to the fact that the suction between soil particles plays an important role in mechanical behavior of the unsaturated soils, the UU triaxial tests were followed by two different test sets (WP4 and SSE tests) to determine the suction value between soil particles.

- As mentioned earlier, it was essential to measure suction and its effect on the soil modulus. To establish the relationship between soil modulus and suction, all UU triaxial tests were followed by WP4 tests adopted to measuring the suction value between soil particles of samples with different water contents. In addition, the results of these tests can be used to draw soil water retention curves (SWRC). The SWRC, a characteristic for various types of soil, is a plot of suction in the soil pores as a function of soil water content. It is also a hydraulic property of the soil considered in this experimental study. In the current study, two laboratory test sets were applied to achieve SWRC: WP4

and SSE tests. SWRCs plots obtained from both WP4 and SSE tests confirmed that suction in the soil pores increases as soil becomes drier. The slope of the suction variation as a function of water content is steeper when soil is in an unsaturated state. The same results were obtained when Young modulus was charted versus water content. These outcomes from UU triaxial tests and WP4 tests revealed that in an unsaturated state, the water tension or suction between soil pores plays a significant role in mechanical behavior of soils. To have a better understanding of the effect of suction between soil particles on the Young modulus as an important mechanical parameter of soils, the outcomes of two tests (UU triaxial tests and WP4 tests) were combined. A plot of Young modulus as a function of suction illustrated the relationship that exists between these two parameters (suction and Young modulus). It was clearly observed that the Young modulus of the soil increases considerably with suction when soil is in an unsaturated state.

- In addition to the WP4 test, the SSE test, which is a proper method of measuring suction in wide range was selected to study the hydraulic properties of porcelain clay. It was also chosen because it is a more reliable method to draw SWRC. It was expected that similar graphs would be obtained from the two tests; however, an obvious difference can be seen between the results obtained from WP4 and SSE tests. This was explained as being due to some experimental limitations. The most important reason was that the WP4 test is not a suitable test for a wide range of suction, and it can be applicable only in a limited range. Although the values of suction in some points are different,

the trend of the results is the same. The results of both tests revealed that suction value between soil particles ascends as soil becomes drier. Suction between soil pores increases with higher slope as water content decreases when soil is unsaturated.

In final analysis, this study shows that because water level variation exists in the compacted embankment and underlying soil layers can cause serious problems as a result of soil softening, appropriate drainage is vitally important. Different design solutions were reviewed as a part of this study.

6.1.2 Breaking the Rayleigh Wave Barrier

One of the most complicated issues regarding HSR lines which has been the concern of different researchers is breaking the Rayleigh wave barrier and the consequences of doing so. Track, compacted embankment and subsoil experience large deflection when train speed approaches the Rayleigh wave speed of the track/embankment/ground system. Different research has confirmed that the maximum track deflection (resonance) occurs at the threshold speed called the critical speed, which is very close to the subsoil Rayleigh wave speed when track is constructed on top of a very shallow embankment (embankment thickness less than 1.0 m ($H_e < 1.0\text{m}$)). This threshold speed is also known as Ground Mach 1.0 (GM1.0). In fact, when a train approaches the threshold speed of the equivalent Rayleigh wave speed of a track/embankment/ground system, it is subjected to the same

phenomena as an airplane going through the sound barrier. Reviewing past studies including various experimental and numerical ones revealed that the vibration induced in the track/embankment/ground structures increases with train speed. The results obtained from instrumented tests performed at different sites indicated that this problem becomes more severe when a HST is operating on tracks located on top of a very shallow embankment underlaying very soft soils. Indeed, in this case, the Rayleigh wave speed of the whole track/embankment/ground system is very low (the Rayleigh wave speed is almost equal to the Rayleigh wave speed of the ground or subsoil). As a result of passing the threshold speed, large dynamic amplification happens, leading to large track vertical movement which may result in high maintenance cost and/or train derailment in the worst-case scenario. The current study aimed at addressing this main geodynamic challenge through extensive finite element modeling. Using LS-DYNA, a well-tested 4-D FEM was developed and verified using measurements and lab experiment results obtained from literature. A summary of the major findings of the 4-D finite element simulations are listed below:

- The reliability of the 4-D FEM was assessed using field measurements from a site in Sweden. The measurements included the time history of the vertical track displacement for different train speeds and the maximum track displacement under the moving train load versus train speeds. These outcomes were used for model verification. The track vertical displacement time history obtained from both measurements and simulations confirmed that as trains run at train speeds much less than critical speed ($V_T \leq 0.3 V_C$ or $V_T \leq 0.3 V_{Req}$), displacement in term of magnitude is almost equal to the displacement due to

the static load. This means that at this range of train speed, displacements are quasi-static and there are no signs of dynamic effects of wave propagation through the soil skeleton. The displacement pattern is almost symmetric, a mirror image of the train axle load and downward. As train speed passes 30% of the critical speed but does not reach the threshold critical speed ($0.5 V_C \leq V_T \leq 0.7 V_C$ or $0.5 V_C \leq V_T \leq 0.7 V_{Req}$), the displacement pattern changes from a symmetric pattern. The effect of wave propagation can be observed in this range of train speed. The maximum displacement of the track starts increasing. However, the dynamic effect of Rayleigh wave propagation at this range of train speeds is negligible. On the other hand, when train speed approaches the critical speed ($0.7 V_C \leq V_T \leq V_C$ or $0.7 V_C \leq V_T \leq V_{Req}$), an asymmetrical displacement pattern with a tail of free oscillation following the moving train load can be clearly seen. A graph of maximum track vertical displacements as a function of train speeds illustrated that at critical speed ($V_T = V_C = V_{Req}$), maximum track vertical displacement occurs. By means of this well-developed FEM, the essential feature of the HSR track/embankment/ground responses as train speed varies can be suitably reproduced. The results obtained from simulations match well with measurement, meaning that the developed FEM used in the current study is valid and reliable. This reliable FEM was used to perform an extensive parametric study leading to proposing a design procedure that prevents breaking of the Rayleigh wave barrier and the consequences of doing so.

- Moreover, a full-scale experimental study conducted in China was used for model validation. The results obtained from the experimental model and simulation showed that significant increases in track displacement, vibration and stress in the embankment and subgrade were observed as train speed approached the critical speed. Also, the higher the train speed, the deeper the vibration that can be experienced. Simulations confirmed that as train speed increases, the depth of influence increases, as was also seen experimentally.
- As the train approaches the threshold speed of the equivalent Rayleigh wave speed of the medium (the critical speed), the wave generated by train reaching this speed propagates through the medium, which results in the same phenomena as an airplane breaking the sound barrier. In aerospace engineering, Mach number (M) is a dimensionless quantity representing the ratio of airplane speed (V_A) to the speed of sound (V_S). Mach 1.0 ($M1.0$) is defined as an airplane moving at the speed of sound, leading to a sharp disturbance inducing a shock wave that affects the airplane. In the same way, the Ground Mach number (GM) can be defined as the ratio of train speed (V_T) to the Rayleigh wave speed (V_R). Ground Mach 1.0 ($GM1.0$) happens when a train operates at the Rayleigh wave speed of the medium. At $GM1.0$, the maximum track response can be clearly observed. Subsonic conditions occur for Ground Mach numbers less than one ($GM < 1.0$) and supersonic conditions occur for Ground Mach numbers greater than one ($GM > 1.0$). These criteria were used to define safe and unsafe train speed zone in the design charts with guidelines that were developed in this study. The results of the simulations

showed that the displacement contour shapes change as train speed increases from subsonic speed to supersonic speed. When trains run at subsonic speeds ($GM < 1.0$ or $V_T < V_R$), the displacement contour is symmetrical and under the moving load. On the other hand, as train speed passes $GM 1.0$ (critical speed) the Ground Mach cone induced under the moving load, and the bulb of displacement contours lag behind the train wheels. As trains go faster in supersonic conditions, the cone tip angle becomes steeper. Near the supersonic condition ($GM > 0.7$), the dynamic effect of wave propagation leads to a high level of vibration through the medium, resulting in high track/embankment/soil responses. Therefore, this range of train speed is considered as an unsafe zone which should be avoided.

- Through an extensive parametric study, the influences of different parameters on the track responses were investigated. The results obtained from these parametric studies were used to establish well-tested guideline charts. These parameters were chosen to check their effects on the equivalent Rayleigh wave speed of the whole medium. According to the different design techniques reviewed in the current study, an effective proposed solution to the problem of breaking the Rayleigh wave barrier is to increase the Rayleigh wave speed of the whole track/embankment/ground system so that it is at least 1.5 to 1.7 times greater than the operational train speed. Through reviewing the previous study, it was confirmed that almost all design methods solve this problem by either strengthening the soft ground under the embankment or stiffening the embankment. Therefore, in this project, the most influential parameters,

including subsoil and embankment modulus in addition to embankment height, were chosen to determine their effects on the equivalent Rayleigh wave speed of the whole system. In all cases, the presence of a track critical speed at which the dynamic amplification leads to maximum track vertical displacement was confirmed. It was shown that this is not always around the Rayleigh wave speed of the subgrade. The critical speed magnitude depends on different factors such as both embankment and subgrade mechanical properties and embankment height. For conventional track with shallow and soft embankment on top of a very soft subgrade soil, it has been confirmed that the critical speed is around the Rayleigh wave speed of the subgrade, which is very low and becomes the researchers' big concern. On the other hand, the results of the parametric study showed that either stiffer and deeper embankments or stiffer subgrades can be effectively used to improve the track responses by increasing the critical speed and decreasing track displacement. Indeed, in a well-designed track, the critical speed is equal to the Rayleigh wave speed of the whole system, not only the subgrade. The deeper and stiffer embankment plays an influential role in defining the Rayleigh wave speed of the whole track/embankment/ground system called the equivalent Rayleigh wave speed (V_{Req}) of the whole system. This equivalent Rayleigh wave speed is much higher than subgrade Rayleigh wave speed when deeper and stiffer embankment is constructed under the track.

- As mentioned earlier, extensive numerical simulations were conducted to propose guideline charts for the design of safe embankment for HSRs. A

design procedure is comprised of two main steps including defining the GM number of the whole system and defining the speed zone based on threshold values. In the first step, like conventional railway lines, it was assumed that embankment does not have a great impact on estimating the GM number, and the only soil layer involved in GM assessment is the subgrade layer. Using equations, an acceptable value for GM can be obtained. In the next step, this GM value should be compared with the threshold value. In the current study, it was confirmed that when GM was kept below 0.7, substructures and super structures would not experience high levels of vibration induced by running HSTs. If GM determined that the first step is already below 0.7, it can be concluded that the main goal of safe design is achieved; on the other hand, if GM is greater 0.7, a design technique should be chosen properly to decrease the GM. In order to decrease the GM below threshold value, either train speed should be decreased or Rayleigh wave speed of whole system should be increased. Since the operational train speed is considered to be constant to provide a fast ride for passengers, the only way to decrease the GM is to increase the Rayleigh wave speed of track/embankment/ground systems to a value which is called the equivalent Rayleigh wave speed. To choose the best method of safe design, the guideline charts prepared through the extensive numerical simulations could be helpful at this step. These guideline charts show that either increasing the strength of subsoil or stiffening the embankment can effectively help the railway engineers to increase equivalent

Rayleigh wave speed of the whole system such that the GM is kept below 0.7 or any other selected threshold values.

- In the current design procedure, in addition to GM criteria, the permissible maximum track vertical deflection was also considered. According to different codes, the maximum track vertical displacement should not exceed 2.0 mm. If the track vertical displacement passes this threshold value, the embankment must be designed to reduce the track vertical displacement.
- To wrap up this part of the study, some well-known design methods were reviewed. The main objective of these design solutions is to prevent soil layer degradation caused by HST vibration. These design solutions seem to be necessary when the HSR lines cross over a very soft area.

6.1.3 Bumps in High-Speed Rails

Among all different causes of developing various types of irregularities, transition zone (for example, near bridges) was our primary concern in the current study. Indeed, the problem of bump or any type of differential settlement in the vicinity of the transition zones is not only the main issue of the railway industry, but also this problem has been addressed as a main concern of highway sectors. The transition zone between compacted embankments and bridge abutments resting on deep foundation has been known as a major source of track bumps or any other type of irregularity.

In this study, to evaluate the effect of track modulus variation alone (non-faulted tracks) and track irregularity (faulted track) on the train/track responses along HSR in transition zones, both faulted and non-faulted tracks was numerically modeled using finite element software, LS-DYNA. The main goal of this valuable work was to establish guidelines included in charts that define the tolerable irregularity size for HSR lines such that both comfort and safety criteria were considered. The main outcomes of this part of the study are summarized below:

- According to the simulations conducted by the coupled finite element model of train/track/embankment, when only stiffness changes at transition zones were considered (non-faulted track), it was seen that having a softer subgrade and an increase in train speed are two effective parameters that play an important role in train/track/soil responses. Both the interaction force between rail and wheel and the maximum vertical train body acceleration increase as either train speed increases or the Young modulus of the subgrade decreases. It should be noted that although stiffness variation in the vicinity of the transition zone influences the train/track responses, this effect is not significant enough to worry about. However, stiffness variation is a big problem because it leads to differential settlement and further development of irregularities. While the interaction force increase caused by stiffness variation is not great enough to be noticed, in the long term it generates differential settlement and affects passenger comfort and safety adversely by increasing the interaction force between rail/wheel and the maximum vertical train body acceleration.

- The effect of track faults (different types of irregularity) on train/track/soil responses was evaluated through an extensive numerical simulation in the second phase of the study. The effects of different parameters including subgrade modulus, train speed, type of irregularity, and irregularity size on the train/track/soil dynamic response were investigated. Based on the simulations conducted by the coupled train/track/soil model of irregularity along railway lines (faulted tracks), it was clearly observed that increased train speed, having a softer subgrade, and irregularity with steeper slope leads to increasing the interaction force considerably in the transition zone, which significantly influences the passenger safety and comfort adversely. Increase in dynamic interaction force between wheel and rail in the vicinity of the transition zone, for example near the bridges, caused more train excitation because of the differential displacement (different types of irregularities) between the rigid and soft sides of the transition zone. The comparison between results obtained from first phase of the parametric study (non-faulted tracks) and the second phase (faulted tracks) indicates that in the presence of no track fault, the stiffness variation on its own does not cause a major problem, particularly at low and medium train speeds and with a stiffer subgrade. On the other hand, the outcomes confirmed that in the presence of track irregularities with high slope, at high train speeds, high interaction force results in large track differential settlement near the bridges. Moreover, the dynamic amplification factor (DAF) and maximum train body acceleration exceeded the threshold values. In fact, the presence

of a track irregularity was clearly seen to be the major source of the increase in interaction force and maximum train body acceleration resulting in passengers' discomfort.

- Using the coupled train/track/soil model in the presence of a rise irregularity near a bridge, an extensive parametric study was performed on the transition issues in terms of the different variables used to define the irregularity size, including irregularity length and irregularity height. Comparing the interaction force and train body acceleration results for two different rise lengths, rise height, train speed, and subgrade modulus values indicate that rise length does not have a noticeable impact on the train/track responses. However, for a given rise length, it was shown that as the deflection difference (rise height) increases (or the rise slope becomes steeper), the DAF and maximum train body acceleration increase and passengers feel uncomfortable and unsafe in this transition zone. It was indicated that irregularity height coming from the resilient behavior of a conventional track plays a significant role in train/track responses. This effect becomes even more severe at higher train speeds.
- In this study, different types of probable irregularities including rise, drop, bump, and dip were assessed for their effects on train/track interaction responses. The results including the DAF and maximum train body acceleration versus train speeds for different irregularity types for a given irregularity size did not indicate an obvious pattern for the results. In total, it can be seen` that the presence of any type of irregularity in the model

leads to more severe train/track responses, especially at high speeds and steeper irregularities, and this affects passenger safety and comfort.

- The main goal of conducting the parametric study was to propose some guideline charts to define the tolerable irregularity size for HSR lines while keeping the DAF and maximum train body acceleration below the identified threshold values. Acceptable irregularity sizes for given subgrade moduli and train speeds both in the form of charts and tables were provided for HSR consultants, designers, and engineers. The primary objective of these guidelines is to define the tolerable irregularity size where a safe and comfortable ride is provided for passengers.
- This part of the study ended with reviewing different applicable transition solutions. The main aim of mitigation methods is to prevent any type of irregularity from developing at transition zones along HSR lines. Most of these design techniques were based on either reducing the potential track faults and permanent deformation in the vicinity of transition zones or providing a smoother track stiffness variation.

6.2 Future Related Research

There are a number of possible areas for further research within the geodynamic issues regarding high-speed railway lines which were addressed in the current study. The following section contains a list of recommendations for future studies.

6.2.1 Long-Term Moisture Softening of Compacted Embankments

The following areas are strongly recommended for future studies within the topic of long-term soil softening due to water content variation:

- In this study, only one type of soil, porcelain clay, was used to run the test. It would be valuable if different types of soil, especially natural soils, were used to evaluate their hydro-mechanical behavior.
- Because problems associated with HSR lines are considered as dynamic problems, it is strongly recommended to conduct cyclic triaxial tests to have a better estimate of resilient behavior of soil due to cyclic loads.
- In this study, due to the fact that weather conditions resulted in both soil drying and wetting, it would be good to draw an SWRC of drying and wetting paths together.

- An extensive parametric study through numerical simulation using for example COD-BRIGHT could be helpful to investigate the effect of water level variation on long-term soil deterioration.

6.2.2 Breaking the Rayleigh Wave Barrier

The possible avenues for continued research within the problem of the breaking Rayleigh wave barrier are listed below:

- The effects of different design techniques on wave propagation in substructure and superstructure, track/embankment/soil dynamic responses, and increasing the critical speed (or equivalent Rayleigh wave speed) can be simulated to evaluate the effectiveness and applicability of each method.
- The effect of train bogie space and train wheels' space on the track response should be evaluated. It was expected that there is a relationship between these space parameters and the predominant soil layer wave length. This relationship can be assessed through conducting a parametric study changing the bogies' or wheels' space running on the layered soil whose wave length is specified.
- A simple one-layer embankment and soil was modeled in the current study. Using the verified 4-D finite element model developed in this

study, more complicated cases, including layered soil which is very close to the reality, can be modeled to estimate the critical speed at which the maximum track responses occurs.

- Numerically, and theoretically, it was confirmed that there is a critical speed at which resonance happens; however, there is no measurement showing that at this special speed, this phenomenon occurs. It would be helpful to measure the track response as a function of train speed to study and assess the reliability of this theory.

6.2.3 Bumps in High-Speed Rails

There are some areas that can be considered for future study:

- It was shown that the effect of rise length on the track responses can be neglected; however, it is crucial to continue the parametric study and check the effect of irregularity length on the track interaction responses when the other types of irregularities are modeled along the HSR lines.
- The effectiveness and applicability of each design mitigation can be numerically evaluated for both faulted and non-faulted tracks.
- Only one type of train with a specific suspension system was considered in the current parametric study. Assessing the impact of the suspension system, including springs and damper on the track/train

interaction responses, can be valuable because to reduce the maximum vertical track acceleration and consequently increase the passengers' comfort, these parameters play an important and influential role. In this study, more focus was the track, embankment, and natural subgrade.

- Comparing the track/train interaction responses when a full train passes faulted and non-faulted tracks to the simple one bogie is strongly recommended for future study.

REFERENCES

- Abu Sayeed, MD., Shahin, M.A. (2016). Three-dimensional numerical modeling of ballasted railway track foundations for high-speed trains with special reference to critical speed. *Transportation Geotechnics. Vol. 6. 55-65*
- Adolfsson, K., Andreasson, B., Bengtsson, P., & Zackrisson, P. (1999). HST X2000 on soft organic clay-measurements in sweden train a grand vitesse X2000 sur argiles molles et organiques-mesures en suede. Paper presented at the *Geotechnical Engineering for Transportation Infrastructure: Theory and Practice, Planning and Design, Construction and Maintenance: Proceedings of the Twelfth European Conference on Soil Mechanics and Geotechnical Engineering, Amsterdam, Netherlands, 7-10*
- Alva-Hurtado, J. E., & Selig, E. T. (1981). Permanent strain behaviour of railroad ballast. *Proceedings of the 10th International Conference on Soil Mechanics and Foundation Engineering, Stockholm, Sweden, pp. 543-546.*
- American Society for Testing and Materials, ASTM D2850-87, Standard Test Method for Unconsolidated, Undrained Compressive Strength of Cohesive Soils in Triaxial Compression.
- AREA (American Railway Engineering Association). (1996). Manual for railway engineering, Washington, DC.
- AREMA 2006 Annual Conference, *Louisville, KY, USA, Sept. 18-20.*
- Ausherman, N. (2016). Federal railroad administration.

- AREMA (American Railway Engineering and Maintenance-of-Way Association).
(2008). *Manual for Railway Engineering*. Washington, DC.
- Arnold, R., Shu, S., Hogan, C., Farritor, S., Fateh, M., and El-Sibaie, M. (2006).
Measurement of Vertical Track Modulus from a Moving Railcar. *Proceedings of
the AREMA 2006 Annual Conference, Louisville, KY, USA, Sept. 18-20.*
- Aubeny, C. & Lytton, R. (2002). PROPERTIES OF HIGH-PLASTICITY CLAYS.
FHWA/TX-02/2100-2, Texas Department of Transportation.
- Aubeny, C. & Lytton, R. (2003). LONG-TERM STRENGTH OF COMPACTED
HIGH-PI CLAYS. *FHWA/TX-03/2100-1, Texas Department of Transportation.*
- Banimahd, M. and Woodward, P.K. (2007). 3-Dimensional Finite Element Modelling of
Railway Transitions. *Proceedings of 9th International Conference on Railway
Engineering, London, June 2007.*
- Banimahd, M. (2008). *Advanced Finite Element Modelling of Coupled Train-Track
Systems: A Geotechnical Perspective, Thesis for the Degree of Doctor of
Philosophy, Heriot-Watt University, UK.*
- Bastin, R. (2005). *Development of German non-ballasted track forms. ICE. UK.*
- Bell, A.L. (1993). Jet Grouting Improvement. *Blachie Academic/Professional.*
- Berggren, E. (2002). Dynamic Track Stiffness Measurement – A New Tool for
Condition Monitoring of Track Substructure. *Licentiate Thesis, Report TRITA
AVE 2005:14, Royal Institute of Technology (KTH), Stockholm.*
- Berggren, E. (2005). The role of vertical track stiffness measurements in condition based
maintenance of railway tracks – A pilot study, *Report TRITA AVE 2005:31,
Royal Institute of Technology (KTH), Stockholm.*

- Berggren, E. (2009). Railway track stiffness: Dynamic measurements and evaluation for efficient maintenance, *Thesis for the Degree of Doctor of Philosophy, Royal Institute of Technology (KTH), Stockholm.*
- Bian, X., Chen, Y., & Hu, T. (2008). Numerical simulation of high-speed train induced ground vibrations using 2.5 D finite element approach. *Science in China Series G: Physics, Mechanics and Astronomy*, 51(6), 632-650.
- Bian, X., Jiang, H., & Chen, Y. (2016). Preliminary testing on high-speed railway substructure due to water level changes. *Procedia Engineering*, 143, 769-781.
- Bian, X., Jiang, H., Cheng, C., Chen, Y., Chen, R., & Jiang, J. (2014). Full-scale model testing on a ballastless high-speed railway under simulated train moving loads. *Soil Dynamics and Earthquake Engineering*, 66, 368-384.
- Briaud, J. (2013). *Geotechnical engineering: Unsaturated and saturated soils* John Wiley & Sons.
- Briaud, J., James, R. W., & Hoffman, S. B. (1997). Settlement of bridge approaches: (the bump at the end of the bridge), *NCHRP, Synthesis of Highway Practice 234, Transportation Research Board, Washington, D.C.*
- Briaud, J.L. & Tafti, S.R. (2017). High Speed Trains Geotechnics: What is a Tolerable Bump?. *Procedia Engineering 2017. Vol. 189, 186-192*
- Burke, G.K., Cacoila, D.M., & Chadwick, K.R. (2000). Super Jet Grouting: A new Technology for In situ Improvement. *Proceeding Transportation Research Board 2000 Annual Meeting, Washington D.C., USA.*
- Definition of high speed rail (2017) BULLET TRAINS. Retrieved from <http://bullettrains.webnode.com/>

- Cai, Z., Raymond, G.P., and Bathurst, R.J. (1994). Estimate of static track modulus using elastic foundation models. *Transportation Research Record 1470, National Academy Press, Washington, D.C., pp. 65-72.*
- Cai, Y., Z. Cao, H. Sun, and C. Xu. (2009). Dynamic Response of Pavements on Poroelastic Half-Space Soil Medium to a Moving Traffic Load. *Computers and Geotechnics*, 36(1), 52–60.
- Carlsten, P. & Ekstrom, J. (1997). Lim and Lim Cement Columns. Guide for project planning, construction and inspections. *Swedish Geotechnical Institute, SGF Report 4:95E, 111p.*
- Ceratti, J.A.P., Gehling, W.Y.Y., Núñez, W.P. (2004). Seasonal variations of a subgrade soil resilient modulus in southern Brazil. *Transportation Research Record, Washington, D.C. Vol. 1874, 165–173.*
- Chang, C.S., Adegoke, C.W., and Selig, E.T. (1980). The GEOTRACK model for railroad track performance. *Journal of Geotechnical Engineering Division, ASCE, Vol. 106, No. GT11, Nov. 1980, pp. 1201-1218.*
- Chen, R., Chen, J., Zhao, X., Bian, X., & Chen, Y. (2014). Cumulative settlement of track subgrade in high-speed railway under varying water levels. *International Journal of Rail Transportation*, 2(4), 205-220.
- Clark, C. W. (1957). Track loading fundamentals-parts 1-7. *Railway Gazette*, 106.
- Costa, Y. D., Cintra, J. C., and Zornberg, J. G. (2003). Influence of matric suction on the results of plate load tests performed on a lateritic soil deposit. *Geotech. Test. J.*, 26 (2), 1–9.

- Clark, M., McCann, D. M., and Forde M. C. (2002). Infrared thermographic investigation of railway track ballast. *NDT&E International*, 35: 83-94.
- Cui, Y. (2014). On the hydro-mechanical behavior of unsaturated soils in railway sub-structures. *Unsaturated Soils: Research & Applications – Khalili, Russell & Khoshghalb (Eds) Taylor & Francis Group, London, ISBN 978-1-138-00150-3*, 117.
- Dahlberg, T. (2001). Some railroad settlement models-a critical review. *Proceedings of Institution of Mechanical Engineers, Part F, Journal of Rail and Rapid Transit*, 215: 289- 300
- Darr, E. & Fiebig, W. Feste. (2006). *Fahrbahn: Konstrktion und Bauarten für Eisenbahn und Strassenbahn, Second edition. Eurailpress. Germany.*
- Davis, D., & Li, D. (2006). Design of track transitions. Research Results Digest 79. *Transportation Technology Center, Inc., Pueblo, Colorado*, 4-15.
- Davis, D., & Plotkin, D. (2009). Track settlement at bridge approaches. *Railway Track and Structures*, 105(2)
- Davis, D. D., Otter, D., Li, D., & Singh, S. (2003). Bridge approach performance in revenue service. *Railway Track and Structures*, 99(12), Issue 12, New York, pp. 18.
- De Nie, F.C. (1948). Undulation of railway embankments on soft sub-soil during passing of trains. *Proceedings of the 2-nd Conf. on Soil Mech. and Found. Engineering 1948, Vol. II*, 8-12

- De Nie, F.C. (1949a). Verbetering van de Spoorbaan Oudewater-Gouda. *Spoor- en Tramwegen*, 22e jaar, Nr.14, 14 juli 1949: pages 209-212 and Nr.15, 28 juli 1949: pages 227-230 (Dutch)
- De Nie, F.C. undated, approx. 1949b. De verbetering van spoorbanen op slappe grond. Archives N.V. Nederlandse Spoorwegen. *Probably unpublished manuscript approx. 1949: Utrecht: Projectorganisatie HSL-Zuid Infra (Dutch).*
- Directive 96/48/EC - Interoperability of the transEuropean high speed rail system.
- Retrieved from
<https://www.transportstyrelsen.se/globalassets/global/jarnvag/english/tsi/tsi-highspeed-operation-techntext-2008-02-01.pdf>
- Doung, TV., Cui, YJ., Tang, AM., Dupla, JC., Calon, N., & Robinet, A. (2014). Investigating the mud pumping and interlayer creation phenomena in railway sub-structure. *Engineering Geology*. Vol 171, 45-58.
- Doyle, N.F. (1980). Railway Track Design-a Review of Current Practice. *Australian Government Publishing Service Canberra.*
- Drainage of railway tracks. (2017). Retrieved from
<http://www.tenax.net/geosynthetics/drainage/railway-track-drainage.htm>
- Dupont, B., & Allen, D. L. (2002). Movements and settlements of highway bridge approaches, *Research Report, Kentucky Transportation Center.*
- Ebersohn, W. and Selig, E.T. (1994). Track Modulus on a Heavy Haul Line. *Transportation Research Record 1470*, pp.73-83.

- Edil, T. B. (1973). *Influence of fabric and soil-water potential on stress-strain response of clay, Thesis for the Degree of Doctor of Philosophy, Northwestern Univ., Evanston, Ill.*
- Edil, T. B., and Krizek, R. J. (1976). "Influence of fabric and soil-water potential on the mechanical behavior of kaolinitic clay." *Geoderma*, 15, 831–840.
- Edil, T.B. & Motan, S.E. (1979) Soil-water potential and resilient behavior of subgrade soils. *Transportation Research Record*, n° 705. 54–63.
- Edil, T. B., Motan, S. E., and Toha, F. X. (1981). Mechanical behavior and testing methods of unsaturated soils. *Laboratory Shear Strength of Soil, ASTM STP 740, ASTM, West Conshohoken, Pa.*
- El Kacimi, A., Woodward, P. K., Laghrouche, O., & Medero, G. (2013). Time domain 3D finite element modelling of train-induced vibration at high speed. *Computers & Structures*, 118(0), 66-73.
doi:<http://dx.doi.org/10.1016/j.compstruc.2012.07.011>
- Eisenmann, J., and Rump, R. (1997). Ein Schotteroberban für hohe Geschwindigkeiten (In German). *Eisenbahntechnische Rundschau*, 3: 99-107.
- Esveld, C. (1997). Innovations in Railway Track. *Conferentie Railtech. Delft University of Technology*.
- Esveld, C. (2001). *Modern railway track*. MRT-Productions Duisburg
- Chandra, S. & Agarwal, M.M. (2016). Failure of Railway Embankment. Retrieved from http://www.brainkart.com/article/Failure-of-Railway-Embankment_4206/

- Farritor, S. (2006). Real-Time Measurement of Track Modulus from a Moving Car, *Final Report, U.S. Department of Transportation, FRA, Washington, DC, January 2006.*
- Feigenbaum, B. (2013). *High-Speed Rail in Europe and Asia: Lessons for the United States.* Reason Foundation
- Feng, YY, Zhang YS, Qu, YX, & Huang, CB. (2001). Mechanism of embankment defects caused by expansive soils in Baise Basin, Nankun railway, China. *Journal of Geotechnical Engineering, 23(4), 463-767.*
- Ferrari, A., Marschall, P., & Laloui, L. (2014). Experimental analysis of the retention behavior of shales. *International Journal of Rock Mechanics and Mining Science*
- Ferreira, T.M. & Teixeira, P.F. (2011). Impact of different drainage solutions in the behavior of railway trackbed layers due to atmospheric action. *9th World Congress on Railway research (WCRR), May 22-26.*
- Fortin, J.P. (1982). La déformée dynamique de la voie ferrée. *Revue Générale des Chemins de Fer, Février 1982, 101e année: pages 93-102.*
- Franz, Q. (2001). Innovative Track Systems Technical Construction. *Project funded by the European Community, Directorate General Energy and Transport Under the 'Competitive and Sustainable Growth' Programme. ProMain. TÜV Intertraffic, Cologne. Oct. 2001.*
- Fredlund, D. G., Bergan, A. T., and Sauer, E. K. (1975). The deformation characteristics of subgrade soils for highways and runways in northern environments. *Can. Geotech. J., 12 (2), 213–223.*

- Fredlund, D. G., Bergan, A. T., and Wong, P. K. (1977). Relation between resilient modulus and stress conditions for cohesive subgrade soils. *Transportation Research Record. 642, Transportation Research Board, Washington, D.C.*
- Fredlund, D. G., and Morgenstern, N. R. (1977). Stress state variables for unsaturated soils. *Journal of Geotechnical Engineering*, 103(GT5), 447–466.
- Fredlund, D. G., Morgenstern, N. R., and Widger, R. A. (1978). The shear strength of unsaturated soils. *Can. Geotech. J.*, 15 (3), 313– 321.
- Fredlund, D.G., & Rahardjo, H. (1993). *Soil Mechanics for Unsaturated Soils. New Yourk: John Wiley & Sons.*
- Frederick, C.O. (1978). The effect of wheel and rail irregularities on the track. *1st International Heavy Haul Conference, Perth, Australia, Sept. 1978.*
- Frederick, C.O., Round, D.J., (1985), Vertical Track Loading, Track Technology: *Proceedings of a Conference, University of Nottingham, UK, Thomas Telford Ltd., July 11-13, pp. 135-149.*
- Grissom, G. (2005). Influence of Cross Ties on Track Stiffness and Track Transition. *Paper Presented to AREMA Committee 30 Meeting, Skokie, Ill., Sept. 28-29, 2005.*
- Hall, N. (May 05 2015). Mach number. Retrieved 10/11, 2016, from <https://www.grc.nasa.gov/www/k-12/airplane/mach.html>
- Grandil, J., and Ramondence, P. (1990). The dynamic behaviour of railways on high-speed lines, *SNCF, Paris.*

- Halkola, H. (1999). Keynote Lecture: Quality Control for dynamic methods. Proceeding International Conference Dry Methods for Deep soil Stabilization, Stockholm, Sweden, 285-294.
- Hall, L. (2000). *Simulations and analyses of train-induced ground vibrations, a comparative study of two and three-dimensional calculations with actual measurements, Thesis for the Degree of Doctor of Philosophy, Royal Institute of Technology, Sweden*
- Hallquist, J.O. (2006). LS-DYNA Theory Manual. Livermore Software Technology Corporation, http://www.lstc.com/pdf/ls-dyna_theory_manual_2006.pdf.
- Hay, W.W. (1982). *Railroad Engineering, Second Edition. John Wiley & Sons, New York.*
- Hendry, M.T. (2007). *Train-induced Dynamic Response of Railway Track and Embankments on Soft Peaty Foundations. Thesis for the Degree of Master of Science, University of Saskatchewan, Saskatoon, Canada.*
- Hetényi, M. (1946). *Beams on Elastic Foundations. University of Michigan Press, Ann Arbor, MI.*
- High speed rail history (2017). UIC. Retrieved from <https://uic.org/High-Speed-History>
- Hillig, J. (1996). Geotechnische Anforderungen an den Eisenbahnunterbau. *Eisenbahningenieur 47, Marz 1996: pages 24-31.*
- Holm, G., Andreasson, B., Bengtsson, P.E., Bodare, A., & Eriksson, H. (2002). Mitigation of Track and Ground Vibrations by High Speed Trains at Ledsgrd,

- Sweden. *Report 10, Svensk Djupstabilisering, Swedish Deep Stabilization Research Centre.*
- Hoppe, E.J. (1999). Guidelines for the use, design, and construction of bridge approach slabs. *Virginia Transportation Research Council, Charlottesville, Virginia.*
- Hunt, G. A. (1994). Analysis of requirements for railway construction on soft ground. *Technical Report LR TM 031, British Rail Research, London, UK.*
- Hunt, H.E.M. (1997). Settlement of railway track near bridge abutments. *Proceedings of the Institution of Civil Engineers, Transportation, Vol. 123, Thomas Telford, pp. 6873.*
- Hunt, H.E.M. and Newland, D.E. (1996). The effect of variable foundation properties on railway-track vibration. *Proceedings of the 4th International Congress on Sound and Vibration, St. Petersburg, Russia, June 24-27, pp. 1065-1072*
- Inci, G., Yesiller, N., and Kagawa, T. (2003). Experimental investigation of dynamic response of compacted clayey soils. *Geotech. Test. J., 26(2), 125–141.*
- Indraratna, B., Khabbaz, H., Salim, W., Christie, D. (2006). Geotechnical properties of ballast and the role of geosynthetics in rail track stabilization. *Ground Improvement, Vol. 10 (3), July, pp. 91-101.*
- International Union of Railways. (1994). Earthworks and track-bed layers for railway lines. *UIC Code 719 R, Paris, France.*
- Iwnicki, S., ed. (2006). *Handbook of Railway Vehicle Dynamics, CRC Press.*
- Jenkins, H.H., Stephenson, J.E., Clayton, G.A., Morland, G.W., Lyon, D. (1974). The Effect of track and Vehicle Parameters on Wheel/Rail Vertical Dynamic Forces, *The Railway Engineering Journal, Jan 2-16.*

- Jenks, C.W. (2006). Design of Track Transitions. *Research Results Digest 79, Transit Cooperative Research Program, Transportation Research Board, October 2006*
- Jiang, H., Bian, X., Chen, Y., & Han, J. (2015). Impact of water level rise on the behaviors of railway track structure and substructure: Full-scale experimental investigation. *Transportation Research Record: Journal of the Transportation Research Board*, (2476), 15-22.
- Kaynia, A. M., Madshus, C., & Zackrisson, P. (2000). Ground vibration from high-speed trains: Prediction and countermeasure. *Journal of Geotechnical and Geoenvironmental Engineering*, 126(6), 531-537.
- Kennedy, J. (2011). *A FULL-SCALE LABORATORY INVESTIGATION INTO RAILWAY TRACK SUBSTRUCTURE PERFORMANCE AND BALLAST REINFORCEMENT. Thesis for the Degree of Doctor of Philosophy, Heriot-Watt University, UK.*
- Kerr, A., and Moroney, B. E. (1993). Track transition problems and remedies. *Proceedings of American Railway Engineering*, 94: 267-298.
- Kerr, A. D., (2000). On the determination of the rail support modulus k. *International Journal of Solids and Structures*, Vol. 37, 4335-4351
- Kerr, A.D. (2002). The Determination of the track modulus k for the standard track analysis. *AREMA Annual Conference, 2002.*
- Khoury, N. N., and Zaman, M. M. (2004). Correlation between resilient modulus, moisture variation, soil suction for subgrade soils. *Transportation Research Record. 1874, Transportation Research Board, Washington, D.C.*

- Koffman, J.L., Fairweather, D.M.S. (1975). Some Problems OF Railway Operation at High Axleloads, *Rail Engineering Inter-national*, Vol. 5, 156-160.
- Kramer, S.L. (1996). *Geotechnical earthquake engineering* Prentice Hall
- Krylov, V. V. (1994). On the theory of railway-induced ground vibrations. *Journal De Physique IV*, 4(5), C5.
- Leal-Vaca, J. C., Gallegos-Fonseca, G., & Rojas-González, E. (2012). The decrease of the strength of unsaturated silty sand. *Ingeniería Investigación y Tecnología*, 13(4), 393-402.
- Lechner, B. (2001). Railway concrete Pavements. *2nd International Conference on Best Practices for Concrete Pavements Florianopolis, November 2011*.
- Lefeuvre-Mesgouez, G., & Mesgouez, A. (2008). Ground vibration due to a high-speed moving harmonic rectangular load on a poroviscoelastic half-space. *International Journal of Solids and Structures*, 45(11), 3353-3374.
- Lei, X., and Mao, L. (2004). Dynamic response analyses of vehicle and track coupled system on track transition of conventional high speed railway. *Journal of Sound and Vibration*, Vol. 271, Elsevier, Academic Press, pp. 1133-1146.
- Leong, E.C., Tripathy, S., & Rahardjo H. (2003). Total suction measurement of unsaturated soils with a device using the chilled-mirror dew point technique. *Géotechnique*, 53, 2: 173-182.
- Li, D., & Selig, E.T. (1995). Evaluation of Railway Subgrade Problems. *Transportation Research Record 1489*

- Li, D., and Selig, E. T. (1998a). Method for railroad track foundation design. I: development. *Journal of Geotechnical and Geoenvironmental Engineering, ASCE 124(4): 316-322.*
- Li, D., and Selig, E. T. (1998b). Method for railroad track foundation design. II: applications. *Journal of Geotechnical and Geoenvironmental Engineering, ASCE, 124(4): 323-332.*
- Li, D., Smith, L., Doe, B., Otter, D., & Uppal, S. (2003). Study of bridge approach and track transition degradation—Factors and mitigation, *Federal Railroad Administration Contract DTFR53-01-H-00305, Washington, D.C.*
- Li, D., Thompson, R., Marquez, P. and Kalay, S. (2004a). Development and Implementation of a Continuous Vertical Track-Support Testing Technique. *Transportation Research Record: Journal of the Transportation Research Board, Issue No. 1863, Transportation Research Board of the National Academies.*
- Li, D., Thompson, R. and Kalay, S. (2004b). Update of TTCI's Research in Track Condition Testing and Inspection. *Proceedings of AREMA 2004 Annual Conference, Nashville, TN, Sept. 19-22, 2004.*
- Li, D., & Davis, D. (2005). Transition of railroad bridge approaches. *Journal of Geotechnical and Geoenvironmental Engineering, 131(11), 1392-1398.*
- Li, D., Hyslip, J., & Chrismer, S. (2016). *Railway Geotechnics. CRC press, Taylor & Francis Group.*
- Lichtberger, B. (2005). *Track compendium, First edition. Eurail Press.*

- Li, YH., Gao, YJ., Ma, HJ., & Yang, YH. (2012). Experimental study of track frost heave in speed-up section of Lanzhou-Xinjiang railway. *Journal of Lanzhou Jiaotong University*. 31(1), 38-42.
- Long, J., Olson, S., Stark, T., & Samara, E. (1998). Differential movement at embankment-bridge structure interface in illinois. *Transportation Research Record: Journal of the Transportation Research Board*, (1633), 53-60.
- Lr, D., & Selig, E. (1995). Evaluation of railway subgrade problems. *Transportation Research Record*, 1489, 17.
- Lu, N., & Likos, W.J. (2004). *Unsaturated Soil Mechanics*. Hoboken, NJ: John Wiley & Sons.
- Lu, S., Hogan, C., Minert, B., Arnold, R., Farritor, S., GeMeiner, W. and Clark, W. (2007). Exception Criteria in Vertical Track Deflection Modulus. *Proceedings of ASME/IEEE Joint Rail Conference & Internal Combustion Engine Spring Technical Conference, Pueblo, CO*.
- Madshus, C. & Kaynia, A.M. (1998). High Speed Railway Lines on Soft Ground: Dynamic Behaviour at Critical Train Speed, *Paper at the 6th International Workshop on Railway Noise, November 1998, France*.
- Madshus, C., & Kaynia, A. (2000). High-speed trains on soft ground: dynamic behavior at critical speed. *Journal of Sounds and Vibration*, 231(3), 689-701.
doi:10.1006/jsvi.1999.2647
- Madshus, C., & Kaynia, A. (2001). 11. High-speed trains on soft ground: Track-embankment-soil response and vibration generation. *Chapter 11 in book: Noise*

and Vibration from High-Speed Trains, Thomas Telford Ltd., Krylov, V.V. (ED.),
315.

Madshus, C., Lacasse, S., Kaynia, A., & Harvik, L. (2004). *Geodynamic Challenges in HSR Projects, ASCE Proc Geotechnical Engineering for Transportation Projects (GSP 126)*

MADSHUS, C., & KEYNIA, A. M. (2000). high_speed railway line on soft ground: dynamic behavior at critical train speed. *Journal of Sounds and Vibration*, 231(3), 689-701. doi:10.1006/jsvi.1999.2647

MANUAL, K. U. (2007). LS-DYNA keyword User's manual.

Manual, L. K. U. *Version 971, Vol.1-2*

Mancuso, C., Vassallo, R., and d'Onofrio, A. (2002). Small strain behavior of a silty sand in controlled-suction resonant column-torsional shear tests. *Can. Geotech. J.*, 39(1), 22-31.

McVey, B., Norman, C., Wood, N., Farritor, S., Arnold, R., Fateh, M., & El-Sibaie, M. (2005). Track Modulus Measurement From A Moving Railcar. *Proceedings of the AREMA Annual Conference, Chicago, IL, September 25-27, 2005.*

Michas, G. (2012). *Slab Track Systems for High-Speed Railways, Thesis for the Master of Science, Royal Institute of Technology.*

Miller, G. F. G., Pursey, H., 1954. On the partition of energy between elastic waves in a semi-infinite solid. *Proceedings of the Royal Society, London, UK, Vol.2333, 55-69.*

Namura, A. and Suzuki, T. (2007). Evaluation of Countermeasures against Differential Settlement at Track Transitions. *Quarterly Report of RTRI, Vol. 48, No. 3, pp. 176182.*

National Geographics (2017). Retrieved from
<http://www.nydailynews.com/news/week-breathtaking-photos-gallery-1.12623?pmSlide=1.12717>

Network Rail. (2005). Company Code of Practice, Formation treatments
NR/SB/TRK/9039, Network Rail, London, UK.

Ng, C. W. W., Zhou, C., Yuan, Q., & Xu, J. (2013). Resilient modulus of unsaturated subgrade soil: Experimental and theoretical investigations. *Canadian Geotechnical Journal, 50(2), 223-232.*

Nicks, J. E. (2009). *The Bump at the End of the Railway Bridge, Thesis for the Degree of Doctor of Philosophy, Texas A&M University, USA.*

Nigel, O. & Franz, Q. (2001). Innovative Track Systems Criteria for their Selection.
Project funded by the European Community, Directorate General Energy and Transport Under the 'Competitive and Sustainable Growth' Programme. ProMain. TÜV Intertraffic, Cologne. Oct. 2001.

Norman, C., Farritor, S., Arnold, R. and Elias, S.E.G. (2003). Preliminary Design of a System to Measure Track Modulus from A Moving Railcar. *Railway Engineering 2003.*

Norman, C., Farritor, S., Arnold, R., Elias, S.E.G., Fateh, M. and El-Sibaie, M. (2004).

Design of a system to measure track modulus from a moving railcar. *Proceedings of the 2004 AREMA National Conference*

ORE (1965) Stresses in Rails, Question 017, *Stresses in the Rails, the Ballast and the Formation Resulting from Traffic Loads, Report D71/RPI/E, Utrecht.*

Penny, C. (2009). Higher Speeds on Existing Networks at an affordable cost – A new Embedded Rail System. *Balfour Beatty Rail Technologies. India.*

Phan, TH., Cushman, M., White, D.J., Jahren, C., Schaefer, V., & Sharma, R. (2008).

Case Study of Seasonal Variation in the Subgrade and Subbase Layers of Highway US 20. IHRB Project TR-516, Iowa Department of Transportation.

Plotkin, D., Davis, D.D., Gurule, S. and Chrismer, S.M. (2006). Track Transitions and the Effects of Track Stiffness. *Proceedings of the AREMA 2006 Annual Conference, Louisville, KY, USA, Sept. 18-20.*

Popp, K., Kruse, H., and Kaiser, I. (1999). *Vehicle-track dynamics in the mid-frequency range Vehicle System Dynamics, 31: 423-464.*

Prajapati, G. (2017). Retrieved from

<https://www.slideshare.net/GhanshyamPrajapati3/railway-track-construction-drainage-maintenance>

Railway Gazette. (1970) Dynamics of Railway Track Systems and Their Economic Consequences, *Vol. 126, No. 1, 19-24.*

Rail Geosynthetics Applications. (2017) TERRAM. Retrieved from

<http://www.terram.com/market-sector/railways/?aaopen=ballast-over-weak-subgrades>

- Read, D., Chrismer, S., Ebersohn, W. and Selig, E. (1994). Track Modulus Measurements at the Pueblo Soft Subgrade Site. *Transportation Research Record 1470*, pp. 55-64.
- Reddy, M.A., Reddy, K.S., & Pandey, B.B. (2004). *Highway Research Bulletin. Bulletin No 73*.
- Rehfeld, E. (1994). Untergrundbeschaffenheit. *Eisenbahningenieur* 46, Nr.4, April 1995 (*Vortrag anlässlich der Fachtagung des VDEI "Bau von Hochleistungsstrecken" am 14 Oktober 1994 in Berlin*): pages 258-264.
- Remennikov, A.M. & Kaewunruen, S. (2007). A review of loading conditions for railway track structures due to train and track vertical interaction. *Journal of Structural Control and Health Monitoring, Vol. 15*, 207–234.
- Ribeiro, C.A., Calçada, R. and Delgado, R. (2008). Dynamic analysis of transition zones of high speed railway lines. *Proceedings of Noise and Vibration on High Speed Railways, Porto, Portugal*.
- Rossetti, M. A. (2007). Analysis of weather events on US railroads. Paper presented at the *23rd Conference on IIPS*.
- Round, D. J. (1993). Non – ballasted tracks. Track Technology Course, *British Rail Research. UK*.
- Salem, H.M. (2005). Effect Of Seasonal Moisture Variation On Subgrade Resilient Modulus. *FHWA-RD-03-049*.
- Salour, F. (2015). *Moisture Influence on Structural Behaviour of Pavements. Thesis for the Degree of Doctor of Philosophy, Royal Institute of Technology (KTH), Stockholm*.

- Sanchez, M. Wang, D. Briaud, J.L., & Douglas, C. (2014). Typical geomechanical problems associated with railroads on shrink-swell soils. *Transportation Geotechnics. Vol. 1, 257-274*
- Sasaoka, C.D. and Davis, D.D. (2005). Implementing Track Transition Solutions for Heavy Axle Load Service. *Proceedings of the AREMA 2005 Annual Conference, Chicago, Illinois.*
- Sasaoka, C.D. (2006). Track transition designs for heavy-axle-load service. *Railway Track & Structures, TTCI R&D, April 2006.*
- Sawanguriya, A., Edil, T. B., and Bosscher, P. J. (2005). Stiffness behavior of an unsaturated pavement subgrade soil. *Proc., of Int. Conf. on Problematic Soils, Eastern Mediterranean University Press, Famagusta, N. Cyprus, 209–217.*
- Sawanguriya, A., Edil, T. B., & Bosscher, P. J. (2009). Modulus-suction-moisture relationship for compacted soils in postcompaction state. *Journal of Geotechnical and Geoenvironmental Engineering, 135(10), 1390-1403.*
- Saxena, SK. & Hsu, TS. (1986). Permeability of geotextile-included railroad bed under repeated load. *Geotextile Geomember. Vol4, 31-51.*
- Schooleman, R. (1996). Overgang kunstwerk-aardebaan voor de hoge-snelheidslijn (In dutch), *Report 7-96-110-10, Technical University of Delft, Netherland.*
- Selig, E.T. & Li, D. (1994). Track Modulus: Its meaning and Factors Influencing It. *Transportation Research Record 1470, National Academy Press, Washington, D.C., pp. 47-54.*
- Selig, E.T., Waters, J.M. (1994). Track Geotechnology and Substructure Management. *Thomas Telford, London.*

- Seo, J. B. (2005). *The Bump at the End of the Bridge: An Investigation, Thesis for the Degree of Doctor of Philosophy, Texas A&M University, USA.*
- Seo, J., Ha, H., & Briaud, J. (2002). Investigation of Settlement at Bridge Approach Slab Expansion Joint: Numerical Simulations and Model Tests, *Report 0-4142-2, Texas Transportation Institute, College Station.*
- Sheng, X., Jones, C. J. C., & Petyt, M. (1999). Ground vibration generated by a load moving along a railway track. *Journal of Sound and Vibration*, 228(1), 129-156.
doi:<http://dx.doi.org/10.1006/jsvi.1999.2406>
- Shenton, M. J. (1985). Ballast deformation and track deterioration. *Proceedings of the Conference on Track Technology, University of Nottingham, pp. 253-265.*
- Smekal, A. & Brggren, E. (2002). Mitigation of track vibration at Ledsgard, Sweden. Field measurement before and after soil improvement. *Proceeding Eurodynamic, 2002.*
- Sonderman, W. & Toth, P.S. (2000). State-of-the-Art of Jet Grouting shown on Different Applications. *Proceeding of 4th International Conference on Ground Improvement Geosystems, Helsinki, 181-194.*
- Stark, T., Olson, S., & Long, J. (1995). Differential movement at the embankment/structure interface-mitigation and rehabilitation. *Final Report, Report no.IAB-H1 FY93, Illinois Transportation Research Center, Illinois DOT, Springfield, Illinois*
- Steenbergen, M. (2006). Modelling of wheels and rail discontinuities in dynamic wheel-rail contact analysis *Vehicle System Dynamics*, 44(10): 763-787.

- Steenbergen, M.J.M.M., Metrikine, A.V., & Esveld, C. (2007). Assessment of design parameters of a slab track railway system from a dynamic viewpoint. *Journal of Sound and Vibration, Vol.306, Pages 361-371*
- Steffens, D.M. (2005). *IDENTIFICATION AND DEVELOPMENT OF A MODEL OF RAILWAY TRACK DYNAMIC BEHAVIOR. Thesis for the degree of Master of Engineering, Queensland University of Technology.*
- Stewart, H.E. & Selig, E.T. (1982). Predicted and Measured Resilient Response of Track. *Journal of the Geotechnical Engineering Division, ASCE, Vol. 108, No. GT11, Nov. 1982.*
- Stewart, H.E. (1985). Measurement and Prediction of Vertical Track Modulus. *Transportation Research Record 1022.*
- Suiker, A. S. J., and Esveld, C. (1997). Stiffness transition subjected to instantaneous moving load passages, *Proceedings, 6th International Heavy Haul Conference, South Africa pp. 1194-1205.*
- Sun, Y. Q., and Dhanasekar, M. (2002). A dynamic model for the vertical interaction of the rail track and wagon system. *International Journal of Solids and Structures 39: 1337-1359.*
- Sunaga, M. & Sekine, E, & Ito, T. (1990). Vibration Behaviours of Roadbed on Soft Grounds under Train Load. *Quar. Rep. of the Railway Technical Research Institute, Vol. 31, No. 1, February 1990: pages 29-35. Japan*
- Sunaga, M. (2001). True-to scale in situ tests determining dynamic performance of earthworks under high speed train loading. *GEOTECHNICS FOR ROADS, RAIL*

TRACKS AND EARTH STRUCTURES, edited by Correia, A.G. & Brandle, H.,
A.A. BALKEMA PUBLICATION, Tokyo. Pages: 203-212.

Tafti, S.R., Briaud, J.L., & Fry, G. (2017). High-Speed Trains and Ground Mach 1:
Numerical Simulation. *Geotechnical Frontiers 2017, March 12-15, Orlando,
Florida.*

Takagi, R. (2005). High-speed railway: The last 10 years. *Japan Railway and Transport
Review, 40*, 4-7.

Talbot, A.N. (1918). Stresses in Railroad Track, *Report of the Special Committee to
Report on Stresses in Railroad Track; First Progress Report, AREA Proceedings,
Vol. 19, 873-1062.*

Talbot, A.N. (1920). Stresses in Railroad Track, *Report of the Special Committee to
Report on Stresses in Railroad Track; Second Progress Report', AREA
Proceedings, Vol. 21, 645- 814.*

Terashi, M. (1997). Deep-Mixing Method-Brief State-of-the-Art. *Proceeding of 14th
International Conference on Soil Mechanics and Foundation Engineering,
Hamburg, 4, 2475-2479*

Thompson, R., Marquez, D., & Li, D. (2001). Track Strength Testing using TTCI's
Track Loading Vehicle, *Railway Track & Structures.*

Thompson, R. and Li, D. (2002). Automated Vertical Track Strength Testing Using
TTCI's Track Loading Vehicle. *Technology Digest.*

Timoshenko, S., and Langer, B. F. (1926). Method of analysis of statical and dynamical
stresses in rail, *Proceedings of 2nd International Congress for Applied
Mechanics, Zürich, Switzerland*

- Towhata, I. (2008). *Geotechnical Earthquake Engineering Springer Science & Business Media*.
- Track Drainage. (2017). CE2303 Railway Engineering. Retrieved from <http://player.slideplayer.com/35/10334372/#>
- Tuller, M. & Or, D. (2003). RETENTION OF WATER IN SOIL AND THE SOIL WATER CHARACTERISTIC CURVE. *Soil Water Characteristic*.
- US HSR network phasing plan (2017). USHSR. Retrieved from <http://ushsr.com/ushsrmap.html>
- US HSR network phasing plan (2017). USHSR. Retrieved from <http://www.ushsr.com>
- Wahls, H. E. (1990). Design and construction of bridge approaches. *NCHRP, Synthesis of Highway Practice 159*, Transportation Research Board, D.C.
- Wang, P., Wang, L., Chen, R., Xu, J., & Gao, M. (2016). Overview and outlook on railway track stiffness measurement. *Journal of Modern Transportation*, 24(2), 89-102
- Wangqing, W., Geming, Z., Kaiming, Z., & Lin, L. (1997). Development of Inspection Car for Measuring Railway Track Elasticity. *Proceedings from 6th International Heavy Haul Conference, Cape Town*.
- Weber, R.C., Gehling, W.Y.Y., & Nunez, W.P. (2014). Effect of wetting and drying path on the resilient modulus of compacted soil. *Unsaturated Soils: Research & Applications – Khalili, Russell & Khoshghalb (Eds) © 2014 Taylor & Francis Group, London*.

- WJRC (West Japan Railway Company) (2002a). Construction and maintenance standards for commuter and local railway track, Osaka, Japan.
- WJRC (West Japan Railway Company). (2002b). Construction and maintenance standards for Shinkansen track. West Japan Railway Company, Osaka, Japan.
- Woldright, B. & New, B.M. (1999). Embankment design for high speed trains on soft Grounds. *Proc XIIth ECSMGE, Amsterdam, Balkema*
- Woodward, P., El Kacimi, A., LAGHROUCHE, O., MEDERO, G., & BANIMAHD, M. (2012). Application of polyurethane geocomposites to help maintain track geometry for high-speed ballasted railway tracks. *Journal of Zhejiang University-Science (Applied Physics & Engineering)*, 13(1),836-849.
- Woodward, P., Laghrouche, O., & El-Kacimi, A. (2013). The development and mitigation of ground mach cones for HSRs. Paper presented at the *ICOVP 2013- International Conference on Vibration Problems*.
- Xiang Liu, M Rapik Saat, Christopher PL Barkan. (2012/12/1). Analysis of causes of major train derailment and their effect on accident rates.2289, 154-163.
- Xiaohong, L., Guolin, Y., & Liangliang, W. (2011). Dynamic response testing and analysis on red-clay cutting bed under ballastless track of high-speed railway. *Geotechnical Investigation and Surveying*, 39(8), 12-18.
- Zarembski, A.M. and Choros, J. (1980). On the measurement and calculation of vertical track modulus. *Proceedings American Railway Engineering Association, Vol. 81, pp. 156-173*.
- Zarembski, A.M. (1989d). Track Stiffness and Impact. *Research Paper, Railway Tie Association, pp. 61-62*.

Zhai, W. M., and True, H. (1999). Vehicle-track dynamics on a ramp and on the bridge: simulation and measurements. *Vehicle System Dynamics, Supplement 33*: 604-615

Zhai, W., Wang, Q., Lu, Z., & Wu, X. (2001). Dynamic effects of vehicles on tracks in the case of raising train speeds. *Proceedings of the Institution of Mechanical Engineers, Part F: Journal of Rail and Rapid Transit*, 215(2), 125-135.